

# Robust optical transmission systems : modulation and equalization

**Citation for published version (APA):**

Borne, van den, D. (2008). *Robust optical transmission systems : modulation and equalization*. [Phd Thesis 1 (Research TU/e / Graduation TU/e), Electrical Engineering]. Technische Universiteit Eindhoven.  
<https://doi.org/10.6100/IR633535>

**DOI:**

[10.6100/IR633535](https://doi.org/10.6100/IR633535)

**Document status and date:**

Published: 01/01/2008

**Document Version:**

Publisher's PDF, also known as Version of Record (includes final page, issue and volume numbers)

**Please check the document version of this publication:**

- A submitted manuscript is the version of the article upon submission and before peer-review. There can be important differences between the submitted version and the official published version of record. People interested in the research are advised to contact the author for the final version of the publication, or visit the DOI to the publisher's website.
- The final author version and the galley proof are versions of the publication after peer review.
- The final published version features the final layout of the paper including the volume, issue and page numbers.

[Link to publication](#)

**General rights**

Copyright and moral rights for the publications made accessible in the public portal are retained by the authors and/or other copyright owners and it is a condition of accessing publications that users recognise and abide by the legal requirements associated with these rights.

- Users may download and print one copy of any publication from the public portal for the purpose of private study or research.
- You may not further distribute the material or use it for any profit-making activity or commercial gain
- You may freely distribute the URL identifying the publication in the public portal.

If the publication is distributed under the terms of Article 25fa of the Dutch Copyright Act, indicated by the "Taverne" license above, please follow below link for the End User Agreement:

[www.tue.nl/taverne](http://www.tue.nl/taverne)

**Take down policy**

If you believe that this document breaches copyright please contact us at:

[openaccess@tue.nl](mailto:openaccess@tue.nl)

providing details and we will investigate your claim.

# **Robust Optical Transmission Systems**

---

*Modulation and Equalization*

Dirk van den Borne

# Robust Optical Transmission Systems

Modulation and Equalization

PROEFSCHRIFT

ter verkrijging van de graad van doctor aan de  
Technische Universiteit Eindhoven, op gezag van de  
Rector Magnificus, prof.dr.ir. C.J. van Duijn, voor een  
commissie aangewezen door het College voor  
Promoties in het openbaar te verdedigen  
op woensdag 19 maart 2008 om 16.00 uur

door

Dirk van den Borne

geboren te Bladel en Netersel

Dit proefschrift is goedgekeurd door de promotoren:

prof.ir. G.D. Khoe

en

prof.ir. A.M.J. Koonen

Copromotor:

dr.ir. H. de Waardt

CIP-DATA LIBRARY TECHNISCHE UNIVERSITEIT EINDHOVEN

Borne, Dirk van den

Robust optical transmission systems : modulation and equalization / by Dirk van den Borne. -  
Eindhoven : Technische Universiteit Eindhoven, 2008.

Proefschrift. - ISBN 978-90-386-1794-7

NUR 959

Trefw.: optische telecommunicatie / modulatie / signaalverwerking / optische polarisatie.

Subject headings: optical fibre communication / electro-optical modulation / signal processing /  
optical fibre polarisation.

Copyright © 2008 by Dirk van den Borne

All rights reserved. No part of this publication may be reproduced, stored in a retrieval system,  
or transmitted in any form or by any means without the prior written consent of the author.

Typeset using L<sup>A</sup>T<sub>E</sub>X, printed in The Netherlands



*"The only constant in technology is change."*

---

Samenstelling van de promotiecommissie:

prof.dr.ir. A.C.P.M Backx, Technische Universiteit Eindhoven, voorzitter  
prof.ir. G.D. Khoe, Technische Universiteit Eindhoven, eerste promotor  
prof.ir. A.M.J. Koonen, Technische Universiteit Eindhoven, tweede promotor  
dr.ir. H. de Waardt, Technische Universiteit Eindhoven, copromotor  
prof.dr.tech. P. Jeppesen, Danmarks Tekniske Universitet  
prof.dr.-ing. P.M. Krummrich, Technische Universität Dortmund  
dr. R.I. Killey, University College London  
dr. J.J.G.M. van der Tol, Technische Universiteit Eindhoven

The work leading to this thesis was part of a cooperation between Nokia Siemens Networks (previously Siemens Communications) in Munich, Germany and the Electro-Optical Communications group, department of Electrical Engineering of the Eindhoven University of Technology, The Netherlands.

The studies presented in this thesis were performed within the long-haul optical transmission R&D department of Nokia Siemens Networks.



---

# Summary

## Robust optical transmission systems Modulation and Equalization

Since the introduction of the first optical transmission systems, capacities have steadily increased and the cost per transmitted bit has gradually decreased. The core of the global telecommunication network consists today of wavelength division multiplexed (WDM) optical transmission systems. WDM is for these systems the technology of choice as it allows for a high spectral efficiency, i.e. the transmitted capacity per unit bandwidth. Commercial WDM systems generally use up to 80 wavelength channels with a 50-GHz channel spacing and a bit rate of 10-Gb/s or sometimes 40-Gb/s per wavelength channel. This translates into a spectral efficiency between 0.2 and 0.8-b/s/Hz. However, to cope with the forecasted increase in data traffic it will be necessary to develop next-generation transmission systems with even higher capacities. These transmission systems are expected to have a 40-Gb/s or 100-Gb/s bit rate per wavelength channel, with a spectral efficiency of between 0.8 and 2.0-b/s/Hz. At the same time, such systems should be robust, i.e. provide a tolerance towards transmission impairments similar to currently deployed systems.

Traditionally, optical transmission systems have used amplitude modulation. However, for the next generation of transmission systems this is not a suitable choice. They normally require a too large channel spacing, have a high optical-signal-to-noise ratio (OSNR) requirement and generate significant nonlinear impairments. Current state-of-the-art transmission systems therefore often use differential phase shift keying (DPSK). Compared to amplitude modulation, DPSK generates less nonlinear impairments and has a lower OSNR requirement. However, due to the high symbol rate (e.g. 40-Gbaud) the robustness against the most significant linear transmission impairments, i.e. chromatic dispersion and polarization-mode dispersion (PMD) is still small. Tunable optical dispersion compensators can be used to improve the chromatic dispersion tolerance and PMD impairments are generally avoided through fiber selection. But optical compensation and fiber selection are generally not suitable for cost-sensitive applications.

The first part of this thesis focuses on modulation formats that can further increase the capacity and robustness of long-haul WDM transmission links. In particular 40-Gb/s differential

---

quadrature phase shift keying (DQPSK) modulation is discussed extensively in this thesis. As a quaternary modulation format, it modulates 2 bits per symbol and therefore requires only a 20-Gbaud symbol rate. The lower symbol rate improves the tolerance towards both chromatic dispersion and PMD. As well, the narrow optical spectrum allows for a high spectral efficiency. On the other hand, DQPSK also requires a more complex transmitter and receiver structure, has a higher OSNR requirement and reduces the nonlinear tolerance. We further verify the feasibility of long-haul 40-Gb/s DQPSK transmission and show that a transmission reach of 2,800-km is viable with a 0.8-b/s/Hz spectral efficiency. In order to realize ultra long-haul transmission we combine DQPSK modulation with optical phase conjugation, which improves the nonlinear tolerance and enables a 4,500-km transmission distance. In addition, we discuss the combination of 40-Gb/s DQPSK modulation with different chromatic dispersion compensation technologies, such as lumped dispersion compensation and fiber-Bragg gratings.

The second part of this thesis discusses polarization-multiplexed (POLMUX) signaling. This is an attractive transmission format as it modulates independent data onto each of the two orthogonal polarizations of an optical fiber. This can double the spectral efficiency and halve the symbol rate in comparison to single-polarization modulation. To further increase the spectral efficiency, POLMUX signaling and DQPSK modulation can be combined to realize optical modulation with 4 bits per symbol. We discuss a transmission experiment with 80-Gb/s POLMUX-RZ-DQPSK and verify the feasibility of long-haul transmission (1,700 km) with a 1.6-b/s/Hz spectral efficiency. However, the interaction between PMD and other transmission impairments makes it challenging to realize transmission systems employing POLMUX signaling without the compensation of PMD-related impairments.

In the third part of this thesis we review electronic equalization techniques. This can be used to mitigate some of the drawbacks of DQPSK modulation and POLMUX signaling. For direct detection receivers, we show that multi-symbol phase estimation (MSPE) can be used to improve the OSNR requirement and nonlinear tolerance of D(Q)PSK modulation. In addition, Maximum likelihood sequence estimation (MLSE) can be used to increase the chromatic dispersion and PMD tolerance. Electronic equalization is particularly attractive when combined with coherent detection. In a coherent receiver, not only the amplitude of the optical signal, but the full base-band optical field is transferred to the electronic domain (amplitude, phase and state of polarization). This enables the equalization of nearly arbitrarily high amounts of chromatic dispersion and PMD, as well as electronic polarization de-multiplexing in the case of POLMUX signaling. We discuss the required system architecture for a digital coherent receiver and demonstrate its feasibility through a 100-Gb/s POLMUX-DQPSK transmission experiment over 2,375 km and with a 2.0-b/s/Hz spectral efficiency.

The work discussed in this thesis shows that multi-level modulation formats enable long-haul transmission systems with a bit rate of 40-Gb/s or 100-Gb/s per WDM channel and a 50-GHz channel spacing. Electronic equalization improves the transmission tolerances, simplifies system design and allows these formats to be used on the existing infrastructure of systems optimized for 10-Gb/s transmission.

---

# Contents

<b>1</b>	<b>Introduction</b>	<b>1</b>
1.1	The global telecommunication hierarchy . . . . .	1
1.2	Motivation . . . . .	3
1.3	Framework & objectives . . . . .	8
1.4	Outline of this thesis . . . . .	8
<b>2</b>	<b>The fiber-optic transmission channel</b>	<b>11</b>
2.1	Fiber attenuation . . . . .	12
2.2	Chromatic dispersion . . . . .	14
2.3	Polarization of light . . . . .	16
2.4	Nonlinear transmission impairments . . . . .	22
<b>3</b>	<b>Long-haul optical transmission systems</b>	<b>35</b>
3.1	Transmitter & receiver structure . . . . .	35
3.2	Fiber loss compensation . . . . .	41
3.3	Chromatic dispersion compensation . . . . .	48
3.4	PMD compensation . . . . .	57
3.5	Narrowband-optical filtering . . . . .	58
3.6	Optical phase conjugation . . . . .	59

## Contents

---

<b>4</b>	<b>Binary modulation formats</b>	<b>67</b>
4.1	On-off-keying . . . . .	67
4.2	Duobinary . . . . .	69
4.3	Differential phase shift keying . . . . .	74
4.4	Partial DPSK . . . . .	83
<b>5</b>	<b>Differential quadrature phase shift keying</b>	<b>87</b>
5.1	Transmitter & receiver structure . . . . .	88
5.2	Back-to-back OSNR requirement . . . . .	92
5.3	Transmitter & receiver properties . . . . .	93
5.4	Nonlinear tolerance . . . . .	99
5.5	Pseudo random quaternary sequences . . . . .	101
5.6	Summary & conclusions . . . . .	104
<b>6</b>	<b>Long-haul DQPSK transmission</b>	<b>105</b>
6.1	21.4-Gb/s RZ-DQPSK transmission . . . . .	106
6.2	42.8-Gb/s RZ-DQPSK transmission . . . . .	108
6.3	Lumped dispersion compensation . . . . .	111
6.4	Chirped-FBGs based dispersion compensation . . . . .	113
6.5	OPC-supported long-haul transmission . . . . .	121
6.6	Comparison of DQPSK transmission experiments . . . . .	126
6.7	Summary & conclusions . . . . .	128
<b>7</b>	<b>Polarization-multiplexing</b>	<b>131</b>
7.1	Principle of polarization-multiplexing . . . . .	132
7.2	Transmitter & receiver structure . . . . .	134
7.3	Transmitter & receiver properties . . . . .	137
7.4	Nonlinear tolerance . . . . .	145

7.5	Summary & conclusions . . . . .	155
<b>8</b>	<b>Polarization-multiplexed DQPSK</b>	<b>157</b>
8.1	Transmitter & receiver structure . . . . .	158
8.2	Long-haul transmission . . . . .	162
8.3	Transmission with a high spectral efficiency . . . . .	169
8.4	Summary & conclusions . . . . .	171
<b>9</b>	<b>Digital direct detection receivers</b>	<b>173</b>
9.1	Multi-symbol phase estimation . . . . .	175
9.2	Maximum likelihood sequence estimation . . . . .	184
9.3	Summary & conclusions . . . . .	201
<b>10</b>	<b>Digital coherent receivers</b>	<b>203</b>
10.1	Analog coherent receivers . . . . .	204
10.2	Digital coherent receivers . . . . .	207
10.3	Digital equalization algorithms . . . . .	210
10.4	Distortion compensation at 43-Gb/s . . . . .	218
10.5	Distortion compensation at 111-Gb/s . . . . .	224
10.6	Long-haul transmission . . . . .	228
10.7	Distortion compensation using baud-rate equalizers . . . . .	234
10.8	Summary & conclusions . . . . .	237
<b>11</b>	<b>Outlook &amp; recommendations</b>	<b>239</b>
11.1	Robust optical modulation formats . . . . .	239
11.2	Robust electronic equalization . . . . .	241
<b>A</b>	<b>List of symbols &amp; abbreviations</b>	<b>243</b>
A.1	List of symbols . . . . .	243

## Contents

---

A.2 List of abbreviations . . . . .	245
<b>B Definition of the Q-factor and eye opening penalty</b>	<b>249</b>
B.1 Q-factor . . . . .	250
B.2 Eye opening penalty . . . . .	251
<b>C Asymmetric 3 x 3 coupler for coherent detection</b>	<b>253</b>
<b>References</b>	<b>257</b>
<b>List of publications</b>	<b>281</b>
<b>Samenvatting</b>	<b>287</b>
<b>Acknowledgement</b>	<b>289</b>
<b>Curriculum Vitae</b>	<b>291</b>
<b>Index</b>	<b>293</b>



# Introduction

## 1.1 The global telecommunication hierarchy

Today's society has been shaped in all its aspects by the progress in telecommunication technology. Ever since the first developments that led to today's Internet and, later on, to the invention of the World Wide Web, data traffic has been increasing exponentially. This exponential bandwidth growth has spurred the development of new technologies, which in turn made it possible to offer services that relied on even higher bandwidth requirements. Today, Internet services such as Skype [1], YouTube [2] or Google earth [3] depend on a backbone of high-speed 'data pipes' so that they can be accessed by people around the world, anywhere, anytime.

Although many people are not aware of it, fiber-optic transmission plays a key role in global transport of telecommunications services. This is best described through the telecommunication network hierarchy. Figure 1.1 shows a simplified model of this network hierarchy, dividing it up into a long-haul core network, regional networks and 'last-mile' access networks. In addition, Table 1.1 depicts the typical distances covered by transmission links in such networks. The core of the global telecommunication network is used for transnational, transcontinental and transoceanic communication. A transmission link in this (ultra) long-haul core network therefore transports the largest amount of data over the longest distances (>1000 km). In the core network, transport technologies are required that enable a long *regenerator-free* transmission distance at the lowest cost. Fiber-optic transmission is ideally suited for this purpose as it allows for both high throughput and long transmission distance. Such systems are engineered to transmit a large capacity over a long-haul transmission distances, and the physical limits of optical fiber as a transmission medium has a significant impact on their design.

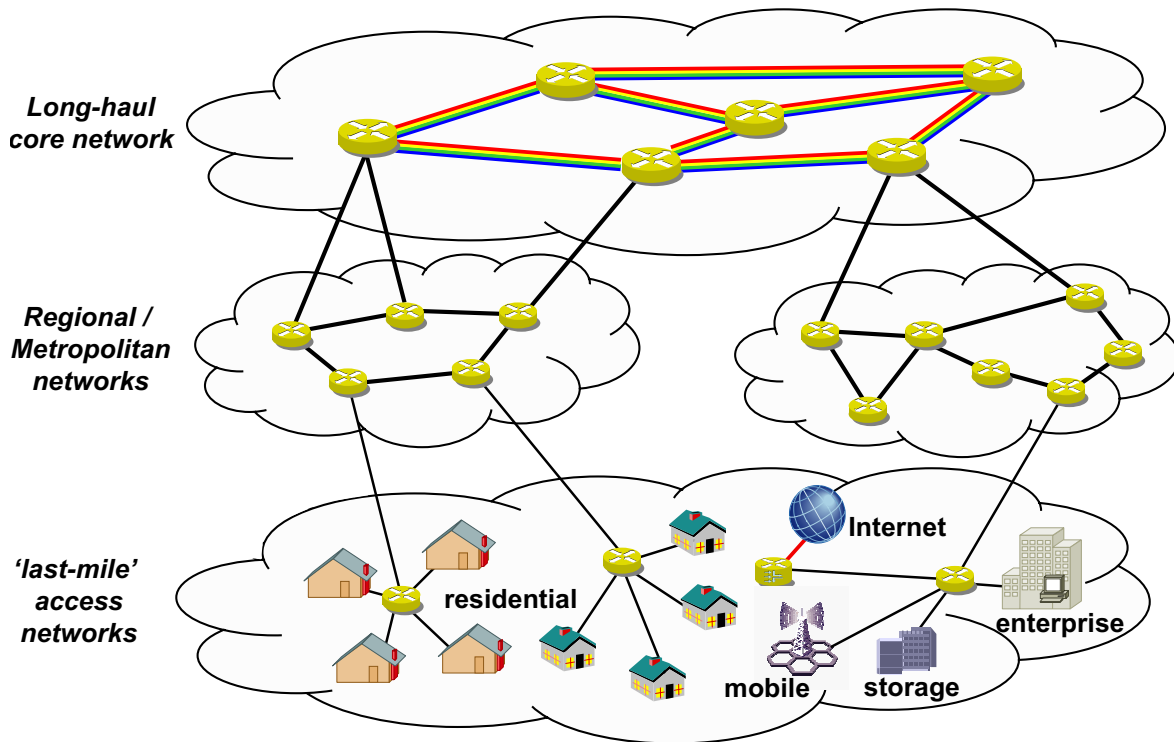


Figure 1.1: *Optical network hierarchy; Long-haul core network, regional/metropolitan and 'last-mile' access network.*

To exemplify the capacity increase in long-haul data transport we look more closely at the *Trans-Atlantic* Internet protocol (IP) traffic. This connection is one of the better documented transmission links in the core network, and serves therefore well as an example. Between 2004 and 2006 traffic has grown over 200%, from 0.5 Tb/s to 1.6 Tb/s [4]. This increase in required capacity is largely fueled by new internet video-on-demand services. When we extrapolate the current annual growth in data traffic over a 10 year period with a conservative 30% per year, we arrive at a figure of 22 Tb/s for the Trans-Atlantic IP traffic in 2016. When we take into consideration that the aggregated traffic is carried over multiple transmission links, each consisting of a number of fibers, the required capacity per fiber will still be in the range of 2 to 3 Tb/s. Considering the vast distances that have to be spanned for a Trans-oceanic link, this presents a significant engineering challenge.

Moving down in the telecommunication hierarchy, and interlinked to the core network, are smaller regional and metropolitan networks. Such networks provide data transport within a smaller geographical region, for example a metropolitan area (<300 km) or a small country (<1000 km). The amount of traffic carried on a typical metropolitan network is much smaller than on a link in the core network. However, the number of exchange points, i.e. the points where data originates from or is destined to, is much larger. Consequently, the challenge for such systems is predominantly the cost-effective realization of a complex network switching architecture. A metropolitan network connects again a number of access or 'last-mile' networks together. Such networks facilitate the connection of the end-user to the global telecommunication hierar-

chy. Many different kinds of end-user applications are possible, spanning from residential internet access to business and storage area networks. As a result, a large variety in access network technologies exists, each with their own requirements and specific end-users. Legacy last-mile networks are still largely based on copper networks, either co-axial or twisted pair. The preferred transmission format to increase bit rates over this infrastructure is digital subscriber line (DSL) technology. However, even with DSL technology the bandwidth of copper networks is limited, especially when the distance between the local exchange point and the end-user is longer than a few kilometers. Optical fibers has a significant advantage over copper networks due to its much higher bandwidth-distance product, which enables high-speed connections over longer distances. Fiber-optic solutions are therefore also gaining momentum in 'last-mile' networks, and 'fiber-to-the-home' or 'fiber-to-the-curb' technology is already deployed on a significant scale. As the infrastructure of an access network is generally not shared by a large number of customers, such networks are predominantly engineered to provide a lowest-cost solution [5]. An overview of fiber-based technologies for 'last-mile' access can be found in [6].

Table 1.1: CLASSIFICATION OF OPTICAL TRANSMISSION SYSTEMS, AFTER [7].

System	Distance (km)
Access	<100
Metro	<300
Regional	300 - 1,000
Long-haul	1,000 - 3,000
Ultra long-haul	>3,000

## 1.2 Motivation

The backbone of the global telecommunication hierarchy consists of long-haul *wavelength-division-multiplexed* (WDM) transmission links. A WDM transmission link transports large amount of data traffic by multiplexing a number of lower capacity wavelength channels onto a single fiber. The use of WDM therefore allows for a manifold increase in the capacity of long-haul optical transmission systems. Or, maybe even more importantly, it allows for a tremendous decrease in the cost of the transmitted bandwidth, i.e. the cost per transmitted bit. To cope with the expected bandwidth demand in the near future, new technologies have to be researched, developed and subsequently deployed in long-haul transmission systems.

The optical transmission links in the backbone of the telecommunication network can be classified, depending on their *regenerator-free* transmission distance, as shown in Table 1.1. We focus here in particular on terrestrial long-haul transmission systems. Figure 1.2 shows the typical layout of a long-haul optical transmission system and Figure 1.3 depicts an example of an optical spectrum for a high-capacity WDM system. In an optical transmitter (Tx), a data sequence is modulated onto an optical carrier, generated by a laser. The separate wavelength channels are then multiplexed together using a wavelength multiplexer, for example an arrayed waveguide

grating (AWG), which typically has a 100-GHz channel spacing. The density of the WDM channels can be further increased through channel interleaving with an optical interleaver (INT). This results in WDM systems with a 50-GHz channel spacing and a total number of 80 WDM channels that are multiplexed on a single optical fiber. Deployed transmission systems with 80 WDM channels are currently state-of-the-art, but in long-haul transmission experiments up to 200 channels are sometimes multiplexed onto a single fiber. Such transmission links rely nowadays on bit rates of 10-Gb/s and sometimes 40-Gb/s per wavelength channel to realize a 1 to 3-Tb/s aggregate capacity<sup>1</sup>. The bit rate and wavelength spacing of a transmission system is often expressed in terms of the spectral efficiency, which is the transmitted capacity per unit bandwidth. For currently deployed systems the spectral efficiency is between 0.2 and 0.8-b/s/Hz. Next-generation transmission links will use bit rates of 40-Gb/s or 100-Gb/s per wavelength channel, which results in a spectral efficiency between 0.8 and 2.0-b/s/Hz. The aggregate capacity of such systems would then increase to 3 to 8-Tb/s over a single fiber. At the receiver side of the transmission link, the WDM channels are de-multiplexed using a combination of de-interleaver and de-multiplexers. Each of the de-multiplexed channels is then fed into an optical receiver (Rx), which converts the signal back to the electrical domain. As most optical transmission systems are bi-directional (on separate fibers) the optical transmitter and receiver are usually combined in a single module, which is referred to as a *transponder*.

The transmission link itself consists of cascaded fiber spans with optical amplifiers in-between. The optical amplifiers amplify the weak input signal from the previous span and launch it again into the next span. This allows long-haul transmission while maintaining a sufficiently high optical signal-to-noise ratio (OSNR) at the output of the fiber link. At bit rates of 10-Gb/s, and in particular 40-Gb/s or 100-Gb/s, transmission impairments such as chromatic dispersion and polarization-mode dispersion (PMD) have to be precisely dealt with. And as such impairments accumulate in a long-haul optical transmission link, this can severely limit the feasible transmission distance. Some transmission impairments are deterministic and therefore straightforward to compensate with proper link design. For example, the accumulated chromatic dispersion is normally compensated using a dispersion compensation module (DCM) placed in-between two fiber spans. Other signal impairments are more difficult to compensate as they fluctuate over time, such as PMD. As not all transmission impairments can be compensated along the transmission link, the receiver should be able to recover the transmitted data sequence in their presence. The tolerance of a transmission system against isolated transmission impairments, such as chromatic dispersion or DGD, is often expressed in terms of the required OSNR margin<sup>2</sup>.

An important aspect of the optical transmission systems that we consider in this thesis is their *robustness*. When an optical transmission system is upgraded, e.g. from a 10-Gb/s to a 40-Gb/s

---

<sup>1</sup>The actual transmitted bit rate includes an overhead for forward error correction (FEC), which is typically 7%. The bit rate used in this thesis is therefore 10.7-Gb/s for 10-Gb/s transmission and 42.8-Gb/s for 40-Gb/s transmission. For 100-Gb/s transmission an additional 4% overhead is normally taken into account for 64B/66B coding, as required for Ethernet transport, which increases the bit rate to 111-Gb/s.

<sup>2</sup>The OSNR margin is dependent on the required bit-error-ratio (BER). In this thesis we used a BER of  $10^{-5}$  to quantify the required OSNR in the analytical simulation as this matches a transmission system that operates with a 3-dB margin with respect to the FEC limit. However, in the transmission experiments or simulations that use a Monte-Carlo approach, a BER of  $10^{-3}$  or  $10^{-4}$  is used to improve the accuracy of the estimation. This is discussed in more detail in Appendix B.

bit rate per wavelength channel, ideally, no modifications are made in the transmission link. This would require a 40-Gb/s transponder that has a similar tolerance to transmission impairments as the deployed 10-Gb/s transponders. However, this is not straightforward as the tolerance against most transmission impairments scales linearly or even quadratically with the symbol rate. To counter the lower transmission tolerances at a higher bit rate, either sophisticated modulation formats, optical compensation or electronic equalization can be used. In this thesis we define a 40-Gb/s or 100-Gb/s transmission format to be robust when its transmission tolerances are sufficiently high to allow deployment on links optimized for transmission with 10-Gb/s bit rate.

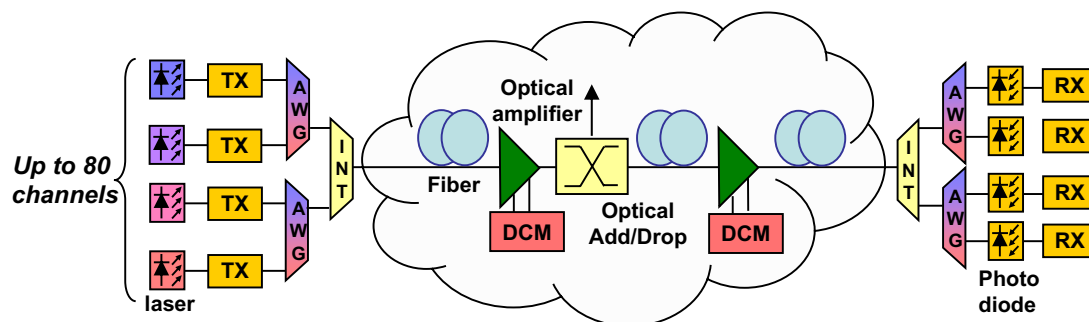


Figure 1.2: Typical layout of a WDM optical transmission link.

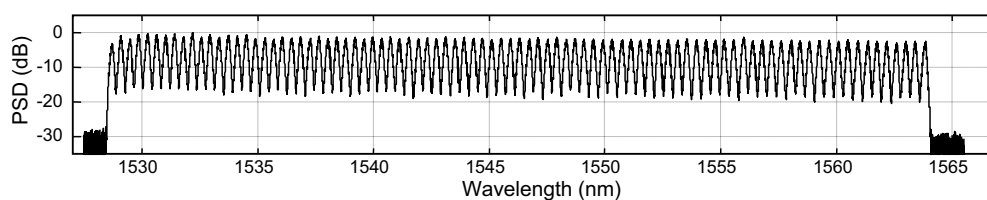


Figure 1.3: Measured WDM spectrum with 89 channels and a 85.6-Gb/s bit rate per channel.

A second important consideration for optical transmission systems, is that they are rapidly evolving from point-to-point *links* to meshed optical *networks*. This requires the flexibility to pass multiple optical add-drop multiplexer (OADM) nodes along the transmission link. At such OADM nodes traffic is routed to other links, thereby creating a meshed network. Today, most deployed long-haul transmission systems have a 50-GHz spacing between the WDM channels. At such a channel spacing, the width of the optical spectrum is not a significant concern for 10-Gb/s systems and WDM channels can be switched *transparently* through an optical network. However, when the symbol rate of the optical signal is doubled or quadrupled, the spectral width scales accordingly. Hence, when transmission systems that are designed for a 10-Gb/s bit rate are upgraded to a 40-Gb/s or 100-Gb/s bit rate per WDM channel, the spectral width of the optical signal can become a key concern [8, 9]. This requires optical modulation formats that are tolerant to the narrowband optical filtering that occurs when multiple OADMs are cascaded along a transmission link.

In this thesis we focus predominantly on two technologies that can enable more robust optical transmission. First of all, we discuss the use of robust multi-level optical modulation formats. Such modulation formats often have favorable transmission properties that can be used to either

increase the capacity of an optical transmission link or increase its robustness against transmission impairments. Secondly, we focus on electronic equalization that can be combined with robust modulation formats to further improve the performance of the transmission link.

### 1.2.1 Robust optical modulation formats

The modulation format defines the characteristics of the optical signal that is transmitted over the transmission link. Until recently, the optical modulation format of choice for nearly all optical transmission systems has been non-return-to-zero on-off keying (NRZ-OOK). NRZ-OOK combines a cost-effective transmitter and receiver structure with a transmission performance sufficient to realize long-haul 10-Gb/s transmission systems. This has largely prevented the use of more complex modulation formats and NRZ-OOK is still used nearly exclusively in deployed 10-Gb/s terrestrial long-haul transmission systems. Only recently the growing interest in more robust optical transmission technologies has opened up the possibility for commercial deployment of different modulation formats. This is particularly true for 40-Gb/s or 100-Gb/s bit rates, where the transmission tolerances of NRZ-OOK modulation are too small to realize robust long-haul transmission systems with a 50-GHz channel spacing.

In addition, for 40-Gb/s or 100-Gb/s bit rates the spectral efficiency is an important consideration. Binary modulation restricts the achievable spectral efficiency to 1-b/s/Hz [10]. And in practical systems, the realizable spectral efficiency is significantly lower than 1-b/s/Hz because WDM is considered to be transparent, i.e. crosstalk from neighboring channels is assumed to be unknown and hence treated as a noise source. And other system design aspects that further reduce the spectral efficiency have to be taken into account, such as the 7% overhead usually required for forward error correction (FEC), wavelength drift in the transmitter laser and (de-)multiplexing filters as well as the limited filter order of optical filters and interleavers. Combined, the required margins restrict the feasible spectral efficiency to approximately  $<0.7$ -b/s/Hz when using NRZ-OOK modulation. Currently deployed 40-Gb/s transmission systems use modulation formats that are more robust against transmission impairments than NRZ-OOK. This includes duobinary, which can be used to improve the tolerance against chromatic dispersion and narrowband optical filtering. But in particular phase modulation, using differential phase shift keying (DPSK), is currently the most widely used state-of-the-art modulation format. Modulation formats such as duobinary or DPSK are more tolerant to narrowband optical filtering and allow a spectral efficiency of up to 0.8-b/s/Hz.

Multi-level modulation with 2 bits per symbol, such as return-to-zero differential quadrature phase shift keying (RZ-DQPSK) modulation, can increase this to  $\sim 1.6$ -b/s/Hz. In addition it is more tolerant to many linear transmission impairments as well as narrowband optical filtering. Another potential candidate to reduce the symbol rate is polarization multiplexing (POLMUX). This doubles the number of bits per symbol by transmitting independent information in each of the two orthogonal polarizations of an optical fiber. Combined with DQPSK modulation, POLMUX signaling enables modulation with 4 bits per symbol.

Multi-level modulation is particularly beneficial for 100-Gb/s transmission. Although 100-Gb/s NRZ-OOK has been demonstrated using ultra-high frequency electronics [11, 12] the use of such a modulation format would pose considerable challenges in deployed transmission systems due its high OSNR requirement and low chromatic dispersion and PMD tolerance. DQPSK is therefore a more likely candidate for long-haul 100-Gb/s transmission and a number of long-haul transmission experiments have demonstrated its feasibility [13, 14, 15]. For 100-Gb/s modulation the main advantage of DQPSK is that it reduces the bandwidth requirement of the electrical components in the transponder as it operates at a 50-Gbaud symbol rate. Taking this approach a step further, POLMUX-RZ-DQPSK modulation enables 100-Gb/s transmission with only a  $\sim 25$ -Gbaud symbol rate. This increases the tolerance to chromatic dispersion and PMD and will enable next-generation optical transmission systems with a spectral efficiency of 2.0-b/s/Hz.

This thesis focuses on multi-level modulation formats that can enable robust 40-Gb/s and 100-Gb/s modulation per wavelength channel. In particular, we look more closely at the potential impact of DQPSK modulation and POLMUX signaling in long-haul transmission systems.

### 1.2.2 Robust electronic equalization

Digital signal processing speeds have increased exponentially over the years [16] and have now started to catch up with bit rates common in optical transmission systems. In particular, high-speed analog-to-digital converters (ADC) have become available to convert the analog signal in an optical receiver to the digital domain for subsequent digital signal processing. Current state-of-the-art ADCs in commercial products have a sample rate of  $\sim 25$ -Gbaud [17, 18] and sample rates up to  $\sim 50$ -Gbaud have shown to be feasible in research and development as well as measurement equipment.

The conversion of the optical signal to the digital domains enables the use of powerful digital signal processing algorithms. Digital signal processing increases the robustness of the transponder and can help to simplify transmission link design. It reduces the need for precise optical compensation of chromatic dispersion and it negates the need for fiber selection to reduce the PMD on an optical transmission link [19, 20]. Digital signal processing can further be used to lower the required OSNR through the use of improved decision variables as well as an increase in nonlinear tolerance. The combination of multi-level modulation formats and digital signal processing is a particularly interesting approach to realize high spectrally efficient transmission. For efficient digital signal processing, the signal has to be sampled at twice the symbol rate. This implies that for binary modulation formats a sample rate of 80-Gbaud and 200-Gbaud is required for 40-Gb/s and 100-Gb/s transponders, respectively. These figures are well beyond the sample rates that seem to be feasible in the foreseeable future. However, combined with multi-level modulation such as POLMUX-DQPSK, the sample rate requirements for a 100-Gb/s transponder are lowered to  $\sim 50$ -Gbaud. A figure that *seems to be* feasible in the foreseeable future.

The electronic equalization schemes that have attracted the most significant interest in recent years include feed-forward and decision-feedback equalizers, maximum likelihood sequence estimation (MLSE), pre-distortion, multi-symbol phase estimation (MSPE) or related approaches

and digital coherent receivers. In particular the combination of coherent receivers with digital signal processing has proven to be useful together with multi-level modulation formats. In addition, it can potentially recover polarization multiplexed data and correct for linear distortions, such as chromatic dispersion and PMD, in the electrical domain. Hence, the combination of digital coherent detection and multi-level modulation formats such as POLMUX-DQPSK seems to be one of the most suitable choices for the next generation of high-capacity optical transmission systems.

### 1.3 Framework & objectives

Long-haul WDM optical transmission systems with a 10-Gb/s bit rate per wavelength channel have been deployed on a significant scale over the last decade. But after the *telecom bust* in 2001, the optical systems industry has become more cost-oriented and moved away from performance-oriented system design that was common during the *telecom boom*. The first generation of transmission systems with a 40-Gb/s bit rate per wavelength channel could therefore not compete on a cost basis with deployed systems that operated with 10-Gb/s bit rates. This has prevented commercial deployment of such systems and limited their use to transmission experiments and field-trials. However, the use of sophisticated optical modulation formats and electronic equalization can enable more robust 40-Gb/s and 100-Gb/s optical transmission systems. This has spurred a significant research and development effort by the optical systems industry into developing these technologies for their next-generation products.

The research discussed in this thesis focuses on a number of next-generation transmission technologies that might significantly impact the design of long-haul transmission systems in the foreseeable future. Ideally, these technologies will allow for 40-Gb/s and 100-Gb/s transmission systems that can be cost-effective in comparison to existing 10-Gb/s systems. This thesis describes in particular the most promising modulation and equalization technologies and demonstrates their feasibility using long-haul optical transmission experiments.

The work described in this thesis has been carried out at Nokia-Siemens networks (previously Siemens Communications) in Munich, Germany, in cooperation with the Electro-Optical Communications group, department of Electrical Engineering of the Eindhoven University of Technology, The Netherlands. This work has been part of the 'MultiTeraNet' and 'Eibone' projects from the German Bundesministerium für Bildung und Forschung (BMBF). In addition, it has been carried out in close cooperation with the work of *Jansen* [21], which focuses on optical phase conjugation in long-haul transmission systems.

### 1.4 Outline of this thesis

In this section we give a general overview of the thesis structure. The first part of the thesis consists of the Chapters 2 and 3, which discuss the fiber-optic transmission channel and long-haul



transmission systems, respectively. The aim of these two chapters is to provide a physical framework of the optical fiber as the transmission medium in long-haul telecommunication systems. In addition, we discuss in detail the relevant technologies for amplification and distortion compensation in a state-of-the-art transmission systems. These technologies are used in the transmission experiments described in the remainder of this thesis.

The second part of the thesis consists of the Chapters 4 to 8, which deal with the relevant optical modulation formats for long-haul transmission systems. Chapter 4 discusses in detail the binary modulation formats which are currently deployed in state-of-the-art 40-Gb/s transmission systems. Next, Chapters 5 and 6 focus on the most significant multi-level modulation format described in this thesis, DQPSK modulation. Chapter 5 introduces the properties of DQPSK modulation, whereas Chapter 6 discusses in detail a number of long-haul transmission experiments that make use of DQPSK modulation. Subsequently, Chapter 7 discusses POLMUX signaling, in particular the specific transmission impairments that occur when two orthogonal polarizations are used to transmit information. Polarization multiplexing is then combined with DQPSK modulation in Chapter 8 to realize high spectrally efficient long-haul transmission.

Finally, the third part of the thesis focuses on electronic equalization and digital signal processing. In Chapter 9, digital signal processing combined with direct detection receivers is discussed in more detail. And in Chapter 10 the use of digital coherent receivers is treated. In addition, long-haul transmission experiments are described that use digital coherent detection together with multi-level modulation formats to realize robust long-haul transmission with a 2.0-b/s/Hz spectral efficiency.



## The fiber-optic transmission channel

Single-mode optical fibers are circular dielectric waveguides that weakly guide a single transverse mode in two orthogonal polarizations. Made from silica glass, single-mode fibers have very advantageous properties for the transmission of guided waves over long-distances. The use of glass fiber for communication at optical frequencies was first proposed by *Kao and Hockham* in 1966 [22]. Since then, progress in material technology and fiber manufacturing [23] has resulted in the widespread availability of optical fiber with near optimal properties.

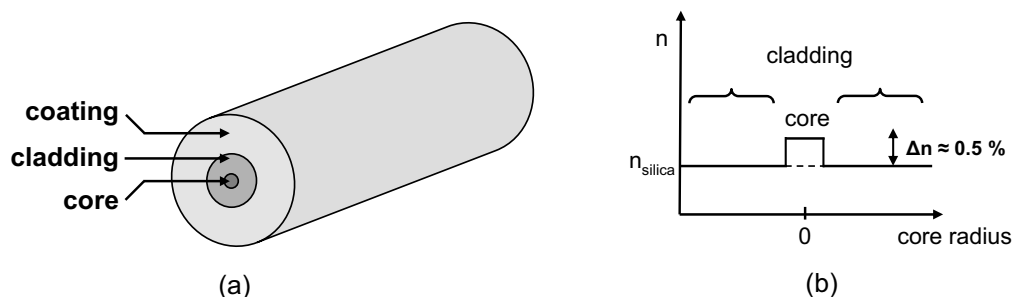


Figure 2.1: (a) Cross-section of an optical fiber and (b) refractive index profile of standard single-mode fiber.

Figure 2.1a shows a cross-section of an optical fiber. In the center of the fiber is the core, which is surrounded by the fiber cladding. For silica fibers the refractive index of the core is  $n \approx 1.48$  (at 1550 nm) and is higher by  $\sim 0.5\%$  than the refractive index of the cladding [24]. This can be achieved either by doping the core with Germanium-Oxide ( $GeO_2$ ), which raises the refractive index, or doping the cladding with fluoride ( $F$ ), which lowers the refractive index. The fiber cladding confines the light to the fiber core through total internal reflection and the low refractive index difference of the core-cladding boundary reduces the scattering loss. Note that the majority,

but not all of the optical wave propagates through the core. The core size is upper-bounded by the need for single-mode propagation in the wavelength range of interest. A too large core diameter with respect to the signal wavelength can result in multi-mode propagation. This is characterized by the cut-off wavelength, which is the lowest wavelength that allows for single-mode operation. Finally, a coating of the optical fiber is necessary for protection of the fiber.

The most widely used fiber type in optical transmission systems is standard single-mode fiber (SSMF), which is sometimes referred to as G.652 fiber [25]. SSMF has a step refractive index profile, as depicted in Figure 2.1b. The fiber core has a typical diameter of  $9\ \mu\text{m}$  and the cut-off wavelength is  $< 1260\ \text{nm}$  so that it provides single-mode operation in the entire low-loss wavelength range of the optical fiber. It was the first single-mode fiber type to be developed, but it is still widely used in optical transmission systems. The core of a SSMF is normally doped with  $\text{GeO}_2$ . As doping with  $\text{GeO}_2$  slightly raises the fiber attenuation, it is preferable to dope the cladding with fluoride for low-attenuation fibers [26]. Such fibers are referred to as pure-silica core fibers and are used in Trans-oceanic optical transmission systems.

Most optical fibers are fabricated (drawn) from a preform in a fiber drawing tower. A preform is a glass rod which has a diameter of a few centimeters and is roughly a meter in length. When heated close to the melting point in a furnace, the preform is pulled into a thin fiber [23]. The preform contains a part with an increased refractive index along its axis, which after fiber drawing becomes the fiber core. The remainder of the preform becomes the cladding of the optical fiber.

This chapter discusses the physical properties of an optical fiber that are the most relevant to long-haul fiber-optic transmission systems. This includes fiber attenuation (Section 2.1), chromatic dispersion (Section 2.2), polarization properties (Section 2.3) and fiber nonlinearities (Section 2.4).

## 2.1 Fiber attenuation

As any physical medium besides vacuum, optical fiber has an intrinsic power loss when a signal propagates along it. The signal power  $P(z)$  in  $[W]$  decreases exponentially with the fiber length, which is referred to a fiber attenuation. After a transmission distance  $z$  in  $[km]$ , the signal power can be denoted by,

$$P(z) = P_0 \cdot \exp(-\alpha z), \quad (2.1)$$

where  $P_0$  is the power coupled into the optical fiber in  $[W]$  and  $\alpha$  is the attenuation coefficient in Neper per kilometer  $[Np/km]$ . The Neper is a logarithmic unit that uses base  $e$ , but it is more convenient to define the fiber attenuation in decibel per kilometer (base 10 logarithmic), following Equation 2.2,

$$\alpha_{dB} = 10 \log_{10}(\exp(\alpha_{Np})) = 10 \log_{10}(e) \cdot \alpha_{Np} = 4.343 \cdot \alpha_{Np}. \quad (2.2)$$

In the remainder of the thesis, the fiber attenuation coefficient in  $[dB/km]$  will be used unless noted otherwise.

The fiber loss as a function of wavelength and frequency is depicted in Figure 2.2. The wavelength ( $\lambda$ ) and the optical frequency ( $f$ ) of a spectral component are related according to  $\lambda = c/f$ , where  $c$  is the speed of light in vacuum which is equal to  $c = 2,9979 \cdot 10^8$  m/s. The minimum fiber loss occurs between  $1.5 \mu\text{m}$  and  $1.6 \mu\text{m}$  and can be as low as  $0.148$  dB/km [27]. In comparison, the attenuation of conventional (window) glass is approximately  $1000$  dB/km. This extremely small attenuation in single-mode silica fiber, allowing for un-repeated transmission links up to  $500$  km [28]. For long-haul transmission links,  $\sim 100$  km spans with re-amplification after each span is widely used.

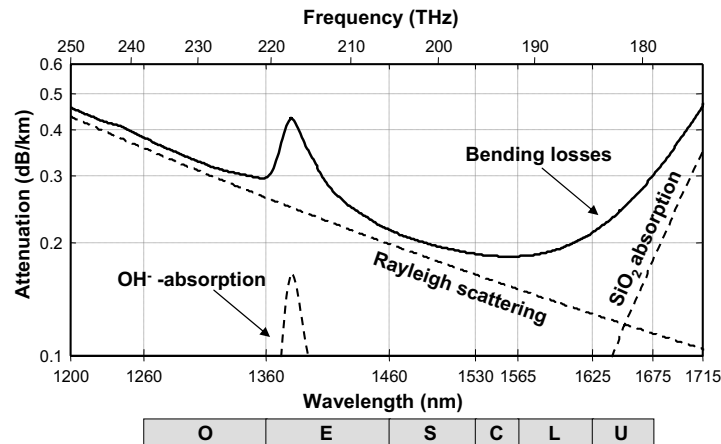


Figure 2.2: Fiber loss as a function of wavelength and frequency.

The remaining contributions to the fiber attenuation in low-loss optical fibers comes from several sources of which the most dominant are: Rayleigh scattering,  $\text{OH}^-$  absorption, bending losses and  $\text{SiO}_2$  absorption [29]. Rayleigh scattering results from microscopic fluctuations in the material density much smaller than the wavelength of the light. It is proportional to the inverse fourth power of wavelength, and therefore attenuates shorter wavelength more than longer wavelength [30]. For longer wavelength ( $> 1600$  nm) the dominant sources of fiber attenuation are bending losses and  $\text{SiO}_2$  absorption. Bending losses are more dominant for longer wavelength because the bending radius relative to the wavelength becomes too small, which increases the scattering losses. For even longer wavelength ( $> 1700$  nm),  $\text{SiO}_2$  absorption becomes the dominant loss mechanism. This results from the harmonic vibrations in the bonds of the silica molecules that make up the glass. Apart from the higher fiber attenuation at lower and higher wavelengths, there is often an  $\text{OH}^-$  absorption peak around  $1.4 \mu\text{m}$  [31]. However, this absorption peak can be nearly eliminated by reducing the concentration of hydroxyl ( $\text{OH}^-$ ) ions in the core of the optical fiber [32, 26]. Optical fibers with a negligible  $\text{OH}^-$  absorption peak are commonly referred to as *water-free* or G.652C/D fibers [25]. Such fibers have a  $\sim 60$ -THz low-loss bandwidth with an attenuation below  $0.4$  dB/km. In principle, this entire wavelength band can be used for optical communication purposes.

The wavelength bands of interest for optical fiber communication are defined by the International Telecommunication Union Standardization (ITU-T) in [33], which span from  $1260$  nm to  $1625$  nm. The wavelength range is lower bounded by the fiber cut-off wavelength and upper bounded by bending and  $\text{SiO}_2$  absorption losses. This wavelength range is divided into 6 wave-

length bands: O, E, S, C, L and U, as depicted in Figure 2.2. For long-haul optical transmission systems the C-band is generally used, which spans the wavelength range between 1528.77 nm and 1568.36 nm. In addition, to increase the transmission capacity the L-band is sometimes used in commercial long-haul systems, which spans the wavelength range between 1568.77 nm and 1610.49 nm. Combined, both bands allow a total of approximately 160 wavelength channels on a 50-GHz WDM grid [34]. The O-band is used extensively for optical communication in metropolitan networks, as cost-effective vertical cavity emitting lasers are available for this wavelength band. [5, 6, 35]. The other wavelength bands are only sporadically used in dense-WDM optical transmission systems due to the higher fiber loss and lack of optical amplifiers with a high efficiency. All wavelength bands combined are also used in metropolitan networks to enable WDM transmission with a large 20 nm channel spacing. Such a channel spacing allows the use of uncooled lasers, and is known as coarse-WDM (CWDM) [36, 37].

## 2.2 Chromatic dispersion

Chromatic dispersion in a single-mode fiber refers to the pulse broadening induced through the wavelength dependence of the fiber's refractive index, and it results for optical transmission systems in inter-symbol interference (ISI). This restricts the dispersion limited reach, i.e. the feasible transmission distance without the need for regeneration or dispersion compensation. In this section the background of chromatic dispersion and the impact on optical transmission links is explained.

The speed at which the phase of any one frequency component of a wave travels along an optical fiber is equal to,

$$v_p(\omega) = \frac{c}{n + n(\omega)}, \quad (2.3)$$

where  $v_p$  is the phase velocity of a spectral component,  $n$  is the refractive index of the guiding material and  $\omega$  is the angular frequency in [rad/s]. As the refractive index  $n$  is larger than 1, the speed of light in an optical fiber is lower than in vacuum. In single-mode optical fibers, the main dispersion effects are material and waveguide dispersion. Waveguide dispersion is related to the optical field being not totally confined to the core of the fiber. A part of the optical field propagates therefore in the cladding, which has a different refractive index. This mismatch in refractive index causes waveguide dispersion. The dependency of the refractive index on the angular frequency is known as material dispersion. The impact of material dispersion on a modulated signal can be described by the mode-propagation constant  $\beta$

$$\beta(\omega) = \frac{\omega}{v_p(\omega)} = [n + n(\omega)] \frac{\omega}{c}, \quad (2.4)$$

The wavelength dependency of  $\beta(\omega)$  can be approximated with a polynomial using a Taylor series expansion. This results in Equation 2.5.

$$\beta(\omega) = [n + n(\omega)] \frac{\omega}{c} \approx \beta_0 + \beta_1(\omega - \omega_0) + \frac{1}{2}\beta_2(\omega - \omega_0)^2 + \frac{1}{6}\beta_3(\omega - \omega_0)^3 + \dots \quad (2.5)$$

## 2.2. Chromatic dispersion

where  $\beta_n$  is defined as the  $n^{\text{th}}$  derivative of  $\beta$  with respect to the angular frequency,

$$\beta_n = \frac{\partial^n \beta}{\partial \omega^n} \Big|_{\omega=\omega_0}. \quad (2.6)$$

In the context of pulse propagation inside an optical fiber, the term  $\beta_0$  in  $[1/km]$  represents a constant phase shift and  $\beta_1$  in  $[ps/km]$  corresponds to the speed at which the envelope of the pulse propagates. The group-velocity of the pulse is then defined by  $\beta_1 = 1/v_g$ . The second order term  $\beta_2$  defines the acceleration of the spectral components in the pulse, which is known as the group velocity dispersion (GVD) in  $[ps^2/km]$ . The third order derivative correspond to  $\beta_3$  in  $[ps^3/km]$  and is known as the GVD slope.

In fiber-optic communication it is common to use the dispersion ( $D$ ) and dispersion slope ( $S$ ), which defines the change in GVD and GVD slope with respect to a reference wavelength  $\lambda$ , respectively. They are related to  $\beta_2$  and  $\beta_3$  as

$$D = \frac{\partial \beta_1}{\partial \lambda} = -\frac{2\pi c}{\lambda^2} \beta_2 \quad S = \frac{\partial D}{\partial \lambda} = \frac{4\pi c}{\lambda^3} (\beta_2 + \frac{\pi c}{\lambda} \beta_3), \quad (2.7)$$

Where  $D$  is expressed in  $[ps/nm/km]$  and  $S$  is expressed in  $[ps^2/nm/km]$ . The wavelength for which  $D$  equals zero is referred to as the zero-dispersion wavelength ( $\lambda_0$ ), it is also the wavelength where waveguide and material dispersion have the same magnitude (but opposite signs). The term *chromatic dispersion* is commonly used to refer to the fiber dispersion. This is in principle not correct as chromatic dispersion implies that different spectral components travel at different velocities. But the fiber dispersion is related to the group-velocity dispersion and not to the group-velocity of the spectral components. However, as it is common terminology in the literature to refer the fiber dispersion as chromatic dispersion, this nomenclature is also adopted in this thesis.

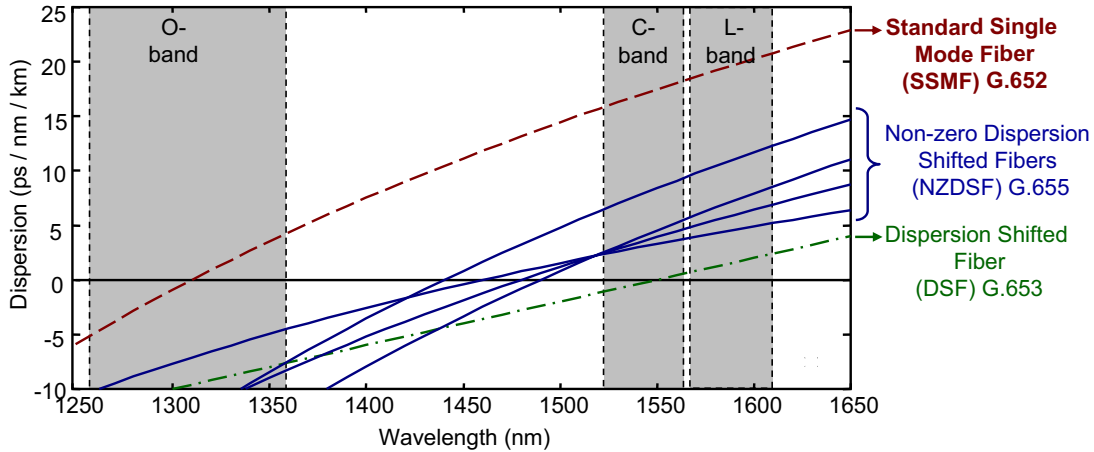


Figure 2.3: Dispersion as a function of wavelength for the most common fiber types in optical communication.

Figure 2.3 shows the dispersion as a function of wavelength for the most common optical fiber types in optical fiber communication. The zero-dispersion wavelength of SSMF is near 1310 nm [38]. This is widely exploited in access and metropolitan networks, as it significantly increases

the dispersion limited reach [35]. In the C-band, the chromatic dispersion of SSMF is typically between  $D = 15.5$  ps/nm/km around 1528 nm and  $D = 17.8$  ps/nm/km around 1568 nm. The dispersion slope for SSMF is approximately  $S = 0.057$  ps<sup>2</sup>/nm/km.

By changing the core-cladding refractive index profile of the fiber, both the material and waveguide dispersion can be modified. For example, by increasing the waveguide dispersion the zero-dispersion wavelength shifts to higher wavelengths. It is also possible to lower the dispersion slope and create a fiber with a nearly flat dispersion profile [39]. Dispersion-shifted fibers (DSF) have a zero-dispersion wavelength in the C-band around 1550 nm and are also known as G.653 fibers [40]. DSF have been developed to extend the dispersion limited reach of optical transmission systems employing the C-band. A low chromatic dispersion coefficient however increases inter-channel nonlinear impairments (see Section 2.4) which makes such fiber unsuitable for WDM transmission systems. A third class of optical fibers that are frequently used in long-haul fiber-optic transmission systems are non-zero dispersion-shifted fibers (NZDSF) or G.655 fiber [41]. There is no common definition for NZDSF, but different manufactures have their own proprietary solutions, e.g. Alcatel TeraLight, Corning LEAF and Lucent TrueWave. The zero-dispersion wavelength of NZDSF fiber is around  $\sim 1460$  nm and the chromatic dispersion in the C-band between 3-8 ps/nm/km, depending on the exact fiber type.

The ISI induced through chromatic dispersion in a fiber-optic transmission link can be quantized by using a normalized dispersion length  $L_D$ , as defined in Equation 2.8 [42].

$$L_D = \frac{T_0^2}{|\beta_2|} \quad (2.8)$$

The normalized dispersion length defines the propagation distance over which the pulse broadens with approximately a factor  $\sqrt{2}$ . The pulsewidth  $T_0$  is the width of a chirp-free transform limited pulse. As  $T_0$  is inverse proportional to the symbol rate, the chromatic dispersion tolerance scales quadratically with the symbol rate. By modifying the refractive index profile it is also possible to create fibers that have a both a negative chromatic dispersion and dispersion slope. Such fibers can compensate for the chromatic dispersion of transmission fibers and are therefore referred to as dispersion compensating fiber (DCF), which is discussed in Section 3.3.

## 2.3 Polarization of light

The polarization of light is the property of electromagnetic waves that describes the direction of the transverse electric field. All electromagnetic waves propagating in vacuum or in a waveguide have electric and magnetic fields that are orthogonal to each other in a transverse plane. The transverse plane is again orthogonal to the direction of propagation  $z$ . In the transverse plane, the electric field vector can be divided into two orthogonal components  $x$  and  $y$ . Note that we do not define a frame of reference for the  $x$  and  $y$  component, and their orientation is therefore arbitrary. The magnetic field vector is normally ignored as it is orthogonal to the electric field vector. The state of polarization (SOP) is then defined as the pattern traced out by the electric field in the



transverse plane as a function of time. In [43], the mathematical background of the polarization of light is discussed in detail.

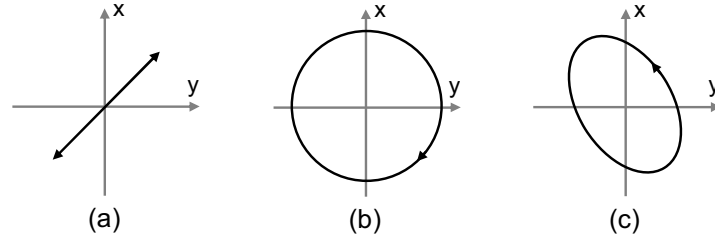


Figure 2.4: Example of different SOP of an electro-magnetic wave; (a)  $45^\circ$  linear, (b) right circular and (c) left elliptical.

In an optical fiber, the two orthogonal components in the transverse plane can be interpreted as the fiber supporting two orthogonal polarizations. The SOP is then defined by relative amplitude and phase of the orthogonal polarization components  $x$  and  $y$ , as shown in Figure 2.4. When there is no phase difference between the  $x$  and  $y$  components, the light is linearly polarized. The angle of the linear polarized light depends on the amplitude in the  $x$  component with respect to the amplitude in the  $y$  component. For horizontally polarized light the pulse travels completely in the  $x$  component, whereas for vertically polarized light the pulse travels in the  $y$  component. When there is a phase difference between the  $x$  and  $y$  component the light is elliptically polarized (Figure 2.4c). In the special case both components contain an equal amplitude and have a  $+90^\circ$  phase difference, the light is right-circular polarized or left-circular polarized for a  $-90^\circ$  phase difference (Figure 2.4b). Note that not all light is polarized, for example sunlight is un-polarized light. However, it is still possible to model un-polarized light as polarized light by assuming a random change in SOP for each fraction of time.

The polarization of an optical signal can be described in a vector notation by separately describing the electric field vector of the  $x$  and  $y$  component,

$$\begin{pmatrix} E_x \\ E_y \end{pmatrix} = \begin{pmatrix} \sqrt{P_x} \exp(j[\omega_0 t + \phi_x(t)]) \\ \sqrt{P_y} \exp(j[\omega_0 t + \phi_y(t)]) \end{pmatrix}. \quad (2.9)$$

The SOP of an optical signal can be described using the vector notation of the complex envelope, which is also known as the Jones vector,

$$\begin{pmatrix} \sqrt{P_x} \exp(j\phi_x) \\ \sqrt{P_y} \exp(j\phi_y) \end{pmatrix} = \sqrt{P_x + P_y} \exp(j\phi_x) \begin{pmatrix} \cos \psi \\ \exp(j|\phi_x - \phi_y|) \sin \psi \end{pmatrix}, \quad (2.10)$$

where  $\psi$  is defined such that  $\tan \psi = \sqrt{P_x}/\sqrt{P_y}$ . The normalized Jones vector with unity amplitude is widely used to characterize the SOP of an optical signal.

An alternative representation to describe the SOP of an optical signal are the Stokes parameters, which can also describe partially or unpolarized light [43]. An additional advantage of using Stokes parameters, is that they express the SOP in term of optical powers instead of the electric field, which is more straightforward to measure. The Stokes vector consists of four stokes

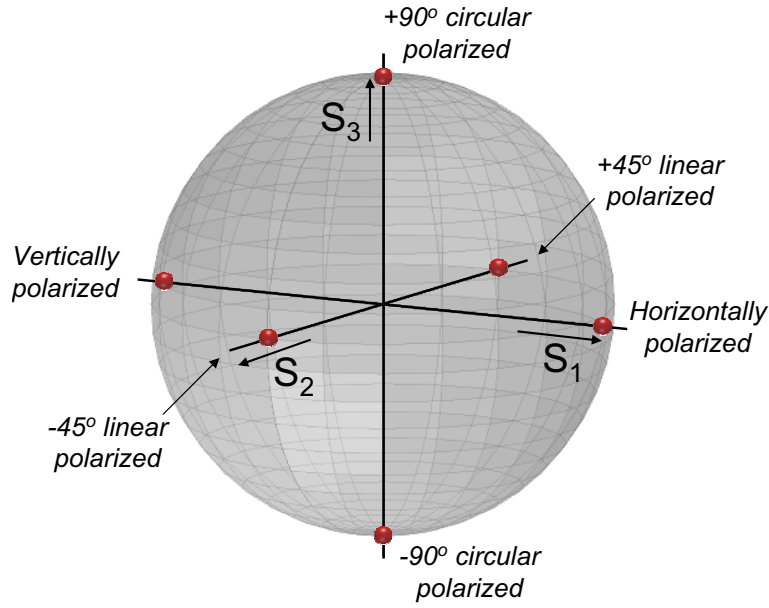


Figure 2.5: The Poincaré sphere.

parameters,  $\vec{S} = [S_0 \ S_1 \ S_2 \ S_3]^T$ , which can be defined in terms of the electrical field vectors using,

$$\begin{cases} S_0 = E_x E_x^* + E_y E_y^* = E_x^2 + E_y^2 \\ S_1 = E_x E_x^* - E_y E_y^* = E_x^2 - E_y^2 \\ S_2 = E_x E_y^* + E_y E_x^* = 2E_x E_y \cos(|\varphi_x - \varphi_y|) \\ S_3 = iE_x E_y^* - iE_y E_x^* = 2E_x E_y \sin(|\varphi_x - \varphi_y|) \end{cases} \quad (2.11)$$

The Stokes parameters are often normalized with respect to the total optical power  $S_0$ . The Poincaré sphere is a graphical representation of the SOP which uses the normalized Stokes parameters as the axis of a 3-dimensional coordinate system, as shown in Figure 2.5. Fully polarized light can be described by a point on the Poincaré sphere, whereas partially or unpolarized light is described by a point within the sphere. The degree of polarization (DOP) defines the distance from  $\vec{S}$  to the center of the Poincaré sphere and it is therefore an important parameter to quantify depolarization. Expressed in term of the Stokes parameters the DOP is equal to,

$$DOP = \frac{\sqrt{S_1^2 + S_2^2 + S_3^2}}{S_0}. \quad (2.12)$$

### 2.3.1 First-order polarization mode dispersion

In an ideal optical fiber with no imperfections and circular symmetry, both orthogonal polarizations have an identical group delay. Hence, the signal will not couple into the orthogonal

polarization and the received SOP is identical to the SOP launched into the fiber. However, the core of the optical fiber is in practice not completely symmetric and the material has imperfections, which results in fiber birefringence  $\Delta n$  and a difference in the group delay  $\Delta\beta_1$  between the two orthogonal polarizations.

$$\Delta\beta_1 = |\beta_{1,x} - \beta_{1,y}| = \frac{\omega}{c} |n_x - n_y|, \quad (2.13)$$

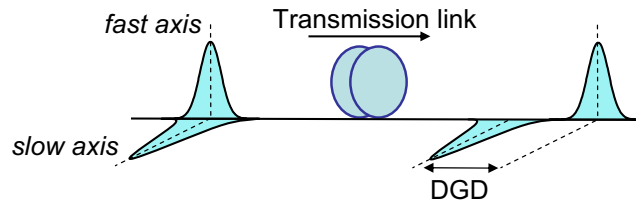


Figure 2.6: Differential group delay in an optical fiber; the signal coupled into the slow axis travels slower than the signal coupled into the fast axis.

In a fiber with constant birefringence, both orthogonal polarizations periodically exchange power with a periodicity equal to the beat length  $2\pi/\Delta\beta_1$  in [km] when the signal is coupled into the fiber in between both orthogonal polarizations. An example of a fiber type with constant birefringence are polarization-maintaining fibers, which are fabricated by artificially enhancing the stress induced birefringence in the fiber core [44]. On the Poincaré sphere the constant birefringence results in a periodic rotation of the output SOP around two orthogonal polarization axes, the principle states of polarization (PSP). When the signal is coupled into one of the PSP, the SOP is constant along the fiber. The PSP with the lower refractive index is referred to as the *fast axis*, because a signal traveling along this axis has a higher group velocity. Following a similar argument the orthogonal PSP, which is on the opposite side of the Poincaré sphere, is then called the *slow axis*. After an optical signal propagated over a distance  $L$ , the differential group delay (DGD) is equal to  $\Delta\tau = \Delta\beta_1 \cdot L$ . Figure 2.6 illustrates DGD in an optical transmission link.

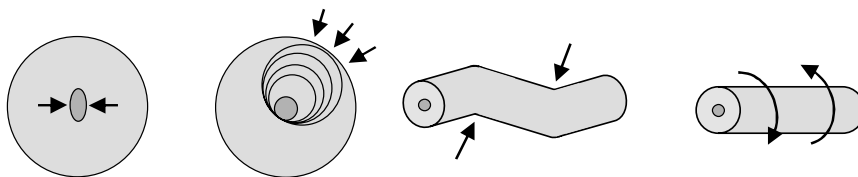


Figure 2.7: Possible causes of random birefringence in non-ideal optical fibers. From left to right, an oval core shape, outside pressure due to mechanical stress, wind or temperature, fiber bending and fiber twisting.

In the fibers used for optical transmission links, birefringence is random, and changes both along the optical fiber and over time. *Rashleigh and Ulrich* were in 1978 the first to note that this random coupling between both orthogonal polarizations could result in signal impairments [45]. The random coupling can be the result of both imperfections introduced in the manufacturing process or external influences as depicted in Figure 2.7. Consequently, the birefringence results

in a random change of the SOP that is analog to the random walk theorem [46]. The random birefringence in a fiber also implies that the DGD is a statistic distribution. This is known as polarization mode dispersion (PMD) in  $[ps]$ , which is defined as the statistical average of the DGD.

$$PMD = \langle \Delta\tau \rangle \quad (2.14)$$

where  $\langle \Delta\tau \rangle$  is the mean DGD and  $\langle \rangle$  denotes an ensemble average. The DGD variance  $var(\langle \Delta\tau \rangle)$  can be denoted through a square relation with the average DGD [47].

$$var(\langle \Delta\tau \rangle) = \frac{3}{\pi/8} \langle \Delta\tau \rangle^2 \quad (2.15)$$

We assume now that the fiber consists of an infinitely large number of infinitely small fiber section, which all rotate the SOP according to the random walk theorem. Then the central limit theorem states that the distribution of the sum of a large number of independent but identically distributed variables is approximately Gaussian distributed, independent of the specific distribution of the variables [48]. For optical fiber with random birefringence this implies that the normalized stokes parameters  $S_{1..3}$  are Gaussian distributed. The PMD properties of an optical fiber can be characterized through the PMD vector  $\vec{\tau}$  [49].  $\vec{\tau}$  is a vector in normalized Stokes space, pointing in the direction of the slow PSP, and with a magnitude equal to the DGD. When the normalized stokes parameters  $S_{1..3}$  are Gaussian distributed, the probability density function of the magnitude of the PMD vector is Maxwellian distributed [50].

$$Pr\{\Delta\tau\} = \frac{32\Delta\tau^2}{\pi^2 \langle \Delta\tau \rangle^3} \exp\left(-\frac{4\Delta\tau^2}{\pi \langle \Delta\tau \rangle^2}\right) \quad (2.16)$$

The Maxwellian distribution of  $Pr\{\Delta\tau\}$  is only correct when the differential group delay is equally distributed over all (infinitely small) fiber sections. When there are points along the fiber with a high local birefringence, the distribution will begin to resemble the square root of a non-central Chi-square distribution with three degrees of freedom [51]. This is also known as the Hinge model [52, 53]. A high local birefringence can result from tight bends in the fiber or points of alleviated mechanical vibrations such a roads or railroad tracks.

For random coupling, the mean DGD ( $\langle \Delta\tau \rangle$ ) does not increase linearly with propagation distance, but with its root-mean-square [29]. The PMD coefficient is the PMD (mean DGD) divided by the square root of the propagation length ( $\sqrt{L}$ ) in  $[ps/\sqrt{km}]$ . The unit  $[ps/\sqrt{km}]$  shows that the maximum allowable PMD decreases with approximately a factor of two when the symbol rate is doubled. Note, however, that the PMD limited transmission distance scales quadratically with the symbol rate.

Due to the statistical nature of PMD there is a finite probability that an arbitrarily high DGD will occur. Usually, one therefore defines a system outage probability, which implies that the DGD can not exceed a certain value during more than a specific fraction of the time. A widely accepted value for the system outage probability is 30 minutes per year or a probability of  $5.7 \cdot 10^{-5}$ . This is equal to an average PMD of between 10% and 15% percent of the symbol rate. For older installed optical fibers the typical PMD coefficient can be as high as  $1 ps/\sqrt{km}$ . But modern optical fibers can have a much lower PMD value, in the order of  $0.05 ps/\sqrt{km}$  [54]. The lower

PMD results mainly from improvements in the manufacturing process, such as fiber spinning during the drawing stage of fiber manufacturing [55]. Due to the improvements in fiber PMD, the PMD-related penalties in state-of-the-art transmission systems are often dominated by PMD in the dispersion compensation and fiber amplifiers. The probability distribution of PMD can, for example, be determined by measuring the change in DGD over either time or frequency and an overview of PMD measurement techniques can be found in [56].

### 2.3.2 Second-order polarization mode dispersion

The change in SOP under the influence of fiber birefringence is wavelength dependent. Using the PMD vector the frequency derivative of the Stokes vector  $S$  is defined as,

$$S_\omega = \frac{\partial S}{\partial \omega} = \vec{\tau} \times S. \quad (2.17)$$

This describes how  $S$  rotates over the Poincaré sphere when the frequency is changed. Using  $S_\omega$  it can be shown that with a change in frequency the output PMD vector rotates around the PSP's, where the magnitude of the DGD determines the rate of rotation. When the PMD vector is aligned with the PSP's there is no rotation on the Poincaré sphere, and the PMD consists only of the DGD. On the other hand, when  $S$  is launched in between the PSP's the rotation angle is maximized because  $\vec{\tau} \times S$  has its largest value.

The magnitude and the orientation of the PMD vector change with wavelength and Equation 2.17 applies only for a narrow wavelength range. The change in the PMD vector with wavelength results in higher-order PMD, which refers to all orders of PMD excluding first-order PMD (DGD). We limit here the description of higher-order PMD to second-order PMD (SOPMD), which is the most important contribution to higher-order PMD for WDM transmission systems. The change of the PMD vector with wavelength can be described by a Taylor expansion of the PMD vector around a carrier frequency  $\omega_0$  [49]. The first frequency derivative describes SOPMD, which is then denoted by,

$$\vec{\tau}_\omega = \frac{d\vec{\tau}}{d\omega} = \Delta\tau_\omega \hat{p} + \Delta\tau \hat{p}_\omega, \quad (2.18)$$

where the subscript  $\omega$  denotes differentiation with respect to frequency. The first term of the SOPMD expression denotes the change of the DGD with wavelength ( $\Delta\tau_\omega$ ), which is known as polarization chromatic dispersion (PCD). The second term denotes the change of the PSP with frequency ( $\hat{p}_\omega$ ) and describes the depolarization of the signal. When visualized on the Poincaré sphere the PSP's would trace out a random path with frequency, due to depolarization. Similar to the DGD variance, the average PCD in  $[ps^2]$  is related to the square of the average PMD,

$$\langle \Delta\tau_\omega \rangle \approx 0.5831 \cdot \langle \Delta\tau \rangle^2. \quad (2.19)$$

The average SOPMD depolarization component is equal to zero which follows directly from the definition of a vector in normalized stokes space. The variance of the statistical distribution of both PCD and the depolarization component of the SOPMD in  $[ps^4]$  can be described by [47],

$$\text{var}(\langle \Delta\tau_\omega \rangle) = \frac{3\pi^2}{64} \cdot \langle \Delta\tau \rangle^4, \quad \text{var}(\langle p_\omega \rangle) = \frac{\pi^2}{192} \cdot \langle \Delta\tau \rangle^4. \quad (2.20)$$

This shows that the SOPMD variance is related to the fourth power of the average DGD. SOPMD can be particularly important for higher symbol rates (e.g. 40 Gbaud), because of the broader spectral width of the signal. Compared with the impact of DGD, the influence of SOPMD is normally small for lower symbol rates (e.g. 10 Gbaud). However, the influence of SOPMD can increase considerably for high average PMD, due to the fourth power dependence between SOPMD variance and average DGD. This can be of particular importance for optical transmission systems that use PMD compensation.

### 2.3.3 Polarization dependent loss

Polarization dependent loss (PDL) refers to the polarization dependence of the insertion loss. It mainly occurs in in-line optical components, such as isolators and couplers. It results in a change of the optical power in the transmission link, which depends on the random evolution of the SOP over time, frequency and along the fiber. The PDL at the end of the transmission link is therefore statistically distributed, and the worst-case cumulative PDL is normally much lower than the added PDL of all components in the link. In the remainder of the thesis we assume 3-dB of PDL as a realistic figure for a long-haul transmission link.

The polarization dependent change in optical power causes depolarization, as both PSP's are no longer orthogonal to each other, and can result in fluctuations in the OSNR. The OSNR consists of both ASE polarized parallel to the signal and ASE polarized orthogonally to the signal. The influence of ASE orthogonal to the signal is minimal as it does not coherently interfere with the optical signal. However, in the presence of severe PDL, the noise emitted in the orthogonal polarization can become polarized parallel to the signal, which causes an OSNR penalty [57]. The amount of average PDL that results in a penalty of 1 dB (with probability of 99.9%) due to PDL-induced OSNR fluctuations is approximately 3 dB [58, 59]. PDL further impacts the probability distribution of DGD and SOPMD, which can cause an increase in DGD and SOPMD related impairments. But as reported by *Shtaif and Rosenberg* in [59], it requires unrealistically high values of PDL before a noticeable penalty occurs.

The impact of PDL is more significant for modulation formats which use the SOP to transmit information, or which periodically change the SOP to enhance the nonlinear tolerance. This is discussed in more detail in Section 7.3.4.

## 2.4 Nonlinear transmission impairments

Optical fibers are essentially a nonlinear guiding medium for electromagnetic waves at deep infrared wavelengths. Although silica is only a weakly nonlinear medium, the nonlinear properties of optical fiber are important to consider. This results from the high confinement of the propagating electromagnetic waves to the core of a single-mode optical fiber. For SSMF, the effective area of the fiber core is typical  $85 \mu m^2$  and it is even smaller for fiber types such as DCF or NZDSF.

For optical powers in the  $mW$  range, the light intensities within the fiber's core are then in the  $MW/m^2$  range. For such intensities, the nonlinear properties of optical fiber become important. This is especially the case for long-haul optical transmission links, where nonlinear impairments add up over long propagation distances.

There are three types of nonlinear processes that are important for optical transmission systems. The first type are the nonlinear processes where there is no energy transfer between the optical field and the dielectric medium. Such nonlinear processes are called non-resonant and can be described as an intensity dependent variation in the refractive index of the silica fiber. This change in the refractive index of a fiber is known as the Kerr effect, discovered in 1875 by *John Kerr*. The most important Kerr nonlinear processes are self-phase modulation (SPM) which is discussed in Section 2.4.2, cross phase modulation (XPM, Section 2.4.3), cross-polarization modulation (XPoLM, Section 2.4.4), four-wave mixing (FWM, Section 2.4.5) and intra-channel XPM and FWM (Section 2.4.6).

The second type of nonlinear processes describes the nonlinear interaction between signal and noise, also known as nonlinear phase noise. The impact of nonlinear phase noise on optical transmission systems is discussed in Section 2.4.7. The third type of nonlinear processes are known as the resonant processes or non-elastic scattering processes. In non-elastic processes the optical field transfers a part of its energy to the dielectric medium. The most important non-elastic scattering processes, stimulated raman scattering (SRS) and stimulated Brillouin scattering (SBS) are discussed in Section 2.4.8.

### 2.4.1 Pulse propagation

The Schrödinger equation, proposed by *Erwin Schrödinger* in 1926 describes the space- and time-dependence of a quantum mechanical system and plays therefore a central role in quantum mechanics. The nonlinear Schrödinger equation (NLSE) is related to the Schrödinger equation used in quantum mechanics and models the evolution of a (single polarization) optical field  $E(z,t)$  in an optical fiber [42]. It can be written as:

$$\frac{\partial E}{\partial z} = - \underbrace{\frac{\alpha}{2} E}_{\text{attenuation}} - \underbrace{j \frac{\beta_2}{2} \frac{\partial^2 E}{\partial T^2}}_{\text{dispersion}} + \underbrace{\frac{\beta_3}{6} \frac{\partial^3 E}{\partial T^3}}_{\text{dispersion slope}} + \underbrace{j \gamma |E|^2 E}_{\text{Kerr nonlinearities}} \quad (2.21)$$

Where  $E$  is the complex envelope of the optical field,  $z$  the propagation distance in  $[km]$ ,  $T = t - \beta_1 z$  is the time measured in a retarded frame and  $\alpha$  is denoted in  $[Np/km]$ .

The term  $j \gamma |E|^2 E$  represents the nonlinear contribution to the NLSE, which is proportional to the power of the optical field times the nonlinear coefficient  $\gamma$ . The nonlinear coefficient can be derived from the wave equation, which describes the propagation of light through an optical fiber and is denoted by,

$$\nabla \times \nabla \times E(z,t) = -\frac{1}{c^2} \frac{\partial^2 E(z,t)}{\partial t^2} - \mu_0 \frac{\partial^2 P(z,t)}{\partial t^2}, \quad (2.22)$$

where  $\nabla$  is the vector differential operator,  $E(z, t)$  the electrical field vector and  $P(z, t)$  the dielectric polarization vector. When the optical frequency of the signal is far away from the resonance frequency of the medium (in this case silica) the dielectric polarization vector  $P(z, t)$  can be described as a power series of the electrical field vector  $E(z, t)$ .

$$P(z, t) = \epsilon_0(\chi^{(1)} \cdot E(z, t) + \chi^{(2)} : E^2(z, t) + \chi^{(3)} : E^3(z, t) + \dots), \quad (2.23)$$

where  $\epsilon_0$  is the vacuum permittivity and  $\chi^{(n)}$  is the  $n^{\text{th}}$  order susceptibility, a tensor of order  $n + 1$ . The first order susceptibility  $\chi^{(1)}$  determines the linear behavior of an optical fiber. The second order susceptibility  $\chi^{(2)}$  vanishes for optical fibers because  $SiO_2$  is a symmetric medium. However other materials can have a strong second order susceptibility. For example, the nonlinear processes that enables optical phase conjugation as discussed in Section 3.6, are related to  $\chi^{(2)}$ . The nonlinear effects that play a role in optical transmission links are included through the third order susceptibility  $\chi^{(3)}$ . Higher order susceptibility are small and can be neglected.

When an intense pulse travels through an optical fiber, it changes the refractive index of the fiber. The dependence of the refractive index on the power of the optical field is denoted by,

$$\tilde{n}(\omega, |E|^2) = n_0(\omega) + n_2|E|^2/A_{eff}, \quad (2.24)$$

where  $|E|^2$  in  $[W]$  is the power of the optical field in the fiber,  $A_{eff}$  in  $[m^2]$  the effective mode area,  $n_0$  the linear refractive index and  $n_2$  in  $[m^2/W]$  the nonlinear contribution to the refractive index. The linear refractive index is related to the first order susceptibility  $\chi^{(1)}$  by:

$$n_0 = \sqrt{1 + Re\{\chi^{(1)}\}}. \quad (2.25)$$

The nonlinear contribution to the refractive index depends on the third order susceptibility  $\chi^{(3)}$  and the linear refractive index,

$$n_2 = \frac{3}{8n_0} Re\{\chi_{xxxx}^{(3)}\}. \quad (2.26)$$

The nonlinear refractive index is a material parameter which is related to the chemical composition of the optical fiber. For silica fiber it is approximately  $n_2 = 2.3 \cdot 10^{-20} m^2/W$ , but this value is slightly higher for fiber doped with  $GeO_2$  [42]. As a smaller core area results in stronger confinement of the light, the nonlinear interaction in an optical fiber depends also on the effective core area  $A_{eff}$  in  $[\mu m^2]$ . The nonlinearity coefficient  $\gamma$  in  $[km^{-1}W^{-1}]$  combines the nonlinear refractive index and the effective core area of the fiber in a single coefficient.

$$\gamma = \frac{2\pi \cdot n_2}{\lambda \cdot A_{eff}}. \quad (2.27)$$

The nonlinearity coefficient for SSMF and a wavelength around  $1.5 \mu m$  is  $\gamma = 1.3 km^{-1}W^{-1}$ . In highly nonlinear fibers for nonlinear signal processing the nonlinearity can be as high as  $\gamma = 21 km^{-1}W^{-1}$  [60] while for a photonic crystal fibers this value can reach  $\gamma = 640 km^{-1}W^{-1}$  [61].

Due to fiber attenuation, the influence of fiber nonlinearities is not evenly divided over the fiber length but the majority of the nonlinear interaction takes place in first part of the fiber. This can



be denoted by the effective length of the fiber, which has an asymptotic behavior for increasing fiber length.

$$L_{eff} = \frac{1 - \exp(-\alpha L)}{\alpha}, \quad (2.28)$$

where  $\alpha$  is defined in  $[Np/km]$ . For long fibers this can be approximated with  $L_{eff} \approx 1/\alpha$ . For example, for a fiber attenuation of 0.2 dB/km and a fiber span of 100 km the effective length is equal to 21.5 km. The signal power as a function of the transmission distance is also referred to as the *power map*. Because nonlinear impairments result from the combined impact of fiber nonlinearities and chromatic dispersion, the asymmetric power map in a fiber has a strong impact on the *dispersion map*, i.e. where along the fiber the chromatic dispersion is compensated. This is discussed in more detail in Section 3.3.1.

### 2.4.2 Self-phase modulation

The nonlinear change in the refractive index causes an intensity dependent nonlinear phase shift, which is referred to as self-phase modulation (SPM). The impact of SPM can be analytically studied using the NLSE in the absence of chromatic dispersion. In this case Equation 2.21 reduces to

$$\frac{\partial E}{\partial z} = - \underbrace{\frac{\alpha}{2} E}_{\text{attenuation}} + \underbrace{j\gamma|E|^2 E}_{\text{Kerr nonlinearities}}. \quad (2.29)$$

This equation can be solved analytically, which results in,

$$E(z, T) = E(0, T) \cdot \exp\left(-\frac{\alpha z}{2}\right) \cdot \exp(j\phi_{SPM}(z, T)) \quad (2.30)$$

where  $E(0, T)$  is the complex field amplitude at  $z = 0$  and the SPM induced nonlinear phase shift is defined as

$$\phi_{SPM}(z, T) = \gamma |E(0, T)|^2 \frac{1 - \exp(-\alpha z)}{\alpha}. \quad (2.31)$$

The maximum nonlinear phase shift is obtained after propagation over length  $L$  and for a peak power  $P_0$  at the center of the pulse ( $T = 0$ ), Equation 2.31 then reduces to,

$$\phi_{SPM,max} = \gamma P_0 L_{eff}. \quad (2.32)$$

Equation 2.31 shows that the nonlinear phase shift changes across the pulse because different parts of the pulse have a different intensity, this results in a SPM-induced chirp, which causes pulse broadening.

The combined effect of SPM-induced nonlinear chirp and chromatic dispersion results in amplitude distortions. The SPM-induced nonlinear chirp shifts the leading edge of a pulse to lower frequencies (red-shift) and the trailing edge of pulse to higher frequencies (blue-shift). In the presence of chromatic dispersion, the red-shifted and blue-shifted parts of the pulse travel at a different speed. When two pulse components with different frequency are overlapping they

interfere, which causes amplitude distortions. Unlike chromatic dispersion, the nonlinear SPM-induced chirp cannot be compensated as this would require a material with a negative Kerr effect. As these amplitude distortions are dependent on the signal power, they are commonly referred to as *nonlinear* impairments.

The combined effect SPM-induced nonlinear chirp and chromatic dispersion can be used to reduce the impact of nonlinear impairments. For a positive chromatic dispersion coefficient ( $D > 0$ ) the nonlinear and dispersion-induced chirp have opposite signs, and therefore (partially) cancel each other out. This can be used to reduce the impact of SPM by appropriately choosing the residual chromatic dispersion at the receiver, which is known as post-compensation [62].

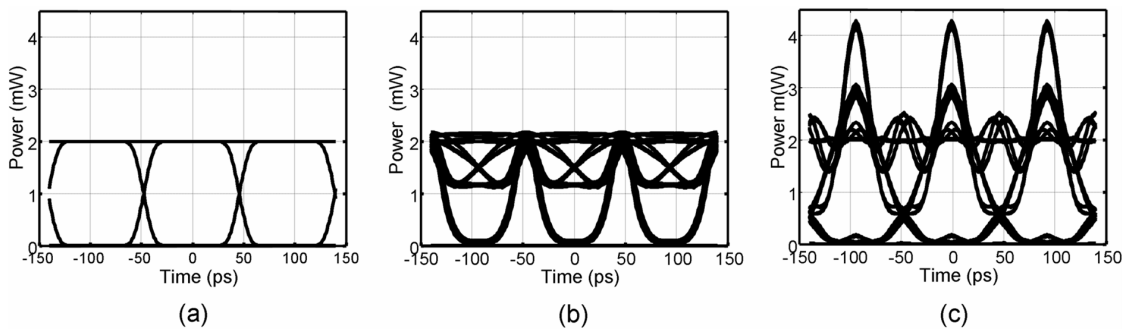


Figure 2.8: Eye diagrams showing the impact of SPM after 100-km SSMF with 15-dBm input power; (a) linear transmission (b) nonlinear transmission, no residual dispersion and (c) nonlinear transmission, 600-ps/nm residual dispersion.

Figure 2.8 depicts an example of SPM-induced signal distortions. The eye diagrams show transmission over a 100-km SSMF span ( $\gamma = 1.3 \text{ km}^{-1} \text{ W}^{-1}$ ,  $D = 17 \text{ ps/nm/km}$ ) with a 15-dBm input power. Figure 2.8b shows the impact of SPM through overshoots near the edge of the pulse. When the SPM induced phase shift is partially compensated with 600-ps/nm of chromatic dispersion (Figure 2.8c) nearly the same eye opening is obtained as in the absence of nonlinear impairments.

The balance between chromatic dispersion and SPM induced chirp can also be used to construct transmission links where the signal propagates undistorted by chromatic dispersion or fiber non-linearity [42]. This is known as soliton propagation and was first demonstrated by *Mollenauer et al.* in 1980 [63]. Ideally, this would require a loss-less fiber as the fiber attenuation destroys the balance between chromatic dispersion and SPM. However, soliton propagation is also possible for lossy fiber, although it requires small amplifier spacings. Soliton propagation has been an extensive field of research throughout the 1990's [64, 65] as it allows for error-free transmission over Trans-oceanic distances. But a drawback of transmission systems using soliton propagation is that they require a low chromatic dispersion coefficient for high bit rates, which increased inter-channel impairments in WDM transmission system [66]. In WDM transmission systems it is therefore preferable to use in-line dispersion management, which is also known as dispersion-managed soliton transmission [67].

### 2.4.3 Cross-phase modulation

Cross phase modulation (XPM) describes the nonlinear phase change through the Kerr effect that results from the interaction with another optical pulse at a different wavelength. There is only a distinction between SPM and XPM in the case both pulses have a clearly separated spectrum, as is the case in WDM transmission systems.

In Equation 2.33 the refractive index is denoted a function of two co-propagating wavelength channels [42].

$$\tilde{n}(\omega, |E_k|_{k=1,2}^2) = n_0(\omega) + n_2(|E_k|^2 + B|E_{3-k}|^2)/A_{eff}. \quad (2.33)$$

where  $B$  is a measure for the difference in polarization between the two channels. When both channels have the same polarization  $B$  is equal to 2 and when they are orthogonally polarized  $B$  is equal to  $2/3$ . The factor two stems from the number of terms of the  $\chi^{(3)}$  susceptibility that contribute to the nonlinear polarization rotation (Equation 2.23), which double for two distinct optical frequencies compared to the single (degenerate) case [42]. The factor  $1/3$  results from the weaker interaction between two orthogonal polarizations. Neglecting chromatic dispersion results in expression 2.34 for the total nonlinear phase shift induced through SPM and XPM when two channels are co-propagating,

$$\phi_k(z) = \gamma(|E_k(0)|^2 + c|E_{3-k}(0)|^2) \frac{1 - \exp(-\alpha z)}{\alpha}. \quad (2.34)$$

When two pulses at different wavelengths propagate along the fiber perfectly overlapping each other (in the absence of chromatic dispersion) the impact of XPM is similar to SPM. The XPM induced nonlinear phase shift is however more detrimental when the two pulses at different wavelengths are partially overlapping in time. One part of the pulse will experience a nonlinear phase shift whereas the other part of the pulse will be unaffected. The nonlinear phase shift interacts with chromatic dispersion along the link, which converts the phase shifts into amplitude distortions.

Chromatic dispersion decreases the XPM induced nonlinear phase shift as both channels have a different group velocity and therefore walk-off from each other. Consider the nonlinear phase shift that a pulse at  $\omega_1$  imposes on a pulse at  $\omega_2$ . The faster the two pulses walk-off, the smaller the difference in nonlinear phase shift will be across the pulse at  $\omega_2$ . In the extreme case, both pulses walk-off fast enough that the nonlinear phase shift is nearly constant across the pulse and the impact of XPM diminishes. The XPM efficiency is therefore related to the walk-off length  $L_W$  in [m].

$$L_W = \frac{T_0}{|\beta_{12} - \beta_{11}|} \approx \frac{T_0}{|\beta_2 \Delta\omega|}, \quad (2.35)$$

where  $\beta_{1k}$  is the group velocity for the  $k^{th}$  co-propagating pulse with  $k = 1, 2$ ,  $\Delta\omega$  is equal to  $|\omega_1 - \omega_2|$  and proportional to the difference in wavelength. The walk-off length is further dependent on the symbol period  $T_0$ . This implies that impact of XPM decreases both for higher chromatic dispersion and a higher symbol rate. XPM is therefore most detrimental for narrow channels spacing or low dispersion fiber [68, 69]. For example, in an optical transmission system with

SSMF and a 10-Gb/s symbol rate, the nonlinear impairment is XPM dominated for a 25-GHz WDM channel spacing [70] and SPM dominated for a 100-GHz WDM channel spacing.

The reduced XPM efficiency between neighboring WDM channels with an orthogonal SOP is exploited in polarization interleaved transmission systems [71, 72], which reduces the XPM caused by the nearest neighbor channels. However, polarization interleaving complicates system design as it requires the transmitter to use polarization maintaining components up to the point where the orthogonally polarized WDM channels are multiplexed. Further techniques to reduce the impact of XPM-induced nonlinear impairments are optimization of the dispersion map (see Section 3.3.1) and shifting or scrambling the relative timing between adjacent WDM channels with optical delay lines [73].

In the context of optical or electrical equalization of nonlinear impairments there is a further significant difference between SPM and XPM. In the case of SPM, the source of the impairment are trailing or leading pulses at the same wavelength. The source of the impairment is thus known to an equalizer with memory, which can therefore (partially) compensate for it [74, 75]. For XPM, the source of the impairment are neighboring WDM channels that are unknown to any (practical) equalizer. In the context of equalization, XPM induced impairments therefore appear as noise.

### 2.4.4 Cross-polarization modulation

Cross-polarization modulation (XPoIM) is an extension of SPM when the two orthogonal polarizations in the fiber are considered. Nonlinear interaction between both polarization components at the same wavelength results in coherent coupling, which can be considered as a XPM-like effect. However, both polarization components carry a portion of the same signal and XPoIM has therefore a similar impact as SPM [42]. This is evident by considering the nonlinear contribution to the refractive index  $\Delta n_x$  and  $\Delta n_y$  for a two-polarization model,

$$\begin{cases} \tilde{n}(\omega, |E_x|^2) = n_0(\omega) + n_2(|E_x|^2 + \frac{2}{3}|E_y|^2) \\ \tilde{n}(\omega, |E_y|^2) = n_0(\omega) + n_2(|E_y|^2 + \frac{2}{3}|E_x|^2). \end{cases} \quad (2.36)$$

Equation 2.36 shows that the strength of XPoIM between orthogonal polarization components is a factor  $\frac{2}{3}$  of the SPM strength when only a the single polarization is considered. However, we can also observe from Equation 2.36 that the refractive index of both polarizations components combined (i.e.  $\tilde{n}(\omega, |E_x|^2) + \tilde{n}(\omega, |E_y|^2)$ ) is independent of the SOP. This is evident by computing the magnitude of the nonlinear refractive index for, respectively,  $E_x = 1, E_y = 0$  and  $E_x = E_y = 1/2 \cdot \sqrt{2}$ . The total nonlinear phase shift in a single WDM channel is therefore independent of the SOP.

The impact of XPoIM becomes more detrimental for multiple co-propagating WDM channels. As an example we assume that a pulse train propagates at a frequency  $\omega_1$  with its power equally divided over the two orthogonal polarizations  $E_x = E_y = 1/2 \cdot \sqrt{2}$ . The SOP of a second co-propagating pulse train at a frequency  $\omega_2$  is such that all power propagates in one of the polari-

zation components  $E_x = 1, E_y = 0$ . The nonlinear phase shift induced on the  $E_y$  component of a pulse at  $\omega_1$  is then smaller by a factor 3 compared to the  $E_x$  component, which follows from Equation 2.33. This results in a change of the relative phase difference between both polarization components  $E_x$  and  $E_y$  of the pulse, which in turn changes the SOP. Because the SOP change depends on the pulse train at  $\omega_2$ , it results in a noise-like change of the SOP and, hence, depolarization. This depolarization can severely degrade the efficiency of PMD compensation [76]. In the presence of PDL, the depolarization is converted into amplitude fluctuations.

XPolM is particularly detrimental when a polarization sensitive receiver is used, as the depolarization translates into amplitude distortions when a single polarization is filtered out [77, 78]. In particular for polarization-multiplexed transmission (Chapter 7) this results in crosstalk between the two polarization tributaries.

### 2.4.5 Four-wave mixing

Four-wave mixing (FWM) is a parametric nonlinear process which involves interaction between four optical waves, in this case different WDM channels, hence the name four-wave mixing. Two or three photons are annihilated and new photons are created at difference frequencies such that the net energy and momentum are conserved.

The FWM efficiency depends on the frequency and phase matching among the four optical waves. There are two distinct four wave mixing processes. In the first process three photons are annihilated and a new photon is created at the sum frequency of the three photons (for example third-harmonic generation). The phase matching condition for this process is hard to satisfy in an optical fiber and is therefore not of significance to optical transmission systems. The second mixing process annihilates two photons and creates two photons. The frequency (left) and phase matching (right) conditions are denoted in Equation 2.37 [79].

$$\omega_1 + \omega_2 = \omega_3 + \omega_4, \quad n_1 \omega_1 + n_2 \omega_2 = n_3 \omega_3 + n_4 \omega_4. \quad (2.37)$$

Where  $\omega_j$  is the frequency and  $n_j$  the refractive index of the fiber at this frequency. The phase condition is most easily satisfied in the case  $\omega_1 = \omega_2$ , which is also referred to as degenerate FWM. In this case, FWM generates two photons at the Stokes and anti-Stokes wavelengths of  $\omega_2$ , which are located at frequencies  $\omega_3$  and  $\omega_4$ . The Stokes shift  $\omega_2 - \omega_3 = \omega_4 - \omega_2$  depends on the fiber parameters.

When two WDM channels at  $\omega_2$  and  $\omega_3$  are co-propagating this results in FWM products at  $\omega_1 = 2\omega_2 - \omega_3$  and  $\omega_4 = 2\omega_3 - \omega_2$ . This is illustrated in Figure 2.9. For equally spaced WDM channels (e.g. on a 50-GHz wavelength grid) FWM has the worst impact, as the FWM products result in crosstalk for other co-propagating channels.

Chromatic dispersion decreases the FWM efficiency considerable as the difference in phase velocity causes the phase matching condition to be only satisfied over a short transmission distance. This decreases FWM efficiency considerable and is therefore only the dominating Kerr nonlinear impairment for small WDM channel spacings and low dispersion fiber, such as DSF [80, 81]. A

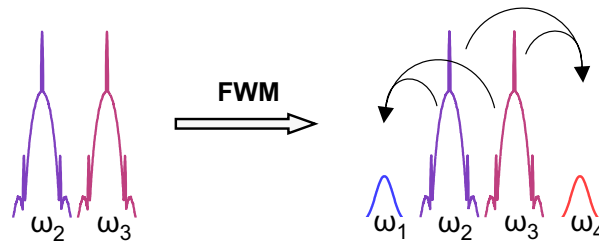


Figure 2.9: Principle of four-wave mixing.

potential solution to reduce the FWM efficiency is the allocation of unequal channel spacings, but this significantly reduces the number of allowable WDM channels [82, 83]. The FWM efficiency is also reduced when the polarization of the neighboring WDM channels is orthogonal, as is the case for polarization interleaved transmission systems [71, 72] or when using the higher dispersion coefficient in the L-band [84]. For C-band transmission systems using SSMF, the impact of FWM can generally be neglected.

### 2.4.6 Intra-channel XPM and FWM

The nonlinear interaction that occurs between subsequent pulses at the same wavelength is very similar to XPM and FWM, and is therefore referred to as *intra-channel* XPM and FWM. Intra-channel XPM (IXPM) and intra-channel FWM (IFWM) are a subdivision of SPM, with pure single pulse SPM sometimes referred to as isolated SPM (ISPM). The XPM and FWM processes explained in the previous section are *inter-channel* nonlinear effects, which describe the interaction between co-propagating WDM channels. Intra-channel XPM and FWM occur mainly in transmission links with high dispersive fiber, as a single pulse is spread out over multiple time slots.

IXPM and IFWM are particularly important for transmission at bit rates of 40-Gb/s or above and high dispersive fiber such as SSMF [85, 86]. For such bit rates, the signal waveforms evolves very fast when propagating along the fiber, which averages out the nonlinear interaction between symbols from the same wavelength channel as well as the interaction between co-propagating WDM channels. This transmission regime is known as *pseudo-linear* because, similar to a linear transmission link, the optimum residual dispersion is close to zero. Pseudo-linear transmission occurs when the normalized nonlinear length (Equation 2.28) is significantly larger than the normalized dispersion length (Equation 2.8).

IFWM results in energy transfer between subsequent time slots [85, 87]. This effect is the most evident for amplitude modulated signals, as it creates ghost pulses in the time slots where a '0' is transmitted. The IFWM induced energy transfer further results in amplitude jitter in the '1' symbols. This is illustrated in Figure 2.10 where a '0' '1' '1' '0' sequence is transmitted over high dispersive fiber. Along the fiber the signal is dispersed and the pulses are spread out beyond their respective time slots. At the same time the Kerr effect causes both pulses interact with each other, which results in two FWM products. When subsequently the accumulated dispersion

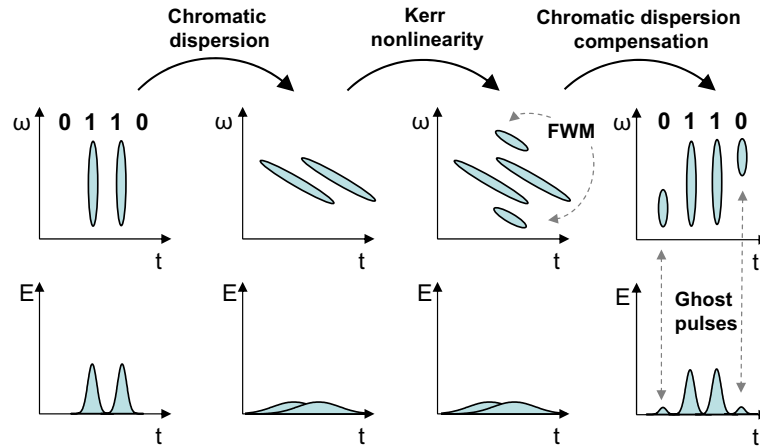


Figure 2.10: Impact of intra-channel FWM (after [85]).

is compensated at the receiver, the two FWM products appear as ghost pulses in the time slots where a '0' is originally transmitted.

IXPM generates a frequency shift due to the intensity change of the overlapping pulses. Through the interaction with chromatic dispersion this frequency shift is subsequently converted into timing jitter [86]. The impact of intra-channel XPM and FWM impairments in high-dispersive transmission links can be reduced through a symmetric transmission link. This is, for example, possible by evenly splitting the chromatic dispersion compensation between the transmitter and receiver [88]. In addition, mid-link optical phase conjugation allows for a symmetrical link design, as discussed in Section 3.6.

### 2.4.7 Nonlinear phase noise

Nonlinear phase noise results from the interaction between the optical signal and ASE induced power fluctuations. These power fluctuations are transformed into phase noise through interaction with the Kerr effect. Nonlinear phase noise was first described by *Gordon* and *Mollenauer* in 1990 and is therefore commonly referred to as the Gordon-Mollenauer effect [89]. It is only of significant importance for modulation formats that encode the information in the phase of the optical signal.

Ideally, a phase modulated signal has a regular pulse shape and each pulse contains an equal amount of optical power. The nonlinear phase shift introduced through the Kerr nonlinearity is then the same for each pulse. When ASE from optical amplifiers is added to the signal along the transmission link, each pulse interferes constructively or destructively with the ASE. This results in a different power for each pulse. When the signal propagates further along the link the pulses then experience a difference in nonlinear phase shift, which is referred to as SPM induced nonlinear phase noise [90]. Figure 2.11 illustrates this origin of nonlinear phase noise through the interaction of ASE with the Kerr effect. Several methods have been demonstrated to reduce or cancel out the impact of nonlinear phase, including optical phase conjugation [91, 92]

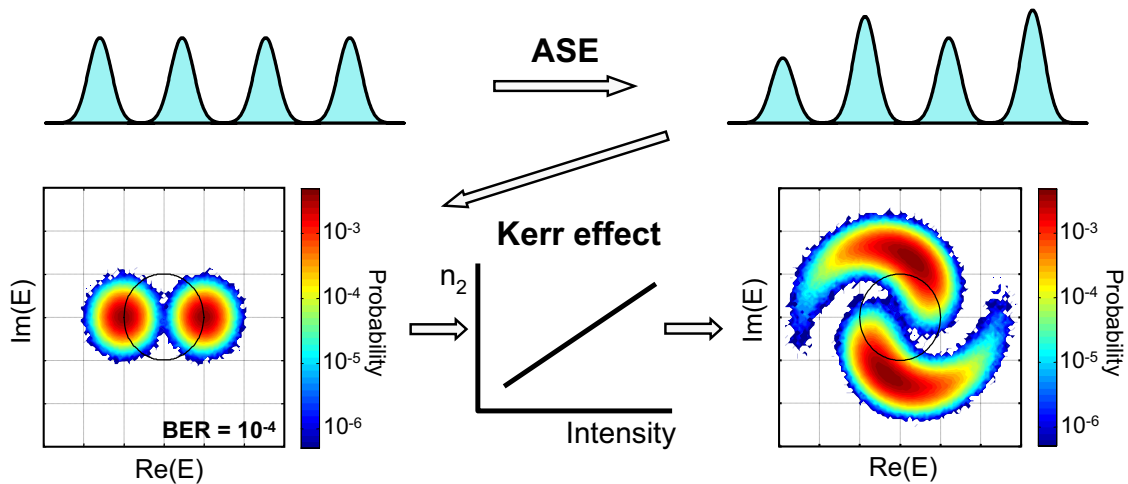


Figure 2.11: Impact of nonlinear phase noise on optical transmission systems.

and semiconductor optical amplifier based optical regeneration [93]. The constellation diagram in Figure 2.11 shows the typical nonlinear phase noise induced *ying-yang* shape. This correlation between signal power and nonlinear phase shift can be used to reduce the impact of SPM induced nonlinear phase noise. For example, in the receiver a phase shift can be applied to each symbol that is dependent on the intensity of the symbol. This is possible through either optical [94, 95] or electronic [96] means. Alternatively, signal processing in the receiver could take the *ying-yang* shape into account when making a decision on the data [95].

Nonlinear phase noise can further result from interaction through XPM. In this case the ASE that is added along the transmission link changes the power level of the co-propagating channels, which either enhances or reduces the XPM-induced nonlinear phase shift. The difference in XPM strength in turn translates into nonlinear phase noise. For XPM induced nonlinear phase noise, there is no correlation between signal power and phase shift in the constellation diagram, which makes it more difficult to compensate for.

The nonlinear phase noise strength is dependent on both the fiber chromatic dispersion coefficient as well as the OSNR along the transmission link [95]. For high dispersive fiber, the power in a symbol period changes rapidly along the fiber which averages out the nonlinear phase shift contribution. The impact of nonlinear phase noise is also strongly dependent on the OSNR along the transmission link, i.e. the path-averaged OSNR. As the OSNR requirement increases for high bit rates, so will the path-averaged OSNR. This reduces the impact of nonlinear phase noise as the ASE power is not large enough to make a significant contribution to the total nonlinear phase shift. Nonlinear phase noise is therefore mainly the dominating impairment for D(Q)PSK modulation at  $< 20$ -Gb/s bit rates or transmission over low dispersion fiber, such as DSF.



### 2.4.8 Non-elastic scattering effects

The second class of nonlinear effects important to optical transmission systems are the non-elastic scattering effects. Non-elastic scattering effects depend on the interaction between the optical pulses and the silica molecules of the optical fiber. The optical pulses transfer a part of the photon energy to the dielectric medium. The most important non-elastic scattering effects in optical transmission are stimulated Raman scattering (SRS) and stimulated Brillouin scattering (SBS).

When a photon collides with a silica molecule of the fiber, it normally scatters through elastic Rayleigh scattering, which does not transfer any energy to the silica molecule. However, for a small fraction of the photon-molecule collisions ( $\sim 10^{-6}$ ) Raman scattering occurs. The origin of Raman scattering is related to the imaginary part of the  $\chi^{(3)}$  susceptibility (see Equation 2.23, whereas the Kerr nonlinearities have their origin in the real part. Raman scattering transfers a part of the photon energy to the silica molecule which makes a transition to a higher-energy vibrational state. In the process a lower frequency photon is generated. The frequency shift of the generated photon is dependent on the propagating material. For silica, which is not a crystalline material, a continuous spectrum is created with a peak value around 13.2 THz  $\approx$  100 nm downshifted from the original frequency, this is called the Stokes band.

Raman scattering can result in stimulated emission when co-propagating WDM channels are present within the Raman bandwidth. SRS is the most effective when both channels have the same polarization and the wavelength difference is close to the 100 nm Raman gain peak. The SRS efficiency dependent on the fiber type and the intensity of the incident pulse [97]. In particular when the optical power is above a critical power, the SRS threshold, the Stokes band will build up nearly exponentially. For long-haul optical transmission systems the input power per channel is generally lower than the SRS threshold, hence SRS-induced impairments are normally not significant. However, SRS can be exploited to create Raman amplifiers [98], which use the fiber as a gain medium by launching a strong pump signal in the fiber. Raman amplifiers are discussed in more detail in Section 3.2.2.

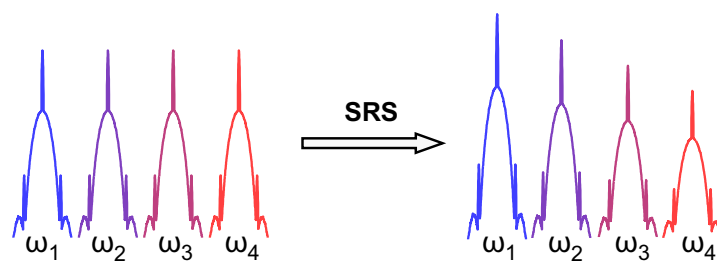


Figure 2.12: *Principle of Stimulated Raman Scattering.*

In WDM transmission, SRS can also occur between neighboring channels, which results in unwanted crosstalk. This transfers energy from the high frequency channels to lower frequency channels and can result in bit-dependent [99] and time averaged SRS crosstalk [100]. Bit-dependent crosstalk behaves similarly as XPM and its impact is therefore relatively small for fibers with a high dispersion coefficient [99]. Time averaged SRS crosstalk results in a gain tilt

in the WDM spectrum as depicted in Figure 2.12 [101]. This crosstalk can be reduced in optical transmission systems using dynamic gain equalizers (DGE) along the transmission link.

Stimulated Brillouin scattering (SBS) results from the interaction between photons and acoustic waves. An optical signal traveling through the fiber generates an acoustic wave, which in turn modulates the refractive index of the optical fiber in a periodic manner. This periodic variation of the refractive index scatters the light of the incident wave through Bragg refraction. This generates a backwards propagating wave, counter-directional to the optical signal. The virtual Bragg grating is moving with a certain acoustic velocity, which causes a Doppler shift of  $\sim 10$  GHz between the backward reflecting wave and the optical signal [42]. The power reflected through SBS increases exponentially when the power is above the SBS threshold. SBS therefore limits the optical power that can be launched into the fiber. However, for optical transmission systems SBS is not of significant importance as it nearly vanishes for pulses shorter than several nanoseconds. Phase modulation of the optical signal is also an effective method to reduce the SBS efficiency.

---

## Long-haul optical transmission systems

In long-haul WDM transmission systems there are basically five dominant limitations: OSNR, optical bandwidth, chromatic dispersion, PMD and nonlinear impairments. The tolerance with respect to these limitations scales linearly, or even quadratically, with the bit rate. Hence, to build robust long-haul transmission systems at high bit rates these transmission impairments should be considered and, if possible, compensated.

This chapter deals with the design of long-haul optical transmission systems and the required technologies to compensate for the dominant transmission impairments. First of all, in Section 3.1 the optical transmitter and receiver are discussed. Subsequently, in Section 3.2 the periodic amplification of optical signals is explained. Section 3.3 then describes the chromatic dispersion compensation in long-haul optical transmission systems and the design of dispersion maps. In Section 3.4 the compensation of PMD is briefly treated and Section 3.5 describes the impact of optical-add-drop multiplexing in transparent optical networks. Finally in Section 3.6, optical phase conjugation is discussed as a potential technology to compensate for nonlinear impairments.

### 3.1 Transmitter & receiver structure

An optical transmission link can be defined as the physical medium over which an information carrying optical signal propagates between a transmitter and a receiver. In the transmitter an optical carrier, generally the output of a laser, is modulated with a bit sequence. At the receiver, the optical signal is again converted into an electrical signal using one or more photodiodes. After a binary decision, ideally, the transmitted bit sequence is again obtained. This section

discusses the most common optical modulation principles (Section 3.1.1) and receiver structure (Section 3.1.2). Section 3.1.3 explains the use of forward error correction in optical communication systems.

### 3.1.1 Optical modulation

Optical modulation is the conversion of a signal from the electrical into the optical domain. This can be achieved by a variety of modulation technologies, which include directly modulated lasers (DML), electro-absorption modulators (EAM) and Mach-Zehnder modulators (MZM). In order to realize high-speed modulation an optical modulator should have (1) a high electro-optical bandwidth, (2) low optical insertion loss, (3) not induce undesired frequency chirp in the signal and (4) have a high enough extinction ratio. The extinction ratio is defined as the ratio of the energy in the '0' compared to the energy in the '1's.

Optical modulation can be most easily realized by direct modulation of the laser drive current. A DML is a very cost-efficient modulation technique as it is compact and does not require any further optical components apart from the transmitter laser. Although DMLs have been shown to operate at bit rates up to 40 Gb/s [102, 103] their modulation bandwidth is limited. High-speed modulation of a DML introduces frequency chirp, a residual phase modulation, alongside the desired intensity modulation and reduces the extinction ratio. The frequency chirp broadens the modulated spectrum, which makes it unattractive to use DML in WDM systems. They are today mainly used in low-bit rate applications, e.g. up to 2.5 Gb/s or short-reach 10-Gb/s transmission. In addition, frequency chirp reduces the chromatic dispersion tolerance. A special application of DMLs that is better suited for high-speed modulation is the use of frequency instead of amplitude modulation. When subsequently a narrowband optical filter is placed after the DML the frequency modulation is converted into intensity modulation with a high extinction ratio [104].

For high-speed modulation, external modulators are generally required as they result in a nearly chirp-free signal. An external modulator switches the incoming continuous-wave laser output ON or OFF, depending on the electrical drive signal applied to the modulator. An EAM modulates the optical field by controlling the absorption of the device material using the externally applied voltage. Modulation with an EAM can result in an optical signal with lower chirp than a DML and a high electro-optical bandwidth can be realized [105]. However, EAMs have a wavelength dependent performance, low extinction ratio (<10 dB typical), high insertion loss (10 dB typical) and a limited optical input power. EAMs mainly find applications in low-cost 10-Gb/s transmitters but have also been used extensively in (single-channel) OTDM transmission experiments.

The most widely used device for optical modulation is the MZM, first proposed by *Ernst Mach* [106] and *Ludwig Zehnder* [107]. A MZM consists of two 3-dB couplers with two interconnecting waveguides of equal length to create an interferometer, as show in Figure 3.1. The MZM waveguides are normally made from a Lithium-Niobate ( $LiNbO_3$ ) electro-optic crystal [108], but sometimes other materials are used such as Gallium Arsenide ( $GaAs$ ) [109], and Indium Phosphide ( $InP$ ) [110]. In such an electro-optic crystal the refractive index depends on the applied

electric field. An electrical drive signal can therefore modulate the refractive index of the crystal, which in turn changes the velocity of the light propagating through the waveguide. By choosing the electrical drive voltage level appropriately, the interference in the second 3-dB coupler can be either constructive or destructive. The difference in drive voltage which changes the interference from constructive to destructive is known as the  $V_\pi$  of the modulator. The two waveguides of a MZM can be modulated separately, which is known as dual-drive operation and which is used in Z-cut modulators. Alternatively, both waveguides can be coupled together, which is known as single-drive operation and which is used in X-cut modulators.

A typical  $V_\pi$  for a single-drive  $LiNbO_3$  MZM modulator is  $\sim 4$  V. In order to amplify the electrical drive signal to the required peak-to-peak voltage ( $V_{pp}$ ), high power and broadband driver amplifiers are therefore required. In a dual-drive modulator the peak-to-peak voltage swing of the electrical drive signal is reduced by a factor of two when a differential drive signal is applied to both waveguides. This is attractive for high-bit rates as there is a trade-off between the electro-optical bandwidth and the  $V_\pi$  of the MZM. A dual-drive modulator, on the other hand, has the drawback that it requires two broadband driver amplifiers to amplify the electrical drive signal to a sufficiently high peak-to-peak voltage.

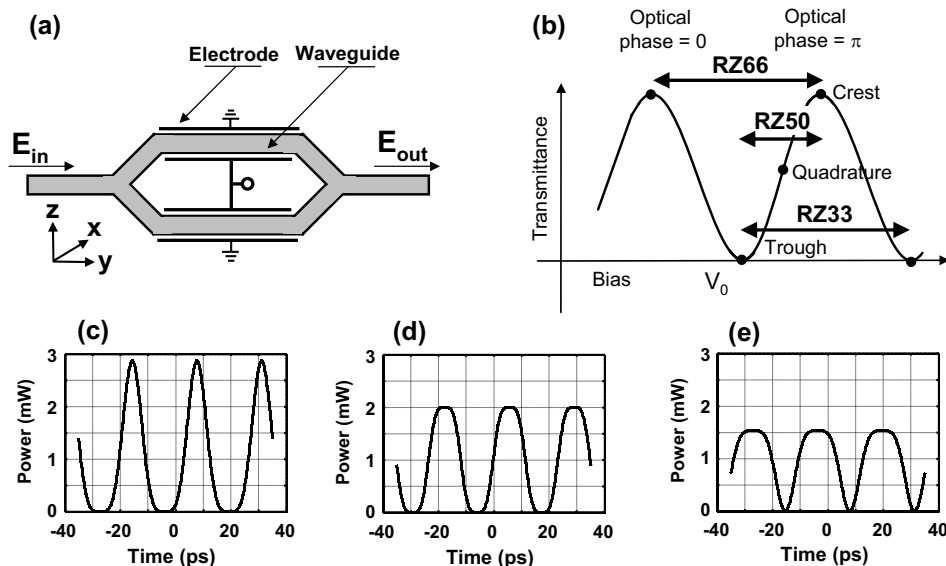


Figure 3.1: (a) Structure of a X-cut MZM, (b) Operation of a MZM for pulse carving, (c-e) RZ eye diagrams for (c) 33%, (d) 50% and (e) 66% pulse carving.

A MZM is particularly suitable for long-haul transmission as it has a high extinction ratio ( $>20$  dB typical), low insertion loss (4 dB typical) and is (nearly) wavelength-independent. The MZM can be used to generate several different optical modulation formats, which is described in more detail in Chapter 4. Another application of a MZM is pulse carving, i.e. the conversion of a non-return-to-zero (NRZ) signal into a return-to-zero (RZ) pulsed signal. RZ pulse carving is widely used for different optical modulation formats as it is less sensitive to imperfections in the transmitter. In high bit rate optical transmitters this can help to reduce the often stringent requirements on, for example, the electro-optical bandwidth of the modulator and driver amplifier voltage swing.

Table 3.1: DRIVE SIGNAL PROPERTIES FOR RZ PULSE CARVING WITH A MZM.

RZ pulse carving duty cycle	Modulator bias voltage	Drive signal voltage swing	Drive frequency
33%	crest	$2 \cdot V_\pi$	$0.5 \cdot \text{symbol rate}$
50%	quadrature	$V_\pi$	symbol rate
66%	trough	$2 \cdot V_\pi$	$0.5 \cdot \text{symbol rate}$

The impact of transmission impairments changes significantly when comparing NRZ and RZ modulation. Because of its more regular pulse shape, RZ modulation improves the tolerance against nonlinear signal impairments. Especially for a 40-Gb/s symbol rate, i.e. transmission limited by intra-channel nonlinear impairments, there is a clear improvement in nonlinear tolerance [111]. The main drawback of RZ modulation is the more complex transmitter structure as well as broadening of the optical spectrum. This reduces the tolerance against narrowband filtering, which is a significant disadvantage for spectrally efficient optical transmission or optical transmission systems with cascaded optical add-drop filtering. In addition, the broadened optical spectrum reduces the chromatic dispersion tolerance somewhat [112]. RZ pulse carving, on the other hand, improves the PMD tolerance as the ISI between adjacent bits is reduced [112, 113].

Using a MZM, three different RZ pulse shapes can be generated, as depicted in Figure 3.1. RZ pulse carving with a 50% duty-cycle is generated by driving a MZM with a sinusoidal drive signal at a frequency equal to the symbol rate. Both 33% or 66% duty-cycle are realized by driving a MZM with a sinusoidal drive signal at half the symbol rate. The drive frequency, bias voltage and drive signal voltage swing are summarized in Table 3.1. Note that RZ modulation with a 66% duty-cycle, in addition to the amplitude modulation, also encodes a  $180^\circ$  phase shift between consecutive symbols. It is therefore often referred to a carrier-suppressed return-to-zero (CSRZ). RZ modulation with a duty-cycle below 33% is possible by cascading two pulse carvers with a time offset between the two drive signals. This has been used in high-bite rate OTDM transmission experiments [114]. The narrower the duty-cycle of the RZ pulse, the broader the optical spectrum and the higher the peak-to-average power. The change in pulse shape is evident from Figure 3.1c-e. Because of the more narrow optical spectrum, RZ modulation with a high duty-cycle is often preferred in WDM transmission.

### 3.1.2 Optical receivers

The most common configuration of an optical receiver is depicted in Figure 3.2. It can be subdivided in the lower speed optical receivers (up to  $\sim 10$ -Gb/s) and high bit-rate receivers for 40-Gb/s transmission systems. Both types of optical receiver use a high-speed photodiode to convert the optical signal to the electrical domain. As a photodiode only detects the power envelope of the optical, any phase information is discarded from the signal. There are several types of high-speed photodiodes, but the most common one found in optical receivers is a *p-i-n* photodiode. A *p-i-n* photodiode is a semiconductor device that contains a *p-n* junction with an

undoped (intrinsic) layer between the  $n$  (negative) and  $p$  (positive) layers. When incident light is absorbed in the depletion region of the intrinsic layer, a photocurrent is generated. Photodiodes for the  $1.5\mu\text{m} - 1.6\mu\text{m}$  wavelengths range are normally made from indium gallium arsenide (In-GaAs). The electro-optical conversion in a photodiode cannot detect arbitrary high frequencies, and a photodiode therefore low-pass filters the signal. The electro-optical 3-dB bandwidth of a photodiode should be in excess of 70% of the symbol rate. A photodiode is further characterized by its responsivity in  $[A/W]$ , which defines the efficiency with which the photodiode converts the optical signal into a photocurrent. Most p-i-n photodiodes have a responsivity of 50%-70%, but high-speed photodiodes often have a somewhat reduced responsivity.

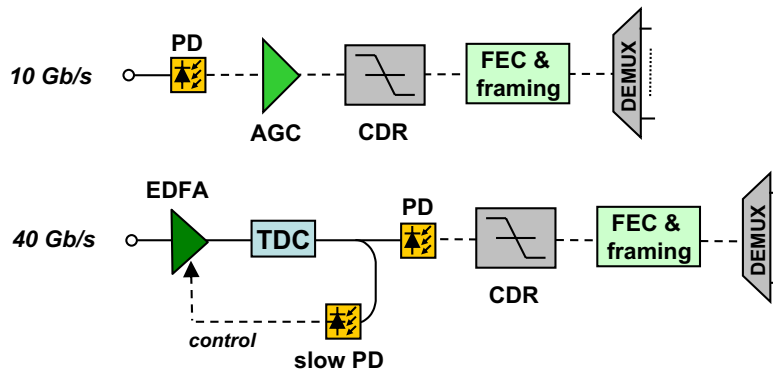


Figure 3.2: Optical receiver configuration.

For lower speed optical receivers, a transimpedance amplifier is typically used for automatic gain control (AGC). The transimpedance amplifier amplifies the photocurrent, which has typical peak-to-peak voltage of 10 mV for  $50\Omega$  termination, and controls the gain such that a constant output voltage is obtained. For high-speed optical receivers, the bandwidth and gain of a transimpedance amplifier can be inadequate. In this case, an optical pre-amplifier is used in the receiver to amplify the signal. In addition, 40-Gb/s receivers require tunable dispersion compensation (TDC) to optimize the accumulated dispersion, this is discussed in more detail in Section 3.3.

In the clock and data-recovery (CDR), the receiver is synchronized with the signal in order to sample at the correct time instant within the symbol period. The data recovery then takes a digital decision on the signal. A variable sampling threshold is normally used for data recovery, as the optimum threshold changes under the impact of transmission impairments such as chromatic dispersion and PMD. This threshold can be optimized using a feedback signal from the forward error correction (FEC) that minimizes the BER. Afterwards, FEC decoding is applied to recover errors that occurred in the received sequence and the transmitted data is extracted from the transport frame (e.g OTN [optical transport network] framing). The signal is then time de-multiplexed for further processing.

### 3.1.3 Forward-error correction

For long-haul transmission systems, the signal quality at the receiver is normally too low to ensure error-free transmission ( $\text{BER} < 10^{-13}$ ). For such systems, FEC enables the correction of bit-errors after transmission by encoding the data appropriately at the transmitter. FEC coding also increases the system robustness against signal impairments such as chromatic dispersion and PMD.

FEC coding requires that some redundant information is added to the transmitted data, which is referred to as the FEC overhead. In optical communication systems the typical FEC overhead is 7%, although in submarine ultra long-haul transmission a FEC overhead of 25% is normally used. This increases the bit rate, for example, from 10 Gb/s to 10.709 Gb/s. The use of FEC results in a coding gain, which defines the difference in required OSNR for a BER of  $10^{-13}$  with and without FEC coding. The highest BER before FEC that can be corrected to a BER below  $10^{-13}$  after FEC is typically referred to as the FEC limit. When the bit-errors are not Gaussian distributed but come in error-bursts (e.g. PMD-induced) the FEC code might not be able to correct all bit-errors at the FEC limit. FEC coding therefore interleaves the data before transmission in order to obtain Gaussian-like error statistics after transmission [115]. In optical transmission experiments, the use of FEC is normally assumed by taking into account the 7% required overhead and measuring the transmission performance at the FEC limit.

FEC has been used since the 1960s in radio communication, but the first application to fiber-optic transmission systems was reported by *Grover* in 1988 [116]. The first commercial applications of FEC were submarine optical transmission systems in the early 1990's [117]. In particular, the Reed-Solomon(RS) code RS(255,239) has been adopted for submarine-transmission systems and has been specified in ITU-T G.975 [118]. This code is known as the first-generation FEC and provides a coding gain of up to 5.8 dB. Nowadays, the most common error correcting codes used in optical transmission are known as second-generation FEC codes. These codes consist of two interleaved codes, where the individual codes can be, for example, RS or Boss-Chaudhuri-Hocquenghem (BCH) codes or a combination of both. Such codes have a code gain of  $\sim 8.5$  dB and have been standardized in ITU-T G.975.1 [119]. An overview of FEC in optical transmission systems is given in [120], where also more advanced codes using turbo codes and soft-decision decoding are discussed.

For the transmission experiments described in this thesis we assume the use of a concatenated RS(1023,1007)/BCH(2047,1952) code with 7% overhead as defined in ITU-T G.975.1 subclause I.4. This code corrects a  $2.23 \cdot 10^{-3}$  BER before FEC to a  $1 \cdot 10^{-13}$  BER after FEC, a coding gain of 8.3 dB. This code is widely used in transmission experiments and deployed long-haul transmission systems [121]. In some long-haul transmission experiments in the literature a more advanced code is used that achieves a coding gain of 8.8 dB with a 6.69% overhead [122, 123]. This code is defined in ITU-T G.975.1 subclause I.9 and consists of interleaved BCH(1020,988) with 10-fold iterative decoding. A  $4 \cdot 10^{-3}$  BER before FEC is corrected by this code to a  $1 \cdot 10^{-13}$  BER after FEC.



## 3.2 Fiber loss compensation

As discussed in Section 2.1, optical fiber is a low-loss transmission medium that allows for considerable transmission distances without re-amplification of the signal. However, in order to realize long-haul transmission systems (1,000 km - 3,000 km) periodic amplification is required after each *fiber span* in order to compensate for fiber loss. The span length varies strongly in deployed transmission systems, but a typical design value is a span attenuation of 21 dB. Depending on fiber quality and splicing losses this translates into a span length between 80 km and 110 km. In between the fiber spans different amplification technologies can be used to compensate for the fiber loss. In this section we discuss doped fiber amplifiers and Raman amplification.

### 3.2.1 Erbium-doped fiber amplifiers

In long-haul optical transmission systems, optical amplification is nearly exclusively used to amplify the signal in between fiber spans. One of the main advantages of optical amplification over optical-electrical-optical conversion is that it can amplify the optical signal independently of modulation format and bit rate. In addition, a single amplifier can amplify the full C-band transmission window. The most common type of optical amplifiers are Erbium doped fiber amplifiers (EDFA). EDFAs are constructed by doping a single mode fiber with Erbium ( $Er^{3+}$ ) ions and pumping the fiber with one or more pump lasers. Early work on EDFAs was pioneered by *Mears* [124] and *Desurvire* [125] in 1987. A detailed overview of EDFA design and technologies can be found in [126].

The general structure of an EDFA is shown in Figure 3.3a. The actual optical amplification takes place in the Erbium-doped fiber with a typical length of  $\sim 10$  meters, which is pumped with light from one or more laser diodes. In Figure 3.3a the fiber is bidirectionally (forward and backward direction) pumped by two laser diodes, which is the most common for optical amplifiers that require a high output power. Either co-directional or counter-directional pumping is also possible when the required output power is not too high. The input signal and output of the pump lasers is combined using a pump combiner, which allows for a low insertion loss. Optical isolators are normally required in optical amplifiers to prevent backreflections. The input isolator prevents light from the counter-directional pump or amplified spontaneous emission (ASE, defined later) to propagate backwards out of the amplifier input. The output isolator prevents that the output light can be reflected back into the amplifier, which could cause lasing. The gain equalizing filter is necessary to ensure that all WDM channels are amplified uniformly and that a flat output spectrum is obtained. Gain equalization can be realized using a variety of filter technologies, such as thin-film filter [127] or long-periodicity fiber Bragg gratings [128].

The wavelength of the pump signal is either around 980 nm or 1480 nm. The energy levels (vibrational states) in Figure 3.3c are not discrete levels but rather a manifold, which is due to the non-crystalline nature of silica. Each energy level that appears as a discrete spectral line in an isolated Erbium ion is split into a manifold when silica glass is doped with the Erbium ions, this

is known as the Stark effect. The Stark effect explains why amplification occurs in a wavelength band rather than at a single wavelength. Pumping with a 1480 nm laser excites the Erbium ions from the ground-state manifold  $^4I_{15/2}$  into the  $^4I_{13/2}$  manifold, from where they can amplify light in the 1500-nm wavelength region via stimulated emission. In the case of pumping with a 980-nm laser the ions are first excited to the  $^4I_{11/2}$  manifold, from where there is a quick ( $\sim 1\mu s$ ) non-radiative transfer (relaxation) to the  $^4I_{13/2}$  manifold. The  $^4I_{13/2}$  manifold is metastable with a half-time of around 10 ms, which is known as the fluorescence time. This is orders of magnitude longer than the bit rates that are normally used in optical communication systems (i.e. 2.5-Gb/s to 40-Gb/s). An exception to this are systems that use burst-mode transmission where the burst-interval can be longer than the fluorescence time [129].

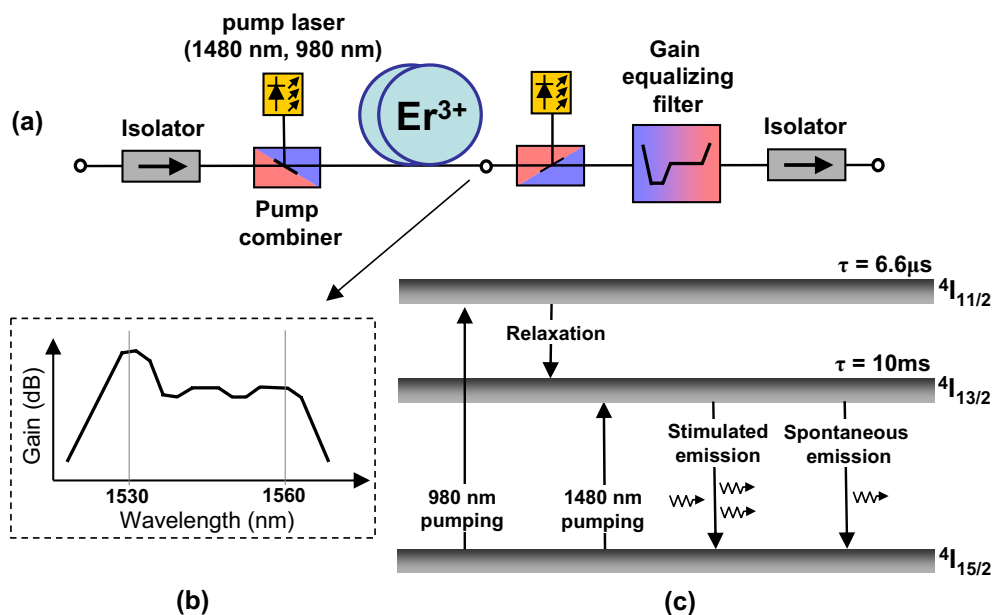


Figure 3.3: (a) schematic of an EDFA; (b) gain spectra of a C-band EDFA and (c) energy level diagram of an erbium-doped silica fiber.

The principle behind optical amplification is stimulated emission. In stimulated emission, as first described by *Einstein* in 1917 [130], a photon from the pump signal transfers a part of its energy to the Erbium ion which makes a transition to a higher-energy vibrational state. When a photon from the input signal collides with the Erbium ion it falls back to the lower vibrational state and at the same time releases a duplicate photon with the same properties (frequency, state of polarization). In optical amplification, this process is repeated numerous times which results in an exponential increase in signal power. The typical gain of an EDFA can therefore be in excess of 40 dB. The output power of an EDFA strongly depends on the number of pump lasers and their respective pump powers. A typical value for the EDFA output power is  $\sim 23$  dBm, which is generally sufficient to amplify up to 80 WDM channels in the wavelength band between roughly 1525 nm and 1570 nm. As depicted in Figure 3.3b, the EDFA generally exhibits a gain peak around 1530 nm. The spectral gain profile can be flattened by doping the Erbium-doped fiber with co-dopants such as Aluminium Oxide ( $Al_2O_3$ ) [126], or through the use of gain flattening filters.

Besides stimulated emission, also spontaneous emission occurs in an optical fiber amplifier. In spontaneous emission, an ion in the high energy  $^4I_{13/2}$  manifold falls back to the ground state, emitting a photon in the process. In contrast to stimulated emission, the emitted photon has an arbitrary frequency and state of polarization. As the spontaneous emission is in turn also amplified along the optical amplifier, this causes amplified spontaneous emission (ASE). ASE is the most dominant for high gain amplifiers, where a large part of the output signal can consist of ASE. The ASE generated by an optical amplifier is added to the amplified signal, which reduces the OSNR. An optical amplifier can therefore be characterized with its noise figure, which denotes the difference in OSNR between the input and output of the amplifier. A practical C-band EDFA normally has a noise figure between 4 dB and 6.5 dB.

Pumping the erbium-doped fiber with a 980-nm laser allows the highest gain efficiency and lowest noise figure. With a 1480-nm pump wavelength a higher power efficiency can be achieved as no transfer to the  $^4I_{11/2}$  manifold occurs. Such a transfer reduces the power efficiency, as part of the energy is lost through relaxation when the ion falls back to the  $^4I_{13/2}$  manifold. On the other hand, stimulated emission of the 1480-nm pump wave occurs along the Erbium-doped fiber. The fraction of Erbium ions in the excited  $^4I_{13/2}$  manifold is therefore much smaller, which reduces the gain efficiency, i.e. the small-signal gain as a function of pump power. As a result, a longer Erbium doped fiber is required which generally results in a higher noise figure. Optical amplifiers for the L-band also used Erbium-doped fiber, but this requires a different optimization of the fiber length ( $\sim 100$  m) and Erbium ion concentration. A single erbium-doped fiber can therefore not amplify both wavelength bands.

The EDFA belongs to a broader family of rare-earth doped fiber amplifiers that also includes neodymium, ytterbium, praseodymium, or thulium doped fiber amplifiers [131]. Doping with other rare-earth elements can be used to construct optical amplifiers for wavelengths other than the C- or L-band. Ytterbium doping can further be used to construct Ytterbium-Erbium co-doped double-clad optical amplifiers [132, 133]. In such amplifiers the 980-nm pump is absorbed by the Ytterbium ions, which are excited to a higher vibrational state. The Ytterbium ions subsequently transfer their energy to the Erbium ions. As the Ytterbium doping density can be much larger than the Erbium doping density this allows for a higher amplifier gain. The co-doping is often combined with double-clad amplifiers. A double-clad amplifier pumps the cladding of the fiber to obtain a more equal distribution of the pump power along the fiber length. Such amplifiers can have output powers as high as 33 dBm. In Section 6.5 such an amplifier is used as pump amplifier for phase conjugation.

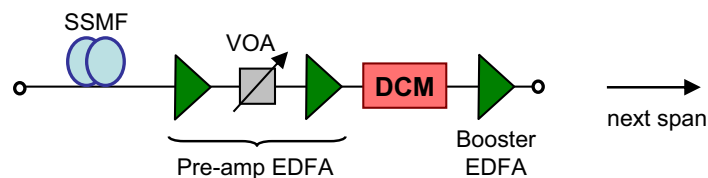


Figure 3.4: EDFA structure used in the long-haul optical transmission experiments.

Figure 3.4 shows the typical EDFA structure used in the long-haul transmission experiments discussed in this thesis. The received optical signal is first fed into a pre-amplifier stage. A pre-

amplifier EDFA is optimized for high gain and a low noise figure. The pre-amplifier stage can consist of two separate EDFAs with a variable optical attenuator (VOA) in between both amplifiers. The VOA is used to dynamically reduce the tilt in the wavelength spectrum, which can either result from SRS along the fiber or the preamplifier amplification itself. After the preamplifier, generally, a dispersion compensation module (DCM) is used for chromatic dispersion compensation. The signal is then fed to the booster EDFA, which is optimized for high output power. The combination of pre-amplifier and booster stage allows the realization of both a low-noise figure and high output power.

### 3.2.2 Raman amplifiers

A Raman amplifier is an optical amplifier based on Raman gain, which results from the effect of SRS (see Section 2.4.8). The use of SRS to construct a Raman amplifier was proposed by *Stolen et. al.* in 1972 [134] and demonstrated by *Hegarty et. al.* in 1985 [135]. The most well known type of Raman amplification is distributed Raman amplification, which uses the transmission fiber as a gain medium. A Raman amplifier can be forward (co-propagating) pumped, backward (counter-propagating) pumped or a combination of both (bi-directional). Backwards pumped Raman amplification is the most common and the power of the pump  $P_p(z)$  and signal  $P_s(z)$  can be expressed as follows,

$$\begin{cases} P_p(z) = P_p(L) \exp(-\alpha_p(L-z)) \\ P_s(z) = P_s(0) \exp(-\alpha_s z) \exp\left(\frac{g_R}{A_{eff}} \frac{P_p(L)}{\alpha_p} [\exp(-\alpha_p(L-z)) - \exp(-\alpha_p L)]\right) \end{cases} \quad (3.1)$$

Where  $g_R$  is the Raman gain coefficient in  $[m/W]$ .  $P_p(L)$  is the Raman pump power in  $[W]$ , which is launched counter-propagating to the optical signal from the back-end of the transmission fiber.  $P_s$  in  $[W]$  is the signal power launched into the transmission fiber. The attenuation coefficients  $\alpha_p$  and  $\alpha_s$  in  $[Np/km]$  denote the fiber attenuation at the pump and signal wavelengths. The attenuation coefficients are normally different for the pump and signal, as the pump is in the 1445 nm wavelength region where the fiber attenuation is slightly higher. The Raman gain coefficient of depolarized light is  $0.428 \cdot 10^{-13}$  m/W for SSMF [98]. Note that pump depletion is not included in this equation.

In Figure 3.5a the optical signal power as a function of transmission distance is depicted for backwards pumped Raman amplification with  $A_{eff} = 72.8 \mu m^2$ ,  $\alpha_s = 0.2$  dB/km,  $P_s = 0$  dBm,  $\alpha_p = 0.25$  dB/km and  $P_p = 24.5$  dBm. This results in Raman ON/OFF gain  $G_{on/off}$  of 12.4 dB. The Raman ON/OFF gain can also be denoted through

$$G_{on/off} = \exp\left(\frac{g_R}{A_{eff}} P_p(L) L_{eff}\right) = \exp\left(\frac{g_R}{A_{eff}} \frac{P_p(L)}{\alpha_p} [1 - \exp(-\alpha_p L)]\right), \quad (3.2)$$

Raman amplification does not necessarily compensate the full span loss, and the remaining part can be compensated using an EDFA. This is known as hybrid EDFA/Raman amplification. This improves the OSNR compared to EDFA-only amplification as the lowest power that occurs along

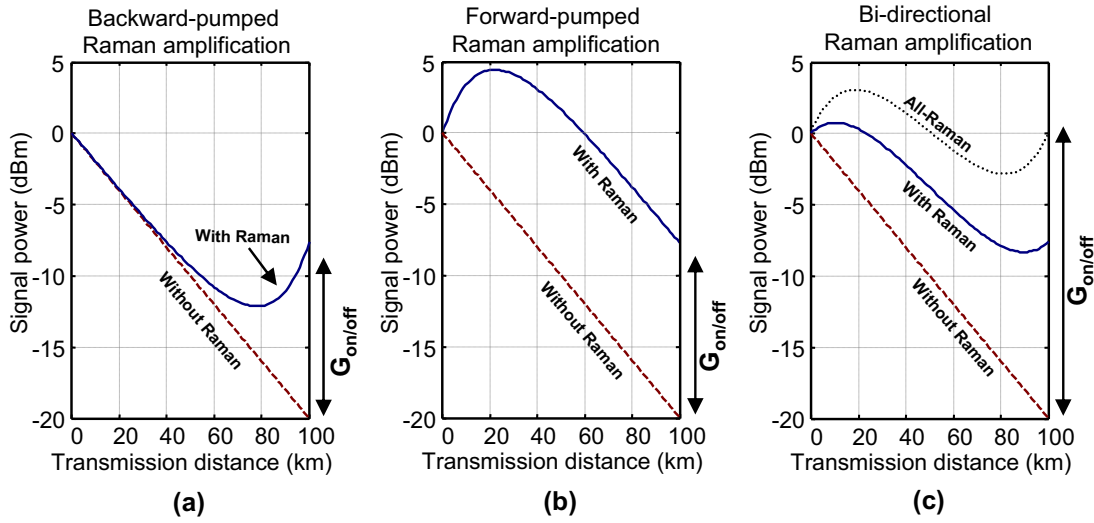


Figure 3.5: Optical signal power as a function of the transmission distance for (a) Backward-pumped Raman, (b) Forward-pumped Raman and (c) bi-directional Raman and all-Raman amplification. All schemes use a total pump power of 24.5 dBm, except for all-Raman amplification which uses a total pump power of 26.5 dBm.

the link is now much higher. The noise figure of a hybrid Raman/EDFA amplifier can be characterized with the effective noise figure. The effective noise figure of a Raman amplifier is defined as the noise figure that EDFA-only amplification would need to have in order to achieve the same OSNR as obtained with Raman amplification. The effective noise figure of a hybrid EDFA/Raman amplifier can be as low as -3 dB [136, 137]. However, intra-band SRS between the Raman pumps increases the noise figure for lower wavelengths and a typical hybrid-EDFA/Raman amplification scheme has therefore an effective noise figure between 0 dB and 1 dB for the worst WDM channel [138].

A further possible amplification scheme is forward-pumped Raman amplification, where the signal and pump are co-propagating along the fiber. This scheme is less desirable as it increases the signal power in the first part of the transmission link, which results in increased nonlinear impairments (see Figure 3.5). For the same pump power, backward and forward-pumped Raman amplification have the same ON/OFF Raman gain. Equation 3.2 is therefore also valid for forward-pumped Raman amplification when  $P_p(L)$  is replaced with  $P_p(0)$ . The evolution of the signal and pump powers along the transmission fiber is now denoted through,

$$\begin{cases} P_p(z) = P_p(0) \exp(-\alpha_p z) \\ P_s(z) = P_s(0) \exp(-\alpha_s z) \exp\left(\frac{g_R}{A_{eff}} \frac{P_p(0)}{\alpha_p} [1 - \exp(-\alpha_p z)]\right) \end{cases} \quad (3.3)$$

Figure 3.5b shows an example of the power evolution for the forward-pumped scheme, using the same parameters as the backward-pumped scheme. Finally, in bi-directional Raman amplification, Raman pumps are both co-propagating as well as counter-propagating with the signal. This can be used for all-Raman amplification. All-Raman amplification is depicted in Figure 3.5c, using a 23.5-dBm pump power for both co-propagating and counter-propagating directions. Be-

cause of the high required pump powers for all-Raman amplification it is desirable to combine it with fiber types that have a high Raman gain coefficient, such as NZDSF.

A Raman amplifier is very suitable for WDM transmission as the 3-dB bandwidth of the Raman gain spectrum is approximately 55 nm. To further flatten and broaden the Raman gain spectrum, multiple Raman pump laser at different wavelengths are often used. This allows for a Raman amplifier with a flat 100-nm gain spectrum [139], which is nearly equal to the Stokes shift in SSMF. A multi-pump Raman amplifier consists often of a single strong pump and several smaller pumps to equalize the gain spectrum [138]. For the transmission experiments in this thesis, Hybrid EDFA/Raman amplification is used with four Raman pumps. A 300-mW polarization-multiplexed pump at 1423 nm and depolarized pumps at 1436 nm (150 mW), 1453 nm (90 mW) and 1467 nm (150 mW) [140].

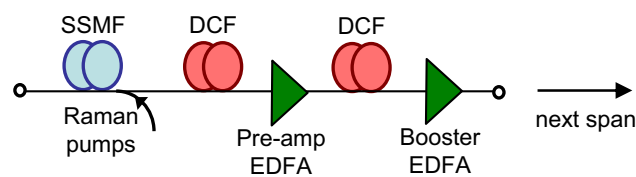


Figure 3.6: Hybrid Raman/EDFA structure used in the long-haul optical transmission experiments.

Figure 3.6 depicts the typical hybrid Raman/EDFA structure used in the long-haul transmission experiments discussed in this thesis. The SSMF is backward pumped with an average Raman gain between 11 dB and 14 dB, depending on the transmission fiber used in the experiment. The insertion loss of the DCF is distributed by placing a DCF module after the Raman pumps, which compensate for part of the chromatic dispersion. The remaining chromatic dispersion is compensated between the pre-amplifier and booster EDFA. Alternatively, the full chromatic dispersion can be compensated with a DCF module placed after the Raman pumps followed by only a pre-amplifier (see Section 10.6.3).

Raman amplification has also some important drawback compared to EDFAs. The pump powers required for Raman amplification are typically significantly higher than the pump powers required in an EDFA. This results in a more expensive amplifier design and the high pump powers can reduce the reliability of the pump lasers [138]. Finally, the distributed nature of high pump powers in Raman amplification makes handling safety precautions important. The high optical powers can cause injuries to skin and eyes and cause optical connectors to damage easily when there is dirt or dust on the connector [141, 142]. As an alternative, discrete Raman amplification can be used. In discrete Raman amplification the high optical powers are contained within the amplifier subsystem and do not propagate into the transmission fiber. Instead DCF or specially designed fiber is used as a Raman gain medium. The high Germanium doping in the core and the small effective area results in  $\sim 7$  times the Raman gain efficiency of SSMF [143]. In Section 3.3.2, discrete Raman amplification is used to investigate the feasibility of lumped chromatic dispersion compensation.

### 3.2.3 Optical-signal-to-noise ratio

The ASE added by the optical amplifiers in a long-haul transmission link ultimately limits the feasible transmission distance. When we consider a long-haul transmission link with  $N_{spans}$ , the total ASE power  $P_{ASE}^{tot}$  in [W] added by all optical amplifiers along the link equals  $P_{ASE}^{tot} = P_{ASE}N_{spans}$ . This is valid under the assumption that a single amplifier adds a noise power  $P_{ASE}$  and that all spans have the same insertion loss. After  $N_{spans}$ , the ratio between ASE power and signal power is known as the OSNR and is defined as,

$$OSNR = \frac{P_{output}}{P_{ASE}N_{spans}} = \frac{P_{output}}{2N_0\Delta f_0}, \quad (3.4)$$

where  $P_{output}$  defines the signal power at the output of the last amplifier of the transmission link and has unit [W]. The noise power can be expressed as the noise power spectral density per polarization  $N_0$ . For measurement purposes the OSNR is often normalized with respect to a certain optical bandwidth, usually 0.1 nm, which is expressed through the reference bandwidth  $\Delta f_0$  in [Hz]. The factor two results from the two orthogonal polarization dimensions in the fiber. Note that, although the ASE is assumed to be unpolarized, only the ASE that is polarized parallel to the signal results in signal-spontaneous beat noise upon detection with the photodiode. The ASE in the orthogonal polarization is added to the signal upon detection with the photodiode, but there is no signal-spontaneous beat noise as the ASE does not coherently interfere with the signal. It therefore worsens the OSNR tolerance with only  $\sim 0.3$  dB [10], which results from spontaneous-spontaneous beat noise.

The noise power spectral density of an amplifier can be expressed as,

$$N_0 = n_{sp}hf_0(G-1)N_{spans} = n_{sp}hf_0(\alpha L_{span} - 1)N_{spans}, \quad (3.5)$$

where  $n_{sp}$  is the spontaneous emission factor of a *single* amplifier,  $f_0$  the reference frequency in [Hz] and  $h$  is Planck's constant ( $6.626068 \cdot 10^{-34}$  m<sup>2</sup>kg/s). The amplifier gain  $G$  is substituted with the fiber span loss  $\alpha L_{span}$  under the assumption that the gain of each amplifier is equal to the span loss.

The noise figure of an EDFA can then be expressed as [144],

$$F = 2n_{sp}\left(1 - \frac{1}{G}\right) + \frac{1}{G} = \frac{2n_{sp}(\alpha L_{span} - 1) + 1}{\alpha L_{span}}. \quad (3.6)$$

In the limit of high gain ( $G = \alpha L_{span} \gg 10$ ) the noise figure therefore approaches  $F = 2n_{sp}$ . This shows that even a perfect optical amplifier  $n_{sp} = 1$  has a noise figure of 3 dB.

Combining Equations 3.4, 3.5 and 3.6 gives an expression for the OSNR as a function of the amplifier noise figure and the span loss.

$$\begin{aligned} OSNR &= \frac{P_{output}}{(\alpha L_{span}F - 1)hf_0\Delta f_0N_{spans}} \\ &= \frac{\alpha L_{span}P_{input}}{(\alpha L_{span}F - 1)hf_0\Delta f_0N_{spans}} \approx \frac{P_{input}}{Fhf_0\Delta f_0N_{spans}}. \end{aligned} \quad (3.7)$$

Denoting Equation 3.7 in [dB] gives,

$$\begin{aligned}
 OSNR[dB] &\approx 10\log_{10}\left(\frac{P_{input}}{N_{spans}Fhf_0\Delta f_0}\right) \\
 &= P_{input}[dBm] - 10\log_{10}(N_{spans}) + 58dBm - F[dB] \\
 &= P_{output}[dBm] - \alpha L_{span} - 10\log_{10}(N_{spans}) + 58dBm - F[dB],
 \end{aligned}
 \tag{3.8}$$

where  $-10\log_{10}(hf_0\Delta f_0)$  equals 58 dBm for a reference frequency  $f_0$  of 193.4 THz (1550 nm) and a reference bandwidth  $\Delta f_0$  of 12.5 GHz (0.1 nm). We can therefore conclude that the OSNR scales linearly with  $P_{output}$  and inversely with the insertion loss of the fiber span. In order to increase the OSNR at the receiver, either the input power into the fiber span (which equals  $P_{output}$ ) has to be increased or the loss of the fiber span  $\alpha L_{span}$  has to be reduced. The input power is ultimately limited by degradations due to nonlinear impairments. The span loss can be reduced by spacing the amplifiers closer together, as is often done for ultra long-haul transmission systems that have to bridge transoceanic distances, or the use of Raman amplification.

### 3.3 Chromatic dispersion compensation

Chromatic dispersion accumulates along an optical fiber which causes ISI and limits the feasible transmission distance, i.e. the dispersion-limited reach. The normalized dispersion length in Equation 2.8 shows that there is a quadratic dependence between the dispersion-limited reach and the symbol rate. This is also evident from Table 3.1, which depicts the dispersion-limited transmission reach over SSMF. Hence, in order to realize long-haul transmission systems, chromatic dispersion compensation is required.

Table 3.2: DISPERSION-LIMITED REACH FOR NRZ-OOK AND A 2-DB OSNR PENALTY.

Symbol rate (Gb/s)	SSMF (km)
2.7	640
10.7	40
42.8	2.5
107	0.4

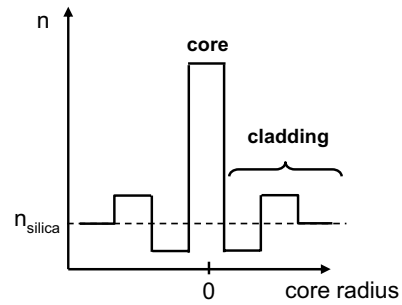


Figure 3.7: Refractive index profile of a DCF.

Chromatic dispersion compensation can generally be subdivided into two categories, in-line and accumulated dispersion compensation. The bulk of the chromatic dispersion in a long-haul transmission link is normally compensated using *in-line* dispersion compensation. Several technologies have been developed for in-line chromatic dispersion compensation, such as dispersion compensating fiber (DCF), dispersion managed cables [145], Higher-order mode DCF [146], fiber Bragg gratings and optical phase conjugation.



Nowadays, DCF is the standard solution to compensate for the chromatic dispersion accumulated in long-haul optical transmission systems. It yields colorless, slope-matched dispersion cancellation with negligible cascading impairments. DCF was first proposed by *Lin et. al.* in 1980 [147] and demonstrated in 1992 by *Dugan et. al.* [148]. DCF has a smaller core effective area ( $\sim 20 \mu\text{m}^2$ ) and different core index profile in comparison to SSMF. Figure 3.7 shows the core index profile of DCF, which normally has triple-cladding structure. The triple cladding index profile has a narrow high-index core surrounded by a deeply depressed cladding followed by a raised ring. The refractive index of the core is raised through  $\text{GeO}_2$  doping. The small core size and triple-cladding structure forces a larger part of the optical field to propagate in the cladding, which increases the significance of waveguide dispersion and results in large negative values of  $D$ . The triple cladding design also changes the sign of the dispersion slope such that the DCF is slope-matched with the transmission fiber. State-of-the-art DCF can therefore accurately compensate the chromatic dispersion of all channels in the C-band. The high ( $\text{GeO}_2$ ) doping in the core of the DCF and the fact that a larger part of the optical field propagates in the cladding slightly raises the attenuation of the DCF, which is typically close to  $\alpha = 0.5 \text{ dB/km}$ . It also makes DCF more vulnerable to core ovality than SSMF, which results in higher module PMD [149] and raises the nonlinear coefficient. An extensive overview of dispersion compensation using DCF can be found in [143].

Despite the fact that the DCF consists of several kilometers of fiber, it is normally used as dispersion compensation module (DCM) where the fiber is coiled around a spool for *discrete* dispersion compensation. This is due to the higher insertion loss per kilometer and the higher complexity of cable installation, which makes it unattractive to use DCF as part of the transmission fiber. The insertion loss of state-of-the-art DCM is  $\sim 6 \text{ dB}$  for a module that can compensate for the chromatic dispersion of 100 km of SSMF (1700 ps/nm). Normally, a two-stage EDFA structure with mid-stage access for the DCM is used to compensate the insertion loss (see Figure 3.4). In such a two-stage amplifier, the input power into the DCF is an important design parameter. The relatively high insertion loss of the DCF must be compensated while keeping at the same time the input powers into the DCF low enough to avoid nonlinear impairments. This relative impact of nonlinear impairments can be quantized using a path-averaged nonlinearity  $\hat{\gamma}$ .

$$\hat{\gamma} = \gamma \int_{z=0}^{z=L} \exp(-\alpha z) dz, \quad (3.9)$$

where  $L$  is the length of the fiber and  $\alpha$  is denoted in  $[Np/km]$ . We now consider 100 km of SSMF and matching DCF and use the fiber parameters in Table 3.3. The path-averaged nonlinearity is then 24.5 dB and 25.0 dB for the SSMF and DCF, respectively. The difference between SSMF and DCF is small, because the impact of the higher DCF nonlinearity is offset through the higher DCF attenuation coefficient. The path average nonlinearity is independent of the input power, but by multiplying with the input power we obtain an expression for the total nonlinear phase shift.

$$\phi_{NL} = \phi_{NL,SSMF} + \phi_{NL,DCF} = \hat{\gamma}_{SSMF} P_{0,SSMF} + \hat{\gamma}_{DCF} P_{0,DCF}. \quad (3.10)$$

The DCF-induced *increase* in the total nonlinear phase shift can be denoted as,

$$\Delta\phi_{NL,DCF} = \frac{\phi_{NL,SSMF} + \phi_{NL,DCF}}{\phi_{NL,SSMF}} = 1 + \frac{\hat{\gamma}_{DCF}}{\hat{\gamma}_{SSMF} \cdot \Delta P_0}, \quad (3.11)$$

Table 3.3: SSMF AND DCF FIBER PARAMETERS, DCF PARAMETERS ARE TAKEN FROM [143].

	SSMF	DCF	unit
Insertion loss ( $\alpha$ )	0.2	0.5	[dB/km]
Dispersion ( $D$ )	17	-170	[ps/km/nm]
Nonlinearity ( $\gamma$ )	1.3	5.24	[W <sup>-1</sup> km <sup>-1</sup> ]

where  $\Delta P_0$  is the difference input power between the SSMF and DCF,

$$\Delta P_0 = \frac{P_{0,SSMF}}{P_{0,DCF}}. \quad (3.12)$$

This shows that when the input power difference between SSMF and DCF increases, the DCF-induced contribution to the total nonlinear phase shift diminishes.

The total noise figure of a two-stage amplifier can be calculated using Friis's formula [126].

$$F_{tot} = F_1 + \frac{\alpha_{DCF} L_{DCF} \cdot F_2 + 1}{G_1} = F_1 + \frac{\alpha_{DCF} L_{DCF} \cdot F_2 + 1}{\alpha_{SSMF} L_{SSMF} / \Delta P_0} \quad (3.13)$$

where  $F_{tot}$  is the total noise figure of the amplifier. The noise figure of the pre-amplifier  $F_1$  and booster  $F_2$  are assumed to be 5.0 dB and 7.5 dB, respectively [143]. The pre-amplifier gain  $G_1$  is equal to the SSMF span loss minus  $\Delta P_0$ . Figure 3.8 depicts the total noise figure and the increase in nonlinear phase shift for a 100 km SSMF span using the fiber parameters of Table 3.3. This shows that a smaller difference in input power leads to an increased nonlinear phase shift but a decrease in total noise figure of the two-stage EDFA. Combining the total noise figure and the increase in nonlinear phase shift gives a measure of the optimal difference in input power between SSMF and DCF. This shows that the optimum power difference is 6.5 dB, which results in a combined penalty of  $\sim 7$  dB. When dispersion compensation is not required, a single-stage EDFA with a 5 dB noise figure would in principle be sufficient to amplify the signal and no nonlinear phase shift would be accumulated in the DCF. Hence, we can conclude that DCF-based chromatic dispersion compensation results in a  $\sim 2$  dB penalty due to the combined effect of an increased nonlinear phase shift and higher effective noise figure. We note that this penalty is independent of the modulation format, as it is based on the DCF-induced increase in nonlinear phase shift and not the absolute nonlinear tolerance. This simplified analysis does not take the amplifier spectral tilt into account, which might change the choice of the SSMF and DCF input powers.

The chromatic dispersion at the receiver is referred to as the *accumulated* dispersion. The accumulated chromatic dispersion of a long-haul link is normally only roughly known as not all fiber is measured accurately before deployment. In addition, the chromatic dispersion slope, different propagation paths in a transparent optical network and temperature dependence [150] also introduce a variation in the accumulated dispersion at the receiver. For  $\leq 10$  Gb/s transmission systems the accumulated dispersion tolerance is generally large enough such that a standard

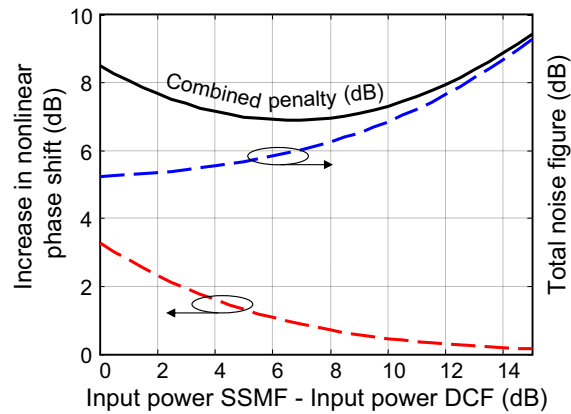


Figure 3.8: Effective noise figure and increase in nonlinear phase shift as a function of the input power difference between SSMF and DCF, the solid curve shows both penalties combined.

direct detection receiver can compensate for the variations that occur. For higher symbol rates (e.g. 40-Gb/s), on the other hand, the accumulated dispersion tolerance is generally too small to compensate for such variations. This can be solved by using optical modulation formats that are more tolerant to chromatic dispersion, as extensively discussed in the remainder of this thesis. Alternatively, *tunable* chromatic dispersion compensation can be employed to improve the chromatic dispersion tolerance at the receiver. A number of different technologies have been proposed for tunable dispersion compensation, including Fiber Bragg gratings [151, 152], thin film etalons [153] and digital signal processing technologies. Digital signal processing such as pre-distortion and digital coherent receivers are an exception to the subdivision of in-line and accumulated dispersion compensation as they can compensate for the full dispersion of the fiber link (see Chapter 10).

#### 3.3.1 Dispersion map

In a long-haul transmission system, chromatic dispersion interacts with the SPM and XPM induced nonlinear phase shifts. Depending on the local dispersion along the transmission link, this can result in severe transmission impairments. It is therefore important to design the local dispersion evolution along the link, which is known as the *dispersion map*.

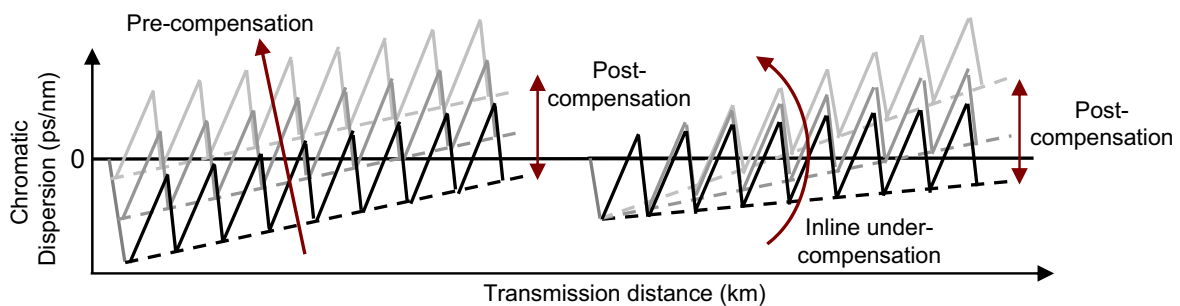


Figure 3.9: Degrees of freedom in the design of a dispersion map.

Figure 3.9 visualizes the degrees of freedom that can be used in the design of a dispersion map. First of all, the *pre-compensation* refers to a DCM with negative dispersion that is added to pre-chirp the signal directly after the transmitter [154]. An optimized pre-compensation makes the dispersion map more symmetric with respect to the zero-dispersion point and minimizes the path-averaged pulsewidth over the high power area of the transmission system. A lower path-average pulsewidth reduces the overlapping of neighboring pulses and, hence, minimizes the distortions due to SPM-induced nonlinearities [155]. A rule of thumb for the design of the dispersion map is to choose the pre-compensation such that the path-averaged nonlinearity corrected for the sign of the local dispersion is close to zero.

$$\gamma \sum_{n=1}^{n=N_{spans}} \int_{z=L_{span}(n-1)}^{z=L_{span}(n)} \text{sign}[D_{local}(z)] \exp(-\alpha z) dz \approx 0. \quad (3.14)$$

When the path-average nonlinearity is close to zero it results in a transmission link where the high-power areas are nearly symmetric with respect to the zero-dispersion point. This is illustrated in Figure 3.10a which indicates the high-power areas along the transmission link directly after each EDFA. Such a link design is possible through the use of a dispersion map that is symmetric with respect to the middle of the link [88, 156].

The second degree of freedom is the *inline under-compensation*, which denotes the difference between the chromatic dispersion of each span and the chromatic dispersion of the subsequent DCF module. The inline under-compensation changes the chromatic dispersion in the high power region at the beginning of each subsequent span. This averages out the interaction between the nonlinear phase shift and chromatic dispersion, as the power envelope is slightly different for each of the following high power regions. The inline under-compensation is particularly important to reduce the impact of XPM, as it is similar to a path-averaged walk-off length. The XPM penalty is, on the other hand, only slightly dependent on the pre-chirp and local dispersion [157]. Finally, the *post-compensation* optimizes the accumulated dispersion at the receiver. The optimal amount of post-compensation can compensate to a certain degree the SPM-induced nonlinear phase shift as discussed in Section 2.4.2. The optimization of the dispersion map for WDM transmission systems is reported in many theoretical (e.g. [158, 159]) and experimental studies (e.g. [160, 157, 161]).

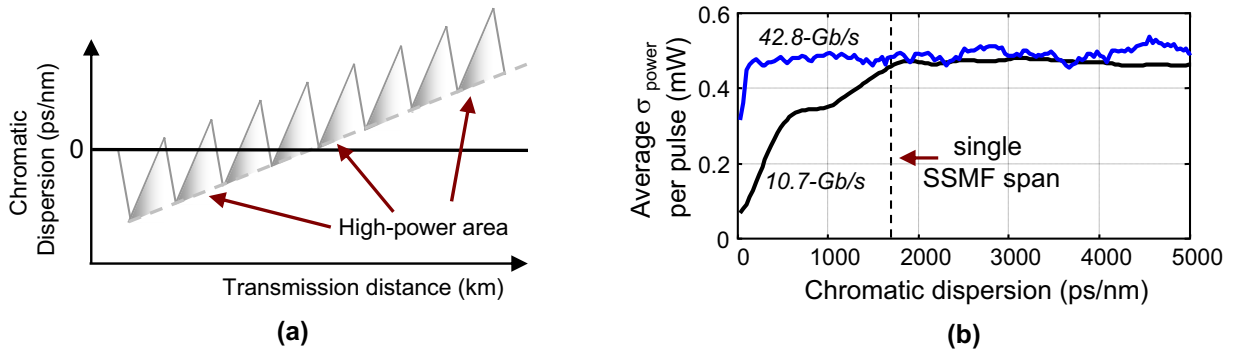


Figure 3.10: (a) Dispersion map with indication of high-power area and (b) average standard deviation of the power in a symbol (75% symbol period) for 10.7-Gb/s and 42.8-Gb/s NRZ-OOK modulation.

### 3.3. Chromatic dispersion compensation

The choice of the dispersion map is particularly important for a  $\sim 10$  Gb/s symbol rate, as the number of interacting pulses is relatively small. This is illustrated in Figure 3.10b which shows the standard deviation of the power in each pulse, averaged out over all pulses in the transmitted sequence, as a function of chromatic dispersion only. In order to exclude the pulse transitions, only the middle 75% of the time slot is used in the calculations. The standard deviation of the power increases with the accumulated chromatic dispersion as the overlapping pulses interfere with each other. For a 10.7-Gb/s symbol rate the standard deviation increase up to an accumulated dispersion of  $\sim 2000$  ps/nm and then saturates. This indicates that if the dispersion map keeps the local dispersion in high-power area below  $\sim 2000$  ps/nm the nonlinear impairments will be lower than when the chromatic dispersion is not periodically compensated. For a 42.8-Gb/s symbol rate, the standard deviation saturates for a  $\sim 150$  ps/nm accumulated dispersion. This indicates that for higher symbol rates, the number of interacting pulses rapidly increases which limits the efficiency of suppressing nonlinear impairments through the choice of the dispersion map. We note that another measure often used to characterize the impact of nonlinearities is the peak power along the transmitted sequence. The peak power shows a similar trend as the average standard deviation, but as there is no averaging in computing the peak power, it is more dependent on the length of the transmitted sequence.

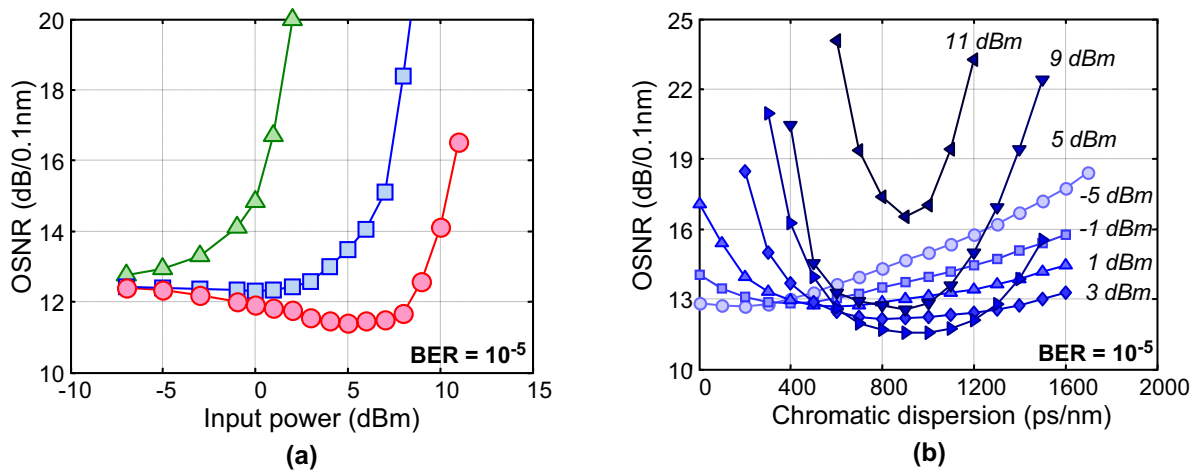


Figure 3.11: (a) Required OSNR for 10.7-Gb/s NRZ-OOK after 2000-km transmission with a  $\bullet$  all optimized dispersion map,  $\square$  optimized in-line and pre-compensation, zero accumulated dispersion and  $\blacktriangle$  zero pre, in-line and accumulated dispersion. (b) accumulated dispersion tolerance for different input powers.

As an example, Figure 3.11 illustrates the impact of dispersion map optimization on the nonlinear and dispersion tolerance in a long-haul transmission system. Depicted in Figure 3.11a is the nonlinear tolerance for 20x100 km transmission with a single 10.7-Gb/s NRZ-OOK channel. When no dispersion map is used and the pre-, in-line- and accumulated dispersion are all equal to zero, an input power of -1 dBm per span results in a 2-dB OSNR penalty. Optimizing the pre- and in-line compensation improves the nonlinear tolerance significantly to 6-dBm input power per span. For this link, the optimum pre-compensation is in the range -1190 ps/nm (lower powers) to -680 ps/nm (higher powers). The optimum in-line under-compensation ranges from 51 ps/nm (lower powers) to 68 ps/nm (higher powers). When furthermore the accumulated dispersion at

the receiver is optimized, the nonlinear tolerance increases to 10 dBm per span. The optimum accumulated dispersion for different input powers per span is depicted in Figure 3.11b for a dispersion map with -680 ps/nm pre-compensation and 68 ps/nm in-line under-compensation. This shows that in the nonlinearity-limited transmission region the accumulated dispersion can be as high as 900-ps/nm. Note that for a zero pre- and in-line compensation, optimizing the accumulated dispersion also improves the nonlinear tolerance (to  $\sim 8$  dBm, not shown). However, for WDM transmission the impact of XPM would be particularly strong in this case, which makes it less relevant. When the pre- and in-line compensation are optimized, the impact of XPM can be reduced. However, even for an optimized dispersion map the impact of XPM will considerably limit the nonlinear tolerance.

In the long-haul transmission experiments described in this thesis, the dispersion map is optimized in order to understand its impact on the transmission properties of different modulation formats (see Chapter 6). The dispersion map is optimized by starting of with an dispersion map as would be optimal for 10.7-Gb/s NRZ-OOK modulation, and then independently varying the pre-compensation and in-line under-compensation. In deployed transmission systems, the optimization of the dispersion map is somewhat restricted because every span has a different length and the DCMs are only available in a certain granularity. A further requirement for optically-switched networks is that at each add-drop points the accumulated dispersion is low in order to minimize the required post-compensation. A practical chromatic dispersion map for such transmission systems is a double-periodic dispersion map [162]. Such a dispersion map typically has a high inline under-compensation for each span, but once every several spans the accumulated dispersion is reduced through a high inline over-compensation.

### 3.3.2 Lumped dispersion compensation

The design of a dispersion map improves the reach in a long-haul transmission system significantly. But it also requires complex system engineering to obtain a near optimal dispersion map in deployed transmission systems. An alternative approach is the use of *lumped dispersion maps*, which compensate the chromatic dispersion every several spans or, in the extreme case, do not apply in-line dispersion compensation at all. For example, the dispersion compensation can be concentrated only at specific points, such as optical add-drop nodes. This allows the replacement of multiple small DCMs with a single "large-dispersion" DCM. Furthermore, it has the advantage that simpler EDFAs can be used in between the dispersion compensation nodes. The use of a lumped dispersion map can potentially also improve transmission performance. When no mid-stage access are required for the EDFAs, less pump lasers are required and the EDFA can have a lower noise figure. As shown previously, this can improve the OSNR with up to 2 dB.

Figure 3.12 depicts the accumulated dispersion along a transmission link for both a conventional and a lumped dispersion map. This illustrated that the local dispersion along the link is significantly higher in the case of a lumped dispersion map. The higher local dispersion can reduce the nonlinear tolerance, which makes lumped dispersion compensation less interesting for ultra long-haul transmission systems or modulation formats that require careful optimization of the dispersion map. For example, for 10.7-Gb/s NRZ-OOK modulation the use of a lumped disper-

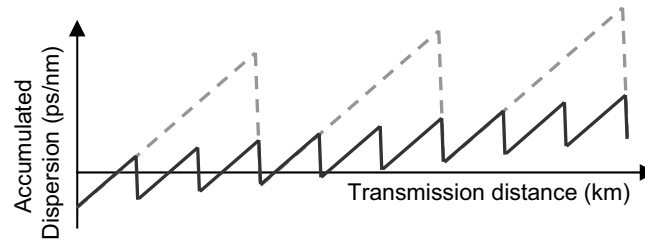


Figure 3.12: Example of a lumped dispersion map.

sion will result in a reduced nonlinear tolerance as this modulation format strongly benefits from an optimized dispersion map [163]. But 40-Gb/s transmission has shown to be highly resistant towards a large accumulated dispersion, particularly when phase shift keyed modulation formats are used [164].

To make lumped dispersion compensation practical an important consideration is the large insertion loss of the single centralized DCM. An efficient amplification scheme to reduce the insertion loss is backwards pumped Raman amplification, as DCF has a high Raman gain coefficient. This allow for a high ON/OFF Raman gain, in the order of 25 dB, while using only low power Raman pumps. A further increase in Raman gain can result in double Rayleigh scattering, which increases the noise figure [165, 166]. When hybrid EDFA/Raman amplification is used the total DCF insertion loss can be  $\sim 30$  dB, which is sufficient to compensate the chromatic dispersion of 500 km of SSMF. An alternative approach for lumped dispersion compensation would be the use of chirped FBGs. This combines a large chromatic dispersion with an insertion loss small enough to be compensated using EDFA-only amplification. An example of long-haul transmission with a lumped dispersion map is discussed in Section 6.3.

#### 3.3.3 Chirped fiber-Bragg gratings

Chirped multi-channel fiber-Bragg gratings (FBG) are an alternative to DCF for the compensation of chromatic dispersion in long-haul transmission links [167, 168]. A FBG is a type of distributed Bragg reflector, first demonstrated by *Hill et. al.* in 1978 [169]. It consists of a short segment of fiber with a periodic variation of the refractive index along the fiber core. The refractive index variation generates a wavelength specific dielectric mirror that reflects a particular wavelength. A FBG can therefore be used to construct a very narrow optical filter that reflects the desired wavelength and transmits all other wavelengths. When a FBG is combined with a circulator, the resulting component transmits only the desired wavelength and attenuates all others, as shown in Figure 3.14. The signal enters the circulator through port 1 and outputs it again through port 2. The FBG connected to port 2 then reflects only the desired wavelengths back into the circulator, which outputs the signal again through port 3.

The refractive index profile of a FBG can have a linear variation in the grating period. Different wavelength are then reflected at different positions along the FBG, which introduces chirp into the signal. Such chirped fiber Bragg gratings can be used for dispersion compensation. A chirped

FBG does not reflect a single wavelength, but rather reflects a range of wavelength defined by the variation of the grating period. This can be used to construct FBGs with a broad bandwidth, for example the full C-band, which can compensate the chromatic dispersion for multiple WDM channels. Alternatively, multiple short gratings can be written on top of each other to reflect multiple WDM channels with a single complex grating. Such a structure enables the manufacturing of full C-band FBGs that can be used on a 100-GHz [170] or 50-GHz grid [171]. The amplitude response of a chirped FBG with 100-GHz channel spacing is depicted in Figure 3.13b. This shows a very flat insertion loss with a ripple of  $<0.5$  dB across a 65-GHz bandwidth and a  $\sim 25$  dB insertion loss in between two pass-bands.

In Figure 3.13c, the phase response of a chirped FBG is depicted. A drawback of chirped FBGs is that they suffer from distortions in their phase response, better known as the group delay ripple (GDR). The GDR is caused by imperfections in the gratings fabrication process and limits the number of FBGs that can be cascaded. Figure 3.13d shows the obtained GDR when the a linear fit is subtracted from the group delay response. In [172], Scheerer *et. al.* showed that the penalty can be calculated from the amplitude and period of the GDR in the frequency domain. The main consideration is the ripples frequency relative to the symbol rate. High-frequency ripples, i.e. ripples with more than one ripple period within the signal bandwidth, create satellite pulses in the time domain. These satellite pulses interfere with adjacent pulses and therefore cause ISI. Low frequency ripples, with only a fraction of the ripple period within the signal bandwidth, cause pulse broadening. This pulse broadening is analog to chromatic dispersion and therefore merely changes the residual dispersion of the signal. The low-frequency ripples can

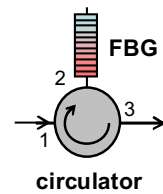


Figure 3.14: FBG with circulator.

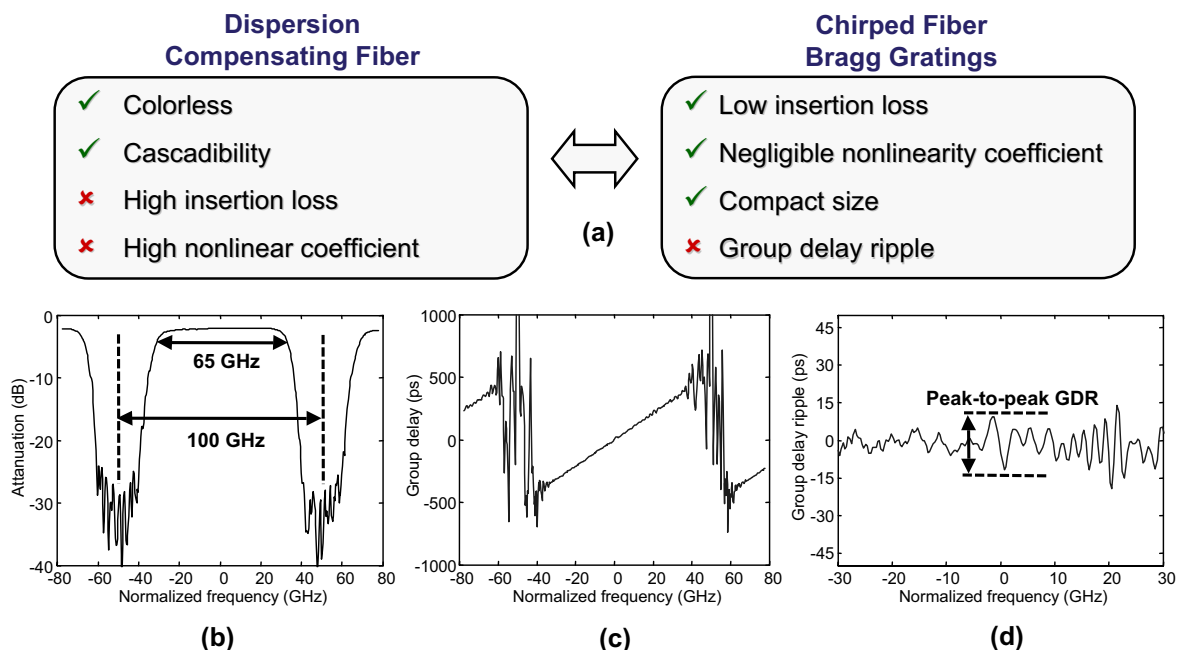


Figure 3.13: (a) Comparison between FBGs and DCF for chromatic dispersion compensation; (b) amplitude, (c) group delay and (d) group delay ripple of a channelized chirped-FBG.



be compensated using tunable dispersion compensation. As a result, mainly the high-frequency ripples cause transmission impairments. Note that the best prediction of the penalty associated with cascaded FBGs is generally the phase ripple (PR) weighted by the signal spectrum [173].

Figure 3.13a lists the most significant differences between DCF and FBGs for dispersion compensation. The main advantage of FBGs is their lower insertion loss and negligible nonlinearity. This potentially allows simpler EDFA design, by cascading the FBG and transmission fiber without a mid-stage amplifier. Another advantage is the compact size, which enables the integration of a (tunable) FBGs in the receiver. A FBG can be made tunable through heating or stretching of the fiber grating, which enables dispersion tuning over a range of typically 800 ps/nm [174]. The main disadvantage of FBGs is the PR-related impairments. However, improved fabrication processes have gradually reduced the PR of slope-matched FBGs, which significantly increases their cascability [175]. A further reduction in PR-related impairments is possible using equalization [176], which enables ultra long-haul transmission using FBGs for dispersion compensation. In Section 6.4 the impact of PR-induced impairments are discussed for a long-haul WDM transmission experiment using 10.7-Gb/s NRZ-OOK and 42.8-Gb/s RZ-DQPSK modulation.

### 3.4 PMD compensation

As there is no easy compensation solution, PMD related penalties are among the most cumbersome for state-of-the-art long-haul optical transmission systems. However, several approaches have been proposed that either mitigated or actively compensated the impact of PMD. Passive PMD mitigation technologies include the use of robust modulation formats, as discussed further in this thesis, and FEC-supported polarization scrambling [177, 178]. Active PMD compensation techniques include PSP coupling [179], the use of optical PMD compensators [180, 181] and optical [182] or electrical signal processing. An extensive overview of PMD compensation technologies is given by *Sunnerud et. al.* in [183].

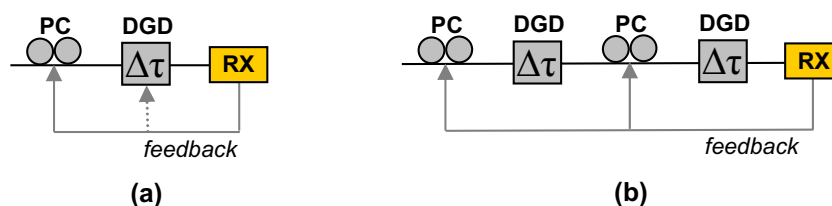


Figure 3.15: (a) single-stage PMD compensator; (b) two-stage PMD compensator.

PSP coupling simply aligns the input SOP with the PSP of the transmission link. This is a fairly easy method to compensate for DGD, but cannot be used to compensate for second-order PMD or in the presence of strong PDL. It also requires a feedback signal from the receiver to the transmitter, which complicates system design. In addition, the time delay in a long transmission link makes it impossible to track fast polarization changes. Optical PMD compensators can either use single-stage [180] or two-stage compensation [181], as illustrated by Figure 3.15. A single stage PMD compensator consists of a polarization controller followed by either a fixed

or tunable birefringent section. Such a PMD compensator has either two (fixed) or three (tunable) degrees of freedom. The degrees of freedom of a PMD compensator is a good figure of merit for the complexity of the control algorithm. With a fixed single birefringent section, the amount of birefringence should match the average PMD of the link and a penalty is introduced when the compensator DGD is larger than the DGD of the transmission link. Note that a single-stage PMD compensator can only compensate for a limited amount of second-order PMD [184]. Hence, for 43-Gb/s transmission a two-stage PMD compensator is desirable. A two-stage PMD compensator (Figure 3.15b) has normally 4 degrees of freedom. This requires both a sophisticated control algorithm as well as a suitable choice of the feedback signal. Most two-stage PMD compensators schemes are known to have the tendency of getting trapped in suboptima [183].

An important design aspect for PMD compensators is the speed of compensation. Polarization changes in an optical fiber are normally on the scale of a few degrees per second. However under the influence of, for example, vibrations, temperature changes, human handling or wind in the case of aerial fibers, the polarization changes can reach a speed of  $\sim 50$  revolutions per second on the Poincaré sphere [185, 186, 187]. In order to track these polarization changes with a ( $\theta < 10^\circ$ ) accuracy, the response time of the automatic polarization control should be in the order of 1 ms. The feedback required for optical polarization controllers makes it difficult to obtain such response times. The combined requirement of a short response time and control algorithms that do not suffer from local suboptima has stalled the deployment of optical PMD compensators in recent years.

### 3.5 Narrowband-optical filtering

The previous three sections discussed the compensation of transmission impairments that occur in a long-haul optical transmission link. This section discusses the impact of optical narrowband filtering, a transmission impairment that typically occurs in an optical transmission network. An optical meshed network requires that signals routed through the network have the flexibility to pass multiple optical add-drop multiplexer (OADM) and photonic cross connects (PXC) nodes along the transmission link [188].

An OADM comprises different optical sub-systems to realize wavelength switching. Generally, the WDM spectrum is de-multiplexed in order to block certain WDM channels and let other WDM channels pass through. This can either be achieved with a wavelength blocker or a wavelength selective switch (WSS), with the difference being that a wavelength blocker has a  $1 \times 1$  structure whereas a WSS can be a  $N \times M$  switch, with  $N$  and  $M$  being the number of input and output ports, respectively. Common types are a  $1 \times 4$  or  $1 \times 9$  WSS. The combination of a wavelength blocker with fiber-optic couplers at the input and output makes it possible to add/drop WDM channels. A wavelength blocker can be realized using planar lightwave circuits or liquid crystal technology [189], whereas a WSS is generally realized using micro-electro mechanical system (MEMS) technology [190].

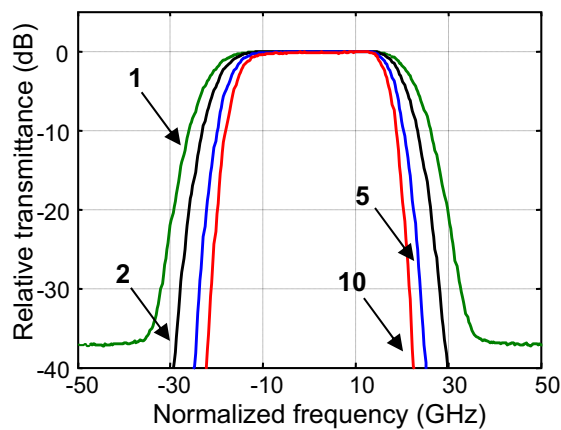


Table 3.4: OPTICAL FILTER BANDWIDTH OF A CASCADED 50-GHZ WSS.

cascaded filters	3-dB bandwidth (GHz)	20-dB bandwidth (GHz)
1	43	59
2	39	52
5	35	45
10	32	40

Figure 3.16: Transmittance of a 50-GHz WSS.

The wavelength de-multiplexing that occurs in an OADM/PXC results in spectral filtering of the WDM channels. Particularly when multiple OADM/PXC are cascaded this filtering can limit the optical bandwidth to a fraction of the channel spacing. Figure 3.16 shows the measured transmittance of a state-of-the-art WSS, which has a (single-pass) 3-dB bandwidth of 43-GHz on a 50-GHz ITU grid. When the measured transmittance is cascaded multiple times to simulate cascaded filtering, the 3-dB bandwidth is reduced significantly, as depicted in Figure 3.16. Note that we here assume that all optical filters have exactly the same transmittance as a function of wavelength. In deployed optical networks, the filter transmittance of the cascaded OADM/PXC is likely to be slightly shifted in wavelength, for example, due to temperature differences or slight variations in the device specifications. This indicates that on a 50-GHz ITU grid, the available 3-dB bandwidth is approximately 35-GHz when a realistic number of 3-4 OADM/PXC is passed along the transmission link. This bandwidth is therefore a suitable figure-of-merit to determine if a modulation format can be used with a 50-GHz channel spacing.

Today, state-of-the-art transmission systems have a 50-GHz WDM channel spacing. This implies a 0.8-b/s/Hz spectral efficiency for 40-Gb/s transmission. For binary formats this is close to the theoretical limit which makes it difficult to cascade multiple OADM with an acceptable OSNR penalty. The more narrow optical spectrum of multi-level modulation formats is therefore one of the more decisive advantages over binary modulation formats. In the remainder of the thesis, a WSS is included in the optical transmission experiments to emulate the strong optical filtering as it occurs in a transparent optical network.

## 3.6 Optical phase conjugation

Nonlinear transmission impairments are clearly the most difficult transmission impairments to compensate in a long-haul transmission link. This mainly results from the lack of a technology that can inverse the nonlinear impairment, e.g. a material with a negative Kerr effect. Optical phase conjugation (OPC) is one of the technologies that can (partially) compensate for nonlinear transmission impairments. It uses the transmission fiber itself to compensate for transmission

impairments and, in effect, invert the sign of the Kerr effect in the second half of the transmission link. With OPC, the impairments that occurred before conjugation can be canceled out by impairments that occur after phase conjugation. OPC is currently not used in deployed optical transmission systems, but it is one of the most promising technologies to increase the robustness against nonlinear transmission impairments.

*Yariv et. al.* proposed in 1979 the use of chromatic dispersion compensation by means of OPC [191]. But apart from the compensation of chromatic dispersion, OPC can also be used to compensate for other (deterministic) linear and nonlinear transmission impairments. This includes the compensation of SPM [192, 193], IXPM/IFWM [194, 195] and nonlinear phase noise [91]. And as OPC compensates the chromatic dispersion along a transmission link, it also allows for simpler EDFA design. The broad range of transmission impairments that can be compensated using OPC makes it a very powerful technology to extend the reach of long-haul transmission systems. This section briefly discusses the theory behind optical phase conjugation. Section 6.5 discusses long-haul transmission experiments using OPC for the compensation of transmission impairments. An in-depth description of optical phase conjugation in long-haul transmission systems can be found in [21].

### 3.6.1 Periodically-poled lithium-niobate

The most promising technology to realize OPC is parametric difference frequency generation (DFG) in a periodically-poled lithium-niobate (PPLN) waveguide. Several other techniques have been proposed to phase conjugate an optical signal and have been used in earlier experiments. This includes highly nonlinear fiber [196], a semiconductor optical amplifiers [197], silicon waveguides [198] and AlGaAs waveguides [199]. Highly nonlinear fibers, semiconductor amplifiers and silicon waveguides are all media with a high  $\chi^3$  and therefore use FWM to conjugate the optical signal. As a result, the phase conjugated signal is degenerated through SPM and XPM that occur simultaneously with the FWM in a  $\chi^3$  nonlinear media.

A PPLN waveguide has a high second order susceptibility  $\chi^2$  but negligible third order susceptibility  $\chi^3$ . Nonlinear interaction resulting from the third-order susceptibility (i.e. SPM, XPM and FWM) can therefore be neglected. Phase conjugation with a PPLN waveguide is realized by second harmonic generation (SHG) and DFG [200, 201]. The principle of the cascaded SHG and DFG process in a PPLN waveguide is illustrated in Figure 3.17. Through SHG, the pump at frequency  $\omega_{pump}$  is up-converted to the frequency  $2 \cdot \omega_{pump}$ . Simultaneously DFG occurs where the second harmonic  $2 \cdot \omega_{pump}$  interacts with the input signal  $\omega_{input}$ . The DFG generates a phase conjugated output signal that mirrors the input signal  $\omega_{input}$  with respect to the pump signal  $\omega_{pump}$ . The frequency of the output signal is therefore  $\omega_{conjugate} = 2 \cdot \omega_{pump} - \omega_{input}$ . It is also possible to phase conjugate the signal using only DFG, in that case the pump signal should have a frequency  $2 \cdot \omega_{signal} + \Delta\omega$  [202], where  $\Delta\omega$  is the frequency difference between the input and phase conjugated output signal. The cascaded SHG/DFG process is instantaneous and phase sensitive in its response, which implies that OPC with a PPLN waveguide is transparent to bit rate and modulation format [203] and has a high conversion efficiency [204]. The DFG and SHG processes can conjugate signals over a broad wavelength range. For example, in [202] conversion is

shown between the  $1.31\mu\text{m}$  and  $1.5\mu\text{m}$  band. The input signal can be a single wavelength channel or multiple WDM signals. In [205], *Yamawaku et. al.*, showed the simultaneous conversion of 103 WDM channels using a single PPLN waveguide.

In an ordinary  $\text{LiNbO}_3$  waveguide, SHG and DFG have a very low efficiency because of the phase mismatch caused by the dispersion of the lithium-niobate. For efficient SHG and DFG, this phase mismatch needs to be compensated, which is possible through quasi-phase matching (QPM). First order QPM can be realized by reversing the sign of the nonlinear susceptibility (periodically poling) with every phase matching period. Typically, the phase matching period of the periodic poling is  $\sim 16.5\mu\text{m}$ . Note that the phase matching period fixes the wavelength of the pump signal, hence a PPLN waveguide has to be designed for a specific pump wavelength. However, slight tuning of the operating wavelength can be realized by changing the operating temperature of the PPLN waveguide. A concern of OPC using a PPLN waveguide is that it suffers from the presence of the photorefractive effect [206]. This can be mitigated by heating the PPLN waveguide. Typically, a PPLN waveguide is operated at  $180^\circ$  to  $200^\circ$  Celsius. Because of the high operating temperature, pigtail fibers cannot be glued to the waveguide and free-space optics have to be used to couple the light in and out of the PPLN waveguide, which complicates sub-system design. Another approach to mitigate the photorefractive effect is doping the  $\text{LiNbO}_3$  slightly with magnesium-oxide [207]. This lowers the operating temperature to between  $50^\circ$  and  $90^\circ$  Celsius [194, 195], which allows gluing the fibers to the waveguide. Hence, magnesium-oxide doped PPLN waveguide are more practical for use as an optical subsystem.

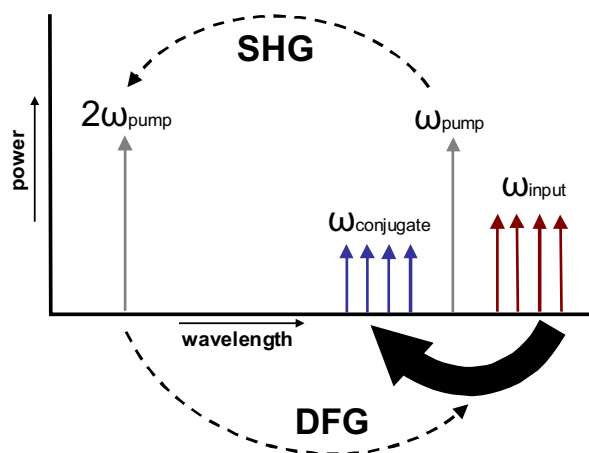


Figure 3.17: Second harmonic generation (SHG) and difference frequency generation (DFG) in a PPLN.

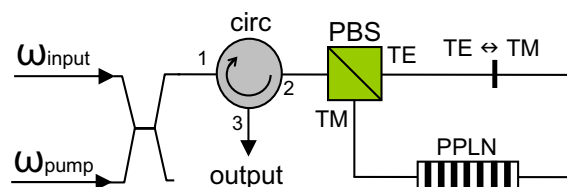


Figure 3.18: Counter directional polarization independent OPC subsystem.

A PPLN waveguide is intrinsically polarization dependent, which is a significant drawback for in-line OPC in a long-haul transmission system. However, two polarization diversity schemes can be used to make the PPLN structure polarization independent. Either using a parallel [208] or a counter-directional [209] approach. In the parallel polarization-diversity scheme, the input signal is split up into two orthogonal polarization components that are separately phase conjugated by two PPLN waveguide. The counter-directional polarization-diversity scheme, on the

other hand, uses a single PPLN waveguide. In the transmission experiments described in Section 6.5 a counter-directional polarization-diversity structure is used, as depicted in Figure 3.17. A polarization beam splitter (PBS) splits the incoming signal with arbitrary polarization into the two orthogonal polarization modes (TM and TE). Counterclockwise rotating, the signal on the TM mode is then phase conjugated in the TM aligned PPLN waveguide, and subsequently converted to the TE mode with a TE  $\leftrightarrow$  TM fusion splice. Clockwise rotating, the TE mode is first converted to the TM mode and afterwards phase conjugated. Both counter propagating modes are again recombined with the same PBS. The pump signal  $\omega_{pump}$  is combined with the input signal  $\omega_{input}$  before the polarization-diversity structure. In order to obtain the same conversion efficiency for both the clockwise and counter-clockwise direction, the pump has to be launched at  $45^\circ$  with respect to the principal axes of the PBS such that the pump power is split with a 50% – 50% ratio. As both the TE and TM mode travel through the same components for the counter-direction polarization-diversity scheme, the structure has an inherently low DGD. And as long as the pump power is high enough that the DFG and SHG processes are not saturated, the PDL is also inherently low. The main disadvantage is the vulnerability to multiple path interference resulting from reflections and the finite extinction ratio of the PBS.

### 3.6.2 Compensation of transmission impairments

As discussed in Section 2.4, the propagation of an optical signal can be expressed by the Nonlinear Schrödinger equation assuming a slowly varying envelope approximation. The complex conjugate of the Nonlinear Schrödinger equation can be denoted as,

$$\frac{\partial E^*}{\partial z} = - \underbrace{\frac{\alpha}{2} E^*}_{\text{attenuation}} + \underbrace{j \frac{\beta_2}{2} \frac{\partial^2 E^*}{\partial T^2}}_{\text{dispersion}} + \underbrace{\frac{\beta_3}{6} \frac{\partial^3 E^*}{\partial T^3}}_{\text{dispersion slope}} - \underbrace{j \gamma |E^*|^2 E^*}_{\text{Kerr nonlinearities}}, \quad (3.15)$$

where  $E^*$  denotes the complex conjugate of the optical field. Comparing Equations 2.21 and 3.15 shows that the contributions of the chromatic dispersion and the Kerr effect have an inverted sign. We now assume that the signal is phase conjugated in the middle of a perfectly symmetrical transmission link. In this case, impairments due to chromatic dispersion and the Kerr effect that occurred along the first part of the link are perfectly canceled out in the second part of the link. The sign of the attenuation and the dispersion slope remains unchanged and are not compensated.

An important consideration for OPC-aided transmission links is that, ideally, compensation of chromatic dispersion and the Kerr effect can only be realized in a transmission link that is perfectly symmetric with respect to the OPC unit. However, due to the attenuation of the optical fiber, the power envelope decreases exponentially with propagation distance along a single span. As a result, the transmission link will not be fully symmetric with respect to the OPC unit. The asymmetry can be reduced by using all-Raman amplification, as discussed in Section 3.2.2 [208]. However, *Chowdhury et. al.* showed that also with hybrid EDFA/Raman amplification, where the power profile along the link is not fully symmetric with respect to the OPC unit, significant nonlinearity compensation can be achieved [194, 195]. And in [210], *Jansen et. al.* showed that also with EDFA-only amplification a significant gain in nonlinear tolerance can be achieved.

Compensation of the dispersion slope can be achieved by optimizing the post-compensation on a per-channel basis after transmission [211, 208, 203]. Alternatively, the third order dispersion can be compensated using a slope compensator [212].

In a long-haul transmission link, the power envelope evolution is a periodic function of the transmission distance. This produces a periodic variation of the fiber refractive index through the Kerr effect. This causes the transmission link to act as a very long FBG with a grating period equal to the amplifier spacing. Such a virtual grating induces a parametric gain which causes exponential growth of the signals spectral sidebands [213]. This parametric gain is known as sideband instability and can be interpreted in the frequency domain as a FWM process which is quasi phase-matched through the virtual grating. The growth of the spectral sidebands is not symmetric with respect to the middle of the transmission link and can therefore not be fully compensated with OPC [193, 214]. Modulation instability can be mitigated with a periodic dispersion map [215], hence it is insignificant in transmission system using periodic dispersion compensation. The lumped dispersion map in OPC-aided transmission systems does not suppress modulation instability, which can therefore result in signal impairments. However, in deployed transmission links not every span will have the same length and power profile, and this significantly reduces the effectiveness of the parametric gain. In the long-haul transmission experiments described in this thesis no modulation instability impairments have been observed, which probably also results from (slight) differences in span length [203, 216].

When hybrid EDFA/Raman amplification is used in a transmission link, the noise figure of the amplifiers can vary across the C-band. This is a result of pump-to-pump interaction between the Raman pumps, which reduces the OSNR of the lower wavelength [138]. This in turn causes a wavelength-dependent performance, where the higher wavelength channels generally have a better performance than the lower wavelength channels. In an OPC-aided transmission link, wavelength conversion occurs in the middle of the transmission link. As a result, all wavelength channels propagate both in the higher and the lower wavelength band for part of the transmission distance. This can ease the design of transmission links somewhat as the wavelength dependent performance among the WDM channels is averaged out.

The most significant drawback of OPC in a long-haul transmission link is its incompatibility with OADM. As an example we assume that an OPC unit is placed in the middle of a transmission link which also contains an OADM, offset from the middle of the transmission link. This implies that the dispersion of the add/drop channels will not be fully compensated by the OPC. OPC-based dispersion compensation in a transmission link with OADMs therefore requires phase conjugating the signal at multiple points in the link. Alternatively, the OPC can be only used for the compensation of nonlinear impairments and the chromatic dispersion is compensated by other means [194, 195].

### 3.6.3 Nonlinear phase noise compensation

The impact of nonlinear phase noise is, due to its statistical nature, one of the most difficult transmission impairments to take into account in the design of a transmission system. OPC can

partially compensate for nonlinear phase noise impairments, as originally proposed by *Loratanasane and Kikuchi* [193].

Figure 3.19 depicts a transmission link of 6 spans with and without mid-link OPC for nonlinear phase noise compensation. We assume every EDFA has the same output power and introduces the same amount of ASE onto the signal. The ASE generated by an EDFA adds amplitude noise to the signal. When the signal plus amplitude noise subsequently propagates over another fiber span, it introduces a nonlinear phase shift to the signal that is dependent on the total power level (i.e. signal plus noise). The total nonlinear phase shift is defined by the number of spans that the ASE propagates along the link and therefore accumulates with  $\langle \rho_{tot,N} \rangle = \langle \rho_{tot,N-1} \rangle + N \cdot \langle \rho \rangle$ , where  $\langle \rho \rangle$  is the nonlinear phase shift added in the first span and  $N$  is the  $n^{th}$  span of the transmission link. It can be shown that this is equal to,

$$\langle \rho_{tot,N} \rangle = \langle \rho \rangle \cdot \sum_{n=1}^{n=N} n = \langle \rho \rangle \cdot \frac{N}{2}(1 + N). \quad (3.16)$$

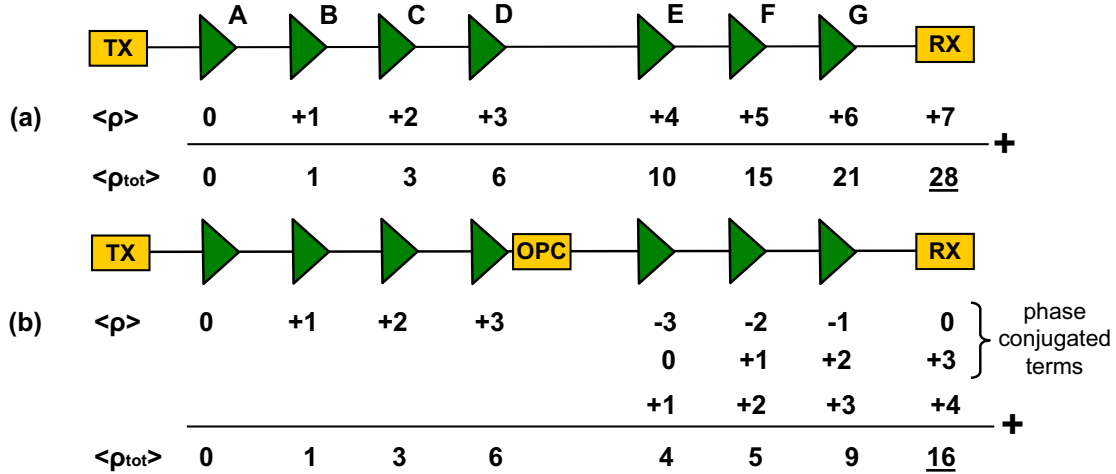


Figure 3.19: Nonlinear phase noise compensation using optical phase conjugation (after [193]).

When mid-link OPC is used in the transmission link, the nonlinear phase noise can be partly compensated. This is depicted in Figure 3.19b, which shows how the nonlinear phase noise adds up along the transmission link. As an example, we now take the amplitude noise generated by amplifier B. After amplifier B, the signal plus noise propagates over two spans before reaching the OPC unit (between amplifiers B and D), generating a nonlinear phase shift equal to  $2\langle \rho \rangle$ . The OPC unit conjugates this signal, which reverses the sign of the nonlinear phase shift but keeps the power of the signal plus noise unchanged. After the OPC unit, transmission over the two more spans (between amplifiers D and F) generates again the same nonlinear phase shift equal to  $2\langle \rho \rangle$ . However, the contribution to the nonlinear phase shift before and after the OPC have an opposite sign and therefore add up to zero. In the last two spans (between amplifier F and Rx) another nonlinear phase shift equal to  $2\langle \rho \rangle$  is generated, which is not compensated anymore. The total nonlinear phase shift generated by the noise of amplifier B, reduces therefore from  $6\langle \rho \rangle$  to  $2\langle \rho \rangle$ . Computing this for all amplifiers shows that the total nonlinear phase shift is reduced from



$28\langle\rho\rangle$  to  $16\langle\rho\rangle$ ). Note that it is beneficial to place the OPC unit at 66% of the transmission link. For example, when in the example in Figure 3.19 the OPC unit is placed after then 5<sup>th</sup> span, the total nonlinear phase shift is reduced to  $7\langle\rho\rangle$ .

The nonlinear phase noise penalty is related to the nonlinear phase noise variance, rather than the average and scales with  $\langle\rho^2\rangle N^3$  [193]. *McKinstrie et. al.* showed in [217] that with mid-link OPC the accumulated nonlinear phase noise variance becomes proportional to  $(2\langle\rho^2\rangle)(N/2)^3 = \langle\rho^2\rangle(N^3/4)$ , resulting in about 6 dB phase noise suppression. When the OPC unit is placed at 66% of the transmission link, the phase noise reduction can be increased to 9.5 dB. However, the OPC can then not fully compensate for the chromatic dispersion of the link. When not every amplifier adds the same amount of noise to the signal, the optimum placement of the OPC unit changes. For example, amplitude distortions in the transmitted signal can be modeled as an amplifier with a high noise factor. The optimum placement of the OPC unit to compensate for transmitter-induced impairments is at 50% of the transmission link. This will shift the optimal position of the OPC unit more towards the middle of the link.

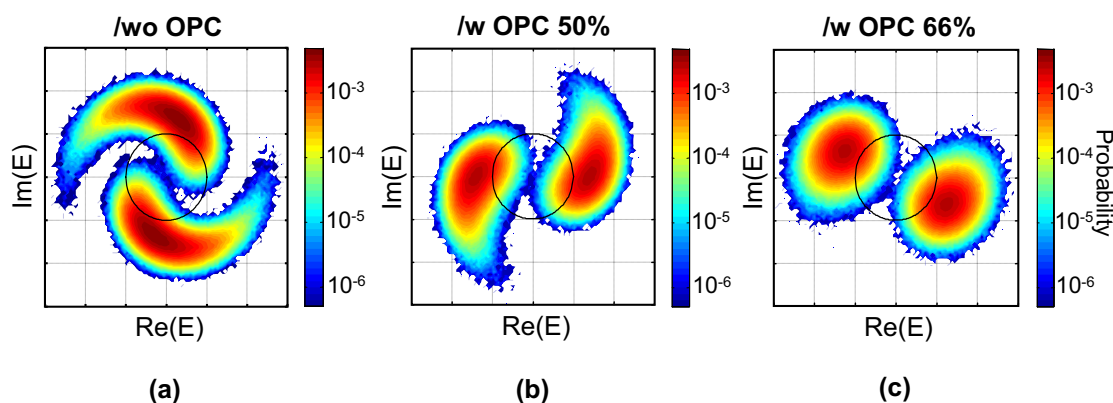


Figure 3.20: Simulated constellation diagrams of DPSK modulation, (a) without OPC, (b) with OPC at 50% of the transmission link and (c) with OPC at 66% of the transmission link.

Figure 3.20 illustrates the compensation of nonlinear phase noise through OPC in a long-haul transmission link. Simulated is single channel DPSK transmission (see Section 4.3) over 30 x 90-km spans with a 3-dBm input power per span and the ASE added along the transmission line. The fiber attenuation is  $\alpha = 0.25$  dB/km, fiber nonlinearity  $\gamma = 1.3$  W<sup>-1</sup>km<sup>-1</sup> and chromatic dispersion is neglected. Without OPC, a constellation plot is obtained that illustrates the typical *ying-yang* shape of a nonlinear phase noise distorted signal. This shape disappears partly or completely when OPC is used to reduce the impact of nonlinear phase noise. In particular when the OPC unit is placed at 66%, the impact of nonlinear phase noise is almost fully compensated.



---

## Binary modulation formats

Many different modulation formats exist that use either amplitude, phase, frequency or polarization modulation to either transmit information or enhance the transmission tolerance. We focus here on the most significant binary modulation formats that are deployed in long-haul transmission systems.

As a reference format we use NRZ-OOK modulation, as this currently still the most widely deployed modulation format for terrestrial long-haul transmission systems. The other modulation formats are evaluated in comparison to OOK. First of all, Section 4.1 introduces briefly the advantages and disadvantages of OOK modulation. Subsequently, Section 4.2 described duobinary modulation, which is currently the most widely used modulation format for 40-Gb/s transmission. We then focus on phase shift keyed modulation formats, which is likely to replace duobinary modulation for long-haul 40-Gb/s transmission. Differential phase shift keying (DPSK) is discussed in Section 4.3. Finally, in Section 4.4 we describe a narrowband filtering tolerant DPSK format, known as partial DPSK.

### 4.1 On-off-keying

From the first application of fiber optics in the middle of the 1970's until only recently, NRZ-OOK has been the modulation format of choice for most commercial applications. NRZ-OOK is an amplitude modulation format, as it encodes the information in the amplitude of the optical field. The transmitter and receiver structure of NRZ-OOK modulation is depicted in Figure 4.1.

At the transmitter, NRZ-OOK is realized by switching the output of a laser ON or OFF, depending on the information to be transmitted. Direct modulation can be used for NRZ-OOK

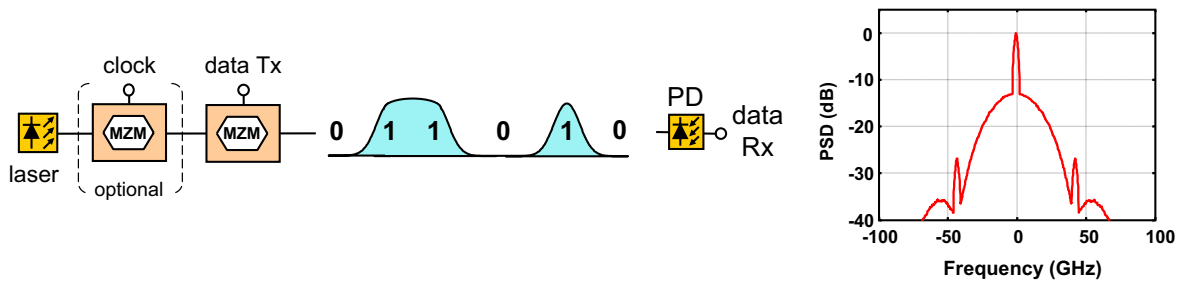


Figure 4.1: NRZ-OOK transmitter and receiver structure and simulated optical spectrum for 42.8-Gb/s NRZ-OOK.

modulation, as well as external modulators. For long-haul transmission systems, external modulation with a MZM is normally preferred to reduce the residual chirp in the modulated signal. The MZM modulates the output of a laser, typically a distributed feedback laser (DFB), which results in a chirp-free signal with high extinction ratio. The operation of a MZM for NRZ-OOK modulation is depicted in Figure 4.2a. The MZM is biased in the quadrature point and is driven from minimum to maximum transmittance. The electrical drive signal requires therefore a peak-to-peak amplitude of  $V_\pi$ . Note that due to the nonlinear transmission function of the MZM, overshoots and ripples on the electrical drive signal can be suppressed during modulation.

The optical spectrum of a NRZ-OOK modulated signal is depicted in Figures 4.1 and 4.2b, respectively. This shows the power spectral density (PSD) as function of optical frequency. NRZ-OOK has a strong component at the carrier frequency, which contains half the optical power and is referred to as the carrier. The spectrum further shows clock tones that are spaced at multiples of the symbol rate, but which are strongly reduced compared to the carrier component. The bandwidth of the optical spectrum is approximately twice the symbol rate.

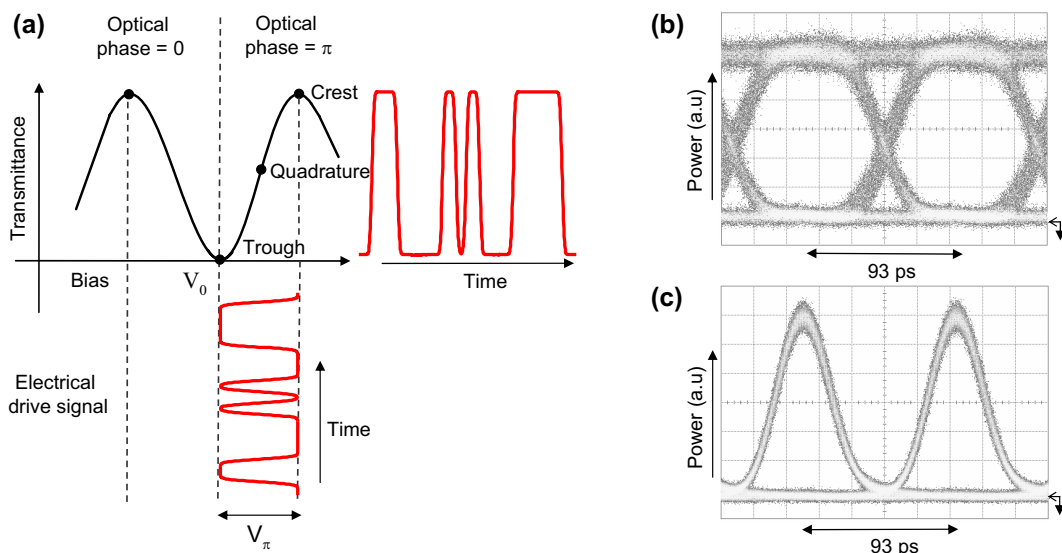


Figure 4.2: (a) Operation of the MZM for OOK modulation and eye diagrams showing, respectively, (b) 10.7-Gb/s NRZ-OOK and (c) 10.7-Gb/s RZ-OOK modulation.

The simple transmitter and receiver structure of OOK modulation comes at the cost of suboptimal transmission properties. In particular the nonlinear tolerance is low due to the strong optical carrier in OOK modulation. The nonlinear tolerance can be improved through RZ pulse carving, which results in RZ-OOK modulation [111, 218]. Without RZ pulse carving, OOK is referred to as NRZ-OOK, which is often abbreviated to NRZ. The most suitable RZ-OOK modulation format for WDM transmission is CSRZ. As discussed in Section 3.1.1, the RZ pulse carving results in a  $180^\circ$  phase change between consecutive symbols for CSRZ. Because of this alternating phase change, the optical field has a positive sign for half the '1' symbols, whereas the other half has a negative sign. This results in a zero-mean optical field envelope, which suppresses the carrier component. The zero-mean optical field also improves the nonlinear tolerance in the pseudo-linear regime where there is strong pulse overlapping.

Another approach to improve the nonlinear tolerance is the use of chirped RZ-OOK modulation, also known as CRZ. In CRZ, a specific amount of phase modulation is imposed on the RZ-OOK signal [219, 220]. Chirped RZ-OOK has an increased nonlinear tolerance in comparison to RZ-OOK modulation, but at the same time the signal chirp results in spectral broadening. This implies there is a trade-off between spectral efficiency and nonlinear tolerance for CRZ, and the optimum phase modulation index therefore depends on the system properties. CRZ modulation can be generated by modulating the phase of the RZ-OOK signal using a phase modulator (PM). Note that CRZ thus requires three modulators in cascade, for data coding, pulse carving and phase modulation, respectively. This either requires careful synchronization of the three drive signals or an integrated CRZ modulator such as reported by *Griffin et. al.* in [221]. Because of its higher nonlinear tolerance, CRZ is used in ultra long-haul (transoceanic) transmission systems.

## 4.2 Duobinary

Duobinary modulation is the best known example of a class of coding formats known as partial response codes, or alternatively known as phase engineering or phase coding formats. Similar to OOK, such modulation formats transmit the information in the amplitude domain and rely on straightforward direct detection at the receiver. But unlike OOK, there is predefined phase relation between consecutive bits that can be used to improve the optical filtering tolerance as well as the chromatic dispersion tolerance. Duobinary is sometimes also referred to as pseudo binary transmission (PSBT) [222].

Duobinary has originally been introduced in the 1960's by *Lender* as a suitable technique to transmit binary data into an electrical cable with a high-frequency cutoff characteristic [223, 224]. The main characteristic of duobinary modulation is a strong correlation between consecutive bits, which results in a more compact spectrum. It can either be generated as a 3-level amplitude signal ('0', '0.5', '1') or as a 3-level signal that combines phase and amplitude signaling ('-1', '0', '1'), which is referred to as AM-PSK modulation [224]. The first optical duobinary experiment using 3-level amplitude modulation was reported at 280 Mb/s by *O'Mahony* in 1980 [225]. However, duobinary generation through 3-level amplitude modulation results in a lower receiver

sensitivity as the symbol distance is reduced by a factor of two [226]. Optical transmission experiments using AM-PSK modulation for duobinary generation have therefore gained interest in the mid-90's [227, 228]. The use of AM-PSK duobinary generation is advantageous in optical communication as it has ideally the same or an even better OSNR requirement than OOK modulation [228]. At the same time the narrower optical spectrum and strong correlation between consecutive bits result in an increased dispersion tolerance [227]. This has made duobinary modulation a useful modulation format to increase the robustness of 10.7-Gb/s and 42.8-Gb/s optical transmission systems where the chromatic dispersion tolerance is a key design parameter.

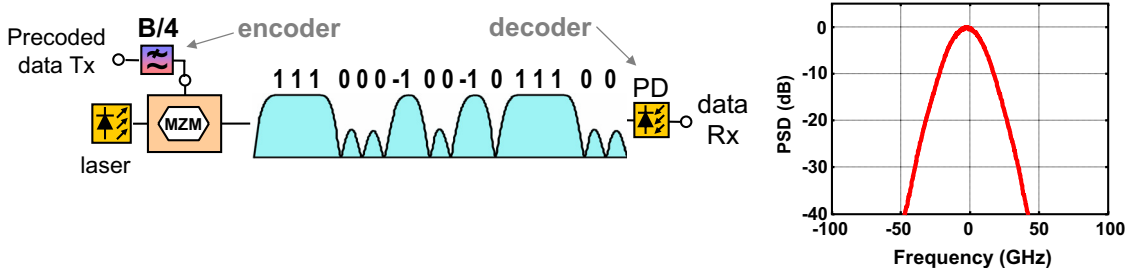


Figure 4.3: Duobinary transmitter and receiver structure and optical spectrum of 42.8-Gb/s duobinary.

The transmitter and receiver structure of duobinary modulation is shown in Figure 4.3. Analogous to OOK modulation, the transmitter consists of a standard MZM. In addition, the electrical signal is encoded before modulation to realize the required correlation between consecutive bits that characterizes duobinary modulation. Prior to encoding, the logical signal is first pre-coded, such that at the receiver the transmitted sequence is again recovered. The pre-coder therefore implements the inverse transfer function of the encoder, modulation and decoder combined. A duobinary pre-coder can be implemented through the operation,

$$b(k) = \overline{d(k)} \oplus b(k-1). \quad (4.1)$$

where  $d(k)$  represents bit  $k$  of the input sequence,  $b(k)$  is the sequence after pre-coding and  $\oplus$  is a logic exclusive OR operation. The pre-coder implementation is therefore a recursive operation, which is difficult to realize with high-speed electronics. An alternative non-recursive implementation consists of an AND operation of the input sequence and clock signal, followed by a toggle flip-flop (T-FF) [229]. Note that pre-coding is not required in transmission experiments that uses a PRBS to evaluate the performance, as the duobinary encoding then merely results in a cyclic shift of the input sequence.

The phase coding in duobinary modulation is exemplified in Figure 4.4. A logical '0' is coded as a zero whereas a logical '1' is coded as either '-1' or '1'. Consecutive logical '1's have a  $180^\circ$  phase shift when they are separated by an odd number of logical '0's. The duobinary signal constellation in Figure 4.4 depicts the three constellation points and the binary logical symbols that they represent. Duobinary encoding can be realized through a delay-and-add,

$$c(k) = b(k) + b(k-1), \quad (4.2)$$

where  $c(k)$  is the output sequence of the encoder that is used for modulation. Note that the encoder operation converts a binary signal into a 3-level amplitude signal. To realize duobinary

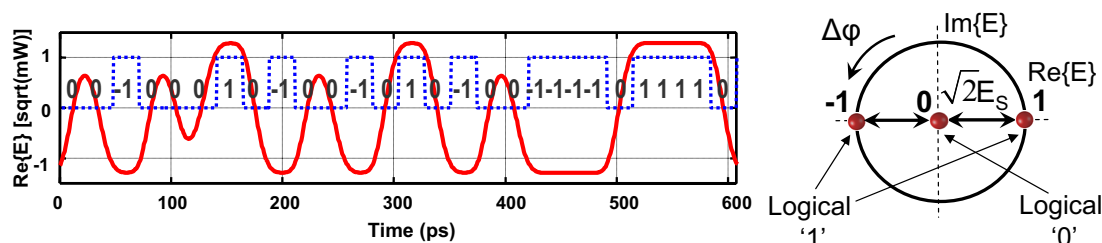


Figure 4.4: Duobinary signal and signal constellation.

modulation with a MZM, the electrical driving voltage should have a peak-to-peak voltage of  $2V_\pi$  and the MZM has to be biased in the trough point. The MZM then switches between two crest points, which have a  $180^\circ$  phase difference. This effectively maps:

$$\begin{aligned} 0 &\rightarrow \exp(j \cdot \pi) = -1 \\ 1 &\rightarrow 0 = 0 \\ 2 &\rightarrow \exp(j \cdot 0) = 1 \end{aligned} ,$$

which is equal to the duobinary partial response code. However, on itself the duobinary partial response code does not result in an improved chromatic dispersion tolerance. To improve the dispersion tolerance the spectral width has to be reduced by electrically low-pass filtering the signal with a  $B_0/2$  bandwidth, where the bandwidth  $B_0$  is twice the inverse of the symbol period ( $B_0 = 1/T_0$ ). For 'standard' binary coding, low-pass filtering with a  $B_0/2$  bandwidth results in severe eye closing. This is best exemplified with a '1 0 1' logical sequence. Low-pass filtering results in energy leakage from the surrounding '1' into the middle '0' which closes the eye. But duobinary encoding does not allow a logical sequence '1 0 1' to occur, instead coding it to '-1 0 1' or '1 0 -1'. The energy from the surrounding '-1' and '1' that leaks into the middle '0' through narrowband filtering now destructively interferes, which limits the eye closing. As a result, strong low-pass filtering does not impact the signal too severely. The delay-and-add operation can be replaced by low-pass filtering the signal with a  $B_0/4$  bandwidth. The narrowband electrical filtering results in a compact optical spectrum, which is evident from comparing the optical spectrum of duobinary modulation (Figure 4.3) and OOK modulation (Figure 4.1).

Duobinary modulation with a MZM preceded by electrical low-pass filtering is depicted in Figure 4.5a, and Figure 4.5b shows the eye diagram for 10.7-Gb/s duobinary modulation. Due to its simplicity this transmitter structure has become the standard duobinary implementation. The low electrical bandwidth allows for a further simplification as the MZM modulator used in duobinary transmitter only requires a  $B_0/4$  electro-optical bandwidth [230, 231]. Hence a 42.8-Gb/s duobinary transmitter can be realized using a  $\sim 10$ -Gb/s modulator. At the receiver, the decoding of duobinary modulation results directly from the square-law detection  $|E|^2$  of the photodiode, i.e.  $-1 \rightarrow 1$ ,  $0 \rightarrow 0$  and  $1 \rightarrow 1$ . Duobinary modulation therefore uses the same direct detection receiver as NRZ-OOK modulation.

The duobinary eye diagram in Figure 4.5b shows a triangular shape with residual energy in the '0's. This results in a 2-3 dB back-to-back OSNR penalty compared to NRZ-OOK modulation. Kim *et al.* showed that the OSNR requirement of duobinary can be significantly improved through narrowband optical filtering at either the transmitter or receiver [232]. The optimal op-

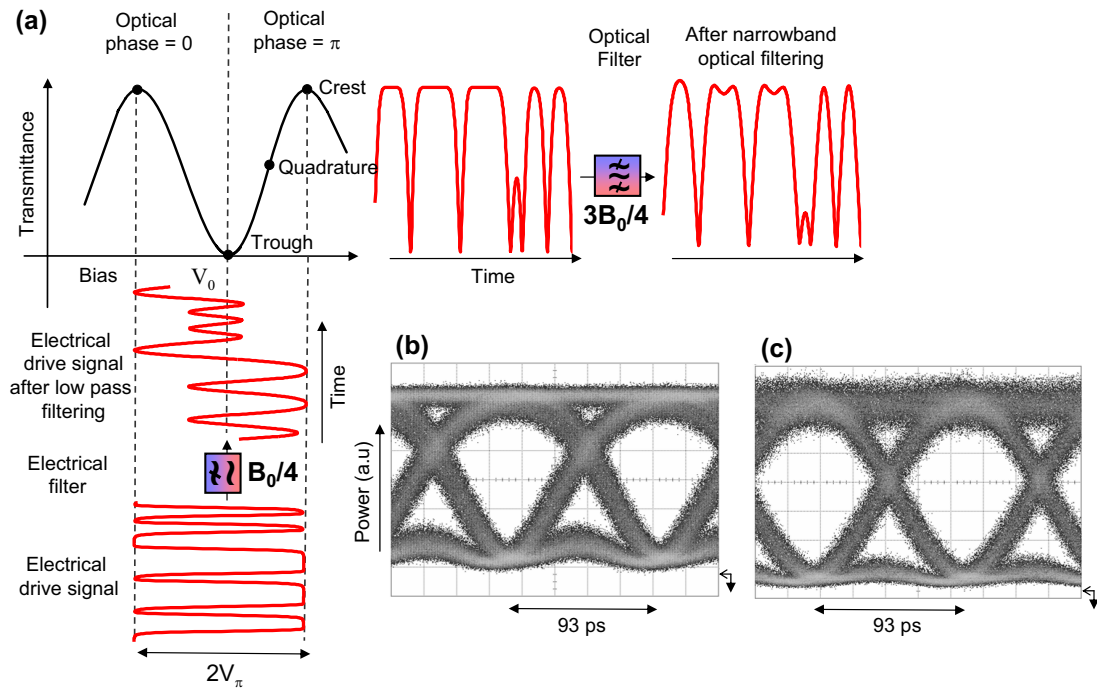


Figure 4.5: (a) Operation of the MZM for duobinary modulation and (b-c) measured eye diagram shows 10.7-Gb/s duobinary (b) without and (c) with additional narrowband optical filtering.

tical filter bandwidth is approximately  $0.8 \cdot B_0$ , with a  $2^{nd}$  order Gaussian shape [233]. After narrowband optical filtering the duobinary signal becomes more NRZ-like, as evident from Figure 4.5c. Figure 4.6a compares the back-to-back OSNR tolerance of duobinary, narrowband filtered duobinary and NRZ-OOK. Narrowband optical filtering at the receiver is particularly interesting as it filters out more noise than a broad de-multiplexing filter, which results in a  $\sim 4$  dB OSNR improvement [234]. Because of the narrower optical bandwidth the OSNR tolerance for filtered duobinary is approximately 1 dB better than NRZ-OOK [235]. The quantum limit for a theoretically optimal duobinary modulation is therefore also  $\sim 1$  dB below the quantum limit of NRZ-OOK modulation [236]. However, the theoretically obtainable performance of duobinary modulation is hard to achieve in practice. In a commercial transponder penalties often arise from variations in the electrical component bandwidth. This can be improved through the integration of a narrowband optical filter, but for a 10-Gb/s receiver this requires a very narrow optical filter with a  $\sim 8$ -GHz bandwidth. For a 40-Gb/s receiver, optical filtering is more practical as the required filter bandwidth scales inversely with the symbol rate. Optical filters with a 32-GHz bandwidth are readily available.

The OSNR tolerance of duobinary is also improved through the use of RZ-duobinary instead of NRZ-duobinary, which can be generated using an additional pulse carver at the transmitter. However, the broader optical bandwidth of RZ-duobinary cancels out the improved chromatic dispersion tolerance that characterizes duobinary, which becomes similar to RZ-OOK modulation. Although the chromatic dispersion tolerance can be recovered through narrowband optical filtering at the receiver this again reduces the OSNR tolerance [237]. RZ-duobinary is therefore only sporadically used in optical transmission experiments and not in deployed transmission sys-



tems. A different application of RZ-duobinary is the reduction of intra-channel impairments, in which it obtains a similar performance as CSRZ [111].

Figure 4.6b shows the chromatic dispersion tolerance of duobinary. In the absence of narrow-band optical filtering, a 'w' shape is obtained in the dispersion curve. This is typical for duobinary modulation. The 'w' shape disappears when the duobinary signal is narrowband optical filtered, which improves the back-to-back OSNR requirement. We note that the narrowband optical filtering strongly reduces the chromatic dispersion tolerance for a 2-dB OSNR penalty. However, this is not due to a reduction in the absolute dispersion tolerance but rather a side-effect of the improved back-to-back OSNR requirement. The residual energy in the '0's that cause the 'w' shape in the dispersion tolerance also reduces the DGD tolerance of duobinary modulation. In the presence of DGD the pulses spread out, which further raises the residual energy in '0's and results in an OSNR penalty. We note though that the SOPMD tolerance of duobinary is more beneficial; the narrow optical spectrum reduces the PSP depolarization and the large chromatic dispersion tolerance reduces the impact of PCF [238].

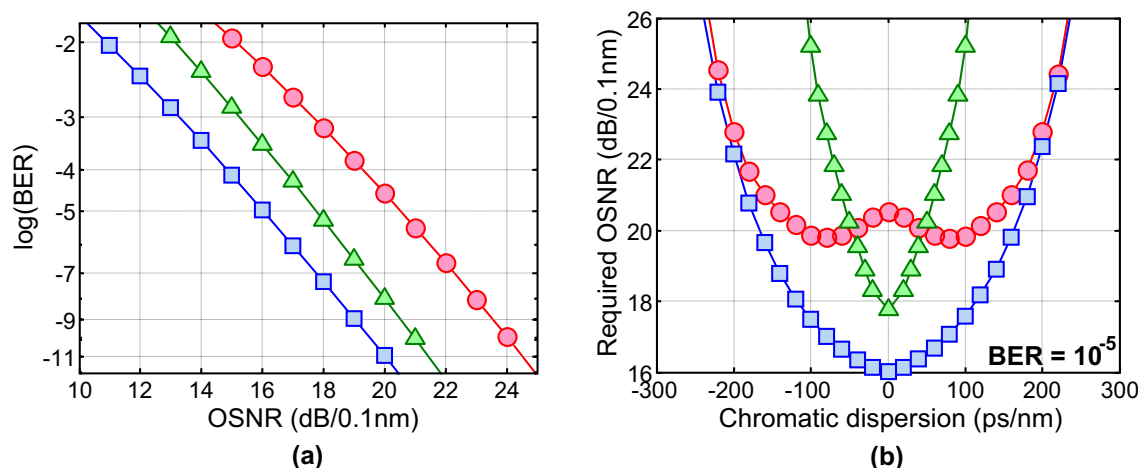


Figure 4.6: Simulated comparison of (a) back-to-back OSNR tolerance and (b) chromatic dispersion tolerance for  $\bullet$  42.8-Gb/s duobinary,  $\square$  42.8-Gb/s filtered duobinary  $\blacktriangle$  42.8-Gb/s NRZ-OOK. The optical filter bandwidths are 90-GHz 3rd order Gaussian for duobinary and OOK, and 34-GHz 2nd order Gaussian for filtered duobinary.

Duobinary modulation has been used extensively in long-haul transmission experiments at 10.7-Gb/s [239] and 42.8-Gb/s [240, 241, 242] bit rates. The narrower spectral width of duobinary makes it a good candidate for DWDM transmission with narrow channel spacing [243]. Hence, duobinary modulation can be used to realize 42.8-Gb/s transmission with a 50-GHz channel spacing, enabling a 0.8-b/s/Hz spectral efficiency [240, 241].

Besides duobinary modulation there are a large number of other partial response codes that offer similar properties [244]. But the simplicity of duobinary encoding through electrical low-pass filtering has made it the most widely used partial response format. Higher-level partial response (polybinary) codes generally do not offer a further improvement in the dispersion tolerance. Although such formats concentrate the power closer to the carrier, they cannot further reduce the total spectral width in comparison to a duobinary signal [245].

### 4.3 Differential phase shift keying

Both OOK and duobinary modulation encode the information in the amplitude of the optical signal. Binary phase shift keying (BPSK), on the contrary, encodes the information in the signal's phase. Because a photodiode is only sensitive to the incident optical power, phase shift keying requires demodulation at the receiver before it can be detected. Various schemes are capable of demodulating BPSK signals. Homodyne demodulation provides the best performance but is complex to realize. In optical transmission systems a low-complexity self-homodyne (interferometric) demodulation scheme is therefore often used [10, 246]. With self-homodyne demodulation, the information is encoded in the differential phase of the optical signal. Hence, the name differential BPSK, or DPSK.

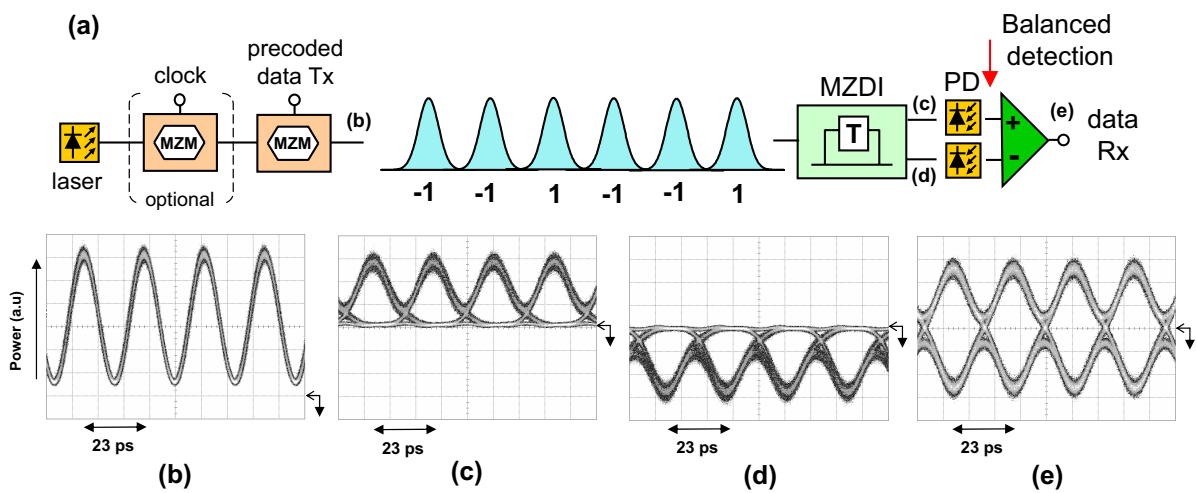


Figure 4.7: (a) Transmitter and receiver structure of RZ-DPSK and (b-e) measured eye diagrams for 42.8-Gb/s RZ-DPSK; (b) before phase demodulation, (c) constructive component, (d) destructive component and (e) after balanced detection.

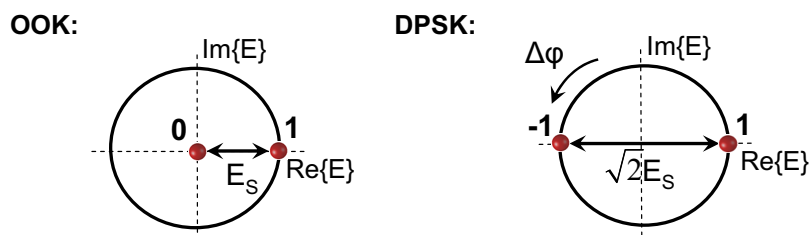


Figure 4.8: Signal constellations for binary OOK and binary DPSK modulation, both signal constellations have the same average optical power.

The transmitter and receiver structure of DPSK modulation is shown in Figure 4.7. DPSK modulation has a number of advantages over OOK modulation that makes it a suitable modulation format for robust long-haul transmission systems. The main benefit of DPSK modulation is the lower OSNR requirement when compared to OOK. This can be understood directly from the signal constellation, as visualized in Figure 4.8. In the case of OOK modulation, the difference

between the two constellation points equals the signal energy  $E_s$ , assuming NRZ pulse coding, an infinite extinction ratio and an average optical power  $1/2 \cdot 0 + 1/2 \cdot |E_s|^2 = 1/2 \cdot |E_s|^2$ . For DPSK, both constellation points have the same signal energy but a differential phase of either  $\Delta\phi = 0$  or  $\Delta\phi = \pi$ . When the difference between the two constellation points equals  $\sqrt{2}E_s$  the average power of DPSK is the same as for OOK, i.e.  $1/2 \cdot |1/\sqrt{2}E_s|^2 + 1/2 \cdot |1/\sqrt{2}E_s|^2 = 1/2 \cdot |E_s|^2$ . However, as the symbol distance is increased with a factor  $\sqrt{2}$  in comparison to OOK modulation, we obtain a  $\sim 3$ -dB advantage in OSNR tolerance.

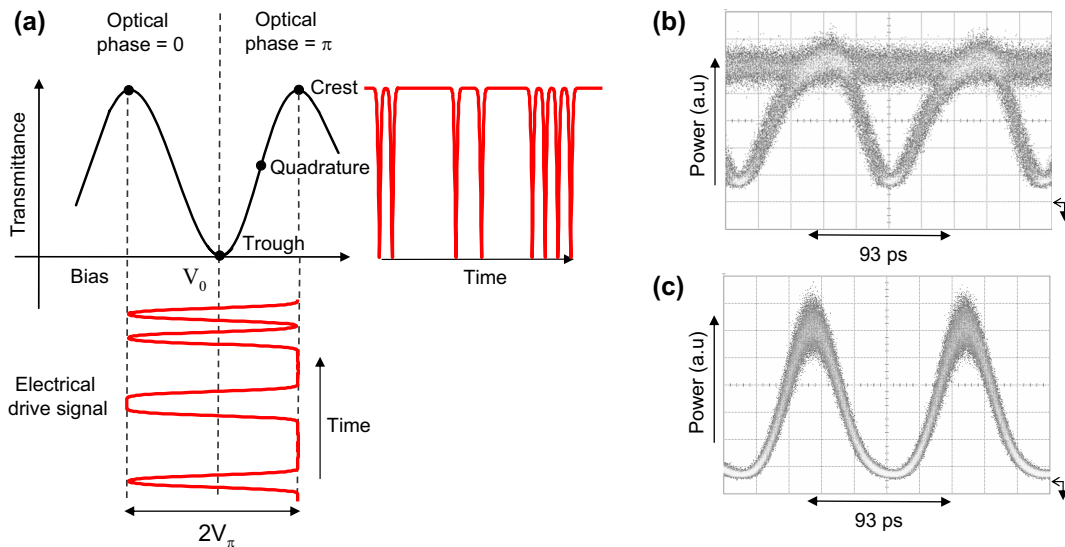


Figure 4.9: (a) Operation of the MZM for DPSK modulation and eye diagrams before phase demodulation showing, respectively, (b) 10.7-Gb/s NRZ-DPSK and (c) 10.7-Gb/s RZ-DPSK modulation.

### 4.3.1 Transmitter structure

As DPSK modulation carries the information in the optical phase, the most straightforward modulator configuration is based on a phase modulator. An (ideal) phase modulator changes only the phase of the optical signal, which results in constant amplitude. However, as the electro-optical bandwidth of a practical phase modulators is limited, the  $180^\circ$  phase transition is not instantaneous, which introduces chirp between symbol transitions. In the presence of chromatic dispersion and/or nonlinear impairments, this chirp limits transmission tolerances.

The more practical DPSK transmitter design is, similar to OOK modulation, based on a MZM. DPSK modulation with a MZM is depicted in Figure 4.9. The MZM is biased in the trough of the modulator curve and the electrical driving voltage has a peak-to-peak voltage of, ideally,  $2V_\pi$ . The MZM therefore switches between two crest points, which encodes the  $180^\circ$  phase jumps. This is visible in the NRZ-DPSK output signal, which shows characteristic intensity dips when the MZM switches from  $-1'$  to  $1'$  or vice-versa. The width of the intensity dips in the NRZ-DPSK signal depends on the electro-optical bandwidth of the MZM and/or the bandwidth of the electrical drive signal. The electro-optical bandwidth of a MZM is similar to what can be

realized for a phase modulator. But as a MZM has exact  $180^\circ$  phase changes, it does not suffer from modulator induced chirp.

When the DPSK modulator is followed by an additional pulse carver the NRZ pulse shape is converted to a RZ shape, similar as discussed for OOK modulation. For DPSK, pulse carving with a 66% duty-cycle does not result in alternating phase coding but merely inverts the encoded information in the DPSK signal. It is therefore not fully correct to refer to CSRZ-DPSK, although the abbreviation is often used in the literature. Figure 4.9b and 4.9c show typical eye diagrams for 10.7-Gb/s NRZ-DPSK and RZ-DPSK, respectively.

As DPSK modulation is based on differential detection, it requires pre-coding of the transmitted sequence. The pre-coder for DPSK is similar to the pre-coder required for duobinary modulation (Section 4.2,[239]). Note that the 'encoding' of the signal is, in contrast to duobinary modulation, not realized at the transmitter but through the phase demodulation at the receiver.

### 4.3.2 Receiver structure

In a DPSK receiver, the differential phase modulation is normally converted into amplitude modulation using a Mach-Zehnder delay-line interferometer (MZDI). An MZDI demodulates the differential phase between each data bit and its successor, which implements the differential decoding of DPSK modulation. Figure 4.10 depicts in more detail the phase demodulation with an MZDI. The optical input signal before demodulation is NRZ-DPSK modulated and has an average optical power of 1 mW (Figure 4.10a). The center spectral lobe of the NRZ-DPSK optical spectrum has a width equal to twice the signal bandwidth,  $2B_0 = 2/T_0$ .

The MZDI splits up the signal in two copies, delays one copy over a single bit period  $\Delta T$  in [s] and recombines both arms to create optical interference. Note that  $\Delta T$  is not necessarily equal to the symbol period  $T_0$  (e.g. for partial DPSK). The transfer function of the MZDI is defined through,

$$u_{\pm}(t) = r(t) \pm \exp(j\Delta\phi)r(t - \Delta T), \quad (4.3)$$

where  $u_{\pm}(t)$  is the constructive and destructive component, respectively.  $r(t)$  is the input signal and  $\Delta\phi$  the phase difference between both interferometer arms. The phase difference is ideally  $\Delta\phi = 0 \pm \pi$ . This can be understood by noting that for this phase shift and an unmodulated input signal, destructive interference occurs at one of the outputs and constructive interference at the other output. Hence, the output ports of the MZDI are referred to as the *constructive* and *destructive* port, respectively. When  $\Delta T$  is the delay in the interferometer arm, the constructive and destructive output ports exhibits a periodic notch response with a 3-dB bandwidth of  $1/(2\Delta T)$  and a free spectral range (FSR) of  $1/\Delta T$ . The constructive and destructive components obtained after demodulation are depicted in Figures 4.10b and 4.10c, respectively. Both signal components have a different optical spectra and signal structure but carry the same (but inverted) information. The optical spectrum of the constructive output port has a central lobe with a spectral width of  $B_0 = 1/T_0$ , which results in duobinary modulation [247, 248]. In the optical spectrum of the destructive output signal the carrier frequency is suppressed, which results in an alternating mark

inversion (AMI) signal. An AMI signal has a  $180^\circ$  phase jump between each consecutive '1', which gives the characteristic RZ shape of the AMI signal.

An MZDI can be realized with different technologies, for example with fiber-optic couplers [249], a fiber-Bragg grating [250] or free space technology [251]. An MZDI based on fiber-optic couplers requires active phase stabilization, as even slight changes in temperature result in a change in the differential delay of a fraction of an optical cycle. The path-length difference changes the interference between the two signals, which would degrade signal quality without an active control. An MZDI based on free-space technology is athermal and therefore does not require active phase stabilization. However, the drawback of an MZDI design without active control is that the phase difference between the two interfering arms cannot be adjusted to the center frequency of the received signal. Hence, such an MZDI must be matched to a predefined wavelength (usually the ITU grid). When the MZDI should be *colorless*, i.e. when it can be used for any WDM channel, this implies a fixed 50-GHz FSR, instead of 43-GHz FSR as would be optimal for a 43-Gb/s bit rate.

Closely related to the phase stabilization of an MZDI, but more difficult to avoid, is the polarization dependent wavelength shift ( $PD\lambda$ ). When both arms of the MZDI have a polarization dependent propagation coefficient, the periodic notch response of the MZDI is dependent on the SOP of the incoming light. As an example, we assume that the phase offset in the MZDI is minimized for a certain input SOP. The worst penalty then occurs when the input SOP changes to the orthogonal SOP on a time scale faster than the phase offset control loop. There is a high probability this will occur, since polarization changes are generally much faster than a thermal control. The penalty that results from a  $PD\lambda$  can be avoided through polarization tracking, but this is impractical as it significantly raises the receiver complexity. Minimizing the  $PD\lambda$  is therefore one of the more important criteria in the design of an MZDI.

Both the constructive and destructive output port of an MZDI carry the full information of the DPSK signal. Therefore, detecting either only the constructive or destructive output is sufficient. This is known as *single-ended* detection. But in order to obtain the  $\sim 3$ -dB OSNR improvement of DPSK over OOK modulation, both MZDI output ports have to be detected simultaneously. This is known as *balanced* detection, which uses two photodiodes followed by a differential amplifier. The transfer function of a DPSK receiver, i.e. the MZDI plus balanced detection is now defined through,

$$\begin{aligned} u(t) &= |u_+(t)|^2 - |u_-(t)|^2 \\ &= \left| \frac{1}{2}r(t) + \exp(j\Delta\phi) \frac{1}{2}r(t - \Delta T) \right|^2 - \left| \frac{1}{2}r(t) - \exp(j\Delta\phi) \frac{1}{2}r(t - \Delta T) \right|^2, \end{aligned} \tag{4.4}$$

where  $u(t)$  is the output after balanced detection. This is depicted in Figure 4.10d, which shows that the peak-to-peak amplitude of the balanced output is twice that of the constructive and destructive signal, separately. Figure 4.7 depicts measured eye diagrams for 42.8-Gb/s RZ-DPSK before demodulation and the constructive, destructive and balanced signals after demodulation.

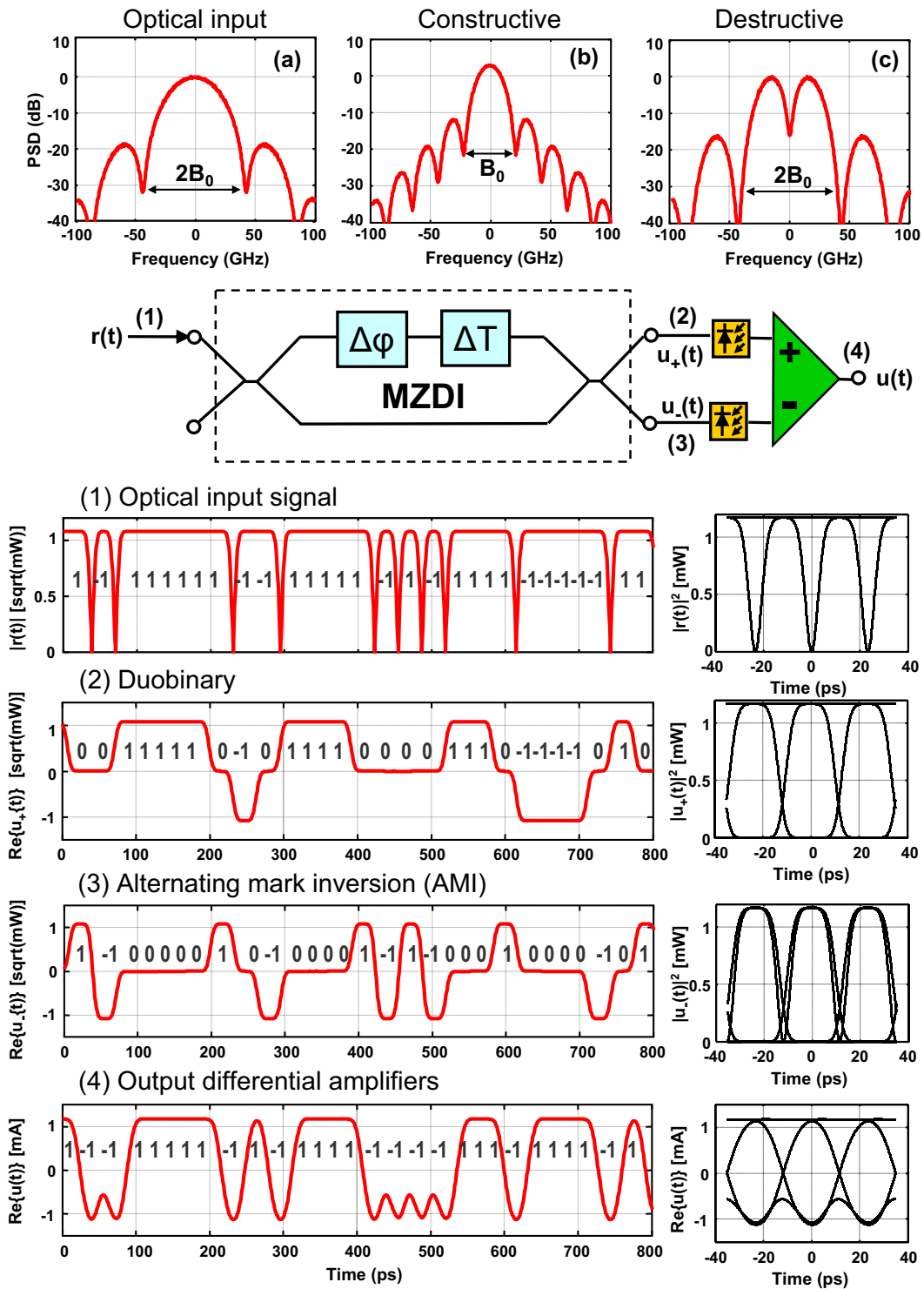


Figure 4.10: Phase demodulation of 42.8-Gb/s NRZ-DPSK showing the input signal before demodulation, as well as the spectra of the constructive, destructive and balanced outputs of the MZDI. The phase difference between the MZDI arms is equal to  $\Delta\phi = \pi$  in the example.

A special application of DPSK demodulation is the optical generation of either duobinary or AMI modulation. This can be achieved using a DPSK transmitter followed by an MZDI to demodulate either the constructive or destructive component. Especially the generation of optical duobinary via this method has some practical applications. The optical duobinary signal has similar properties as the (electrical) duobinary described in Section 4.2. This can be especially interesting in transmission links where strong narrowband filtering occurs [252]. On the other hand, the transmitter is more complicated as it requires an MZDI and higher bandwidth optical and electrical components (drive amplifiers, optical modulator).

### 4.3.3 Back-to-back OSNR requirement

The use of interferometric detection in DPSK allows for a lower-complexity receiver but requires a high OSNR to obtain the same performance as homodyne (coherent) detection. Figure 4.11 compares the theoretical performance of the different detection schemes for 10.7-Gb/s DPSK. The difference in OSNR requirement between 10.7-Gb/s DPSK with coherent and direct detection is 0.6 dB for a  $10^{-3}$  BER. Differential detection is not required in a coherent receiver and this can improve the OSNR requirement with a further 0.55 dB. The total difference in OSNR requirement between 10.7-Gb/s BPSK with coherent detection and DPSK with direct detection is therefore 1.1 dB for a  $10^{-3}$  BER.

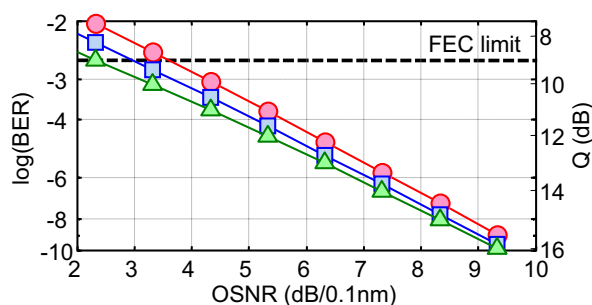


Figure 4.11: Theoretical performance of 10.7-Gb/s DPSK modulation ● direct detection with an MZDI, ■ coherent detection with differential decoding, ▲ coherent detection without differential decoding.

The difference is slightly dependent on the BER and it can be shown that the theoretical receiver sensitivity or 'quantum limit' at a BER of  $10^{-9}$  is 18 photons/bit for coherent BPSK and 20 photons/bit [253] for direct detection DPSK. In comparison, for OOK with direct detection the quantum limit is 38 photons/bit. Hence the theoretical sensitivity difference between OOK and DPSK modulation is 2.8 dB at low BER. Experimental verification has shown receiver sensitivities for direct detection DPSK of 30 photons/bit [254] and 38 photons/bit [255, 112] at a bit rate of 10 Gb/s and 42.7 Gb/s, respectively.

Besides the lower OSNR requirement, coherent detection can have further advantages over interferometric detection in the nonlinear transmission regime. Interferometric detection compares the phase difference between two consecutive symbols; the sensitivity penalty is therefore a product of the phase error in both symbols. When one assumes an ideal transmitter and LO laser in



coherent detection (i.e. no phase noise) the penalty only dependent on the phase error in the received symbol itself. Hence, coherent detection theoretically reduces the impact of nonlinear phase noise by a factor of two in comparison to interferometric detection [256]. The main drawback of homodyne demodulation is the higher complexity of a coherent receiver as it requires the detection of the full optical field, including the state of polarization. Because of its relative simplicity, self-homodyne demodulation is therefore the preferable choice for deployed transmission systems. A practical approach for homodyne demodulation that is currently under consideration is a coherent intra-dyne receiver, which is discussed in Chapter 10. In this section we further discuss the properties of DPSK modulation using a direct detection receiver.

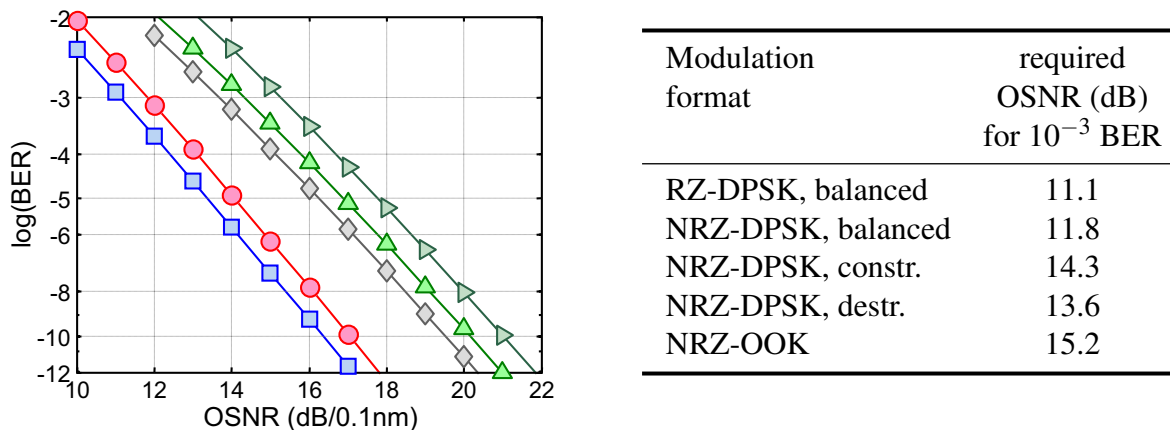


Figure 4.12: Simulated OSNR requirement for  $\bullet$  42.8-Gb/s NRZ-DPSK, balanced,  $\square$  42.8-Gb/s RZ-DPSK, balanced,  $\blacktriangle$  42.8-Gb/s NRZ-DPSK, constructive,  $\blacklozenge$  42.8-Gb/s NRZ-DPSK, destructive,  $\blacktriangleright$  42.8-Gb/s NRZ-OOK. In all cases a 90-GHz optical filter bandwidth is used

The difference in OSNR requirement between DPSK and OOK modulation depends on pulse shape and receiver parameters. For the simulations depicted in Figure 4.12, the difference in required OSNR between NRZ-DPSK and NRZ-OOK is 3.4 dB. The  $>3$ -dB penalty is a result of the broad 90-GHz optical filter bandwidth used in the simulations. For DPSK modulation, the transfer function of the MZDI narrowband filters the signal which reduces the spontaneous-spontaneous beat noise in the signal. For OOK, on the other hand, the OSNR requirement is higher as the spontaneous-spontaneous beat noise is not filtered out. It is further observed that the constructive and destructive components of the NRZ-DPSK signal differ by 0.7 dB in OSNR requirement. This is a consequence of the RZ pulse shape of the destructive (AMI) components in comparison to the NRZ-pulse shape of constructive (duobinary) component. For the same reasons, a 0.7 dB difference in OSNR is observed between NRZ-DPSK and RZ-DPSK. The difference between NRZ-DPSK and the constructive/destructive component is 2.5 dB and 1.8 dB, respectively, for a  $10^{-3}$  BER but increases for lower BER. We note that with narrowband optical filtering the comparison changes as each of the signal has a different optimal filter bandwidth. However, a 90-GHz filter bandwidth is a reasonable assumption for transmission systems with a 100-GHz channel spacing.



## 4.3.4 Receiver imperfections

Imperfection in the phase demodulation have a significant impact on the optical performance characteristics of a DPSK receiver [257, 258]. A direct detection DPSK receiver can be impaired through, for example, an amplitude or time imbalance between the constructive and destructive outputs. The amplitude imbalance results in a shift of the optimum threshold whereas the time imbalance offsets the constructive and destructive components, resulting in a skewed eye diagram. Furthermore, the phase differences and bit-delay between the signal and its delayed copy upon interfere within the MZDI are important to consider. The bit-delay in the MZDI is an important aspect for partial DPSK, and is therefore discussed extensively in the next section. We note that although the simulated results are for a 42.8-Gb/s symbol rate, most of the receiver imperfections are bit rate independent.

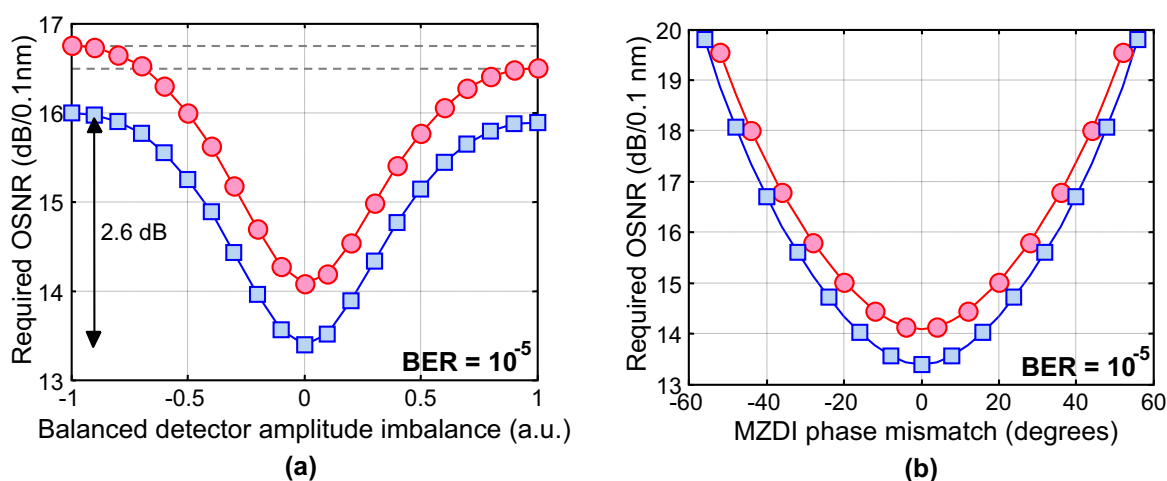


Figure 4.13: Simulated DPSK receiver imperfections, (a) amplitude imbalance and (b) phase mismatch; ● 42.8-Gb/s NRZ-DPSK, ■ 42.8-Gb/s RZ-DPSK.

Figure 4.13a shows the amplitude imbalance between the constructive and destructive components. An amplitude imbalance results from a difference in the pigtail or connector loss in one of the two arms, or a difference in conversion efficiency between the two photodiodes. The amplitude imbalance is defined as [257],

$$\alpha = \frac{|u_+|^2 - |u_-|^2}{|u_+|^2 + |u_-|^2}, \quad (4.5)$$

where  $|u_-|^2$  and  $|u_+|^2$  are the averaged output powers of both photodiodes *before* balanced detection. The amplitude imbalance varies between  $\alpha = \pm 1$  and is in the extremes equal to single-ended detection of either the constructive or destructive component. For NRZ-DPSK, the curve is slightly asymmetric, which results from the difference in OSNR requirement between the constructive component (dominant for  $\alpha < 0$ ) and destructive component (dominant for  $\alpha > 0$ ). For RZ-DPSK, the difference is negligible as both components have a similar OSNR requirement. The simulated penalty is with 2.6 dB slightly lower than the 2.8-dB penalty that one would expect from theory, which is caused by the higher BER ( $10^{-5}$ ) used in the simulations. An  $\alpha = 0.2$

results in a 0.5-dB penalty, which equals approximately a 1.5 dB difference between the two outputs of the MZDI.

The phase offset penalty results from a phase difference upon interference between the two arms of the MZDI, as  $\Delta\phi = 0$  is optimal. For an OSNR penalty of 1 dB, the allowable phase offset is about  $20.5^\circ$  (see Figure 4.13b). Note that the penalty is independent of the pulse coding (RZ or NRZ). A phase offset in the MZDI can be induced through (1) wavelength drift of the transmitter laser, (2) temperature drift of the MZDI and (3) polarization-dependent wavelength shift of the MZDI [259]. The phase offset in degrees is related to the laser wavelength through,

$$\Delta\phi = 360 \cdot \Delta f \Delta T, \quad (4.6)$$

where  $\Delta f$  is the laser frequency drift in  $[Hz]$ . To counter a temperature or laser wavelength drift, the required tracking speed is generally slow and in the seconds range. A (slow) thermal control can therefore be used to change the phase difference between the two arms and as a control signal, the RF power after balanced detection can be measured [260]. When a phase offset is present in the MZDI, the constructive and destructive component are not anymore fully orthogonal to each other, i.e.  $|u_+|^2 \approx -|u_-|^2$ . The subtraction of the constructive and destructive component through balanced detection then result in a lower RF power. Hence, a phase offset in the MZDI lowers the RF power obtained after balanced detection and maximizing the RF power will minimize the phase offset in the MZDI.

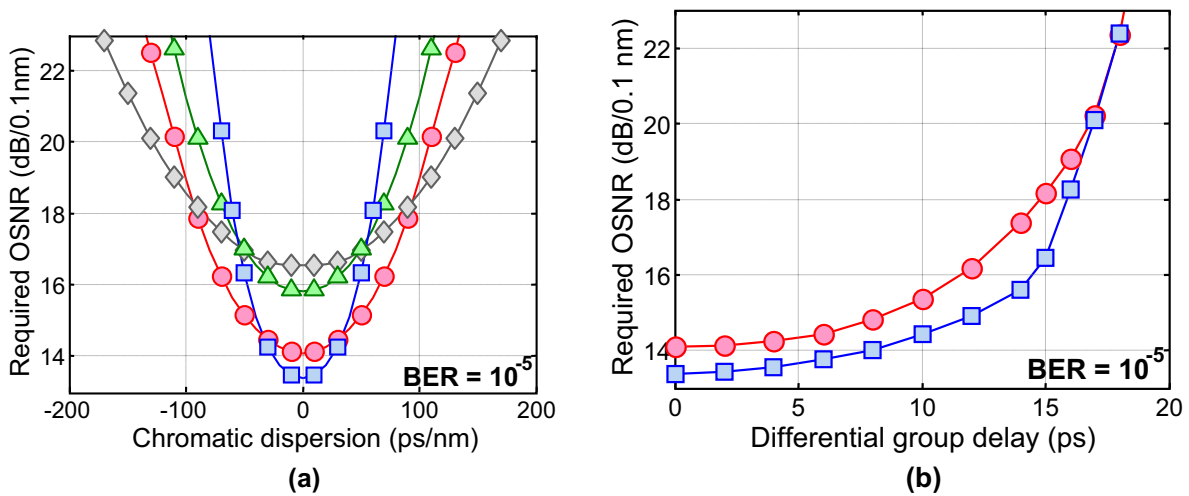


Figure 4.14: (a) chromatic dispersion and (b) DGD tolerance for 42.8-Gb/s NRZ and RZ-DPSK;  $\bullet$  42.8-Gb/s NRZ-DPSK, after balanced detection, 90-GHz filter  $\square$  42.8-Gb/s RZ-DPSK, 90-GHz filter.  $\blacktriangle$  42.8-Gb/s NRZ-DPSK, destructive component, 60-GHz filter  $\blacklozenge$  42.8-Gb/s NRZ-DPSK, constructive component, 40-GHz filter.

### 4.3.5 Chromatic dispersion & DGD tolerance

The chromatic dispersion tolerance of DPSK modulation is depicted in Figure 4.14a. This shows that the dispersion tolerance differs between the destructive and constructive component of DPSK. This difference can be explained by the line coding in both components. Due to its

duobinary coding, the constructive component has similar properties as duobinary modulation. This improves the dispersion tolerance, although the tolerance is somewhat lower compared to conventional duobinary. The destructive component, on the other hand, has a reduced dispersion tolerance. This results from the RZ-shape of the signal, which broadens the optical spectrum. Note that the optical filter bandwidth for both the constructive and destructive component is different and has been optimized. The chromatic dispersion tolerance after balanced detection is determined by both components. However, together with narrowband filtering (not shown) the dispersion tolerance becomes similar to the tolerance of the constructive component. When we furthermore compare the dispersion tolerance of RZ-DPSK with NRZ-DPSK, a significant reduction is evident. This results from the broader optical spectrum of the RZ signal. In addition, there is no significant difference between the constructive and destructive component for RZ-DPSK.

Figure 4.14b shows the DGD tolerance for 42.8-Gb/s NRZ-DPSK and RZ-DPSK. For a RZ pulse shape, there is less ISI for small amounts of DGD because the pulses spread out but not yet interfere with the neighboring pulses. Hence, we find a 9 ps and 10 ps DGD tolerance (1-dB OSNR penalty) for NRZ-DPSK and RZ-DPSK, respectively. For larger amounts of DGD the tolerance of both RZ and NRZ is similar, as the DGD tolerance is mainly determined by the symbol rate.

## 4.4 Partial DPSK

Ideally, 42.8-Gb/s modulated signals can be deployed in transmission systems with a 50-GHz channel spacing. But when OADM/PXCs are passed along the transmission link this result in severe narrowband optical filter, and the optical bandwidth can be reduced to  $\sim 35$  GHz. For 42.8-Gb/s NRZ-DPSK modulation this result in high OSNR penalties, which limits the number of add-drop nodes that can be passed

When a NRZ-DPSK signal is narrowband filtered, the constructive component remains nearly unaffected because most of the energy is close to the carrier. In addition, the constructive component has a duobinary line coding which significantly improves its tolerance to narrowband filtering. For the destructive component, on the other hand, most of the energy is relatively far away from the carrier. Narrowband filtering therefore reduces the power in the destructive component, which becomes distorted. As a result, the signal after balanced detection is asymmetric and the optimum threshold shift towards the constructive component.

The use of a shortened MZDI in the DPSK receiver, which has a  $\Delta T < T_0$  bit-delay between both arms, improves the narrowband filtering tolerance. This is known as partial DPSK, and was first demonstrated in 2003 by *Yoshikane et. al.* [261]. Figures 4.15a and 4.15b depicts the concept of partial DPSK and the OSNR requirement as a function of the bit-delay, respectively. This shows that for 42.8-Gb/s NRZ-DPSK there is a strong asymmetry with respect to the 1-bit delay. For  $\Delta T < T_0$ , the signal and its delayed copy are only partially overlapping upon interference, which results in deterministic interference at the beginning and end of the symbol

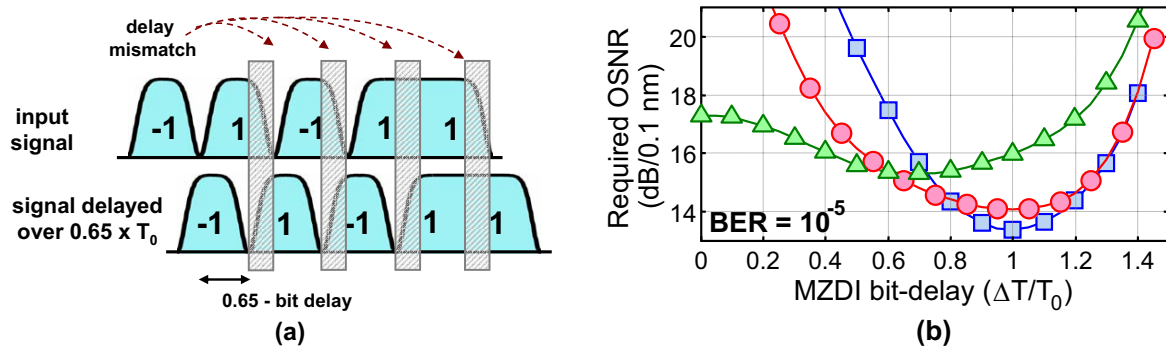


Figure 4.15: (a) phase demodulation with  $< 1$ -bit delay, (b) OSNR penalty for different MZDI bit-delays  
 ● 42.8-Gb/s NRZ-DPSK, 90-GHz filter bandwidth    ■ 42.8-Gb/s RZ-DPSK, 90-GHz filter bandwidth    ▲ 42.8-Gb/s NRZ-DPSK, 35-GHz filter bandwidth.

period. After balanced detection the electrical signal appears, apart from a negative offset, similar to a duobinary signal. This is evident from Figure 4.16, which shows simulated eye diagrams of the balanced output for several MZDI bit-delays. The shortened bit-delay in the MZDI results in a somewhat higher OSNR requirement. This is explained by the observation that the constructive and destructive components are not fully orthogonal anymore, which results in a lower signal power after balanced detection. For  $\Delta T \ll T_0$ , the destructive component fades out and the penalty is solely determined by the constructive component. For  $\Delta T > T_0$ , the symbol transition of the delayed copy occurs in the middle of the symbol period which results in crosstalk. The penalty reduces for  $\Delta T \gg T_0$  and is close to zero for  $\Delta T \sim 2T_0$  as the symbol transitions are again aligned with each other [262].

The impact of a shortened bit-delay on the narrowband filtering tolerance is shown in Figure 4.15b. Depicted is the penalty for 42.8-Gb/s NRZ-DPSK with a 35-GHz, 3<sup>rd</sup> order Gauss filter as a

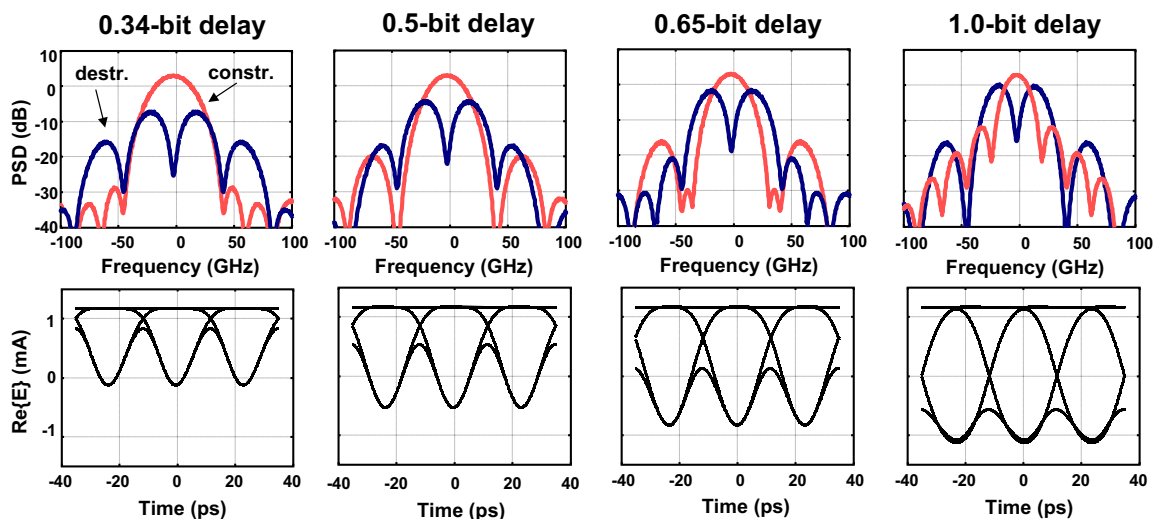


Figure 4.16: Impact of  $< 1$ -bit MZDI delay. The upper row shows the optical spectra (0.1-nm res.) of the constructive and destructive output port. The lower row shows the electrical signal after balanced detection.

function of the MZDI bit-delay. For a 1 bit-delay, a 16.0-dB OSNR is required, a 1.9-dB OSNR penalty. When the bit-delay is reduced, the narrowband filtering penalty reduces accordingly, with a minimum penalty for a 0.65 bit-delay. Note that for a 0.65 bit-delay there is a negligible difference in OSNR requirement between NRZ-DPSK with (35 GHz) and without (90 GHz) optical filtering. This is particularly interesting from a system design point of view, as no performance variation has to be accounted for. We further observe that with narrowband filtering, the bit-delay can be reduced to zero with only a minor penalty. In this case the DPSK signal is demodulated through narrowband optical filtering [263]. The improved narrowband filtering tolerance for a shortened bit-delay is best explained with the optical spectra of the constructive and destructive component, as shown in Figure 4.16. When the bit-delay is decreased, the 3-dB bandwidth of the MZDI's periodic notch response broadens. As a result, a larger part of the signals energy passes through the constructive port. The destructive component, on the other hand, is attenuated and fades out for shorter bit-delays. The optical narrowband filtering mainly affects the destructive component, which is attenuated anyway through the demodulation with a shortened MZDI. The constructive component (with the duobinary line coding) becomes the dominant signal compo-

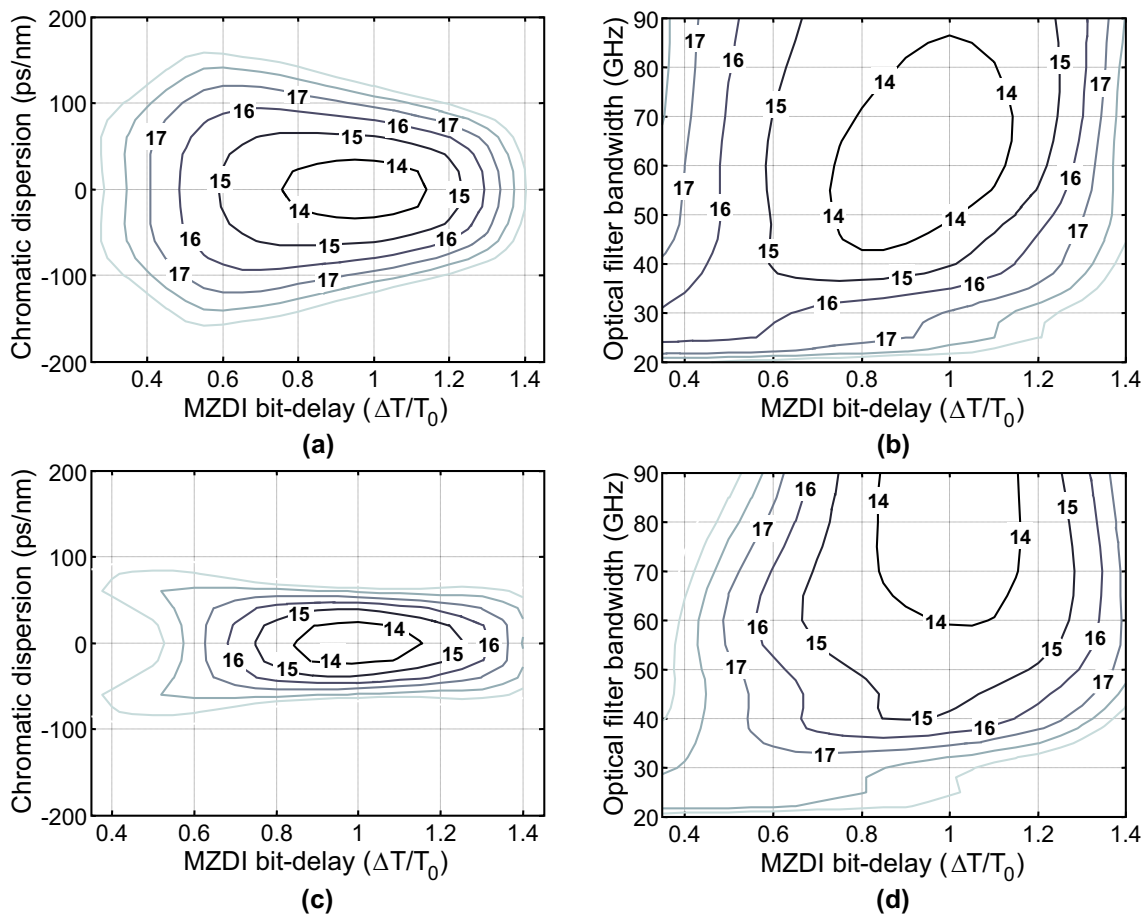


Figure 4.17: Chromatic dispersion (a,c) and optical filter bandwidth (b,d) tolerance for NRZ-DPSK (a,b) and RZ-DPSK (c,d) as a function of MZDI differential delay. The contour plots show the required OSNR for a  $10^{-5}$  BER.

ment, which in turn reduces the narrowband filtering penalties. As a result, partial DPSK is the DPSK format of choice for deployed transmission systems. The improvement in optical filter tolerance for 42.8-Gb/s NRZ-DPSK with a shortened MZDI is discussed in [264, 265]. For RZ-DPSK, the penalty is more or less symmetrical with respect to the 1 bit-delay. A shortened bit-delay results in a signal that has similar properties as RZ-duobinary, including a broad optical spectrum. No significant improvement in narrowband filtering tolerance is therefore observed at low OSNR penalties [266].

Finally, we note that the chromatic dispersion tolerance and the filter bandwidth are dependent on each other as well as on the MZDI bit-delay. This is depicted in Figure 4.17. When narrowband optical filtering or a shortened MZDI are considered separately, an OSNR penalty is observed for NRZ-DPSK. For an OSNR requirement of 16-dB (2.5-dB penalty), the narrowband filter tolerance is 35-GHz. However, combined with a shortened 0.65 bit-delay MZDI the narrowband filter tolerance is improved to 24 GHz. At the same time, the chromatic dispersion tolerance increases from 80-ps/nm to 95-ps/nm, for an 16-dB required OSNR. We note that this is computed with a 60-GHz optical filter bandwidth. When the shortened bit-delay is combined with narrowband filtering, the tolerance can be further increased. For RZ-DPSK (Figure 4.17c-d), the dependence is significantly reduced. Only for high OSNR penalties a similar improvement in narrowband filtering tolerance is observed. The observed 'w'-shape in the dispersion tolerance for small bit-delays confirms that the signal is similar to duobinary in the absence of narrowband filtering.

---

## Differential quadrature phase shift keying

For high-speed optical transmission systems, multi-level modulation formats are a logical upgrade to either increase the spectral efficiency above 1-b/s/Hz, or to improve the robustness against transmission impairments. A significant number of different multi-level modulation formats have been proposed, using either modulation in the amplitude, phase or polarization domain [267, 245, 268]. In order to minimize the OSNR requirements and maximize nonlinear tolerance for long-haul transmission systems, especially modulation formats based on either phase and/or polarization modulation appear to be the most suitable. Phase modulated formats have only modestly worse OSNR requirements compared to DPSK [10]. As well, the lack of a strong optical carrier reduces the generation of XPM when compared to amplitude modulation formats [269]. The higher OSNR requirement, as well as the reduced nonlinear tolerance of multi-level modulation in the amplitude domain [270] makes it impractical for long-haul transmission. The use of polarization as a selective agent is discussed in Chapter 7

The multi-level modulation format that received the most interest in recent years is return-to-zero differential quadrature phase shift keying (RZ-DQPSK). This chapter discusses the properties of DQPSK modulation. In Section 5.1 the structure of a DQPSK transmitter and receiver are explained. Subsequently, in Section 5.3 the properties of DQPSK modulation are discussed, including the tolerance against narrowband filtering, chromatic dispersion and PMD. Section 5.4 analyzes the nonlinear tolerance of DQPSK modulation and in Section 5.5 we discuss in detail the use of multi-level random sequences for evaluation of DQPSK transmission performance. In Chapter 6 we subsequently focus on long-haul transmission using DQPSK modulation.

---

<sup>1</sup>The results described in this chapter are published in c11, c24, c35, c42, c50, c53

## 5.1 Transmitter & receiver structure

Figure 5.1 depicts the signal constellations of both binary DPSK and quaternary DQPSK modulation. Comparing DPSK and DQPSK modulation, it is evident that the number of constellation points is doubled and the distance between the constellation points is halved. Taking, for example, '00' as a reference, then the symbols '01', '10' and '11' correspond to a phase difference  $\pi/2$ ,  $\pi$  and  $3\pi/2$ , respectively. At the same symbol rate, DQPSK therefore doubles the total bit rate. However, as the distance between the constellation points is halved it requires, at least, a 3-dB higher OSNR for the same BER. More commonly, DQPSK is used at half the symbol rate of binary modulation to obtain the same total bit rate. DQPSK has then, ideally, no OSNR penalty in comparison to DPSK modulation.

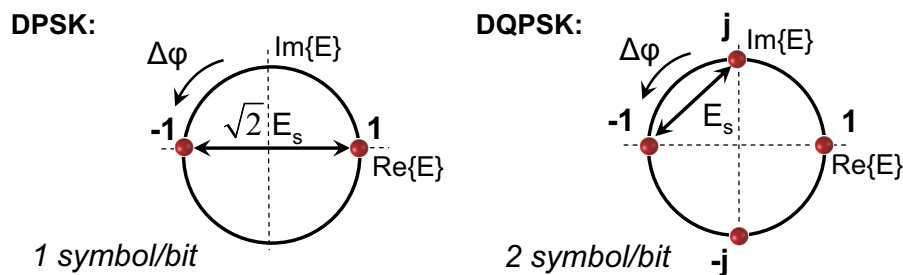


Figure 5.1: Signal constellations for binary DPSK and quaternary DQPSK modulation.

DQPSK modulation can be realized using a variety of modulator configurations. The most common DQPSK modulator configuration is depicted in Figure 5.2 using a so called 'Super Mach-Zehnder' structure as first introduced by *Griffin et. al.* [271]. In such a parallel DQPSK modulator, the signal is split and each tributary is, in effect, DPSK modulated. DQPSK modulation is subsequently obtained by interfering the two tributaries with a suitable chosen phase shift (either  $-\pi/2$  or  $\pi/2$ ). Two independent electrical drive signals are fed to the DQPSK modulator and only binary drive signals are required. This has the advantage that standard drive amplifiers at half the bandwidth of DPSK modulation can be used to amplify the electrical drive signals to a  $2 \cdot V_\pi$  voltage swing. The eye diagram in Figure 5.2 shows a double intensity dip when the MZM switches over either  $\Delta\phi = \pi/2$  or  $\Delta\phi = \pi$ , this is characteristic for DQPSK modulation with a parallel modulator.

Other modulator configurations for DQPSK modulation include a MZM and phase modulator in series [272], a single phase modulator with a 4-level drive signal [273, 274] and two EAMs in a three-arm interferometer structure [275]. Figure 5.3 depicts the signal constellation for several of the DQPSK modulator configurations. The main drawback of using a phase modulator for DQPSK modulation is the higher residual chirp in the signal, which reduces the tolerance against chromatic dispersion and nonlinear impairments [273, 274]. We note that modulation with a parallel DQPSK modulator also result in residual chirp, but in somewhat reduced amounts as it occurs only during the symbol transitions. The higher signal chirp is also evident from the signal constellations of both the MZM and phase modulator in series as well as the 4-level phase modulator. RZ pulse carving reduces the residual chirp in the modulated signal and is



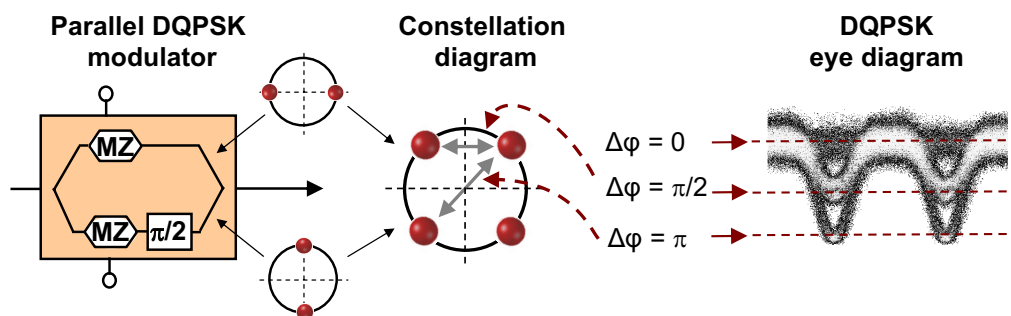


Figure 5.2: Operation of the 'super' Mach-Zehnder structure for DQPSK modulation.

therefore desirable for DQPSK modulation. The performance of all three modulation structures is nearly identical for 33% RZ pulse carving [273]. This is illustrated by optical time-division-multiplexing experiments where a MZM plus phase modulator has been used for DQPSK modulation with excellent performance [276].

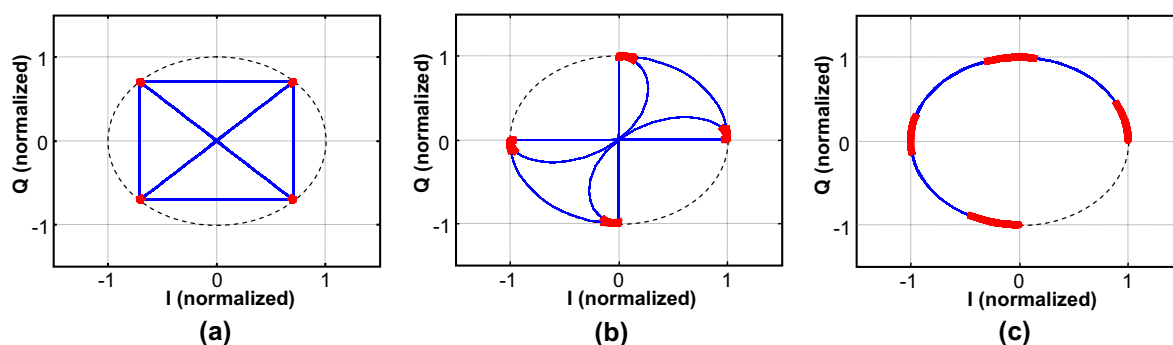


Figure 5.3: Simulated signal constellations for DQPSK modulation with (a) a parallel 'Super Mach-Zehnder' structure, (b) a cascaded MZM and PM and (c) a PM with 4-level drive signal. The thick line shows the signal in the middle 50% of the symbol period.

Figure 5.4 depicts the transmitter and receiver structure using a parallel DQPSK modulator. In most reported transmission experiments, two separate MZDIs are used in the receiver to convert the modulation from the phase to amplitude domain. Although it is also possible to demodulate both tributaries at the same time using a 1x4 star coupler [277, 278], or a  $90^\circ$  hybrid with one of its inputs delayed over one symbol period [279]. When two separate MZDI interferometers are used, the phase shift between the two arms of the MZDI is  $+45^\circ$  and  $-45^\circ$  to demodulated the in-phase (I) and quadrature (Q) component, respectively. A phase control for DQPSK demodulation is described in [280]. Each MZDI has a constructive and destructive output and therefore 4 photodiodes are required for balanced detection of DQPSK. For experimental evaluation of DQPSK modulation, a pseudo random quaternary sequence (PRQS) can be used to ensure that all possible sequences up to a given length are tested (see Section 5.5). The data sequences obtained after balanced detection are, due to the differential demodulation in the 1-bit delay MZDI, a mix of the two transmitted data sequences. Either pre-coding or post-coding is therefore required to evaluate DQPSK modulation. For experimental evaluation the BER tester is normally programmed for the expected output sequence (post-coding). This limits the PRBS length to  $\sim 2^{15} - 1$  because

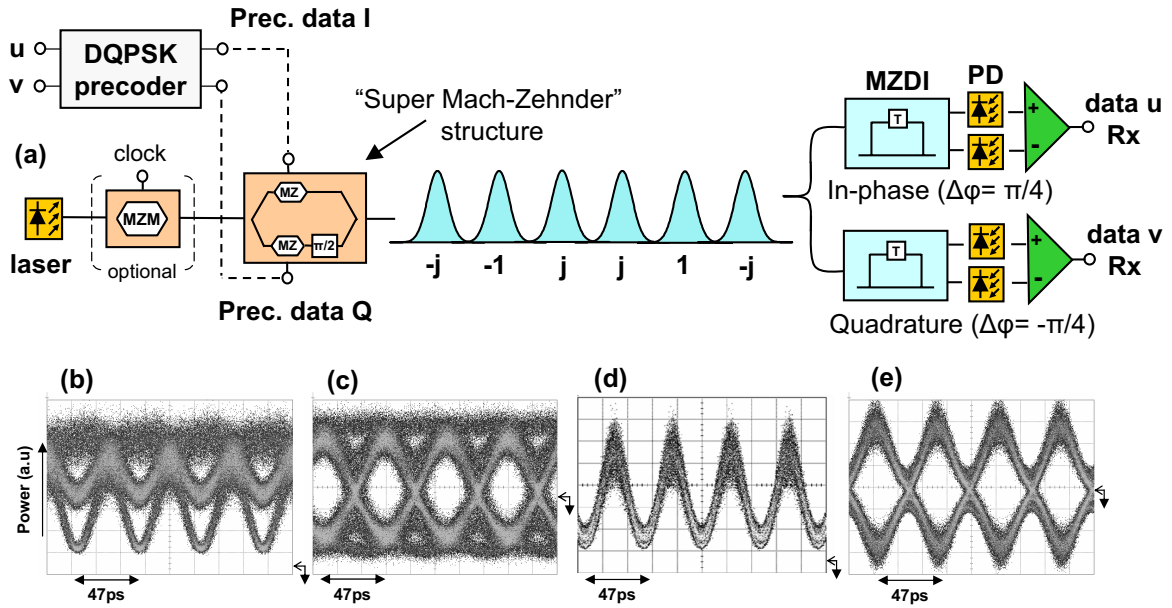


Figure 5.4: (a) Transmitter and receiver structure of RZ-DQPSK, (b-e) Measured eye diagrams showing; (b) 42.8-Gb/s NRZ-DQPSK, (c) 42.8-Gb/s NRZ-DQPSK after phase demodulation, (d) 42.8-Gb/s RZ-DQPSK, (e) 42.8-Gb/s RZ-DQPSK after phase demodulation.

programming the expected output sequence makes longer sequences impractical. Each bit  $I(k)$  and  $Q(k)$  in the post-coded sequences is dependent on four bits of the transmitted sequence,  $u(k)$ ,  $v(k)$ ,  $u(k-1)$  and  $v(k-1)$ . The post-coded bits for a parallel DQPSK modulator are given by,

$$I(k-1) = \frac{1}{2} \left( u(k-1) \oplus u(k) + v(k-1) \oplus v(k) - u(k-1) \oplus v(k) + v(k-1) \oplus u(k) \right) \quad (5.1)$$

$$Q(k-1) = \frac{1}{2} \left( u(k-1) \oplus u(k) + v(k-1) \oplus v(k) + u(k-1) \oplus v(k) - v(k-1) \oplus u(k) \right) \quad (5.2)$$

In a commercial transponder, on the other hand, pre-coding of the transmitted sequence is required [281, 282, 283]. Each bit of the pre-coded sequence is dependent on the bits  $u(k)$ ,  $v(k)$ ,  $I(k-1)$  and  $Q(k-1)$ . This shows that each pre-coded bit depends on its predecessor, which implies that a high-speed feedback is required that operates at the symbol rate. Such a high-speed feedback path can be avoided by using toggle flip-flops, as shown by *Serbay et. al.* in [281]. Alternatively, a parallel implementation can be used to reduce the speed of the feedback path

[283]. The pre-coded bits of a parallel DQPSK modulator are given by [271],

$$\begin{aligned}
 I(k) &= \left( \overline{I(k-1) \oplus Q(k-1)} \right) \cdot \left( \overline{I(k-1) \oplus v(k)} \right) \\
 &+ \left( I(k-1) \oplus Q(k-1) \right) \cdot \left( \overline{I(k-1) \oplus u(k)} \right)
 \end{aligned} \tag{5.3}$$

$$\begin{aligned}
 Q(k) &= \left( \overline{I(k-1) \oplus Q(k-1)} \right) \cdot \left( \overline{I(k-1) \oplus u(k)} \right) \\
 &+ \left( I(k-1) \oplus Q(k-1) \right) \cdot \left( I(k-1) \oplus v(k) \right)
 \end{aligned} \tag{5.4}$$

which can be re-written as [283],

$$\begin{aligned}
 I(k) &= u(k) \cdot v(k) \cdot I(k-1) + u(k) \cdot \overline{v(k)} \cdot Q(k-1) \\
 &+ \overline{u(k)} \cdot \overline{v(k)} \cdot \overline{I(k-1)} + \overline{u(k)} \cdot v(k) \cdot \overline{Q(k-1)}
 \end{aligned} \tag{5.5}$$

$$\begin{aligned}
 Q(k) &= u(k) \cdot v(k) \cdot Q(k-1) + \overline{u(k)} \cdot v(k) \cdot I(k-1) \\
 &+ u(k) \cdot \overline{v(k)} \cdot \overline{I(k-1)} + \overline{u(k)} \cdot \overline{v(k)} \cdot \overline{Q(k-1)}
 \end{aligned} \tag{5.6}$$

Figure 5.4 further shows the measured eye diagrams for NRZ- and RZ-DQPSK modulation before and after demodulation. This shows a relatively broad '1'-rail in the NRZ-DQPSK modulated eye diagram due to amplitude noise. The amplitude noise results from modulator imperfections. Typical modulator imperfections result from mismatches between the  $V_\pi$  of the modulator and the  $2 \cdot V_\pi$  amplitude swing of the driver amplifiers. But for a parallel DQPSK modulator, in particular the phase and amplitude mismatches between the two DPSK modulated tributaries is important. Such imperfections depend on the specifications of the modulator, but can be minimized by controlling the bias voltage of the three interferometers within a parallel DQPSK modulator. In the transmission experiments reported here these bias voltages are set manually, but for a commercial transponder they have to be controlled, for example, by minimizing the power envelope variance. In this case three different pilot tones can be used, where each pilot tone separately controls one of the three bias voltages. Alternatively, an additional light source at the modulator output can be used to implement a control of the bias voltages by minimizing the power of the backward propagating light [284]. The broadened '1'-rail in a DQPSK signal can be partially suppressed through RZ pulse-carving, but the amplitude of the pulse remains noisy. We note that the amplitude noise in the signal is not clearly evident in the back-to-back OSNR requirement, but results in an increased impact of nonlinear phase noise along the transmission link.

## 5.2 Back-to-back OSNR requirement

The OSNR requirement of DQPSK modulation is, ideally, the same as for DPSK modulation at the same total bit rate. However, for direct detection receivers the OSNR requirement differs between both modulation formats as DQPSK suffers from a higher MZDI demodulation penalty. The higher OSNR requirement for DQPSK demodulation can be explained as follows. For DPSK, the constructive component is duobinary modulated and the destructive component is AMI modulated. In an ideal DPSK receiver, both components are (nearly) orthogonal to each other. For DQPSK modulation both the constructive and destructive outputs are neither duobinary or AMI modulated. This is clearly visible in Figure 5.7 which depicts eye diagrams of the constructive and destructive components as well as the (slightly skewed) eye diagram after balanced detection for the in-phase tributary of 42.8-Gb/s RZ-DQPSK modulation. The constructive and destructive components show a ghost pulse in the '0', which in a sense results from crosstalk of the other tributary. The crosstalk is removed through balanced detection as the ghost pulse is subtracted from the other component. This causes a loss of signal power, which translates into a higher OSNR requirement.

Figure 5.5 shows the measured OSNR requirement for 42.8-Gb/s RZ-DQPSK modulation, with 21.4-Gb/s RZ-DPSK as a reference. This indicates that the difference in OSNR requirement between RZ-DPSK and RZ-DQPSK is BER dependent. For a  $10^{-9}$  BER the difference is 6.2 dB, whereas for a  $10^{-3}$  BER the difference reduces to 4.4 dB. When we do not take the 3-dB difference into account that results from doubling the bit rate, a measured penalty is left that varies between 1.4 dB and 3.2 dB. Figure 5.6 depicts this excess OSNR penalty for both the measurements as well as simulations. The measured penalty is slightly higher than the penalty predicted by simulations, which is  $\sim 0.6$  dB for a BER close to the FEC limit and increases to 1.6 dB for a  $10^{-9}$  BER. The difference between simulated and measured penalty results from transmitter and receiver imperfections.

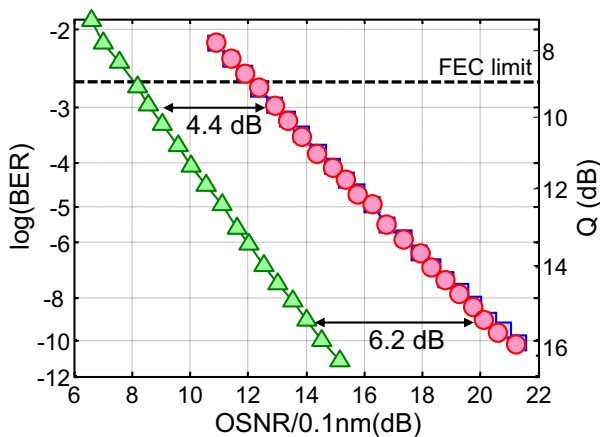


Figure 5.5: Measured BER versus OSNR for  $\bullet$  42.8-Gb/s RZ-DQPSK, In-phase  $\square$  42.8-Gb/s RZ-DQPSK, Quadrature  $\blacktriangle$  21.4-Gb/s RZ-DPSK.

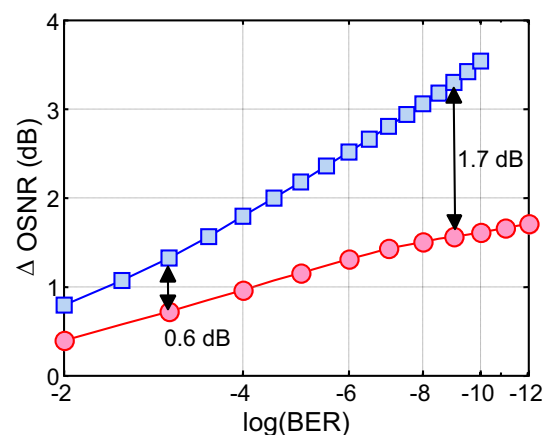


Figure 5.6: OSNR difference between DPSK and DQPSK modulation at a 42.8-Gb/s bit rate;  $\bullet$  simulated  $\square$  measured.

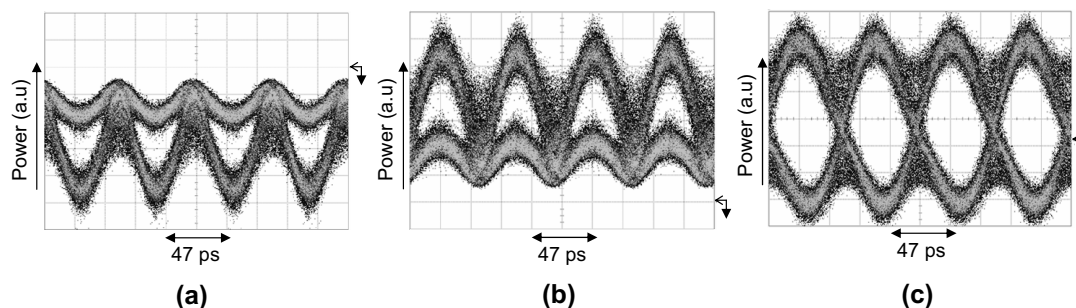


Figure 5.7: Measured eye diagrams for the in-phase tributary of 42.8-Gb/s RZ-DQPSK with 34-GHz optical filtering, (a) destructive, (b) constructive and (c) after balanced detection.

The higher OSNR requirement of DQPSK modulation can be computed using Equation 4.4. As an example, we assume that the input signal is an ideal unmodulated signal,  $r(t) = 1$ , and that the phase shift in the MZDI is ideal, i.e.  $\Delta\phi = \pi/4$ . The output signal after balanced detection can then be denoted as,

$$u(t) = \left| \frac{1}{2} + \frac{1}{2} \exp(j\frac{\pi}{4}) \right|^2 - \left| \frac{1}{2} - \frac{1}{2} \exp(j\frac{\pi}{4}) \right|^2 = \sqrt{2}. \quad (5.7)$$

In comparison, for DPSK modulation, i.e.  $\Delta\phi = 0$ , this gives  $u(t) = 1$ . The difference is equal to 1.5 dB when converted to logarithmic units.

For homodyne demodulation in a coherent receiver, DPSK and DQPSK modulation have the same OSNR requirement. Figure 5.8 depicts the BER as a function of OSNR for self-homodyne demodulation of DQPSK and homodyne demodulation of DQPSK and QPSK. For a  $10^{-3}$  BER the difference between coherent and interferometric detection is 1.85 dB for DQPSK. Comparing DQPSK with coherent QPSK detection the OSNR difference increases to 2.4 dB, as the differential decoding of DQPSK doubles the BER. We note that the curve for 42.8-Gb/s DQPSK modulation with interferometric detection is computed using Monte-Carlo simulations. The simulation assumes ideal signal constellations and matched filtering at the receiver to match with the theoretical performance of the coherent detection schemes. Note that the simulated penalty is slightly higher than the difference between the theoretical curves in Figure 5.8 as we assume ideal matched filtering. The excess OSNR penalty of DQPSK demodulation with an MZDI can be compensated using electrical post-processing algorithms such as multi-symbol phase estimation (see Chapter 9).

## 5.3 Transmitter & receiver properties

Similar to DPSK, a direct detection DQPSK receiver is vulnerable to receiver impairments such as amplitude or time imbalance between the photodiodes and an offset in the phase and time-delay of the MZDI. The eye diagrams in Figure 5.10 show the impact of some of the receiver impairments on the demodulated signal after balanced detection. Figure 5.9a depicts the tolerance of NRZ-DQPSK against phase offsets in the MZDI, with NRZ-DPSK as a reference.

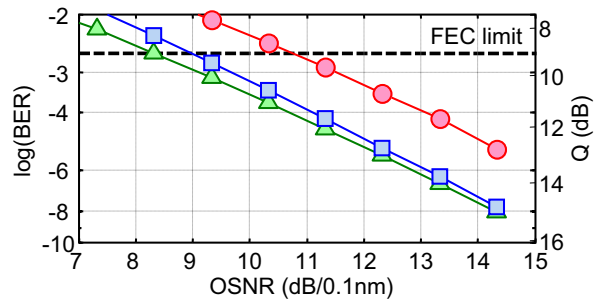


Figure 5.8: Theoretical performance of 42.8-Gb/s DQPSK with  $\circ$  conventional direct detection,  $\square$  coherent detection with differential decoding,  $\triangle$  42.8-Gb/s QPSK with coherent detection.

Because the phase difference between the constellation points is halved, DQPSK is about a factor of three more sensitive than DPSK to MZDI phase offsets. For a 1-dB OSNR penalty, the allowable phase offset is  $6.5^\circ$  for a DQPSK signal compared to  $20.5^\circ$  for DPSK [285]. When the penalty is expressed as a percentage of the bit rate, as for example used by *Kim and Winzer* in [259], the phase offset tolerance is a factor of six lower due to the factor of two difference in symbol rate. Measurements of the phase offset penalty in [259] shows a slightly larger penalty which most likely results from transmitter impairments.

Figure 5.9b depicts the impact of an offset in the MZDI differential delay. The penalty as a function of differential delay offset is very similar to DPSK modulation. For a  $<1$ -bit delay MZDI the partially deterministic interference results in a smaller penalty than for a  $>1$ -bit delay where three symbols are interfering and the symbol transition of the delayed symbol falls within the symbol period. Although the use of a  $<1$ -bit delay MZDI improves the narrowband filtering tolerance somewhat [286, 287], its effectiveness is reduced through the mixing of the duobinary and AMI component in the MZDI. This indicates that partial-DQPSK does not provide a significant benefit over DQPSK modulation.

### 5.3.1 Narrowband optical filtering

One of the more important advantages of DQPSK modulation over binary modulation formats is its robustness against narrowband filtering in densely spaced WDM transmission. Figures 5.11a and 5.11b show for 42.8-Gb/s RZ-DQPSK the tolerance towards narrowband optical filtering for back-to-back simulations and measurements, respectively. The receiver structure in the simulations is modeled to match the experimental receiver, with a 3<sup>rd</sup> order Gaussian optical filter and a 15-GHz 5<sup>th</sup> order Bessel electrical low-pass filter. The BER is computed with the eigenfunction evaluation method [288]. The OSNR at the receiver is set to 17 dB in the measurements and 15 dB in the simulation, which results for both cases in a BER of approximately  $4 \cdot 10^{-6}$ . Comparing Figures 5.11a and 5.11b show a similar tendency but a different optimal filtering bandwidth of 32 GHz (experimental) and 45 GHz (simulations), respectively. We conjecture that the more narrow filtering bandwidth is beneficial in the measurements because it removes impairments in the optical signal resulting from imperfections in the modulator. In the simulations an ideal RZ-DQPSK signal is used and hence no modulator imperfections are taken into account.

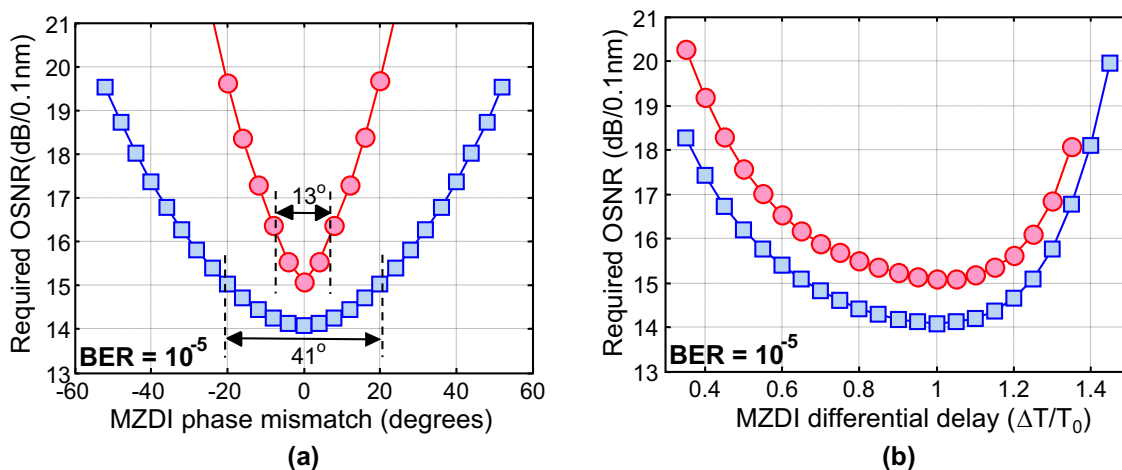


Figure 5.9: Simulated (a) MZDI phase mismatch and (b) MZDI differential delay mismatch;  $\circ$  42.8-Gb/s NRZ-DQPSK,  $\square$  42.8-Gb/s NRZ-DPSK.

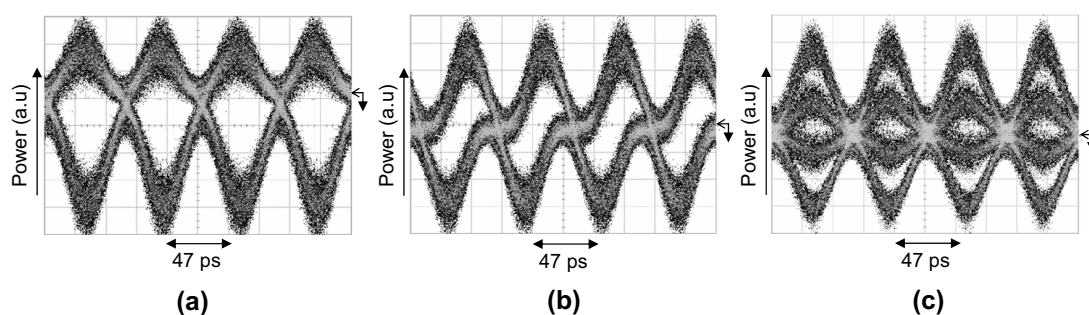


Figure 5.10: Measured eye diagrams for the quadrature tributary of 42.8-Gb/s RZ-DQPSK with 100-GHz optical filtering, (a) amplitude imbalance, (b) time imbalance and (c) phase offset.

The modulator imperfections are also evident from the eye diagrams depicted in Figure 5.12a, which show the amplitude fluctuations in the broadened '1'-rail of the optical signal. Note that the eye diagrams are measured at high OSNR, so that practically no ASE is present. With narrowband filtering (36 GHz) the amplitude fluctuations are reduced, as evident from Figure 5.12b. The '0' level is broadened due to ISI, but this does not impact the signal quality after the MZDI. Hence, narrowband optical filtering results in a performance improvement for a filtering bandwidth down to  $\sim 34$  GHz. For an even narrower filtering bandwidth, the additional ISI causes performance impairments. However, only a 1-dB penalty is measured for a 24-GHz filtering bandwidth (Figure 5.12c). This indicates that 42.8-Gb/s RZ-DQPSK is compatible with a narrow channel spacing down to 25 GHz. In [289], it has been shown that 21.4-Gb/s RZ-DQPSK is compatible with a 12.5-GHz WDM grid and in [290] the performance of 85.6-Gb/s RZ-DQPSK on a 50-GHz WDM grid is measured. For optical meshed networks, as discussed in Section 3.5, the available optical bandwidth after cascaded optical filtering is approximately 35-GHz. This shows that 42.8-Gb/s RZ-DQPSK modulation is well suited for optical meshed networks [291].

Besides the optical filter bandwidth, the filters center frequency is an important parameter to take into account. An offset between the filters center frequency and the optical spectrum result in asymmetric filtering. For most optical filters the center frequency will change slightly over the



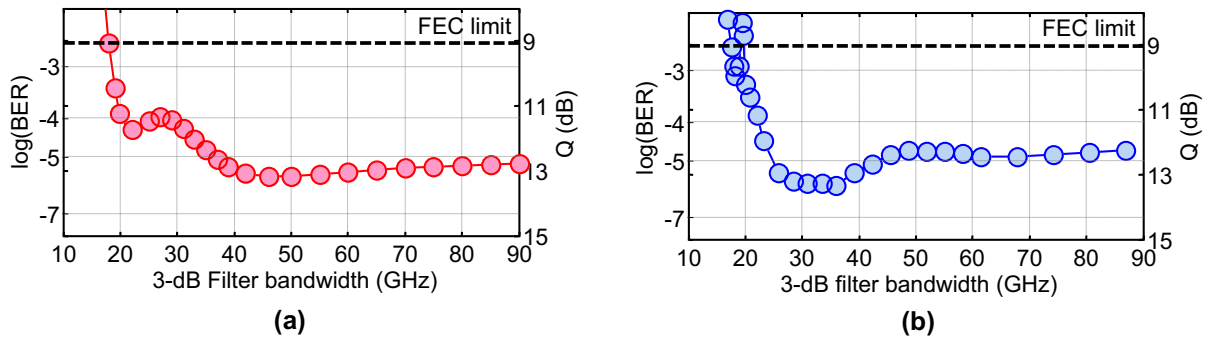


Figure 5.11: (a) simulated and (b) measured narrowband filtering penalty for 42.8-Gb/s RZ-DQPSK.

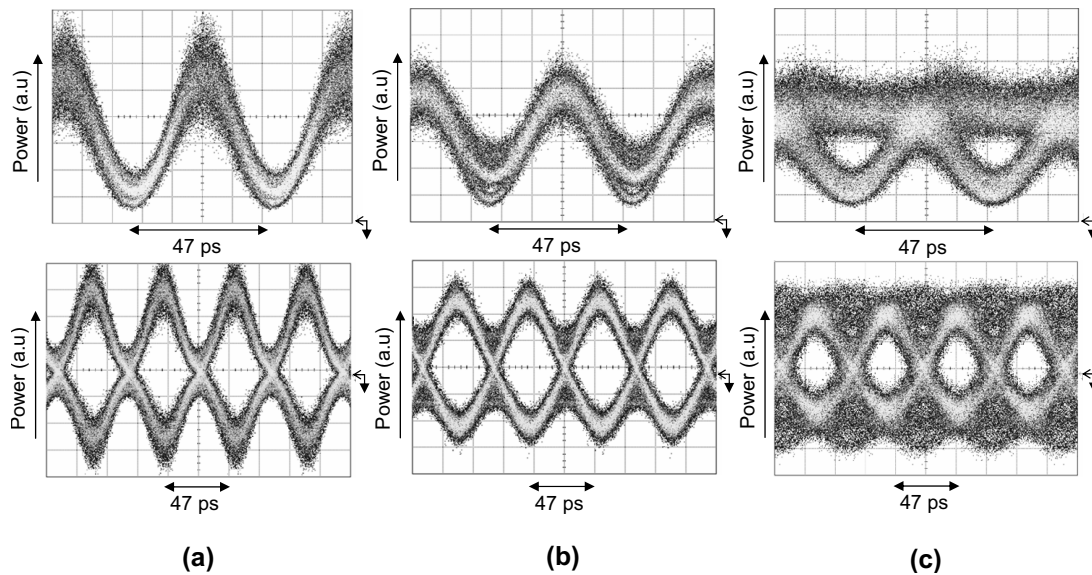


Figure 5.12: Measured eye diagrams for 42.8-Gb/s RZ-DQPSK before (upper row) and after (lower row) phase demodulation for (a) 50-GHz filtering (b) 36-GHz filtering and (c) 24-GHz filtering.

course of the filters lifetime. This can, for example, results from temperature induced changes or component aging. Furthermore, in the case of cascaded optical filters, every filter can have a slightly different center frequency. Figure 5.13a shows the measured tolerance with respect to filter center frequency offset. For a broad 50-GHz optical filter, the allowable frequency offset window with a penalty below 1 dB is as large as 32-GHz. This shows that 42.8-Gb/s RZ-DQPSK modulation on a 50-GHz WDM grid is still very tolerant to de-tuning of the optical filter [292]. The depicted measurements are for a single WDM channel. When other channels would be present at a 50-GHz channels spacing, the filter offset results in crosstalk as some energy of the other channel is passed through. Note that for a center frequency offset of up to  $\pm 10$  GHz, the performance slightly improves. This is similar as observed for narrowband optical filtering and we attribute this to a reduction in modulator imperfections.

When the optical filter bandwidth is reduced, the tolerance to center frequency offsets is consequently lowered. An important consideration is therefore the tolerance for filter bandwidths in the range of 35 to 40 GHz, as this is typical for cascaded optical filtering on a 50-GHz grid. Figure 5.13a shows that for a 37.5-GHz optical filter bandwidth the allowable filter offset range



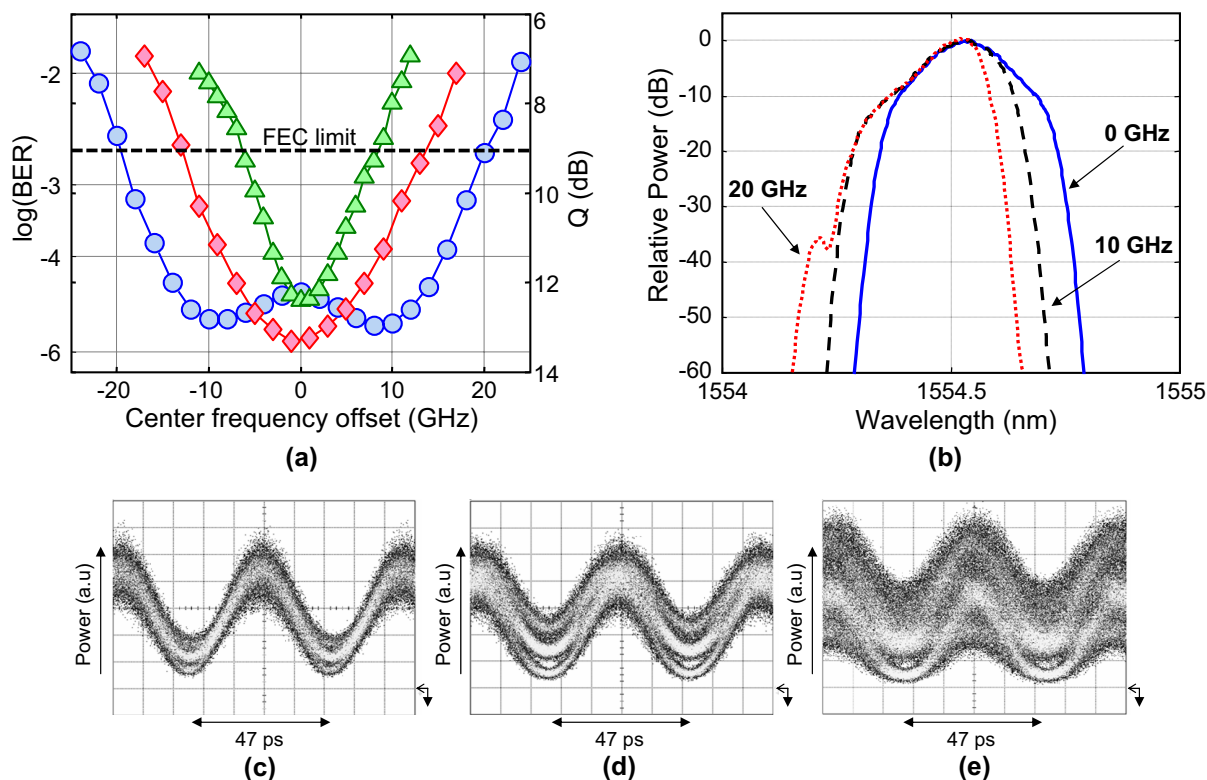


Figure 5.13: (a) measured filter center frequency offset for 42.8-Gbit/s RZ-DQPSK for a 3-dB filter bandwidth of  $\circ$  50 GHz,  $\diamond$  37.5 GHz and  $\blacktriangle$  25 GHz; (b-e) 42.8-Gb/s RZ-DQPSK after passing through a 40-GHz 3-dB bandwidth filter for different offsets from the center frequency, (b) measured spectra and eye diagrams for an offset of (c) 0 GHz; (d) 10 GHz and (e) 20 GHz.

is still  $\sim 10$  GHz with a penalty below 1 dB. The impact of asymmetric filtering is also evident from the measured spectra and eye diagrams in Figures 5.13b and 5.13c-e. For a 10-GHz center frequency offset, mainly the '0' level in between two symbols is broadened due to ISI, but no significant degradation is observed in the middle of the symbol period. Combined, a 37.5-GHz optical filter bandwidth and 10-GHz center frequency offsets tolerance should be sufficient to counter the (random) drift in center frequency of a number of cascaded 50-GHz optical filters (with 42-GHz 3-dB bandwidth) over the course of their lifetime.

### 5.3.2 Chromatic dispersion & DGD tolerance

A further advantage of DQPSK over DPSK modulation is the higher tolerance against linear transmission impairments, such as chromatic dispersion and PMD. Figure 5.14a shows simulations that compare the chromatic dispersion tolerance of 42.8-Gb/s NRZ-DPSK, NRZ-DQPSK and duobinary modulation. For DQPSK, the increased tolerance against chromatic dispersion results from the doubled symbol period as well as the more narrow optical spectrum. When we compare 42.8-Gb/s NRZ-DPSK and NRZ-DQPSK, the chromatic dispersion tolerance increases from 96 ps/nm to 221 ps/nm for a 1-dB OSNR penalty, a factor of 2.3. This is lower than the factor of four that one would expect by simply scaling the symbol rate. The difference results

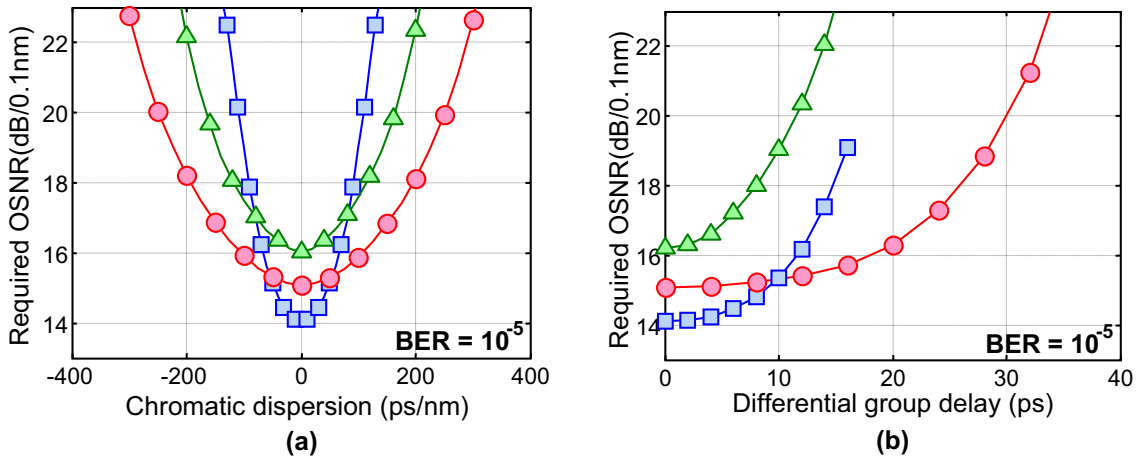


Figure 5.14: Simulated comparison of (a) chromatic dispersion and (b) DGD tolerance;  $\circ$  42.8-Gb/s NRZ-DQPSK,  $\square$  42.8-Gb/s NRZ-DPSK,  $\triangle$  42.8-Gb/s filtered duobinary.

Table 5.1: CHROMATIC DISPERSION TOLERANCE FOR A 1-DB OSNR PENALTY.

	Optical filter [GHz]	NRZ [ps/nm]	RZ [ps/nm]
DPSK	90	96	63
DQPSK	42	221	226
Duobinary	90	350	-
Duobinary	32	157	-

Table 5.2: DGD TOLERANCE FOR A 1-DB OSNR PENALTY. PMD-LIMITED REACH FOR  $0.1 - ps/\sqrt{km}$  PLUS 0.3-PS OF DGD PER SPAN.

	DGD tolerance [ps]	PMD-limited reach [km]
NRZ-DPSK	9.5	650
NRZ-DQPSK	18.5	1,800
Duobinary	6	300

from the residual chirp in the signal, which decreases the chromatic dispersion tolerance. This can be reduced through 50% RZ pulse carving, which improves the chromatic dispersion tolerance. When we now compare 42.8-Gb/s RZ-DPSK and RZ-DQPSK, the chromatic dispersion tolerance increases from 63 ps/nm to 226 ps/nm for a 1-dB OSNR penalty, a factor of 3.6. This is summarized in Table 5.1. In order to compare NRZ-DQPSK with duobinary modulation, the optical filter bandwidth plays a critical role. Without narrow-band optical filtering, duobinary has a larger chromatic dispersion tolerance but also an increased OSNR requirement. With optimal narrowband filtering (32-GHz), duobinary has a somewhat lower chromatic dispersion tolerance for a 1-dB OSNR penalty.

Figure 5.14b shows the DGD tolerance for the same modulation formats. The DGD tolerance is, in contrast to the chromatic dispersion tolerance, mainly dependent on the symbol period. This gives DQPSK modulation a clear advantage over either DPSK or duobinary modulation. For a 1-dB OSNR penalty, the DGD tolerance equals 18.5 ps, which translates into a  $\sim 6$ -ps PMD tolerance. We now consider a link with  $0.1 - ps/\sqrt{km}$  PMD coefficient for the transmission fiber and 0.3-ps DGD for each span to account for PMD in the EDFAs and DCF. This gives a 1,800-km feasible transmission distance for DQPSK, which compares favorably with other 42.8-

Gb/s modulation formats as denoted in Table 5.2. In particular the feasible PMD-limited reach of duobinary modulation is limited in comparison to both DPSK and DQPSK modulation, as discussed in Section 4.2.

## 5.4 Nonlinear tolerance

The smaller phase difference between the constellation points in DQPSK modulation results also in a reduced nonlinear tolerance. Particularly the SPM-induced nonlinear phase shift has a more severe impact on DQPSK modulation compared to DPSK. This is illustrated in Figure 5.16 by comparing the nonlinear tolerance of 10.7-Gb/s RZ-DPSK and 21.4-Gb/s RZ-DQPSK on a 800-km SSMF transmission link.

In this experiment, the outputs of 1 to 9 ECL on a 50-GHz grid (center wavelength at 1550.9 nm) are combined in a 16:1 coupler. A MZM driven with a 10.7-Gb/s clock signal is used for pulse-carving. The second modulator is a standard MZM driven with a  $2^{31} - 1$  PRBS for 10.7-Gb/s DPSK modulation or a parallel DQPSK modulator for 21.4-Gb/s DQPSK modulation. In this case, two 10.7-Gb/s  $2^{15} - 1$  PRBS sequences with a relative delay of 5 bits for de-correlation of the bit sequences are used for modulation of the DQPSK signal. Before transmission, the channels are de-correlated with -510 ps/nm of pre-compensation. The transmission line consists of eight 100 km spans of SSMF with EDFA amplification in between the spans, as depicted in Figure 5.15. After each span the chromatic dispersion is compensated with an average under-compensation of 78.4 ps/nm. The loss of the SSMF spans and DCF varied between 21 dB ... 24 dB and 8 dB ... 11 dB, respectively. At the receiver a 37-GHz CSF selects the desired WDM channel and the accumulated dispersion is compensated to approximately 0 ps/nm. Subsequently, the OSNR is set such that a  $10^{-9}$  back-to-back BER is obtained, which is 10.9 dB and 15.9 dB for 10.7-Gb/s RZ-DPSK and 21.4-Gb/s RZ-DQPSK, respectively.

We now take a  $10^{-5}$  BER as a measure for the nonlinear tolerance in Figure 5.16. For the single-channel case, the nonlinear tolerance reduces from 12.8 dB for 10.7-Gb/s RZ-DPSK to 6.2 dB for 21.4-Gb/s RZ-DQPSK, a difference of 6.6 dB. For WDM transmission, the impact of XPM reduces the difference between both modulation formats. With a 50-GHz WDM channel spacing and 9 co-propagating channels the nonlinear tolerance is 4.5 dB (DQPSK) and 8.3 dB (DPSK), respectively. The 4.5 dB lower nonlinear tolerance indicates a severe XPM penalty for DPSK. For DQPSK modulation, on the other hand, the difference between single-channel and 50-GHz spaced WDM transmission is only slightly over 1 dB, and this includes degradations due

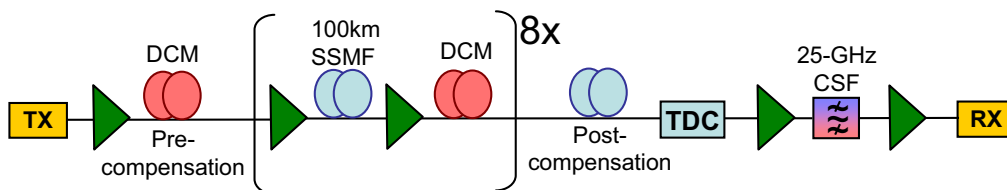


Figure 5.15: *Experimental setup*

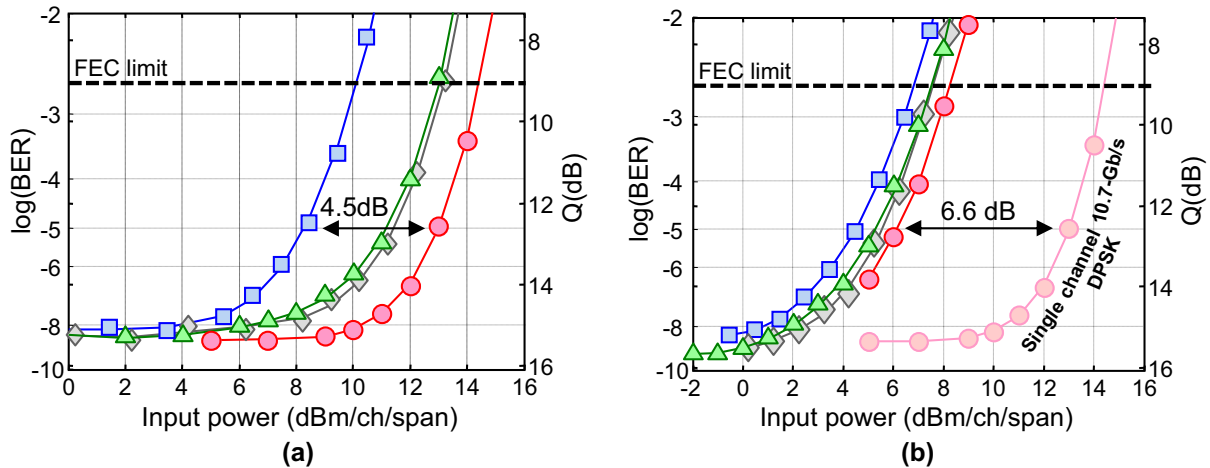


Figure 5.16: Measured nonlinear tolerance for 800-km transmission (a) 10.7-Gb/s RZ-DPSK and (b) 21.4-Gb/s RZ-DQPSK with  $\bullet$  single channel,  $\square$  9 channels on a 50-GHz grid,  $\blacktriangle$  5 channels on a 100-GHz grid and  $\blacklozenge$  3 channels on a 200-GHz grid.

to amplifier gain tilt. We can therefore conclude that RZ-DQPSK is strongly SPM-limited, even at a 10.7-Gb/s symbol rate, whereas RZ-DPSK is largely XPM limited. We note that 21.4-Gb/s RZ-DPSK modulation will have a reduced nonlinear tolerance compared to 10.7-Gb/s RZ-DPSK, and hence the comparison is here somewhat undue. However, at the same bit rate, i.e. 42.8-Gb/s DPSK compared to 42.8-Gb/s DQPSK, the difference in nonlinear tolerance is still  $\sim 2$ -3dB.

The small inter-channel impairments that are observed for DQPSK in Figure 5.16 are not the result of a high XPM tolerance. On the contrary, the denser signal constellation of DQPSK in comparison to DPSK modulation makes it more sensitive to XPM-induced distortions. An important consideration for 42.8-Gb/s RZ-DQPSK modulation is therefore the impact of co-propagating 10.7-Gb/s NRZ-OOK channels, as first observed by *Spinnler et. al.* in [293]. Such a configuration might occur when a deployed system, carrying 10.7-Gb/s NRZ-OOK channels, is upgraded to a 42.8-Gb/s bit rate. As this is an important aspect for the deployment of 42.8-Gb/s DQPSK transmission, it has been extensively studied in the literature [294, 295, 296, 297]. Figure 5.17 shows the impact of XPM-induced impairments using signal constellations. Simulated is a 2000-km transmission link with -2-dBm input power per channel. In the case of DQPSK-only transmission, a very similar constellation diagram is obtained with either single-channel or five WDM channels on a 50-GHz grid. However, when the four co-propagating channels are 10.7-Gb/s NRZ-OOK modulated, the XPM impact is much stronger. In particular the signal constellation before phase demodulation is clearly degraded through a pattern-dependent XPM-induced phase shift. We can therefore conclude that 42.8-Gb/s RZ-DQPSK is XPM rather than SPM limited with co-propagating 10.7-Gb/s NRZ-OOK channels. The strong XPM impact can be reduced through a lower input power. This is however difficult, and often impossible, as the system design of the deployed NRZ-OOK channels is based on high input powers (typically 3 dB per channel). Alternatively, the wavelength spacing between the DQPSK and NRZ-OOK channels can be increased to  $\geq 100$  GHz. Figure 5.17 further shows that the phase distortions are strongly reduced through differential demodulation, which indicates a strong correlation between the XPM-induced phase shift of consecutive symbols. This is important for digital coherent receivers, as discussed in Chapter 10, which do not necessarily use differential demodulation.

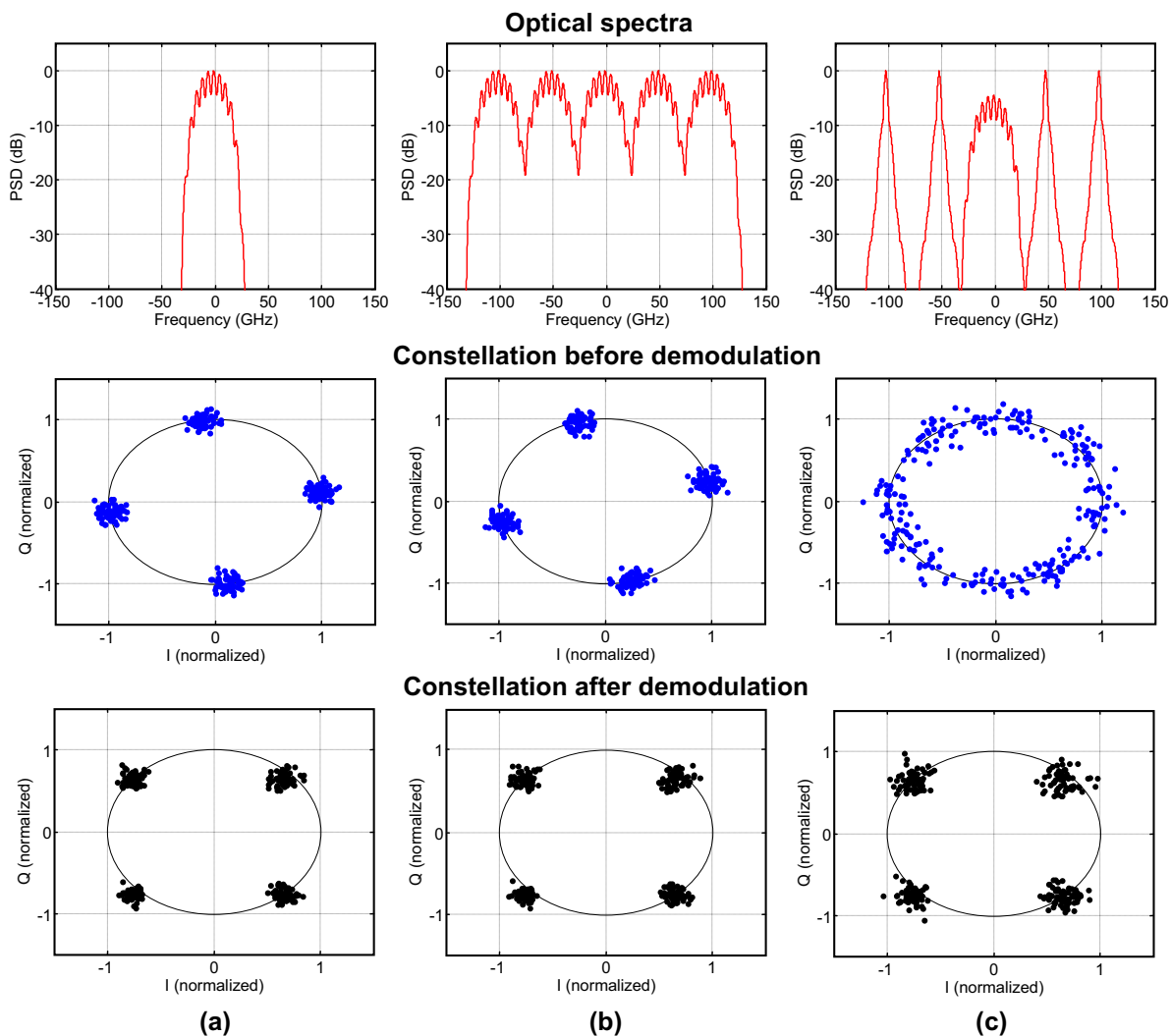


Figure 5.17: Simulated impact of XPM on 42.8-Gb/s RZ-DQPSK; (a) single-channel 42.8-Gb/s RZ-DQPSK, (b) 5 co-propagating 42.8-Gb/s RZ-DQPSK channels and (c) a 42.8-Gb/s RZ-DQPSK center channel with 4 co-propagating 10.7-Gb/s NRZ-OOK channels.

## 5.5 Pseudo random quaternary sequences

We now discuss in more detail the impact of the pseudo-random bit sequence in DQPSK transmission experiments. Binary modulation formats are routinely modeled using a PRBS, but for quaternary modulation formats no such standard exists. For DQPSK modulation, two bit streams at half the bit rate are fed to the modulator. In transmission experiments, generally, the same data stream is used twice with a relative delay for de-correlation. To assess the linear and nonlinear transmission properties of DQPSK, inter-symbol interference as occurs along the transmission line should be properly modeled. For example in [298], *Wickham et. al.* showed that for transmission systems limited by intra-channel nonlinear impairments the bit pattern length can be critical in correctly evaluating the transmission performance. For DQPSK modulation, the transmission performance is best assessed by using pseudo-random quaternary sequences (PRQS).

A pseudo-random sequence should, ideally, contain all possible combinations of symbols up to a given length. Assume a sequence to have length  $k^n$ , where  $k$  is the alphabet size and  $n$  an integer value. A pseudo random sequence (also know as de Bruijn sequence) can then be defined as a sequence that contains all possible combinations of symbols up to length  $n$  (subsequences) exactly once. Note that De Bruijn sequences are equal to standard PRBS with length  $k^n - 1$  with the exception that the subsequence with  $n$  consecutive zeros is omitted. Two PRBS with a cyclic shift for de-correlation can be multiplexed to construct a 4-level sequence. However, this results in a sequence with length  $4^{n/2} = 2^n$  which is generally not a pseudo-random sequence, i.e. it does not contain all possible subsequences up to length  $n/2$ .

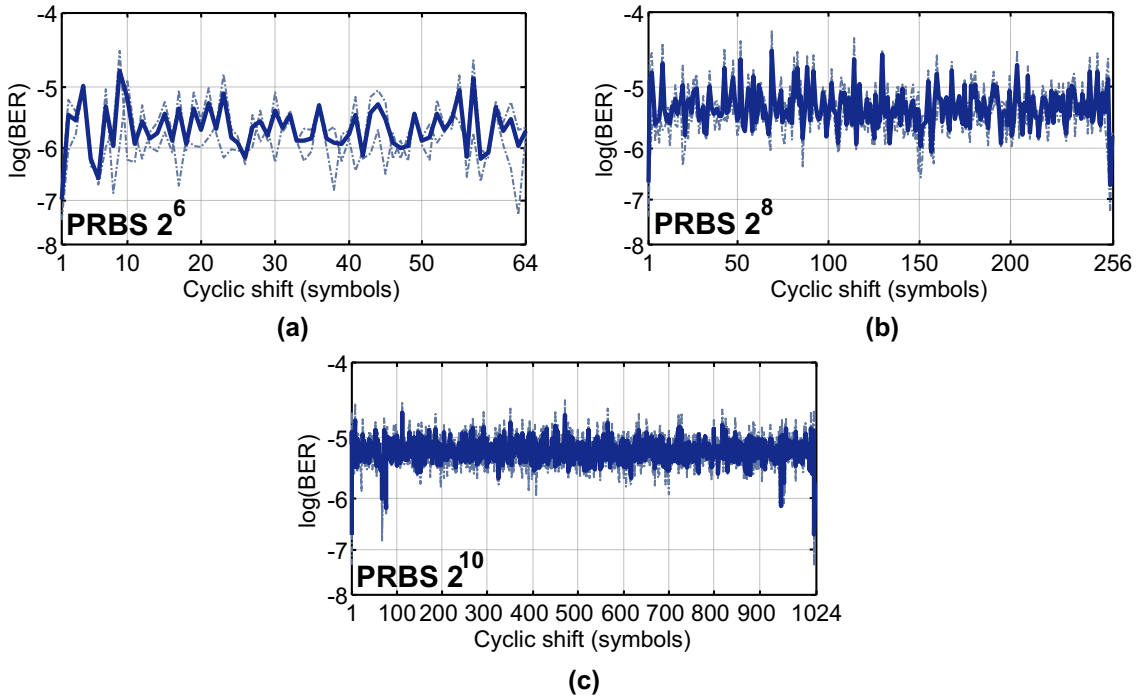


Figure 5.18: Simulated BER for 42.8-Gb/s NRZ-DQPSK after 1140 km for all possible cyclic shifts and (a) PRBS  $2^6$ , (b) PRBS  $2^8$ , (c) PRBS  $2^{10}$ , dotted lines denote in-phase and quadrature tributaries, solid line denote the average of both tributaries.

Comparing multi-level ( $k > 4$ ) modulation with binary modulation, the required sequence length to consider all possible subsequences of a given length  $n$  grows exponentially. Hence, for multi-level modulation formats it becomes difficult in both simulations as well as experimental verification to correctly model the interaction of long bit patterns. To verify the impact of bit pattern dependence we now simulated the influence of different 4-level sequences on 42.8-Gb/s NRZ-DQPSK transmission. We use NRZ rather than RZ-DQPSK modulation here as RZ carving would somewhat mask the impact of bit-sequence dependence. Single channel transmission over 12x95-km (1140 km) of SSMF is simulated with a pre-compensation of 680-ps/nm, 85-ps/nm/span in-line under-compensation and zero residual dispersion. The input power is 4 dBm per channel into the SSMF and -1 dBm into the DCF. At the receiver, the signal is filtered with a 45-GHz optical Gauss filter, phase demodulated with an MZDI, differentially detected and subsequently filtered with a 17-GHz electrical Bessel filter. The OSNR is set to 18.3 dB, which results in a back-to-back BER of  $10^{-9}$ . The BER is computed using a Karhunen-Loeve series expansion



[299]. Figure 5.18 shows the obtained BER after transmission for different bit pattern lengths. For each bit pattern length, two PRBS ( $u$  and  $v$ ) are used to modulate the in-phase and quadrature component of the DQPSK signal. The bit pattern dependence is observed by cyclically shifting both sequences with respect to each other and computing the BER for each cyclic shift. As evident from Figure 5.18 this results in significant performance differences, clearly indicating that the choice of bit pattern severely affects the obtained transmission performance. Comparing Figure 5.18a-c shows that a shorter bit pattern length result on average in a lower BER. For a longer bit pattern length (e.g. 1024 symbols) the variation in BER as a function of the cyclic shift is reduced, but differences of more than an order of magnitude are still apparent. This shows that even for long sequences an arbitrary cyclic shift can potentially result in inaccurate modeling of transmission penalties.

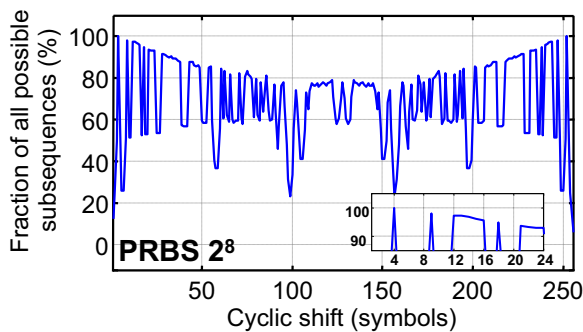


Figure 5.19: Fraction of existing sequences with length 4 as a function of the cyclic shift.

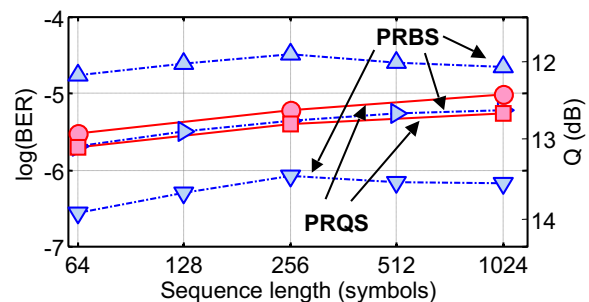


Figure 5.20: Worst-case, median and best-case BERs for all cyclic shifts compared to the BER of a PRQS.

The observed transmission performance difference can be avoided by a proper choice of the bit pattern. For this purpose we analyze which fraction of all possible 4-level subsequences with length  $n/2$  exists as a function of the cyclic shift between the two PRBS sequences  $u$  and  $v$  with length  $2^n$ . Figure 5.19 shows the obtained results for a PRBS length of  $2^8$  and a subsequence length of 4. It is evident that all possible subsequences of length 4 exist only when  $v$  is cyclically shifted over  $\pm 4$  symbols with respect to  $u$ . It can be shown that for a  $2^n$  PRBS and a cyclic shift of  $\pm n/2$  symbols (for  $n$  is even) always a PRQS with length  $4^{n/2}$  is obtained. Note that shifting  $v$  over  $-n/2$  symbols is equal to shifting  $v$  over  $+n/2$  symbols and inverting it. This gives a straightforward and simple method to generate true PRQS for the simulation and experimental verification of 4-level modulation formats such as DQPSK<sup>1</sup>. This method can also be extended to create pseudo-random sequences for modulation formats with  $k > 4$ , such as polarization-multiplexed DQPSK modulation (see Chapter 8). From Figure 5.18 we now take the worst-case, median and best-case obtained BER for all possible cyclic shifts between  $u$  and  $v$  larger than two (to ensure all symbol transitions exist), as depicted in Figure 5.20. The proposed PRQS results in a BER close to the median value over all possible cyclic shifts. This indicates that such sequences are suitable for the assessment of DQPSK transmission performance. For a bit

<sup>1</sup>The use of PRQS for DQPSK modulation is based on more recent work and is therefore not used in most of the transmission experiments discussed in this thesis. An exception is the transmission experiment discussed in Section 10.6.3.

pattern length larger than 256 symbols the median value is relatively constant, which indicates this bit pattern length is sufficient to properly determine transmission penalties. We note that PRQS can also be generated using 4-level generator polynomials [300], similar to the method used for PRBS.

### 5.6 Summary & conclusions

DQPSK modulation is one of the most suitable multi-level modulation formats for long-haul transmission links. As it encodes 2 bits per symbol, it allows for a higher spectral efficiency and a higher tolerance towards linear transmission impairments compared to binary modulation formats. The most significant properties of DQPSK modulation can be summarized as follows:

- DQPSK modulation is possible using a variety of modulator architectures, of which the *parallel 'Super Mach-Zehnder' structure* is most widely used. An important consideration for the choice in modulator architecture is the residual frequency chirp in the modulation signal. In addition, DQPSK modulation has an increased transponder complexity compared to DPSK or duobinary modulation. This makes a higher degree of optical integration attractive for DQPSK modulation.
- DQPSK is normally demodulated with two separate MZDI with a  $\pm\pi/4$  phase shift between both arms. Due to the suboptimal phase demodulation, DQPSK has a higher *OSNR requirement* in comparison to DPSK modulation. Near the FEC limit, the difference is limited to approximately 1 dB.
- The *narrowband filtering* tolerance is one of the most significant advantages of DQPSK in comparison to binary modulation formats. No significant narrowband filtering penalty is evident down to a 28-GHz filter bandwidth. On a 50-GHz grid, DQPSK further allows for a 10-GHz filter offset with an OSNR penalty smaller than 1-dB.
- The *chromatic dispersion* tolerance of DQPSK modulation is lowered due to the residual chirp in the modulated signal. This residual frequency chirp can be reduced through RZ pulse carving, which potentially makes the tolerance comparable to DPSK at the same symbol rate. For 50% RZ-DQPSK modulation the chromatic dispersion tolerance is approximately a factor of three higher when compared to DPSK at the same bit rate.
- DQPSK modulation has a doubled *PMD* tolerance compared to DPSK modulation. This negates the need for active PMD compensation on fibers with even moderately high PMD.
- DQPSK modulation is strongly limited by *inter-channel nonlinear impairments*. This significantly reduces the nonlinear tolerance of DQPSK modulation compared to DPSK modulation. For a 10.7-Gbaud symbol rate, the difference is approximately 4 dB for a 50-GHz WDM system. At the same bit rate the difference in nonlinear tolerance is 2-3 dB.



# 6

---

## Long-haul DQPSK transmission

The previous chapter focused on the properties of DQPSK modulation in comparison to binary modulation formats. In this chapter we focus in more detail on the properties of DQPSK in long-haul transmission. In particular, we discuss the optimization of the dispersion map and the use of different technologies for chromatic dispersion compensation. First of all, in Section 6.1 we discuss an ultra long-haul transmission experiment using 21.4-Gb/s RZ-DQPSK modulation. Subsequently, in Section 6.2 the bit rate is doubled and we focus on long-haul transmission with 42.8-Gb/s RZ-DQPSK modulation.

The second part of this chapter focuses on alternative dispersion compensation technologies for long-haul transmission systems. In Section 6.3 we simplify dispersion compensation using a lumped dispersion map. This allows for simplified EDFAs in most of the transmission link, at the cost of a less optimized dispersion map that somewhat reduces the nonlinear tolerance. In Section 6.4, chirped-FBGs are discussed as a means of dispersion compensation in more cost-sensitive transmission systems. Here, we particularly focus on the impact of phase ripple induced impairments on 42.8-Gb/s RZ-DQPSK modulation. Subsequently, Section 6.5 focuses on the combination of DQPSK modulation and OPC-supported long-haul transmission. We show that OPC can enable both lumped dispersion compensation as well as a significant increase in transmission distance through the compensation of intra-channel nonlinear impairments. Finally, in Section 6.6 we compare some of the DQPSK transmission experiments that have been reported in the literature.

---

<sup>1</sup>The results described in this chapter are published in c1, c5, c8-c10, c12, c27, c32-c33, c38, c40-c41, c44, c46, c51

## 6.1 21.4-Gb/s RZ-DQPSK transmission

Figure 6.1 depicts the experimental setup for ultra long-haul 21.4-Gb/s RZ-DQPSK modulation. At the transmitter, the outputs of 44 DFB lasers on a 50 GHz ITU grid are multiplexed using an AWG. Subsequently, two cascaded modulators are used for RZ pulse-carving with a 50% duty cycle and DQPSK modulation. The parallel DQPSK modulator is driven with two 10.7-Gb/s PRBS with length  $2^{15} - 1$  and shifted over 5 bits for de-correlation. The transmission link consists of three 94.5 km spans of SSMF, with an average span loss of 21.5 dB. Using hybrid EDFA/Raman amplification, with an average 11-dB ON/OFF Raman gain from counter-directional pumping, the SSMF span loss is compensated. After each span a DCF module is used to compensate for the chromatic dispersion. Approximately 20% of the DCF is placed between the Raman pump and the first amplifier stage to balance the DCF insertion loss.

In order to emulate ultra long-haul transmission, the signal is re-circulated and passes multiple times through the same transmission link. Two optical switches are used to control the propagation of the signal. When the first switch (Tx switch) is open, an optical burst from the transmitter enters the re-circulating loop. Afterwards, the first switch closes and the second switch (Loop switch) is opened which allows the optical burst signal to propagate around the re-circulating loop. Once the signal has propagated over the predetermined transmission distance (a multiple of the re-circulating loop length) a trigger signal to the receiver starts the measurements. Afterwards, the first switch opens again and another optical burst starts to propagate around the re-circulating loop.

The re-circulating loop further contains a loop-synchronous polarization scrambler (LSPS) in order to obtain the correct polarization distribution and a WSS to emulated cascaded optical filtering and power equalization. At the receiver, a 25-GHz CSF selects the desired WDM channel. Afterwards, the accumulated dispersion is optimized on a per-channel basis. The signal is then fed into a one-bit ( $\Delta T = 94\text{ps}$ ) MZDI and subsequently detected with a balanced photodiode. The transmission performance is evaluated using a BER tester programmed for the expected output sequence.

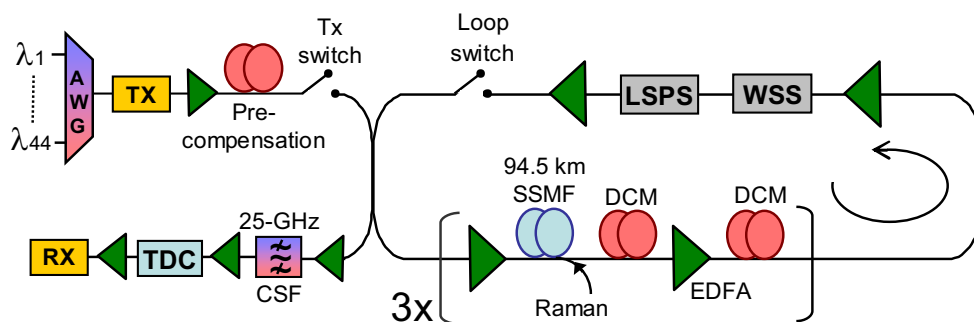


Figure 6.1: Experimental setup for long-haul 21.4-Gb/s RZ-DQPSK transmission.

In order to maximize transmission performance, the SSMF input power, inline-under compensation and pre-compensation are optimized after 4,500-km transmission. The input power is set to

-4 dBm/channel; the pre-compensation to -850 ps/nm and the inline-under compensation is fixed at 80 ps/nm/span. Subsequently each parameter is varied to assess its influence on the transmission performance (Figure 6.2). The optimum input power per channel is lowered through the hybrid EDFA/Raman amplification and has its optimum at -4 dB/channel. For lower input powers, transmission is OSNR limited, whereas for higher input powers the penalty is dominated by nonlinear impairments. However, the transmission performance is relatively tolerant to power variations as the input power can be varied between -7 dBm and -1 dBm for a 1-dB Q-factor penalty. Secondly, we optimize the pre-compensation. This has only a minor impact on the transmission performance, but we observe that a higher amount of pre-compensation is slightly better. Next, we optimize the inline under-compensation per span. A clear penalty is evident for low inline under-compensation per span as this results in an enlarged impact of XPM due to insufficient spreading between the channels [301]. For an inline under-compensation higher than >60 ps/nm/span the performance differences are insignificant.

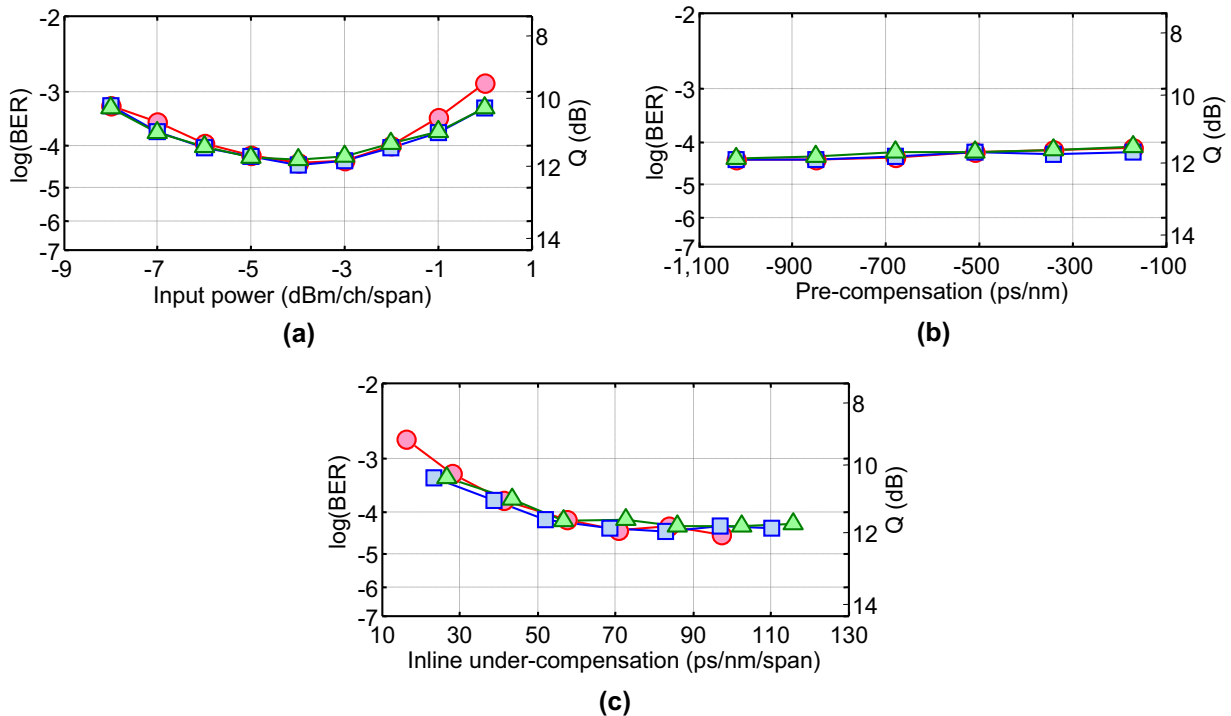


Figure 6.2: BER as function of (a) input power per channel, (b) pre-compensation and (c) inline-under compensation; with  $\circ \lambda = 1533.7 \text{ nm}$ ,  $\square \lambda = 1549.7 \text{ nm}$ ,  $\triangle \lambda = 1553.5 \text{ nm}$ .

Using the optimized parameters, the BER of a typical channel (in-phase tributary, 1550.7 nm) is assessed as a function of the transmission distance (Figure 6.3a). For shorter distances, the  $\log(\text{BER})$  increases linearly with an exponential increase in transmission distance. After 5,000-km transmission, the measured  $\log(\text{BER})$  deviates from the linear increase due to the accumulated nonlinear impairments. We conjecture that this accelerated BER increase results partially from the impact of SPM-induced nonlinear phase noise which is more significant at low OSNR, as previously observed in [302]. This limits the feasible transmission distance in this configuration to 7,100 km. We note that the optimum input power per channel will be slightly lower after transmission over 7,100 km compared to 4,500 km. A lower input power would therefore

somewhat improve the feasible transmission distance beyond the limit measured here as less non-linear impairments accumulate and transmission is more limited by the OSNR. In Figure 6.3b the BER of both the in-phase and quadrature components of all 44 WDM channels is assessed after 7,100 km. It can be seen that the performance is similar for all WDM channels and no spectral dependence is measured. The highest measured BER is  $1.6 \cdot 10^{-3}$  after 7,100-km transmission, which is a 0.4-dB Q-factor margin with respect to the FEC limit<sup>1</sup>.

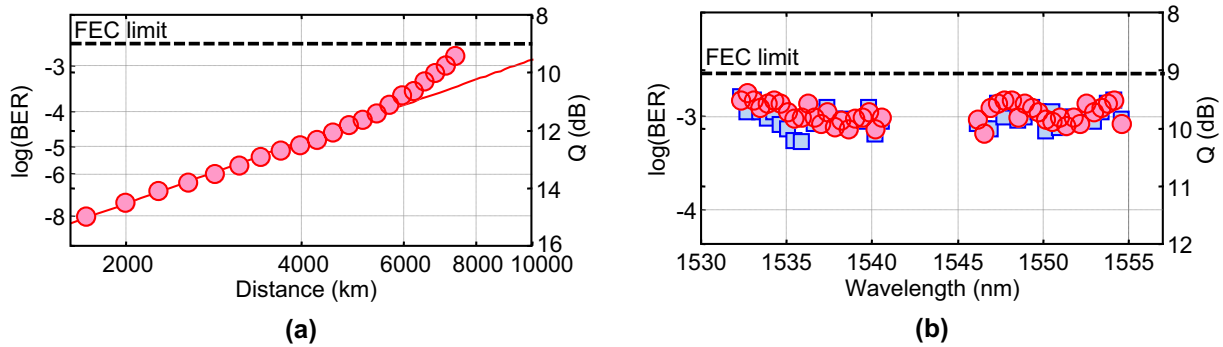


Figure 6.3: (a) Measured BER as a function of transmission distance (b) BER of all channels after 7,100-km transmission (25 re-circulations);  $\circ$  In-phase tributary,  $\square$  Quadrature tributary.

## 6.2 42.8-Gb/s RZ-DQPSK transmission

RZ-DQPSK modulation is the most promising for a 42.8-Gb/s bit rate (21.4-Gbaud symbol rate). This enables robust 42.8-Gb/s transmission on a 50-GHz wavelength grid, as is used by the majority of the deployed transmission systems. In addition, at a 21.4-Gbaud symbol rate, the bandwidth requirement for the electrical components in the transponder is still modest. In this section we optimize the power and dispersion map for 42.8-Gb/s RZ-DQPSK modulation and analyze the long-haul transmission performance.

Figure 6.4 depicts the transmitter and receiver structure for 42.8-Gb/s RZ-DQPSK modulation. The WDM channels are modulated using two parallel modulator chains for separate modulation of the even and odd channels. Each RZ-DQPSK modulator chain consists of a MZM for RZ pulse-carving, followed by a parallel DQPSK modulator. The pulse-carver MZM is driven with a 21.4-GHz clock signal to carve out pulses with a 50% duty cycle. The 21.4-Gb/s electrical bit sequences for DQPSK modulation is created by electrically multiplexing two 10.7-Gb/s PRBS signals with a length of  $2^{15} - 1$  and a relative delay of 16 bits. The 21.4-Gb/s data stream is subsequently split and fed to both inputs of the 42.8-Gb/s DQPSK modulator with a relative delay of 10 bits. After modulation, the spectral width of an unfiltered 42.8-Gb/s RZ-DQPSK signal is  $>50$  GHz. Optical filtering is therefore required to reduce the linear crosstalk between neighboring WDM channels. Here, the channels are filtered when the odd and even WDM channels are combined in the 50-GHz interleaver.

<sup>1</sup>The absolute performance is expressed here in terms of the BER, whereas a penalty or margin is expressed in terms of the Q-factor, see Appendix B for the difference.

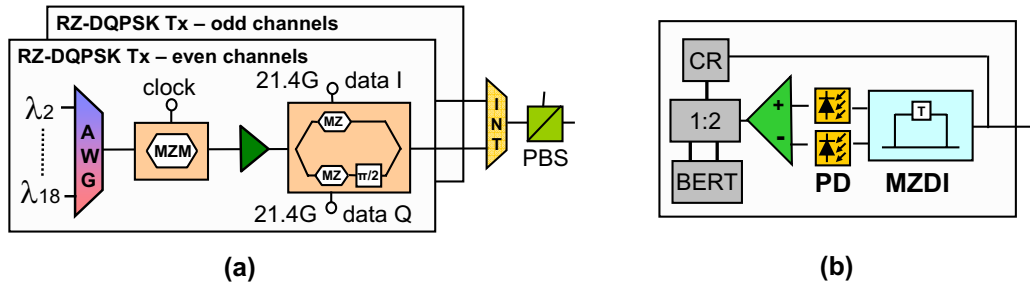


Figure 6.4: Experimental setup for long-haul 42.8-Gb/s RZ-DQPSK transmission (a) transmitter and (b) receiver.

In this experiment, 18 WDM channels are multiplexed on a 50-GHz ITU grid, as depicted in Figure 6.5a. The 18 WDM channels are divided over the lower and higher part of the C-band, 9 channels in the lower part of the C-band (from 1534.25 nm to 1537.40 nm) and 9 channels in the higher part of the C-band (from 1549.32 nm to 1552.52 nm). The two separate wavelength bands are used here to investigate the presence of wavelength dependent performance differences due to a change in amplifier noise figure or gain tilt across the C-band. For this purpose, the BER is measured for the center channels of both the higher and lower wavelength band (1535.9 nm and 1551.0 nm). In order to model worst-case nonlinear interaction between the WDM channels, a PBS after the interleaver ensures that all WDM channels are co-polarized. The re-circulating loop setup is the same as used in the 21.4-Gb/s RZ-DQPSK transmission experiment (see Figure 6.1).

At the receiver, the chromatic dispersion is optimized on a per-channel basis and a narrowband 25-GHz CSF is used to select the desired WDM channel. Note that the 25-GHz bandwidth of the optical filter results in a 1-dB OSNR penalty. Subsequently, the signal is split and one part is used for clock-recovery. The other part is fed to a two-bit ( $\Delta T = 94$  ps) MZDI, followed by balanced detection. The use of a two-bit instead of a one-bit MZDI might result in slightly higher penalties [262] but it is used here to simplify the post-coding of the DQPSK sequences. After balanced detection, the signal is de-multiplexed to 10.7-Gb/s with a 1:2 de-multiplexer and evaluated using a BER tester programmed for the expected bit sequence. With a two-bit MZDI, the BER tester requires only programming for the expected 10.7-Gb/s tributary instead of the multiplexed 21.4-Gb/s signal. As the BER is measured using a 10.7-Gb/s BER tester this considerably simplifies the DQPSK post-coding. The performance of the two tributaries is averaged through loop operation; hence it is sufficient to measure only one 10.7-Gb/s tributary of the 21.4-Gb/s signal.

Figure 6.5 shows the optimization of the dispersion map for 42.8-Gb/s RZ-DQPSK after 2,260-km transmission. First of all, the measured BER as a function of the input power per channel is depicted in Figure 6.5b. The inline under-compensation is set to  $\sim 33$  ps/nm/span and the pre-compensation is fixed at -1020 ps/nm. For high input powers a slight performance difference is measured between both channels. This is due to amplifier gain tilt and intra-band SRS, which increases the noise factor of the lower wavelengths. The optimal input power is found to be -3.5 dBm per channel. Subsequently, the inline under-compensation per span is optimized, as shown in Figure 6.5c. The inline under-compensation is changed by stepwise substituting the DCF spools in the link such that the average inline under-compensation increases or decreases. A pre-compensation of -1020 ps/nm is used as well as a -3.5-dBm channel input power. For a

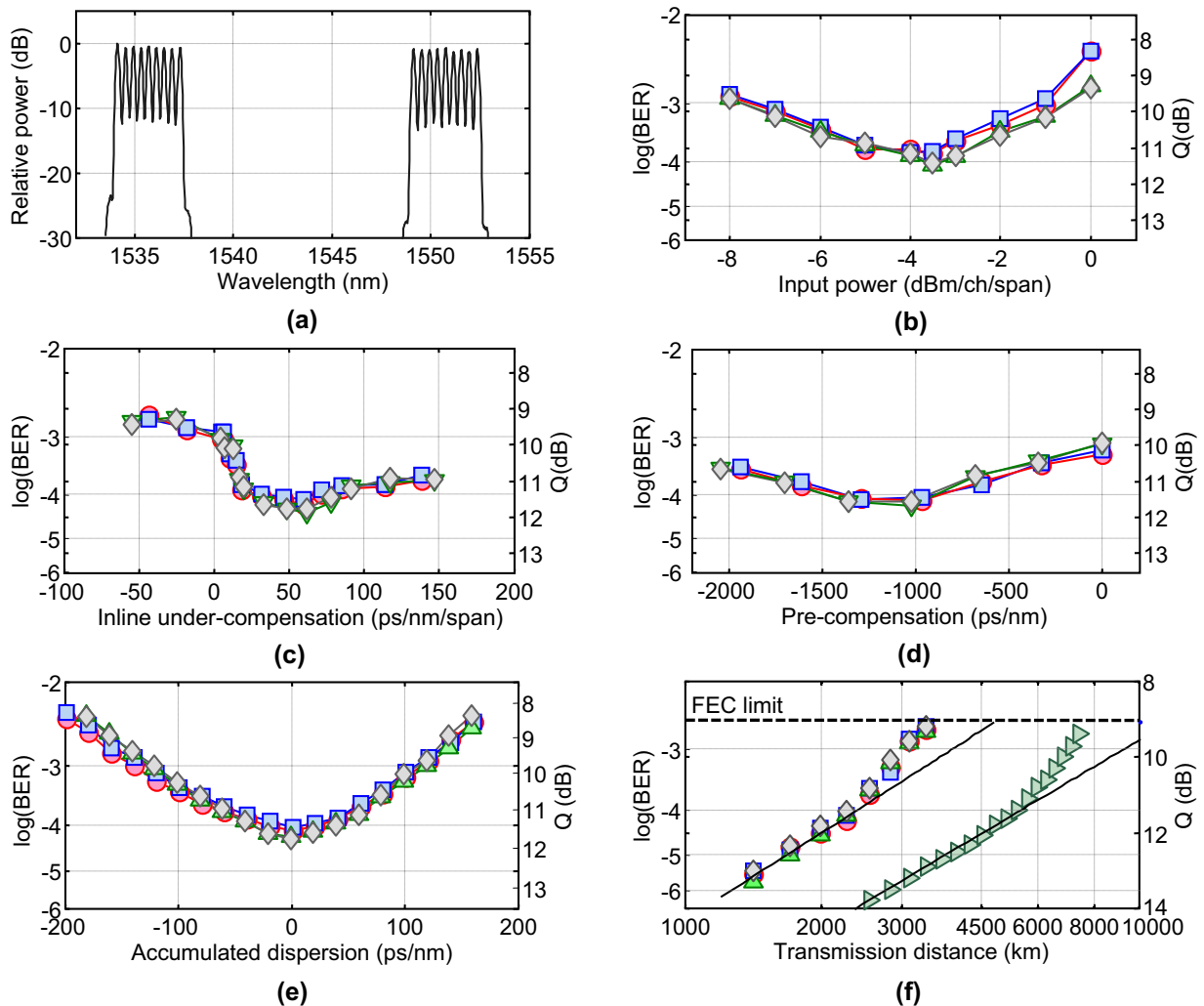


Figure 6.5: Dispersion and power map optimization for 42.8-Gb/s RZ-DQPSK after 2,260 km, (a) Optical spectra of the 18 WDM channels, (b-e) BER as a function of (b) input power per channel, (c) pre-compensation, (d) inline under-compensation per span, (e) accumulated dispersion and (f) transmission distance;  $\circ$   $\lambda = 1535.9$  nm, In-phase tributary,  $\square$   $\lambda = 1535.9$  nm, Quadrature tributary,  $\triangle$   $\lambda = 1551.0$  nm, In-phase tributary,  $\diamond$   $\lambda = 1551.0$  nm, Quadrature tributary,  $\blacktriangleright$  21.4-Gb/s RZ-DQPSK.

lower under-compensation the walk-off between the WDM channels is reduced which clearly raises the transmission penalty. The optimal value is found to be an inline under-compensation of  $\sim 60$  ps/nm/span. A further increase in inline under-compensation decreases the measured performance only by a small amount, which indicates a large tolerance for 42.8-Gb/s RZ-DQPSK modulation towards suboptimal dispersion maps. Next, Figure 6.5d plots the BER performance as a function of pre-compensation. In this experiment the input power is again set to  $-3.5$  dBm per channel and the inline under-compensation is fixed at  $\sim 60$  ps/nm/span. Similar to the measured results for 21.4-Gb/s RZ-DQPSK, the amount of pre-compensation has no strong influence on the transmission performance. Only when the pre-compensation value is close to zero, insufficient pulse spreading occurs and the measured performance decreases. The optimal pre-compensation is  $-1020$  ps/nm.

The optimal dispersion map for 42.8-Gb/s RZ-DQPSK modulation is similar to other modulation formats as well as to the optimum values found in the previous section for 21.4-Gb/s RZ-DQPSK transmission. This indicates that 42.8-Gb/s RZ-DQPSK should be compatible with a dispersion maps optimized for 10.7-Gb/s NRZ-OOK legacy transmission systems. Figure 6.5e shows the BER after 2,260-km as a function of the accumulated dispersion excursion. For a 1-dB and 2-dB Q-factor penalty, the chromatic dispersion window is in excess of 160 ps/nm and 250 ps/nm, respectively. This is somewhat lower as the simulated back-to-back tolerance in Figure 5.14a, which probably results from the accumulation of nonlinear impairments after 2,260-km transmission.

Figure 6.5f depicts the measured BER of both center channels (1535.9 nm and 1551.0 nm) as a function of the transmission distance. Up to a 2,500 km transmission distance the  $\log(\text{BER})$  degrades in a linear fashion. But for longer transmission distances, the  $\log(\text{BER})$  degradation accelerates due to the accumulation of nonlinear impairments. For a  $10^{-3}$  BER, the feasible transmission distance is therefore approximately 3,500 km. Compared to the reach of 21.4-Gb/s RZ-DQPSK, which is depicted as a reference, this is a reduction by a factor 2.3 in feasible transmission distance. After 2,260-km transmission the measured BER is  $9 \cdot 10^{-5}$ , which gives a  $\sim 2.4$ -dB margin with respect to the FEC limit.

## 6.3 Lumped dispersion compensation

In order to explore the possibility of simplified dispersion management, we now discuss 42.8-Gb/s RZ-DQPSK transmission with a lumped dispersion map. In this experiment 16 DFB outputs are combined on a 50-GHz ITU grid, from 1549.0 nm to 1555.0 nm. The transmitter and receiver structure that is used for 42.8-Gb/s RZ-DQPSK modulation is identical to the one described in Section 6.2, with the exception that a 34-GHz CSF is now used to de-multiplex the WDM channels. This improves the back-to-back OSNR requirement with  $\sim 1$  dB.

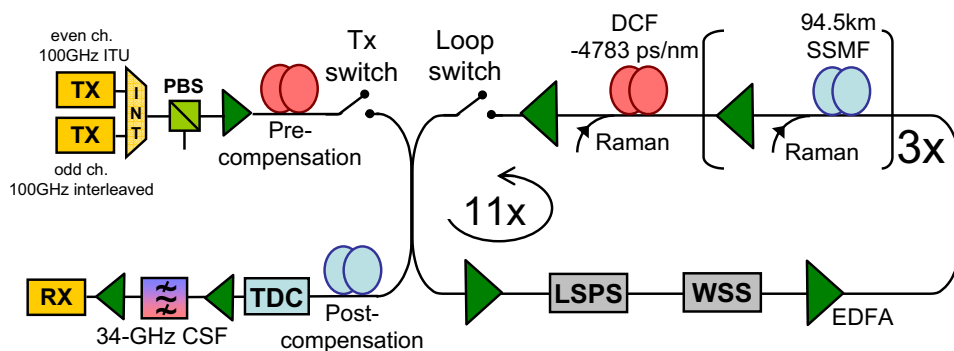


Figure 6.6: Re-circulating loop setup with lumped dispersion compensation.

Figure 6.6 depicts the re-circulating loop setup. Before entering the re-circulating loop, the WDM channels are de-correlated with -1020 ps/nm of pre-compensation. The re-circulating loop consists of three 94.5-km spans of SSMF with an average span loss of 21.5 dB. A Hybrid



Raman/EDFA structure with backward pumping is used for signal amplification with an average ON/OFF Raman gain of  $\sim 11$  dB. The chromatic dispersion of the three 94.5-km SSMF spans combined ( $-4783$  ps/nm), is compensated using DCF placed after the third span. The DCF insertion loss is compensated using backwards Raman pumping with an ON/OFF Raman gain of 18 dB. As the combined loss of DCF and Raman coupler is 17.6 dB, the dispersion compensation has effectively no insertion loss. However, in order to avoid nonlinear impairments in the DCF, the input power is  $\sim 5$  dB reduced with respect to the SSMF. Hence, the total gain of the EDFA/Raman amplification for dispersion compensation is 23 dB. Note that the Raman pump powers launched into the DCF are significantly lower than the pump powers used for Raman amplification in the SSMF.

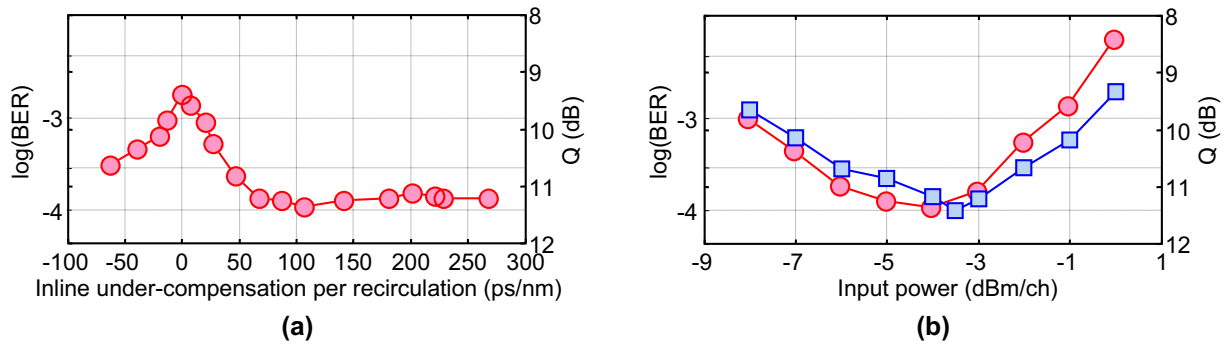


Figure 6.7: Measured BER after 2,550km transmission versus (a) inline under-compensation and (b) input power variation;  $\bullet$  lumped dispersion map,  $\square$  periodic dispersion map.

Figures 6.7a and 6.7b show the dependence of the transmission performance on the inline under-compensation per *recirculation* and input power, respectively. The BER is measured for the center channel at 1552.12 nm and after 2,550-km transmission. From Figure 6.7a it is clear that even though the accumulated dispersion is only compensated every 285 km, the influence of the inline under-compensation on the measured BER is still significant. This can be attributed to a reduction of XPM-induced impairments from co-propagating channels. The worst performance is obtained with full dispersion compensation after every three spans, which results in approximately a 2-dB penalty. When either inline under- or over-compensation is used, the performance improves and optimal performance is obtained for an inline under-compensation of more than 60 ps/nm. Figure 6.7b shows the input power variation for a 107-ps/nm inline under-compensation per re-circulation. 42.8-Gb/s RZ-DQPSK with a periodic dispersion map, as described in the previous section, is shown as a reference. Note that the transmission distance is slightly different in both experiments (2,260 km and 2,550 km). The optimal input power is -4 dBm and -3.5 dBm for the lumped and periodic dispersion map, respectively. The 0.5 dB difference indicates that the lumped dispersion map suffers from a somewhat larger influence of nonlinear impairments. However, with the lumped dispersion map the number of EDFA's in the re-circulating loop is reduced (single-stage versus double-stage amplifiers). This slightly increases the OSNR at the receiver. Hence, there is a trade-off between nonlinear tolerance and OSNR requirement and only a negligible difference in BER is measured between the lumped and periodic dispersion map.



## 6.4. Chirped-FBGs based dispersion compensation

Figure 6.8a shows the BER as a function of transmission distance for both the periodic and lumped dispersion map. The dispersion map and input powers are separately optimized for the periodic and lumped dispersion map. From this comparison we conjecture that the use of a lumped dispersion map does not reduce the transmission performance of 42.8-Gb/s RZ-DQPSK modulation. This indicates that more cost effective dispersion management is feasible by accumulating the DCF at specific points and using single-stage amplifiers in the remainder of the transmission link. Figure 6.8b shows the measured BER for all 16 channels after 3,100-km transmission. The worst-case WDM channel still has a  $\sim 1$  dB margin with respect to the FEC limit.

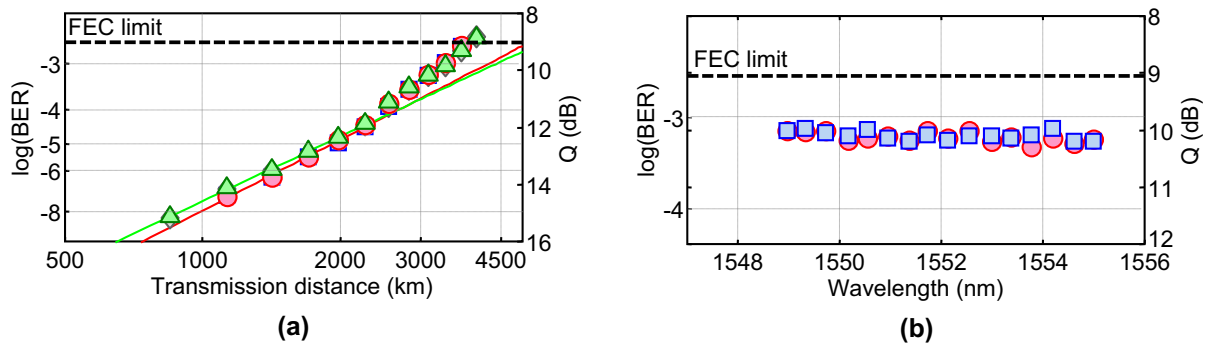


Figure 6.8: Measured BER (a) as a function of transmission distance and (b) for all 16 WDM channels after 3,100-km transmission;  $\circ$  Lumped map, In-phase tributary,  $\square$  Lumped map, Quadrature tributary,  $\triangle$  Periodic map, In-phase tributary,  $\diamond$  Periodic map, Quadrature tributary.

## 6.4 Chirped-FBGs based dispersion compensation

Cost-sensitive optical transmission systems nowadays might use chirped-FBGs for dispersion compensation. As discussed in Section 3.3.3, the low insertion loss and negligible nonlinearity of a FBG allow for a simpler EDFA structure. But the accumulation of phase ripple (PR)-induced transmission impairments limit the feasible transmission distance. This is particularly important for 42.8-Gb/s transmission systems, where the PR-induced transmission impairments might make it difficult to realize long-haul transmission. For chirped-FBGs that have a channelized dispersion compensation profile, as discussed here (see Figure 3.14), the broad optical spectrum can further increase the penalty because the FBGs incur narrowband filtering and have an increased PR near the edge of the pass-band. It is therefore advantageous to use a 42.8-Gb/s modulation format with a relatively narrow optical spectrum such as 42.8-Gb/s RZ-DQPSK. This has the further advantage that the PR penalty is generally smaller for phase modulated formats in comparison to amplitude modulation [303]. This section describes a long-haul transmission experiment using 42.8-Gb/s RZ-DQPSK modulation. In order to assess the impact of using cascaded FBGs for chromatic dispersion compensation we compare long-haul transmission with either FBGs or DCF based chromatic dispersion compensation.

In the transmitter, 32 DFB outputs are combined on a 100-GHz ITU grid, from 1538.2 nm to 1563.0 nm. The channel spacing is limited to 100 GHz because of the channelized profile of

the FBGs. The 32 WDM channels are 42.8-Gb/s RZ-DQPSK modulated with the transmitter discussed in Section 6.2 and the re-circulating loop setup as shown in Figure 6.9. It consists of 6 x 95-km SSMF spans with an average span loss of 19.5 dB. The span loss is  $\sim 2$  dB lower in this experiment compared to the previous experiments as no Raman coupler are included. The chromatic dispersion is compensated with chirped-FBGs and a double periodic dispersion map is used in the transmission experiments. This has the advantage that the accumulated dispersion after every six spans is close to zero. The double-periodic dispersion map is realized using a FBG-based DCM with  $-1020$  ps/nm of chromatic dispersion (at 1550 nm) before the first span, which at the same time is also used as pre-compensation. The FBG-based DCM have an average insertion loss of 2 dB and an average GDR of  $0.074rad$  with a standard deviation of  $0.02rad$ . As the motivation of this experiment is the feasibility of FBG-based dispersion compensation for cost-effective transmission systems, EDFA-only amplification is used (see Section 3.2.2). The SSMF input power is  $\sim 0.5$  dBm per channel, which is found to be the optimum for this configuration. When DCF-based DCMs are used for chromatic dispersion compensation, the input power into the DCF is  $\sim 7$  dB reduced with respect to the SSMF input power. The FBG and transmission fiber are not cascaded here because the EDFA used in this experiment are optimized for DCF-based dispersion compensation. The use of a double-stage EDFAs structure is therefore necessary to control the tilt of the WDM spectrum. At the receiver the desired WDM channel is selected using a narrowband 34-GHz CSF and the residual chromatic dispersion is per channel optimized with a (DCF/SSMF-based) TDC. Afterwards, the signal is fed into the 42.8-Gb/s RZ-DQPSK receiver discussed in Section 6.2.

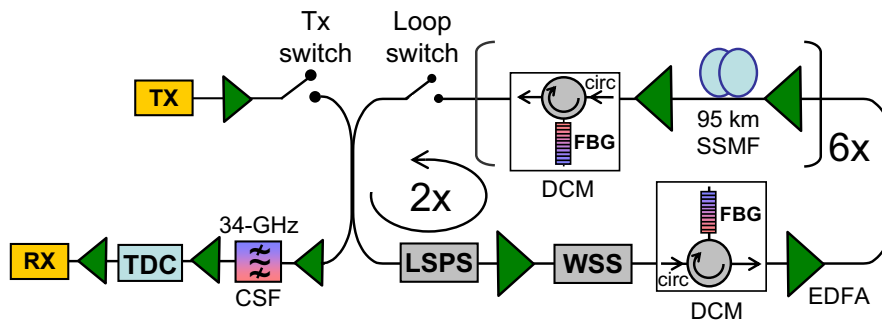


Figure 6.9: Re-circulating loop setup with FBG-based dispersion compensation.

To analyze the impairments that result from cascaded FBGs, the performance for all 32 WDM channels is measured after two circulations (1140 km). First, in-line dispersion compensation with only FBG-based DCMs is considered. The 6 in-line DCMs in the re-circulating loop have either a chromatic dispersion of  $-1345$  ps/nm (5x) or  $-1681$  ps/nm (1x). Hence, after two circulations a total number of 14 FBGs is cascaded. Figure 6.10a depicts the measured BER for all WDM channels. The PR penalty is clearly visible through the large (3.0 dB) spread in performance between the 32 WDM channels. For cascaded FBGs the PR can add up constructively or destructively, as a result some WDM channels will be affected significantly where other WDM channels show only minor PR related impairments. However, despite the significant PR-induced penalty the measured BER is below the FEC limit for all channels.

## 6.4. Chirped-FBGs based dispersion compensation

Figure 6.11 shows measured eye diagrams before and after phase demodulation (Quadrature tributary). After transmission, the combination of residual dispersion and PR impairments results in a WDM channel dependent eye shape. The eye diagram in Figure 6.11b shows a more severe PR penalty (BER  $1.5 \cdot 10^{-4}$ ) than the eye diagram in Figure 6.11c (BER  $1.9 \cdot 10^{-5}$ ). Note that in the experiment the residual dispersion is optimized on a per-channel basis to minimize the BER. The measured difference in optimal post-compensation between the channels shown in Figures 6.11b and 6.11c is approximately 220 ps/nm. This indicates that the residual dispersion optimization can be important to reduce the PR associated penalty [303, 304]. In deployed systems this would require per-channel tunable dispersion compensation at the receiver, for example through the use of a thermally-tuned FBG [151, 152]. Note that in the absence of PR impairments the residual dispersion would be close to zero.

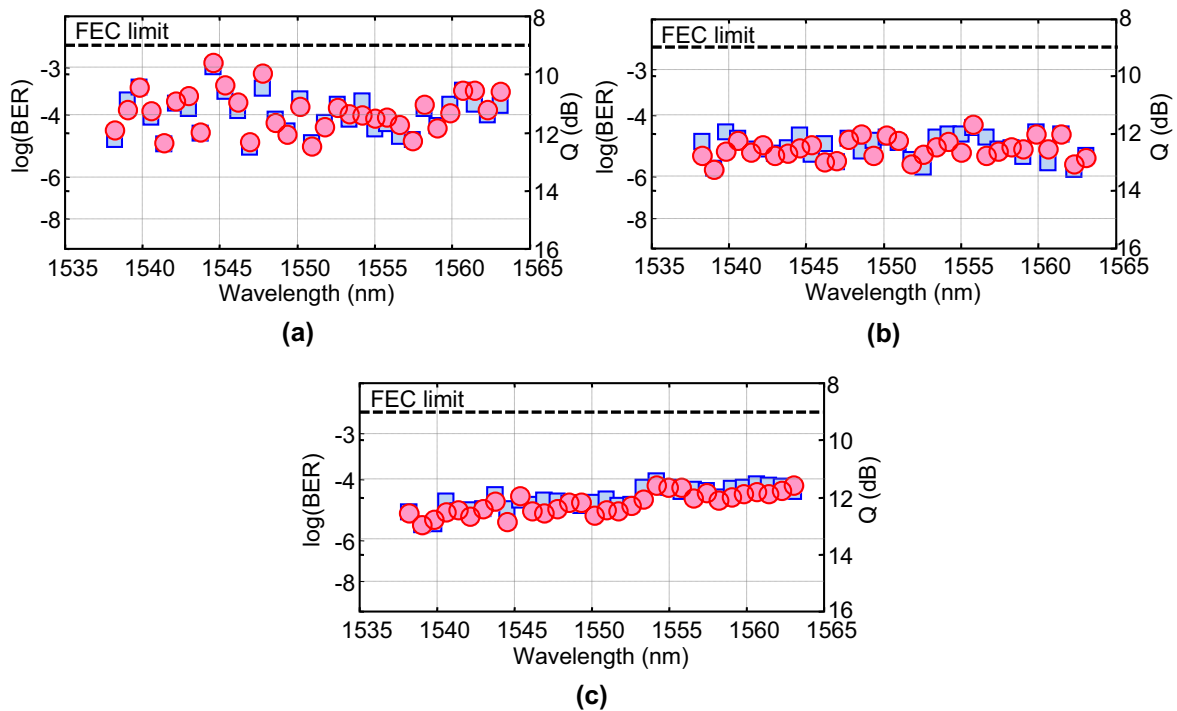


Figure 6.10: Measured BER for 32 WDM channels after 1140-km (12 x 95 km) of SSMF using dispersion compensation with (a) only FBGs, (b) mixed DCF and FBGs and (c) only DCF; ● In-phase tributary, ■ Quadrature tributary.

Next, every second FBG-based DCMs is replaced with DCF-based DCMs and the measured performance for all WDM channels is depicted in Figure 6.10b. The in-line dispersion compensation now consist of FBG-DCMs (-1345 ps/nm, 3x) and DCF (-1512 ps/nm, 3x). The smaller number of cascaded FBG clearly improves the transmission performance. This reduces the spread between the WDM channels to below 1.5 dB and decreases the average BER to  $1.2 \cdot 10^{-5}$ , which results in nearly a 3 dB margin with respect to the FEC limit. Finally, Figure 6.10c shows the measured performance when all FBG DCMs are replaced by DCF except for the pre-compensation DCM. The in-line dispersion map consists now of DCF modules with either -1345 ps/nm (3x) or -1512 ps/nm (3x) of chromatic dispersion. Using DCF-only for dispersion compensation further reduces the spread between adjacent WDM channels to approximately 1 dB, but the average

BER is  $2.8 \cdot 10^{-5}$ , slightly higher compared to the mixed FBG/DCF in-line dispersion compensation. This is a results of the performance difference between the lower and higher part of the WDM spectrum. We conjecture that this difference is due a spectral tilt, which increases the power of the channels in the upper part of the WDM spectrum. The higher power increases nonlinear impairments, which in turn increases the measured BER. This illustrates that the lower insertion loss and nonlinearity of FBG-based inline dispersion compensation can simplify EDFA spectral tilt control.

We can now compute the Q-factor penalty from using FBGs instead of DCF-based dispersion compensation. The Q-factor of the *best-case* channel with DCF for dispersion compensation is 13.0 dB and the Q-factor of the *worst-case* WDM with FBG-based dispersion compensation is 9.6 dB. This translates into a Q-factor penalty per FBG of 0.24 dB. Although this penalty is clearly overestimated, long-haul transmission with only FBGs for in-line dispersion compensation might not be feasible. This particularly results from the small margins available with 42.8-Gb/s transmission, which makes it difficult to allocate a 2-dB penalty to PR-related impairments. However, a smaller number of FBGs (up to  $\sim 10$ ) result in an acceptable penalty, comparable to or smaller than the increased nonlinear penalty when DCF is used for in-line dispersion compensation.

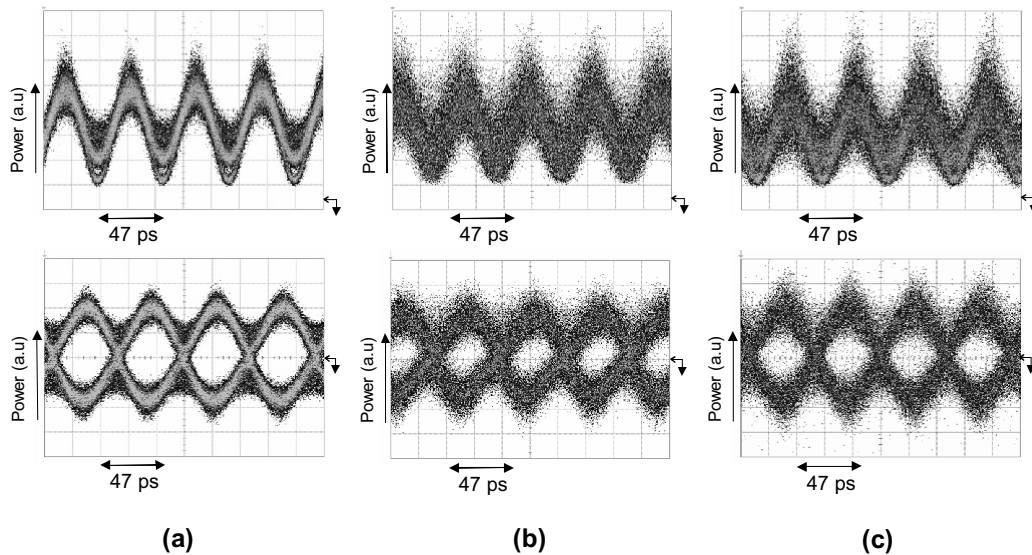


Figure 6.11: Eye diagrams showing the signal before phase demodulation (upper row) and the quadrature tributary after demodulation (lower row). Back-to-back (a) and after 1140 km transmission for  $\lambda = 1553.3$  nm (b) and  $\lambda = 1538.2$  nm (c).

### 6.4.1 Wavelength de-tuning

Figure 6.10 depict the measured BER when the WDM channel is centered on the ITU grid, whereas PR-induced penalties can change significantly with only a small change in center wavelength [305]. We now assess the impact of laser de-tuning on the PR-induced penalties. Figure 6.12 depicts the measured BER as a function of the wavelength de-tuning. Note that the

## 6.4. Chirped-FBGs based dispersion compensation

channelized WSS used in the re-circulating loop has a 42-GHz 3-dB bandwidth, which is more narrow than the 65-GHz 3-dB bandwidth of a single FBG. The wavelength de-tuning range is thus in principle not limited by the bandwidth of the channelized FBGs. To measure the penalty as a function of wavelength de-tuning, both the wavelength of the transmitter laser and the center wavelength of the receiver-side CSF are changed. Figure 6.12a shows the measured BER for the WDM channel at 1538.2 nm, which suffers only from a small PR penalty whereas the channel at 1544.5 nm is severely affected (Figure 6.12b). However, both channels show that the PR penalty can easily change with up to 3 dB within a  $\pm 5$ -GHz de-tuning range. Note though that a typical laser wavelength drift over the system lifetime would be  $\pm 1.5$  GHz. As evident from Figure 6.12b, the measured BER increases to above the FEC limit within the de-tuning range. But the PR-induced penalty is artificially enlarged in these results as each of the FBGs is passed twice within the re-circulating loop. When independent FBGs are cascaded, the peak-to-peak PR would increase statistically in comparison to a linear addition when the same FBGs are passed multiple times. Hence, the peak-to-peak PR will be higher for a re-circulating loop with two re-circulations in comparison to straight-line transmission. For two re-circulations, the peak-to-peak PR increases by a factor of  $\sqrt{2}$ , but the difference in OSNR penalty can be more significant. The impact of using a re-circulating loop in the evaluation of PR-induced penalties is discussed in more detail in the next section.

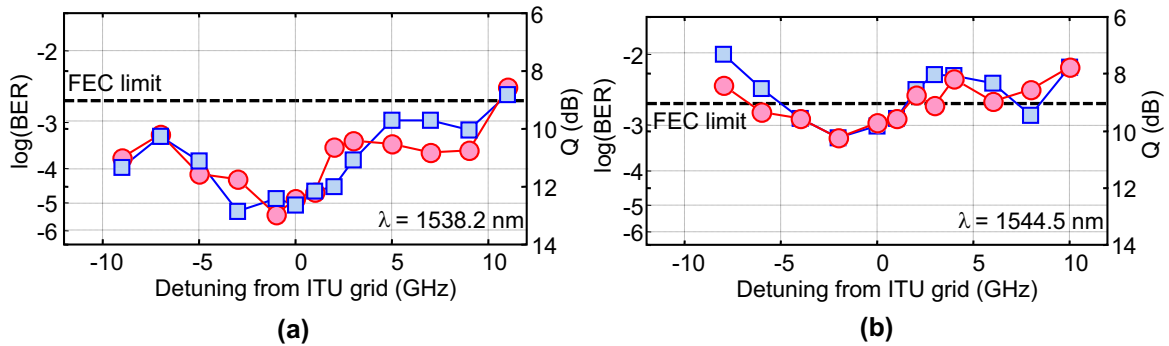


Figure 6.12: Measured BER versus wavelength detuning from the ITU grid after 1140-km, for the WDM channels at (a) 1538.2 nm and (b) 1544.5 nm;  $\bullet$  In-phase tributary,  $\square$  Quadrature tributary

### 6.4.2 10.7-Gb/s NRZ-OOK

In order to analyze the PR-induced penalties that occur when multiple FBG are cascaded, we now discuss a long-haul transmission experiment using 10.7-Gb/s NRZ-OOK modulation and chirped-FBGs for dispersion compensation. In this experiment, the same 32 channels are used as in the previous section (from 1538.2 nm to 1563.0 nm) and the transmitter and receiver structure are depicted in Figure 6.13. The same re-circulating loop setup is used here as described in the previous section (Figure 6.9), with the difference that the number of spans in the re-circulating loop is increased to 8. For the in-line dispersion compensation, the DCMs have a chromatic dispersion equivalent to 80 km (1345 ps/nm, 5x) or 100 km of SSMF (1681 ps/nm, 3x). The SSMF input power is increased to  $\sim 3$  dBm per WDM channel, which is consistent with the input powers that are used in deployed 10.7-Gb/s transmission systems. At the receiver the

desired WDM channel is selected using a 18-GHz CSF and the residual chromatic dispersion is per channel optimized with a (DCF/SSMF-based) TDC. Afterwards, the signal is fed to a standard 10.7-Gb/s receiver (Rx), which consists of a photo-diode, CDR and BER tester.

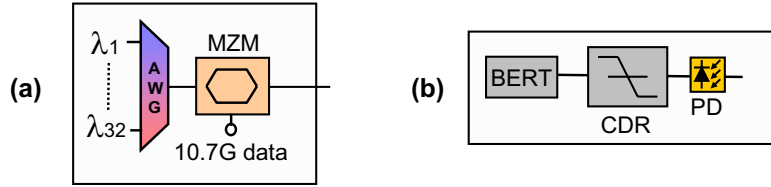


Figure 6.13: Transmitter and receiver structure for 10.7-Gb/s NRZ-OOK.

Figures 6.14a and 6.14b show the measured BER after 3,040-km and 3,800-km of transmission, cascading 36 and 45 FBGs, respectively. The impact of PR-related impairments is apparent through the large  $\sim 5$  dB spread in performance between the WDM channels whereas the spread would be in the range of  $\sim 1$  dB for a similar DCF-based transmission experiment. By measuring a large number of WDM channels a certain measured of statistics for the PR penalties is obtained. This shows that after 3,040-km transmission the measured BER is below  $10^{-4}$  for the worst channel, which gives a 2.5 dB margin with respect to the FEC limit. And even for a 3,800-km transmission distance, the measured BER is below the FEC limit for all 32 WDM channels.

Figure 6.15 shows in the upper row the measured eye diagrams after 3,800-km transmission. The eye diagrams at (a) 1543.7 nm and (b) 1551.7 nm show WDM channels where the PR has a relatively small influence. On the other hand, for the channels at (c) 1552.5 nm and (d) 1554.1 nm the PR has evidently a more severe impact, limiting the feasible transmission distance to 3,800 km. The lower row in Figure 6.15 shows the eye diagrams for the same WDM channels when the amplitude and phase response of the cascaded FBGs are simulated. In the simulations the measured amplitude and phase response of the FBGs from the transmission experiment are used, but no transmission is simulated ("back-to-back"). Hence, the simulation shows only the PR related impairments resulting from the cascaded FBGs. Both the simulated and measured eye diagrams in Figure 6.15 show a strong broadening of the '1' rail through phase distortions. Based on this similarity we conjecture that the phase distortion in the measured eye diagrams result mainly from PR-induced penalties.

We now compute the OSNR penalty between FBG and DCF-based dispersion compensation. After transmission the average OSNR is 19.7 dB and 18.8 dB, for respectively a 3,040-km and 3,800-km transmission distance. For comparison, back-to-back the required OSNR is 9.7 dB and 15.3 dB for a  $10^{-3}$  and  $10^{-9}$  BER, respectively. The OSNR penalty is now computed by subtracting the required back-to-back (B2B) OSNR for the measured BER from the measured OSNR after transmission,

$$\Delta OSNR = OSNR_{Rx} - OSNR_{B2B}(BER_{Rx}). \quad (6.1)$$

We compute this way the OSNR penalty for the best-case and worst-case measured BER, which gives a variation in OSNR penalty between 4 dB and 8.5 dB after 3,040 km transmission. After a 3,800 km transmission distance, the OSNR penalty range increases and we measure penalties



## 6.4. Chirped-FBGs based dispersion compensation

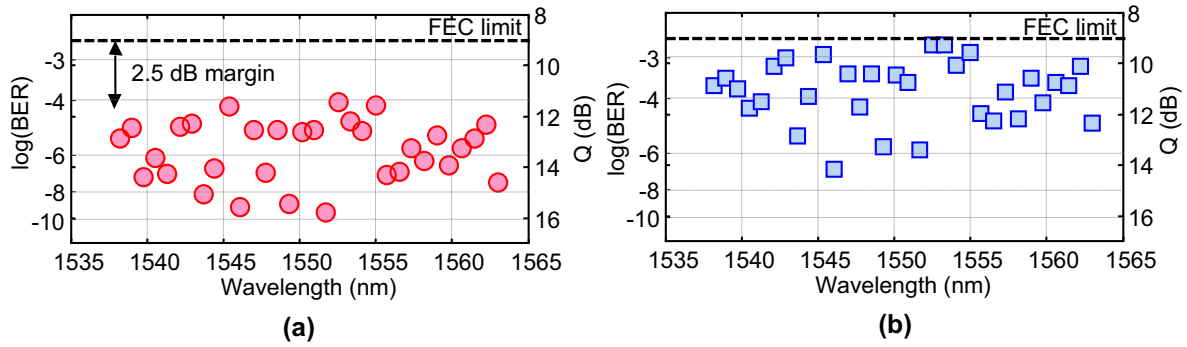


Figure 6.14: Measured BER for 32 WDM channels after (a) 3,040-km and (b) 3,800-km transmission.

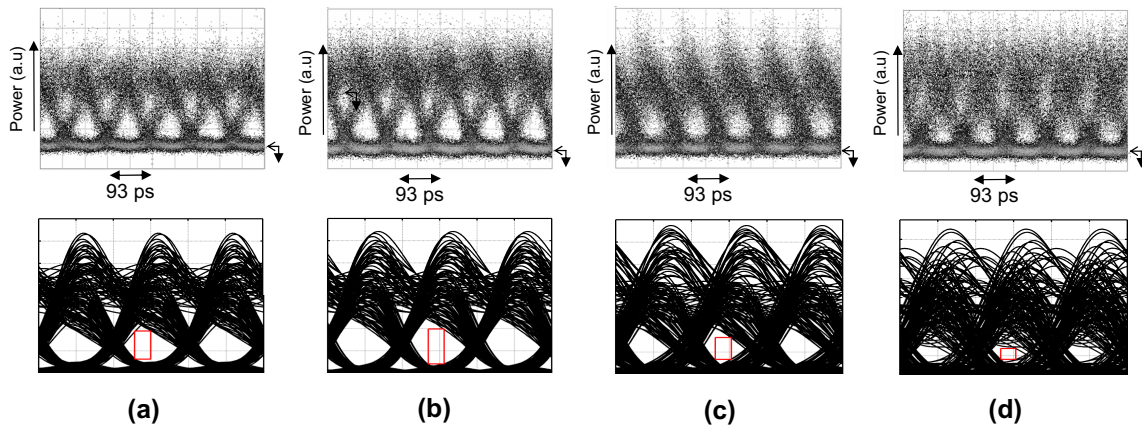


Figure 6.15: upper row: Eye diagrams after 3,800 km with small (a and b) and large (c and d) PR related penalties, lower row: simulated back-to-back eye diagrams using measured amplitude and phase response, (a) 1543.7 nm; (b) 1551.7 nm; (c) 1552.5 nm; (d) 1554.1 nm.

between 5 dB and 10 dB. When we now assume that the OSNR penalty is only related to PR-induced impairments, we can compute the OSNR penalty per FBG. Dividing the penalty through the number of FBGs passed along the transmission link, we obtain an OSNR penalty per cascaded FBG between 0.11 dB and 0.24 dB.

Figure 6.16b shows the BER increase with transmission distance for a number of WDM channels, including channels that suffer from small as well as large PR penalties. The Q-factor decrease with  $\sim 6.5$  dB when the transmission distance is doubled, in comparison to 3 dB for an ideal (linear) transmission line<sup>2</sup>. Hence, we can conclude that the PR related impairments become more severe with an increasing number of cascaded FBGs. However, in the re-circulating loop experiment, the measured penalty is artificially increased due to the cascade of the same FBGs for each re-circulation. This is visualized through simulations in Figure 6.16b and 6.16c, which show the growth of the peak-to-peak GDR (GDRpp) when an increasing number of FBGs is cascaded. The mean value and the standard deviation of the GDRpp are computed from a large number ( $> 100$ ) of measured FBGs for statistical averaging. Both the mean GDRpp and the mean GDRpp plus twice the standard deviation ( $2 \cdot \sigma$ ) are shown. In Figure 6.16b we assume

<sup>2</sup>This is slightly different in a nonlinear transmission link. If the Q-factor is assessed as a function of the transmission distance for a fixed input power, the decrease is  $\sim 2.2$  dB for a doubling in transmission distance.

that arbitrary FBGs are cascaded, as occurs in field deployment. The PR of the cascaded FBGs is then uncorrelated and grows statistically (square-root) [305]. However, in this transmission experiment 8 FBGs are cascaded in a re-circulating loop and the optical signal is thus passed multiple times through the same FBG. Consequently, the peak-to-peak GDR grows linearly, tremendously worsening the associated penalty. Figure 6.16c depicts the case when 8 arbitrary FBG are cascaded in a re-circulating loop. Hence, we conjecture that for arbitrary cascaded FBGs the drop-off with transmission distance is less steep and a significant larger number of FBGs can be cascaded with acceptable PR-induced impairments.

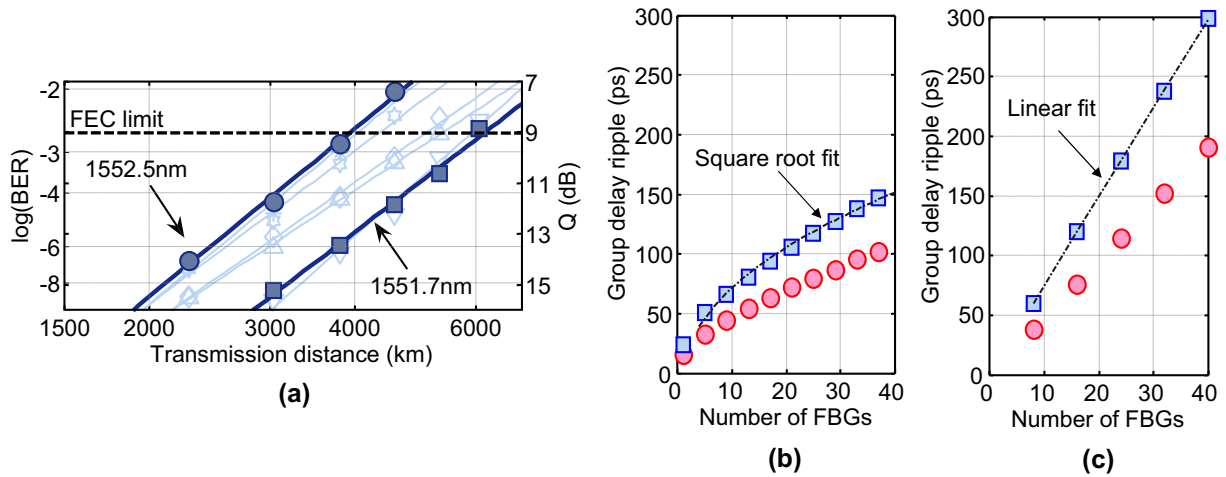


Figure 6.16: (a) Measured BER versus transmission distance for a channel with small (1551.7 nm) and large (1552.5 nm) PR penalties as well as several arbitrary WDM channels. Peak-to-peak group-delay ripple (b) when arbitrary FBGs are cascaded and (c) when 8 FBGs are cascaded in a re-circulating loop; ● mean GDRpp, ■ mean GDRpp + 2 · σ.

The transmission experiment shows that the PR of state-of-the-art FBGs is small enough for dispersion compensation in a long-haul transmission link. In a straight-line, where the PR of the cascaded FBGs adds randomly, the worst-case OSNR penalty per FBG is  $\sim 0.1$  dB when we assume that a larger number of FBGs are cascaded. When we allow a maximum 2-dB penalty resulting from PR-induced impairments this implies that FBG fabrication technology has matured into an appealing alternative for cost-sensitive long-haul links, up to approximately 2000 km. However, the penalties associated with cascading an even large number of FBGs ( $> 30$ ) implies that FBGs are not yet suitable for ultra long-haul applications. In addition, the penalty we find here assume per-channel optimization of the accumulated dispersion. Without tunable dispersion compensation the OSNR penalty per FBG will be higher.

We note that it is not straightforward how the PR related penalty scales as a function of the bit rate. The FBG peak-to-peak ripple amplitude is a much larger fraction of the bit period for 42.8-Gb/s modulated signals in comparison to 10.7-Gb/s modulation. The ripple period on the other hand is usually well below the modulation frequency for 42.8-Gb/s modulation, which reduces the ripple impact [172]. In [152] it was shown that the PR penalty is somewhat larger for a 42.8-Gb/s compared to a 10.7-Gb/s bit rate, but the difference is relatively small. Comparing the PR-induced penalty for 10.7-Gb/s NRZ-OOK and 42.8-Gb/s RZ-DQPSK appears to support this conclusion.



## 6.5 OPC-supported long-haul transmission

DQPSK has a somewhat lower nonlinear in comparison to DPSK modulation, as observed in Section 5.4. This makes OPC of particular interest to DQPSK modulation, as it can be used to improve the nonlinear tolerance and thereby increases the feasible transmission reach. In this section we therefore discuss OPC-aided long-haul transmission experiments using RZ-DQPSK modulation and compare it with the DCF-aided transmission experiment discussed in Section 6.1. The experimental setup of the OPC-aided transmission link is depicted in Figure 6.17a, the link with DCF for dispersion compensation in Figure 6.1. In both experiments, the same transmitter and receiver structure is used.

### 6.5.1 21.4-Gb/s RZ-DQPSK transmission

In this transmission experiment, 44 wavelengths on a 50-GHz ITU grid are 21.4-Gb/s RZ-DQPSK modulated. The wavelengths range from 1532.3 nm to 1540.6 nm in the lower part of the C-band and from 1546.1 nm to 1554.5 nm in the upper part of the C-band. After half the re-circulations (18x), the signals are optically phase conjugated. Mid-link OPC is realized here with a re-entrant re-circulating loop structure, as depicted in Figure 6.17a. The re-circulating loop is split in two branches, with one branch containing the OPC subsystem. The other branch contains only a VOA to match the output power of both branches. After half the re-circulations, the loop switch is closed and the re-entrant switch is opened for one re-circulation. This feeds the phase conjugated signal into the loop, which then propagates for another 18 re-circulations.

The OPC subsystem first removes the 22 channels in the lower part of the C-band, which range from 1532.3 nm to 1540.6 nm, as these channels are only used to balance the amplifiers in the re-circulating loop. Subsequently, the remaining 22 channels, from 1546.1 nm to 1554.5 nm, are optical phase conjugated. The OPC subsystem that is used in this experiment is based on the counter-propagating polarization-diversity scheme discussed in Section 3.6.1 and has a measured PDL of less than 0.4 dB. In order to reduce the photo-refractive effect in the PPLN waveguide, it is operated at 202.3° Celsius. QPM inside the PPLN waveguide is realized by reversing the sign of the nonlinear susceptibility every 16.3 μm. The OPC subsystem is pumped, after amplification to ~26 dBm, with the output of an ECL at 1543.4 nm.

The input power of the WDM channels is approximately 10 dBm per channel at the input of the polarization diversity structure. The optical spectrum at this point is depicted in Figure 6.17b, which consists only of the 22 WDM channels in the upper part of the C-band. The optical spectrum at the output of the OPC subsystem consists of the pump signal, input signals and phase conjugated signals, as depicted in Figure 6.17c. The phase conjugated signals are present mirrored with respect to the pump and range from 1532.3 nm to 1540.6 nm. The conversion efficiency of the PPLN waveguide, i. e. the difference between the input signal and the conjugated signal at the output of the OPC subsystem, is 9.2 dB. This is shown in Figure 6.17c, where the conversion efficiency is the difference between the lower (after OPC) and upper (before OPC) wavelength band. The insertion loss of the OPC subsystem and subsequent filters is comparable

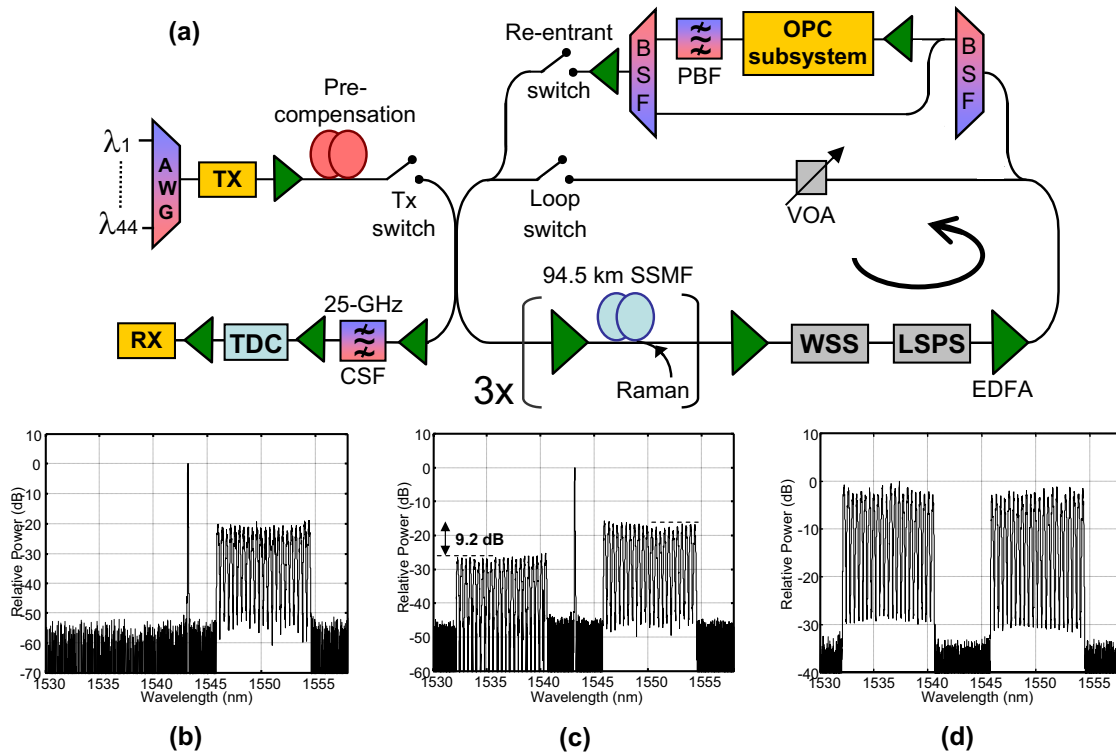


Figure 6.17: (a) Experimental setup for OPC-aided long-haul 21.4-Gb/s RZ-DQPSK transmission; (b) spectra at the input of the OPC subsystem; (c) spectra at the output of the OPC subsystem and (d) received spectra after 10,200-km transmission (all spectra 0.01 nm res. bw.)

to a single fiber span (with hybrid EDFA/Raman amplification), and the OPC has therefore no significant impact on the OSNR after transmission. After the OPC subsystem, the pump signal is suppressed through a pump block filter (PBF) and the original input signals are removed using a band selection filter (BSF). Finally, the input channels, ranging from 1546.1 nm to 1554.5 nm, are recombined with the phase conjugated channels to balance the amplifiers when the signal propagates for another 18 re-circulations through the re-circulating loop.

In the OPC-aided transmission experiment, the optimal SSMF input power is -3 dBm per channel. This is 1 dB higher than the optimal input power in the transmission experiment with DCF-based dispersion compensation. Figure 6.18 depicts the BER as a function of the transmission distance. For the OPC-aided transmission experiment the in-phase tributary at 1535.1 nm is measured, whereas for the configuration with DCF the in-phase tributary at 1550.7 nm is depicted. At shorter distances, the Q-factor of the configuration with DCF is about 0.5 dB lower than that of the OPC-aided transmission system. But after 5,000-km transmission, the performance of the DCF configuration deviates from the linear increase in  $\log(\text{BER})$  whereas the OPC based performance is virtually unaffected. As RZ-DQPSK is mainly limited by single channel impairments this likely results from SPM induced nonlinear impairments and the impact of nonlinear phase noise. In the absence of OPC, the nonlinear impairments are not compensated, which results in worsening of the performance after 5,000-km transmission. As well, an extra penalty arises in this experiment due to transmitter-side imperfections of the parallel DQPSK modulator. The amplitude fluctuations result in signal dependent nonlinear phase shift variations, which

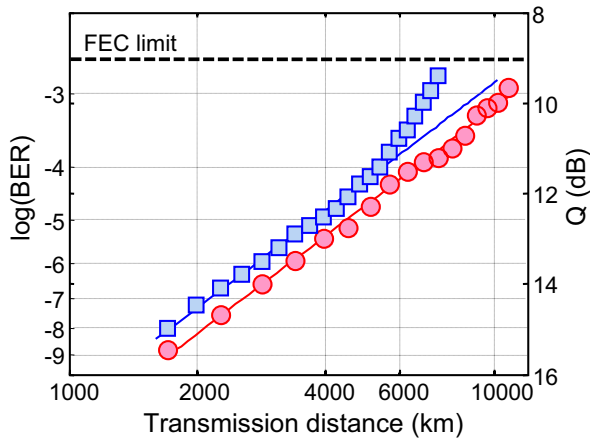


Figure 6.18: BER of a typical channel as a function of the transmission distance,  $\bullet$  with OPC and  $\blacksquare$  without OPC.

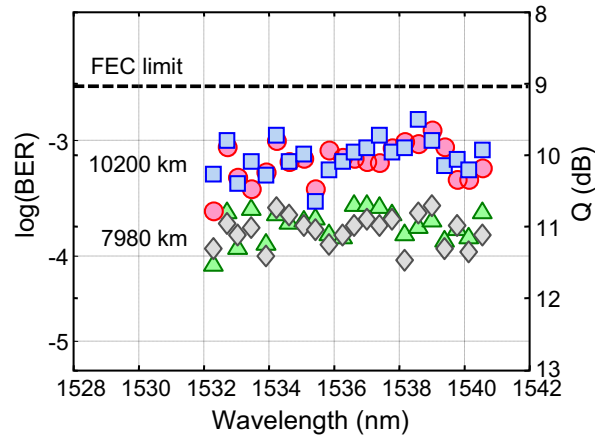


Figure 6.19: BER of all channels after transmission for the OPC-aided configuration;  $\blacksquare$  10,200 km, In-phase,  $\bullet$  10,200 km, Quadrature,  $\blacklozenge$  7,980 km, In-phase,  $\blacktriangle$  7,980 km, Quadrature.

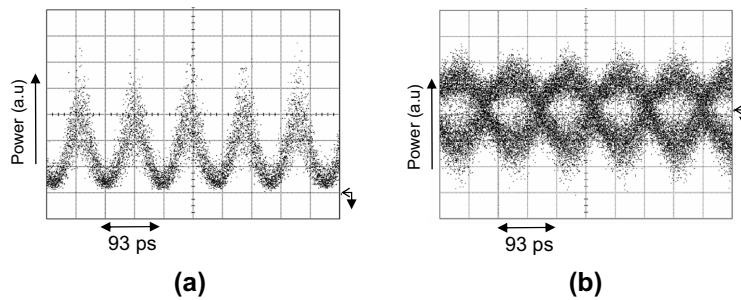


Figure 6.20: Eye diagrams after 10,200-km transmission (a) before demodulation; (b) after demodulation, Quadrature.

causes additional nonlinear phase noise impairments along the transmission link. In the OPC-aided transmission experiment, mid-link OPC reduces both conventional SPM-induced nonlinear impairments as well as the increased nonlinear phase noise due to modulator imperfections. Figure 6.20 depicts the measured eye diagrams after 10,200 km transmission, before as well as after phase demodulation.

The BER of all WDM channels after 7,980 km (28 circulations) and 10,200 km (36 circulations) is depicted in Figure 6.19. The performance is only evaluated for the 22 phase conjugated channels. In order to conjugate the other 22 channels, a second OPC subsystem would be required. After 7,980 km there is an average 2 dB margin with respect to the FEC limit. And even after 10,200 km transmission all WDM channels are well below the FEC limit. Note that for a 10,200 km transmission distance, the single OPC unit compensates for an accumulated chromatic dispersion of over 160,000 ps/nm. When we compare mid-link OPC and the configuration with DCF for dispersion compensation, the transmission reach of 21.4-Gb/s RZ-DQPSK is 10,200 km and 7,200 km, respectively. This indicates that the use of a single mid-link OPC unit increases the transmission distance by 44%.

### 6.5.2 42.8-Gb/s RZ-DQPSK transmission

The concept of mid-link OPC for simultaneous chromatic dispersion and nonlinearity compensation is even more promising for higher bit rates. As an increase in bit rate severely reduces the feasible transmission distance, the gain in transmission reach provided through OPC can be an enabling technology for long-haul transmission.

We now discuss a transmission experiment where mid-link OPC is combined with 42.8-Gb/s RZ-DQPSK modulation. In this transmission experiment, 52 wavelengths on a 50-GHz ITU grid are used, ranging from 1530.8 nm to 1540.6 nm in the lower wavelength band and from 1546.1 nm to 1556.1 nm in the higher wavelength band. The channels are 42.8-Gb/s RZ-DQPSK modulated using the transmitter architecture discussed in Section 6.2 and the re-circulating loop has the same configuration as shown in Figure 6.17a. The input power per channel into the SSMF is -2.9 dBm in the OPC-aided configuration, compared to -3.5 dBm for the configuration with DCF for dispersion compensation. The channels are first de-correlated with -2040 ps/nm of pre-compensation before entering the re-circulating loop. The signal then propagates for 8 re-circulations (2270 km) around the re-circulating loop. Mid-link, the signals are fed through the re-entrant branch of the loop and the signal is phase conjugated using the same polarization-diversity OPC subsystem as described in the previous section. The conversion efficiency is with 7.2 dB slightly higher in this experiment, which results from further optimization as well as a higher pump power (27 dBm). After phase conjugation, the signal is transmitted for another 8 circulations around the re-circulating loop and subsequently fed into the 42.8-Gb/s RZ-DQPSK receiver. The optical spectrum at the receiver is depicted in Figure 6.21b.

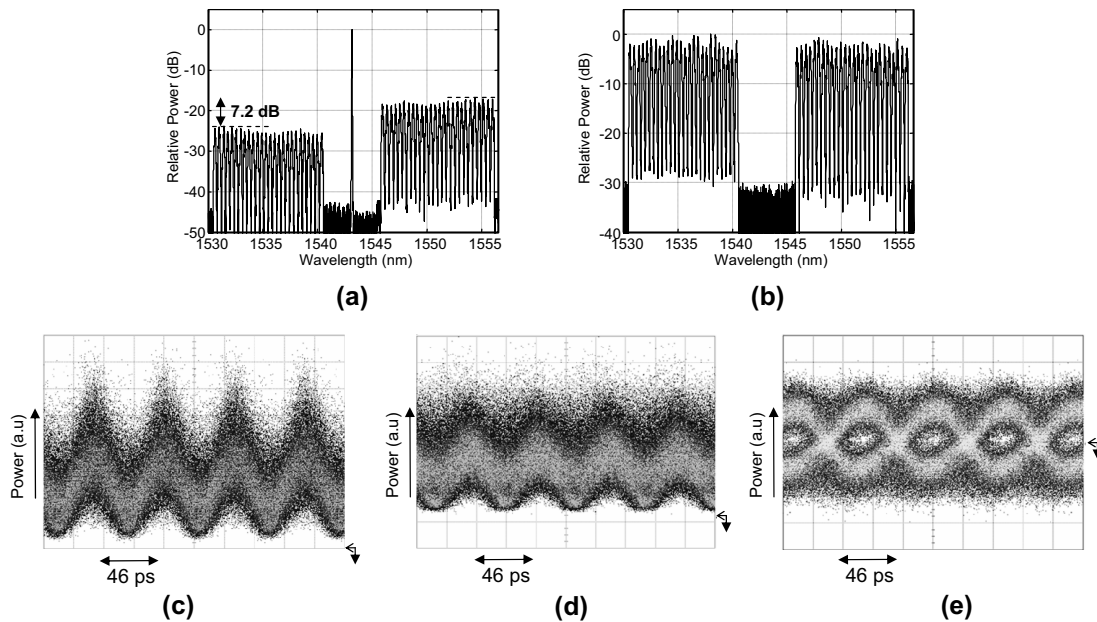


Figure 6.21: (a) Optical spectrum after the PPLN subsystem, (b) Optical spectrum at the receiver after 4,500-km transmission, (c) eye diagram before demodulation without narrowband filtering, (d) eye diagram before demodulation with narrowband filtering and (e) eye diagram after demodulation (all spectra 0.01nm res.bw.).

Figure 6.21c depicts the measured eye diagram after 4,500-km transmission when the nearest neighbors are switched off and the signal is not passed through the 25-GHz CSF. Although the low OSNR after transmission ( $\sim 15.5$  dB) is evident from the eye diagram, the RZ shape is clearly recognizable. When the nearest neighbors are switched on and the signal passes at the receiver through the 25-CSF, the eye diagram in Figure 6.21d is obtained. The narrowband optical filtering is clearly visible in the eye diagram. As discussed in Section 5.3.1, narrowband filtering with a 25-GHz bandwidth results in approximately a 1-dB penalty. Figure 6.21e depicts the eye diagram after phase demodulation and balanced detection.

The measured performance as a function of transmission distance is depicted in Figure 6.22. For this measurement, the same 18 WDM channels are used as in the configuration with the periodic dispersion map. In this case the upper 9 channels are phase conjugated (from 1549.32 nm to 1552.52 nm), and the additional 9 channels (from 1534.25 nm to 1537.40 nm) are used to balance the amplifiers. Reducing the number of WDM channels resulted in a slight improvement in transmission performance because the more narrow spectrum requires less gain tilt compensation in the EFDA, which improves the amplifier noise figure. The measured difference between the 9 channel and 52 channel WDM spectrum is approximately 1 dB in Q-factor. For the center channel (at 1535.8 nm), the BER is measured as a function of transmission distance from 1,700 km up to 5,700 km. Figure 6.22 further depicts the BER versus transmission distance of 42.8-Gb/s RZ-DQPSK with a periodic DCF-based dispersion map. When we compare the performance of both configurations, a clear advantage is evident for mid-link OPC. Similar to the 21.4-Gb/s RZ-DQPSK experiment, we measure for the mid-link OPC a linear dependency between transmission distance and  $\log(\text{BER})$ , which indicates that the nonlinear impairments are (partially) compensated. This increases the feasible transmission distance from 3,500 km with a periodic dispersion map to 6,000 km with the mid-link OPC. Hence, a single OPC provides a  $>50\%$  improvement in transmission reach.

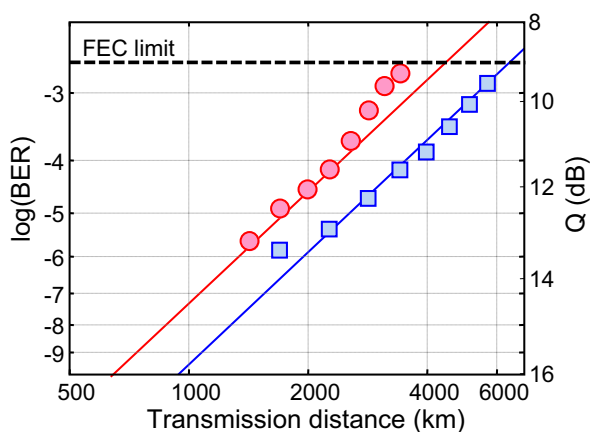


Figure 6.22: BER of a typical channel as a function of transmission distance;  $\bullet$  without OPC and  $\blacksquare$  with OPC.

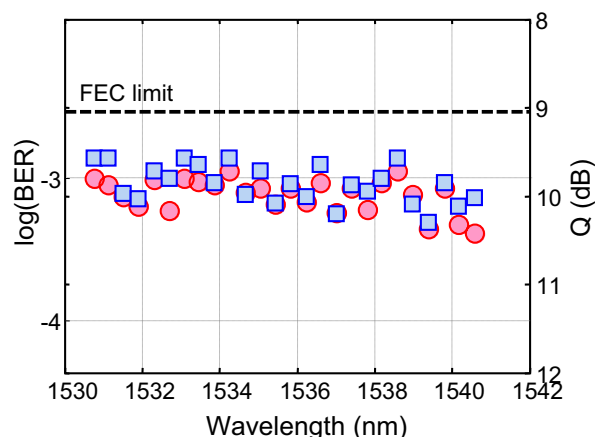


Figure 6.23: BER of the in-phase and quadrature tributary after 4,500 km for the OPC-aided configuration;  $\bullet$  In-phase,  $\blacksquare$  Quadrature.

The WDM performance with mid-link OPC is evaluated after 4,500-km transmission for the 26 phase conjugated WDM channels. In Figure 6.23, the BER of both the in-phase and quadrature channels are depicted. Both tributaries show a similar average BER, with a slightly better performance for the in-phase tributary due to modulator imperfections. The BER of the worst measured channel is  $1.3 \cdot 10^{-3}$ ; hence all measured channels are below the FEC limit. The received OSNR of all channels after 4,500-km transmission is approximately 15.5 dB averaged over all WDM channels, which corresponds to a 2-dB OSNR penalty compared with the back-to-back performance. This indicates that there is only a minor impact of nonlinear distortions, and we observe no evidence of severe nonlinear phase noise impairments. Hence, OPC effectively improves the nonlinear tolerance and thereby extends the reach of 42.8-Gb/s RZ-DQPSK transmission.

### 6.6 Comparison of DQPSK transmission experiments

The previously discussed long-haul transmission experiments focus on the feasible transmission distance near the FEC limit. However, deployed transmission systems operate often with a considerable margin with respect to the FEC limit. This is used to account for chromatic dispersion and PMD penalties as well as aging, component variations and temperature differences. In addition, the vast majority of the deployed transmission system uses EDFA-only amplification.

Figure 6.24 shows two 42.8-Gb/s RZ-DQPSK transmission experiments with a  $\sim 3$ -dB margin with respect to the FEC limit. Both experiments are discussed in more detail in Section 6.4 and Section 8.2, respectively. The transmission experiment in Figure 6.24a uses EDFA-only amplification, whereas in Figure 6.24b hybrid EDFA/Raman amplification is used. This shows that the use of hybrid EDFA/Raman amplification increases the feasible transmission distance with  $\sim 60\%$ . This percentage can be used as a figure of merit to estimate the feasible transmission distance for the other transmission experiments discussed in this chapter when EDFA-only amplification would be used. We note that in the first experiment a 100-GHz channel spacing is used, but due to the small impact of XPM on DQPSK modulation this will not significantly affect the comparison.

The transmission experiment in Figure 6.24a shows that a  $\sim 1000$ -km reach is feasible for 42.8-Gb/s RZ-DQPSK modulation with EDFA-only amplification and a 3-dB margin with respect to the FEC limit. For long-haul transmission systems that can use hybrid EDFA/Raman amplification the feasible transmission distance can be extended to around 1,700 km.

Table 6.1 summarizes some of the long-haul transmission experiments that have been reported in recent years using  $>40$ -Gb/s DQPSK modulation. In [291], *Gnauck et. al.* were the first to show that 42.8-Gb/s RZ-DQPSK enabled long-haul transmission with a 0.8-b/s/Hz spectral efficiency in the presence of strong optical filtering. But the lower nonlinear tolerance of RZ-DQPSK coupled with the higher OSNR requirement, severely restricts the feasible transmission distance when compared to DPSK modulation. For example, comparing the long-haul transmission experiments using 42.8-Gb/s RZ-DPSK modulation in [306] and 42.8-Gb/s RZ-DQPSK modulation in [122], the feasible transmission distance is reduced from 6,120 km to 4,080 km.

## 6.6. Comparison of DQPSK transmission experiments

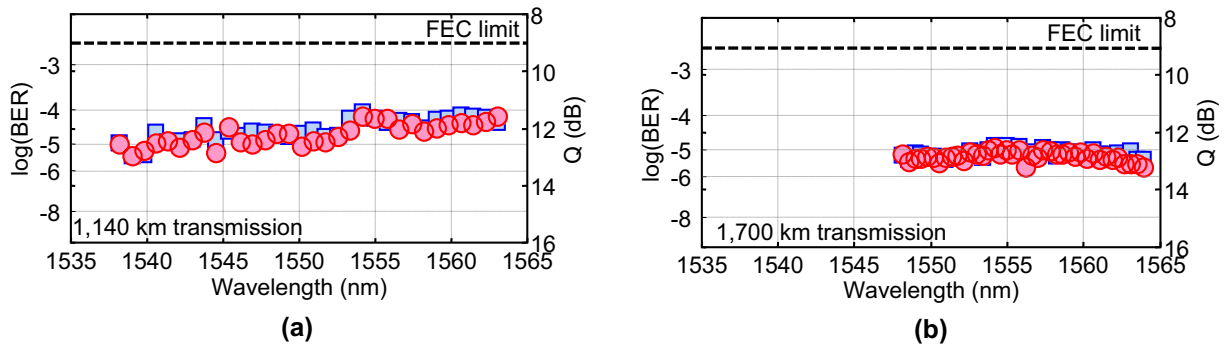


Figure 6.24: Long-haul 42.8-Gb/s RZ-DQPSK transmission, (a) BER after 1,140-km transmission with EDFA-only amplification (b) BER after 1,700-km with hybrid EDFA/Raman amplification;  $\circ$  In-phase tributary,  $\square$  Quadrature tributary.

Hence, the OSNR requirement (1 dB) and lower nonlinear tolerance (2-3 dB) result on average in a 50% reduction in feasible transmission distance. However, the nonlinear tolerance of RZ-DQPSK can potentially be improved through all-Raman amplification [122], CRZ modulation [307], bit-wise alternating polarization (APol) [307] or optical phase conjugation (OPC) [308]. Note that bit-wise alternating polarization or phase modulation results in spectral broadening, which reduces the feasible spectral efficiency and therefore offsets one of the main advantage of DQPSK modulation. Finally, in [294] a field trail using 43-Gb/s DQPSK modulation was reported with full implementation of the transmitter and receiver control circuits. A commercial 43-Gb/s RZ-DQPSK transponder is discussed by *Hoshida et. al.* in [309].

For the next generation of 100-Gb/s transmission systems, the lower symbol rate of DQPSK modulation is of particular interest. Binary modulation formats are challenging to use at such bit rates, as the required bandwidth of the electrical components in the transponder is difficult and costly to realize. As shown by *Winzer et. al.* in [15], 107-Gb/s DQPSK transmission can enable long-haul transmission with a 1.0-b/s/Hz spectral efficiency. The performance of 100-Gb/s DQPSK modulation is currently limited by the immature components, predominantly the DQPSK modulator, in the transponder. However, this performance is likely to increase in the near future as components are better optimized for the required  $\sim 55$ -Gbaud symbol rate.

The disadvantage of 100-Gb/s DQPSK modulation is the limited transmission reach. When we assume the use of EDFA-only amplification and taking into account a 3 dB margin with respect to the FEC limit, even for an optimized 100-Gb/s DQPSK signal, the feasible transmission distance is not likely to exceed  $\sim 600$  km. In [310], a field trail was reported using 107-Gb/s DQPSK modulation to cover a 500 km distance, albeit using all-Raman amplification. A further drawback of 100-Gb/s DQPSK modulation is its spectral width, which makes it unsuitable for a 50-GHz channel spacing. When used with a 100-GHz channel spacing, the advantage over 40-Gb/s transmission with a 50-GHz channel spacing is limited, particularly as there is a considerable difference in feasible transmission reach. We note that 100-Gb/s DQPSK modulation can be compatible with a 50-GHz wavelength grid using asymmetric interleavers [311]. Asymmetric interleavers have a broad and a narrow pass-band, which allows to use modulation formats with different spectral width for the odd and even wavelength grid.

Table 6.1: SELECTED LONG-HAUL (> 1,000 KM) TRANSMISSION EXPERIMENTS USING DIRECT DETECTED >40-Gb/s RZ-DQPSK MODULATION.

year	bit rate (Gb/s)	# of WDM channels	Spectral efficiency (b/s/Hz)	Distance (km)	Spans (km) / fiber type	Remarks	Company / Ref
2004	42.7	25	0.8	2,800	100	EDFA/Raman SSMF	Lucent [291]
2005	42.8	26	0.8	4,500	93.5 SSMF	EDFA/Raman OPC	TU/e, Siemens [308]
2005	43	151	0.8	4,080	65 -D/+D/-D	all-Raman	Alcatel [122]
2006	42.8	18	0.8	2,800	93.5 SSMF	EDFA/Raman	TU/e, Siemens [312]
2006	42.7	28	0.3	6,550	45 -D/+D/-D	EDFA-only APoL/CRZ	Tyco [307]
2006	43	1+38	-	1,047	~90 SSMF	EDFA-only field-trail	Ericsson, CoreOptics [294]
2006	107	10	0.66	2,000	100 NZDSF	EDFA/Raman	Lucent [14]
2007	107	10	1.0	1,200	100 NZDSF	EDFA/Raman NRZ	Alcatel-Lucent [15]

## 6.7 Summary & conclusions

In this chapter, we described a number of long-haul transmission experiments using RZ-DQPSK modulation.

- In an ultra long-haul transmission experiment using **21.4-Gb/s RZ-DQPSK** modulation, the feasible transmission distance is 7,100-km. This shows that ultra-long haul transmission with a 0.4-b/s/Hz spectral efficiency is possible using only 10-Gb/s optical and electrical components and a 50-GHz channel spacing.
- For **42.8-Gb/s RZ-DQPSK** transmission we obtain a feasible transmission distance of 2,800 km with a 0.8-b/s/Hz spectral efficiency. The re-circulating loop used in the transmission experiment contains a narrowband optical filtering nodes with 42-GHz bandwidth. This shows that a large number of cascaded optical filtering nodes can be passed in a long-haul transmission link using 42.8-Gb/s RZ-DQPSK modulation.
- Both for a 21.4-Gb/s and 42.8-Gb/s bit rate, the optimized *dispersion map* for DQPSK modulation is comparable to a dispersion map optimized for 10.7-Gb/s NRZ-OOK modulation as used in most deployed transmission systems.



- For deployed transmission systems with EDFA-only amplification and a 3 dB margin with respect to the FEC limit, a ***~1000 km transmission reach*** seems feasible for 42.8-Gb/s RZ-DQPSK modulation.

We further discussed long-haul transmission experiments using a number of different technologies for chromatic dispersion compensation.

- ***Lumped dispersion compensation*** requires only minor changes to the transmission link design. The lumped dispersion map discussed here compensates the DCF insertion loss with backwards-pumped raman amplification. A single DCM unit can then compensate the chromatic dispersion between two OADM nodes (up to  $\sim 500$  km) and simpler EDFAs can be used in the remainder of the link. The long-haul transmission experiments shows that a high accumulated chromatic dispersion does not severely affect the nonlinear tolerance of 42.8-Gb/s RZ-DQPSK. When 10.7-Gb/s NRZ-OOK modulated channels are co-propagating on the same link, the lumped dispersion map might result in a lower nonlinear tolerance.
- ***Fiber Bragg gratings (FBG)*** have a low insertion loss (2 dB to compensate for 100 km of SSMF) and negligible nonlinearity. The FBG can therefore be cascaded with transmission fiber, which negates the need for inter-stage access in the EDFA. The use of chirped-FBGs for dispersion compensation results in PR-induced impairments that limit the feasible transmission distance. This PR-related penalty can be significantly reduced by optimizing the chromatic dispersion at the receiver. When the accumulated dispersion is optimized, the cascade of a large number of FBGs results in an OSNR penalty of  $\sim 0.1$  dB per FBG. This implies that FBG-based dispersion compensation can be used for links up to 2000 km with 10.7-Gb/s NRZ-OOK modulation. For 42.8-Gb/s RZ-DQPSK the penalty per FBG is only slightly higher than for 10.7-Gb/s NRZ-OOK modulation, but the smaller available margin for 42.8-Gb/s makes it challenging to use FBG-based dispersion compensation at this bit rate.
- ***Optical phase conjugation (OPC)*** allows the compensation of both chromatic dispersion and intra-channel nonlinear impairments in a long-haul transmission link. OPC is modulation format and bit rate transparent and a single device can conjugate multiple WDM channels. In a long-haul transmission experiment with 42.8-Gb/s RZ-DQPSK, the use of a single mid-link OPC unit increases the feasible transmission distance with  $>50\%$  when compared to a conventional transmission link with an optimized periodic dispersion map. This indicates that use of OPC extends the feasible transmission reach and enables transmission links without any periodic dispersion compensation. It can therefore be instrumental in the realization of long-haul transmission systems with a high spectral efficiency.

The results discussed in Chapters 5 and 6 shows that DQPSK modulation has a number of significant advantages over binary modulation formats in terms of chromatic dispersion and PMD tolerance, as well as spectral efficiency. On the other hand, the higher OSNR requirement and lower nonlinear tolerance somewhat restrict the feasible transmission distance. In summary,

43-Gb/s DQPSK modulation seems to be particularly promising for transmission systems that require a high tolerance against transmission impairments rather than maximize the transmission reach. The compensation of nonlinear impairments through, for example, optical phase conjugation might be instrumental in realizing ultra long-haul transmission with 43-Gb/s DQPSK modulation.

---

## Polarization-multiplexing

So far, we have limited the discussion to modulation formats that employ either the amplitude or phase dimension to transmit information. A different approach towards multi-level modulation formats is the use of the polarization dimension of the optical signal. In comparison to the extensive use of amplitude or phase shift keying in fiber-optic research, modulation using the polarization dimension has attracted only modest attention. This is mainly due to the fact that such modulation formats require a polarization sensitive receiver. Polarization-multiplexed (POLMUX) transmission, sometimes also referred to as polarization division multiplexing (PDM), is the most widely used polarization-sensitive modulation format. It transmits two independent tributaries in each of the orthogonal polarizations and can therefore be used to double the spectral efficiency in comparison to single polarization modulation. In addition, POLMUX signaling reduces the symbol rate by a factor of two when compared with binary modulation formats at the same total bit rate. This can be useful to increase both linear and nonlinear transmission tolerances. For instance, POLMUX-DPSK features a comparably high chromatic dispersion tolerance and narrow spectral width as DQPSK modulation, but at the same time has a lower OSNR requirement and higher SPM tolerance.

*Evangelides et. al.* first proposed in 1992 the use of polarization-multiplexing in long-haul transmission systems using soliton transmission [313]. Later on, different groups used POLMUX signaling in transmission experiments as a means to increase the bit rate in a single wavelength channel [314, 315]. This ultimately resulted in a transmission experiment where POLMUX-DQPSK was used to transmit 2.56-Tb/s in a single wavelength channel [276]. After the advent of WDM transmission systems, POLMUX signaling has mainly be used to double the spectral efficiency for high-capacity WDM transmission experiments. In 1996, *Chraplyvy et. al.* used POLMUX transmission to demonstrate for the first time a 1-Tb/s transmission capacity [316].

---

<sup>1</sup>The results described in this chapter are published in c13, c16-c18, c37, c48-c49, c55

Later on, POLMUX signaling has been used in a number of record-capacity breaking laboratory experiments [317, 318, 319, 320, 321, 34] and field trials [322]. However, such record-capacity breaking experiments are generally limited to comparably short transmission distances. This is in part due to the sensitivity of POLMUX to PMD-related impairments in long-haul transmission systems.

POLMUX is only one representative of a broader family of polarization sensitive modulation formats, which includes bit-wise alternating-polarization (APol) modulation and polarization-shift-keying (PolSK). APol modulation can be used either with a polarization sensitive or polarization insensitive receiver. The main advantage of POLMUX over APol modulation is the potentially higher spectral efficiency. POLMUX, on the other hand, has a more complicated transmitter and receiver structure. PolSK uses the SOP of the signal to encode the information rather than multiplexing two orthogonal polarizations. It therefore requires an even more complicated transmitter and receiver structure, but can potentially provide an even higher spectral efficiency.

Due to the random birefringence in optical fibers, a polarization sensitive receiver requires polarization de-multiplexing at the receiver. This can be realized either in the optical or electrical domain. This chapter discussed POLMUX modulation with a direct detection receiver, i.e. with polarization de-multiplexing in the optical domain. Chapter 10 will consider digital coherent detection, which opens up the possibility of electrical polarization de-multiplexing. Because POLMUX signaling transfers the information in the polarization of the optical signal, it is more sensitive to polarization related impairments. In particular, optical polarization de-multiplexing reduces the PMD tolerance, which makes this a key issue to consider. This chapter therefore focuses on the interaction between PMD and various signal impairments.

In Section 7.1 we introduce the concept of POLMUX mathematically and show that up to three channels can be multiplexed. Subsequently, Section 7.2 discusses the transmitter and receiver architecture required for POLMUX signaling. Section 7.3 then reviews the tolerance of POLMUX signaling with respect to linear transmission impairments with a focus on PMD related impairments. Finally, Section 7.4 analyzes the impact of single-channel and WDM nonlinear impairments on POLMUX signaling.

### 7.1 Principle of polarization-multiplexing

The possibility to multiplex two channels in the polarization domain is intuitive when considering the two degenerate polarization modes of an optical fiber. Mathematically, the possibility of multiplexing using the polarization as a selective agent can be derived by considering the matrix multiplication that is required for polarization (de-)multiplexing. We assume therefore that the signals  $E_1, E_2, \dots, E_k$ , in total  $K$  logical channels, are multiplexed and transmitted over an optical fiber. The  $K$  signals have an equally spaced linear SOP,

$$\theta_k = (k-1) \frac{\pi}{K}. \quad (7.1)$$

In the receiver the intensity received for channel  $k$  after a polarizer with polarization angle  $\theta_k$  is given by *Malus* law [43] and can be denoted through  $E'_k$ ,

$$E'_k = \frac{1}{K} \sum_{n=1}^K E_n \cos^2[\theta_k - \theta_n] = \frac{1}{K} \sum_{n=1}^K E_n \cos^2[(k-n)\frac{\pi}{K}], \quad (7.2)$$

where the summation over the  $K$  channels describes the amount of energy of input channel  $E_k$  that contributes to  $E'_k$ . Hence, a  $K \times K$  matrix  $A_K$  characterizes the received signal for all channels by denoting the transferred power from the input to the output signals. It is straightforward that proper decoding of the transmitted signal at the receiver is only possible when this matrix can be inverted. The possibility of transmitting  $K$  signals multiplexed in the polarization domain is therefore dependent on the existence of an inverse matrix  $A_K^{-1}$ . It can be shown that the inverse matrix  $A_K^{-1}$  only exists when the determinant of matrix  $A_K$  is nonzero [323]. This is possible when  $K \leq 3$ .

First, we look at the case that two channels are multiplexed in the polarization. The channel matrix  $A_2$  is then given by Equation 7.3

$$A_2 = \begin{pmatrix} \frac{1}{2} \cos^2(0) & \frac{1}{2} \cos^2(-\frac{\pi}{2}) \\ \frac{1}{2} \cos^2(\frac{\pi}{2}) & \frac{1}{2} \cos^2(0) \end{pmatrix} = \begin{pmatrix} 1 & 0 \\ 0 & 1 \end{pmatrix}. \quad (7.3)$$

Where it should be noted that  $A_2$  equals  $A_2^{-1}$ . This shows that multiplexing two channels in the polarization is possible with each channel having a linear polarization. When we extend this to multiplexing three channels in the polarization domain, the transfer matrix  $A_3$  and its inverse  $A_3^{-1}$  are denoted by,

$$A_3 = \frac{1}{3} \begin{pmatrix} 1 & \frac{1}{4} & \frac{1}{4} \\ \frac{1}{4} & 1 & \frac{1}{4} \\ \frac{1}{4} & \frac{1}{4} & 1 \end{pmatrix}, \quad A_3^{-1} = \frac{1}{3} \begin{pmatrix} 10 & -2 & -2 \\ -2 & 10 & -2 \\ -2 & -2 & 10 \end{pmatrix}. \quad (7.4)$$

The negative elements in the inverse matrix  $A_3^{-1}$  shows that not all of the three channels can have a linear SOP. The three-fold multiplexing is therefore only possible by employing the ellipticity of the transmitted signals, i.e. the phase difference between the polarization states [324]. This is in a sense very similar to PolSK, although only binary signals are multiplexed at the transmitter. The distribution on the Poincaré sphere for two and three-fold POLMUX signaling is visualized in Figure 7.1, which shows that for three-fold POLMUX the symbol are also spaced more closely together. This results in a slightly higher OSNR requirement for the same total bit rate.

The maximum of three multiplexed channels can also be related to the generalized description of a two-by-two Jones matrix. This describes the polarization change in an optical device, including optical fiber. In its most general form the Jones matrix is denoted through [325],

$$\begin{pmatrix} \cos \theta \exp(j\phi) & -\sin \theta \exp(-j\psi) \\ \sin \theta \exp(j\psi) & \cos \theta \exp(-j\phi) \end{pmatrix}, \quad (7.5)$$

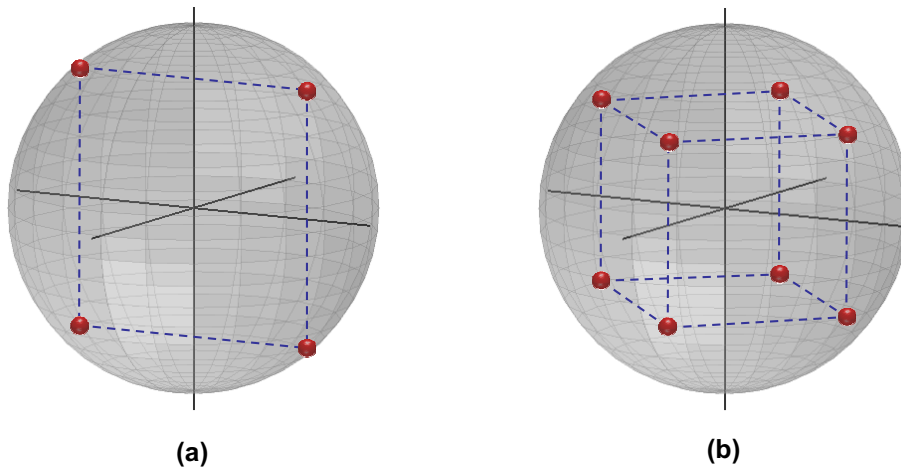


Figure 7.1: *Poincaré sphere for (a) two-fold and (b) three-fold polarization-multiplexing, each polarization tributary is DQPSK modulated*

where  $\theta$ ,  $\phi$  and  $\psi$  are independent real variables. This also implies that in the case of three-fold multiplexing in the polarization domain, not all channels have a linear SOP. Multiplexing three channels in the polarization domain is generally not used in optical transmission because it would require careful control of the relative phase differences between the polarization states. For two-fold multiplexing, on the other hand, only the linear part of the SOP has to be controlled. In addition, the impact of PMD and fiber nonlinearities in realistic optical fiber links are likely to make three-fold multiplexing impractical. We therefore focus in the remainder of this thesis on POLMUX signaling with two orthogonal polarization channels.

## 7.2 Transmitter & receiver structure

Following Equation 7.3, two channels can be multiplexed using linear, but orthogonal, SOPs. In this section we discuss the transmitter and receiver structure required for POLMUX signaling with two orthogonal polarizations.

Figure 7.2 depicts the basic layout of a POLMUX transmitter and receiver. The transmitter can either use a single laser source or two different laser sources, but a single laser source is generally used as this is more cost-effective and prevents impairments through beating between the two lasers in the presence of PMD [326]. The output of the laser source is split into two branches, with a MZM in each branch to modulate the orthogonal signal components with independent electrical drive signals. Afterwards a PBS recombines the two polarization tributaries channels into a single POLMUX channel. Note that the laser output, PBS and modulators should use polarization maintaining fiber to ensure that both polarization tributaries have an equal optical power.

Figure 7.2 depicts the transmitter and receiver structure for POLMUX-RZ-OOK modulation, as well as eye diagrams for (N)RZ-OOK and (N)RZ-DPSK with POLMUX signaling. Fig-

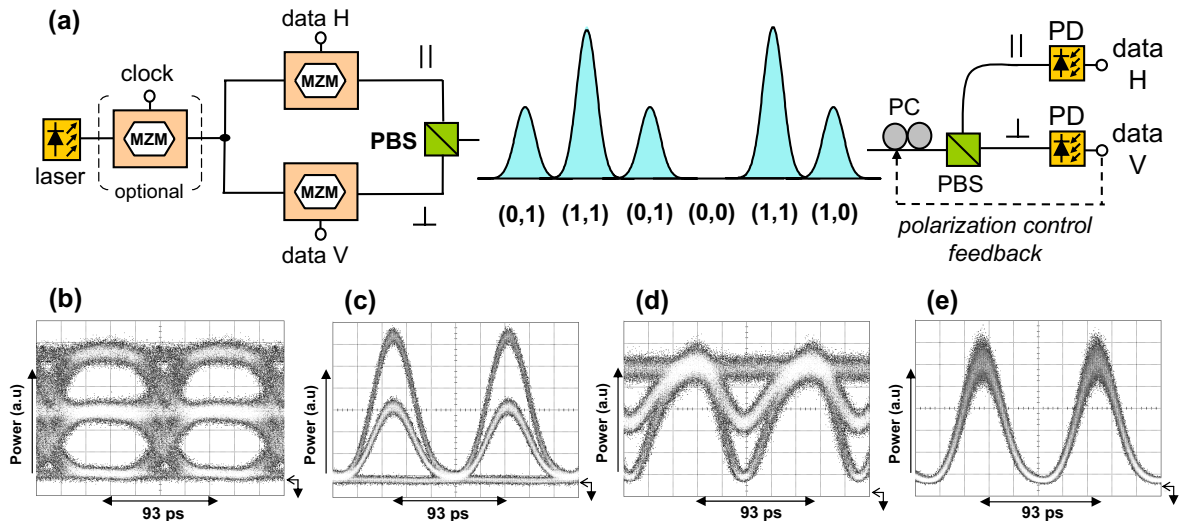


Figure 7.2: Transmitter and receiver structure for POLMUX modulation; 21.4-Gb/s back-to-back eye diagrams for (b) POLMUX-NRZ-OOK, (c) POLMUX-RZ-OOK, (d) POLMUX-NRZ-DPSK and (e) POLMUX-RZ-DPSK.

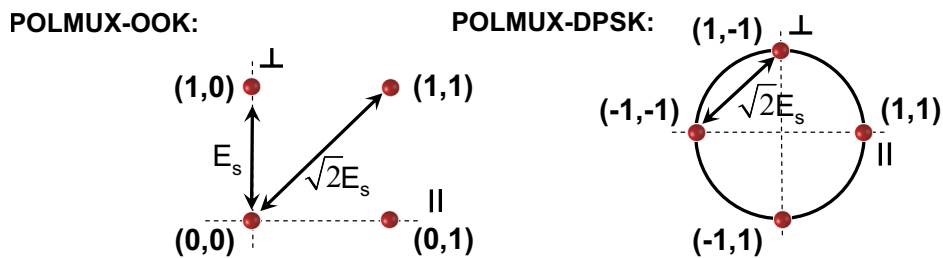


Figure 7.3: Signal constellations for POLMUX-OOK and POLMUX-DPSK modulation.

Figure 7.3 depicts the signal constellation for POLMUX-OOK and POLMUX-DPSK modulation. This shows that combined with DPSK modulation, POLMUX-DPSK is still a constant intensity modulation format. POLMUX-OOK modulation, on the other hand, results in a 'quasi' 3-level amplitude signal.

POLMUX signaling requires a polarization-sensitive receiver in order to separate both polarization tributaries. The optical polarization de-multiplexing consists of a PBS preceded by an automatic polarization control. After polarization de-multiplexing, two conventional polarization-independent receivers can be used. As discussed in Section 2.3, the birefringence in an optical fiber results in a random and time-variant SOP at the receiver. When the polarization axis of the PBS are not aligned with the two polarization tributaries, a misalignment penalty occurs. This misalignment penalty as a function of the angle  $\theta$  is depicted in Figure 7.4 for linearly polarized 21.4-Gb/s POLMUX-NRZ modulation. This shows that a  $4.5^\circ$  and  $9^\circ$  misalignment angle between the PBS axis and the polarization tributaries results in a 1-dB and 2-dB OSNR penalty, respectively. Note that the penalty curve for both polarization tributaries is asymmetric because the misalignment results in crosstalk that adds either constructively or destructively with the signal on the orthogonal polarization. Destructive crosstalk results in a higher OSNR penalty. When

the polarization of both polarization tributaries is not linear but elliptical, the crosstalk interferes only partially. Averaged over time, the randomly varying interference results in a noise-band that characterize suboptimal polarization de-multiplexing. This is evident by comparing the optical signals in Figures 7.4b and 7.4c.

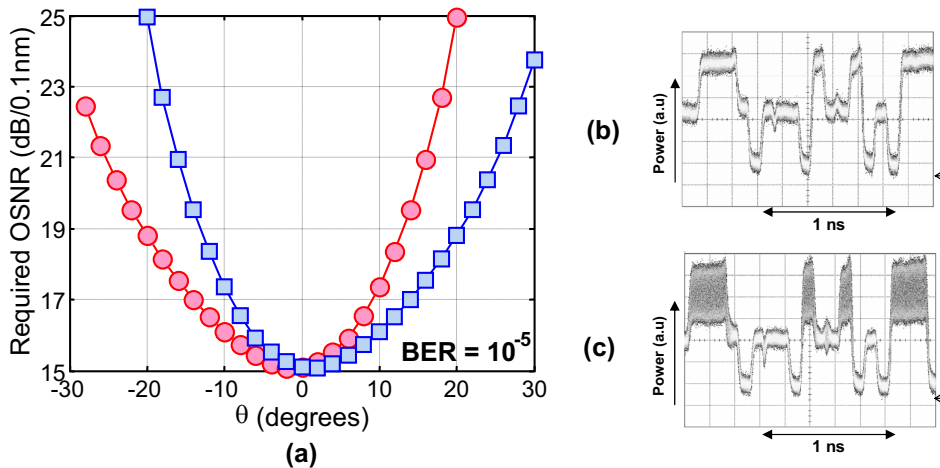


Figure 7.4: (a) OSNR penalty versus misalignment angle  $\theta$  for 21.4-Gb/s POLMUX-NRZ-OOK with  $\circ$  the  $0^\circ$  tributary and  $\square$  the  $90^\circ$  tributary; measured optical signals show de-multiplexing (b) without crosstalk and (c) with crosstalk.

The automatic polarization control in front of the PBS should be both accurate to minimize the de-multiplexing penalty, and fast in order to track the randomly changing polarization that can occur in optical fibers (see Section 3.4). The tracking speed of an automatic polarization control for polarization de-multiplexing needs to be faster than the tracking speed required for PMD compensation in a polarization insensitive receiver. To limit the OSNR penalty to  $< 0.5$  dB the de-multiplexing needs to have an accuracy of  $\theta < 2^\circ$ , compared to approximately  $\theta \leq 10^\circ$  for a polarization insensitive receiver. The response time of the automatic polarization control should therefore be in the order of  $200 \mu\text{s}$  when we assume that a full revolution around the Poincaré sphere can occur in 20 ms [185, 186, 187]. In order to track the polarization, the automatic polarization control requires a feedback signal that provides a measure of the interference between the two polarization tributaries. A number of feedback principles have been proposed in the literature. Including the use of pilot tones [322, 327], FEC error counting, different line rates for each polarization tributary [328] or the magnitude of the clock recovery output [77, 316]. The most practical approach is to add a low-frequency phase modulated pilot tone to one of the polarization tributaries [327]. The phase modulation varies the crosstalk between constructive and destructive interference which, after filtering and signal processing in order to integrate over time, provides a measure for the degree of misalignment.



## 7.3 Transmitter & receiver properties

The lower symbol rate of POLMUX signaling compared to binary modulation formats, combined with the impact of optical polarization de-multiplexing has a significant impact on the tolerance against linear transmission impairments. The chromatic dispersion tolerance and OSNR requirement are improved. But polarization related signal impairments, such as PMD and PDL, are more critical. This section discusses the tolerance of POLMUX signaling with respect to OSNR (Section 7.3.1), PMD (Section 7.3.2), chromatic dispersion (Section 7.3.3) and polarization dependent loss (Section 7.3.4).

### 7.3.1 Back-to-back OSNR requirement

The use of different multi-level modulation formats such as amplitude phase shift keying and DQPSK (with direct detection) results in a  $>3$  dB increase in OSNR for a doubling in the bit rate. One of the main advantages of POLMUX signaling is therefore that it allows a doubling of the bit rate with a  $\leq 3$  dB increase in OSNR requirement. This is valid under the assumption that without POLMUX signaling a polarization-insensitive receiver is used. The combination

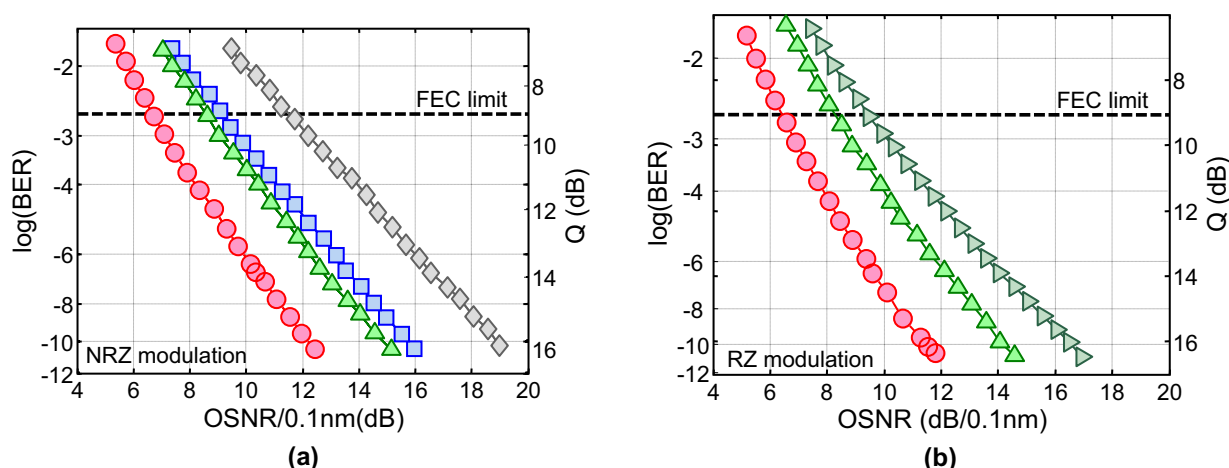


Figure 7.5: Measured OSNR requirement for (a) NRZ and (b) RZ modulation;  $\circ$  10.7-Gb/s OOK,  $\square$  10.7-Gb/s DPSK,  $\triangle$  21.4-Gb/s POLMUX-OOK,  $\diamond$  10.7-Gb/s POLMUX-DPSK and  $\blacktriangledown$  21.4-Gb/s DQPSK.

of POLMUX signaling with different binary modulation formats is depicted in Figure 7.5a and the OSNR requirements for a  $10^{-3}$  and  $10^{-9}$  BER are listed in Table 7.1. At a  $10^{-9}$  BER the required OSNR for NRZ-OOK and POLMUX-NRZ-OOK is respectively 15.7 dB and 18.4 dB. The 2.7-dB difference in OSNR requirement results from a 3-dB penalty due to the doubled bit rate and a 0.3-dB improvement which results from the use of a polarization sensitive receiver. The OSNR tolerance improves with  $\sim 0.3$  dB in a polarization sensitive receiver because the ASE in the orthogonal polarization is filtered out, which worsens the OSNR tolerance through spontaneous-spontaneous beat noise in a polarization insensitive receiver. Note that the advantage of using a polarization sensitive receiver increases slightly for higher BER, where the impact

Table 7.1: MEASURED OSNR TOLERANCE FOR DIFFERENT MODULATION FORMATS AT 10 GBAUD (BER  $10^{-3}$  AND  $10^{-9}$ )

	single polarization (10.7-Gb/s)	POLMUX (21.4-Gb/s)
NRZ-OOK	9.7 / 15.7	12.2 / 18.4
RZ-OOK	8.7 / 14.2	11.2 / 17.2
NRZ-DPSK	7.1 / 11.7	9.0 / 14.3
RZ-DPSK	6.8 / 10.9	9.0 / 13.7
	single polarization 21.4-Gb/s)	
RZ-DQPSK	10.1 / 15.9	

of spontaneous–spontaneous beat noise is stronger for a polarization independent receiver. The difference between NRZ-DPSK and POLMUX-NRZ-DPSK is only 1.9 dB at a  $10^{-3}$  BER. This lower difference might result from the absence of a  $PD\lambda$  induced penalty in the polarization sensitive DPSK receiver. As a polarization sensitive receiver filters out the orthogonal polarization, the  $PD\lambda$  of the MZDI is irrelevant. It indicates that the advantage of a polarization sensitive receiver is somewhat higher for D(Q)PSK compared to OOK modulation. We note that for DPSK modulation there is some measurement uncertainty as the drift of both polarization and MZDI phase offset is controlled manually in the experiment. For a high BER this measurement uncertainty is averaged out, but for  $10^{-9}$  BER it results in some residual penalty, which explains the smaller difference between OOK and DPSK at low BER.

Figure 7.5b compares the OSNR tolerance of 21.4-Gb/s POLMUX-RZ-DPSK with 21.4-Gb/s RZ-DQPSK. This shows that POLMUX modulation allows for a 1.1 dB improvement in OSNR requirement compared to direct detection RZ-DQPSK. The improved OSNR requirement is a combination of the use of a polarization sensitive receiver and the absence of a phase demodulation penalty as observed for direct detection DQPSK.

### 7.3.2 Polarization-mode dispersion

In the absence of PMD and nonlinear impairments both orthogonal polarization modes do not interact with each other. In this case POLMUX can truly be considered a transparent multiplexing technique. Even in the presence of random fiber birefringence, the SOP is only rotated and both polarization modes remain orthogonal to each other. However, in the presence of PMD, the coupling between the polarization modes will generally result in a transmission impairment for POLMUX signaling. Only when the POLMUX tributaries are exactly coupled into the PSP's of the fiber, the DGD results only in a time delay and no de-multiplexing penalty occurs.

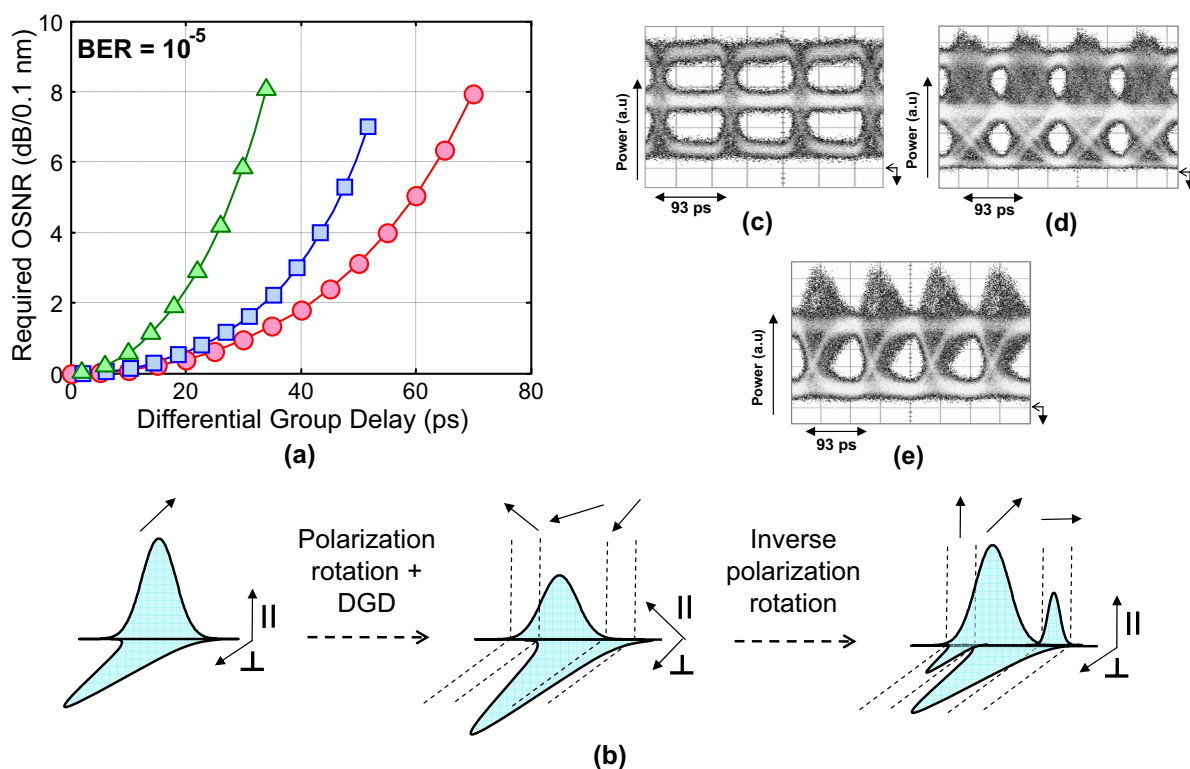


Figure 7.6: (a) Simulated OSNR penalty versus DGD for  $\bullet$  10.7-Gb/s NRZ-OOK,  $\blacksquare$  21.4-Gb/s POLMUX-NRZ-OOK and  $\blacktriangle$  21.4-Gb/s NRZ-OOK; (b) polarization changes within a symbol period resulting due to DGD; (c-e) measured eye diagrams for 21.4-Gb/s POLMUX-NRZ-OOK with (c) back-to-back, (d) with 40-ps DGD and (e) with 40-ps DGD after polarization de-multiplexing.

PSP coupling is however not realistic for a deployed transmission systems and the polarization de-multiplexing will therefore introduce a DGD induced penalty. This is most easily understood by noting that DGD results in ISI between neighboring bits. For POLMUX signaling this results in higher penalties because the DGD changes the SOP along the symbol period, which results in amplitude fluctuations when the tributaries are polarization de-multiplexed. This is illustrated in Figure 7.6b for a '010' sequence in both polarization tributaries. When DGD is added to the POLMUX signal, the part of the signal in the slower PSP is delayed. If the POLMUX tributaries are not coupled into the PSPs, the ISI results in mixing of the tributaries at the leading and falling edges of the symbol. At the receiver, the polarization tracking aligns the polarization tributaries again with the PSPs. But the polarization control cannot correct for polarization changes on the time scale of a single symbol period. We assume therefore that the polarization control will align the polarization in the middle part of the symbol period, which contains the majority of the pulse energy, to the axis of the PBS. The part of the pulse at the leading and falling edge which has been coupled to the orthogonal polarization will then appear as a ghost pulse. For other sequences (e.g. '011' or '110'), the ghost pulse will interfere either constructively or destructively with the trailing or leading pulse, which results in over- and undershoots. The over- and undershoots are in effect crosstalk between the polarization tributaries. The measured eye diagrams in Figure 7.6c-e clearly show the DGD induced over- and undershoots in a 21.4-Gb/s POLMUX-NRZ-OOK signal with 40-ps DGD.

Figure 7.6a shows a comparison between the DGD tolerance of 10.7-Gb/s NRZ-OOK and 21.4-Gb/s POLMUX-NRZ-OOK for a worst-case  $45^\circ$  offset with respect to the PSP's. Although POLMUX is more sensitive to PMD-induced impairments, the difference with single polarization modulation is relatively small. This can be understood by noting that the crosstalk occurs mainly at the rising and falling edge of the pulse and not in the middle of the symbol period. The allowable DGD for a 2-dB OSNR penalty reduces from 42 ps to 34 ps for POLMUX signaling, while the bit rate is doubled. In comparison, when the symbol rate is doubled the DGD tolerance is reduced by a factor of two (e.g. for 21.4-Gb/s NRZ-OOK). This indicates a clear advantage of POLMUX signaling over an increase in symbol rate.

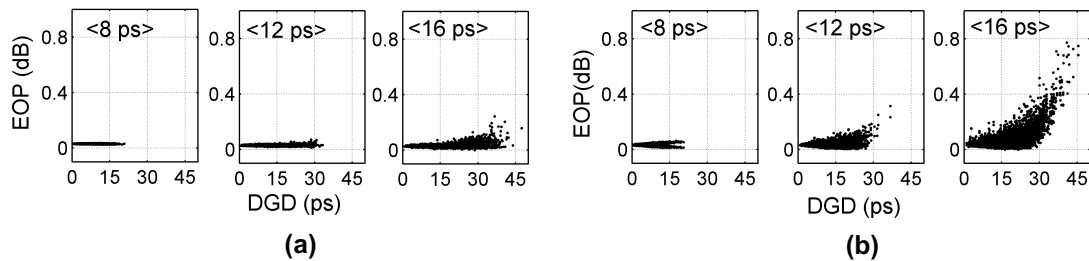


Figure 7.7: Simulated scatter plots showing the penalty for different average PMD (a) 10-Gb/s NRZ-OOK and (b) 20-Gb/s POLMUX-NRZ-OOK.

We now extend the discussion to randomly distributed PMD. Figure 7.7 shows the distributions obtained with 10-Gb/s NRZ-OOK and 20-Gb/s POLMUX-NRZ-OOK with different amounts of average PMD. The PMD is generated with a wave-plate model that uses 100 randomly oriented wave-plates. In the wave-plate model, the average PMD per wave-plate is constant whereas the coupling angles between the 100 wave-plates change for each of the 10,000 simulations, this approximates a Maxwellian PMD distribution [329]. To quantify the PMD penalty, the optical EOP is used. This gives a performance indication with less computational effort, but the resulting penalty is approximately a factor of 2-3 smaller than the OSNR penalty [330]. The difference results from the use of the optical EOP to quantify the penalty rather than the OSNR requirement, which is based on the error probability in the electrical signal. To compute the OSNR requirement, the signal is low-pass electrical filtered with  $0.7 \cdot B$  bandwidth, which shift the DGD induced over- and undershoot more towards the middle of the symbol. In Figure 7.7, the worst-case penalty for a 12-ps average PMD is approximately a 0.35 dB EOP. When we adapt this to OSNR penalties ( $3x$ ) and scale it to a 21.4-Gb/s bit rate to account for FEC, the worst-case penalty is approximately 1.1 dB. This indicates that 21.4-Gb/s POLMUX-NRZ-OOK has a  $\sim 11$ -ps PMD tolerance for a 1-dB OSNR penalty. The results depicted in Figure 7.6 show a 34-ps DGD tolerance for a 1-dB OSNR penalty. When we take into account that the average PMD tolerance for a  $10^{-5}$  outage probability is approximately a factor of three lower than the DGD tolerance, this also translates into a  $\sim 11$ -ps PMD tolerance. Using the same approach to compute the PMD tolerance of 10.7-Gb/s NRZ-OOK, we find a 16-ps tolerance for a 1-dB OSNR penalty.

The impact of DGD becomes more complicated when other impairments are present in the signal. A good example is the inter-symbol delay between both polarization tributaries (see Figure 7.8b). We can consider the case when both POLMUX tributaries are exactly interleaved. In the absence of DGD, both tributaries are orthogonal and the offset between the two polarization tributaries

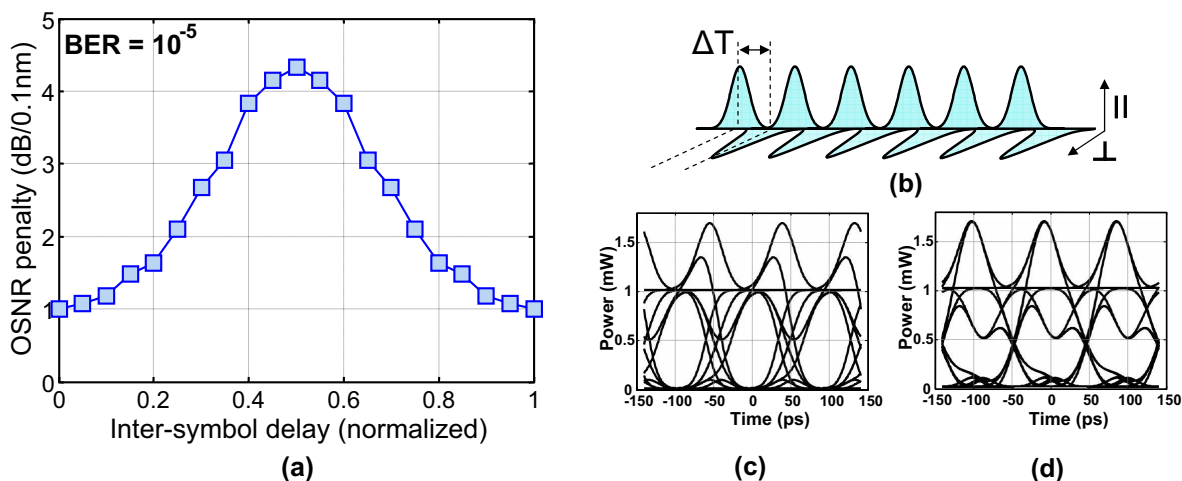


Figure 7.8: (a) Simulated OSNR penalty versus the inter-symbol delay between the POLMUX tributaries with 34-ps of DGD; (b) definition of the inter-symbol delay between the POLMUX tributaries; (c-d) simulated eye diagrams for 20-Gb/s POLMUX-NRZ-OOK with (c) tributaries aligned and (d) tributaries interleaved.

does not result in an OSNR penalty. But when DGD is added to the signal, the crosstalk between both polarization tributaries occurs not anymore at the leading and falling edge of the symbol, but is shifted to the middle of the symbol period [331]. This is depicted in Figure 7.8a for worst-case coupling of the POLMUX tributaries in between the PSP. When both polarization tributaries are synchronized, 25 ps of DGD results in a 1-dB OSNR penalty. When, on the other hand, the polarization tributaries are time-interleaved, the OSNR penalty increases to more than 4 dB. This shows that in order to minimize the OSNR penalty, both polarization tributaries should be synchronized such that the rising and falling edges of the pulse occurs at the same time. The alignment of both tributaries can be easily realized by a proper design of the transmitter, but signal impairments such as chromatic dispersion and nonlinear impairments have a similar effect on the PMD tolerance. The interaction between these transmission impairments will be discussed in the remainder of this chapter.

In addition to ISI between consecutive symbols, DGD induces also a periodic change of the SOP [332]. The polarization control at the receiver aligns the signal such that crosstalk is minimized. In effect the SOP of the carrier wavelength, which contains the majority of the transmitted power, is aligned with the axes of the PBS. In the presence of DGD this results in crosstalk between both polarization channels for all other components of the signal spectrum, i.e. depolarization. The impact of DGD induced depolarization is illustrated in Figure 7.9. A DGD equal to one symbol period is added to a (single-polarization) NRZ-OOK signal which is coupled exactly in between both PSP's. Afterwards the signal is passed through a polarizer, which shows the depolarization in the signal. Note that the periodicity between the minima in the optical spectrum in [THz] is equal to the inverse of the DGD in [ps]. The impact of SOPMD on POLMUX signaling is similar, as it also incurs a wavelength dependent change in the SOP.

For high symbol rates (and hence a broad optical spectrum) the wavelength dependent polarization change can be dominating. The difference in PMD tolerance between POLMUX and

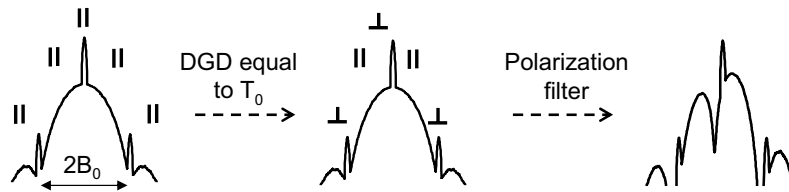


Figure 7.9: Depolarization when a signal is passed through a polarizer in the presence of a DGD equal to the symbol period.

non-POLMUX therefore increases for higher symbol rates. Especially at a high symbol rate (e.g. 40 Gbaud), depolarization can become the dominant impairment and significantly worsens the PMD tolerance of POLMUX signaling [326, 333, 334]. On the other hand, for POLMUX signaling at a 10.7-Gbaud symbol rate, the contribution of time domain ISI is normally dominant (in the absence of DGD compensation). This difference is for example evident by comparing the PMD induced penalties with and without POLMUX signaling for 10-Gb/s NRZ-OOK, as discussed here, with the results reported by *Nelson and Kogelnik* in [326]. They investigate POLMUX signaling combined with 40-Gb/s RZ-OOK modulation and find a reduction in PMD tolerance up to a factor of 5 compared to single-polarization modulation.

### 7.3.3 Chromatic dispersion

The lower symbol rate of POLMUX signaling compared to binary modulation formats improves the chromatic dispersion tolerance with a factor of 4. This is evident from the comparison in Figure 7.10a, which shows a nearly identical chromatic dispersion tolerance for 10.7-Gb/s NRZ-OOK and 21.4-Gb/s POLMUX-NRZ-OOK, but a sharply reduced tolerance for 21.4-Gb/s NRZ-OOK.

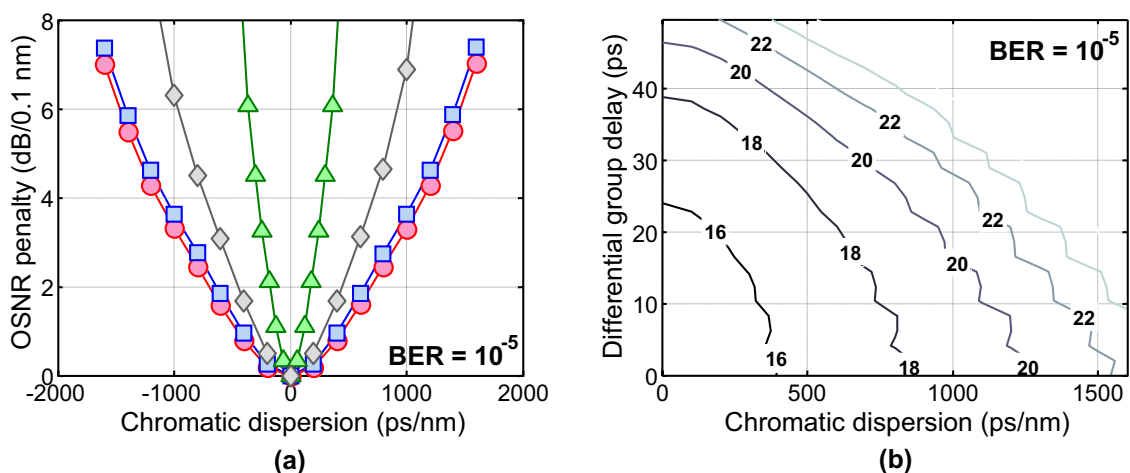


Figure 7.10: (a) Simulated OSNR penalty versus chromatic dispersion;  $\bullet$  10.7-Gb/s NRZ-OOK,  $\square$  21.4-Gb/s POLMUX-NRZ-OOK,  $\blacktriangle$  21.4-Gb/s NRZ-OOK and  $\blacklozenge$  21.4-Gb/s POLMUX-NRZ-OOK with 34-ps of DGD. (b) OSNR penalty versus chromatic dispersion and DGD.

However, when we consider PMD and chromatic dispersion simultaneously, the dispersion tolerance is somewhat reduced. The over- and undershoots in the signal that normally occur near the symbol transition are now broadened and shift more towards the middle of the symbol period. In Figure 7.10b the required OSNR is depicted as a function of both chromatic dispersion and DGD. This clearly indicates that both signal impairments are strongly correlated. For a 2-dB OSNR penalty, either 650-ps/nm of chromatic dispersion or 34-ps of DGD can be tolerated. When on the other hand both signal impairments are present simultaneously, 340-ps/nm of chromatic dispersion and 20-ps of DGD together result in a 2-dB OSNR penalty. The combined penalty is further evident from Figure 7.10a, when comparing the tolerance without DGD and with 34-ps of DGD (2-dB OSNR penalty). In comparison, for single polarization modulation both signal impairments can be considered nearly independently of each other.

### 7.3.4 Polarization dependent loss

For polarization insensitive receivers PDL is a relatively insignificant impairment, as only large amount of PDL results in a noticeable penalty (see Section 2.3.3). For POLMUX signaling, on the other hand, the impact of PDL is more detrimental as it effects the *orthogonality* between both tributaries. To simplify the discussion on PDL, we assume here for the moment a single PDL element. The PDL induced penalty in POLMUX signaling then depends on the alignment between the POLMUX tributaries and the axis of the PDL element. With a  $0^\circ$  offset between the POLMUX tributaries and the axis of the PDL element, the PDL attenuates one tributary and leaves the other tributary unaffected. This is shown in Figure 7.11b. At the receiver, and assuming a constant *total* signal power, this reduces the OSNR of one tributary while increasing the OSNR of the other tributary. The OSNR for each of the POLMUX tributaries can then be denoted as,

$$\begin{aligned} \Delta OSNR_{best-case} &= 10 \log_{10} \left( \frac{2}{S+1} \right) \\ \Delta OSNR_{worst-case} &= 10 \log_{10} \left( \frac{2 \cdot S}{S+1} \right) \end{aligned}, \quad (7.6)$$

where  $0 < S < 1$  denotes the PDL-induced attenuation in linear units. In the absence of PDL,  $S$  equals 1. The performance of the worst-case POLMUX tributary is generally used as a measure of the OSNR penalty. In this case a 2-dB OSNR penalty is obtained for  $\sim 3.5$  dB of PDL.

PDL results in depolarization of the signal when the POLMUX tributaries are  $45^\circ$  offset with respect to the axis of the PDL element. Figure 7.11c illustrates this by showing the impact of PDL-induced depolarization on the signal constellation. The POLMUX tributaries are no longer orthogonal to each other, which results in crosstalk upon polarization de-multiplexing. Normally, a polarization-sensitive receiver demultiplexes the POLMUX tributaries using only a single PBS. But this is suboptimal when the signal is severely depolarized due to PDL. A lower de-multiplexing penalty is then obtained when each of the polarization tributaries is de-multiplexed with a separate polarizer and polarization control [313, 316]. If we assume that in the absence of PDL the optimum de-multiplexing angles are  $\theta = 0^\circ$  and  $\theta = 90^\circ$ , respectively,



the two polarizers should filter the signal with an angle,

$$\theta = \frac{180^\circ}{\pi} \left( \frac{\pi}{4} \pm \arctan(\sqrt{S}) \right). \quad (7.7)$$

Even in the presence of severe PDL, this separates the two POLMUX tributaries without any crosstalk. However, there still is an OSNR penalty when two separate polarizers are used. This penalty is a result of the smaller fraction of the total signal power that now passes through the polarizers, which lower the signal power by  $\gg 3$  dB. The noise power, on the other hand, is reduced with only 3-dB when the signal passes through the polarizer. The combination of a lower signal power but constant noise power results in a reduced OSNR. This assumes that the noise is unpolarized, which results in the worst-case penalty. The OSNR decrease is negligible when the noise is polarized through the PDL. Figure 7.11a depicts the impact of PDL-induced depolarization when unpolarized noise is assumed, both with a single PBS and with separate polarizers. This shows that PDL-induced depolarization results in a slightly lower OSNR penalty than PDL-induced attenuation of one of the polarization tributaries. We note that the case of two separate polarizers applies to the digital coherent receiver discussed in Chapter 10.

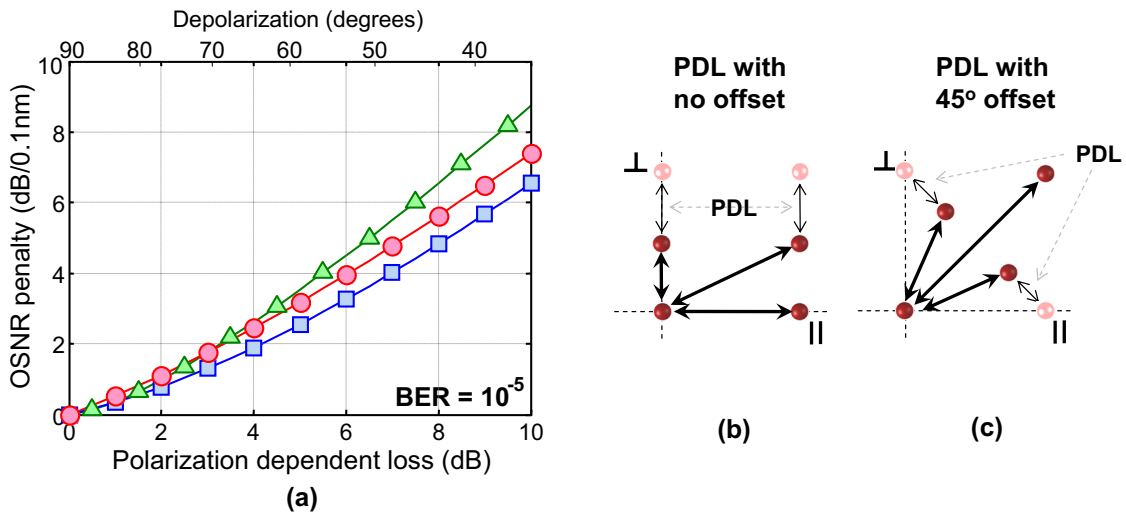


Figure 7.11: (a) Simulated OSNR tolerance versus polarization dependent loss, all curves show the worst-case of both POLMUX tributaries; (b,  $\bullet$ ) impact of PDL parallel to one of the polarization tributaries; (c) impact of PDL with a  $45^\circ$  offset to the polarization tributaries with separate polarizers ( $\square$ ) and for a single PBS ( $\triangle$ ).

The impact of PDL in a long-haul transmission link is more difficult to estimate as it also interacts with other transmission impairments such as PMD. We therefore only consider here the impact of PDL-induced depolarization on a POLMUX signal, which is likely to be the dominant PDL-related impairment. Figure 7.11 then shows that if we take 3 dB of PDL as a typical value for a long-haul link, the OSNR penalty due to depolarization is limited to 2-dB.



## 7.4 Nonlinear tolerance

We now extend the discussion on POLMUX signaling to include nonlinear transmission impairments. Section 7.4.1 discusses the nonlinear tolerance of POLMUX signaling in the absence of co-propagating WDM channels. Subsequently, Section 7.4.2 studies in more detail the interaction between PMD and single-channel nonlinear impairments. We then focus on POLMUX signaling in a WDM transmission system. In WDM systems, POLMUX signaling suffers from polarization scattering through XPM-induced depolarization, which is analyzed in Section 7.4.3. Finally, Section 7.4.4 introduces polarization-interleaved POLMUX transmission as a concept to reduce the impact of XPM-induced depolarization.

### 7.4.1 Self-phase modulation

The nonlinear interaction between both orthogonal polarization modes at the same wavelength results in XPolM. For modulation formats that do not modulate the polarization of the optical signal, both polarization modes carry a portion of the same signal and the XPolM interaction is similar to SPM. For POLMUX signaling, on the other hand, XPolM results in a crosstalk between both tributaries that is more similar to XPM.

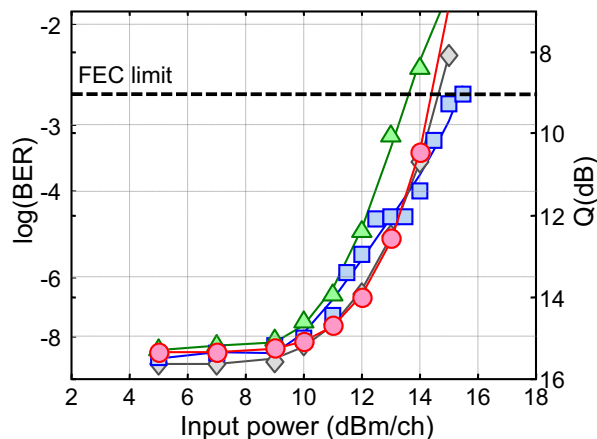


Figure 7.12: Measured single channel nonlinear tolerance for  $\circ$  10.7-Gb/s RZ-DPSK,  $\square$  10.7-Gb/s RZ-OOK,  $\triangle$  21.4-Gb/s POLMUX-RZ-OOK,  $\diamond$  21.4-Gb/s POLMUX-RZ-DPSK.

We now assess the nonlinear tolerance of POLMUX signaling on an 800-km transmission link, which is depicted in Figure 5.15. The outputs of 1 to 9 ECL on a 50-GHz grid (center wavelength at 1550.9 nm) are combined in a 16:1 coupler. A MZM driven with a 10.7-Gb/s clock signal is used for pulse-carving and a 10.7-Gb/s  $2^{31} - 1$  PRBS is used to drive a second MZM for modulation. The second MZM generates either OOK or DPSK modulation, depending on the bias voltage and drive signal amplitude swing applied to the modulator. The signal is subsequently polarization-multiplexed by splitting the signal, delaying one tributary by 23 ns and then recombining both tributaries with orthogonal polarizations. The 800-km transmission link

consists of 8x100-km SSMF spans and the dispersion map is described in Section 5.4. At the receiver a 37-GHz CSF selects the desired WDM channel. The signal is then manually polarization de-multiplexed using a PBS preceded by a polarization controller (PC). For RZ-DPSK the detector consists of a 1-bit MZDI followed by balanced detection and for RZ-OOK direct detection is used.

Figure 7.12 shows the single channel<sup>1</sup> nonlinear tolerance of 10.7-Gb/s NRZ-OOK and 10.7-Gb/s NRZ-DPSK with both single polarization and POLMUX signaling. Without POLMUX signaling, a slightly higher nonlinear tolerance is measured for DPSK compared to OOK modulation. And when the signals are polarization-multiplexed, there is no significant change in the nonlinear tolerance for either OOK or DPSK modulation. This similarity in nonlinear tolerance can be understood when we take into account that POLMUX signaling divides the channel power over both polarization modes. Because the SOP of the signal changes on the bit-level, the average propagating power is equally divided over both orthogonal PSP. Substituting the power per polarization channel into Equation 2.36 indicates that the nonlinear phase shift in a single channel is the same for both POLMUX signaling and single polarization modulation. The nonlinear phase shift is therefore not related to the power per *polarization* channel, but to the power per *wavelength* channel, as is also the case in the absence of POLMUX signaling. However, the interaction between the nonlinear phase shift and chromatic dispersion is slightly different. When the signal is not coupled into the PSP's, the propagating signal in each of the polarization modes is a mix between both POLMUX tributaries. When we take POLMUX-NRZ-OOK modulation as an example, this implies that a quasi '3-level' amplitude modulated signal propagates along the fiber. Due to the interaction with chromatic dispersion, the nonlinear penalty for such a '3-level' signal will generally be slightly higher compared to a conventional NRZ-OOK signal.

### 7.4.2 Self-phase modulation & PMD

As a next step, we consider the impact of PMD on the single channel nonlinear tolerance. In conventional transmission systems, the impact of PMD on the nonlinear tolerance is small. A significant amount of PMD can even reduce nonlinear impairments to a certain degree [335]. However, as the PMD-induced penalty is normally much larger than the improvement in nonlinear tolerance, it is desirable to avoid PMD in the transmission link. In POLMUX transmission the interaction between PMD and nonlinear impairments results unfortunately in increased transmission impairments.

This is illustrated through the simulated eye diagrams in Figure 7.13. The SPM-induced nonlinear impairments shift the DGD-induced over- and undershoots more to the middle of the symbol period. As a result, both impairments combined results in higher penalties as when they would occur separately. For 10-Gb/s NRZ-OOK, on the contrary, we observe no significant penalty for the same amount of DGD and nonlinear phase shift, as evident from Figure 7.13.

---

<sup>1</sup>Single channel refers to a single *wavelength* channel.

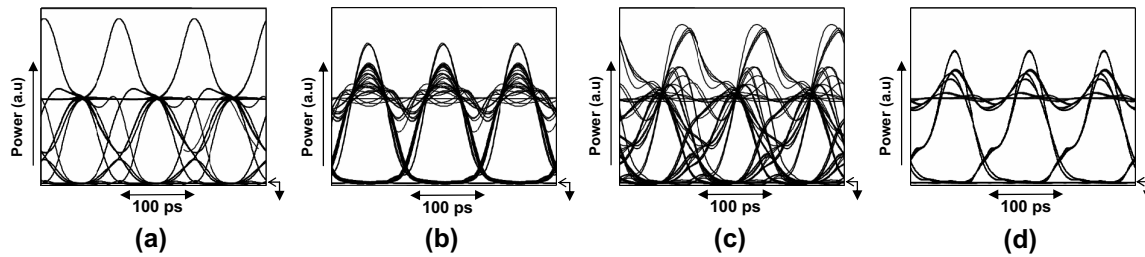


Figure 7.13: Simulated eye diagrams for (a) 20-Gb/s POLMUX-NRZ-OOK with 40 ps of DGD, (b) 20-Gb/s POLMUX-NRZ-OOK after transmission over 100-km SSMF with 15-dBm input power (c) 20-Gb/s POLMUX-NRZ-OOK after transmission and with 40 ps of DGD, (d) 10-Gb/s NRZ-OOK after transmission and with 40 ps of DGD.

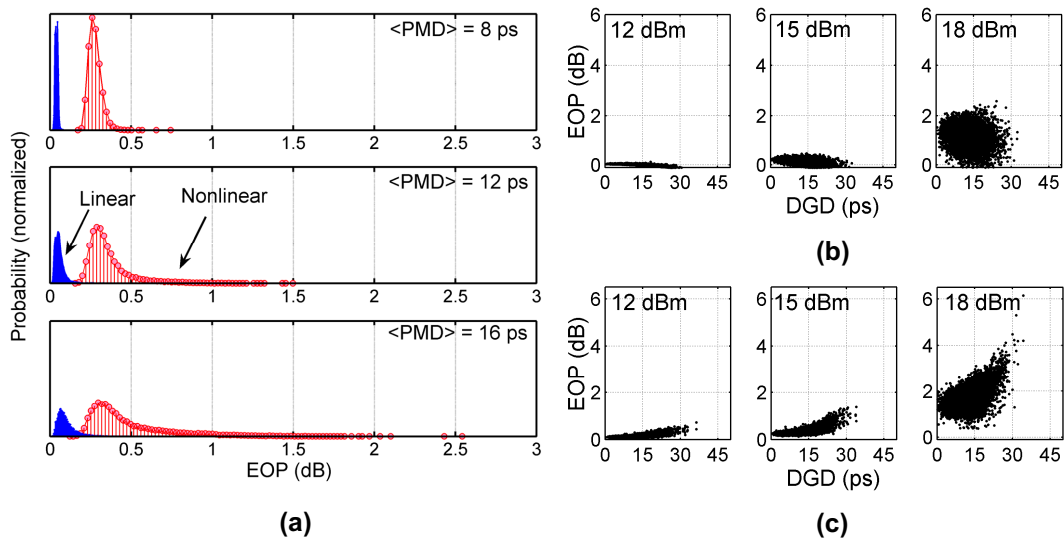


Figure 7.14: Statistical simulation results for 10-Gb/s NRZ-OOK and 20-Gb/s POLMUX-NRZ-OOK; (a) Monte-Carlo simulation (10,000 simulations) of the probability distribution for 8-ps, 12-ps and 16-ps of PMD, dots denote linear and circles denote nonlinear simulations for a 100-km link and 15-dBm input power. (b-c) PMD scatter plots for a 100-km link and 12-ps of average PMD with (b) 10-Gb/s NRZ-OOK and (c) 20-Gb/s POLMUX-NRZ-OOK.

The precise interaction between DGD and fiber nonlinearity is rather difficult to quantize as it depends on the evolution of the SOP along the fiber. As an alternative, the interaction between PMD and nonlinear impairments is quantified using statistical simulations. Figure 7.14 shows statistical simulations of the combined penalty for 10-Gb/s NRZ-OOK and 20-Gb/s POLMUX-NRZ-OOK modulation. Only the interaction between nonlinearity and DGD is considered, ASE noise is neglected in the simulations and the performance is evaluated using the EOP. A single 100-km SSMF fiber span is simulated with -510-ps/nm pre-dispersion and zero accumulated dispersion. The input power is equal to 15 dBm into the SSMF and 5.5 dBm into the DCF. Different amount of PMD are added distributed along the SSMF through random coupling between the wave-plates. The fiber parameters for the SSMF and DCF are depicted in Table 7.2. At the receiver, the polarization channels are de-multiplexed using a PBS. We assume here perfect alignment between the SOP at the carrier frequency and the axis of the PBS. In addition, the worst-case EOP of both POLMUX tributaries is used.

Table 7.2: SIMULATED FIBER PARAMETERS.

	SSMF	DCF	unit
Insertion loss ( $\alpha$ )	0.2	0.5	<i>dB/km</i>
Dispersion (D)	17	-102	<i>ps/km/nm</i>
Dispersion slope (S)	0.057	-0.34	<i>ps/km/nm<sup>2</sup></i>
Nonlinearity ( $\gamma$ )	1.3	2.95	<i>1/W/km</i>

The linear and nonlinear simulation for an average PMD of 8 ps, 12 ps, and 16 ps are depicted in Figure 7.14a. For the linear simulations, only a small penalty is obtained. The penalty is Maxwellian distributed and shows a longer tail for higher average PMD. In the nonlinear simulations the worst-case penalty is significantly increased beyond the penalty for the linear case. As an example we consider the simulation with 16-ps average PMD, where the worst-case PMD-only penalty extends to 1.1 dB. But combined with nonlinear impairments, the worst-case penalty equals 2.5 dB whereas the mean nonlinear penalty is only 0.4 dB. This interaction is also evident from a comparison between Figures 7.14b and 7.14c. Whereas we observe a clear correlation between PMD and nonlinear impairments for 20-Gb/s POLMUX-NRZ-OOK, the penalty for 10-Gb/s NRZ-OOK is uncorrelated or decreases slightly with higher PMD. When we take the worst-case penalty from the statistical simulations as a measure, the interaction between nonlinear impairments and PMD results in a  $\sim 2$  dB decrease in nonlinear tolerance.

Next, a fixed set of coupling angles between the birefringent wave plates is used and the strength of the birefringence is varied to simulate different amounts of DGD. The polarization channels are launched with a worst-case  $45^\circ$  misalignment angle with respect to the PSP. This simplification allows for significantly reduced computation effort in the study of the interaction between DGD and nonlinearity. For a fixed DGD and input power a single EOP is now obtained instead of a probability distribution. Note that the results only represent an average case with respect to DGD and nonlinear tolerance due to the fixed evolution of the SOP along the fiber link. For the selected set of coupling angles the SOPMD is  $0.228 \text{ ps}^2$  for a 1-ps DGD, and can therefore be neglected. Figure 7.15 shows the EOP as a function of both DGD and input power into the SSMF. In order to compare penalties, both 20-Gb/s POLMUX-NRZ-OOK (Figure 7.15a) as well as NRZ-OOK transmission with 10 Gb/s and 20 Gb/s (Figures 7.15b and 7.15c) are shown.

First of all, we compare 10-Gb/s NRZ-OOK and 20-Gb/s POLMUX-NRZ-OOK. In this case the simulations show a clear reduction in both nonlinear and DGD tolerance. In the absence of nonlinear interaction, the DGD tolerance is respectively 54 ps and 42 ps for a 1-dB EOP. The nonlinear tolerance in the absence of DGD decreases from 17.5 dBm to 16.2 dBm, which is comparable to the measurements in Figure 7.12. As well, and similar to the previously discussed statistical simulations, the penalty increases when both DGD and nonlinear impairments are present. This contrasts with 10-Gb/s NRZ-OOK modulation where no interaction between DGD and nonlinear impairments is observed. Although a comparison between 20-Gb/s POLMUX-NRZ-OOK and 10-Gb/s NRZ-OOK gives insight in how POLMUX signaling changes the transmission penalties, it is more realistic to compare the penalties at the same total bit rate, i.e. 20-Gb/s POLMUX-NRZ-OOK with 20-Gb/s NRZ-OOK. This results in a very different comparison between the DGD and nonlinear tolerances. Similar to Figure 7.6, the DGD tolerance

of NRZ-OOK is approximately halved and the nonlinear tolerances decrease even more when the symbol rate is doubled. Consequently, 20-Gb/s POLMUX-NRZ-OOK has a clear advantage over 20-Gb/s NRZ-OOK in both DGD and nonlinear tolerances. The DGD tolerance of 20-Gb/s POLMUX-NRZ-OOK is 42 ps compared with 26 ps for 20-Gb/s NRZ-OOK and the nonlinear tolerance equals 16.2 dBm and 11.9 dBm, respectively. We note that this difference in nonlinear tolerance gives only an indication and might change slightly when long-haul transmission with an optimized dispersion map is considered.

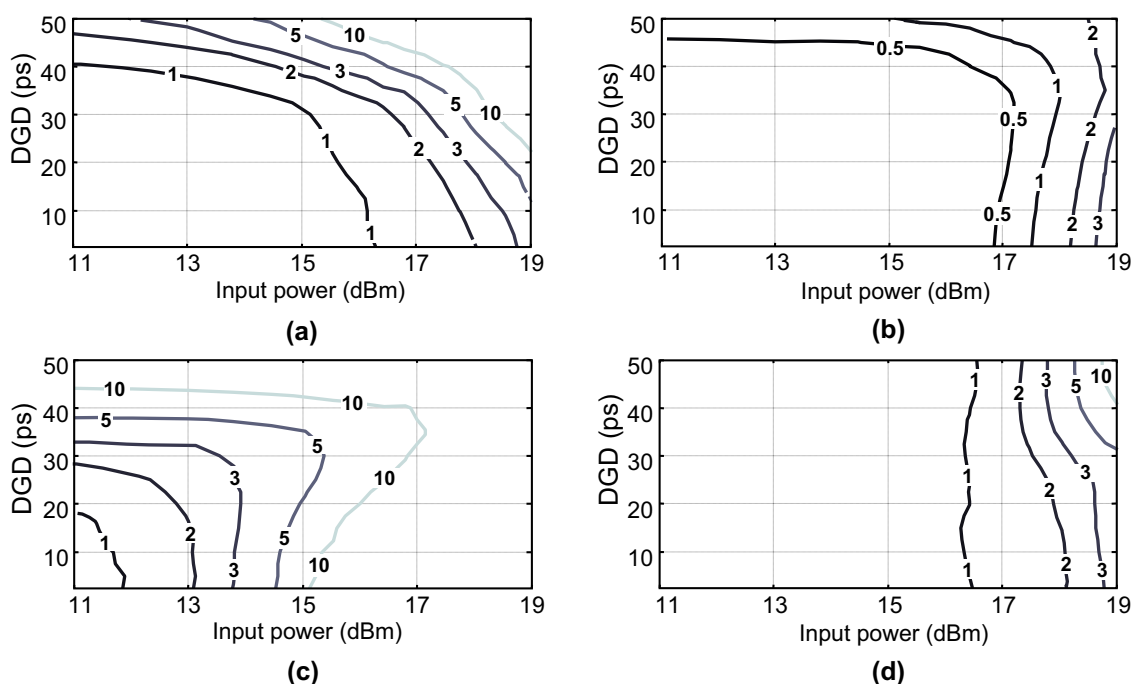


Figure 7.15: Simulated EOP as a function of DGD and input power for transmission over 100 km of SSMF, (a) 20-Gb/s POLMUX-NRZ-OOK, (b) 10-Gb/s NRZ-OOK, (c) 20-Gb/s NRZ-OOK and (d) 20-Gb/s POLMUX-NRZ-OOK with DGD compensation.

We now investigate the de-multiplexing penalties when the DGD is compensated at the receiver. First-order PMD compensation is used, i.e. the DGD at the carrier frequency is reduced to zero, and any influence of higher-order PMD is not compensated. In this case, Figure 7.15d shows that no penalties are associated with the de-multiplexing of the polarization multiplexed channels. The nonlinear tolerance is comparable to the case without DGD compensation (Figure 7.15a) and no further penalties are observed up to a 50-ps DGD. This confirms that the increased penalties in POLMUX signaling result from the polarization de-multiplexing at the receiver and do not result from nonlinear interaction along the transmission link. This implies that for a DGD compensated transmission link, PMD and nonlinear effects can be treated independently, similar as observed in Figures 7.15b and 7.15c for NRZ-OOK. A final consideration is that PMD compensation normally uses the DOP as a feedback signal. In a POLMUX transmission system, the PMD compensation cannot be based on DOP measurement as the time-averaged DOP is close to zero. An alternative feedback signal that has been reported for POLMUX signals is the monitoring of spectral components in the electrical spectrum [336]. Alternatively, the impact of PMD can be compensated using a digital coherent receiver, as discussed in Chapter 10.

### 7.4.3 Cross polarization modulation

We now extend the discussion to POLMUX-specific inter-channel nonlinear impairments. In POLMUX transmission systems, XPM-induced XPolM results in a polarization dependent nonlinear phase shift. This nonlinear phase shift depends on the transmitted bit-sequence in the co-propagating channels which leads to a noise-like change of the SOP, and hence depolarization. Due to the polarization sensitive receiver, the depolarization is converted into crosstalk between the POLMUX tributaries. This was first observed for two co-propagating polarization-multiplexed solitons by *Mollenauer et. al.* in [77]. The nonlinear induced depolarization does not affect polarization insensitive modulation formats, as the penalty occurs only in the receiver when the POLMUX tributaries are de-multiplexed [78].

In order to study the effects of XPM-induced XPolM, we compare the nonlinear tolerance for transmission with and without POLMUX signaling. The nonlinear tolerance is measured for RZ-OOK or RZ-DPSK modulation with different numbers of co-propagating channels and different channel spacings. The experimental setup consists of an 800-km transmission link, as discussed in Section 5.4. Figures 7.16a-d shows the BER as a function of the channel input power with co-propagating channels on a 50-GHz ITU grid. First of all, we compare single channel and WDM transmission with 9 co-propagating channels for RZ-OOK and RZ-DPSK. This shows that the nonlinear tolerance decreases with 2.4 dB and 4.8 dB, respectively, which results mainly from XPM impairments between the co-propagating WDM channels. Linear crosstalk between neighboring channels can also contribute slightly to the penalty as the channels are multiplexed using a 16:1 coupler, which does not filter out the out-of-band components. This comparison shows that at a 10.7-Gb/s symbol rate, RZ-DPSK is more affected by XPM impairments than RZ-OOK. This is straightforward when we take into account that for DPSK, the XPM-induced nonlinear phase shift results in a *direct* penalty. For OOK, on the other hand, the XPM-induced nonlinear phase shift results only *indirectly* in a transmission penalty through the interaction with chromatic dispersion. We note that for RZ-DPSK, the large inter-channel penalty could partially be a result of the high input powers used in this comparison, which enhances the influence of nonlinear phase noise.

Next, we compare the nonlinear tolerance of RZ-OOK and POLMUX-RZ-OOK, which is shown in Figures 7.16a and 7.16c, respectively. For RZ-OOK, the nonlinear tolerance decreases with 2.4 dB when we compare single channel transmission with 9 co-propagating WDM channels on a 50-GHz grid. On the other hand, for POLMUX-RZ-OOK modulation the decrease equals 6.7 dB. This indicates a strong impact of XPM-induced XPolM impairments for POLMUX-RZ-OOK modulation. Where RZ-OOK is mainly limited by (intra-channel) SPM, POLMUX-RZ-OOK is clearly limited by inter-channel nonlinear impairments. A comparison between RZ-DPSK (Figure 7.16b) and POLMUX-RZ-DPSK (Figure 7.16d), on the other hand, shows only an additional 0.9-dB penalty. This is related to the more symmetric signal constellation of POLMUX-DPSK, which reduces the impact of XPolM. In summary; RZ-OOK has a higher nonlinear tolerance when compared to RZ-DPSK on a 50-GHz WDM grid. But for POLMUX signaling, the impact of XPolM results in a lower nonlinear tolerance for POLMUX-RZ-OOK when compared to POLMUX-RZ-DPSK.

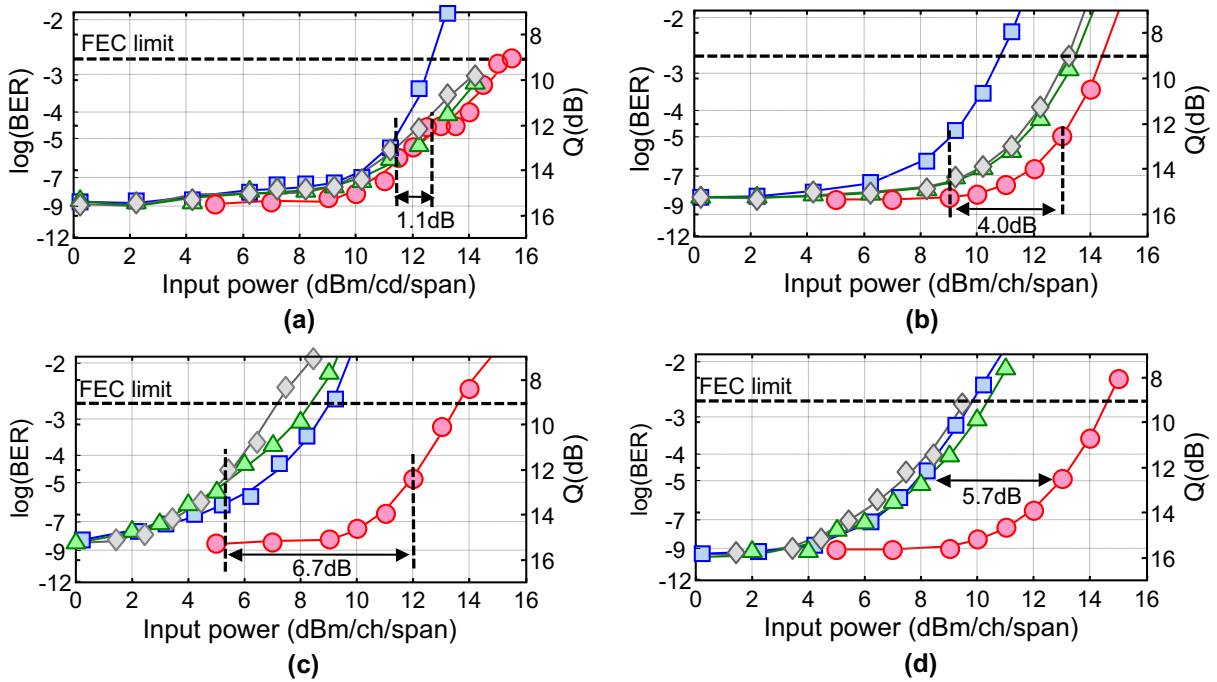


Figure 7.16: Measured nonlinear tolerance after 800-km for (a) 10.7-Gb/s RZ-OOK, (b) 10.7-Gb/s RZ-DPSK, (c) 21.4-Gb/s POLMUX-RZ-OOK and (d) 21.4-Gb/s POLMUX-RZ-DPSK with  $\circ$  single channel,  $\square$  3 WDM channel, 50-GHz spacing,  $\triangle$  5 WDM channel, 50-GHz spacing,  $\diamond$  9 WDM channel, 50-GHz spacing.

Figures 7.17e-h compares the influence of different channel spacings with 3 co-propagating channels on a 50-GHz, 100-GHz and 200-GHz WDM grid. For both RZ-OOK (Figure 7.17e) and RZ-DPSK (Figure 7.17f), the penalty is sharply reduced for a channel spacing larger than 50 GHz. With POLMUX-RZ-OOK (Figure 7.17g) and POLMUX-RZ-DPSK (Figure 7.17h), on the other hand, a reduced nonlinear tolerance is also observed when the co-propagating channels are spaced 100-GHz and 200-GHz away. In particular POLMUX-RZ-OOK shows still a significant penalty (2.9 dB) between single channel and 3 co-propagating channels on a 200-GHz grid. For RZ-OOK, on the other hand, almost no difference is measured between 3 channels on a 200-GHz grid and single-channel transmission. This larger bandwidth is typical for XPolM-induced depolarization in POLMUX transmission. In *conventional* transmission systems, where the receiver is not polarization sensitive, a low-pass behavior characterizes the influence of XPM [337] and therefore results in a penalty which scales strongly with the channel spacing. Whereas XPM is normally not significant for a channel spacing in excess of 100-GHz (for SSMF and 10-Gbaud), XPolM can be a significant impairment for channel spacing up to 200-GHz. The difference in nonlinear penalty as a function of channel spacing is less significant for RZ-DPSK and POLMUX-RZ-DPSK, which confirms the observation that DPSK is mainly XPM and not XPolM limited. We note that this results in particularly large transmission impairments when a D(Q)PSK signal co-propagates with an OOK modulated channel. This case is discussed in Section 10.6.2.



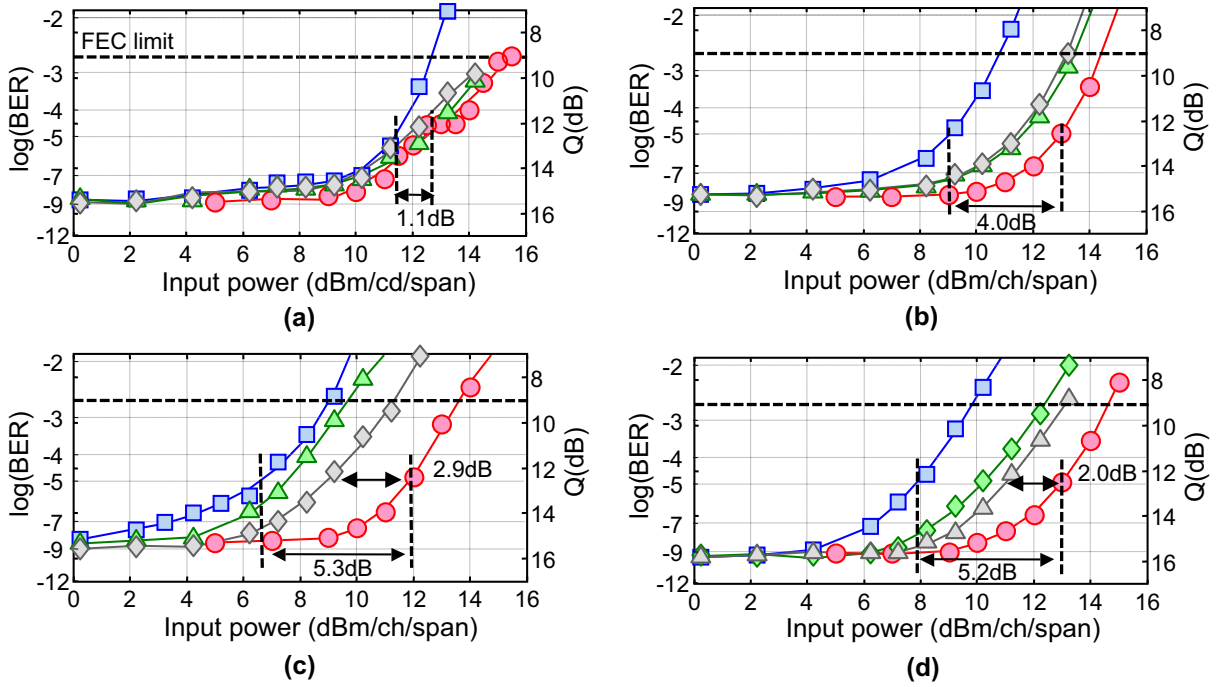


Figure 7.17: Measured nonlinear tolerance after 800-km for (a) 10.7-Gb/s RZ-OOK, (b) 10.7-Gb/s RZ-DPSK, (c) 21.4-Gb/s POLMUX-RZ-OOK and (d) 21.4-Gb/s POLMUX-RZ-DPSK with  $\bullet$  single channel,  $\square$  3 WDM channel, 50-GHz spacing,  $\blacktriangle$  3 WDM channel, 100-GHz spacing,  $\blacklozenge$  3 WDM channel, 200-GHz spacing.

#### 7.4.4 Polarization-interleaved POLMUX systems

The impact of XPolM-induced transmission penalties can be reduced through orthogonal polarization interleaving of adjacent POLMUX channels. Interleaved POLMUX transmission deterministically spreads out the SOP of the channels over the Poincaré sphere, by changing the SOP of the even wavelength channels with respect to the uneven channels. Polarization interleaved POLMUX transmission therefore bears a strong similarity to *conventional* polarization interleaved transmission, where adjacent WDM channels are transmitted in orthogonal SOPs [71, 72].

In polarization interleaved POLMUX systems, a signal is transmitted in both orthogonal SOPs of each co-propagating wavelength channel, as illustrated in Figure 7.18. The decrease in transmission penalties is based on the observation that the sum of the Stokes vectors of two co-propagating wavelength channels is constant during transmission, which cancels the influence of XPolM. Using the Manakov Equation [338], one can show that the nonlinear polarization shift induced on a pulse in channel  $\omega_1$  through a second co-propagating pulse in channel  $\omega_2$  is equal to,

$$\frac{S_{\omega_1}}{z} = \frac{8}{9} \gamma P_0 (S_{\omega_1} \times S_{\omega_2}), \quad (7.8)$$

where  $S_n$  denotes the Stokes vector of channel  $n$ ,  $P_0$  is the channel input power and  $z$  the transmission distance. Assuming a sum vector  $S_0$  with  $S_0 = \frac{1}{2}(S_{\omega_1} + S_{\omega_2})$  it can be shown that this is



equal to,

$$\frac{S_{\omega_1}}{z} = \frac{16}{9} \gamma P_0 (S_{\omega_1} x S_0), \quad (7.9)$$

which only depends on  $S_{\omega_1}$  and the sum vector  $S_0$ . When the two pulses in channels  $\omega_1$  and  $\omega_2$  have an orthogonal SOP, the sum vector  $S_0$  equals zero and the nonlinear polarization shift only depends on the pulse in channel  $\omega_1$  itself. Using a similar argument it can be shown that also for multiple co-propagating channels polarization interleaving minimizes the variance in nonlinear polarization shift.

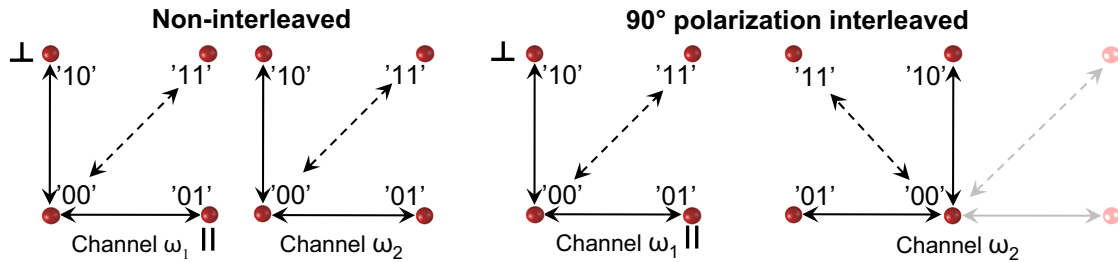


Figure 7.18: Principle of interleaved POLMUX transmission.

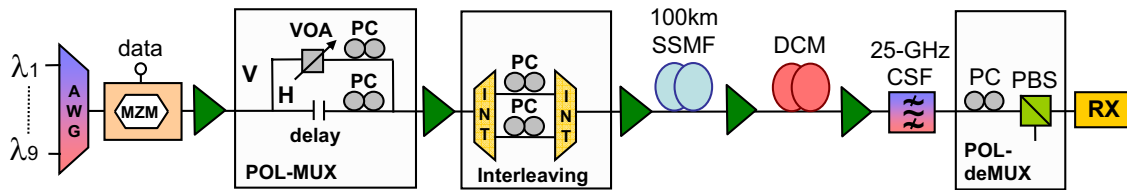


Figure 7.19: Experimental setup for interleaved POLMUX transmission.

We experimentally verify the principle of interleaved POLMUX transmission with the setup depicted in Figure 7.19. The output of up to 9 DFB lasers, spaced on a 50-GHz grid, are 10-Gb/s NRZ-OOK modulated (PRBS  $2^{31}-1$ ). Afterwards, the signals are polarization-multiplexed to 20-Gb/s POLMUX-NRZ-OOK. The WDM channels are polarization interleaved by splitting the channels into two subsets using a 50-GHz interleaver and afterwards recombining the channels with a second 50-GHz interleaver. The SOP of the POLMUX channels are adjusted using the polarization controllers in between both interleavers. As it is difficult to measure the SOP difference between the WDM channels, we adjust the SOP of one of the channel subsets such that the measured BER is minimized. In effect, the polarization interleaving rotates the linear polarization components of the even WDM channels  $90^\circ$  with respect to the uneven WDM channels. The signals are then transmitted over 100 km of SSMF and matching DCF, where the same input power is used for both SSMF and DCF to generate sufficient nonlinear impairments. After transmission, a 25-GHz CSF filters out the center channel and the signal is manually polarization de-multiplexed with a PBS preceded by a polarization controller. Afterwards, the signal is fed into a direct detection receiver and the nonlinear tolerance is measured for the center channel at 1551.6 nm.

In Figure 7.20a, the impact of polarization interleaving on 10-Gb/s NRZ-OOK is depicted. This shows an improvement of 0.9 dB and 0.5 dB for 3 and 5 co-propagating channels, respectively

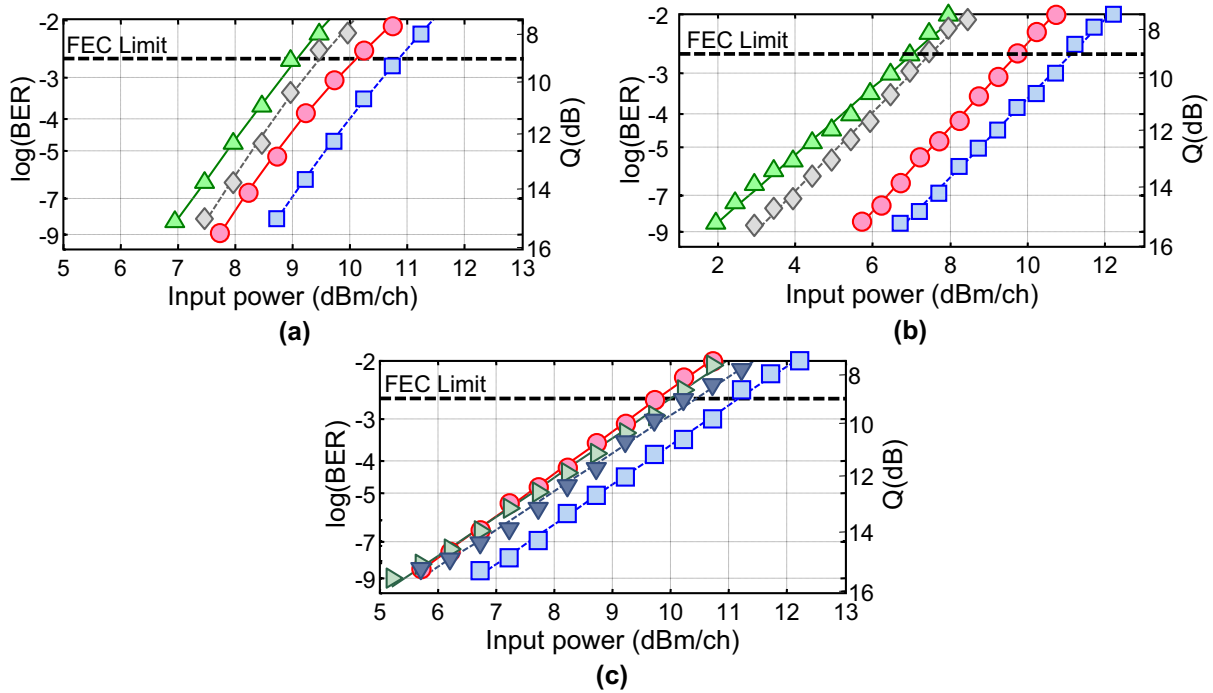


Figure 7.20: Measured nonlinear tolerance after 100-km for (a) 10-Gb/s NRZ-OOK and (b-c) 20-Gb/s POLMUX-NRZ-OOK with  $\bullet$  3 channel 50-GHz spacing,  $\square$  3 channel 50-GHz spacing, interleaved,  $\blacktriangle$  9 channel 50-GHz spacing,  $\diamond$  9 channel 50-GHz spacing, interleaved,  $\blacktriangleright$  3 channel 300-GHz spacing,  $\blacktriangledown$  3 channel 300-GHz spacing, interleaved.

(at  $10^{-5}$  BER). This improvement results mainly from a reduction in XPM impairments between the co-propagating channels. For 20-Gb/s POLMUX-NRZ-OOK, as depicted in Figure 7.20b, a much lower nonlinear tolerance is measured compared to 10-Gb/s NRZ-OOK. The difference between 3 and 9 co-propagating channels is more significant here than previously discussed (Figure 7.16c), as there is no dispersion map used here to reduce the impact of XPM. For 3 co-propagating channels, polarization interleaving increases the nonlinear tolerance with 1.2 dB. But when the number of co-propagating channels increases, the beneficial influence of polarization interleaved transmission decreases as channels spaced further away contribute to the XPolM penalty. The influence of the channel spacing is evident from the measurement results depicted in Figure 7.20c, which compares a 50 GHz and a 300-GHz channel spacing for 3 co-propagating channels. When the channel spacing is increased, the nonlinear tolerance improvement reduces from 1.2 dB to 0.2 dB.

The efficiency of interleaved POLMUX transmission is relatively small compared to the XPolM penalty. This is mainly due to the impact of DGD and SOPMD, which changes the SOP as a function of wavelength. In particular for WDM channels that are spaced further apart, the orthogonality between the WDM channels is maintained only over a short transmission distance. This reduces the benefit of polarization interleaving, as it requires an accurate alignment of the SOP of the WDM channels. We can therefore conclude that polarization interleaved POLMUX transmission does not sufficiently reduce the impact of XPolM to be practical in long-haul transmission systems.

## 7.5 Summary & conclusions

In this chapter we analyzed and compared the transmission tolerances of POLMUX signaling with polarization insensitive modulation formats. This shows that for most linear and nonlinear transmission impairments separately, POLMUX signaling significantly increases the transmission tolerance when compared to binary modulation at the same bit rate.

- A polarization-sensitive receiver improves the *OSNR requirement* by filtering out the noise in the orthogonal polarization. For POLMUX-OOK modulation, the difference is  $\sim 2.7$  dB for a doubling in the total bit rate. In comparison to DQPSK modulation, POLMUX-DPSK modulation has a 1.1 dB advantage in OSNR requirement.
- *PMD* results in crosstalk between the POLMUX tributaries due to over- and undershoots near the edge of the pulse. But at the same bit rate, the PMD tolerance of POLMUX signaling is significantly higher in comparison to binary modulation formats.
- The lower symbol rate increases the *chromatic dispersion* tolerance by a factor of 4 in the absence of a PMD. However, the combination of chromatic dispersion and PMD, shifts the DGD induced edge over- and undershoots from the edge to the center of the pulse. This reduces the tolerance by  $\sim 30\%$  (2-dB OSNR penalty) in comparison to single-polarization transmission at the same symbol rate.
- For POLMUX signaling, *PDL* can either result in an OSNR fluctuation for one of the tributaries or a loss of orthogonality between the tributaries. A 3-dB PDL results approximately in a 2-dB worst-case OSNR penalty.
- At a 10-Gbaud symbol rate, the *single-channel nonlinear tolerance* is comparable with and without POLMUX signaling. In the presence of PMD, the nonlinear tolerance decreases due to the cumulative edge effects of DGD and SPM. Statistical simulations show for this case a reduction in nonlinear tolerance with up to  $\sim 2$  dB in comparison to single-polarization transmission at the same symbol rate.

In addition we find that for WDM transmission systems, the impact of XPolM results in a reduced nonlinear tolerance for POLMUX transmission systems.

- The *XPolM*-induced nonlinear phase shift result in a noise-like change in the SOP. This causes crosstalk between the POLMUX tributaries after the polarization sensitive receiver.
- For *POLMUX-OOK* modulation, the impact of XPolM results in a reduction of the nonlinear tolerance with 4-5 dB in comparison to WDM transmission without POLMUX signaling (10 Gbaud, 50-GHz grid). This makes POLMUX-OOK modulation generally impractical for long-haul transmission.
- *POLMUX-DPSK* modulation has a more symmetric signal constellation, which reduces the impact of XPolM. It suffers therefore only a  $\sim 1$  dB penalty from XPolM impairments.

This indicates that POLMUX-DPSK can be a suitable modulation format for long-haul transmission systems. POLMUX-DPSK has a 3-dB advantage in nonlinear tolerance compared to DQPSK modulation at a 10-Gbaud symbol rate and 50-GHz channel spacing.

- Deterministically spreading the SOP of co-propagating WDM channels reduces the impact of XPolM. *Polarization interleaving* of the WDM channels therefore, ideally, cancels out the XPolM penalty. However, the orthogonality between the co-propagating channels is lost through PMD, which decreases the efficiency of polarization interleaving.

The interaction between PMD, chromatic dispersion and nonlinear impairment complicates system design for POLMUX transmission systems. This is undesirable for long-haul transmission systems which, if possible, have to be designed with simple engineering rules. It is therefore attractive to apply PMD compensation for POLMUX transmission systems, either through optical or electrical means. When the PMD-related impairments are compensated, the high transmission tolerances combined with the doubled spectral efficiency of POLMUX signaling make it an attractive option for high-capacity transmission systems. However, optical compensation of PMD might not be practical due to high polarization tracking speeds that are required. The use of phase modulation reduces the impact of XPolM and makes POLMUX signaling practical for long-haul transmission systems.

---

## Polarization-multiplexed DQPSK

Future state-of-the-art optical transmission systems are expected to transmit high bit rates in even more densely spaced WDM channels. However, as shown in the previous chapter the use of multi-level modulation formats is challenging for long-haul transmission systems. It can result in reduced transmission reach through higher OSNR requirements and a lower nonlinear tolerance. This requires transmission formats with a narrow optical bandwidth while maintaining sound linear and nonlinear transmission tolerances to enable long-haul transmission with  $>1$  b/s/Hz. Chapters 5 and 7 have discussed, respectively, DQPSK modulation and POLMUX signaling as possible approaches to double the spectral efficiency over binary modulation.

To further increase the number of bits per symbol, orthogonal coding can be used to exploit two or more degrees of freedom at the same time. An example of orthogonal coding that combines amplitude and phase shift keying is amplitude differential phase shift keying [339]. The simultaneous modulation of the amplitude, phase and polarization dimensions of an optical signal has allowed multi-level modulation at high bit rates with up to 5 and 6 bits per symbol [340, 341]. This chapter combines DQPSK modulation and POLMUX signaling to realize modulation with 4 bits per symbol. Such a high-density signal constellation opens up the possibility for a  $\geq 1.6$  b/s/Hz spectral efficiency in long-haul transmission systems.

Section 8.1 describes the transmitter and receiver structure of POLMUX-RZ-DQPSK modulation, the OSNR requirement as well as the tolerance against narrowband filtering. Subsequently, Section 8.2 discusses long-haul POLMUX-RZ-DQPSK transmission with a 1.6-b/s/Hz spectral efficiency. We particularly focus on the influence of interleaved polarization multiplexing, which presents a trade-off between the nonlinear and PMD tolerance. In Section 8.3 we then compare the high-spectrally efficient transmission experiments that have been studied in the literature.

---

<sup>1</sup>The results described in this chapter are published in c7, c36

## 8.1 Transmitter & receiver structure

A POLMUX-DQPSK transmitter consists of two DQPSK transmitters which are afterwards multiplexed on the two orthogonal polarizations of the signal. This results in a transmitted signal,

$$\vec{r}(t) = \begin{pmatrix} E_h \\ E_v \end{pmatrix} = \begin{pmatrix} \sqrt{P_h} \exp(j[\omega_0 t + \varphi_h(t)]) \\ \sqrt{P_v} \exp(j[\omega_0 t + \varphi_v(t)]) \end{pmatrix}. \quad (8.1)$$

As POLMUX-DQPSK modulation encodes the information in the differential phase  $\Delta\phi$ , we can also denote the signal as,

$$\vec{r}(t) = \begin{pmatrix} \sqrt{P_h} \cdot \exp(j[\omega_0 t + \varphi + \Delta\phi_h(t)]) \\ \sqrt{P_v} \cdot \exp(j[\omega_0 t + \varphi + \Delta\phi_v(t) + \Delta\psi]) \end{pmatrix}, \quad (8.2)$$

where  $\varphi$  is the absolute phase of the transmitter laser and  $\Delta\psi$  is the phase difference between both orthogonal polarization components. The information is carried in  $\Delta\phi_h(t)$  and  $\Delta\phi_v(t)$  which are independent of each other and take a value from the set  $[0, \pi/2, \pi, 3\pi/2]$ . Assuming  $\varphi$  and  $\Delta\psi$  are equal to zero this gives  $\sqrt{P_h} \exp(j\Delta\phi_h(t)) = h_I(t) + j \cdot h_Q(t)$  as the complex envelope of the horizontal polarization components and  $\sqrt{P_v} \exp(j\Delta\phi_v(t)) = v_I(t) + j \cdot v_Q(t)$  as the complex envelope of the vertical polarization component. The signals in each of the 4 signaling dimensions can therefore be defined as,

$$\begin{aligned} h_I(t) &= \Re\{E_h\} = \Re\{\sqrt{P_h} \exp(j\Delta\phi_h(t))\} \\ h_Q(t) &= \Im\{E_h\} = \Im\{\sqrt{P_h} \exp(j\Delta\phi_h(t))\} \\ v_I(t) &= \Re\{E_v\} = \Re\{\sqrt{P_v} \exp(j\Delta\phi_v(t))\} \\ v_Q(t) &= \Im\{E_v\} = \Im\{\sqrt{P_v} \exp(j\Delta\phi_v(t))\}. \end{aligned} \quad (8.3)$$

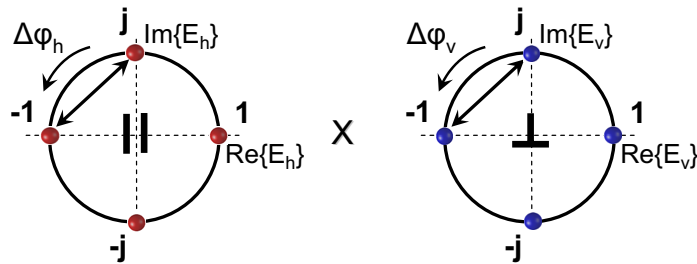


Figure 8.1: 2-dimensional signal constellation diagram for POLMUX-DQPSK modulation

Figure 8.1 shows the signal constellation diagram for POLMUX-DQPSK, as a DQPSK modulated signal on each of the two orthogonal polarizations. Each DQPSK signal encodes 2 bits per symbol, which results in a total  $2 \cdot 2 = 4$  bits per symbol for POLMUX-DQPSK modulation. This can be slightly counterintuitive, as the constellation diagram in Figure 8.1 shows only 8

signal points. As an alternative representation, Figure 8.2 depicts both orthogonal polarizations combined in a single constellation diagram. The signal constellation diagram is now shown as a 4-dimensional hypercube. Different hypercubes can be used to represent the signal constellation but we use here a torus, which is the product of two coplanar circles. We use here one circle to denote  $\exp(j\Delta\phi_h)$ , whereas the other circle denotes  $\exp(j\Delta\phi_v)$ . Assuming that  $\Delta\psi$  is equal to zero, the signal constellation can be defined in a three-dimensional coordinate system  $(x, y, z)$  as,

$$\begin{aligned} x(\Delta\phi_h, \Delta\phi_v) &= [R + r \cdot \cos(\Delta\phi_v)] \cdot \cos(\Delta\phi_h) \\ y(\Delta\phi_h, \Delta\phi_v) &= [R + r \cdot \cos(\Delta\phi_v)] \cdot \sin(\Delta\phi_h) \\ z(\Delta\phi_h, \Delta\phi_v) &= r \cdot \sin(\Delta\phi_v), \end{aligned} \tag{8.4}$$

where  $R$  and  $r$ , with  $R > r$  defines the distance from the center of the tube to the center of the torus and the radius of the tube, respectively. Note that when visualized on a Poincaré sphere, the constellation diagram of POLMUX-DQPSK modulation consist of 4 signal points as only the phase difference between both polarization modes is denoted (i.e.  $\Delta\phi_v - \Delta\psi - \Delta\phi_h$ , see Figure 7.1a).

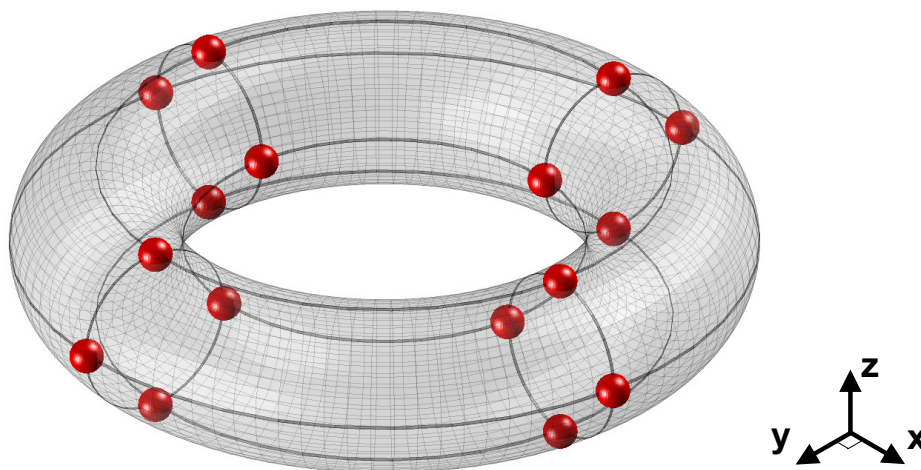


Figure 8.2: 4-dimensional signal constellation diagram for POLMUX-DQPSK modulation

The transmitter and direct detection receiver structure for POLMUX-RZ-DQPSK modulation are both depicted in Figure 8.3. For RZ modulation, the output of the laser is first RZ pulse carved. Afterwards, the signal is split and each of the tributaries is DQPSK modulated with a parallel DQPSK modulator. With a PBS, both tributaries are then multiplexed together on orthogonal polarizations. Hence, a total of 4 independent binary electrical data streams are modulated onto the POLMUX-DQPSK signal. We note that all fibers in the transmitter would normally be polarization-maintaining. The polarization rotation for one of the DQPSK tributaries is shown explicitly here, but is normally integrated into the PBS.

At the receiver, the signal is first split into two orthogonal polarization tributaries with a polarization controller followed by a PBS. Each of the polarization tributaries is split again with a 3-dB

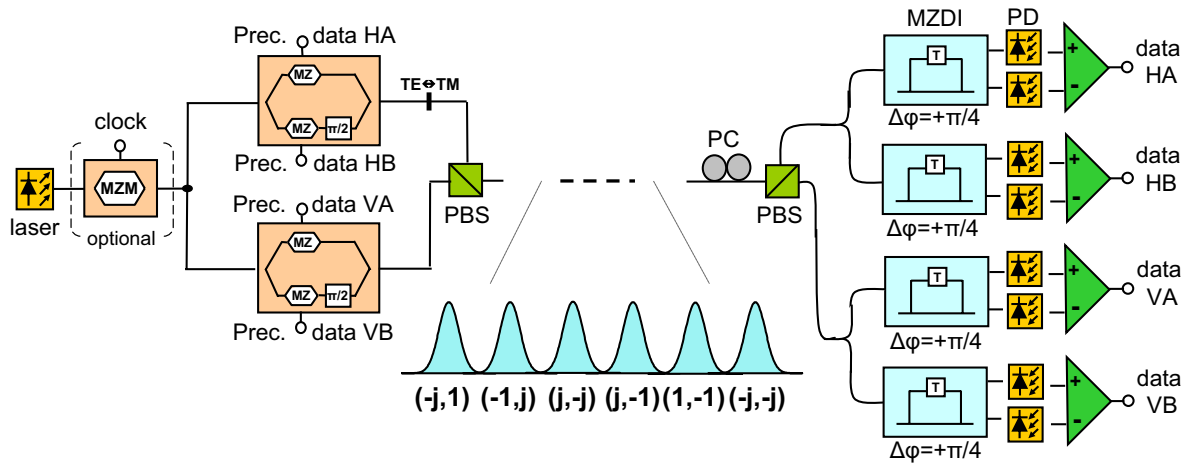


Figure 8.3: Transmitter and receiver structure for POLMUX-(RZ)-DQPSK modulation

fused-fiber coupler and all four tributaries are fed to separate MZDIs. The MZDIs demodulate the in-phase and quadrature tributaries of each of the polarization components which is followed by balanced detection. This shows that the number of optical components in both the transmitter and receiver is significant for POLMUX-RZ-DQPSK modulation. Hence, to make such a modulation format more practical further optical integration of the components is a prerequisite. This would for example be possible using InP technology, which enables multiple components on a single optical dei [342, 278, 343].

### 8.1.1 Back-to-back OSNR requirement

Figure 8.4 depicts the configuration of the 85.6-Gb/s POLMUX-RZ-DQPSK transmitter and receiver as used in the experimental verification. For simplicity, the transmitter and receiver structure is somewhat different from the one discussed in Section 8.1. At the transmitter, the output signals of 40 DFB lasers, aligned on a 50-GHz ITU grid between 1548.15 nm and 1563.88 nm, are modulated using two parallel modulator chains for separate modulation of the even and odd wavelength channels. The RZ-DQPSK modulator is the same as discussed in Section 6.2. After DQPSK modulation, the even and odd channels are combined with a 50-GHz interleaver, having a 3-dB bandwidth of 44 GHz. Subsequently, the channels are fed to a polarization-multiplexing stage. The signal is power split to create two tributaries (H and V), which are delayed with 16.6 ns relative to each other. One branch of the polarization-multiplexing stage contains an optical switch and phase modulator. The optical switch can be triggered (switch 1) to change between POLMUX-RZ-DQPSK, and (single polarization) RZ-DQPSK modulation for the reference measurements. The phase modulator (PM) causes synchronization loss in tributary V when switched on (switch 2), and is hence used to identify which polarization tributary is measured. Note that it is switched off in the actual measurement and has no influence on the discussed results. The tributaries H and V are recombined with orthogonal polarizations in a PBS to generate 85.6-Gb/s POLMUX-RZ-DQPSK modulation. The two polarization tributaries can be bit-aligned or they can be offset from each other. This is discussed in more detail in Section 8.2.1.



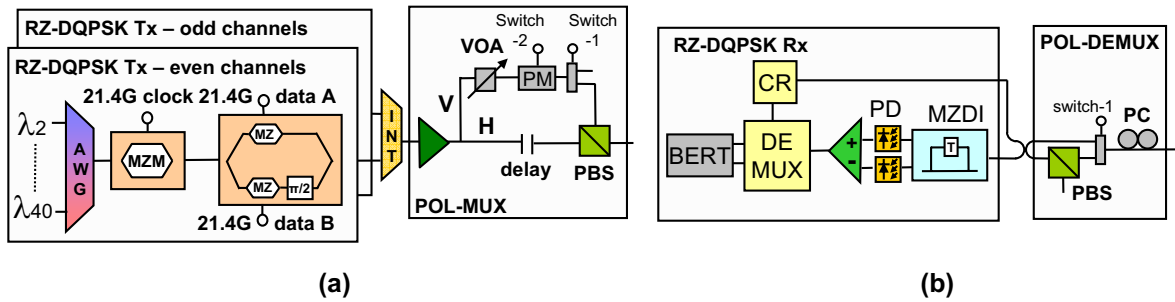


Figure 8.4: Experimental setup: (a) transmitter and (b) receiver.

Figure 8.5 shows the back-to-back OSNR requirement of 42.8-Gb/s RZ-DQPSK and all four tributaries of 85.6-Gb/s POLMUX-RZ-DQPSK modulation. The simulated back-to-back OSNR requirements are shown as a reference. For both simulations and experiments the respective optimized filter bandwidths discussed in the Section 5.3.1 are used. The required OSNR for a  $10^{-3}$  BER is 13.0 dB and 15.8 dB for 42.8-Gb/s RZ-DQPSK and 85.6-Gb/s POLMUX-RZ-DQPSK, respectively. Hence, 85.6-Gb/s POLMUX-RZ-DQPSK requires a 2.8 dB higher OSNR with respect to 42.8-Gb/s RZ-DQPSK. This sensitivity reduction is similar to the reduction observed in Section 7.3.1 and results from a 3-dB penalty due to the doubled bit rate and a 0.2-dB benefit which originates from the polarization sensitive receiver. In the simulations, the required OSNR is 11.8 dB and 14.6 dB for 42.8-Gb/s RZ-DQPSK and 85.6-Gb/s POLMUX-RZ-DQPSK, respectively. Hence, the simulative and experimentally measured OSNR requirement are in good agreement and show only a 1.2 dB difference due transmitter and receiver impairments (for a  $10^{-3}$  BER). For a fixed OSNR, the back-to-back Q-factor difference between RZ-DQPSK and POLMUX-RZ-DQPSK equals 2.4 dB and 3.0 dB for measurements and simulations, respectively.

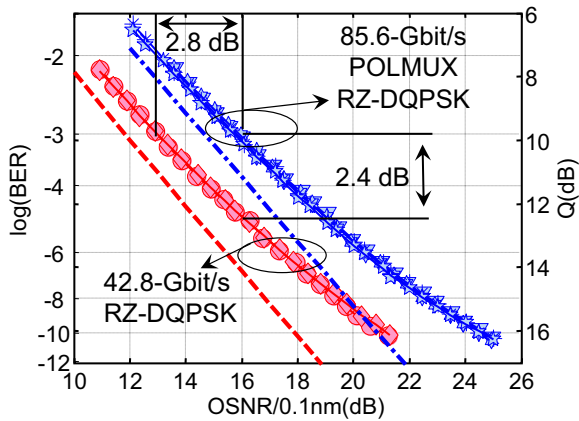


Figure 8.5: Measured (points) and simulated (lines) back-to-back sensitivity for 42.8-Gb/s RZ-DQPSK (dashed line) and 85.6-Gb/s POLMUX-RZ-DQPSK (dotted line).

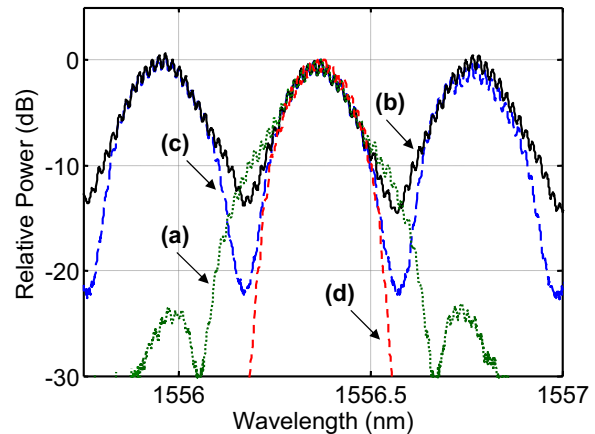


Figure 8.6: High resolution optical spectrum with: (a) single channel, (b) transmitted spectrum (c) received spectrum before the CSF (d) received spectrum after the CSF.

### 8.1.2 Narrowband optical filtering

In order to transmit 85.6-Gb/s POLMUX-RZ-DQPSK with a 50-GHz channel spacing, the bandwidth of the optical filters is important to consider. The narrowband filtering tolerance of 85.6-Gb/s POLMUX-RZ-DQPSK is similar to 42.8-Gb/s RZ-DQPSK as both modulation formats are DQPSK modulated and have the same symbol rate. Figure 8.6 shows in more detail the narrowband filtering as it occurs along the transmission line in the long-haul transmission experiment discussed later in this chapter. Spectra (a) shows the single channel optical spectrum of 85.6-Gb/s POLMUX-RZ-DQPSK before optical filtering. A comparison of spectra (a) and (b) shows the influence of the 50-GHz interleaver at the transmitter. The optical filtering in the in-line WSS reduces the optical bandwidth with every pass through the re-circulating loop. The transmittance spectrum of the in-line WSS used in the experiment is shown in Figure 3.16. The in-line spectral filtering is evident by comparing the spectral dip between WDM channels in spectra (b) after the 50-GHz interleaver and spectra (c) after 6 passes through the re-circulation loop. At the receiver, the WDM signal is de-multiplexed using a CSF with a 34-GHz 3-dB bandwidth, further narrowing the optical bandwidth. Spectra (d) is obtained after de-multiplexing of the WDM channels. It shows that the spectral width of the received signal after 6 passes through the re-circulating loop is similar to the back-to-back optimized de-multiplexing filter bandwidth of 34-GHz. This indicates that 85.6-Gb/s POLMUX-RZ-DQPSK can be transmitted over multiple cascaded add-drop nodes on a 50-GHz WDM grid. This enables a high 1.6-b/s/Hz spectral efficiency while maintaining a sound tolerance with respect to narrowband optical filtering.

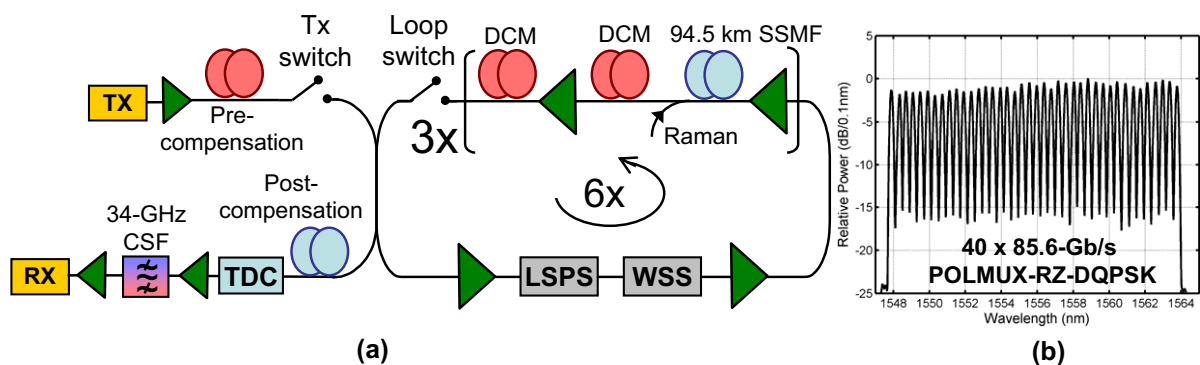


Figure 8.7: (a) re-circulating loop setup, (b) optical spectrum after transmission.

## 8.2 Long-haul transmission

In this section we discuss a long-haul transmission experiment with 85.6-Gb/s POLMUX-RZ-DQPSK modulation on a 50-GHz WDM grid. The re-circulating loop consists of three 94.5-km spans of SSMF with an average span loss of 21.5 dB. Before transmission the channels are de-correlated with -1020 ps/nm of pre-compensation. The inline under-compensation per span is 33.5 ps/nm (at 1550 nm), which is close to the optimum for 42.8-Gb/s RZ-DQPSK as discussed in Section 6.2. The input power into the SSMF is -3 dBm per WDM channel and a

hybrid backward pumped Raman/EDFA structure is used for signal amplification with an average ON/OFF Raman gain of  $\sim 11$  dB. A LSPS with a deterministic sequence of polarization states equal to the number of re-circulations is used in the re-circulating loop. The polarization in each re-circulation of the loop is thus randomized with respect to the other re-circulations, averaging out PMD and PDL influences. However, the LSPS does not influence the polarization at the receiver and is as such not used to de-multiplex the polarization tributaries. Power equalization of the WDM channels is provided by the WSS, configured as a channel-based DGE.

The optical spectrum at the receiver is depicted in Figure 8.7b. Using a TDC, the accumulated dispersion at the receiver is optimized on a per-channel basis. Subsequently, the desired channel is selected with a narrowband 34-GHz CSF and afterwards fed into the receiver (depicted in Figure 8.3b). The signal is first manually polarization de-multiplexed using a PC followed by a PBS. Afterwards, the signal is fed into the conventional 42.8-Gb/s DQPSK receiver as discussed in Section 6.2.

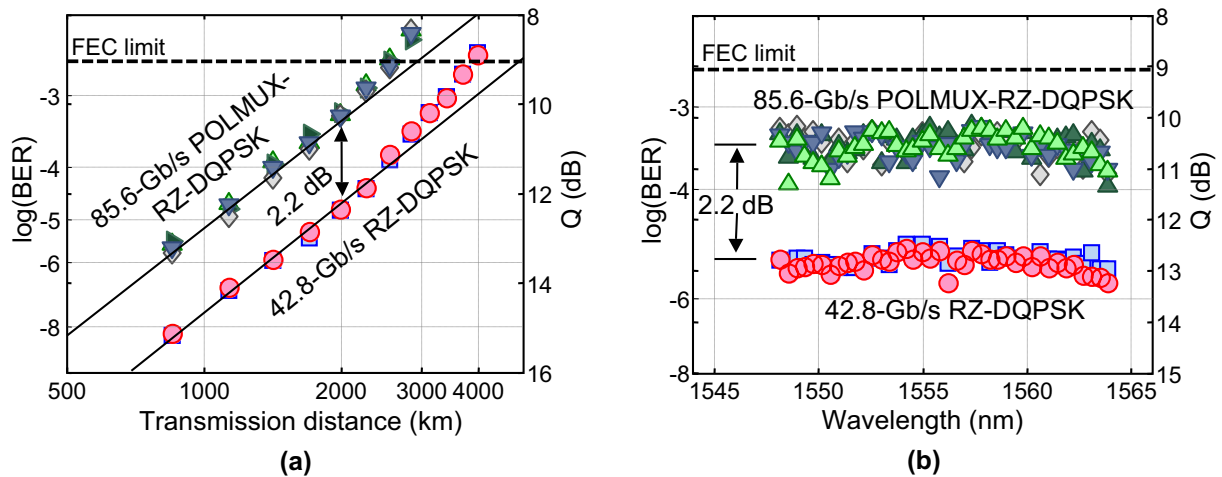


Figure 8.8: (a) Measured BER as a function of transmission distance, (b) Measured BER of all 40 WDM channels after 1,700 km, for RZ-DQPSK  $\square$  In-phase,  $\circ$  Quadrature and POLMUX-RZ-DQPSK  $\diamond$  In-phase, pol.H,  $\blacktriangleright$  Quadrature, pol.H,  $\blacktriangledown$  In-phase, pol.V,  $\blacktriangle$  Quadrature, pol.V.

To analyze the suitability of the 85.6-Gb/s POLMUX-RZ-DQPSK modulation format for long-haul transmission, the performance is assessed as a function of the transmission distance. This is depicted in Figure 8.8a. Initially the measured log(BER) shows a linear increase with an exponential increase in transmission distance. After 2,000 km it deviates from the linear increase due to an increased impact of nonlinear impairments such as SPM and nonlinear phase noise. A similar performance decrease is observed for 42.8-Gb/s RZ-DQPSK modulation and it can thus be concluded that no POLMUX specific impairments are measured. The 2.4-dB back-to-back difference in Q-factor between 42.8-Gb/s RZ-DQPSK and 85.6-Gb/s POLMUX-RZ-DQPSK is slightly reduced to 2.2 dB. This is likely a result of the lower peak power in comparison to RZ-DQPSK, which results in an improved nonlinear tolerance. We note though that the difference is small and can also partially result from measurement inaccuracies. The lack of POLMUX specific impairments such as XPM induced cross polarization modulation confirms that 85.6-Gb/s POLMUX-RZ-DQPSK is strongly limited by single-channel impairments and that the influence of XPM-induced depolarization is minimal.

Figure 8.8a shows the BER for all WDM channels and tributaries for both 42.8-Gb/s RZ-DQPSK and 85.6-Gb/s POLMUX-RZ-DQPSK. After 1,700-km transmission, all 40 RZ-DQPSK channels have more than 3-dB margin with respect to the FEC limit. For 85.6-Gb/s POLMUX-RZ-DQPSK the worst channel is more than 1 dB above the FEC limit. The small performance variance among the WDM channels indicates that there is no strong wavelength dependency across the upper part of the C-band.

### 8.2.1 Interleaved vs. bit-aligned polarization-multiplexing

The optical inter-pulse delay is defined as the delay between both polarization tributaries within one symbol period (see Section 7.3.2). It can be changed such that both tributaries are either bit-aligned or interleaved. The difference in inter-pulse delay can be denoted by the optical extinction ratio before polarization de-multiplexing and phase demodulation, which is defined as the peak power divided by the minimum power in the eye diagram. In Figure 8.9 the influence of the inter-pulse delay on the optical extinction ratio is depicted for 85.6-Gb/s POLMUX-RZ-DQPSK. In the case both polarization tributaries are interleaved, a quasi CW signal is obtained and the extinction ratio is close to zero. When the polarization tributaries are bit-aligned on the other hand, the RZ pulse shape of RZ-DQPSK is to a high degree maintained and a high extinction ratio is measured, as evident from the eye diagrams in Figure 8.9.

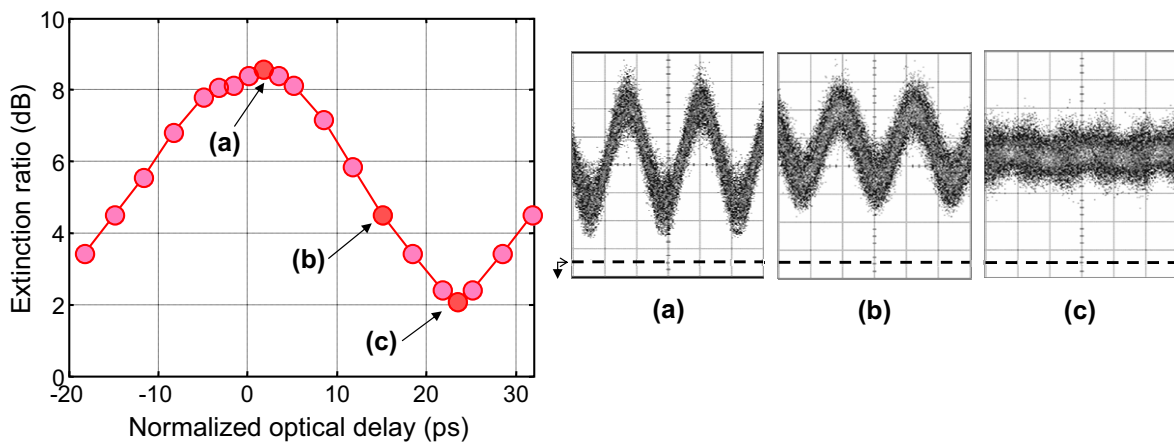


Figure 8.9: Extinction ratio of the 85.6-Gb/s POLMUX-RZ-DQPSK signals before polarization de-multiplexing and phase demodulation as a function of the normalized inter-pulse delay.

For RZ pulse carved signals, it can be particularly interesting to interleave both polarization tributaries as this lowers the peak power of the signal and therefore improves the nonlinear tolerance. It is observed in the transmission experiment that interleaving the polarization tributaries reduces nonlinear impairments considerably; a maximum 2 dB difference in Q-factor is measured. On the other hand the influence of PMD related impairments is enhanced for interleaved polarization tributaries, as shown in Section 7.3.2. In the experimental results reported here, the inter-pulse delay is set in between both extremes, partly because the quasi CW signal of interleaved polarization tributaries caused unstable operation of the phase-locked loop based clock-recovery.

Additionally, the performance fluctuations might be attributed to the reduced PMD tolerance of 85.6-Gb/s POLMUX-RZ-DQPSK with interleaved tributaries. Setting the inter-pulse delay in between both extremes resulted in more stable operation but a  $\sim 0.5$  dB decrease in measured Q-factor. With a simulative comparison the influence of the inter-pulse delay on the PMD and nonlinear tolerance of POLMUX-RZ-DQPSK is discussed in more detail.

### 8.2.2 Differential group delay

The polarization de-multiplexing in the POLMUX receiver, results in a penalty when the signal polarization is not constant (1) over the symbol period or (2) across the optical spectrum. A DGD results in a polarization change across the symbol period, which causes over- and under-shoots near the edges of the symbol. For high bit rates, the impact of SOPMD is also important to consider as it results in a polarization change along the optical bandwidth. For 85.6-Gb/s POLMUX-RZ-DQPSK the influence of a wavelength dependent polarization mismatch should be relatively small due to the 21.4-Gb/s symbol rate. In particular the difference between interleaved and bit-aligned POLMUX is not likely to be significantly affected by higher order PMD, because the inter-pulse delay has no influence on the optical spectrum. We therefore restrict our comparison here to the DGD tolerance, which is modeled as linear birefringence. For the POLMUX signals, the simulated DGD is chosen such that the output SOP equals the input SOP. This is true when the DGD times the center frequency (193.1 THz) is an integer multiple [331]. In the simulations the penalties are denoted through the EOP. Hence, it does not include the difference in OSNR requirement for the various modulation formats. In addition, the EOP is normalized with respect to the back-to-back EOP. For RZ-DQPSK the results shown here are the worst-case (maximum) EOP obtained from the in-phase or quadrature channel. In the case of POLMUX signaling, the generated RZ-DQPSK signal is split, delayed over 17 bits and recombined with orthogonal polarizations, the denoted EOP is the maximum EOP obtained among the 4 tributaries.

Figure 8.10a shows the simulated DGD tolerance for both cases, with 42.8-Gb/s RZ-DPSK and 42.8-Gb/s RZ-DQPSK as a reference. Comparing the DGD tolerance of 42.8-Gb/s RZ-DPSK and 42.8-Gb/s RZ-DQPSK shows an increase in DGD tolerance with about a factor of two for 42.8-Gb/s RZ-DQPSK [122]. For 85.6-Gb/s POLMUX-RZ-DQPSK the DGD tolerance is strongly dependent on the inter-pulse delay between the two polarization tributaries. When the polarization tributaries are bit-aligned the DGD tolerance is only slightly worse than 42.8-Gb/s RZ-DPSK, for the doubled bit rate. For interleaved polarization tributaries, on the other hand, the DGD tolerance is further reduced by about a factor of two in comparison to bit-aligned 85.6-Gb/s POLMUX-RZ-DQPSK. In this case the misalignment between the received polarization and the axis of the PBS does not occur in between two symbols, as is the case for bit-aligned polarization tributaries, but in the middle of the symbol period. The reduced DGD tolerance of interleaved POLMUX-RZ-DQPSK is even more evident from Figure 8.10b, which depicts the penalty versus the inter-symbol delay between the polarization tributaries in the presence of 8.0 ps of DGD. This clearly shows a relatively low penalty for aligned polarization tributaries and a large increase in penalty when the tributaries are interleaved. The inset eye diagrams show

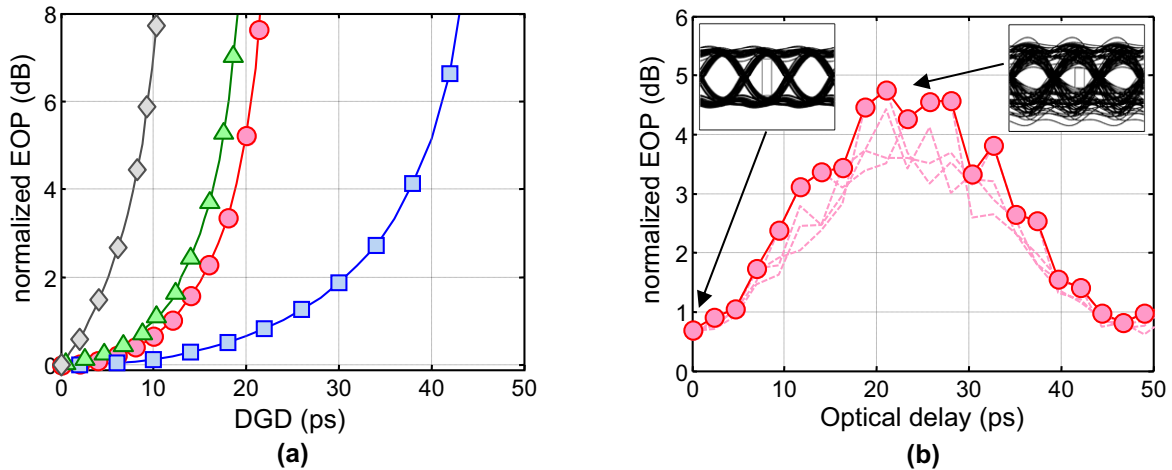


Figure 8.10: (a) Simulated comparison of the DGD tolerance with  $\circ$  42.8-Gb/s RZ-DPSK,  $\square$  42.8-Gb/s RZ-DQPSK  $\triangle$  85.6-Gb/s POLMUX-RZ-DQPSK, bit-aligned  $\diamond$  85.6-Gb/s POLMUX-RZ-DQPSK, interleaved; (b) normalized EOP as a function of the inter-pulse delay for 85.6-Gb/s POLMUX-RZ-DQPSK with 8-ps DGD. Dotted lines denote tributaries whereas the  $\circ$  denote worst case result among all tributaries.

Table 8.1: SIMULATED LINK AND RECEIVER PARAMETERS.

Link parameters		unit
Transmission length	8 x 100	km
Amplification	EDFA	-
Pre-compensation	-510	ps/nm
Inline under-compensation	90	ps/nm
Post-compensation	0	ps/nm

the additional degradation for interleaved polarization tributaries. When the tributaries are bit-aligned the DGD mainly results in jitter between consecutive symbols and the penalty is below 1 dB. For interleaved polarization tributaries on the other hand, severe overshoots are evident in the middle of the eye diagram which clearly shows the cause of the reduced DGD tolerance. This increases the EOP to in excess of 4 dB.

### 8.2.3 Nonlinear tolerance

The more constant intensity level of interleaved POLMUX-RZ-DQPSK modulation reduces the impact of nonlinear impairments through a lower peak power. To show the relation between nonlinear tolerance and inter-pulse delay we simulate single-channel transmission over an 8x100-km link of SSMF. The simulation parameters of the transmission link are listed in Table 8.1 whereas the fiber parameters are the same as denoted in Table 7.2. In the simulated transmission link, the polarization is randomized through random coupling between wave-plates every 1 km. EDFA-only amplification is used and the dispersion map is chosen such that it is typical for a transmission link optimized for 10-Gb/s bit rate.



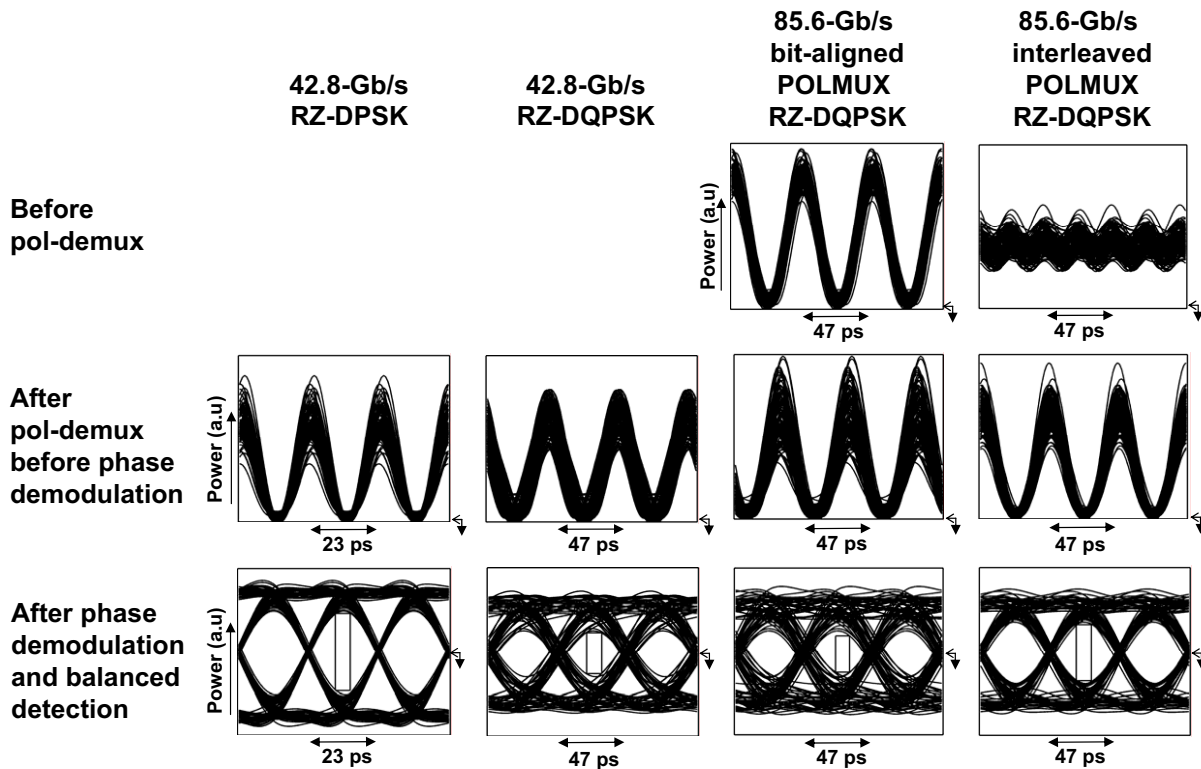


Figure 8.11: Simulated eye diagrams; before polarization de-multiplexing as well as before and after phase demodulation and balanced detection.

Figure 8.11 depicts the simulated eye diagrams for the four considered modulation formats with a 9-dBm input power into each span. This relatively high input power is chosen here to point out the difference in nonlinear tolerance between the modulation formats. The received eye diagram of bit-aligned and interleaved POLMUX-RZ-DQPSK before polarization de-multiplexing shows the RZ and quasi CW shape, respectively. After polarization de-multiplexing, increased broadening of the '1'-rail is evident for bit-aligned POLMUX, whereas for interleaved POLMUX a much cleaner RZ shape is obtained. After phase demodulation and balanced detection the increased eye closing is evident, showing the lower nonlinear tolerance for bit-aligned POLMUX. The variance of the '1' rail in the eye diagrams after polarization de-multiplexing is comparable for bit-aligned POLMUX-RZ-DQPSK and 42.8-Gb/s RZ-DPSK. However, for RZ-DPSK the phase demodulation is more ideal in comparison to RZ-DQPSK. This results in an eye diagram after balanced detection that is wide open despite the broadened '1'-rail in the phase domain. The nonlinear tolerance of 42.8-Gb/s RZ-DPSK is therefore clearly higher than for both POLMUX and single polarization RZ-DQPSK, which is in agreement with the measured results in Section 6. The eye diagram of 42.8-Gb/s RZ-DQPSK shows a strong timing jitter, which is not as evident in the POLMUX eye diagrams. The reduced jitter for POLMUX-RZ-DQPSK might be due to a more constant spread of the optical power over both polarization modes. From the eye diagrams after balanced detection, it follows that the nonlinear tolerance of interleaved 85.6-Gb/s POLMUX-RZ-DQPSK is slightly better than 42.8-Gb/s RZ-DQPSK. For bit-aligned POLMUX-RZ-DQPSK, on the other hand, the nonlinear tolerance is somewhat reduced compared to 42.8-Gb/s RZ-DQPSK. This indicates that, although the bit rate is doubled, the nonlin-

ear tolerance could be improved using POLMUX signaling. This also confirms the observation in the experimental results that 85.6-Gb/s POLMUX-RZ-DQPSK has a slightly higher nonlinear tolerance in comparison to 42.8-Gb/s RZ-DQPSK. Figure 8.12a shows the nonlinear tolerance of the four considered modulation formats. For a normalized EOP penalty of 2 dB, the difference in input power between 42.8-Gb/s RZ-DPSK and 42.8-Gb/s RZ-DQPSK is 2.5 dB. For 85.6-Gb/s POLMUX-RZ-DQPSK with respect to 42.8-Gb/s RZ-DQPSK the nonlinear tolerance is increased with 1.0 dB for interleaved polarization tributaries and decreased with 1.8 dB for bit-aligned polarization tributaries.

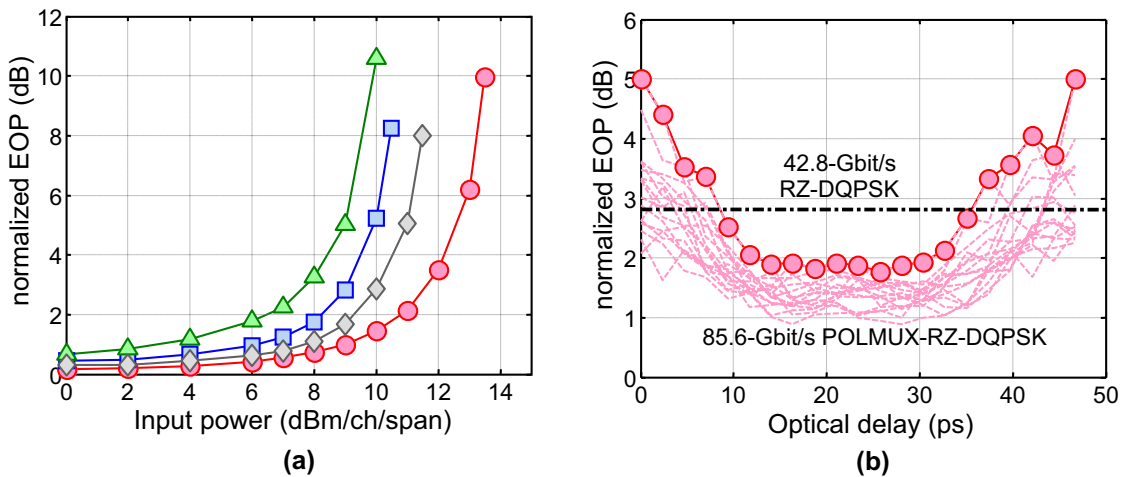


Figure 8.12: (a) Simulated comparison of the nonlinear tolerance for 800-km transmission with  $\circ$  42.8-Gb/s RZ-DPSK,  $\square$  42.8-Gb/s RZ-DQPSK  $\triangle$  85.6-Gb/s POLMUX-RZ-DPSK, bit-aligned  $\diamond$  85.6-Gb/s POLMUX-RZ-DPSK, interleaved; (b) normalized EOP versus inter-pulse delay for a 9-dBm input power. Dotted lines denote tributaries whereas  $\circ$  denote worst case result among all tributaries.

Figure 8.12b shows a similar observation when the inter-pulse delay is varied. A severe bit-pattern dependence is observed in the simulations due to the limited length of the De Bruijn sequence. Therefore simulations have been conducted with different delay between the two polarization tributaries (13, 16, 17, 21 symbols), and worst-case results are denoted here. The dotted horizontal line denotes the penalty obtained for 42.8-Gb/s RZ-DQPSK modulation. The trade-off between nonlinear and DGD tolerance for interleaved in comparison to bit-aligned POLMUX-RZ-DQPSK has significant implications for the use of POLMUX-RZ-DQPSK as a modulation format for long-haul transmission. The use of ultra-low PMD fiber would be required to enable long-haul transmission with interleaved POLMUX-RZ-DQPSK and benefit from its higher nonlinear tolerance. In the absence of PMD compensation, only the DGD tolerance of bit-aligned POLMUX-RZ-DQPSK seems to be large enough to enable medium or long-haul transmission with realistic fiber PMD coefficients. Together with PMD compensation, interleaved POLMUX-RZ-DQPSK transmission can be used to enable long-haul transmission with a high spectral efficiency. Since POLMUX signaling requires anyhow polarization control at the receiver the additional effort of PMD compensation does not significantly increase the transponder complexity. In addition, a digital coherent receiver can realize both polarization control as well as PMD compensation simultaneously.



## 8.3 Transmission with a high spectral efficiency

We now consider the feasibility of high-spectrally efficient transmission in more detail. For binary modulation formats, experimental long-haul transmission results have been reported with a spectral efficiency of 0.8 b/s/Hz. Using terrestrial length fiber spans, a transmission distance of 2,700-km [344] and 3,200-km [345] is feasible for duobinary and RZ-DPSK, respectively. For shorter span length, as common for undersea deployment, transmission distances up to 8,200-km have been bridged [346]. For RZ-DQPSK modulation with a 0.8-b/s/Hz spectral efficiency, long-haul transmission has been reported over 2,800-km (see Chapter 6 and [291]) using terrestrial length fiber spans and over 4,080-km with shorter fiber spans [122], respectively. This shows that a spectral efficiency  $< 1$ -b/s/Hz can be realized in long-haul transmission systems using a number of different modulation formats.

A higher spectral efficiency of 1-b/s/Hz can be realized using DQPSK modulation and a direct detection receiver [15]. In [290], *Yoshikane et. al.* showed the feasibility of 1.6-b/s/Hz spectral efficiency using narrowband filtered RZ-DQPSK. However, RZ-DQPSK modulation has to be severely bandlimited to reach a 1.6-b/s/Hz spectral efficiency, which might not be practical in the presence of optical add-drop multiplexing. Most other transmission experiments with a high spectral efficiency have been reported using POLMUX-RZ-DQPSK modulation, i.e. at 1.6 b/s/Hz [347, 348, 349, 350, 351], 2.0 b/s/Hz [352, 321, 353], 2.5 b/s/Hz [354] and 3.2 b/s/Hz [34]. The transmission experiments are listed in Table 8.2.

In order to realize a  $> 1$ -b/s/Hz spectral efficiency, a suitable choice of both the channel spacing and bit rate is necessary. For a 10...12.5-Gbaud symbol rate [348, 352, 354], the main challenge to obtain a high spectral efficiency is the (de-)multiplexing of the  $\leq 25$ -GHz spaced WDM channels. This requires narrow (de-)multiplexing filters with a near rectangular bandwidth profile at the transmitter, receiver and add-drop points along the link. Using less optimal filters results in linear crosstalk between neighboring WDM channels as well as asymmetric filtering due to the limited wavelength stability of the laser sources. In addition, for closely spaced WDM channels the XPM induced crosstalk can be a significant source of transmission impairments. On the other hand, the OSNR requirement, chromatic dispersion and PMD tolerance are more relaxed for a  $\sim 10$ -Gbaud symbol rate.

At a 40...55-Gbaud symbol rate, multiplexing and de-multiplexing is significantly relaxed as only a 100-GHz [347, 349, 321] channel spacing is required. In addition, the wider channel spacing and higher symbol rate increase the walk-off between WDM channels, making intra-channel nonlinearities the dominant transmission impairment. On the other hand, the reduced chromatic dispersion and PMD tolerance at a  $> 40$ -Gbaud symbol rate will require tunable compensators for most long-haul transmission systems. In particular, the need for active PMD compensation makes it difficult to realize POLMUX signaling at such a symbol rate. The higher symbol rate poses furthermore challenges to the electrical components in the transmitter (MZM, phase modulator) and receiver, which often have a limited bandwidth. In addition, the OSNR requirement and nonlinear tolerance might limit the feasible transmission distance.

## Chapter 8. Polarization-multiplexed DQPSK

Table 8.2: SELECTED TRANSMISSION EXPERIMENTS WITH A SPECTRAL EFFICIENCY  $\geq 1.6$ -B/S/Hz. UNLESS NOTES OTHERWISE ALL EXPERIMENTS USE POLMUX-DQPSK MODULATION.

year	bit rate (Gb/s)	# of WDM channels	Spectral efficiency (b/s/Hz)	Distance (km)	Spans (km) / fiber type	Remarks	Company / Ref
2001	160	40	1.6	80	40 -D/+D	EDFA-only	NICT [347]
2003	40	8	1.6	200	100 SSMF	EDFA-only	U. Kiel, Siemens [348]
2004	85.4	64	1.6	320	80 SSMF	EDFA/Raman RZ-DQPSK	KDDI [290]
2004	50	14	2.0	400	100 SSMF	EDFA-only	CeLight [352]
2005	40	3	2.5	200	100 DSF	EDFA/Raman	U. of Tokyo [355]
2005	160	8	1.6	324	81 SSMF	EDFA/Raman	U. Paderborn [349]
2006	85.6	40	1.6	1,700	94.5 SSMF	EDFA/Raman	TU/e, Siemens [350]
2007	222	102	2.0	240	80 NZDSF	EDFA/Raman	NTT [321]
2007	170.8	160	3.2	240	80 SSMF	EDFA/Raman	Alcatel-Lucent, NICT, Sumitomo [34]
2007	111	10	2.0	2,375	95 SSMF	EDFA/Raman	CoreOptics, TU/e, Siemens [353]
2007	85.6	160	1.6	2,550	65 +D/-D/+D	all-Raman	Alcatel-Lucent [351]

The majority of the deployed WDM transmission systems uses a channel spacing of 50-GHz. A symbol rate around 20...30 Gbaud [350, 351, 353] is therefore the most suitable choice to realize high-spectrally efficient transmission with a sound tolerance towards (de)-multiplexing and optical filtering on a 50-GHz WDM grid. As shown in this chapter, the 21.4-Gbaud symbol enables long-haul transmission due to a combination of component maturity and low OSNR requirement. The nonlinear tolerance of a 20...30 Gbaud symbol rate also compares favorably with lower symbol rates, as intra-channel nonlinear impairments are generally dominant for SSMF-based transmission systems. This limits the penalty due to either XPM or XPolM, hence avoiding POLMUX-specific nonlinear impairments. Although, for other fiber types with a lower chromatic dispersion coefficient (e.g NZDSF) inter-channel nonlinear impairments might still be significant.

In [34], *Gnauck et. al.* showed that a 3.2-b/s/Hz spectral efficiency can be realized using 170.8-Gb/s POLMUX-DQPSK modulation and a 50-GHz channel spacing. This indicates that future

high-capacity optical transmission systems might use a spectral efficiency well above 2-b/s/Hz. However, this will likely require the use of modulation formats with more than 4 bits per symbol in order to realize a sound tolerance to narrowband optical filtering. A potential candidate for modulation with more than 4 bits per symbol is orthogonal frequency division multiplexing (OFDM). As OFDM inherently uses multi-level signals at the transmitter, it is more straightforward to use more dense signal constellations. For example in [356] *Jansen et. al.* showed OFDM-based POLMUX-QPSK modulation and in [357], *Schmidt et. al.* showed the implementation of 4 and 5 bits per symbol using (single-polarization) quadrature amplitude modulation.

## 8.4 Summary & conclusions

Using direct detected 85.6-Gb/s POLMUX-RZ-DQPSK modulation the feasibility of high spectrally efficient long-haul transmission is discussed in this chapter. This shows that the transmission characteristics of POLMUX-RZ-DQPSK modulation are well suited for long-haul transmission as long as PMD is not the dominant transmission impairment.

- An **OSNR requirement** of 15.8-dB is measured for 85.6-Gb/s POLMUX-RZ-DQPSK modulation combined with a direct detection receiver ( $10^{-3}$  BER). The theoretical OSNR requirements for 85.6-Gb/s POLMUX-RZ-DQPSK modulation is 14.6 dB.
- An **optical filter bandwidth** of 34-GHz is found to be optimal for 85.6-Gb/s POLMUX-RZ-DQPSK modulation. This enables long-haul transmission with cascaded optical filtering in a 50-GHz wavelength grid, realizing a 1.6-b/s/Hz spectral efficiency.
- For POLMUX modulation, the **inter-pulse delay** has a significant impact on both the DGD tolerance as well as the impact of intra-channel nonlinear impairments. When both POLMUX tributaries are bit-aligned the DGD tolerance is maximized. In contrast, when both tributaries are interleaved the nonlinear tolerance is increased by about 2 dB. This allows an increase in nonlinear tolerance when POLMUX signaling is used to double the bit rate.
- Using POLMUX-RZ-DQPSK modulation combined with a direct detection receiver, **long-haul transmission** with a 1,700-km feasible transmission distance and 1.6-b/s/Hz spectral efficiency is discussed. This shows that long-haul transmission with a  $>1$ -b/s/Hz spectral efficiency is feasible over a long-haul transmission distance.



---

## Digital direct detection receivers

As discussed in Chapters 4 to 8, the choice of the optical modulation format can substantially increase the transmission tolerances in long-haul transmission links. However, no modulation format has the ideal combination of transmission properties. For example, POLMUX-DPSK modulation has an excellent OSNR requirement and nonlinear tolerance but suffers from a reduced PMD tolerance. DQPSK modulation, on the other hand, supports a high PMD tolerance but has a reduced OSNR requirement and lower tolerance against nonlinear impairments. It is therefore advantageous to combine robust optical modulation formats with analog or digital signal processing, as this can further improve transmission tolerances and can negate some of the drawbacks of the modulation format.

Digital signal processing can be applied either at the transmitter to pre-distort the optical signal or at the receiver. At the transmitter, digital signal processing can be used to electronically pre-compensate for chromatic dispersion [358, 359], intra-channel nonlinear impairments [360, 361] or both impairments simultaneously [362]. The main drawback of pre-distortion is the significant reduction in nonlinear tolerance that occurs when chromatic dispersion is fully compensated at the transmitter [363]. Although intra-channel nonlinear impairments can be compensated using pre-distortion, this is not possible for inter-channel nonlinear impairments. In addition, pre-distortion can not compensate for PMD, which can be a limiting transmission impairment in high bit rate long-haul transmission. This makes pre-distortion a less likely candidate for high bit-rate systems. In this chapter we therefore focus on digital signal processing at the receiver.

In the receiver, the applications of digital signal processing are more extensive and includes the compensation of chromatic dispersion, PMD, nonlinear impairments as well as electrical polarization de-multiplexing and improvements in the back-to-back OSNR requirement [364]. To

---

<sup>1</sup>The results described in this chapter are published in c3, c19, c23, c39, c43

realize most of these receiver-side digital signal processing applications with a minimal performance penalty, the full optical field has to be transferred to the electrical domain. This is the case for a (digital) intra-dyne coherent receiver, as will be discussed in Chapter 10. However, digital signal processing is not limited to coherent receivers. In direct detection receivers, only the amplitude information is transferred to the electrical domain. This reduces the efficiency of digital signal processing, but it can still allow for a significant increase in transmission robustness.

A number of different signal processing algorithms can be used together with direct detection receivers, for example:

- Linear feed-forward or decision-feedback equalizers
- Nonlinear equalizers
- Optical field reconstruction algorithms
- Maximum likelihood sequence estimation (MLSE)

In order to compensate for signal distortions, an equalizer can be used that approximates the inverse of the channel impulse response. The simplest equalizer structure is a linear feed-forward or decision-feedback equalizer [365, 366, 367]. However, such a linear equalizer can only compensate for limited signal distortions as a direct detection receiver is inherently nonlinear due to the squaring function of the photodiode. This can be alleviated through the use of nonlinear equalizers, as shown by *Xia et. al.* in [368] using structures based on nonlinear Volterra theory.

Optical field reconstruction algorithms do not equalize signal impairments but rather generate an improved decision variable. Such algorithms use the amplitude information from the in-phase and quadrature tributary to (partially) reconstruct the optical field in the receiver. This includes multi-symbol phase estimation (MSPE) and field reconstruction based on the inverse tangent of the direct detected components [369]. Once the optical field is reconstructed in the receiver, linear equalizers can be used with higher efficiency. In Section 9.1, MSPE is discussed as a means to improve the OSNR requirement and nonlinear tolerance of D(Q)PSK modulation.

MLSE is another approach to increase the tolerance against linear and nonlinear transmission impairments. It improves the decision variable by basing it on a sequence of symbols rather than on a single symbol. MLSE is a more complex, but also a more versatile approach to distortion compensation than a linear equalizer. The use of MLSE can improve the tolerance against chromatic dispersion, PMD and narrowband filtering [19, 20, 370]. In addition, it can under certain conditions improve the tolerance towards nonlinear transmission impairments [74, 75]. MLSE has shown to provide excellent performance when combined with NRZ-OOK and duobinary modulation [371]. In Section 9.2 we discuss the application of MLSE to DPSK and DQPSK modulation.

## 9.1 Multi-symbol phase estimation

In a direct detection D(Q)PSK receiver, the received signal is demodulated using one or more MZDIs. As discussed in Chapters 4 and 5, this demodulation is suboptimal and results in an OSNR penalty when compared to a coherent receiver. MSPE is a signal processing algorithm that can be used to overcome some of the drawbacks of direct detection and achieve an OSNR requirement close to theoretical optimal performance. It is based on techniques previously proposed for wireless communications [372, 373, 374]. In addition, MSPE can reduce impairments due to nonlinear phase noise and therefore improve the nonlinear tolerance.

Section 9.1.1 introduces the concept of MSPE and Section 9.1.2 discusses the MSPE algorithm. The improvement in back-to-back OSNR requirement is subsequently discussed for 10.7-Gb/s DPSK and 42.8-Gb/s DQPSK (Section 9.1.3). In Section 9.1.4 we analyze the implications of a finite laser linewidth to the MSPE demodulation scheme. Finally, in Section 9.1.5 we focus on reducing the nonlinear phase noise penalty using MSPE demodulation.

### 9.1.1 Multi-symbol phase estimation

MSPE generates an improved decision variable in the electrical domain by using not only the last received symbol but a sequence of the latest received symbols. As this improved decision variable is based on a long sequence of previous symbols, the phase noise in the individual symbols is averaged out. The main difference of the MSPE in comparison to conventional MZDI-based demodulation schemes is therefore that the improved decision variable is less degraded by phase noise. Ideally, the improved decision variable is only impaired by the phase noise of the last received symbol  $x(k)$  instead of the last two symbols as is the case with the decision variable  $x(k)x^*(k-1)$  in a conventional direct detection receiver. Note that this is equal to coherent detection, where the decision variable is also based only on the last received symbol  $x(k)$ . Hence, MSPE potentially closes the performance gap between direct detection and coherent detection.

MSPE demodulates the signal by comparing each symbol from the DPSK signal with the previous symbol of the demodulated sequence. Since the previous symbol is itself based on its predecessor a decision variable is generated that is based on a long sequence of received symbols. In other words, MSPE uses the received in-phase and quadrature components to generate a decision variable that depends recursively on the past received symbols. The recursive algorithm gives a correction term which is added to the conventional decision variable to generate an improved decision variable. In order to make the scheme adaptive and prevent an infinite memory, a forgetting factor  $w$  slowly fades out the contribution from previous symbols. Because MSPE is based on interferometric phase demodulation and does not involve a local oscillator, the forgetting factor  $w$  can be chosen relatively close to 1 without any performance impairments. The scheme proposed in [374] is based on coherent detection and as such suffers a penalty due to the phase drift of the local oscillator, which limits the highest acceptable value of  $w$ . In [375, 376] a similar approach is discussed, which used MZDIs with different bit-delays to generate a more accurate phase estimation in the optical domain.

Figure 9.1 shows the receiver structure that is required for MSPE demodulation. In order to generate the improved decision variable, the MSPE demodulation scheme requires the phase information in the electrical domain. However, as no coherent detection is applied, the phase information cannot be directly transferred to the electrical domain. This is solved by detecting both the in-phase and quadrature component of the received symbol, which together also contain the phase of the received signal. Hence, two MZDIs are necessary with a  $\pi/2$  difference in the phase shift between both arms. This can be either a  $-\pi/4$  and  $\pi/4$  phase difference as in a conventional DQPSK receiver or a 0 and  $\pi/2$  phase difference for the two MZDIs, respectively.

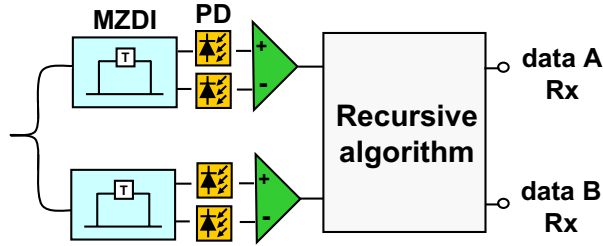


Figure 9.1: MSPE receiver structure for either DPSK or DQPSK modulation.

The MSPE algorithm can also be used for modulation formats that combine phase and amplitude modulation. This requires a third branch in the receiver with a single-ended photodiode to detect the intensity of the optical field [377].

### 9.1.2 The MSPE algorithm

The recursive MSPE algorithm is now based on the following principle. Consider a received signal,

$$r(t) = \sqrt{P_s} \exp(j[\omega_0 t + \varphi(t)]), \quad (9.1)$$

where  $\sqrt{P_s} \exp(j\varphi(t)) = x_I(t) + j \cdot x_Q(t)$  is the complex envelope of the signal  $x(t)$  in the absence of phase noise. After balanced detection and electrical low-pass filtering two components  $u_I(t)$  and  $u_Q(t)$  are obtained containing the in-phase and quadrature components, respectively:

$$\begin{cases} u_I(t) = \Re\{x(t)x^*(t - \Delta T)\} \\ u_Q(t) = \Im\{x(t)x^*(t - \Delta T)\}. \end{cases} \quad (9.2)$$

This can be realized with two MZDIs, one with a phase shift between the arms of  $\Delta\phi = 0$  and one with a phase shift of  $\Delta\phi = \pi/2$

For simplicity we now introduce a time discrete notation where  $t = kT_0 + t'$ , with  $-T_0/2 \leq t' \leq T_0/2$ . Considering the optimal sampling point in the bit interval we assume  $t' = 0$  and the signals are further denoted as time discrete samples. The recursive algorithm now replaces the *conventional* decision variable  $x(k)x^*(k-1)$  with the *improved* decision variable  $x(k)z^*(k-1)$  [374], where  $x(k)$  is the currently received symbol.  $z(k)$  is a recursive component,

$$z(k-1) = x(k-1) + w \cdot \exp(+jc(k-1)) \cdot z(k-2), \quad (9.3)$$



where  $0 \leq w \leq 1$  is the forgetting factor. The binary factor  $c(k-1)$  rotates the previous symbol  $z(k-2)$  to align it with  $x(k-1)$ . However, Equation 9.3 can only be implemented together with coherent detection because not  $x(k)$ , but only  $x(k)x^*(k-1)$  is available after demodulation with an MZDI. As a result, Equation 9.3 cannot be directly implemented. The recursive component  $z(k)$  in Equation 9.3 is therefore replaced by the following approximation,

$$y(k) = u_I(k) + w \cdot u(k) \cdot \exp(-jc(k-1)) \cdot y(k-1), \quad (9.4)$$

where  $u(k) = u_I(k) + j \cdot u_Q(k)$ . Note that the term  $\exp(-jc(k-1))$  is a straightforward multiplication with either  $-1$  or  $1$ , depending on the binary value of  $c(k-1)$ .

We now show that a similar OSNR requirement can be expected for a receiver that uses either the algorithm in Equations 9.3 or 9.4. When we assume that the MSPE receiver demodulates the correct symbol we can express  $y(k-1)$  as,

$$\tilde{y}(k-1) = y(k-1) \cdot \exp(-jc(k-1)). \quad (9.5)$$

Equation 9.4 can then be written (for DPSK modulation) as,

$$y(k) = u_I(k) + w \cdot u(k) \cdot \tilde{y}(k-1). \quad (9.6)$$

The output of the MZDI  $u(k)$  equals  $x(k)x^*(k-1)$  which changes Equation 9.6 into,

$$y(k) = \Re\{x(k)x^*(k-1)\} + w \cdot x(k)x^*(k-1) \cdot \tilde{y}(k-1). \quad (9.7)$$

We can unroll the recursion in Equation 9.6, but for simplicity we assume that for symbol  $y(k-1)$  the conventional and improved decision variable are equal, e.g.  $y(k-1) = u(k-1) = x(k-1)x^*(k-2)$ . Using this approximation in Equation 9.7 results in,

$$y(k) \approx \Re\{x(k)x^*(k-1)\} + w \cdot x(k)x^*(k-1) \cdot \tilde{x}(k-1)x^*(k-2), \quad (9.8)$$

where  $\tilde{x}(k) = x(k) \cdot \exp(-jc(k))$ . This gives,

$$y(k) \approx \Re\{x(k)x^*(k-1)\} + w \cdot x(k)\tilde{x}^*(k-2), \quad (9.9)$$

The improved decision variable thus consists partly of the most recent symbol  $x(k)$  and a contribution from the previous symbols  $x(k-1)$  and  $\tilde{x}(k-2)$ . In Equation 9.3 there is no contribution from previous symbols, and it therefore results in the theoretically optimal performance. The contribution from the previous symbols in Equation 9.4 somewhat impacts the performance of the MSPE algorithm, and this causes the slight difference in OSNR requirement that we will find between MSPE and the theoretically optimal performance of a coherent receiver.

In Figure 9.2 the principle of MSPE is visualized using a signal constellation diagram *after interferometric demodulation*. Combining the in-phase and quadrature components, each received symbol can be considered as a vector in the complex phase plane. In a conventional direct detection receiver, the binary decision would be '0' for  $\Re\{u(k)\} < 0$  and '1' for  $\Re\{u(k)\} > 0$ .

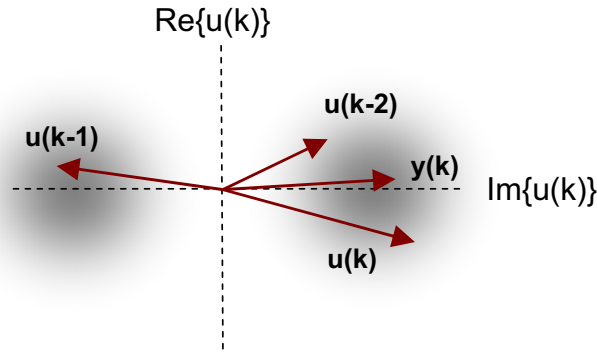


Figure 9.2: Generation of the improved decision variable.

The MSPE algorithm now constructs an improved decision variable  $y(k)$  using the sequence of received symbols in Figure 9.2 such that,

$$\begin{aligned}
 y(k) &= \Re\{u(k)\} + w \cdot u(k) \cdot \Re\{u(k-1)\} \\
 &- w^2 \cdot u(k-1) \cdot \Re\{u(k-2)\} + w^3 \cdot u(k-2) \cdot \Re\{u(k-3)\} + \dots
 \end{aligned}
 \tag{9.10}$$

The MSPE demodulation scheme can be implemented with either analog, as discussed here, or digital signal processing [378]. In the case of digital signal processing, the most straightforward implementation is to convert the decision variables  $u_I(k)$  and  $u_Q(k)$  into digital samples. Note that the performance of the MSPE demodulation scheme with a digital implementation depends on the granularity of the ADCs, which is not considered here. An analog implementation of the MSPE demodulator for DPSK modulation is shown in Figure 9.3. This implementation requires a complex four-quadrant multiplication, an attenuation to implement the forgetting factor  $w$  and a delay line with a bit-delay  $\Delta T$  to multiply  $u(k)$  with the previous decision variable  $x(k-1)$ . The improved decision variable  $c(k)$  is obtained from the real part of the improved decision variable  $x(k)$  after binary decision with a D-flip-flop (D-FF). Note that the upper MZDI on itself demodulates the in-phase tributary of the DPSK signal, which gives the conventional decision variable  $u_I(k)$  and is therefore equivalent to a conventional direct detection DPSK receiver.

### 9.1.3 MSPE demodulation for 10.7-Gb/s DPSK & 42.8-Gb/s DQPSK

Figure 9.4a shows the improvement in OSNR requirement with MSPE demodulation when only Gaussian noise is present. Simulations are based on the Monte-Carlo approach with a random bit sequence of  $5 \cdot 10^6$  bits. The simulated BER is compared for a  $10^{-4}$  BER because lower BERs are impractical to simulate using the Monte-Carlo approach. The sensitivity improvement due to MSPE increases for higher values of the forgetting factor  $w$ , approaching the performance of coherent detection with differential decoding. For a  $10^{-4}$  BER, the difference between MSPE ( $w = 0.9$ ) and conventional direct detection is  $\sim 0.5$  dB. The difference between MSPE ( $w = 0.9$ ) and differential coherent detection is negligible, effectively closing the gap in OSNR requirement between coherent detection and direct detection.

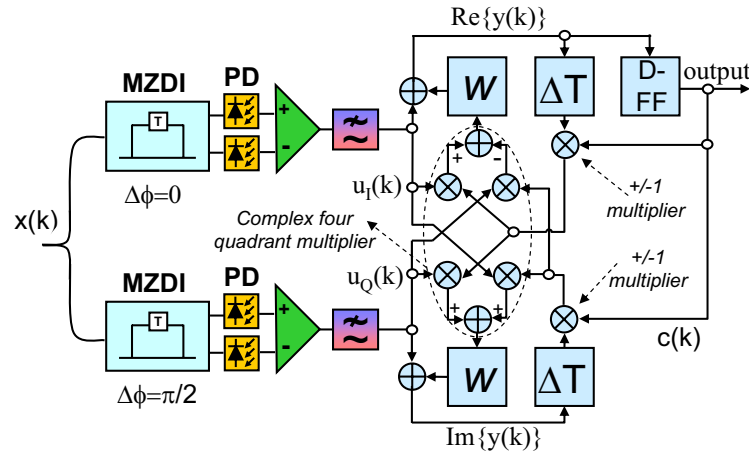


Figure 9.3: Implementation of the MSPE algorithm for DPSK.

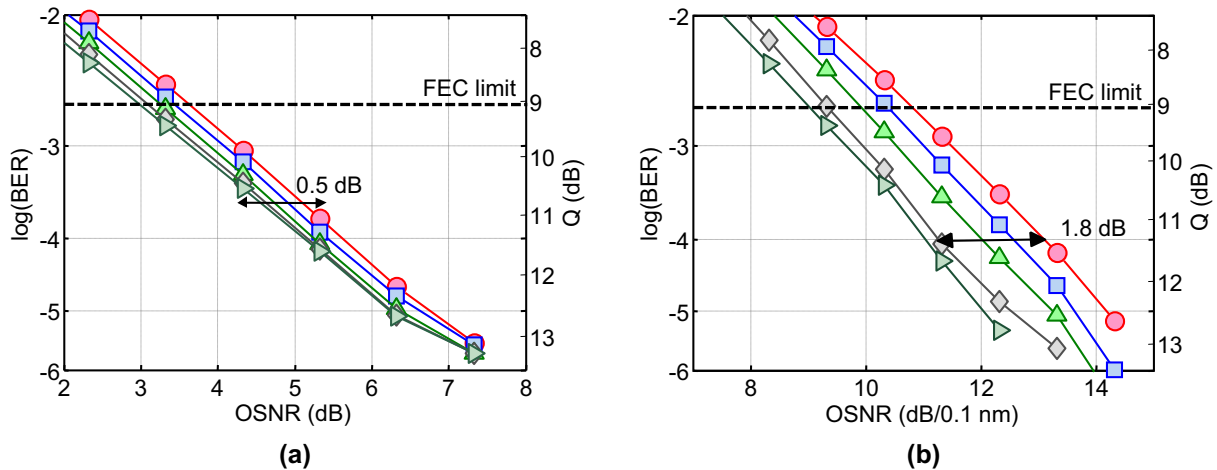


Figure 9.4: Performance of (a) 10.7-Gb/s DPSK and (b) 42.8-Gb/s DQPSK modulation with MSPE for Gaussian noise and several values of the forgetting factor  $w$ ;  $\circ$  conventional direct detection  $\square$  MSPE with  $w = 0.2$ ,  $\triangle$  MSPE with  $w = 0.5$ ,  $\diamond$  MSPE with  $w = 0.9$ ,  $\triangleright$  differential coherent detection

The MSPE demodulation scheme can be easily extended to DQPSK modulation. An analog implementation of the MSPE demodulator for DQPSK modulation is shown in Figure 9.5. Similar to a conventional direct detection DQPSK receiver, two MZDIs are necessary to demodulate the signal. In comparison to the MSPE implementation for DPSK, the quadrature part of the signal is used to obtain the second output  $c_Q(k)$  from the imaginary part of the improved decision variable  $y(k)$ . The  $\pm 1$  multipliers are exchanged with a complex  $\pm 1$  multiplier because both the  $c_I(k)$  and  $c_Q(k)$  outputs have to be taken into account and  $c(k)$  now takes a value of the set  $\{1, j, -1, -j\}$ . Note that the forgetting factor  $w$  now has to be scaled with a factor  $\sqrt{2}$ . The optical components necessary to realize the MSPE demodulation scheme are the equal to a conventional DQPSK receiver. Hence, the overhead of using MSPE in combination with DQPSK modulation is limited to (potentially inexpensive) electronic signal processing.

Figure 9.4b shows the performance of the MSPE demodulation scheme with DQPSK modulation when only Gaussian noise is present. Similar to the results for DPSK modulation, Monte-Carlo

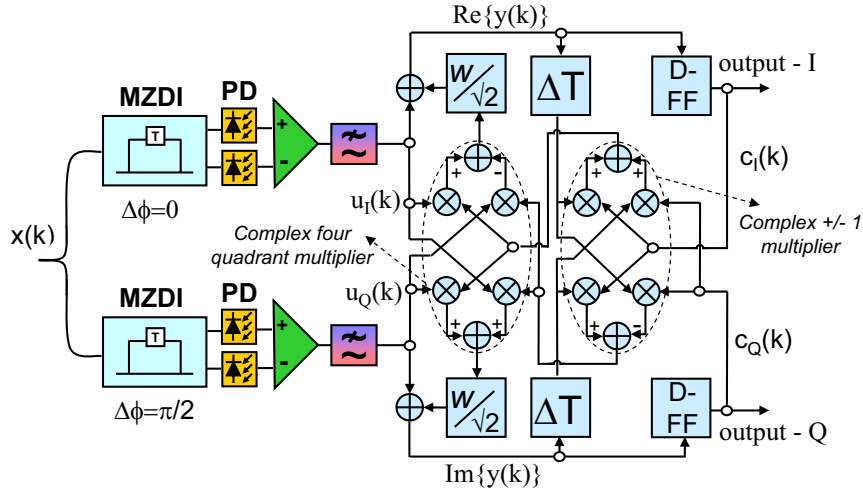


Figure 9.5: Implementation of the MSPE algorithm for DQPSK.

simulations are used and every point is simulated with a  $2 \cdot 10^6$  symbols long random sequence. The performance gain with MSPE demodulation is considerably larger due to the larger theoretical difference between coherent and direct detection DQPSK. For MSPE with  $w = 0.9$ , the difference amounts to 1.8 dB for a  $10^{-4}$  BER, which is only a 0.2-dB difference with respect to coherent detection (with differential decoding). When one considers that the same optical components and nearly the same signal processing is required for MSPE with either DPSK or DQPSK modulation, DQPSK seems to be the most logical application of MSPE demodulation.

### 9.1.4 Laser linewidth requirements

PSK modulation is generally sensitive to phase noise, for example, resulting from a finite laser linewidth. With conventional direct detection, only the phase difference between two subsequent symbols determines the sensitivity penalty. This makes direct detection robust against phase noise. At a 10.7-Gb/s bit rate and for a 0.5-dB OSNR penalty the transmitter laser requires a linewidth less than 30-MHz linewidth [379]. Savory and Hadjifotiou derived for a similar penalty the maximum allowable linewidth with DQPSK modulation and a self-homodyne receiver, which equals 8 MHz [380]. Standard DFB lasers can have a linewidth in the order of 1-3 MHz [381], which is sufficient for both DPSK and DQPSK direct detection at a 10.7-Gb/s bit rate.

MSPE uses a sequences of symbols to compute the improved decision variable. When the phase noise between those symbols is uncorrelated (zero mean) the estimate will be improved by using more symbols. However, the phase noise resulting from a finite laser linewidth is correlated and therefore does not average out when more symbols are taken into account. The phase noise of a Lorentzian-shaped laser linewidth can be described as a random walk Wiener process using

$$\phi_{PN}(t) = \sum_{m=-\infty}^{m=t} v_m, \tag{9.11}$$

where  $v_m$  are independently Gaussian distributed random variables with zero mean and variance  $\sigma^2 = 2\pi\Delta\nu T_0$ .  $\Delta\nu$  is the beat linewidth, which is the sum of the 3-dB linewidth of the signal and LO lasers, and  $T_0$  is the symbol period [382]. In the time discrete simulations the laser linewidth is now modeled as random walk phase noise [383].

$$\phi_{PN}(t) = \phi_{PN}(t - T_0) + N(0, 2\pi\Delta\nu T_0), \quad (9.12)$$

where  $N(0, \sigma^2)$  is a Gaussian distribution random variable. The phase-noise degraded signal is then defined according to,

$$s_{PN}(t) = s(t)\exp[i\phi_{PN}(t)]. \quad (9.13)$$

With MSPE demodulation, the number of symbols that is taken into account to compute the decision variable depends strongly on the forgetting factor. When the laser linewidth is not negligible, the forgetting factor is upper bounded. A too high linewidth will result in a performance penalty because linewidth-induced phase noise reduces the accuracy of the improved decision variable. Figure 9.6a shows the performance of MSPE as a function of laser linewidth for 10.7-Gb/s DPSK. A laser linewidth lower than  $\sim 4$  MHz is required for a  $w = 0.9$  forgetting factor. This is a significant reduction in comparison to conventional direct detection, but the tolerance is still sufficient to use a typical DFB laser. For 42.8-Gb/s DQPSK modulation the linewidth requirements are significantly higher, as shown in Figure 9.6b. For a  $w = 0.9$  forgetting factor the maximum allowable linewidth is now 1.5 MHz (for a 1-dB penalty). However, when a  $w \cong 0.8$  forgetting factor is used the linewidth tolerance increases to  $\sim 3$  MHz. And for a 2-dB penalty, the linewidth requirement increases to 10 MHz by sufficiently lowering the forgetting factor to  $w = \cong 0.5$ . Hence, it can be beneficial to make the forgetting factor  $w$  adaptive in order to obtain the maximum performance for a certain laser linewidth.

We can compare the linewidth tolerance of MSPE with (analog) coherent detection. For coherent detection, a too high laser linewidth results in phase noise degradations through beating between transmitter and local oscillator (LO) laser. Coherent detection therefore, generally, requires a much narrower linewidth compared to direct detection. For 10-Gbaud (D)PSK modulation and a 0.5-dB sensitivity penalty, *Norimatsu* derived in [384] that both transmitter and LO laser require a laser linewidth below 8 MHz. For coherent detection of QPSK, the allowable laser linewidth is reduced even further. In [385], *Barry and Kahn* reported that a beat linewidth lower than 500 kHz is required (at 5-Gbaud and for a 0.5-dB penalty). This implies that both the transmitter and LO laser require a laser linewidth narrower than 250 kHz. When we scale this to a 42.8-Gb/s bit rate, we obtain 500 kHz or 1 MHz for 10-Gbaud POLMUX-QPSK and 20-Gbaud QPSK modulation, respectively. This tolerance is not sufficient to use standard DFB lasers and an analog coherent receiver requires therefore ECL. With ECL a linewidth below 200 kHz is feasible [386]. However, such lasers are generally not used in conventional optical transponders as it is difficult to realize full C-band tunable ECL.

*Digital* coherent detection is largely similar in terms of its tolerance against laser linewidth. For 42.8-Gb/s POLMUX-QPSK with a digital coherent receiver, a beat linewidth of 1.4 MHz is reported for a 1-dB OSNR penalty at  $10^{-3}$  BER [382]. Scaling this to a 20-Gbaud symbol rate gives a beat linewidth of 2.8 MHz, which is similar to the requirement for MSPE. With the exception that MSPE uses only a transmitter laser whereas for digital coherent detection the

beat linewidth is divided over the LO and transmitter laser. Another detection scheme that is very tolerant to laser linewidth is proposed in [387], where a LO is used in combination with differential detection. However this scheme comes at the cost of an  $>3$  dB increase in OSNR requirement.

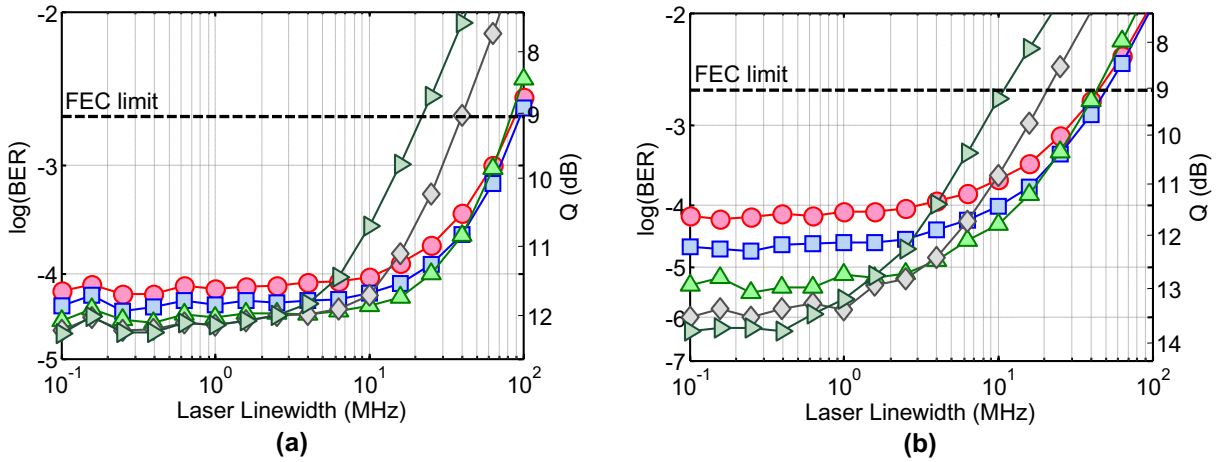


Figure 9.6: Performance of (a) 10.7-Gb/s DPSK and (b) 42.8-Gb/s DQPSK modulation with MSPE for different laser linewidth and several values of the forgetting factor  $w$ ;  $\bullet$  conventional direct detection,  $\square$  MSPE with  $w = 0.2$ ,  $\blacktriangle$  MSPE with  $w = 0.5$ ,  $\blacklozenge$  MSPE with  $w = 0.8$ ,  $\blacktriangleright$  MSPE with  $w = 0.9$ .

### 9.1.5 Nonlinear phase noise compensation

Besides a finite laser linewidth, nonlinear phase noise can also degrade signal quality in PSK systems, as discussed in Section 2.4.7. The reduction of nonlinear phase noise through MSPE results from the recursive decision variable, which averages out the phase uncertainty over a long sequence of received symbols. With MSPE, the decision variable ideally only depends on a single symbol  $x(k)$  instead of  $x(k)x^*(k-1)$  as for interferometric demodulation. MSPE therefore potentially halves the magnitude of nonlinear phase noise, which can significantly reduce the associated penalty. Another advantage of the nonlinear phase noise reduction through MSPE is that it is unimportant what the source of the phase noise is. Compensation schemes that use the correlation between intensity and nonlinear phase shift in the received symbol are restricted to compensation of SPM induced nonlinear phase noise. However, MSPE reduces the influence of phase noise in general; as long as the noise sequence is uncorrelated and has a zero-mean distribution. Hence, the impact of XPM induced nonlinear phase noise is also reduced through the use of MSPE. This can for example be important for D(Q)PSK transmission in the presence of co-propagating OOK modulated channels [293].

Figure 9.7a shows for 10.7-Gb/s DPSK the performance improvement of MSPE in the presence of nonlinear phase noise. Simulated is single channel transmission over 30 x 90-km spans with the ASE added along the transmission line. Fiber attenuation is  $\alpha = 0.25$  dB/km and fiber non-linearity  $\gamma = 1.3 \text{ W}^{-1}\text{km}^{-1}$ , the influence of dispersion is neglected for simplicity [95]. In order to change the OSNR, the noise figure of the in-line amplifiers along the link is changed. For low

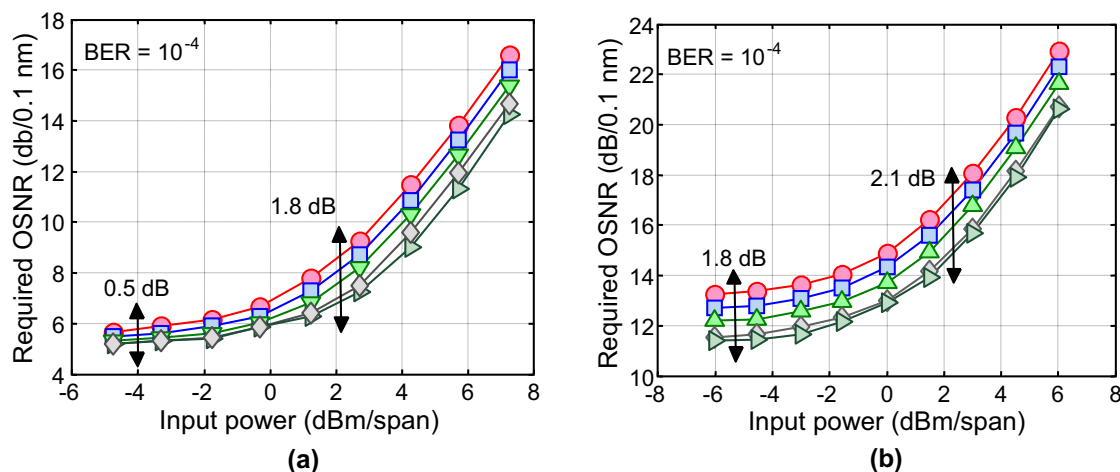


Figure 9.7: Nonlinear tolerance of (a) 10.7-Gb/s DPSK and (b) 42.8-Gb/s DQPSK with MSPE and several values of the forgetting factor  $w$ ;  $\bullet$  conventional direct detection  $\square$  MSPE with  $w = 0.2$ ,  $\blacktriangle$  MSPE with  $w = 0.5$ ,  $\blacklozenge$  MSPE with  $w = 0.9$ ,  $\blacktriangleright$  differential coherent detection.

input power the simulated OSNR requirement differs 0.5 dB between MSPE and conventional direct detection, which is also observed in the back-to-back case. When the input power is increased to 2.1 dBm per span, the required OSNR for the conventional direct detection receiver is 8.7-dB (3-dB penalty). However, for MSPE ( $w=0.9$ ) the required OSNR is only 6.9 dB, which gives a 1.8 dB improvement over conventional direct detection. Alternatively, we can define the nonlinear tolerance as the input power for which a 3-dB OSNR penalty is obtained. In this case MSPE increases the nonlinear tolerance from 2.1 dBm to 3.6 dBm per span. For 42.8-Gb/s DQPSK transmission, the performance of MSPE in the presence of nonlinear phase noise is shown in Figure 9.7b. The link parameters used in the simulation are the same as for 10.7-Gb/s DPSK. The MSPE improvement with ( $w = 0.9$ ) for a  $10^{-4}$  BER is with 2.1 dB comparable to the performance gain in the presence of only Gaussian noise. This can be understood from the constellation diagrams in Figure 9.8, which show a 10.7-Gb/s DPSK and 42.8-Gb/s DQPSK signal with nonlinear phase noise. The same link parameters are used as in Figure 9.7, with a 3-dBm input power per span. The received OSNR is 5.6 dB and 13.1 dB, respectively, which result back-to-back in a BER of  $10^{-4}$ . Comparing the two constellation diagrams shows a significantly larger nonlinear phase noise impact in the case of 10.7-Gb/s DPSK, despite the fact that the nonlinear phase shift is the same for both cases. The more pronounced impact of nonlinear phase noise for 10.7-Gb/s DPSK modulation is a result of the lower OSNR along the link. This indicates that the lack of an improvement in nonlinear tolerance through MSPE demodulation is a result of the smaller impact of nonlinear phase noise for 42.8-Gb/s DQPSK modulation. Comparing Figures 9.7a and 9.7b further shows that the different in nonlinear tolerance between DPSK and DQPSK is 0.8 dB (for a 3-dB OSNR penalty). This indicates that the larger difference observed in Section 5.4 results from the interaction between fiber nonlinearity and chromatic dispersion, rather than from nonlinear phase noise.

We note that the simulations discussed here do not include chromatic dispersion and therefore only the reduction in nonlinear phase noise is observed. When chromatic dispersion is included, the improvement in nonlinear tolerance can be more significant, as experimentally shown by *Lui*



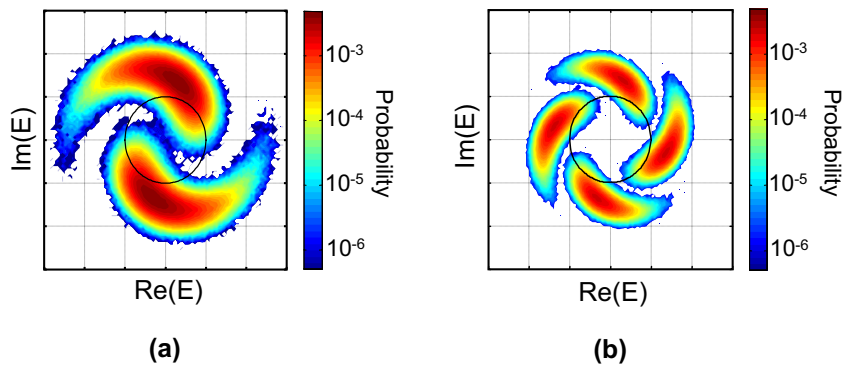


Figure 9.8: Simulated constellation diagrams of (a) DPSK and (b) DQPSK modulation with nonlinear phase noise.

*et. al.* in [378]. A further improvement in nonlinear tolerance might be realized by combining MSPE with a nonlinear phase noise compensation scheme that employs the correlation between intensity and nonlinear phase shift. This has been shown to provide an improvement of the nonlinear tolerance when a digital coherent receiver is used [256].

## 9.2 Maximum likelihood sequence estimation

Arguably the most important application of signal processing in an optical receiver is increasing the tolerance with respect to (linear) transmission impairments such as chromatic dispersion and PMD. This allows for simpler system design and can alleviate the need for optical compensation of these transmission impairments. A maximum likelihood sequence estimation (MLSE) receiver searches for the transmitted sequence that has the highest probability of producing the received sequence. Such a receiver is therefore the theoretically optimal receiver for a transmission channel with ISI.

In Section 9.2.1 we introduce the principle of MLSE and a Viterbi receiver. Subsequently, in Sections 9.2.2 and 9.2.3 we discuss the performance of MLSE with OOK and DPSK modulation, respectively. To improve the performance of MLSE with DPSK modulation, either joint-decision MLSE (Section 9.2.4) or partial DPSK (Section 9.2.6) can be used. Finally, for DQPSK modulation we discuss in Section 9.2.7 the use of joint-symbol MLSE.

### 9.2.1 The MLSE algorithm

Figure 9.9a shows a received OOK modulated sequence with significant chromatic dispersion induced pulse broadening. The amplitude of the middle '0' of a '101' sequence (at  $4T$ ) is broadened through the ISI of the trailing and leading '1's. This implies that the '0' amplitude differs depending on the two surrounding symbols and will be higher for a '101' than for a '001' sequence (e.g. at  $6T$ ). As this difference is deterministic, the receiver can assign a different



probability to each of the possible received sequences as a function of the received amplitude in the '0'. This can be described using conditional probability density functions (PDF), with the surrounding symbols as the condition. The accuracy in which the PDF models the channel characteristics is determined by the channel memory, e.g. the number of surrounding symbols that is taken into account. For example, if the PDF takes only the two surrounding symbols into account, it assumes that the channel has an impulse response of three symbol periods.

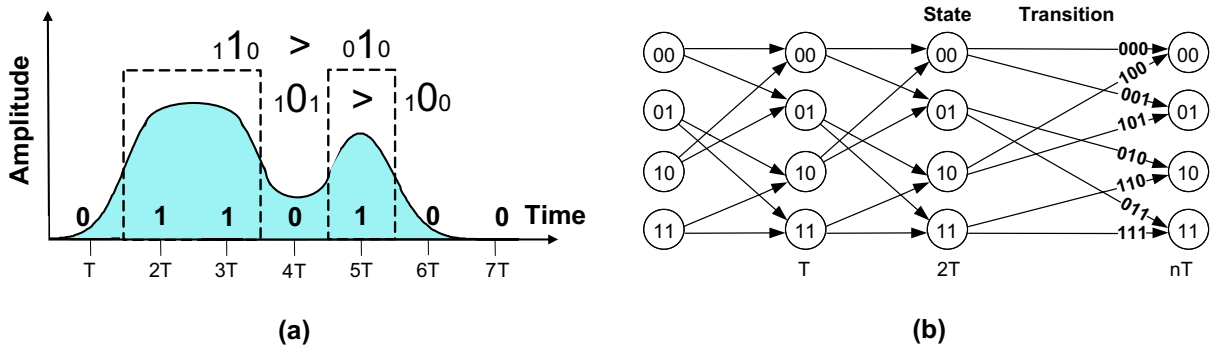


Figure 9.9: (a) Deterministic ISI resulting from chromatic dispersion and (b) trellis diagram with 4 states.

To discuss the concept of MLSE we first consider a channel with no memory. The signal's alphabet  $A = \{A_1, A_2, \dots, A_N\}$  consists of  $N$  possible symbols and each symbol is transmitted with an equal probability  $1/N$ . Note that the alphabet size is defined through the bits per symbol of the modulation format (e.g. 2 for OOK/DPSK and 4 for DQPSK). The received sequences is a vector  $r(k)$ , which contains  $K$  samples taken from the continuous received signal  $r(t)$  at sample points  $t = kT_0 + t'$ , with  $-T_0/2 \leq t' \leq T_0/2$ .

The *a posteriori* probability  $P(A_i|r_k)$  can now be defined as the probability that the symbol  $A_i$  is transmitted when the sample  $r_k$  is detected. The optimal decision then looks for the symbol that has the maximum a posteriori probability among all of the symbols in the alphabet  $A$ ,

$$P(A_i|r_k) > P(A_j|r_k) \quad \forall \quad i \neq j. \tag{9.14}$$

This is known as the a posteriori probability, because the decision is made after receiving the sample  $r_k$  [388]. According to Bayer's theorem of probability, the a posteriori probability can be written as,

$$P(A_i|r_k) = \frac{P(r_k|A_i) \cdot P(A_i)}{P(r_k)}. \tag{9.15}$$

The terms  $P(r_k)$  and  $P(A_i)$  are equal for all a posteriori probabilities and can therefore be neglected. This simplifies Equation 9.14 to,

$$\hat{A} = \underset{i}{\operatorname{argmax}}(P(r_k|A_i)) \quad \forall \quad i = 1, 2, \dots, N, \tag{9.16}$$

where  $P(r_k|A_i)$  is the probability that  $r_k$  is received when the symbol  $A_i$  is transmitted. The term  $\operatorname{argmax}(P(r_k|A_i))$  defines the value of  $A_i$  that maximizes  $P(r_k)$ . For example, for a binary signal  $A = \{0, 1\}$  the decision can then be written as,

$$\hat{A} = \begin{cases} 0 & P(r_k|A_0) > P(r_k|A_1) \\ 1 & \text{otherwise} \end{cases} \tag{9.17}$$

This is equal to the decision of a conventional CDR receiver as discussed in Section 3.1.2. An MLSE receiver does not consider only the received symbol, but rather the received sequence in order to obtain the maximum a posteriori probability decision. This can be written as,

$$\hat{S} = \underset{i}{\operatorname{argmax}} \left( \prod_{k=1}^K P(r_k | A_i^k) \right) \quad \forall \quad i = 1, 2, \dots, N, \quad (9.18)$$

where  $\hat{S}$  is the sequence with the maximum a posteriori probability and  $A_i^k$  is the set of all the possible symbols representing sample  $r(k)$ . This can be simplified by changing the multiplication into a summation by taking the natural logarithm function of the a posteriori probability. The natural logarithm function is monotonic and Equation 9.18 can now be rewritten as,

$$\hat{S} = \underset{i}{\operatorname{argmax}} \left( \sum_{k=1}^K \ln[P(r_k | A_i^k)] \right) \quad \forall \quad i = 1, 2, \dots, N. \quad (9.19)$$

Equation 9.19 implies that  $N^K$  sequences have to be taken into account to determine the maximum a posteriori probability. This increases exponentially with the length of the sequence and the alphabet size, which is not practical. The MLSE estimation process is therefore based on the Viterbi algorithm as first proposed by *Forney* in 1972 [389]. The Viterbi algorithm can be represented by means of a trellis diagram that consists of  $N^L$  states and  $N^{L+1}$  states transitions, where  $N$  is the alphabet size and  $L$  is the memory length. Each transition  $m_i(k)$  in the trellis diagram is associated with one of the PDFs of the channel. Figure 9.9b shows an example of a trellis diagram for a two bit channel memory and binary modulation. The trellis diagram has  $2^2$  possible states and  $2^3$  state transitions. After sample  $k$  is received and quantized with quantization level  $r_k$ , the channel histogram is used to find the conditional probability  $P(r_k | S_i)$  associated with each of the channels conditional PDFs. For instance, for  $L = 2$  the transition '010' is associated with the PDF  $P(r_k | 010)$ , which is the probability that the sample  $r_k$  represents a '1' symbol, preceded and followed by '0' symbols. This means that a received '1' has four different conditional PDF functions.

To make the optimum decision on a received symbol, MLSE requires that the PDFs correctly represent the distortions in the optical channel. This is possible by training the MLSE with a known sequence. Alternatively, blind estimation can be used through feedback signals from the forward error correction or more advanced blind channel estimation algorithms [390]. Once the PDFs are obtained this information can be used to calculate the metrics of the trellis's state transitions. This is possible through different algorithms of which we use here both the histograms method and the Gaussian model method. The histograms technique builds discrete PDFs for all of the possible transitions in the trellis diagram, which are quantized with a vertical resolution of  $Q$  bits. Subsequently, the a posteriori probabilities for each state transition at each quantization level  $P(r | S_i)$  are determined, which gives the PDFs or histograms [391]. The histograms are stored in a look-up table, which contains a total of  $2^Q \cdot N^{L+1}$  values. The look-up tables are then used to compute the metric for each of the transitions in the trellis. For example, the metric of the state transition  $m_i(k)$  can be expressed as,

$$m_i(k) = m_j(k-1) + \ln[P(r_k | S_i)], \quad (9.20)$$

where  $m_j(k-1)$  is the metric of the transition that leads to state  $S_i$ . For each of the  $N^L$  states in the trellis, the metrics of the  $N$  incoming paths are compared and the path with the highest metric survives, while the others are canceled out. Repeating this procedure for  $K$  samples results in  $N^L$  surviving paths, each having a different total metric and a different path through the trellis. The trellis path of the sequence with the maximum probability is considered to represent the maximum likelihood sequence. This implies that using the Viterbi algorithm, the complexity is reduced from searching through  $N^K$  down to  $K \cdot N^{L+1}$  sequences.

Figures 9.10a and 9.10b depict two examples of histograms, for back-to-back and 2000 ps/nm of chromatic dispersion, respectively. The y-axis shows the transitions in the trellis diagram for a channel with a 2-symbol memory, where the x-axis represents the quantization bins for a 4-bit vertical resolution. The z-axis shows the probability for each quantization bin/transition.

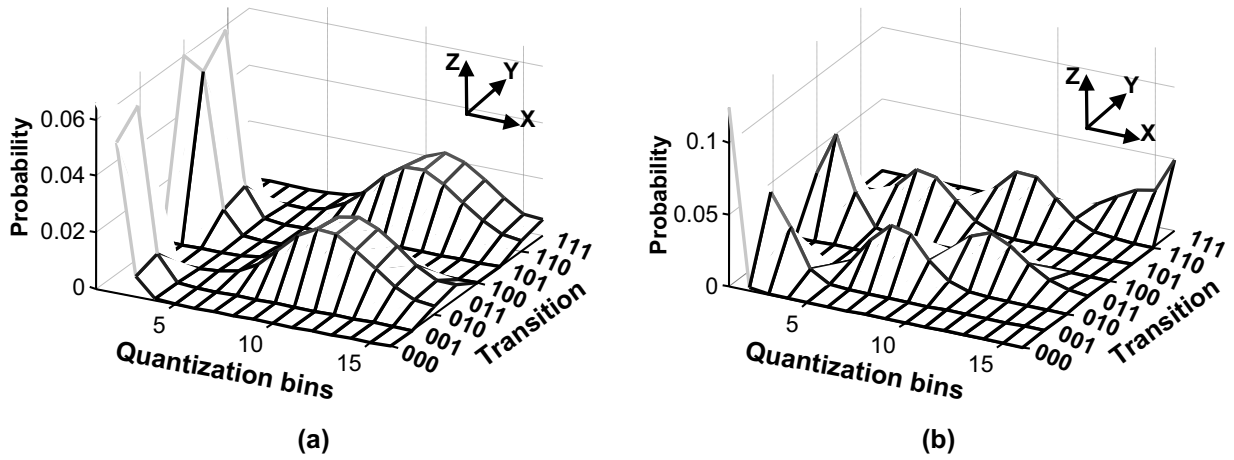


Figure 9.10: MLSE histograms for (a) 0-ps/nm chromatic dispersion and (b) 2000-ps/nm chromatic dispersion.

The Gaussian model method uses a somewhat simpler channel model as it assumes that the PDF functions associated with a specific channel have Gaussian distributions. This method determines the sequence that maximizes the Gaussian a posteriori probability defined as,

$$\hat{S} = \underset{i}{\operatorname{argmax}} \sum_{k=1}^K \ln \left( \frac{1}{\sqrt{2\pi}\sigma_i} \exp \left( -\frac{(r_k - \mu_i)^2}{2\sigma_i^2} \right) \right) \quad \forall i = 1, 2, \dots, N, \quad (9.21)$$

where  $\mu_i$  is the mean of the Gaussian PDF associated with state transition  $m_i$ , and  $\sigma_i$  is the PDF variance. When the variance of all PDFs is assumed to be equal, Equation 9.21 can be simplified into,

$$\hat{S} = \underset{i}{\operatorname{argmin}} \sum_{k=1}^K (r_k - \mu_i)^2 \quad \forall i = 1, 2, \dots, N. \quad (9.22)$$

The Gaussian model method assumes that the sample belongs to the state  $S_i$  of which the mean is nearest to the received sample  $r_k$  [392]. Minimizing the sum of these distances for  $K$  successive samples maximizes the probability that the sequence has been correctly estimated. Only the

mean of each of the PDFs is now extracted from the training sequence and a total of  $N^{L+1}$  values are stored in the look-up table. Hence, the Gaussian model method is somewhat less complex in comparison to the histogram technique. The assumption that all PDFs have the same variance is generally valid in the presence of significant signal distortions.

An additional property of electronic equalization is that only limited signal distortions can be tolerated using baud rate sampling (1 sample per symbol)[392]. It is therefore advantageous to sample at a multiple of the baud rate in an MLSE receiver. Equations 9.19 and 9.20 then changes into,

$$\hat{S} = \underset{i}{\operatorname{argmax}} \sum_{k=1}^K \sum_{h=1}^H \ln[P(r_{h,k}|A_i^k)] \quad \forall \quad i = 1, 2, \dots, N \quad (9.23)$$

$$m_i(k) = m_j(k-1) + \sum_{h=1}^H \ln[P(r_{h,k}|S_i)], \quad (9.24)$$

where  $H$  is the number of samples per symbol. Note that this increases the size of the look-up table but does not change the size of the trellis. Sampling at twice the baud rate ( $H=2$ ) is generally used in the literature. An MLSE receiver with two-fold over-sampling can tolerate an arbitrary amount of chromatic dispersion given that it uses a sufficiently large channel memory, as shown by *Poggiolini et. al.* in [393]. For MLSE receivers without over-sampling, the dispersion tolerance can be increased through narrowband optical filtering in the receiver [394, 395].

### 9.2.2 MLSE combined with OOK

For 10.7-Gb/s OOK modulation, MLSE can substantially increase the tolerance against linear transmission impairments [19]. This is verified using the experimental setup depicted in Figure 9.11. At the transmitter side, a MZM is driven with a 10.7-Gb/s  $2^{31} - 1$  PRBS to generate NRZ-OOK modulation. Chromatic dispersion between -4500 ps/nm and 4500 ps/nm is subsequently added to the signal using SSMF and DCF of different lengths, while a low input power (<5 dBm) is used to avoid nonlinear impairments. The DGD is measured by splitting the signal in two orthogonal polarizations with equal power and recombining them with a time delay between 0 ps and 200 ps. At the receiver, the signal is filtered with a CSF having a 27-GHz 3-dB bandwidth. After detection with a single-ended photodiode, either a conventional threshold CDR or an MLSE receiver is used. The real-time MLSE receiver has a 3-bit ADC with a two-fold over-sampling rate of 21.4 Gsample/s and a 2-bit channel memory [19]. The channel model is based on the analysis of amplitude histograms. Figures 9.11b and 9.11c depict the CDR and MLSE receiver, respectively.

Figure 9.12a shows the measured chromatic dispersion tolerance of the MLSE receiver compared with the CDR receiver. The chromatic dispersion tolerance of 10.7-Gb/s NRZ-OOK is  $\pm 800$  ps/nm for a 2-dB OSNR penalty. But combined with the MLSE receiver, the tolerance increases to  $\pm 2000$  ps/nm for a 2-dB OSNR penalty. Hence, the MLSE receiver outperforms the threshold CDR receiver by more than a factor of two. Figure 9.12b shows that the use of an MLSE receiver also significantly improves the DGD tolerance. However, the most significant

improvement occurs only when the allowable OSNR penalty is in excess of 6 dB where the DGD tolerance is doubled. For a 2-dB OSNR penalty the allowable DGD is 60 ps, a 30% improvement over a conventional CDR receiver.

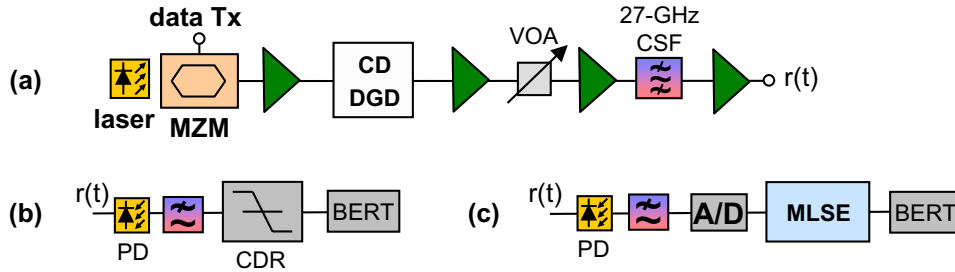


Figure 9.11: (a) Experimental setup, (b) conventional CDR receiver and (c) MLSE receiver.

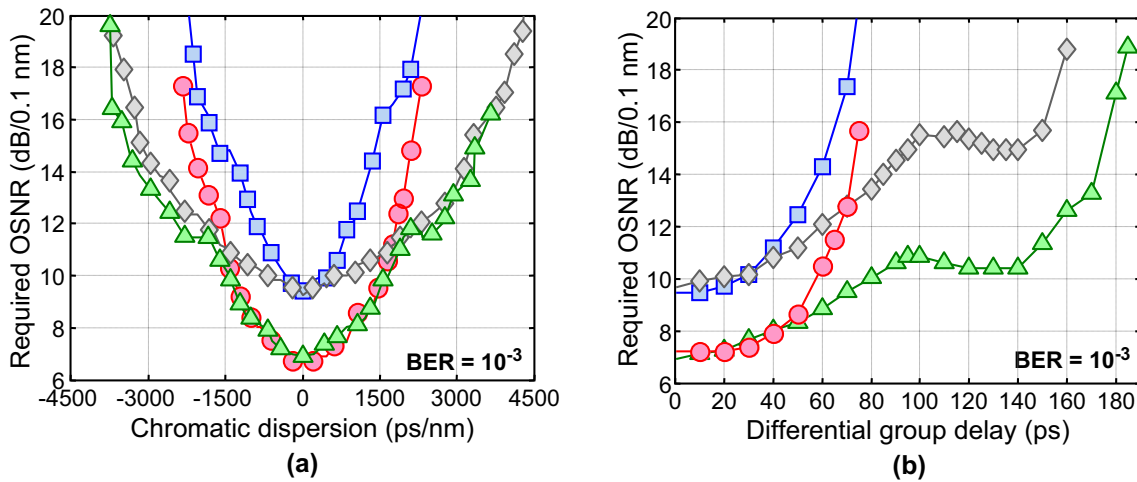


Figure 9.12: Measured OSNR requirement versus (a) chromatic dispersion and (b) differential group delay; ● DPSK with balanced detection and CDR receiver, ■ OOK with CDR receiver, ▲ DPSK with balanced detection and MLSE receiver, ◆ OOK with MLSE receiver.

### 9.2.3 MLSE combined with DPSK

The improved chromatic dispersion and DGD tolerance of an MLSE receiver would be ideally combined with DPSK modulation. This would combine the high tolerance against linear impairments of MLSE with the improved OSNR requirement and nonlinear tolerance of DPSK.

The experimental setup depicted in Figure 9.16 is used to evaluate MLSE with DPSK modulation and Figure 9.12a depicts the measured dispersion tolerance of MLSE combined with DPSK modulation. This shows that the improvement in dispersion tolerance that is observed for OOK is not replicated for DPSK modulation. When we compare the performance of DPSK with a CDR and MLSE receiver, no performance improvement is measured between 0 ps/nm to 1600 ps/nm of chromatic dispersion. For higher chromatic dispersion the improvement is small and approaches the results obtained with NRZ-OOK modulation. This shows that the 3-dB benefit of DPSK with

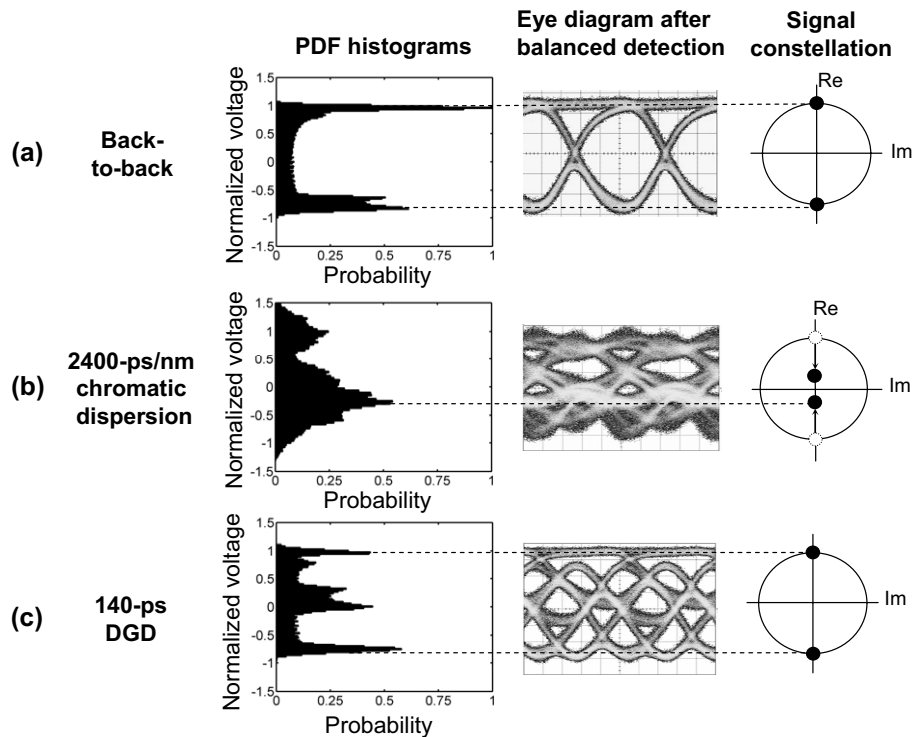


Figure 9.13: Simulated PDF histograms of signal samples, measured eye diagrams at the output of the balanced photodiode and signal constellation for (a) back-to-back, (b) 2400-ps/nm chromatic dispersion and (c) 140-ps differential group delay.

balanced detection fades away when chromatic dispersion is the dominant impairment, even when used together with an MLSE receiver. The insignificant advantage of MLSE combined with DPSK modulation was also reported in [396]. In contrast, Figure 9.12b shows that when the DGD tolerance is considered, the 3-dB benefit of DPSK remains when using an MLSE receiver.

Figure 9.13 shows measured eye diagrams at the output of the balanced photodiode in the presence of significant chromatic dispersion and DGD. The eye diagrams are complemented with simulated PDF histograms of the signal samples and the simulation parameters are set according to the measurement conditions. Figure 9.13a shows that back-to-back the eye diagram is wide open and the samples have a high probability in the *normalized* voltage range around 1 and -1. As chromatic dispersion becomes more dominant, the majority of the samples shift towards the middle of the histogram. This is particularly true for the destructive signal component, which confirms the difference in dispersion tolerance of the constructive and destructive components as discussed in Section 4.3.5. For 2400-ps/nm chromatic dispersion, the samples are concentrated with a high probability around a voltage of -0.5 and 0.2, reducing the symbol distance that is the basis for the 3-dB OSNR benefit of DPSK. For DGD, on the other hand, Figure 9.12c shows that for 140 ps the eye is highly distorted which confirms the high measured OSNR penalty. However, in contrary to chromatic dispersion there is still a high probability that the samples occur around  $\pm 1$  in the histogram. Hence, the constructive and destructive outputs of the MZDI are correlated to a lesser degree which preserves more of the symbol distance, and therefore the 3-dB OSNR benefit of DPSK.

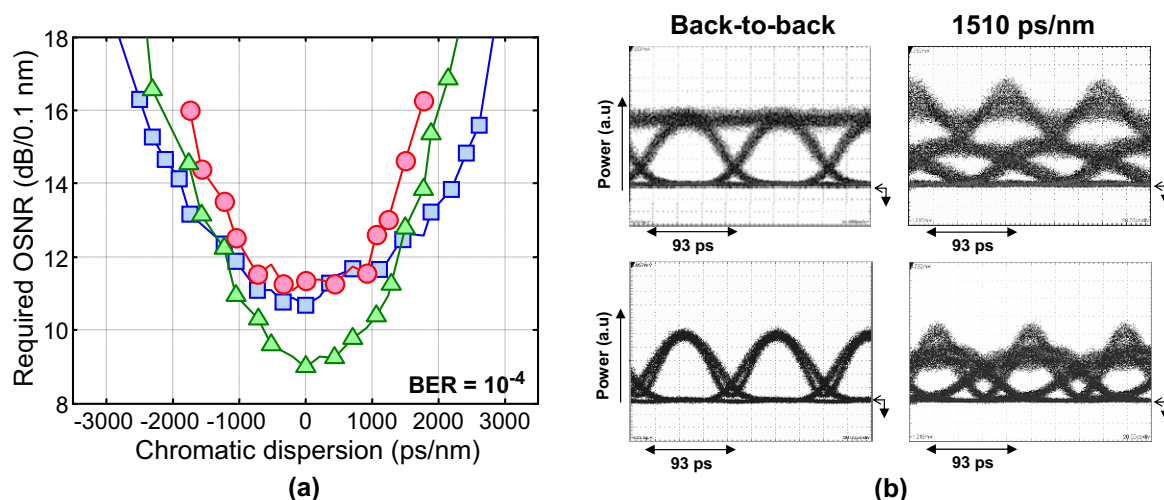


Figure 9.14: (a) Experimental comparison of DPSK with single-ended or balanced detection input to the MLSE receiver;  $\bullet$  destructive,  $\square$  constructive,  $\blacktriangle$  balanced detection and (b) measured eye diagrams comparing constructive (upper row) and destructive (lower row) components back-to-back and with chromatic dispersion.

To better understand the ineffectiveness of MLSE with DPSK modulation, we measure the dispersion tolerance of the constructive and destructive ports, separately (Figure 9.14a). The destructive component clearly shows a smaller dispersion tolerance than the constructive component. This is similar to the difference in chromatic dispersion tolerance as observed with a CDR receiver (see Section 4.3.5). Hence, the duobinary modulation of the constructive components improves the dispersion tolerance, whereas the AMI modulation on the destructive components broadens the optical spectrum and results in a lower dispersion tolerance. Figure 9.14b show measured eye diagrams of the constructive and destructive components for back-to-back and with 1900 ps/nm of chromatic dispersion. This confirms that in the presence of chromatic dispersion the destructive component is, in comparison to the constructive component, more severely distorted. The lower dispersion tolerance of the destructive component closes the eye diagram after balanced detection, which reduces the MLSE performance. However, this does not explain why, in the presence of  $>1200$  ps/nm chromatic dispersion, the OSNR requirement with balanced detection is worse compared to the constructive component. We conjecture that this results from a correlation between the constructive and destructive components in the presence of chromatic dispersion. As a result of this correlation, the constructive and destructive component partially cancel each other out with balanced detection. This reduces the signal power, which in turn results in a higher OSNR requirement.

### 9.2.4 Joint-decision MLSE

To overcome the low chromatic dispersion tolerance of D(Q)PSK combined with MLSE, *Cavalari et al.* proposed in [397] the use of joint-decision MLSE (JD-MLSE). JD-MLSE is characterized by having more than one input into the MLSE receiver in order to provide it with additional information about the signal. A joint-decision MLSE can thus be considered as a two input,

single output receiver. In the case of DPSK modulation, the two inputs of the JD-MLSE are the constructive and destructive output ports of the MZDI. The JD-MLSE therefore maximizes the a posteriori probability,

$$\hat{S} = \underset{i}{\operatorname{argmax}} \sum_{k=1}^K \ln[P(u_k^-, u_k^+ | S_i)], \quad (9.25)$$

where  $u_k^-$  and  $u_k^+$  represent the constructive and destructive components of the demodulated DPSK signal that are used as input sequences of the JD-MLSE.  $P(u_k^-, u_k^+ | S_i)$  is the a posteriori probability that samples  $u_k^-$  and  $u_k^+$  are received when the state  $S_i$  is transmitted [397].

The principle of JD-MLSE is similar to the histograms method, since both methods build discrete PDFs containing the probability of occurrence for each state transition. But the JD-MLSE constructs  $N^{L+1}$  3-dimensional discrete PDFs instead of the conventional 2-dimensional PDFs used in the histograms method. This increases the size of the look-up table, which now has to store the 3-dimensional PDFs, to a total of  $4^Q \cdot N^{L+1}$  values. JD-MLSE therefore requires a significantly larger look-up table to compute the trellis metrics. In addition, more information is necessary to compute the PDFs with a high enough accuracy. This increases the required training sequence length or the accuracy of the blind estimation algorithms. On the other hand, the trellis diagram has the same complexity for the conventional MLSE with balanced detection (B-MLSE) and JD-MLSE. The computational effort required for the JD-MLSE is therefore comparable to the B-MLSE based on histograms (except for slightly higher memory requirements due to the larger number of PDFs). In addition slightly more hardware is required, as two ADC are necessary to convert the received signals into the digital domain.

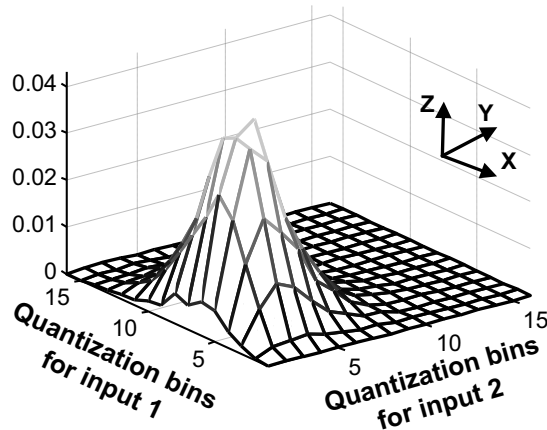


Figure 9.15: Joint-decision MLSE histogram for transition '010' with 2000-ps/nm chromatic dispersion.

Figure 9.15 shows a 3-dimensional PDF for the '010' state transition with a two bits memory length. The  $x$ -axis represents the quantization bins for the first input, where the  $y$ -axis represents the quantization bins for the second input. The  $z$ -axis gives the probability for each point in this 2-dimensional plane. Obviously, when the two input signals are the same, the PDF will be symmetric with respect to the  $x$  and  $y$ -axis. However, when two different signals (carrying the same information) are input into the JD-MLSE, another degree of confinement is added to the conditional PDF.



## 9.2.5 Joint-decision MLSE combined with DPSK

We now evaluate the impact of JD-MLSE on DPSK modulation using the experimental setup shown in Figure 9.16<sup>1</sup>. It is similar as discussed in Section 9.2.2 with the exception that a 50-GHz CSF filter is used in the receiver, this slightly increases the back-to-back OSNR requirement.

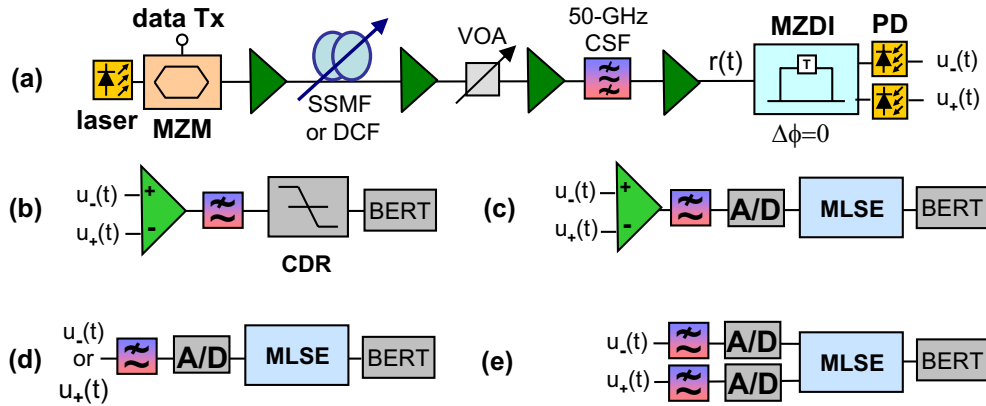


Figure 9.16: (a) Experimental setup and (b-e) different receiver configurations; (b) CDR receiver, (c) MLSE with balanced detection, (d) MLSE with single-ended detection and (e) joint-decision MLSE.

At the receiver, the signal is input into either a threshold CDR receiver or a DSO. The bandwidth of the DSO is 8 GHz and it samples at a sampling rate of 20 Gsample/s. To obtain exactly 2 samples/symbol, the stored signal is re-sampled to a sample rate of 21.4 Gsample/s. Subsequently, the signal is re-timed using the digital filter and square timing recovery algorithm, as discussed in Section 10.3.1. After re-timing, the signal is sampled at  $-T_0/4$  and  $+T_0/4$ , where  $T_0$  is the symbol period. Using off-line processing, MLSE is applied to the sequences stored with the DSO. The MLSE has a 4-bit quantization resolution and 4-state Viterbi decoder. To determine the MLSE performance, data sequences of  $1 \cdot 10^6$  bits are processed by the MLSE algorithm, which gives an accuracy of 99.99% for a BER of  $10^{-3}$  [398]. The measured dispersion tolerance for both the conventional CDR receiver, B-MLSE as well as JD-MLSE are depicted in Figure 9.17. The balanced MLSE show no significant improvement in dispersion tolerance over the conventional CDR receiver, which is similar to results obtained in the previous section with the real-time MLSE (see Figure 9.12). Only for large accumulated dispersion we find a difference between the real-time MLSE and off-line MLSE. This is attributed to the re-timing required for the off-line MLSE, which is sub-optimal in the presence of large signal distortions.

The JD-MLSE used here has a 2-symbol memory and it builds therefore eight 3-dimensional histograms similar to the one shown in Figure 9.15. Figure 9.17a compares the chromatic dispersion tolerance of the B-MLSE and JD-MLSE. This shows a clear advantage for the JD-MLSE, which nearly doubles the chromatic dispersion tolerance over both the B-MLSE as well as the CDR receiver. For a 2-dB OSNR penalty the measured chromatic dispersion tolerance is 2000 ps/nm

<sup>1</sup>A real-time JD-MLSE receiver was not available in this experimental evaluation and the measurements discussed here are therefore 'off-line'. In the off-line measurements, a set of data is stored using a DSO (Tektronix TDS 6804B) and afterwards post-processed on a desktop computer.

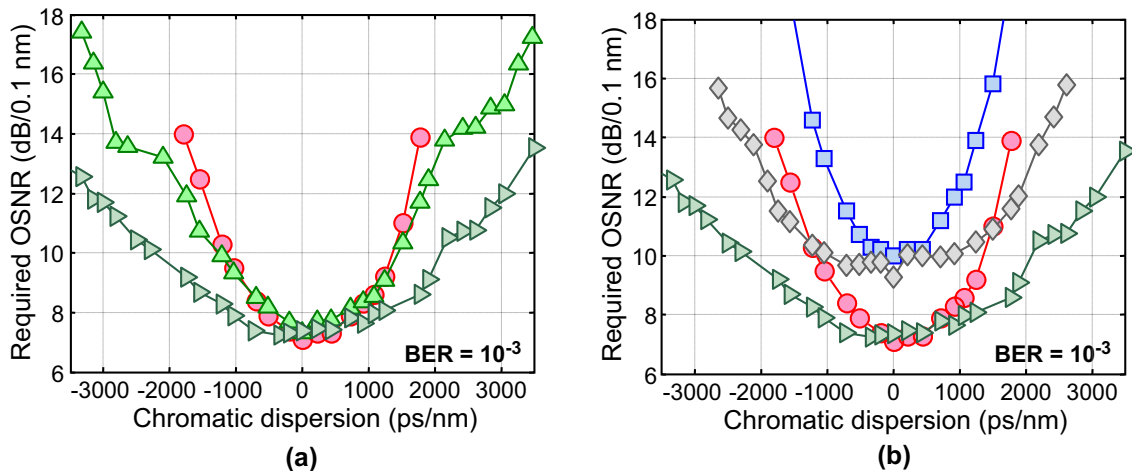


Figure 9.17: (a) DPSK with different MLSE configurations and (b) comparison between OOK and DPSK modulation;  $\circ$  DPSK with balanced detection and CDR receiver;  $\square$  OOK with CDR receiver;  $\triangle$  DPSK with balanced detection and MLSE receiver;  $\diamond$  OOK with MLSE receiver;  $\blacktriangledown$  DPSK with joint-decision MLSE receiver.

for the JD-MLSE, compared to only 1100 ps/nm for the CDR and B-MLSE receivers. In Figure 9.17b, the chromatic dispersion tolerance obtained for 10.7-Gb/s OOK and 10.7-Gb/s DPSK is compared when JD-MLSE is used for the DPSK receiver. This shows that JD-MLSE preserves the 3-dB difference in OSNR requirement between OOK and DPSK in the dispersion-limited regime.

### 9.2.6 MLSE combined with partial DPSK

A different approach to improve the chromatic dispersion tolerance of DPSK modulation and MLSE is the use of partial DPSK. As shown in Section 4.4, the use of MZDI with a delay of less than one bit can considerably increase the chromatic dispersion tolerance. In this section we show that combined with MLSE the improvement is further enhanced.

Figures 9.18a and 9.18b depict the simulated influence of the MZDI bit-delay on the chromatic dispersion tolerance of the CDR and MLSE receiver, respectively. The simulations use a similar configuration as shown in Figure 9.16. A  $2^7$  bits long 10.7-Gb/s PRBS sequence is repeated 4 times to obtain a total block length of  $2^9$  bits, which is then used to construct a DPSK modulated signal. To determine the chromatic dispersion tolerance, this signal is multiplied with the impulse response of the desired amount of chromatic dispersion. At the receiver, a data sequence with a length of  $10^6$  bits is constructed from the received  $2^9$  bits by using the overlap-and-add-method [398]. Additive white Gaussian noise is added to the signal, which is subsequently filtered with a  $2^{nd}$ -order Gaussian shaped 50-GHz filter. To determine the impact of partial DPSK, the MZDI bit-delay is varied from  $0.5 \cdot T_0$  to  $1.0 \cdot T_0$  bit in steps of  $0.1 \cdot T_0$ . After balanced detection, the electrical signal is filtered with a  $10^{th}$ -order Bessel filter with a bandwidth of 7 GHz. Either a conventional CDR receiver or MLSE receiver is subsequently used to determine the chromatic dispersion tolerance.

Figure 9.18a shows that for the CDR receiver the chromatic dispersion tolerance improves from 1140 ps/nm to 1890 ps/nm when the bit-delay is decreased from  $1.0 \cdot T_0$  to  $0.5 \cdot T_0$  (2-dB OSNR penalty). It further shows that there is a trade-off between chromatic dispersion tolerance and back-to-back OSNR requirement, which increases by 1.7 dB when a 0.5-bit delay MZDI is used. Figure 9.18b depicts the chromatic dispersion tolerance when we apply an MLSE receiver to the output of the balanced photo-diode. The chromatic dispersion tolerance is now increased from 1140 ps/nm to 3750 ps/nm when the bit-delay is decreased from  $1.0 \cdot T_0$  to  $0.5 \cdot T_0$ , again for a 2-dB OSNR penalty. The back-to-back OSNR requirement is somewhat higher with 2.6 dB, which indicates that MLSE causes a slight OSNR penalty for partial DPSK. For a 0.5-bit-delay, the use of MLSE results in a nearly identical OSNR requirement for chromatic dispersion ranging from 0 ps/nm to in excess of 3000 ps/nm. Figure 9.18b shows that the chromatic dispersion tolerance is optimum for a bit-delay of 0.5 or 0.6. But on the other hand, a shorter bit-delay results in an increased back-to-back OSNR requirement. The choice of the optimum MZDI bit-delay should therefore take both the back-to-back OSNR requirement and chromatic dispersion tolerance into account. Consequently, a slightly higher bit delay (e.g. 0.65-bit delay) is a more optimal choice in order to balance the chromatic dispersion tolerance and back-to-back OSNR requirement.

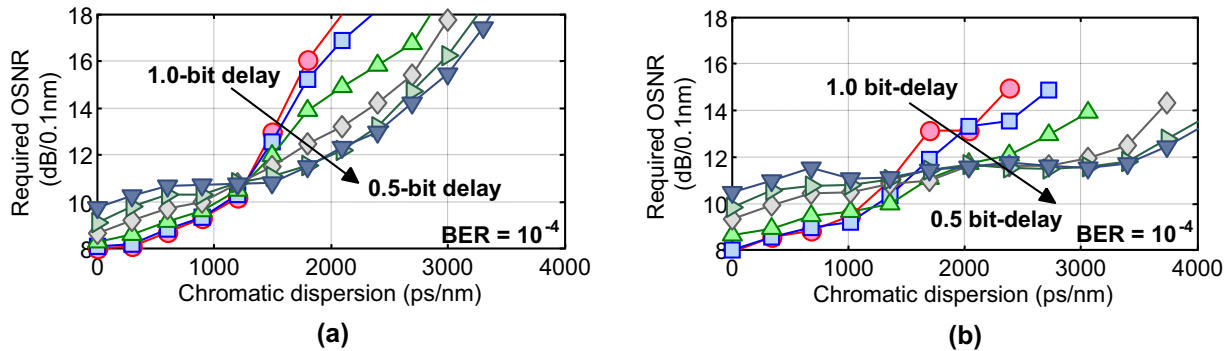


Figure 9.18: Simulated chromatic dispersion tolerance of 10.7-Gb/s NRZ-DPSK with different MZDI bit-delay (a) conventional CDR receiver and (b) MLSE receiver;  $\bullet$  1.0-bit delay,  $\blacksquare$  0.9-bit delay,  $\blacktriangle$  0.8-bit delay,  $\blacklozenge$  0.7-bit delay,  $\blacktriangleright$  0.6-bit delay,  $\blacktriangledown$  0.5-bit delay.

We now use the experimental setup depicted in Figure 9.16 to verify the chromatic dispersion tolerance of partial DPSK combined with MLSE. Two different MZDIs are employed; one with a 1-bit delay, the other with a 0.5-bit delay, followed by a balanced photodiode. Subsequently, the output of the balanced photodiode is used as the input signal for (1) a real-time MLSE receiver [19], (2) a software based MLSE receiver for off-line processing and (3) a conventional CDR receiver. The measured chromatic dispersion tolerance for both the CDR and real-time MLSE with a 0.5 and 1.0-bit delay MZDI is depicted in Figure 9.19a. A comparison between the CDR and MLSE receiver for a 1-bit delay MZDI confirms the inefficiency of an MLSE for DPSK modulation. On the other hand, when a 0.5-bit delay MZDI is used a considerable improvement in chromatic dispersion tolerance is evident. For partial DPSK combined with MLSE no significant increase in OSNR requirement is measured for a chromatic dispersion up to 3500 ps/nm, which confirms the improvement observed through simulations. To further point out the improvement obtained with partial DPSK and MLSE, Figure 9.19b compares the chromatic dispersion tolerance of partial DPSK with duobinary modulation. This shows both a clear OSNR improvement

( $\sim 2.5$  dB) and a slightly higher chromatic dispersion tolerance for the partial DPSK scheme with MLSE. In addition, the back-to-back OSNR requirement of partial DPSK can be improved by optimizing the MZDI bit-delay, which would further increase the difference with duobinary modulation.

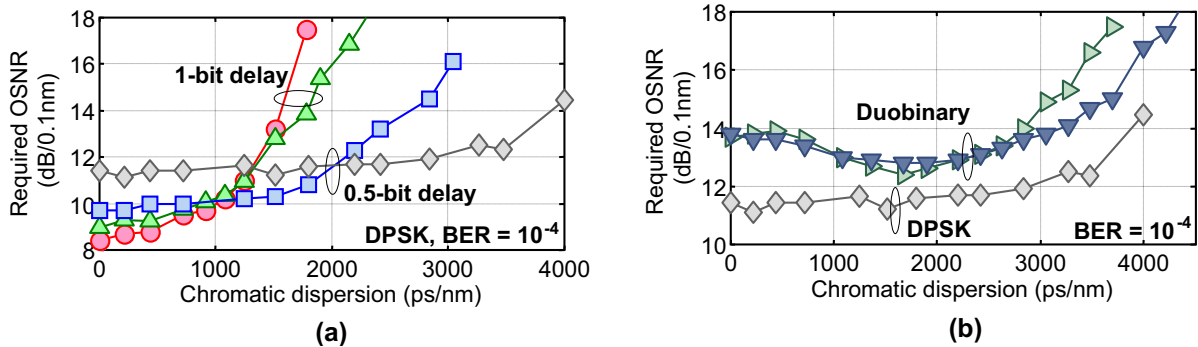


Figure 9.19: Measured chromatic dispersion tolerance of  $\bullet$  DPSK with CDR and 1.0-bit delay,  $\blacksquare$  DPSK with CDR and 0.5-bit delay,  $\blacktriangle$  DPSK with MLSE and 1.0-bit delay,  $\blacklozenge$  DPSK with MLSE and 0.5-bit delay,  $\blacktriangleright$  duobinary with CDR,  $\blacktriangledown$  duobinary with MLSE.

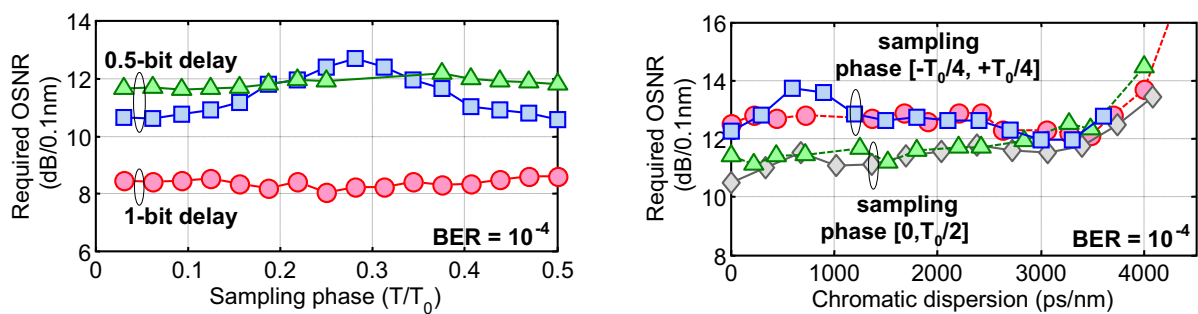


Figure 9.20: Sampling instant optimization with MLSE;  $\bullet$  1.0-bit delay, 0-ps/nm,  $\blacksquare$  0.5-bit delay, 0-ps/nm,  $\blacktriangle$  0.5-bit delay, 3000-ps/nm.

Figure 9.21: Difference between real-time and off-line processing;  $\bullet$  real-time measured,  $\blacksquare$  real-time simulated,  $\blacktriangle$  off-line measured,  $\blacklozenge$  off-line simulated.

In [266] it is shown that due to the deterministic interference between consecutive symbols in an MZDI with  $\Delta T < T_0$  bit-delay, the output signal resembles an inverted RZ signal. For a RZ signal, the choice of the sampling phase is more sensitive in comparison to NRZ. Figure 9.20 shows the OSNR requirement of (partial)-DPSK with different sampling instants. The x-axis depicts the sampling instant  $t$  of the first sample along the symbol period, whereas the second sample is taken at  $t + T_0/2$ . When we compare the sample phase sensitivity of a 0.5-bit delay MZDI and a 1-bit delay MZDI, the higher sensitivity of the RZ pulse shape becomes apparent. Conventional DPSK with a 1-bit delay MZDI is insensitive to the sampling phase when a two-fold over-sampled MLSE receiver is used. This is similar to what has been reported in [399] for NRZ-OOK. However, in the case of a 0.5-bit delay MZDI and 0-ps/nm chromatic dispersion, the required OSNR shows a significant dependence on the sampling phase offset. The optimum sampling phase of the two samples is at  $t = 0$  and at  $t = T_0/2$  as most of the information in RZ can be extracted from the middle of the symbol. On the other hand, the dependence on the sampling phase disappears in the dispersion-limited regime. This can be better understood from

the partial DPSK eye diagram demodulated with a 0.5-bit delay MZDI, as shown in Figure 9.22. Comparing the eye diagrams back-to-back and with 1900 ps/nm of chromatic dispersion, shows that the signal loses the RZ shape in the dispersion-limited regime. As a result the impact of the sample phase is significantly reduced.

Figure 9.21 now compares the chromatic dispersion tolerance of the off-line processed MLSE with the real-time MLSE. The real-time MLSE shows a slight OSNR penalty for low chromatic dispersion, but this difference disappears in the dispersion-limited regime. This can be attributed to the sub-optimal choice of the sample phase, which is not adapted to the partial DPSK signal but to a NRZ-OOK modulated signal. The real-time MLSE samples the signal therefore at a different part of the symbol period ( $t = -T_0/4$  and  $t = +T_0/4$ ), which results in a higher OSNR requirement. In the chromatic dispersion limited regime, on the other hand, the choice of the sampling instant is less critical. This explains why the OSNR requirement of the real-time and off-line MLSE converges in the dispersion-limited regime. Simulated curves confirm the choice in sampling phase as the source of the difference in OSNR requirement. Note that the real-time MLSE receiver could be easily modified to sample at the optimal sampling point. In addition, it might be beneficial to over-sample more than two-fold with partial DPSK. Sampling at  $-T_0/4$ , 0 and  $+T_0/4$  could somewhat reduce the  $\sim 1$  dB OSNR penalty that occurs when partial DPSK is combined with MLSE.

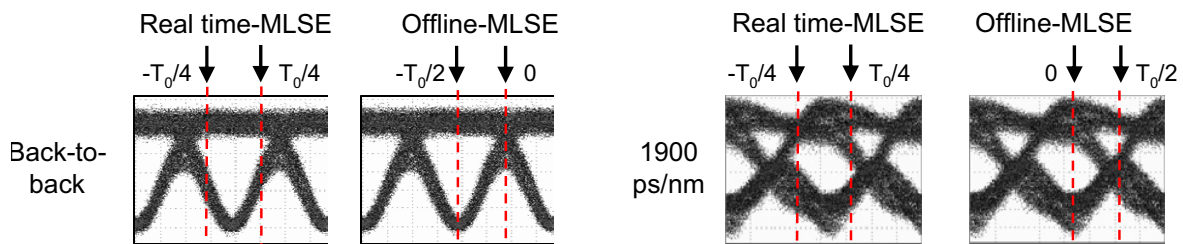


Figure 9.22: Measured eye diagrams after phase demodulation with a 0.5-bit delay MZDI and balanced detection (a) back-to-back (b) 1900-ps/nm of chromatic dispersion.

### 9.2.7 Joint-decision and joint-symbol MLSE combined with DQPSK

We now combine MLSE with DQPSK modulation. DQPSK modulation on itself supports already an improved tolerance to chromatic dispersion and PMD, and combined with MLSE the necessity of an optical tunable dispersion compensation for a 43-Gb/s transponder might be alleviated<sup>2</sup>. As well, the higher PMD tolerance can be beneficial in PMD-limited transmission links. In this section we discuss the combination of 21.4-Gb/s NRZ-DQPSK modulation with MLSE, limited by the sampling rate of the ADCs in the DSO that is used for experimental verification.

Figure 9.23 shows the different MLSE receivers for DQPSK modulation. We compare three different MLSE schemes and a conventional CDR receiver. In order to assess MLSE combined

<sup>2</sup>The required chromatic dispersion tolerance for a robust 43-Gb/s transponder depends on system design, but as a figure-of-merit we assume here a 1000-ps/nm chromatic dispersion window for a 1-dB OSNR penalty.



with DQPSK modulation, the DSO has been used to store the in-phase and quadrature tributaries, simultaneously. As DQPSK modulation has a low tolerance to phase mismatches in the MZDI, the random drift of two MZDI poses a significant problem to the experimental assessment (see Section 5.3). This causes some residual penalty in the measurements.

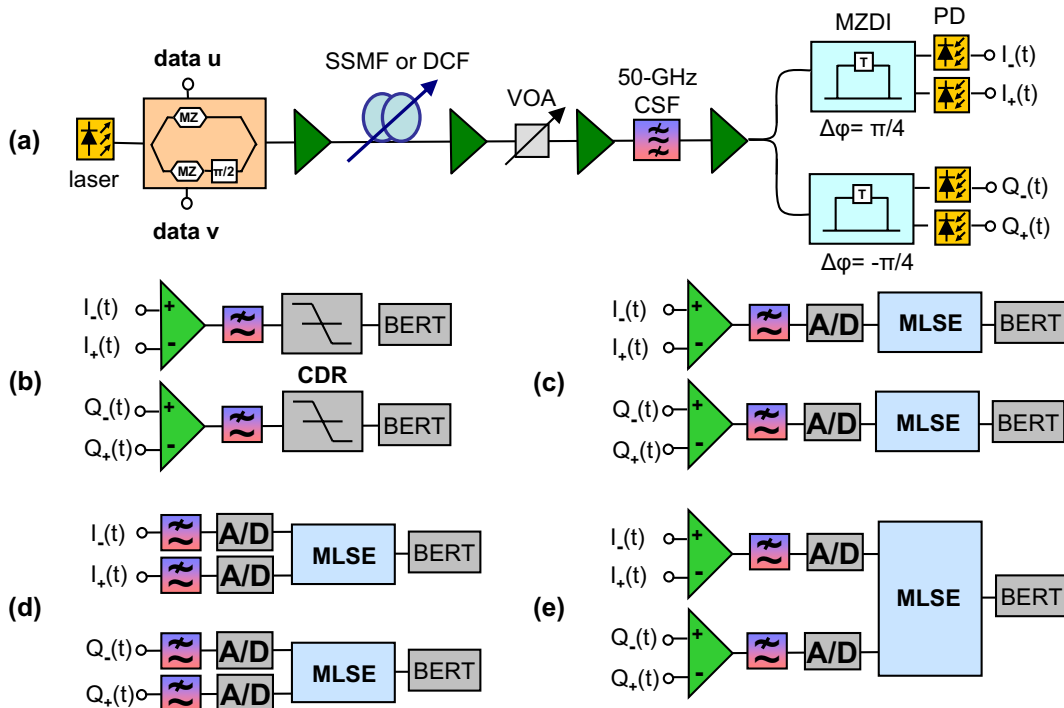


Figure 9.23: (a) Experimental DQPSK setup with (b) conventional CDR receiver; (c) MLSE with balanced detection, (d) MLSE with joint-decision estimation and (e) MLSE with joint-symbol estimation.

As inputs to an MLSE receiver for DQPSK modulation, we can use the constructive and destructive components of the in-phase and quadrature tributaries. This gives a total of 4 signals that are detected with either balanced or single-ended photodiodes. The three considered MLSE schemes consists of MLSE with balanced detection (B-MLSE), MLSE with joint-decision estimation (JD-MLSE) and MLSE with joint-symbol estimation (JS-MLSE). A 5-bit vertical quantization resolution, 2-symbol channel memory and two-fold over-sampling is used in all cases. Both the B-MLSE and JD-MLSE consider the in-phase and quadrature tributaries independent of each other and use a  $2^2 = 4$ -state Viterbi decoder. For JD-MLSE the same approach is used as described for DPSK modulation in Section 9.2.4.

The principle of JS-MLSE is the same as discussed for JD-MLSE, with the exception that a quaternary alphabet ( $N = 4$ ) is used instead of a binary alphabet ( $N = 2$ ). JS-MLSE uses the samples from the in-phase and quadrature tributaries simultaneously to compute the branch metrics in the Viterbi decoder. The JS-MLSE uses the same parameters as the JD-MLSE, except that due to the quaternary alphabet the Viterbi decoder now has  $4^2 = 16$  states. Either the histogram method or Gaussian model method is used. The Gaussian model method minimizes the Euclidean distance,

which is now defined as,

$$\hat{S} = \underset{i}{\operatorname{argmin}} \sum_{k=1}^K (I_k + j \cdot Q_k - \mu_i)^2 \quad \forall i = 1, 2, \dots, N. \quad (9.26)$$

Equation 9.26 follows from Equation 9.22, except that the term  $r_k$  is replaced by  $I_k + j \cdot Q_k$ , where  $I_k$  and  $Q_k$  are the samples from the in-phase and quadrature tributary, respectively and  $\mu_i$  is a complex number. In [400] it has been shown that the Gaussian model is a valid assumption for the channel statistics of DQPSK modulation with a direct detection receiver.

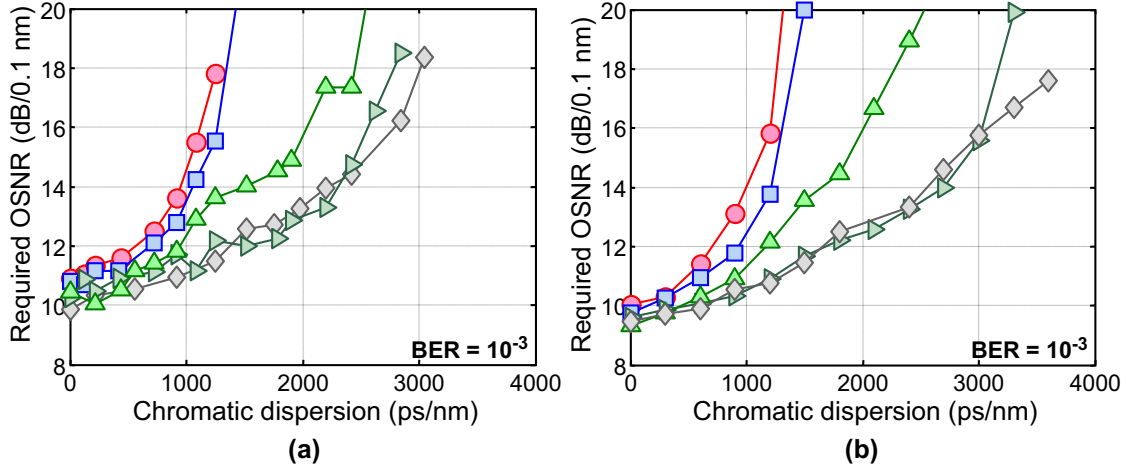


Figure 9.24: DQPSK with different MLSE configurations for (a) experimental and (b) simulated results;  $\bullet$  conventional CDR receiver,  $\square$  MLSE with balanced detection,  $\blacktriangle$  JD-MLSE,  $\blacklozenge$  JS-MLSE and histogram method,  $\blacktriangledown$  JS-MLSE and Gaussian model method.

Figures 9.24a and 9.24b show the OSNR requirement as a function of the chromatic dispersion for experiments and matching simulations, respectively. The small mismatch between simulations and experiments can be attributed to the phase drift in the MZDIs and suboptimal digital clock recovery at high accumulated dispersion. It is evident that B-MLSE provides little or no advantage in comparison to a conventional CDR receiver, which is similar to the results obtained for DPSK modulation. When JD-MLSE is used instead of the CDR receiver, the dispersion tolerance is increased by  $\sim 50\%$  at an OSNR penalty of 2-dB. But when we compare the impact of JD-MLSE for both DPSK and DQPSK modulation, it is evident that the performance improvement is less significant for DQPSK. We conjecture that this difference results from the suboptimal phase demodulation in the case of DQPSK modulation. As discussed in Section 5.2, this results in crosstalk between the in-phase and quadrature tributaries and therefore in a higher back-to-back OSNR requirement. In the presence of significant chromatic dispersion this crosstalk can limit the MLSE efficiency. JS-MLSE takes the decision on both tributaries simultaneously, and it can take the crosstalk between the two tributaries into account. Figure 9.24a shows that JS-MLSE provides a significantly higher dispersion tolerance of  $\sim 1500$  ps/nm compared to 700 ps/nm for the CDR receiver (at a 2-dB OSNR penalty). When we scale the measured dispersion tolerance of DQPSK with JS-MLSE to a 43-Gb/s bit rate, we obtain a 800 ps/nm window. This might be sufficient to alleviate the need for optical tunable dispersion compensation. As well, improvement in the signal processing (e.g. a larger number of states in the MLSE decoder) will further increase this figure and meet the requirement of dispersion tolerance modulation format.

Table 9.1: ESTIMATED COMPLEXITY OF THE DIFFERENT MLSE SCHEMES APPLIED TO DQPSK MODULATION.

	B-MLSE histograms	JD-MLSE histograms	JS-MLSE histograms	JS-MLSE Gaussian
Number of trellis	2	2	1	1
Trellis states	$2^L$	$2^L$	$4^L$	$4^L$
Dimensions of the PDF	2-D	3-D	3-D	N.A.
Size of the look-up table	$2^Q \cdot 2^{L+1}$	$4^Q \cdot 2^{L+1}$	$4^Q \cdot 4^{L+1}$	$4^{L+1}$

Table 9.2: BACK-TO-BACK OSNR REQUIREMENT OF DQPSK MODULATION FOR A  $10^{-3}$  BER AND DIFFERENT MLSE SCHEMES.

	CDR	B-MLSE histograms	JD-MLSE histograms	JS-MLSE histograms	JS-MLSE Gaussian
Measured (dB)	10.9	10.8	10.4	10.3	9.9
Simulated (dB)	10.0	9.8	9.3	9.5	9.6

Figure 9.24a further shows that both joint-symbol algorithms to calculate the metrics of the trellis's state transitions (histograms and Gaussian model) have a similar performance. This confirms that the Gaussian channel model is a valid assumption for direct detected DQPSK modulation. The advantage of the Gaussian model method is a significantly reduced complexity to store and compute the branch metric. As only the mean value for each state is stored, the size of the look-up tables is  $4^{L+1} = 64$  and  $4^Q \cdot 4^{L+1} = 65536$  for the Gaussian model and histogram method, respectively. In addition, when the Gaussian model method is used only the Euclidean distance has to be computed in the trellis diagram. The complexity of the different MLSE schemes is summarized in Table 9.1.

From Figure 9.24 it is evident that both JD-MLSE as well as JS-MLSE have a slightly lower back-to-back OSNR requirement, which is also summarized in Table 9.2. As MLSE creates an improved decision variable based on a number of symbols, in this case equal to the channel memory length, this is similar to the improvement observed for MSPE. The back-to-back OSNR requirement of JS-MLSE is 1.0 dB and 0.4 dB lowered in comparison to the CDR receiver for the measurements and simulation, respectively. We note that the difference between the measurements and simulation probably results from phase offsets in both MZDIs. The limited improvement for MLSE compared to MSPE is due to the smaller number of symbols used to compute the improved decision variable. This suggests that a combination of MSPE and MLSE might be a suitable approach to realize robust DQPSK modulation, which has been confirmed by *Zhao et. al.* in [401, 402]. In this work the MSPE is implemented in the optical domain using multiple MZDIs with different bit-delays, but similar results could be obtained using a digital signal processing implementation.



## 9.3 Summary & conclusions

In this chapter, signal processing algorithms have been discussed that can increase the robustness of D(Q)PSK modulation with a direct detection receiver. *Multi-symbol phase estimation (MSPE)* generates an improved decision variable using a recursive signal processing algorithm.

- MSPE approaches the *OSNR requirement* of coherent detection. It therefore allows for a 0.5-dB and 1.8-dB improvement in back-to-back OSNR requirement for DPSK and DQPSK modulation, respectively.
- In the presence of *nonlinear phase noise*, the advantage of MSPE over conventional direct detection increases. This allows for a 1.5-dB improvement in nonlinear tolerance for 10.7-Gb/s DPSK modulation. For DQPSK modulation, no significant compensation of nonlinear phase noise is observed.
- MSPE demodulation has only a modest laser *linewidth requirement* as it is based on interferometric demodulation with an MZDI. It is more tolerant to laser linewidth than a digital coherent receiver with optimized carrier recovery. For lasers with a  $\gg 1$  MHz linewidth, the forgetting factor can be lowered as a trade-off between linewidth requirement and OSNR improvement.

*Maximum likelihood sequence estimation (MLSE)* improves the tolerance with respect to transmission impairments by basing the decision variable not only on the most recent symbol, but on a received sequence of symbols.

- Using the signal after balanced detection as the input of a *conventional MLSE* receiver does not significantly improve the tolerance against chromatic dispersion for both DPSK and DQPSK modulation. On the other hand, a conventional MLSE receiver does improve the DGD tolerance of DPSK modulation.
- For DPSK modulation, the use of *joint-decision MLSE* significantly improves the chromatic dispersion tolerance. A joint-decision MLSE operates using both the constructive and destructive component as separate inputs to the MLSE receiver.
- The combination of *partial DPSK* with a conventional MLSE provides a significant increase in chromatic dispersion tolerance at the cost of somewhat higher back-to-back OSNR requirement. For 10.7-Gb/s NRZ-DPSK, a 3750-ps/nm dispersion tolerance is measured for a 2-dB OSNR penalty.
- For DQPSK modulation, *joint-symbol MLSE* provides the best chromatic dispersion tolerance. This makes a simultaneous decision on the in-phase and quadrature tributaries of the demodulated DQPSK signal. It can therefore compensate for the crosstalk between both tributaries, which degrades the performance of a direct detection DQPSK receiver.

In summary, signal processing in direct detection receivers seems promising to realize more robust optical transmission. The chromatic dispersion tolerance and PMD tolerance of, in particular, 43-Gb/s DQPSK modulation can be increased to the extent that no optical chromatic dispersion or PMD compensation is required.

---

## Digital coherent receivers

In this chapter we discuss digital coherent receivers, also known as digital intra-dyne receivers, for amplitude, polarization and phase-sensitive detection. Such receivers combine coherent detection with digital signal processing to compensate for transmission impairments, and therefore are a suitable candidate for robust optical transmission systems.

Coherent detection of an optical signal implies that the received signal is mixed with the output signal of a LO laser. The LO is normally a receiver-side semiconductor laser. Coherent detection has initially received significant research interest in the 1980's. At that time, no pre-amplification was used in front of the receiver, which results in detection mostly limited by the *thermal noise* of the photo diode and electrical amplifiers. As the LO signal typically has a much higher power than the received signal, it can be used for *coherent amplification*. Hence for coherent detection, the receiver sensitivity is only limited by optical *shot noise*. This can potentially increase the receiver sensitivity with up to 20 dB in comparison to optically unamplified direct detection [403]. However, after the development of the EDFA as an optical pre-amplifier, the interest in coherent detection declined. With EDFA pre-amplification and direct detection, nearly the same receiver sensitivity can be obtained without many of the drawbacks of coherent detection, such as active polarization and phase control.

Although the receiver sensitivity of direct detection is close to the theoretical optimum, a small difference remains. As discussed in Chapter 4, the phase demodulation with an MZDI results in an OSNR penalty of 1.1 dB (DPSK) or 2.4 dB (DQPSK) when compared to coherent detection. For state-of-the-art transmission systems, this difference in receiver sensitivity can potentially improve the OSNR requirement and increase the feasible transmission distance. In addition, differential detection provides relatively poor performance with respect to digital equalization as

---

<sup>1</sup>The results described in this chapter are published in c4, c6, c21-c22, c25-c26

discussed in Chapter 9. Using coherent detection not only the amplitude, but the full (base-band) optical field, i.e. the amplitude, phase and polarization information from the received signal is transferred into the electrical domain. This opens up the possibility of distortion compensation and polarization de-multiplexing in the electrical domain and has recently revived the interest in coherent detection.

This chapter is organized as follows. The principle of coherent detection is briefly treated in Section 10.1. In more detail, the implementation of a digital coherent receiver is discussed in Section 10.2 and the required signal processing algorithms are reviewed in Section 10.3. In Sections 10.4 and 10.5 the compensation of linear impairments is discussed for 43-Gb/s POLMUX-NRZ-DQPSK and 111-Gb/s POLMUX-RZ-DQPSK, respectively<sup>1</sup>. Subsequently, Section 10.6 discusses the performance of digital equalization in long-haul transmission experiments. Finally, Section 10.7 analyzes the possibilities of baud-rate distortion compensation.

### 10.1 Analog coherent receivers

Figure 10.1 shows the basic layout of a coherent receiver. The received signal is mixed with the output of the LO in an optical hybrid. There are a number of different technologies that allow the construction of an optical hybrid [404]. The most straightforward realization is a 2x2 coupler, which simply produces an interference between the received signal and the LO at the output.

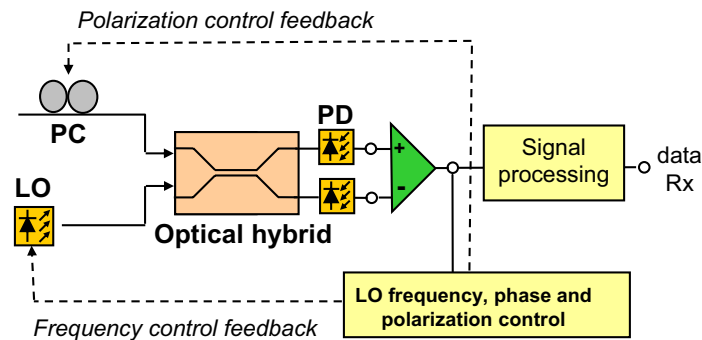


Figure 10.1: Principle of a coherent receiver.

In order to analyze coherent detection, we define the received signal and LO signal at the input of the optical hybrid as,

$$\begin{aligned} r_s(t) &= \sqrt{P_s} \exp(j[\omega_s t + \phi_s]) \\ r_{LO}(t) &= \sqrt{P_{LO}} \exp(j[\omega_{LO} t + \phi_{LO}]). \end{aligned} \quad (10.1)$$

<sup>1</sup>A coherent receiver does not necessarily require differential detection, and POLMUX-QPSK would therefore be the correct acronym of the modulation format. However, in the work described in this chapter, *electrical* differential decoding is used (see Section 10.3.4) and hence the modulation format is still referred to as POLMUX-DQPSK.

Where the LO and transmitter laser are assumed to have different frequency and phase. After mixing, the optical signal at the input of the two photodiodes is then equal to,

$$\frac{1}{\sqrt{2}} \begin{pmatrix} r_s(t) + j \cdot r_{LO}(t) \\ j \cdot r_s(t) + r_{LO}(t) \end{pmatrix}. \quad (10.2)$$

The current after the photodiode is given by  $i(\vec{t}) = R \cdot |\vec{y}(t)\vec{y}^*(t)| + \eta_{sh}(t)$ .  $R$  is the responsivity of the photodiode and  $\eta_{sh}(t)$  the photocurrent shot noise. Thermal noise has been neglected. The coherent mixing term after detection with the photodiode is subsequently defined by the photocurrent,

$$\vec{i} = \frac{R}{2} \begin{pmatrix} P_s + P_{LO} + 2\sqrt{P_s P_{LO}} \sin[(\omega_s - \omega_{LO})t + \varphi_s - \varphi_{LO}] \\ P_s + P_{LO} - 2\sqrt{P_s P_{LO}} \sin[(\omega_s - \omega_{LO})t + \varphi_s - \varphi_{LO}] \end{pmatrix} + \eta_{sh}(t). \quad (10.3)$$

The information is contained in the term  $\pm 2\sqrt{P_s P_{LO}} \cdot \sin[\omega_s - \omega_{LO}t + \varphi_s - \varphi_{LO}]$ . This shows directly the advantage of coherent detection in a system without pre-amplification. As  $P_{LO} \gg P_s$ , the magnitude of the coherent detected term becomes much larger with respect to the photocurrent shot noise  $\eta_{sh}(t)$  as can be the case for direct detection. The direct detection terms  $P_s$  and  $P_{LO}$  can be filtered out through balanced detection. Whereas for single-ended detection, only  $\langle P_s \rangle$  and  $\langle P_{LO} \rangle$  can be removed through D.C. blocking. This leaves a direct detection contribution from the modulation in  $P_s$  as well as amplitude noise contributions in  $P_{LO}$ , better known as relative intensity noise (RIN). When balanced detection is used the RIN of the LO is canceled out [405].

Coherent detection can be realized using a homodyne, heterodyne or intra-dyne receiver. The difference between the three receiver types is the required frequency difference between LO and transmitter laser. In a homodyne receiver the LO and transmitter laser have the same frequency and the phase difference should be zero (or a multiple of  $2\pi$ ). The LO and received signal are mixed in the  $180^\circ$  hybrid (for example a  $2 \times 2$  coupler), which generates the desired coherent mixing products. Homodyne detection is the ideal coherent detection scheme in the sense that it allows for the optimal receiver sensitivity. When detection is quantum noise limited it requires 9 photon/bit for BPSK modulation to obtain a  $10^{-9}$  BER [403]. However, active control of the frequency and phase of the LO is required in a homodyne receiver as the phase difference between the LO and the transmitter laser should be zero. Optical transmission using homodyne detection with a phase-locked-loop was first shown by *Malyon* in 1984 [406]. The phase-locked-loop operation puts however stringent requirements on the laser linewidth for both the LO and transmitter laser, which makes homodyne detection difficult to realize using semiconductor lasers.

In heterodyne detection the difference between the LO and transmitter laser frequency is non-zero and equals a fixed intermediate frequency (IF), i.e.  $\omega_s - \omega_{LO} = \omega_{IF}$ . Such a receiver has a reduced sensitivity of  $>3$  dB in comparison to homodyne detection, as the signal energy with homodyne detection is twice the signal energy of a heterodyned signal [407, 408]. The linewidth requirements are however about an order of magnitude less stringent in comparison to homodyne detection, which makes such a receiver easier to realize. The main drawback of heterodyne detection is that it requires a receiver bandwidth of at least twice the bit rate [409]. A heterodyne receiver therefore needs broadband photodiodes and electrical amplifiers, which makes it challenging to realize high-speed transmission. Recently, bit rates up to 10-Gb/s have been shown for

heterodyne detection [410], but non-ideal electrical components in the receiver make it difficult to match the performance of direct detection with an optical preamplifier.

Intra-dyne detection is similar to homodyne detection, with the exception that the frequency difference between the LO and transmitter laser is not exactly zero, but *approximately* zero. The frequency difference between LO and transmitter laser than can be tolerated by an intra-dyne receiver depends on the signal processing. Intra-dyne detection relies on detection of both the in-phase and quadrature component of the received signal, and is therefore also referred to as a *phase-diversity* receiver. In order to detect both the in-phase as well as the quadrature component, a  $90^\circ$  hybrid is required [404]. The phase-diversity reception makes the receiver robust against phase offsets between the LO and transmitter laser. When the signal in one of the arms fades to zero the other signal is still present, and the summation of both signals (for BPSK) will be independent of the phase difference. As the signal has to be split in two components, intra-dyne detection has a 3-dB sensitivity penalty in comparison to homodyne detection for shot noise limited reception. Intra-dyne coherent detection at 680-Mbit/s was first shown by *Davis et. al.* in 1986 [411]. Similar to heterodyne detection, an intra-dyne receiver that uses single-ended detection is vulnerable to RIN from the LO. This can be solved through balanced detection, which requires a total of 4 photo-diodes and an optical hybrid with 4 outputs, each shifted by  $90^\circ$  degrees.

As an intra-dyne coherent receiver converts both the in-phase and quadrature component into the electrical domain, it can as well be used for QPSK detection. In comparison to a BPSK intra-dyne receiver demodulation, only the electrical baseband processing has to be modified [412, 413]. This is similar for heterodyne demodulation, which can separate both components through electrical baseband processing. For homodyne QPSK demodulation, on the contrary, a second receiver is required which results in a 3-dB sensitivity penalty. Hence, there is no sensitivity difference between homodyne, heterodyne or intra-dyne QPSK demodulation. The main disadvantage of coherent QPSK demodulation is that the laser linewidth tolerance is strongly reduced in comparison to PSK demodulation, as discussed in Section 9.1.4. This makes it difficult to demodulate QPSK with an optical phase-locked loop. The optical phase-locked-loop can be avoided by analog-digital conversion after the photodiode and subsequent phase drift compensation through digital signal processing, as first shown by *Derr* in 1991 [412, 414].

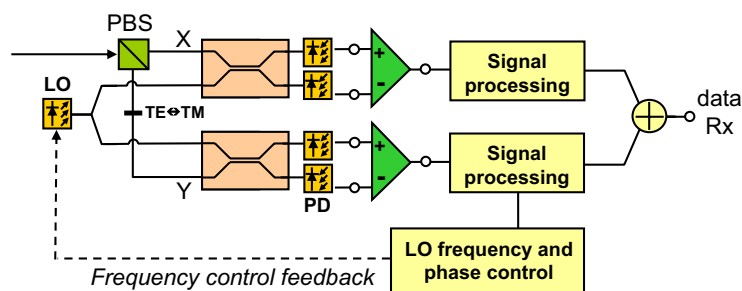


Figure 10.2: Principle of a polarization-diversity coherent receiver.

Coherent optical transmission systems require, in addition to active phase control, that the polarization of the received signal and the LO are matched. This can be achieved either through

active polarization control, as discussed in Chapter 7 for POLMUX with direct detection, or polarization diversity [415]. A polarization-diversity receiver was first demonstrated by *Okoshi et al.* in 1983 [416]. In this scheme two IF signals (heterodyne demodulation) obtained from orthogonal polarizations are combined after phase adjustment, and the combined IF signal is then demodulated. A more practical approach is to separately demodulate the two polarization components, as it does not require phase adjustment at an IF frequency [417]. Such a polarization-diversity scheme results only in a 0.4 dB receiver sensitivity penalty with respect to an ideal single-polarization receiver [418]. Figure 10.2 shows the basic layout of a polarization-diversity coherent receiver. Note that the polarization rotation  $TM \leftrightarrow TE$  is shown here explicitly, but is normally integrated into a PBS.

The combination of an intra-dyne receiver with polarization diversity, results in a coherent receiver that translates all properties of the optical signal into the electrical domain, as first demonstrated by *Okoshi et al.* in 1987 [419]. Together with digital signal processing this allows for a receiver implementation that is robust against the most significant transmission impairments.

## 10.2 Digital coherent receivers

As discussed in Chapter 9 the development of high-speed digital electronics allows for the use of powerful digital signal processing algorithms for distortion compensation. A digital coherent receiver enables the compensation of linear transmission impairments and polarization demultiplexing in the electrical domain. This provides in particular a high tolerance towards PMD and chromatic dispersion. The high tolerance against transmission impairments of a digital coherent receiver enables the upgrade of existing, 10-Gb/s optimized, infrastructure to 43-Gb/s and 111-Gb/s bit rates.

### 10.2.1 The optical front-end

The digital coherent receiver discussed here uses polarization-diversity intra-dyne detection to convert the full optical field (i.e. amplitude, phase and polarization information) to the electrical domain. This requires the detection of both the in-phase and quadrature components for two arbitrary, but orthogonal, polarization states - a total of four signals. Because the full (base-band) optical field is transferred to the electrical domain, a digital coherent receiver can operate with any kind of optical modulation format. The most advantageous modulation format to use is POLMUX-(D)QPSK [355, 420, 421, 422]. As POLMUX-DQPSK encodes 4 bits per symbol, the coherent receiver only has to operate at 10.75 Gbaud to achieve a 43-Gb/s bit rate. This allows the use of optical and electrical components with a  $\sim 10$ -GHz bandwidth. The typical setup of a digital coherent receiver using POLMUX-RZ-DQPSK modulation is shown in Figure 10.3. The transmitter laser is either a DFB laser or an ECL. The allowable product of linewidth times symbol period for a digital coherent receiver is approximately  $1.3 \cdot 10^{-4}$  [382]. This translates for a 10.75-Gbaud symbol rate into a  $\sim 1.4$ -MHz beat linewidth, which is difficult to achieve with

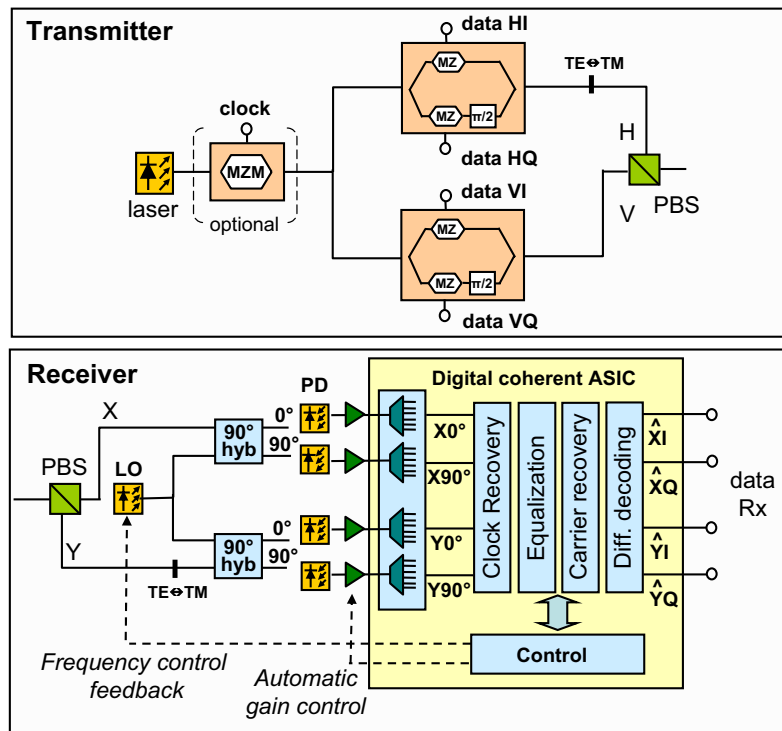


Figure 10.3: A digital coherent transmitter and receiver using POLMUX-DQPSK modulation.

standard DFB lasers. An ECL, with a typical linewidth of several hundred Kilohertz, provides therefore the optimum performance. In addition, the requirements on the LO laser might be somewhat higher than on the transmitter laser as it should have both a narrow linewidth as well as a low RIN. Typically, ECLs will therefore be used as LO in coherent transponders. In the off-line measurements<sup>2</sup> described in this chapter a  $\sim 1$  dB OSNR tolerance degradation has been observed when using a DFB laser at the transmitter. We therefore use ECL lasers for both the LO and transmitter laser in the results discussed in this chapter.

The POLMUX-RZ-DQPSK modulator chain starts with a MZM for RZ pulse carving. After the RZ pulse carver the signal is split up in two components using a power splitter. Each of the components is then fed to an integrated QPSK modulator. After DQPSK modulation, both polarization components are recombined using a PBS, which results in POLMUX-RZ-DQPSK modulation. For a 43-Gb/s bit rate it might be desirable to use NRZ instead of RZ pulse carving as this removes the need for the additional pulse carver. For a 111-Gb/s bit rate, on the other hand, it can be more attractive to use RZ pulse carving as it reduces (nonlinear) transmission impairments as well as residual chirp in the transmitted optical signal. Moreover, when NRZ coding is used, the required electro-optical bandwidth of the integrated QPSK modulator is higher, which might be difficult to achieve at a 111-Gb/s bit rate. A too low modulator bandwidth results in increased transmission impairments due to the broad amplitude level of the transmitted signal.

<sup>2</sup>A real-time digital coherent receiver requires implementation of the digital signal processing into integrated circuits. The measurements discussed here are therefore 'off-line'. In the off-line measurements, a set of data is sampled and stored using a DSO and afterwards processed on a personal computer



The digital coherent receiver structure is shown in Figure 10.3. First, a PBS splits up the signal into two arbitrary, but orthogonal, polarization components X and Y. The polarization components X and Y are therefore an arbitrary rotation of the two polarization components at the transmitter (H and V). The polarization rotation  $TM \leftrightarrow TE$  is once more shown explicitly, but is normally integrated into the PBS. Each of the polarization components is then fed into a  $90^\circ$  hybrid and mixed with the output of a LO laser. The LO is free-running and should be aligned with the transmitter laser within an approximate frequency range of several hundred megahertz. The allowable frequency range depends on the signal processing algorithms that are used for carrier phase estimation, which is discussed in Section 10.3.3. The LO can be fixed within this frequency range using a slow feedback signal generated through signal processing, as shown in [423]. The mixing of the received signal and LO in the  $90^\circ$  hybrids gives the in-phase and quadrature components, which are then fed to single-ended Pin/TIA photodiodes. Balanced photodiodes are not used in order to test a cost-efficient and lower complexity receiver architecture. The distortions from direct detected signal components are minimized using a high LO-signal power ratio of approximately 18 dB. In the electrical signal, the direct detected LO component can be removed using a D.C. block. Afterwards the four signals are digitalized using an ADCs.

### 10.2.2 Analog-to-digital converters

After the photodiodes, the four signals are quantized using ADCs, which are typically sampling at 2 samples/symbol. A 43-Gb/s transponder therefore requires  $\sim 25$ -Gsample/s ADCs, whereas a 111-Gb/s transponder would use  $\sim 60$ -Gsample/s ADCs. A  $\sim 25$ -Gbaud ADC implementation has been shown in different semiconductor technologies [17, 424, 18]. Particularly BiCMOS technology allows for the realization of high speed ADCs. The most promising architecture is a full-flash topology where  $2^Q - 1$  parallel comparators are used to convert the signal with a resolution of  $Q$  bits in a single step [17, 425]. ADCs can also be made with CMOS technology, but this requires the use of a number of slower converters which are then time interleaved to achieve a high total sampling rate [424, 18]. Realizing the ADCs in CMOS technology has the important advantage that they can be combined on a single chip with the subsequent digital signal processing. And as the digital signal processing has an inherently parallel architecture this fits well with the parallel ADC architecture required for CMOS implementation. At the time of writing, a 50-Gsample/s ADC design has only been realized for digital storage oscilloscopes [426], where the power dissipation requirements are less strict than for a transponder. The required vertical resolution of the ADCs to have a negligible penalty resulting from quantization distortions is 5-6 bits [427]. In order to use available vertical resolution as effectively as possible the dynamic range of the ADC should be fully used. This requires an automatic gain control in front of the ADCs to adapt to changes in the received optical power, for example resulting from optical transients or component aging. Finally, also the electrical bandwidth of the ADCs is an important design parameter. Generally, an electrical 3-dB bandwidth of 0.5 times the baudrate is sufficient [428]. However, the required bandwidth depends strongly on the roll-off with frequency and specifying only the 3-dB ADC bandwidth can be somewhat misleading.

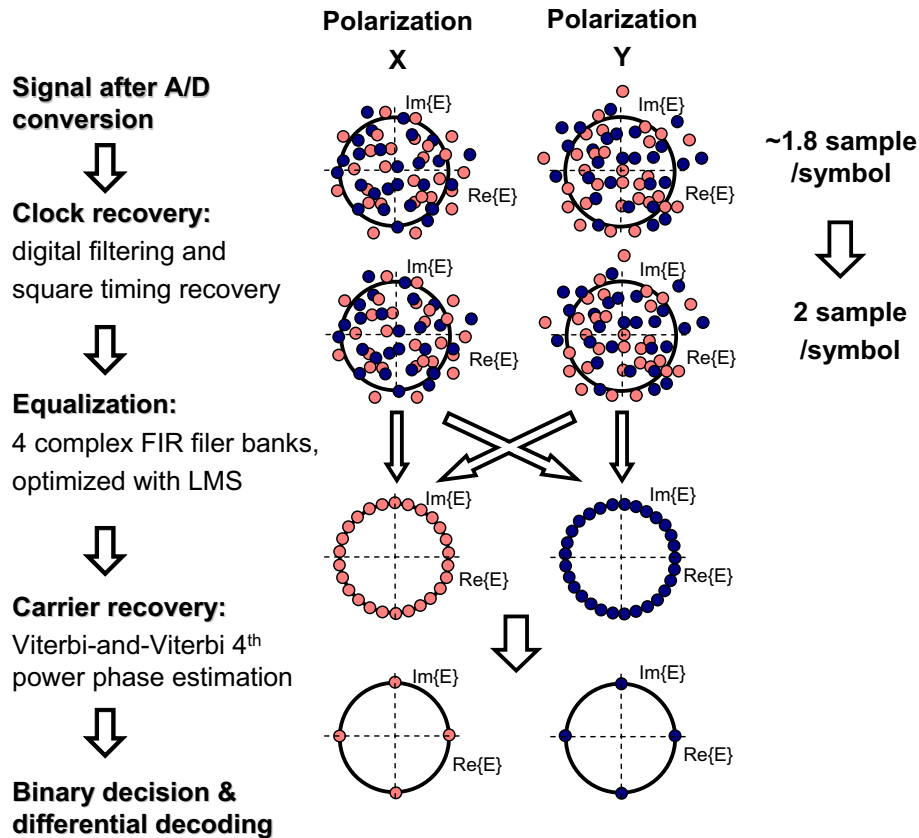


Figure 10.4: Overview of the signal processing steps in a digital coherent receiver, signal constellations exemplify the signals obtained after each processing step.

### 10.3 Digital equalization algorithms

In this section, the digital signal processing algorithms that enables the electronic distortion compensation are discussed in detail. Figure 10.4 shows the different steps used in the digital coherent receiver as discussed in this thesis. After detection and quantization, first of all, clock recovery is applied. Afterwards the linear distortions in the signal are equalized using finite impulse response (FIR) filters, this step also realizes the polarization de-multiplexing. Subsequently, carrier phase estimation (CPE) is applied to cancel out the phase and frequency offset between the LO and transmitter laser. In the final step a digital decision is taken and differential decoding is applied to prevent cycle slips between the LO and transmitter laser.

We note that the digital signal processing algorithms would normally process the data in blocks in order to parallelize the processing and reduce the required clock rate of the hardware. This requires an overlap between consecutive blocks, such that the full impulse response of every symbol within the block is taken into account. The block-wise processing results therefore in an overhead to the processing and memory requirements, which scales linearly with the number of equalizer taps and inversely with the block length. The overlap between consecutive blocks can be implemented using, for example, the overlap-and-add method [429].

### 10.3.1 Clock recovery and re-timing

For the transmission experiment discussed in this chapter, a DSO is used to convert the analog signal to the digital domain and subsequently store the received signal for later off-line processing. The DSO samples at 20 Gbaud (for the 10.75-Gbaud experiments) or at 50 Gsample/s (for the 27.75-Gsample/s experiments). This translates in both cases to  $\sim 1.8$  sample/symbol, and hence the sequence must be re-timed to obtain an integer number of samples per symbol (either 1 or 2). In the first step the signal is approximately re-sampled to  $\sim 2$  sample/symbol.

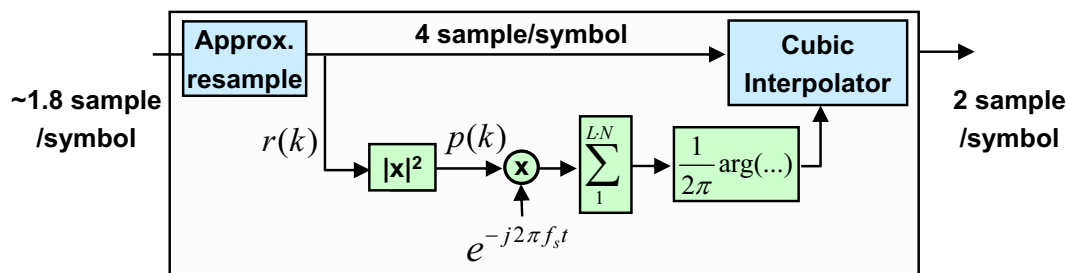


Figure 10.5: Clock recovery and re-sampling.

This is achieved by increasing the sampling rate from  $\sim 1.8$  sample/symbol to 4 sample/symbol through up-sampling, based on knowledge of the symbol rate and oscilloscope sampling rate. This typically leaves some residual timing offset caused by timing error and jitter that must be compensated using a clock-recovery scheme. In order to exactly re-sample to 2 sample/symbol the digital filter and square timing recovery algorithm is used as described by *Oeder and Meyer* in [430]. In this scheme the timing function is derived from the power envelope of the received signal by block-wise computing the complex Fourier coefficient at the symbol rate  $\chi_m$ .

$$\chi_m = \sum_{k=mLN}^{(m+1)LN-1} p(k) e^{-j2\pi k/L}, \quad (10.4)$$

where  $m$  is the block index for blocks of length  $N$ ,  $L$  is the over-sampling factor. The power envelope  $p(k)$  is calculated from the square of the four received signal components ( $X_{0^\circ}^2 + X_{90^\circ}^2 + Y_{0^\circ}^2 + Y_{90^\circ}^2$ ). Note that the fraction  $k/L$  corresponds to the sample period  $f_s t$ . The normalized phase  $\hat{\epsilon}$  of the Fourier coefficient  $\chi_m$  is then a measure of the sampling phase error for block  $m$  and can be used to re-sample the data using a cubic interpolator,

$$\hat{\epsilon} = \frac{1}{2\pi} \arg(\chi_m). \quad (10.5)$$

Re-timing the signal with the "filter and square timing recovery" algorithm becomes very critical in the presence of large signal distortions. In a digital coherent receiver specifically designed for a 10.75/27.75-Gbaud symbol rate, the ADCs would therefore sample at an exact multiple of the baud rate, and no re-timing of the signal is required. In addition this also saves the implementation complexity of the re-timing algorithm.

### 10.3.2 Distortion compensation & polarization de-multiplexing

In the next step, the electronic equalization implements both polarization de-multiplexing as well as the compensation of (linear) transmission impairments. The electronic equalization, as depicted in Figure 10.6a, is implemented by a bank of 4 FIR filters with complex tap weights ( $h_{xx}$ ,  $h_{yx}$ ,  $h_{xy}$  and  $h_{yy}$ ). The FIR filters are arranged in a butterfly structure to enable polarization de-multiplexing, this structure is also known as a cross polarization interference canceler (XPIC) [431, 432]. Note that the polarization de-multiplexing can, in principle, be implemented with a single tap structure and that longer FIR filters are necessary to compensate for chromatic dispersion and PMD. The output signal of the equalization stage can be described as

$$\underbrace{\begin{bmatrix} \hat{X} \\ \hat{Y} \end{bmatrix}}_{\text{equalized signal}} = \underbrace{\begin{bmatrix} \hat{h}_{xx}^{-1}(f) & \hat{h}_{yx}^{-1}(f) \\ \hat{h}_{xy}^{-1}(f) & \hat{h}_{yy}^{-1}(f) \end{bmatrix}}_{\text{equalizer}} \cdot \underbrace{\begin{bmatrix} X \\ Y \end{bmatrix}}_{\text{detected signal}}, \quad (10.6)$$

where in principle the matrix  $\hat{h}^{-1}$  is an approximation of the inverse of the channel matrix  $h$  which is defined as,

$$\underbrace{\begin{bmatrix} X \\ Y \end{bmatrix}}_{\text{detected signal}} = \underbrace{\begin{bmatrix} h_{xx}(f) & h_{yx}(f) \\ h_{xy}(f) & h_{yy}(f) \end{bmatrix}}_{\text{channel}} \cdot \underbrace{\begin{bmatrix} H \\ V \end{bmatrix}}_{\text{transmitted signal}}, \quad (10.7)$$

$H$  and  $V$  are the polarization tributaries of the transmitted signal,  $X$  and  $Y$  are the detected polarization components and  $\hat{X}$  and  $\hat{Y}$  are the recovered polarization tributaries after signal processing.

Figure 10.6b shows the FIR filter bank in more detail. Each bank consists of a number of taps, which are either baud-rate ( $T_0$ -spaced, 1 sample/symbol) or fractionally-spaced ( $T_0/2$ -spaced, 2 sample/symbol). Fractionally-spaced equalizers generally provide better performance than baud-rate equalizers since they serve as both matched filter and equalizer. Fractionally-spaced equalizers can however have difficulty converging because the neighboring tap signals are highly correlated [433].

Figure 10.6c shows the complex multiplication required for each filter tap. Adapting the filter tap as a single complex filter tap is only possible when the signal is perfectly symmetrical, i.e. when the real and imaginary components have the same magnitude, which is normally not the case. The single complex-valued tap is therefore structured as four real-valued filter taps, which are optimized independently. The filter taps can be optimized using least mean squares (LMS) algorithms such as the constant modulus algorithm (CMA) [434, 435] or the decision-directed least mean squares (DD-LMS) algorithm [436].

CMA exploits the property of PSK modulation (e.g. BPSK, QPSK) that all points in the signal constellation are located on a circle, as shown in Figure 10.7. It therefore tries to choose the tap coefficients in such a way that the variance between the samples and the circle is minimized, which translates into minimizing an error function,

$$\begin{aligned} \epsilon_x &= R^2 - |\hat{x}|^2 \\ \epsilon_y &= R^2 - |\hat{y}|^2 \end{aligned}, \quad (10.8)$$

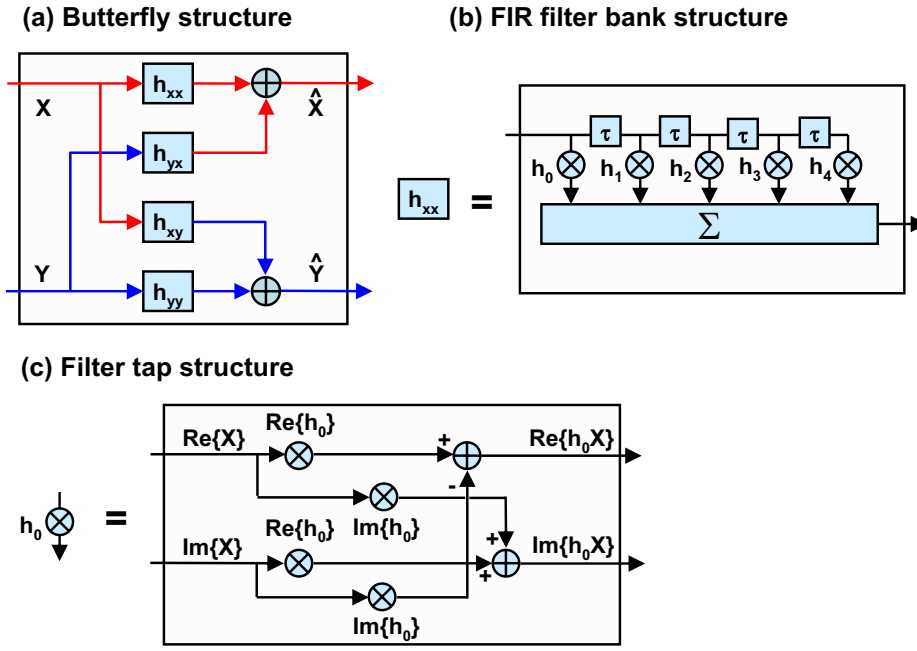


Figure 10.6: Digital Equalization using linear FIR filters (a) butterfly structure for polarization demultiplexing; (b) linear FIR filter structure and (c) filter tap structure. The tap delay  $\tau$  is equal to  $T_0$  for a baud-rate equalizer or  $T_0/2$  for fractionally-spaced equalizers.

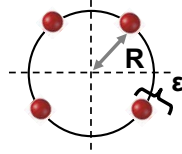


Figure 10.7: Principle of CMA.

where  $R$  is the radius of the constellation points, which can be easily computed from the average optical power. Because of the squaring in the error function, CMA is not influenced by a phase rotation between consecutive symbols. CMA is therefore robust against a large frequency offset between the LO and transmitter laser. Using the error function, the tap coefficients are now updated until the algorithm converges and the error function becomes small enough. The update of the tap coefficients follows according to,

$$\begin{aligned} \hat{h}_{xx}^{-1} &= \hat{h}_{xx}^{-1} + \mu \varepsilon_x \hat{x} \cdot x^* & \hat{h}_{xy}^{-1} &= \hat{h}_{xy}^{-1} + \mu \varepsilon_x \hat{x} \cdot y^* \\ \hat{h}_{yx}^{-1} &= \hat{h}_{yx}^{-1} + \mu \varepsilon_y \hat{y} \cdot x^* & \hat{h}_{yy}^{-1} &= \hat{h}_{yy}^{-1} + \mu \varepsilon_y \hat{y} \cdot y^* \end{aligned} \quad (10.9)$$

where  $\mu$  is a convergence parameter and  $x^*$  is the complex conjugate of  $x$ . Note that for  $N$  taps, each tap  $n$  of the FIR filter is updated separately,

$$\hat{h}_n^{-1} = \hat{h}_n^{-1} + \mu \varepsilon_x \hat{x}_n \cdot x_n^* \quad (10.10)$$

The tapweights  $\hat{h}_n^{-1}$  therefore increase or decrease with  $\mu \varepsilon$ . The speed of convergence depends on the magnitude of  $\mu$ , where a larger value results in faster convergence but also increases the

residual error as well as the possibility that the algorithm does not converge to a solution. The more severe the channel distortions are, the smaller  $\mu$  generally should be chosen.

The second algorithm that can be used for equalization is DD-LMS. This is a decision-directed algorithm, which implies that the algorithm makes a decision on the data in order to estimate the error function. However, DD-LMS is still a blind equalization algorithm, and it can be used either before or after the carrier phase estimation. Equation 10.11 gives the DD-LMS error function.

$$\begin{aligned}\varepsilon_x &= R \cdot \text{csgn}(\hat{x})/\sqrt{2} - \hat{x} \\ \varepsilon_y &= R \cdot \text{csgn}(\hat{y})/\sqrt{2} - \hat{y} \end{aligned} \quad (10.11)$$

where  $\text{csgn}(x)$  and  $\text{csgn}(y)$  are the complex sign functions defined by,

$$\text{csgn}(x) = \begin{cases} 1 + j & [\text{Re}\{x\} > 0, \text{Im}\{x\} > 0] \\ 1 - j & [\text{Re}\{x\} > 0, \text{Im}\{x\} < 0] \\ -1 + j & [\text{Re}\{x\} < 0, \text{Im}\{x\} > 0] \\ -1 - j & [\text{Re}\{x\} < 0, \text{Im}\{x\} < 0] \end{cases} \quad (10.12)$$

The tap coefficients are then updated according to,

$$\begin{aligned}\hat{h}_{xx}^{-1} &= \hat{h}_{xx}^{-1} + \mu \varepsilon_x \cdot x^* & \hat{h}_{xy}^{-1} &= \hat{h}_{xy}^{-1} + \mu \varepsilon_x \cdot y^* \\ \hat{h}_{yx}^{-1} &= \hat{h}_{yx}^{-1} + \mu \varepsilon_y \cdot x^* & \hat{h}_{yy}^{-1} &= \hat{h}_{yy}^{-1} + \mu \varepsilon_y \cdot y^* \end{aligned} \quad (10.13)$$

As there is no squaring in the DD-LMS algorithm, it is sensitive to phase distortions. In the presence of significant phase distortion the convergence parameter  $\mu$  should therefore be suitably small. Note that it is also possible to combine the DD-LMS algorithm with CPE, which should make it more robust to a larger frequency offset between transmitter and LO laser [435]. A further possibility is to use DD-LMS with training sequences instead of the blind equalization [437]. In this case the error function is computed by comparison of the output sequence with a known training sequence.

Ideally, both CMA and DD-LMS converge to the same solution. However, in practice CMA is more robust to channel distortions and especially phase rotations. The DD-LMS algorithm, on the other hand, is less robust to channel distortions and phase offset but is more likely to converge to the optimum solution. When only the DD-LMS algorithm is used for channel equalization, the convergence parameter  $\mu$  should be smaller and the optimization process will require more iterations. For the off-line measurements described in the remainder of this chapter this results in slow processing as each new measurement starts by assuming an ideal channel model. In a realtime equalizer, each processed block can start with the channel model of the previous block and update this using a limited number of iterations. Under such conditions, the DD-LMS optimization algorithm is more practical. Alternatively, first CMA can be applied to the data to roughly equalize the majority of the channel distortions. In a second step this is then followed by the DD-LMS algorithm, which can be preceded or combined with the carrier recovery, to equalize the remaining distortions [435]. Figure 10.8 shows an example of the resulting equalizer taps after optimization with the CMA algorithm.

A further consideration for the digital coherent receiver is the required number of taps to compensate for channel distortions. The described equalization scheme can compensate for linear

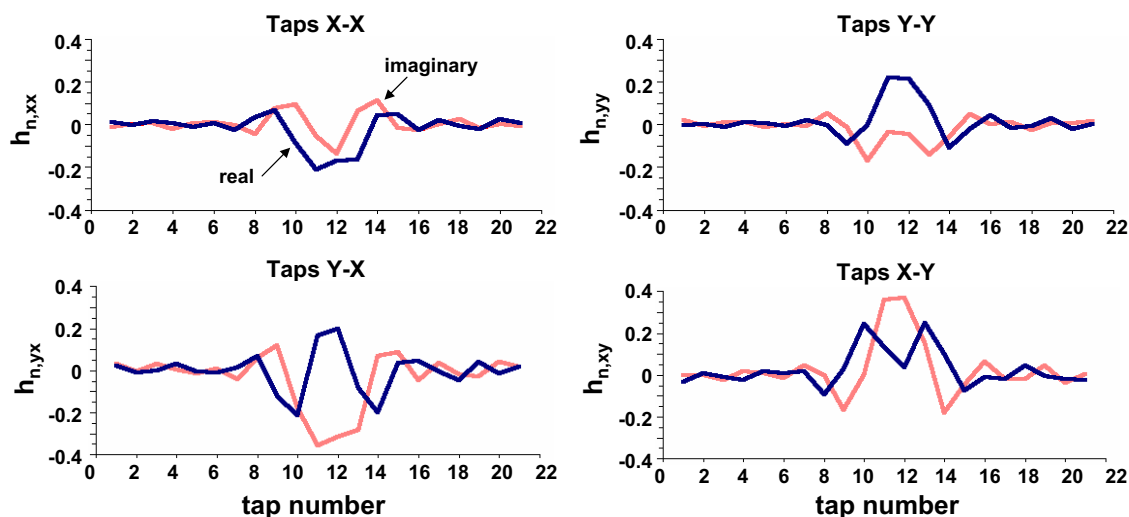


Figure 10.8: Resulting tap coefficients for a 21 tap FIR filter with 111-Gb/s POLMUX-RZ-DQPSK modulation, 2000-ps/nm and a  $30^\circ$  polarization offset. The lines depict the real and imaginary part part of the tap vector.

distortions as long as the impulse response length of the equalizer is at least equal to the impulse response length of the channel distortion. The chromatic dispersion and PMD that can be compensated increases therefore linearly with the number of FIR filter taps. For certain applications it can be desirable that a digital coherent receiver can compensate for the full chromatic dispersion in a long-haul transmission link [422, 435, 438]. Assuming, for example, transmission over 3000-km of SSMF this requires the compensation of  $\sim 50,000$  ps/nm of chromatic dispersion. At a 10.75-Gbaud symbol rate, the impulse response of such a channel broadens an impulse over  $\sim 100$  symbol periods. This would require a FIR filter bank with  $>100$  taps, which would be difficult, if not impossible, to realize in a real-time implementation. As well, it is questionable if the optimization algorithms would always converge properly for a FIR filter bank with such large tap counts. For a larger number of taps ( $>16$ ), it is therefore more efficient to implement a fixed FIR filter by converting the signal to the frequency domain using a fast-Fourier transform (FFT). An arbitrary amount of chromatic dispersion can then be compensated by a single multiplication with the desired frequency response. Afterwards the signal is converted back to the time domain with an inverse FFT. The polarization tracking and compensation, as well as the compensation of any residual chromatic dispersion is implemented afterwards with shorter (typically 5 taps) FIR filter banks. This uses again the above mentioned butterfly structure and is optimized with either the CMA or the DD-LMS algorithm. The drawback of such a scheme is that it is not based on blind estimation, i.e. the amount of chromatic dispersion that should be compensated has to be roughly known. This implementation has the further advantage that the carrier phase be approximately estimated before equalization, as discussed in the next section and shown in [435], which makes the subsequent equalization stage more efficient. The digital equalization steps in such a receiver architecture are shown in Figure 10.9.

A further advantage of digital coherent receivers is that the FIR tap values can be used to estimate the transmission impairments for optical performance monitoring [439, 440]. When we assume a linear transmission channel with *only* chromatic dispersion and DGD the channel matrix can

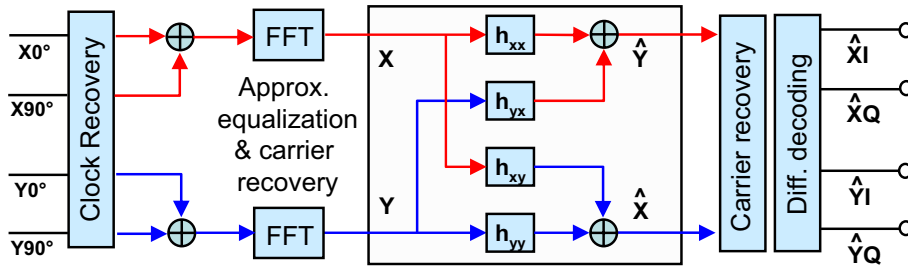


Figure 10.9: Digital Equalization using a combination of FFT and linear FIR filters .

be written as,

$$H(f) = \begin{bmatrix} h_{xx}(f) & h_{yx}(f) \\ h_{xy}(f) & h_{yy}(f) \end{bmatrix} = \begin{bmatrix} u(f) \cdot d(f) & v(f) \cdot d(f) \\ -v^*(f) \cdot d(f) & u^*(f) \cdot d(f) \end{bmatrix}, \quad (10.14)$$

where

$$\begin{bmatrix} u(f) & v(f) \\ -v^*(f) & u^*(f) \end{bmatrix}, \quad (10.15)$$

is a unitary matrix which denotes the transfer function of the DGD.  $d(f)$  is the chromatic dispersion transfer function, which is equal to

$$d(f) = \exp(jf^2 \frac{\beta_2 L}{2}). \quad (10.16)$$

A property of a unitary matrix is, that the absolute value of its determinant is equal to one,

$$|u(f) \cdot u^*(f) - v(f) \cdot -v^*(f)| \cdot d(f)^2 = d(f)^2 = \exp(jf^2 \beta_2 L), \quad (10.17)$$

where  $\beta_2 L/2$  is the accumulated dispersion. The absolute value of  $u(f)$  or  $v(f)$  can subsequently be used to estimate the DGD, which is shown in [439]. The accumulated PDL in the received signal can as well be estimated using signal processing in digital coherent receiver, which is discussed in [440].

### 10.3.3 Carrier phase estimation

After the electronic equalization a CPE stage is used to correct for the frequency and phase offset between transmitter and LO laser as described by *Viterbi and Viterbi* in [441]. For analog coherent receivers the frequency deviations between the transmitter and LO laser is one of the most critical design parameters. For a digital coherent receiver, the signal processing enables a much larger tolerance towards frequency deviations. Depending on the signal processing algorithms a frequency de-tuning range of several hundred Megahertz [353] to several Gigahertz [435] is possible. However, a feedback from the signal processing to LO, as shown in Figure 10.3, is still desirable to tune the LO approximately to the center of this frequency range.

The principle behind CPE is shown in more detail in Figure 10.10. As a first step the frequency can be corrected approximately. This is for example possible by integrating the phase change



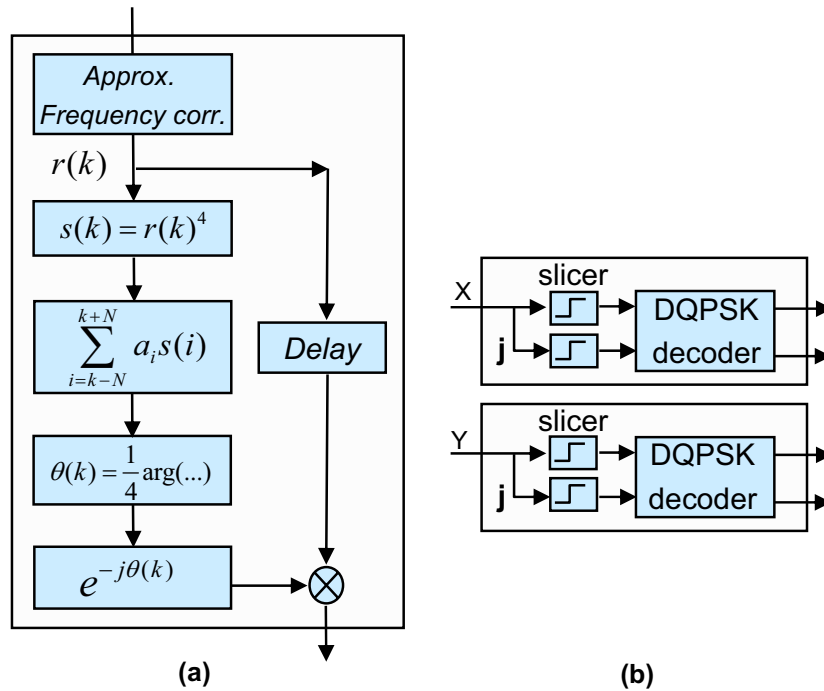


Figure 10.10: (a) Carrier phase estimation and (b) slicer followed by a DQPSK decoder.

over a large number of symbols or by estimating the shift in the frequency domain after FFT, as shown by Savory *et. al.* in [435]. Note that the CPE algorithm works also when it is not preceded by approximate frequency correction, but this will generally result in smaller frequency offset window and/or a performance penalty. The CPE algorithm first takes the 4<sup>th</sup> power of the symbols in order to remove the phase modulation from the QPSK modulated signal,

$$s(k) = r(k)^4, \quad (10.18)$$

where  $r(k)$  is either the  $x'$  or  $y'$  vector obtained from the equalization stage. Subsequently a running average is used over a predefined number of symbols of the complex vectors  $s(k)$ ,

$$\sum_{i=k-N}^{k+N} a_i s_i. \quad (10.19)$$

For an  $2N + 1$  symbol CPE the  $N$  pre-cursor and  $N$  post-cursor symbols are considered. The parameter  $a_i$  can implement a windowing function, such as for example a Wiener filter [383]. The argument then gives the phase correction factor  $\theta(k)$  that is used to apply a correction to the original symbols.

The number of symbols over which the CPE averages can have a critical influence on the performance of the digital coherent receiver. When ASE is the dominant impairment a larger number of symbols for CPE is more optimal as this will average out the (zero mean) Gaussian noise and obtain a better phase estimate. On the other hand, in the presence of significant phase noise a smaller number of symbols will be preferable as this allows better tracking of the fast change in phase offset. The most likely sources of phase noise are a LO or transmitter laser with a broad

laser linewidth ( $\sim$ MHz) or XPM-induced phase noise from neighboring WDM channels. The impact of XPM is especially severe when the adjacent channels are 10.7-Gb/s NRZ modulated. For 43-Gb/s POLMUX-NRZ-QPSK the optimum CPE length is found to be averaging over 17 symbols. When DFB lasers are used for the transmission and/or LO laser, a shorter CPE length will result in better performance, as for example shown in [442] where a CPE length of 9 is found to be optimum. Note that using 2 symbols for CPE is similar to differential detection in a direct detection receiver.

### 10.3.4 Differential decoding & error counting

In the final stage of the electronic signal processing, a digital decision on each symbol is made on the symbols using a slicer. In the experiments discussed in this chapter we use digital differential decoding. The digital differential decoding is used to avoid the possibility of cycle slips. A cycle slip result in loss of synchronization, for example because of a sudden jump in phase difference between LO and transmitter laser. The possibility of cycle slips is effectively avoided through differential detection. However, the differential decoding doubles the BER which results in a  $\sim$ 0.5-dB OSNR penalty [10]. However, there are other algorithms that can be used to detect and correct for cycle slips. This might be desirable as it lowers the OSNR requirement by 0.5 dB.

## 10.4 Distortion compensation at 43-Gb/s

Section 10.3 discussed the algorithms that are used for the distortion compensation with a digital coherent receiver. In this section we discuss the compensation of different impairments using experimental results obtained with a coherent receiver for 43-Gb/s POLMUX-NRZ-DQPSK.

The digital coherent receiver setup discussed in Section 10.2 is for simplicity somewhat modified in the experiments, as shown in Figure 10.11a. The output signal of an ECL at a wavelength of 1550.12 nm is modulated using an integrated DQPSK modulator. A 10.75-Gb/s PRBS with a length of  $2^{15} - 1$  and a relative delay of 9 bits for de-correlation is split and fed to both inputs (data I and Q) of the DQPSK modulator. Afterwards, a POLMUX signal is generated by dividing the signal into two tributaries (H and V) and recombining those with orthogonal polarizations and a 106 symbol delay between the tributaries for de-correlation. This results in 43-Gb/s POLMUX-NRZ-DQPSK modulation. Figures 10.11b and 10.11c show the directly detected eye diagrams for NRZ-DQPSK with (43 Gb/s) and without (21.5 Gb/s) POLMUX signaling, respectively.

At the receiver the OSNR is set using a VOA followed by an EDFA and a 37-GHz CSF. The signal is then fed into the coherent receiver, with an input power of approximately -9 dBm. The PBS splits the signal into two arbitrary, but orthogonal, polarization components X and Y. Each of the polarization components is then fed into a fiber based  $90^\circ$  hybrids where it is mixed with the output of the LO laser. The LO is a tunable ECL with 100-kHz linewidth, manually aligned to within 400 MHz of the transmitter laser. The output power of the LO is 9 dBm. The  $90^\circ$  hybrids

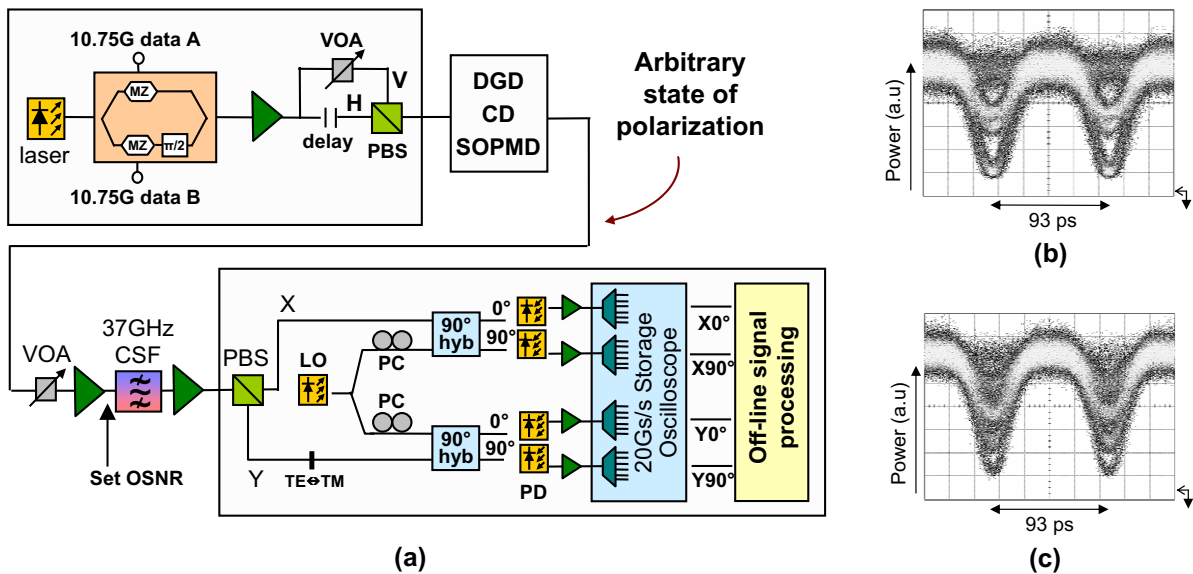


Figure 10.11: (a) Experimental setup for the 43-Gb/s POLMUX-NRZ-DQPSK transmitter and coherent receiver; eye diagrams for (b) 21.5-Gb/s NRZ-DQPSK and (c) 43-Gb/s POLMUX-NRZ-DQPSK.

consist of asymmetric 3x3 fiber couplers with a 20%:40%:40% coupling ratio [420]. Mixing of LO and signal components in the hybrids leads to orthogonal signals on the 20% and one of the 40% outputs. This is discussed in more detail in Appendix C. The polarization controllers (PC) between the LO and the 90° hybrids are required because the latter are not polarization-maintaining. The in-phase and quadrature components of both polarizations are detected using four single-ended pin/TIA photodiodes. The absolute power on the photodiodes (dominated by the LO) is between -2 and +1 dBm, where the power variation results from the use of an asymmetric 2:2:1 coupler. Using a Tektronix TDS6154 digital storage oscilloscope, each of the four signals is then sampled with 20-Gbaud ADCs to obtain four data sets of 524,184 bits each (in total  $\sim 2 \cdot 10^6$  bits). The four data sets are subsequently off-line post-processed with the digital equalization algorithms described in Section 10.3. After processing the differentially decoded sequence is compared to the transmitted PRBS, taking into account the differential decoding. For back-to-back measurements, the BER is measured at a number of different OSNR values, and the OSNR required for a BER of  $10^{-4}$  is interpolated.

### 10.4.1 Back-to-back OSNR requirement

Figure 10.12a depicts the required OSNR for single polarization 21.5-Gb/s NRZ-DQPSK and 43-Gb/s POLMUX-NRZ-DQPSK with the digital coherent receiver. This shows the expected 3-dB difference in OSNR tolerance with the doubling of the bit rate. This indicates that a digital coherent receiver is capable of electrical polarization de-multiplexing without a noticeable performance penalty. Note that, unlike the results described in Chapter 7, the receiver is polarization sensitive for both cases and the OSNR difference is therefore exactly 3 dB. With 43-Gb/s POLMUX-NRZ-DQPSK, the required OSNR is 11.2 dB and 13.1 dB for a  $10^{-3}$  and  $10^{-4}$  BER, respectively.

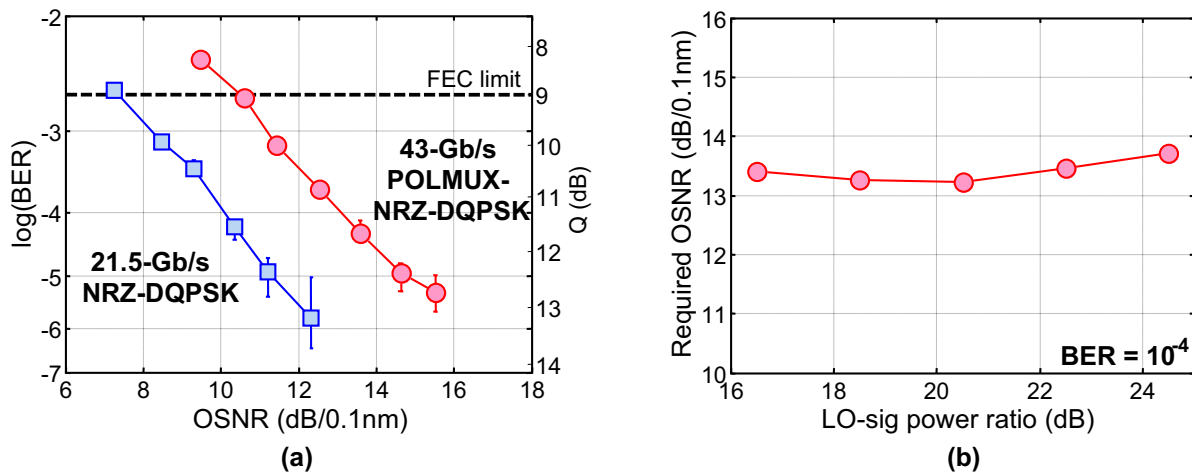


Figure 10.12: (a) Back-to-back sensitivity for 43-Gb/s POLMUX-NRZ-DQPSK with the OSNR requirement for 21.5-Gb/s NRZ-DQPSK as a reference; (b) Required OSNR versus LO-signal ratio.

The required OSNR as a function of the LO-signal power ratio is shown in Figure 10.12b. A high LO-signal power ratio is beneficial as it reduces the impairments resulting from direct detection components. However, the measured results shows that the OSNR penalty is minimal for a relatively broad range of LO-signal power ratios. The optimum LO-signal power ratio is between 18 dB and 20 dB, and 18 dB is used in the remainder of the experiments. A too high LO-signal power ratio results here in a higher OSNR requirement as the signal power becomes too small (the LO power is kept constant).

### 10.4.2 Differential group delay

Probably the most significant impairment that can be compensated with a digital coherent receiver is PMD, as there is no easy optical compensation approach. Since a digital coherent receiver detects the linear optical field for both polarization states and DGD is a linear distortion in the optical field, the inverse channel constructed by the FIR filters can effectively cancel out the distortion induced through DGD.

As a first step, only the DGD is considered using a DGD emulator. The input SOP into the DGD emulator is set to a  $45^\circ$  offset with respect to the transmitted polarization tributaries, which results in a worst-case alignment. Figure 10.13a shows the DGD tolerance for different numbers of FIR taps. For 13 taps no significant penalty is measured for a DGD up to 200 ps. This corresponds to an mean DGD of about 60 ps for a  $10^{-5}$  outage probability, which is approximately the DGD tolerance of a direct detection 2.5-Gb/s NRZ-OOK receiver. When the number of FIR taps is reduced to 5, a 1-dB OSNR penalty is evident for 60 ps of DGD. It can also be observed that the OSNR requirement is slightly reduced at 0-ps DGD when the number of filter taps increases. We conjecture that this results from the equalization of transmitter and receiver imperfections.

### 10.4.3 Polarization dependent loss

Figure 10.13b shows the influence of PDL on the digital coherent receiver. PDL is more detrimental for POLMUX signaling in comparison to polarization insensitive modulation as it results in a performance difference between the polarization channels. Here, PDL is added to the signal as a power imbalance by attenuating one of the polarization tributaries in the transmitter, which equals the case shown in Figure 7.11b. As a result, both tributaries will also have a different OSNR at the receiver. In Figure 10.13b the worst-case tributary is depicted for 2 dB and 5 dB of PDL, respectively. The lower signal power in the worst-case tributary reduces the OSNR by 1.1 dB and 3.2 dB compared to the average OSNR, respectively. This indicates that even with a severe power imbalance between both channels, coherent equalization can still recover the polarization tributaries. When the PDL is combined with up to 120 ps of DGD, slightly higher penalties are evident. This is most likely the result of the attenuated tributary having insufficient signal power to use the full dynamic range of the ADCs. Note that PDL induced depolarization is not considered here, but as shown in Section 7.3.4 the difference in penalty between both cases is marginal for a direct detection receiver. Hence, for this case we also expect to observe similar penalties with a digital coherent receiver. The combined impact of PMD and PDL might have a more significant impact, but is not considered here.

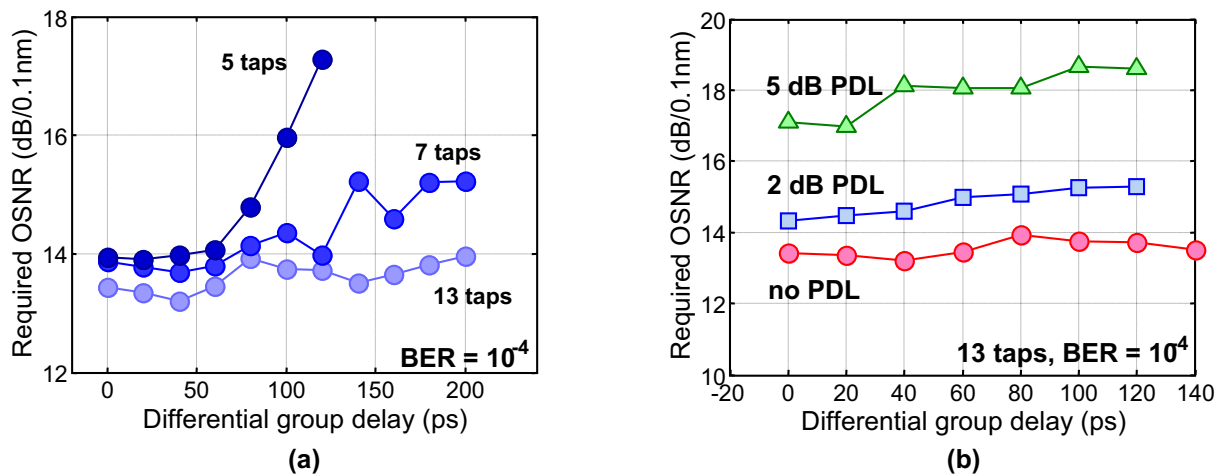


Figure 10.13: (a) required OSNR versus DGD for various tap lengths and (b) DGD tolerance  $\circ$  without PDL and in the presence of  $\square$  2-dB and  $\triangle$  5-dB of PDL.

### 10.4.4 Higher-order polarization-mode dispersion

Higher-order PMD can have a severe impact for POLMUX signaling as the polarization demultiplexing becomes wavelength dependent, which results in depolarization [326]. The experimental setup that is used here to evaluate the combined effect of DGD and SOPMD is depicted in Figure 10.14a. The signal passes first through a polarization scrambler to randomize the state of polarization, followed by a DGD emulator. Subsequently, SOPMD is added to the signal using a NewRidge NRT-40133A emulator preceded by a second polarization scrambler. The SOPMD

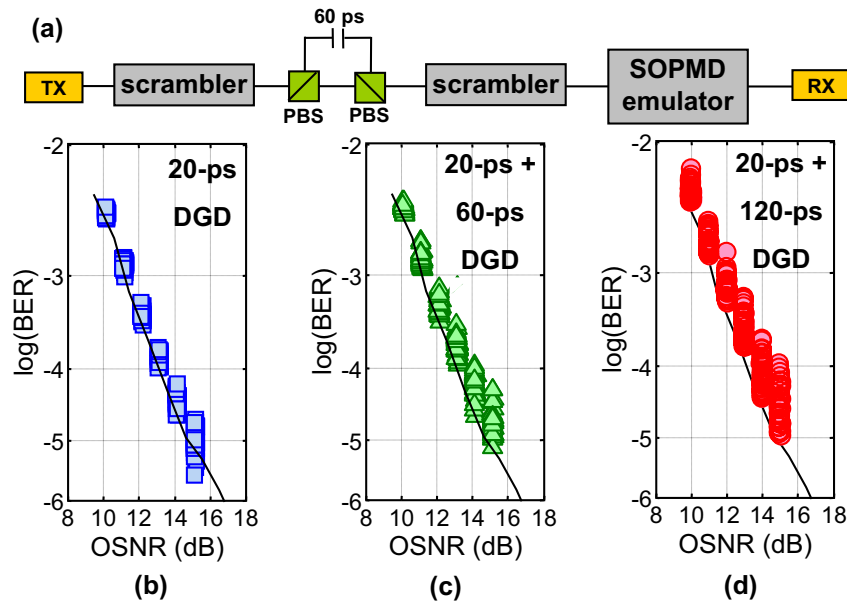


Figure 10.14: (a) Experimental setup used for higher order PMD evaluation, (b-d) 270-ps<sup>2</sup> SOPMD combined with different amounts of DGD, the line indicates back-to-back performance and a 13 tap FIR filter is used.

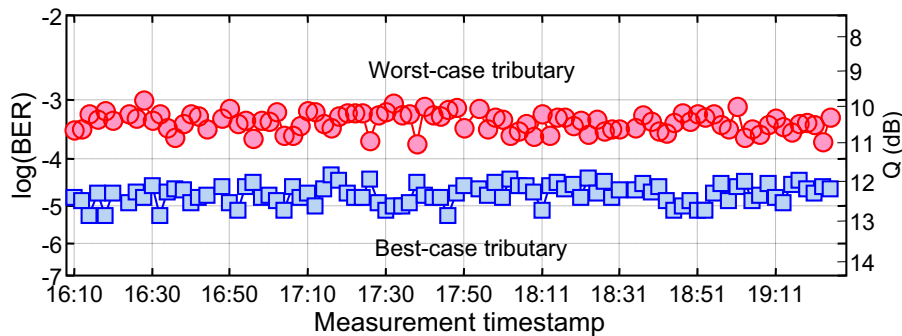


Figure 10.15: Stability test over three hours with 2-dB PDL, 80-ps + 20-ps DGD, 270-ps<sup>2</sup> SOPMD and a 13 tap FIR filter, both best-case and worst-case polarization tributaries are depicted.

emulator is set to add the maximum amount of 20 ps of DGD and 270 ps<sup>2</sup> of SOPMD to the signal. For this configuration (Figure 10.14b, 40 measurements for each setting/OSNR) no relevant penalty is observed. The measured points below the back-to-back OSNR requirement are due to measurement uncertainty. Note that for a 10-Gbaud symbol rate, 270 ps<sup>2</sup> of SOPMD will normally not result in a significant penalty due to the small spectral width of the signal. In Figure 10.14d the amount of DGD is increased to 120 ps + 20 ps of DGD and 270 ps<sup>2</sup> of SOPMD and still the worst-case OSNR penalty is below  $\sim 2$  dB for a  $10^{-4}$  BER. This indicates that coherent equalization is not overly sensitive to SOPMD and meets the requirements of a 43-Gb/s transponder. Further statistical measurements are required to understand the fundamental limits of coherent equalization with respect to higher order PMD impairments.

In Figure 10.15, measurements are depicted over a time period of three hours to show system stability. The measurement are taken with a 2 minutes interval. To illustrate the successful

compensation of PMD related impairments, PDL, DGD and SOPMD are added to the signal. The 2-dB of PDL is once again added by attenuating one of the tributaries at the transmitter. DGD and SOPMD are added in the same way as previously described for the results depicted in Figure 10.14b-d. The results show that despite the presence of severe PMD impairments, only a small BER variation ( $\sim 1$  dB) is evident over time.

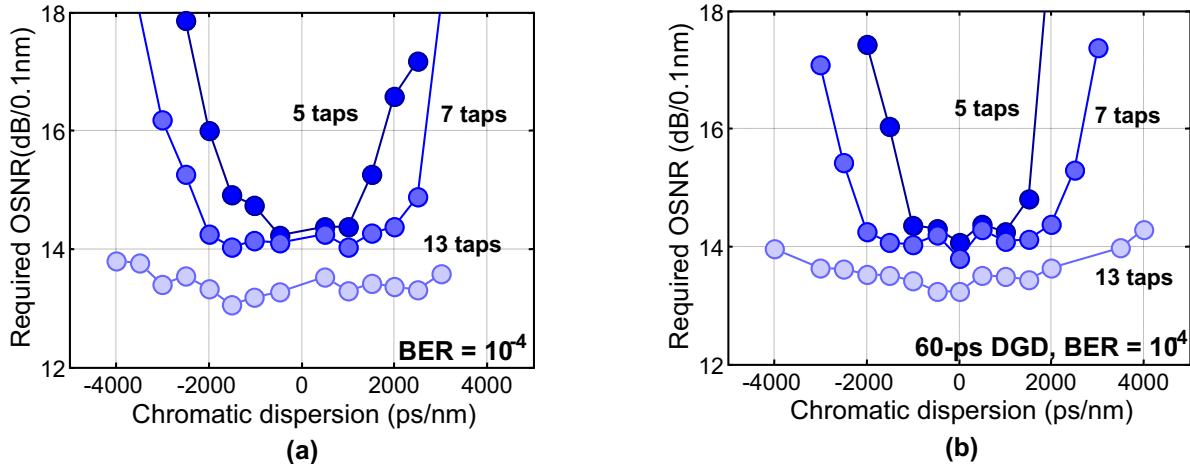


Figure 10.16: Required OSNR versus chromatic dispersion for various tap lengths; (a) only chromatic dispersion and (b) chromatic dispersion plus 60 ps of DGD.

### 10.4.5 Chromatic dispersion

The channel impulse response of chromatic dispersion is typically longer than the impulse response of DGD, and the impulse energy is therefore spread out over multiple symbol periods. However, when the length of the FIR filters is sufficient to accurately synthesize the inverse transfer function of the channel impulse response, an arbitrary amount of chromatic dispersion can be compensated. To verify the feasibility of chromatic dispersion compensation, the tolerance is measured using a combination of DCF/SSMF spools and a fiber-based TDC. The resulting chromatic dispersion tolerance for different numbers of FIR taps is depicted in Figure 10.16. With 13-tap  $T_0$ -spaced FIR filters in the equalizer, only a small penalty is measured and the tolerance is in excess of  $\pm 3000$  ps/nm. When the number of taps is reduced to 7, the dispersion tolerance for a 1 dB penalty is about  $\pm 2000$  ps/nm. The combined compensation of chromatic dispersion and DGD impairments is shown by adding 60 ps of DGD together with different amounts of chromatic dispersion (see Figure 10.16b). Even for 60 ps of DGD and 4,000 ps/nm of chromatic dispersion the OSNR penalty is only in the order of 1 dB for a 13-tap equalizer. For a reduced number of taps the chromatic dispersion tolerance decreases accordingly.

The chromatic dispersion and DGD tolerance measured with the digital coherent receiver, confirms the expectation that for such a receiver the chromatic dispersion and DGD tolerance is only limited by the number of FIR taps in the equalizer. This indicates that a digital coherent receiver does not require tunable optical chromatic dispersion or PMD compensation at the receiver.



## 10.5 Distortion compensation at 111-Gb/s

Besides 43-Gb/s transmission, the possible application of digital coherent receivers to 111-Gb/s transmission is also of major interest. As chromatic dispersion scale quadratically with the bit rate, the need for either optical or electrical adaptive distortion compensation becomes increasingly more important for higher bit rates. And as a digital coherent receiver combines an excellent OSNR tolerance with the compensation of linear transmission impairments it is an attractive solution to realize robust 111-Gb/s long-haul transmission. Similar to the 43-Gb/s bit rate, POLMUX-DQPSK is also the modulation format of choice for 111-Gb/s to combine with a digital coherent receiver. The use of POLMUX-DQPSK modulation is particularly important at a 111-Gb/s bit rate, because the 27.75-Gbaud symbol rate is low enough to enable conversion to the digital domain using state-of-the-art ADCs. Figure 10.18 shows NRZ and RZ eye diagrams for both DQPSK and POLMUX-DQPSK at a 27.75-Gbaud symbol rate.

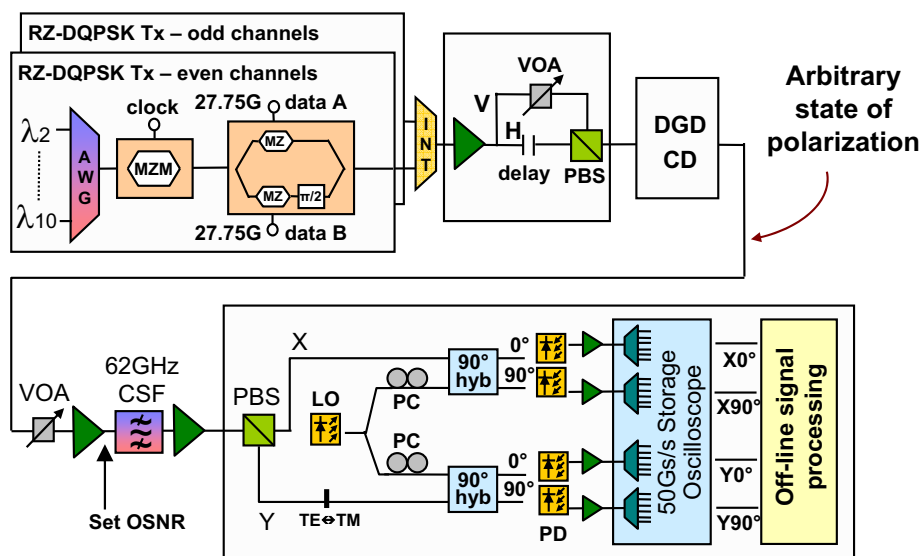


Figure 10.17: Experimental setup for the 111-Gb/s POLMUX-RZ-DQPSK transmitter and receiver.

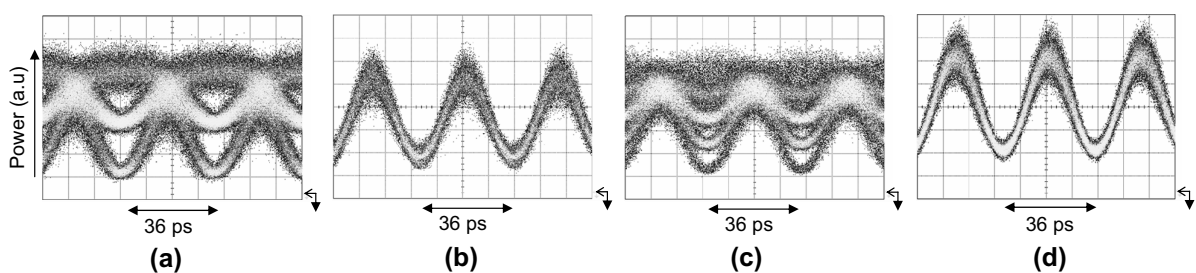


Figure 10.18: Eye diagrams for (a) 55.5-Gb/s NRZ-DQPSK, (b) 55.5-Gb/s RZ-DQPSK, (c) 111-Gb/s POLMUX-NRZ-DQPSK and (d) 111-Gb/s POLMUX-RZ-DQPSK modulation

In order to verify the electronic distortion compensation at a 111-Gb/s bit rate, the transmitter and receiver structure shown in Figure 10.17 are used. The output of 10 ECL between 1548.5 nm and 1552.2 nm centered on a 50-GHz ITU grid are fed to two modulator chains for separate



modulation of the odd and even WDM channels. Because of the somewhat limited electro-optic bandwidth of the modulators, a RZ pulse carver is included to generate RZ-DQPSK. The electrical drive signals consist of a  $2^{16}$  PRBS that is split and fed to both inputs of the integrated DQPSK modulators with a 8 bit de-correlation, which results in a  $4^8$  PRQS. After DQPSK modulation a 50-GHz interleaver with a 45-GHz 3-dB bandwidth is used to combine the even and odd WDM channels. Note that the optical spectrum of 55.5-Gb/s RZ-DQPSK is significantly broader than 45-GHz, and the interleaver is therefore bandlimiting the signal. For the back-to-back measurement the nearest neighbor channels are turned off to allow OSNR measurements. Finally, a POLMUX signal is generated by dividing the signal in two tributaries and recombining those with orthogonal polarizations and a 353 symbol delay between the tributaries for de-correlation. The digital coherent receiver is identical to the one described in Section 10.4 with the exception that photodiodes with a  $\sim 30$ -GHz bandwidth are used. After detection, the signals are sampled with 50-Gsample/s photodiodes using a Tektronix DSA72004 DSO.

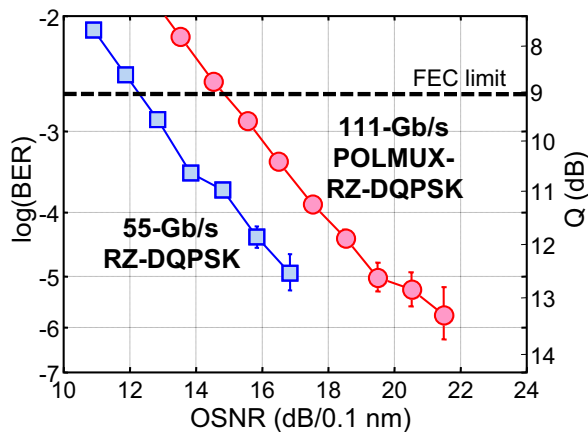


Figure 10.19: Back-to-back sensitivity for 111-Gb/s POLMUX-RZ-DQPSK with a coherent receiver; the OSNR requirement of 55.5-Gb/s RZ-DQPSK is shown as a reference.

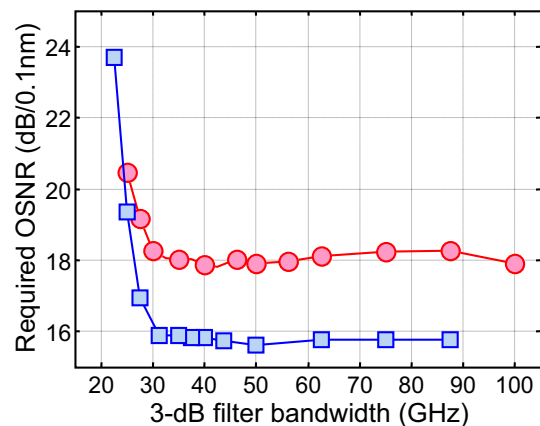


Figure 10.20: Required OSNR for a  $10^{-4}$  BER versus 3-dB optical filter bandwidth,  $\bullet$  111-Gb/s POLMUX-RZ-DQPSK with coherent detection;  $\square$  55-Gb/s RZ-DQPSK with direct detection.

### 10.5.1 Back-to-back OSNR requirement

For a 111-Gb/s bit rate, the OSNR requirement of the modulation format is particularly significant as it is much higher than for a 10.7-Gb/s and 43-Gb/s bit rate. For a 10.7-Gb/s bit rate, NRZ-OOK is conventionally used as the modulation format for terrestrial long-haul systems. 10.7-Gb/s NRZ-OOK requires a  $\sim 10$  dB of OSNR for a  $0^{-3}$  BER. When we simply scale the bit rate, the required OSNR scales with 6 dB when increased from 10.7 Gb/s to 43 Gb/s. But this difference can be effectively reduced by using advanced modulation formats. For example, DPSK requires only a  $\sim 12$  dB of OSNR. And the use of POLMUX-NRZ-DQPSK with coherent detection would further reduce this to  $\sim 11$  dB. However, when upgrading from a 43-Gb/s to a 111-Gb/s line rate, the OSNR requirement cannot be further reduced. This will result in a significant reduction in feasible transmission distance for 111-Gb/s in comparison to 43-Gb/s

transmission. It is therefore advantageous to keep the OSNR requirement as low as possible for 111-Gb/s transmission by using POLMUX-RZ-DQPSK modulation with coherent detection.

The back-to-back OSNR requirement of both 55.5-Gb/s RZ-DQPSK and 111-Gb/s POLMUX-RZ-DQPSK is depicted in Figure 10.19. As expected, the doubling of the channel capacity results in a 3-dB OSNR penalty. For 111-Gb/s POLMUX-RZ-DQPSK, a 15.8-dB and 17.8 dB OSNR is required to obtain a BER of  $10^{-3}$  and  $10^{-4}$ , respectively. This compares favorably with previously reported 100-Gb/s OSNR requirements as it is a 2.3-dB improvement over 107-Gb/s RZ-DQPSK [14] and a >4-dB improvement over 107-Gb/s NRZ-OOK (with an optical equalizer) [12]. The lower OSNR requirement of POLMUX-DQPSK modulation combined with a digital coherent receiver can therefore be instrumental in realizing long-haul transmission systems with a 111-Gb/s bit rate per wavelength channel

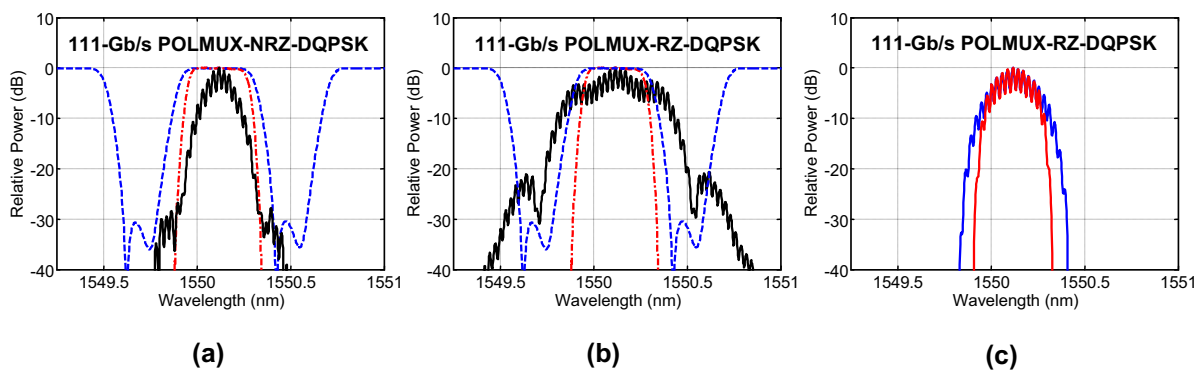


Figure 10.21: Measured optical spectra (0.01nm/res); (a) 111-Gb/s POLMUX-NRZ-DQPSK with filter curves, (b) 111-Gb/s POLMUX-RZ-DQPSK with filter curves and (c) 111-Gb/s POLMUX-RZ-DQPSK after filtering; ■ Interleaver with 44-GHz 3-dB bandwidth; ■ CSF with 40-GHz 3-dB bandwidth.

### 10.5.2 Narrowband optical filtering

The lower symbol rate of POLMUX-RZ-DQPSK in comparison to binary modulation formats is a significant advantage in term of achievable spectral efficiency. It supports a 111-Gb/s bit rate on a 50-GHz WDM grid, which realizes a spectral efficiency of 2.0-b/s/Hz. The tolerance of 111-Gb/s POLMUX-RZ-DQPSK with respect to narrowband optical filtering is shown in Figure 10.20. The optical filter used to assess the tolerance is a NetTest X-Tract filter with a nearly rectangular pass-band. This clearly shows the absence of a noticeable filtering penalty until the 3-dB optical filtering drops below 30 GHz. Note that a nearly similar narrowband filtering tolerance is obtained when a direct detection receiver is used, as evident from Figure 10.20. This indicates that the narrowband filtering tolerance is not significantly improved by the coherent receiver, but results mainly from the choice in modulation format. The sound tolerance toward narrowband optical filtering enables transmission through a large number of cascaded 50-GHz OADMs for 111-Gb/s POLMUX-RZ-DQPSK.

Figure 10.21 depicts the measured optical spectra for 111-Gb/s POLMUX-(N)RZ-DQPSK with the filter curves of a 44-GHz interleaver and 40-GHz CSF superimposed. This shows that both filters result in strong spectral narrowing in the case of RZ pulse carving. Figure 10.21c depicts

the spectra obtained after filtering for 111-Gb/s POLMUX-RZ-DQPSK. The RZ spectra after passing through the 40-GHz CSF shows a very similar shape as the NRZ spectra without filtering. This indicates that the narrowband filtering results in a quasi-NRZ eye shape. Because the symbol rate is lowered by a factor of two, 111-Gb/s POLMUX-RZ-DQPSK requires only half the optical bandwidth of 111-Gb/s (direct-detection) RZ-DQPSK. Whereas 111-Gb/s POLMUX-RZ-DQPSK can be used on a 50-GHz WDM grid, 111-Gb/s RZ-DQPSK is normally limited to a 100-GHz WDM grid.

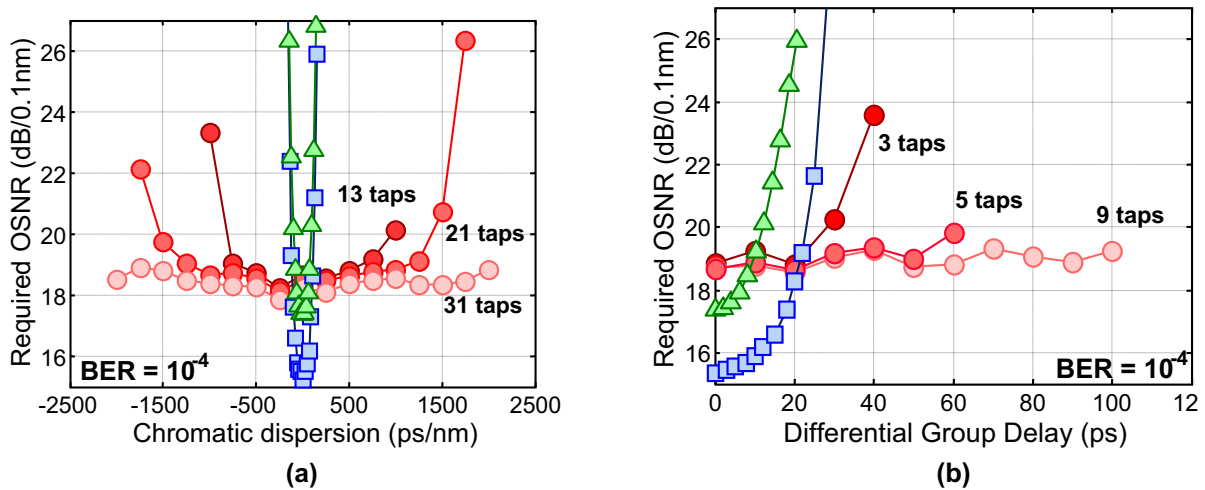


Figure 10.22: Required OSNR for various tap lengths (a) chromatic dispersion and (b) DGD, both in comparison to direct detection (CDR receiver),  $\circ$  111-Gb/s POLMUX-RZ-DQPSK with coherent detection;  $\square$  55-Gb/s RZ-DQPSK with direct detection;  $\triangle$  111-Gb/s POLMUX-RZ-DQPSK with direct detection (simulated).

### 10.5.3 Chromatic dispersion & differential group delay

The OSNR requirement for a  $10^{-4}$  BER as a function of the chromatic dispersion is shown in Figure 10.22. The OSNR penalty is depicted for different numbers of filter taps in the FIR equalizer. For 31 taps, no significant penalty is evident for a dispersion window ranging from -2000 ps/nm to +2000 ps/nm. And even for 13 taps the measured chromatic dispersion tolerance is in excess of 750 ps/nm. When one compares this tolerance to the  $\sim 8$ -ps/nm chromatic dispersion tolerance of 107-Gb/s NRZ-OOK [14], or  $\sim 25$  ps/nm using 55.5-Gbaud RZ-DQPSK [13], the increased robustness is nearly two orders of magnitude. Although this improvement is in part due to the 27.75-Gbaud symbol rate of POLMUX-RZ-DQPSK, the most significant contribution results from the coherent detection of the optical field and the subsequent distortion equalization.

The DGD tolerance for various FIR filter tap lengths is shown in Figure 10.22. It can be observed that a 3-tap FIR filter is effective for a DGD up to 30 ps, while a 9-tap FIR filter shows no penalty for a DGD in excess of 100 ps. When we take into account that 100 ps of DGD equals 2.8 symbol periods for a 27.75-Gsymbol/s baud rate, this clearly demonstrates the flexibility of a digital coherent receiver. This compares favorably with a  $\sim 3$ -ps DGD tolerance using 107-Gb/s NRZ-OOK and  $\sim 6$  ps using 107-Gb/s RZ-DQPSK.

## 10.6 Long-haul transmission

The results discussed in Sections 10.4 and 10.5 show that the combination of POLMUX-DQPSK modulation coupled with a digital coherent receiver has excellent tolerance against linear transmission impairments. Nonlinear transmission impairments are however a different challenge as a digital coherent receiver has limited capability to compensate for such impairments. In this section we discuss the transmission performance of POLMUX-DQPSK coupled with a digital coherent receiver for both a 43-Gb/s and 111-Gb/s bit rate.

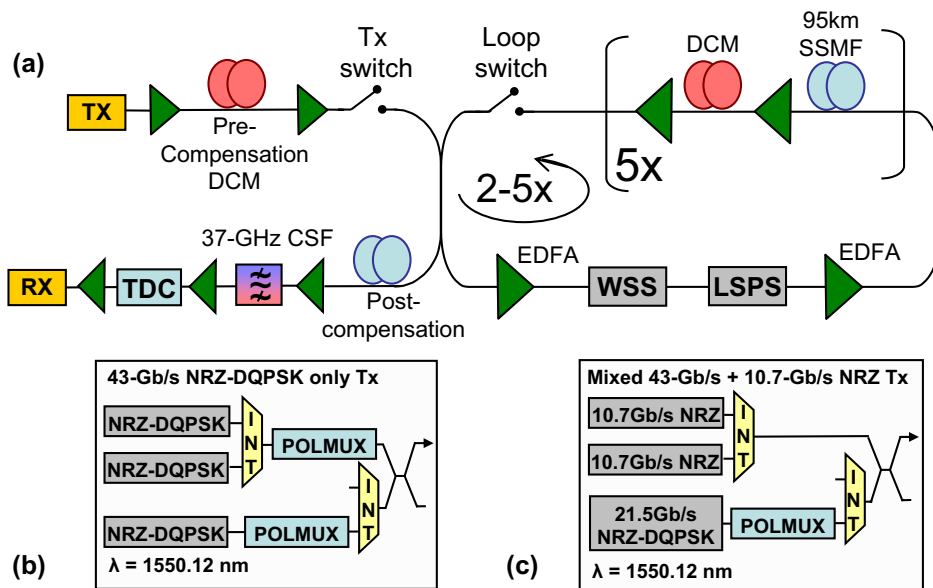


Figure 10.23: (a) Experimental transmission link; (b) transmitter with only 43-Gb/s POLMUX-NRZ-DQPSK modulated channels and (c) transmitter with a single 43-Gb/s POLMUX-NRZ-DQPSK channel surrounded with 10.7-Gb/s NRZ-OOK modulated channels.

### 10.6.1 43-Gb/s POLMUX-NRZ-DQPSK transmission

In order to evaluate the performance of 43-Gb/s POLMUX-NRZ-DQPSK modulation in a long-haul WDM transmission system, 9 co-propagating channels between 1548.5 nm and 1552.2 nm are added to the channel under test on a 50-GHz WDM grid. The output of the 9 additional ECLs are modulated using two DQPSK modulators for separate modulation of the even and odd channels, as depicted in Figure 10.23b. The re-circulating loop (Figure 10.23a) consists of five 95-km spans of SSMF with an average span loss of 18.5 dB. The signal is pre-dispersed with DCF having -1360 ps/nm of chromatic dispersion and the in-line under compensation is  $\sim 85 \text{ ps/nm/span}$ . Double-stage EDFA-only amplification is used and the input power per channel into the DCF is 6 dB reduced with respect to the SSMF. Loop-induced polarization effects are reduced using a LSPS and power equalization of the WDM channels is provided by a channel-based WSS. At the receiver the channel at 1550.12 nm is selected with a 37-GHz CSF. Using

post-compensation and a TDC, the chromatic dispersion at the receiver is either set close to zero, or offset from zero to measure the chromatic dispersion tolerance of the receiver. Afterwards the signal is fed into the coherent receiver. To obtain sufficient measurement accuracy, each measurement is repeated on 10 separate time instants, to obtain a total of  $2 \cdot 10^7$  bits for error detection.

First of all, the transmission distance and input power per channel are both varied to obtain an estimate for the transmission reach. Figure 10.24a shows the feasible transmission distance for the optimum input power per channel, which is found to be -3 dBm. Note that the optimum input power of -5 dBm per channel after 900 km is likely due to measurement uncertainty. When compared to 10.7-Gb/s NRZ, the nonlinear tolerance of 43-Gb/s POLMUX-NRZ-DQPSK is reduced by 4-5 dB. The nonlinear tolerance of 43-Gb/s POLMUX-DQPSK is mainly limited by SPM, which is similar to 43-Gb/s DQPSK modulation. On the other hand, the POLMUX signaling will also somewhat reduce the nonlinear tolerance due to XPM induced nonlinear polarization modulation, as discussed in Chapter 7.

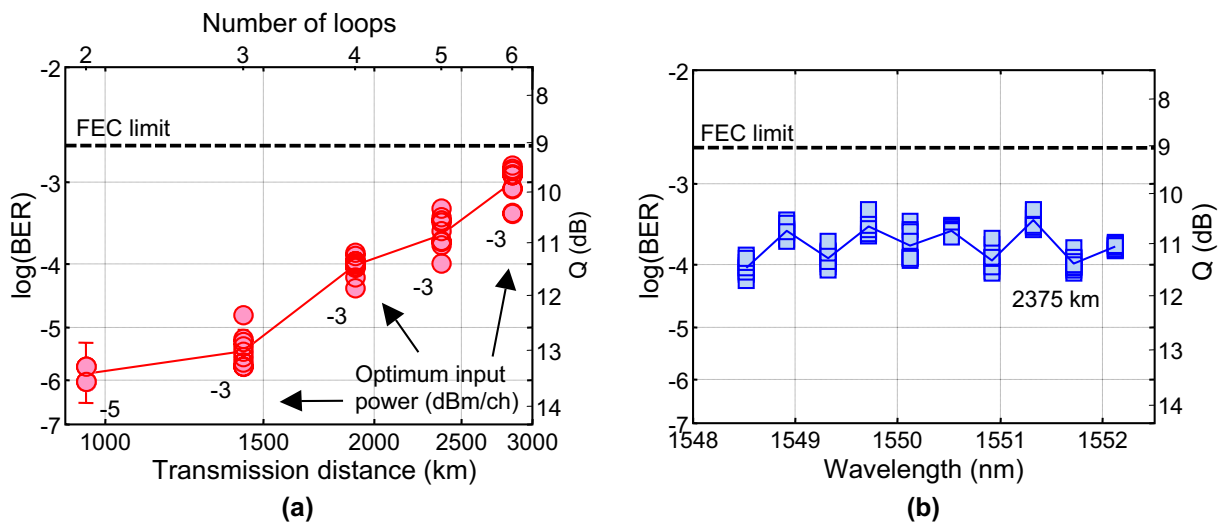


Figure 10.24: Long-haul transmission results with 43-Gb/s POLMUX-NRZ-DQPSK; (a) BER versus transmission distance and (b) BER for all WDM channels.

Figure 10.24a shows that the feasible transmission distance of 43-Gb/s POLMUX-NRZ-DQPSK with EDFA-only amplification is approximately  $\sim 3000$  km. Figure 10.24b further depicts the BER for the 10 co-propagating WDM channels after 2375-km (5 loops) transmission. There is a slight variance between the even and odd WDM channels, which results from a slight performance difference between both DQPSK modulators. This results from a drift in bias voltages of the modulator.

### 10.6.2 Co-propagating 10.7-Gb/s NRZ-OOK channels

Section 10.6.1 discussed the nonlinear tolerance under the assumption that all co-propagating channels are 43-Gb/s POLMUX-NRZ-DQPSK modulated. However, the currently installed base of WDM links carries predominantly 10.7-Gb/s NRZ-OOK modulated channels. Such links are likely to be upgraded in the near future to a 43-Gb/s bit rate. We therefore consider the case that the neighboring channels of a 43-Gb/s POLMUX-NRZ-DQPSK modulated channel are 10.7-Gb/s NRZ-OOK modulated. The transmitter is modified such that only the center channel is modulated with 43-Gb/s POLMUX-NRZ-DQPSK and that the 9 surrounding channels are 10.7-Gb/s NRZ-OOK modulated (as depicted in Figure 10.23c)

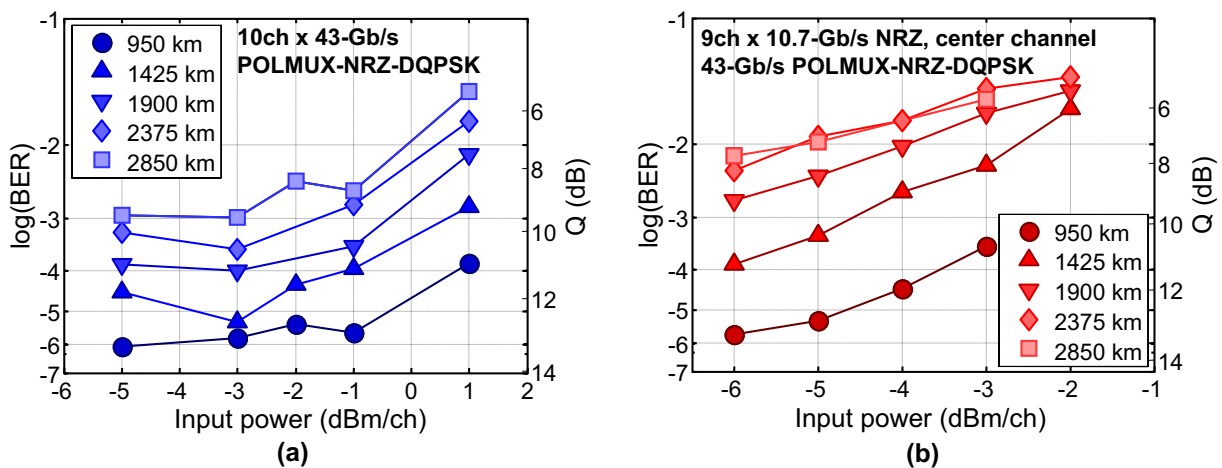


Figure 10.25: BER of the center channel versus input power per channel for (a) all channels 43-Gb/s POLMUX-NRZ-DQPSK modulated and (b) 43-Gb/s POLMUX-NRZ-DQPSK center channel with 9 co-propagating 10.7-Gb/s NRZ-OOK channels

As shown in Section 5.4, co-propagating NRZ-OOK channels can result in significant XPM impairments for DQPSK modulated signals. However, whereas in a direct detection receiver the impact of XPM is reduced through differential detection, this is not the case for a digital coherent receiver. In this case the transmission penalty can be even more severe as the XPM induced phase noise can potentially impair the CPE in the digital signal processing. In addition, POLMUX signaling can result in XPolM-induced polarization modulation, as discussed in Chapter 7. The XPM tolerance of 43-Gb/s POLMUX-NRZ-DQPSK is therefore a key parameter to determine its suitability for overlay on an existing 10-Gb/s infrastructure. Figure 10.25 compares the nonlinear tolerance for 43-Gb/s POLMUX-NRZ-DQPSK with and without 10.7-Gb/s NRZ-OOK neighbors, respectively. For all measurements the CPE averages over 17 symbols. In this case the co-propagating 10.7-Gb/s NRZ-OOK modulated channels clearly reduce the transmission performance. The optimum input power is lowered from -4 dBm to below -6 dBm. As a result the feasible transmission distance for 43-Gb/s POLMUX-NRZ-DQPSK modulation is reduced from  $\sim 3000$  km to  $\sim 1800$  km. This confirms that XPM-induced phase noise from co-propagating 0.7-Gb/s NRZ-OOK neighbors is an important design consideration for 43-Gb/s POLMUX-NRZ-DQPSK. The impact of XPolM is illustrated using the Poincaré spheres in Figure 10.26. This shows simulated results for transmission over 20x100-km of SSMF with a -2 dBm input power per WDM channel. When only a single channel is transmitted, the spread in



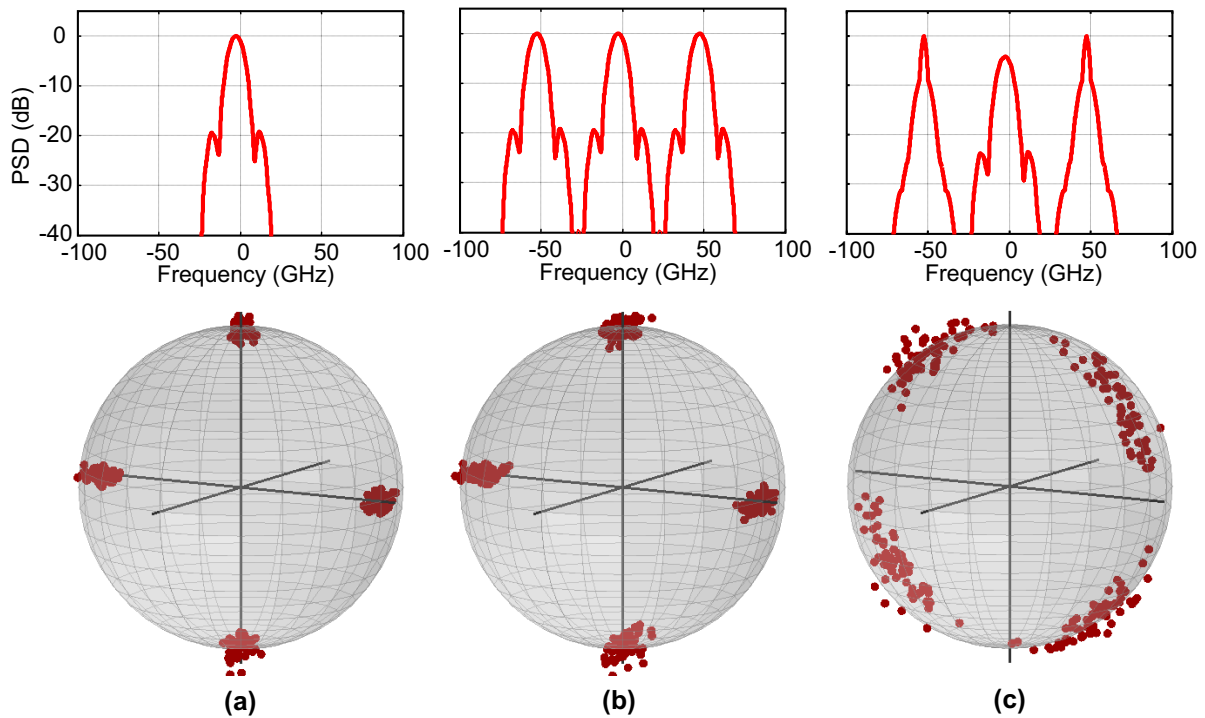


Figure 10.26: Simulated spectra and Poincaré spheres showing 43-Gb/s POLMUX-NRZ-DQPSK modulation after 2000-km transmission; (a) single-channel, (b) 43-Gb/s POLMUX-NRZ-DQPSK neighbors and (c) 10.7-Gb/s NRZ-OOK neighbors.

the constellation points is minimal, and no evidence of severe nonlinear impairments is observed. When we add co-propagating WDM transmission on a 50-GHz channel grid, the spread of the constellation point is marginally increased as long as the co-propagating channels are 43-Gb/s POLMUX-NRZ-DQPSK modulated (Figure 10.26b). However, when the neighboring channels are 10.7-Gb/s NRZ-OOK modulated the spread of the constellation points increases dramatically (Figure 10.26c). This directly results from the increased XPM and XPolM impairments generated through the co-propagating NRZ-OOK channels. We now obtain similar depolarization penalties as observed for transmission with POLMUX-NRZ-OOK modulation in Chapter 7.

The increased impact of XpolM can be partially alleviated by optimizing the number of symbols used for CPE. As discussed in Section 10.3.3, the XPM induced phase noise depends on the bit sequence of the neighboring channels and therefore does not average out when more symbols are taken into account. Figure 10.27a shows, for transmission over 1900 km, the impact of reducing the averaging in CPE. For high input powers XPM induced phase noise is the dominant impairment and CPE with a smaller number of symbols gives better performance. For low input powers, XPM induced impairments are less dominant and the performance is more OSNR limited. In this case a longer CPE length is beneficial, this is evident from the smaller difference between the measured CPE lengths. We find that the optimum input power per channel and CPE lengths are respectively -5 dBm and a 5 symbol CPE length. Figure 10.27b now depicts the feasible transmission distances for 43-Gb/s POLMUX-NRZ-DQPSK with 10.75-Gb/s neighbors when the CPE length is optimized. The shorter CPE ( $\sim 5$  symbols) improves the reach from  $\sim 1800$  km to  $\sim 2800$  km. With an optimized CPE length there is still a penalty evident when

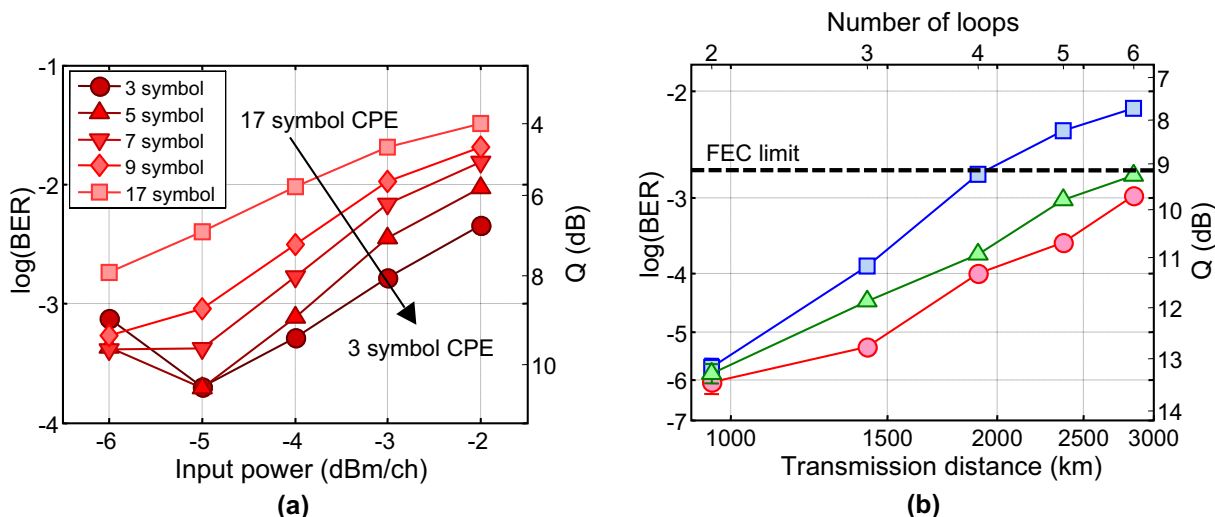


Figure 10.27: (a) BER versus input power per channel after 1.900 km for 43-Gb/s POLMUX-NRZ-DQPSK with 10.7-Gb/s NRZ neighbors transmission; (b) BER versus transmission distance for,  $\circ$  all 43-Gb/s POLMUX-NRZ-DQPSK neighbors;  $\square$  10.7-Gb/s NRZ neighbors and a 17 symbol CPE length;  $\triangle$  10.7-Gb/s NRZ neighbors and an optimized CPE length.

compared to transmission with 43-Gb/s POLMUX-NRZ-DQPSK modulated neighbors, but this penalty is relatively small. This indicates that 43-Gb/s POLMUX-NRZ-DQPSK modulation can be used to upgrade transmission systems that carry legacy 10.7-Gb/s NRZ-OOK channels. However, the residual penalty due to XPoIM might make it beneficial to increase the wavelength spacing between the 43-Gb/s and 10.7-Gb/s modulated channels to  $\geq 100$  GHz.

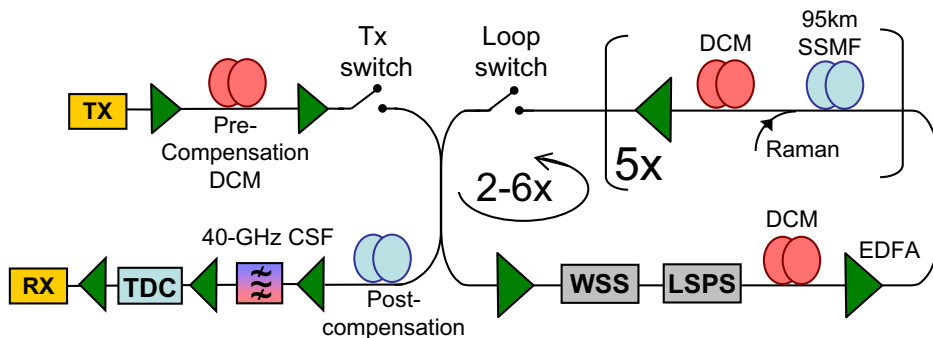


Figure 10.28: Experimental transmission setup.

### 10.6.3 111-Gb/s POLMUX-RZ-DQPSK transmission

In this section we discuss the transmission performance of 111-Gb/s POLMUX-RZ-DQPSK modulation when combined with a digital coherent receiver. The combination of 111-Gb/s POLMUX-RZ-DQPSK modulation with a 50-GHz WDM grid enables long-haul transmission with a 2.0-b/s/Hz spectral efficiency. The same transmitter and receiver structure with 10 WDM



channels is used as depicted in Figure 10.17. The re-circulating loop setup used for the 111-Gb/s transmission experiment is shown in Figure 10.28.

The re-circulating loop consisting of 5x95 km of SSMF and uses hybrid EDFA-Raman amplifiers. The dispersion map is similar as discussed in Section 10.6.1 for 43-Gb/s POLMUX-NRZ-DQPSK, with -1530 ps/nm of pre-compensation and 85 ps/nm of inline under-compensation per span. The ON/OFF Raman gain in the SSMF provided by the backwards pumped Raman amplifiers is  $\sim 14$  dB. Note that the same Raman pump powers are used here as previously described in this thesis. The higher Raman gain results from the use of "water free" SSMF, which has a lower attenuation around 1450 nm, which is approximately the wavelength range of the Raman pumps. A WSS with a 3-dB channel bandwidth of 43-GHz equalizes the power spectrum for each re-circulation and emulates strong optical filtering as it would occur in cascaded OADMs. Because of the broad optical spectrum of 111-Gb/s POLMUX-RZ-DQPSK, the signal is severely bandlimited through the 43-GHz filtering. After 5 re-circulations, the received spectra of the signal has a bandwidth of 32 GHz and 36.5 GHz (3 dB and 10 dB point respectively). However, as shown in Section 10.5.2 this does not result in a significant penalty for 111-Gb/s POLMUX-RZ-DQPSK modulation. In the receiver the 40-GHz CSF selects the desired channel, and the chromatic dispersion is set to the desired value (either zero or a preselected offset). Subsequently, the signal is fed into the digital coherent receiver.

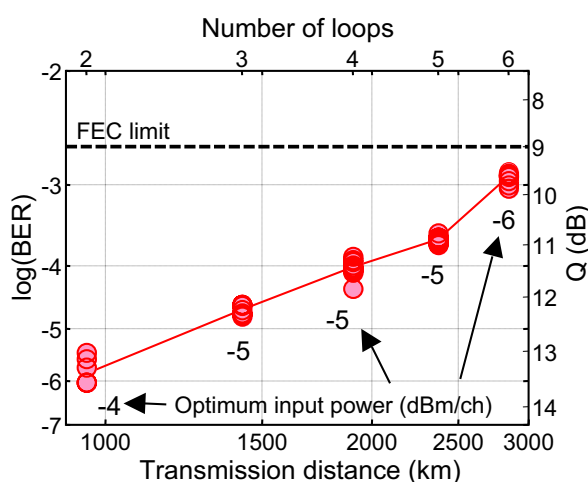


Figure 10.29: 111-Gb/s POLMUX-RZ-DQPSK; BER versus transmission distance for the optimum input power per channel.

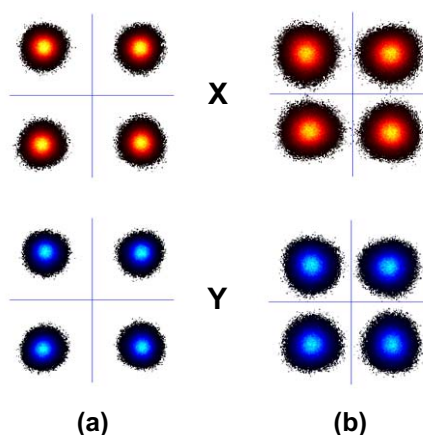


Figure 10.30: Measured signal constellation for (a) back-to-back with 25-dB OSNR and (b) after 2375-km transmission ( $BER = 2 \times 10^{-4}$ ).

First of all, the performance of 111-Gb/s POLMUX-RZ-DQPSK is determined by measuring the BER of the center channel at 1550.1 nm as a function of both input power per channel and transmission distance (see Figure 10.29a). The optimum input power per channel is found to be -4 dBm after 950 km and decreases to -6 dBm after 2850 km of transmission. Note that Figure 10.29 plots the BER for each of the 10 separate measurements, which gives a good indication of the loop induced BER variation. The BER variance also increases for higher input powers as nonlinear impairments become more dominant. However, the BER variation is minimal for the optimum input power of -4 to -6 dBm. Figure 10.30 shows a comparison of the signal

constellations measured back-to-back and after 2375-km transmission. In the presence of strong nonlinear phase noise, the constellation point would normally become asymmetric, as discussed in Section 2.4.7. The symmetry of the constellation points therefore indicates that the impact of nonlinear phase noise is small.

Figure 10.32 shows the measured performance for all 10 wavelength channels after 1900 km and 2375 km. All channels show a similar BER between  $1 \cdot 10^{-4}$  and  $5 \cdot 10^{-4}$  after 2375 km of transmission. Hence, all measured channels have a margin with respect to the FEC limit of  $\sim 1.5$  dB. By varying the post-compensation and the TDC at the receiver, the chromatic dispersion tolerance is measured after 2375 km (see Figure 10.32). Using a 13-tap FIR filter, a dispersion tolerance window of  $\sim 1500$  ps/nm is measured without a significant penalty. This is equal to the tolerance observed in the back-to-back measurement.

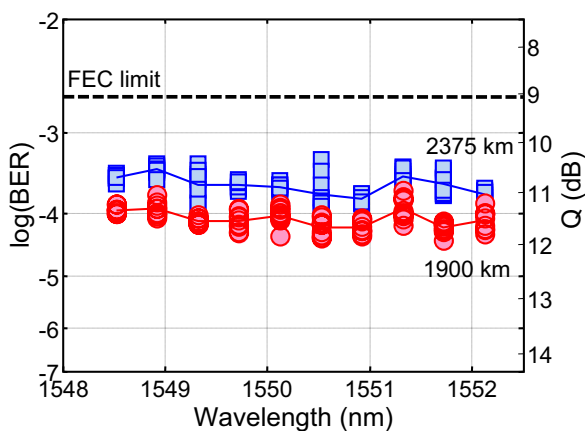


Figure 10.31: BER for all 111-Gb/s POLMUX-RZ-DQPSK WDM channels after 1,900-km and 2,375-km transmission.

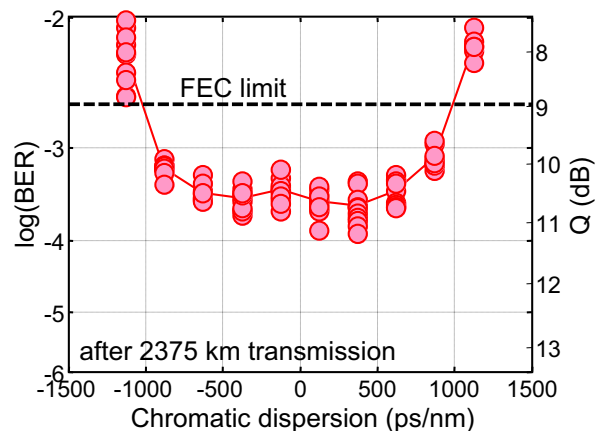


Figure 10.32: Chromatic dispersion tolerance with a 13-tap equalizer after 2375-km transmission

## 10.7 Distortion compensation using baud-rate equalizers

Although the current state-of-the-art ADCs allows for sampling rate as high as 50-Gsample/s in DSOs, the power consumption makes it unrealistic to integrate such ADCs in a commercial transponder. In addition, the ADCs in DSO are usually based on BiCMOS or SiGe technology, whereas integration in CMOS technology would be desirable for a single-chip solution. It might therefore takes some time before  $\sim 60$ -Gsample/s ADCs can be integrated into optical transponders. A further concern besides the raw sample rate itself, is the total signal processing required in a 111-Gb/s digital coherent receiver. Assuming that a digital coherent receiver requires 5-6 bits of vertical resolution, over-sampling with 55.5 Gsample/s on 4 input channels requires the processing of 1100-1300 Gb/s. There is no doubt that given the exponential increase in capability of CMOS integrated circuits [16] this will be realizable in the long-term. In the short-term, sampling with only 1 sample/symbol would allow a receiver implementation with a lower complexity and less digital signal processing. On the other hand, sampling with 1 sample/symbol requires the

use of a baud-rate ( $T_0$ -spaced) equalizer for the polarization de-multiplexing and distortion compensation. A  $T_0$ -spaced equalizer is normally not capable of compensating an arbitrary amount of chromatic dispersion and DGD, and the tolerance will therefore reduce accordingly.

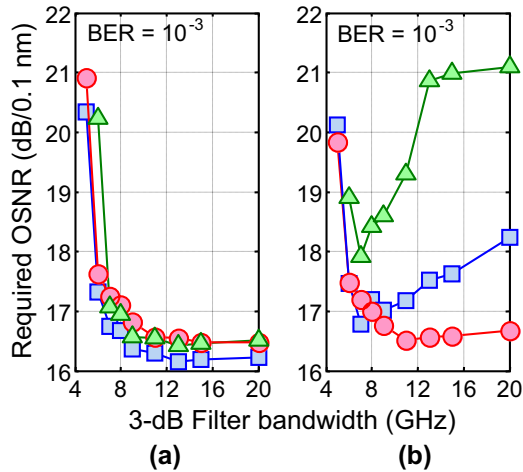


Figure 10.33: Required OSNR versus Bessel filtering bandwidth for (a)  $T_0/2$ -spaced and (b)  $T_0$ -spaced equalization;  $\circ$  0 ps/nm,  $\square$  -250 ps/nm and  $\triangle$  -500 ps/nm chromatic dispersion.

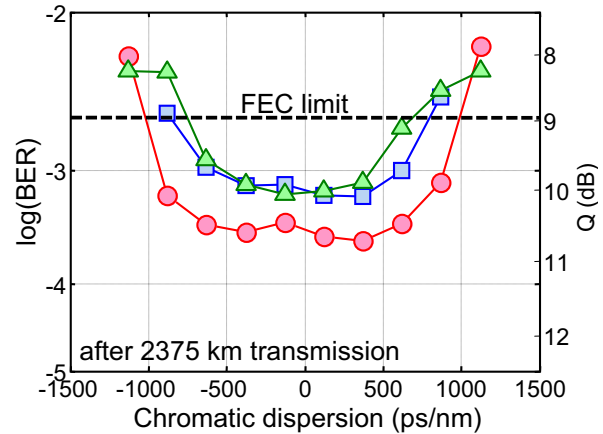


Figure 10.34: (c) BER versus chromatic dispersion after 2375-km transmission and with 13-tap equalizers  $\circ$   $T_0/2$ -spaced, no filtering  $\square$   $T_0/2$ -spaced, 7-GHz filter  $\triangle$   $T_0$ -spaced, 7-GHz filter.

The lower performance of a  $T_0$ -spaced equalizer can be somewhat alleviated with strong electrical filtering in the receiver [443]. Low-pass electrical filtering increases the ISI and spreads therefore the energy of the received signal to the  $T_0$ -spaced sampling points. In addition it removes the aliasing induced through baud-rate sampling. The equalizer must in turn compensate for both the additional ISI resulting from the low-pass filtering, as well as the channel distortions. To illustrate the feasibility of a  $T_0$ -spaced equalizer, we determine the OSNR requirement as a function of low-pass filter bandwidth in the presence of chromatic dispersion. This is achieved by low-pass filtering the input samples with an electrical 5<sup>th</sup> order Bessel filter. Afterwards, the samples are re-quantized using 5 bit resolution to ensure that subsequent signal processing using floating point arithmetic does not reverse the low-pass filtering. Subsequently, the digital signal algorithms as described in Section 10.3 are applied, but with the difference that now  $T_0$ -spaced FIR filters are used. Note that the sampling time instant has a large impact when using only 1 sample/symbol. This implies that for such a digital coherent receiver the clock recovery implementation is much more critical. Here, the sample time instant is optimized to give the lowest mean-square error at the output of the equalizer.

Figures 10.33a and 10.33b shows the required OSNR with 0, -250 and -500 ps/nm of chromatic dispersion for  $T_0/2$ -spaced and  $T_0$ -spaced signal processing, respectively, where a 13-tap FIR is used in all measurements. It is evident that for 2 sample/symbol signal processing, the chromatic dispersion tolerance is independent of the electrical low-pass filtering bandwidth. The required OSNR increases only when the filtering 3-dB bandwidth is below 10 GHz as the low-pass filtering starts to incur a significant penalty. For 1 sample/symbol signal processing, on the other hand, the chromatic dispersion tolerance improves significantly as the electrical low-pass filtering bandwidth is reduced. For a 7-GHz low-pass filtering bandwidth, there is a  $\sim 0.7$  dB

back-to-back penalty from the low-pass filtering. For -500 ps/nm of chromatic dispersion, the additional OSNR penalty is less than 1 dB. For a low-pass filtering bandwidth below 6 GHz, the performance is limited by the filtering, both back-to-back and with chromatic dispersion.

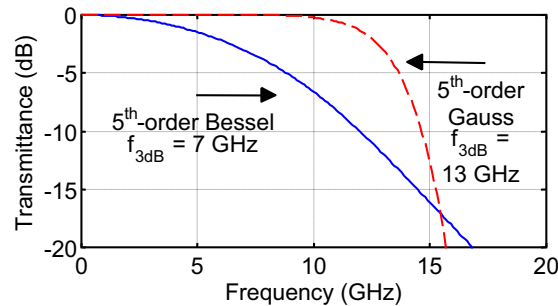


Figure 10.35: *Transmittance spectrum of a 7-GHz Bessel and 13-GHz Gauss filter.*

The measured optical filter tolerance (as depicted in Figure 10.20) shows a 1-dB OSNR penalty for a  $\sim 27$  GHz filtering bandwidth, which is a factor of four difference with the 7-GHz optimal electrical filter bandwidth. In theory, there should be equivalence between the optical and electrical filtering after coherent detection. A factor of two is accounted for by noting that the optical filter is defined as a band-pass, double-sided, bandwidth. On the other hand, the electrical filter bandwidth is defined as a low-pass, single-sided, bandwidth. The other factor of two results from the *Bessel* filter shape, as the narrowband filtering tolerance is not only defined through the 3-dB bandwidth but strongly dependent on the exact filter curve. A Bessel filter has a very flat roll-off, whereas a *Gauss*-shaped filter has a steeper roll-off with frequency. When a Gauss-shaped electrical filter is used in the receiver, the filter bandwidth for a 1-dB penalty increases to 13-GHz, a factor of two difference with the (Gauss-shaped) optical filter bandwidth of 27-GHz. This is illustrated in Figure 10.35, which depicts the filters curves of a 5<sup>th</sup> order Bessel and Gauss filter, with a 7-GHz and 13-GHz 3-dB bandwidth, respectively

Next, the  $T_0$ -spaced equalizer with 7-GHz 5<sup>th</sup> order Bessel filtering is used to process the data obtained after long-haul transmission. For both  $T_0$ - and  $T_0/2$ -spaced FIR filters, this results in  $\sim 0.5$ -dB penalty. When using a  $T_0$ -spaced FIR filter, a chromatic dispersion window of  $\sim 1000$  ps/nm is obtained without a significant penalty, as shown in Figure 10.34. Hence, we can conclude that a 111-Gb/s digital coherent receiver can be realized using only 27.75-Gbaud ADCs. The tolerance towards chromatic dispersion is sufficient to enable the use of 111-Gb/s transponders on network infrastructure that has been designed for 10-Gb/s systems, without the use of tunable dispersion. The compensation of PMD using  $T_0$ -spaced equalizers is not determined here, but in [351, 444] it is shown that it is not possible to compensate for an arbitrarily high PMD. An alternative might be to sample at a slightly higher sample rate, for example with 1.5 sample/symbol, and re-time the samples through signal processing. In [444], *Ip and Kahn* show that this allows for the compensation of arbitrarily high DGD. In addition, this shows that a 111-Gb/s digital coherent receiver can be realized using an electrical component with a  $\sim 15$  GHz bandwidth, which significantly reduces the cost and complexity of the transmitter and receiver.

## 10.8 Summary & conclusions

The digital coherent receiver architecture discussed in this chapter clearly shows the potential of signal processing in optical communication systems. It allows for high bit-rate transmission systems where the system design complexity is shifted more to the electrical domain instead of the optical domain, as is the case for convention transmission systems. The main benefits of a digital coherent receiver can be summarized as:

- A digital coherent detection translated the *full optical field* into the digital domain. This enables efficient signal processing that can theoretically compensate for any (linear) distortion accumulated along the transmission link.
- The *optical front-end* of a digital coherent receiver consists of a LO, PBS and two 90° hybrids, it is therefore much simpler in comparison to a direct detection POLMUX-DQPSK receiver. The four signal components (in-phase & quadrature on both polarizations) are detected with single-ended photodiodes. The resulting direct detection impairments are reduced through a high  $\sim 18$ -dB LO to signal ratio.
- For both 43-Gb/s and 111-Gb/s POLMUX-DQPSK modulation we have shown the effective compensation of *linear transmission impairments*, i.e. chromatic dispersion, DGD and SOPMD. This confirms that as long as a large enough number of FIR filter taps is used, any linear signal distortion can be compensated.
- The impact of *PDL* results in a penalty for a digital coherent receiver, either due to a OSNR difference between the tributaries or a loss of orthogonality. However, 3 dB of PDL can be tolerated with less than a 2-dB OSNR penalty.

We further analyzed the transmission performance of 43-Gb/s and 111-Gb/s POLMUX-DQPSK modulation when combined with a digital coherent receiver:

- For *43-Gb/s* POLMUX-NRZ-DQPSK, a 2375 km reach is feasible using EDFA-only amplification and an optimal input power of -3 dBm per channel.
- A significant drawback for POLMUX-DQPSK modulation is the severe *XPM and XPolM* penalty incurred through co-propagating NRZ-OOK channels, which reduces the feasible transmission reach. This penalty can be reduced by optimizing the number of symbols used for CPE. However, it remains desirable to increase the channel spacing to  $\geq 100$  GHz between 43-Gb/s and 10.7-Gb/s modulated channels.
- For *111-Gb/s* POLMUX-RZ-DQPSK, a transmission reach of 2375 km is measured using hybrid EDFA/Raman amplification. The optimum input power per channel is approximately -5 dBm.
- With 111-Gb/s POLMUX-RZ-DQPSK modulation, a *spectral efficiency* of 2.0-b/s/Hz is feasible while maintaining a sound tolerance towards narrowband filtering. In a long-haul

transmission experiment, 5 add/drop nodes on a 50-GHz grid are passed. This results in a 32-GHz spectral width after transmission, which does not incur a noticeable penalty.

- The higher sampling rate of the ADCs in a 111-Gb/s transponder can be reduced through 1-sample/symbol quantization and subsequent *T-spaced signal processing*. This requires electrical low-pass filtering with a 7-GHz Bessel filter to spread the energy to the T-spaced sampling points. A  $>1000$ -ps/nm chromatic dispersion tolerance with only 0.7-dB OSNR penalty is obtained using a T-spaced 13-tap equalizer.

On the basis of these results we can conclude that long-haul transmission with a 43-Gb/s and 111-Gb/s bit rate can be realized using POLMUX-DQPSK modulation and digital coherent receivers. The feasibility of upgrading an existing transmission systems that already carries 10.7-Gb/s NRZ-OOK modulation remains a question for further research.

The results discussed in this chapter are all based on off-line processing, and the step to real-time processing is a critical one to determine the feasibility of such transmission systems. For example, in [428], *Sun et. al.* reported the first real-time ASIC implementation of a digital coherent receiver at 43-Gb/s. The described ASIC requires 20 million transistors and has a power dissipation of 21 Watts, which underlines the state-of-the-art nature of this technology. However, the advantages of digital coherent detection are such that it is likely that this technology will be broadly adapted in the upcoming years.

---

## Outlook & recommendations

In upcoming years, the steady growth in Internet bandwidth will fuel the need to develop and deploy 40-Gb/s and 100-Gb/s optical transmission systems. In this section we aim to compare the various options that can be considered for such transmission systems based on the results described in the thesis. Table 11.1 shows a summary of the advantages and disadvantages of the different modulation formats.

It should also be stressed here that technology changes constantly. In the little over three years that have been covered by the work in this thesis, DQPSK modulation went from the first experimental demonstration at 43-Gb/s to commercial products [309]. And whereas 100-Gb/s DQPSK was not even on the horizon three years ago, a field trial has now already demonstrated its feasibility in a deployed network [310]. This is even more true for POLMUX signaling. Until recently, many people in the fiber-optic industry considered it only suitable for transmission experiments and never stable enough for commercial deployment. But when digital coherent detection provided a practical alternative to optical polarization de-multiplexing, this technology went in the course of less than two years from the first lab demonstrations to commercial deployment [428]. The comparison in this section is therefore based on the current state-of-the-art and bound to be soon outdated.

### 11.1 Robust optical modulation formats

The choice of the optical modulation format is a trade-off between a number of different requirements: (1) spectral efficiency and optical filter tolerance, (2) OSNR requirement, (3) nonlinear tolerance, (4) chromatic dispersion tolerance, (5) PMD tolerance and (6) transponder complexity.

The importance of each of these requirements differs depending on the optical transmission system. It is therefore unlikely that a 'standard' modulation format will be the best choice for a wide range of transmission systems. More likely, the optimal choice of the modulation format will depend on such factors as the bit rate, fiber type, transmission distance and network architecture.

We first consider the modulation formats of interest in the absence of electronic equalization. This makes it difficult to use POLMUX signaling as the interaction between PMD-related impairments and other transmission impairments complicates system design too much. Hence, the choice is reduced to duobinary, (partial-)DPSK or DQPSK modulation<sup>1</sup>. When we consider the *OSNR requirement* and *nonlinear tolerance*, which determine the transmission reach, the differences are significant and particularly poor for duobinary modulation. Duobinary is currently (beginning of 2008) the most widely deployed modulation format for 40-Gb/s transmission. But it is likely that, at least for long-haul transmission, it will be replaced by other options as soon as they become available. However, due to its low *transponder complexity* 40-Gb/s duobinary might be the best choice for regional networks (300 km - 800 km).

DPSK and DQPSK both have a significantly lower OSNR requirement, with only a 1-dB advantage for DPSK. However, this 1-dB advantage combined with a 2-3 dB advantage in nonlinear tolerance makes DPSK the more suitable choice for long-haul transmission (1,000 km - 1,500 km). In comparison, the feasible transmission distance of 40-Gb/s DQPSK modulation is not likely to exceed 1,000 km. The poor *filter tolerance* of 40-Gb/s DPSK when used on a 50-GHz wavelength grid is its most significant drawback, in particular when a transmission link contains multiple OADM/PXC. In this case, either partial DPSK or DQPSK modulation is a better choice because of their higher narrowband filtering tolerance. A further concern for DPSK modulation is the smaller *chromatic dispersion* and *PMD tolerance*. It therefore requires both tunable dispersion compensation as well as PMD compensation for transmission over high-PMD fiber. DQPSK modulation has a better chromatic dispersion tolerance, but it is insufficient to negate the need for tunable dispersion compensation (generally 500 ps/nm for a 1-dB OSNR penalty). However, the higher PMD tolerance is a definite advantage of DQPSK modulation, which might be useful for *PMD-limited* transmission links. DQPSK modulation seems therefore the better choice for PMD-limited transmission links and/or systems with multiple OADM/PXC nodes. However, the higher *transponder complexity* of a DQPSK transponder in comparison to DPSK might negate these advantages.

For 100-Gb/s transponders, both duobinary and DPSK are difficult to realize due the high symbol rate. This puts stringent requirements on the bandwidth of the electrical components in the transponder. But more importantly, binary modulation formats do not provide a (significant) increase in spectral efficiency when the bit rate is increased from 40-Gb/s to 100-Gb/s. At the same time, the higher OSNR requirement will limit the feasible transmission distance. This combination of a limited spectral efficiency and feasible transmission distance, is likely to stall the deployment of such formats. DQPSK modulation, on the other hand, is a much more attractive option as it allows for a 1.0-b/s/Hz spectral efficiency as well as a reduction in the electrical

---

<sup>1</sup>We assume here EDFA-only amplification, SSMF fiber with a 21-dB span loss, multiple cascaded OADM/PXC in the link and a 3-dB margin with respect to the FEC limit. Only those options are discussed that are likely to have a spectral efficiency of >0.8-b/s/Hz and a reach in excess of 500-km.



bandwidth of the transponder components. But, similar as observed for 40-Gb/s transmission, the limited nonlinear tolerance and high OSNR requirement will restrict the feasible transmission distance. For 100-Gb/s DQPSK, it is not likely to exceed  $\sim 600$  km in commercial systems. In addition, 100-Gb/s DQPSK modulation is not directly compatible with the 50-GHz channel spacing of most deployed long-haul transmission systems.

## 11.2 Robust electronic equalization

We now consider the impact of electronic equalization on the choice of the modulation format. The main difference with the previously discussed modulation formats is that electronic equalization makes it feasible to use POLMUX signaling. On the other hand, the limited speed of state-of-the-art ADCs restrict the symbol rate to  $< 30$ -Gbaud. This disqualifies the use of binary modulation formats for electronic equalization at either 40-Gb/s or 100-Gb/s bit rates. We therefore consider the following options: direct detection DQPSK modulation combined with MSPE/MLSE and POLMUX-BPSK or POLMUX-QPSK modulation combined with a digital coherent receiver.

The *OSNR requirement* is close to optimum in all three cases with a slight exception for DQPSK, as differential detection is required. For all three formats, the nonlinear tolerance can be improved through digital signal processing. However, (POLMUX-)DQPSK modulation is more vulnerable to phase perturbations as it has a more dense signal constellation. POLMUX-BPSK is therefore likely to have the highest *nonlinear tolerance*, which makes it the most suitable choice with respect to transmission reach. The improvement in *chromatic dispersion* and *PMD tolerance* is one of the main benefits of electronic equalization. For a digital coherent receiver, the chromatic dispersion and PMD tolerance depend only on the signal processing and can therefore be nearly arbitrarily high. With a direct detection receiver, on the other hand, the chromatic dispersion compensation is somewhat limited as the signal processing cannot compensate for arbitrary large distortions without penalty. The same is true for the PMD tolerance as no polarization-diversity receiver is used. However, both the chromatic dispersion and PMD tolerance can be sufficiently high such that no tunable optical compensation is required in the receiver. The main drawback of all three formats is the high *transponder complexity*, which results from both multi-level modulation as well as the required electronic signal processing.

For 40-Gb/s transponders all three modulation formats seem to be a suitable choice. POLMUX-QPSK has the advantage of a lower symbol rate, which reduces the requirements on the ADCs. On the other hand, it requires the most complex transmitter structure of all three modulation formats. When the difference in symbol rate is less significant, POLMUX-BPSK might be the best choice for long-haul transmission as the higher nonlinear tolerance improves transmission reach. DQPSK plus MSPE/MLSE can be an option in transmission links where it is desirable to have a polarization-insensitive receiver, for example in the presence of co-propagating 10-Gb/s NRZ-OOK channels. For a 100-Gb/s transponders, only POLMUX-QPSK seems to be a viable option as the symbol rate of both DQPSK and POLMUX-BPSK is too high to combine with digital signal processing. A transmission reach of  $\sim 1000$  km seems feasible with POLMUX-

Table 11.1: COMPARISON OF MODULATION FORMATS<sup>2</sup>.

	Spectral Efficiency	OSNR requirement	Nonlinear tolerance <sup>3</sup>	CD tolerance	PMD tolerance	Transponder Complexity <sup>4</sup>
OOK	✘✘	✘	✘✘	✘	-	✓
duobinary	✓	✘✘	✘✘	✓	✘	✓
RZ-DPSK	✘	✓	✓✓	✘	-	✘
partial DPSK	-	-	-	-	-	-
DQPSK	✓✓	-	✘	✓	✓	✘✘
DQPSK, MSPE/MLSE	✓✓	✓	✓	✓✓	✓✓	✘✘
POLMUX-BPSK, coherent	✓✓	✓✓	✓✓	✓✓✓	✓✓✓	✘✘
POLMUX-QPSK, coherent	✓✓✓	✓✓	✓	✓✓✓	✓✓✓	✘✘✘

QPSK modulation and a digital coherent receiver. This in turn indicates that for a 100-Gb/s data rate per wavelength, it becomes challenging to realize long-haul transmission even when the best possible solution is considered. A further improvement in transmission reach is only possible through an improvement in nonlinear tolerance. It is therefore likely that the compensation of nonlinear transmission impairments will become one of the most significant fields of research in the upcoming years. This can either be realized through nonlinear signal processing, in the transmitter and receiver, or through optical compensation along the link, for example with optical phase conjugation.

In summary, the combination of multi-level modulation formats and digital signal processing has very advantageous properties to realize robust high-capacity transmission. However, this combination comes also at the cost of a higher transponder complexity. This could be alleviated through a higher level of optical integration, for example using InP photonic integrated circuits. We therefore conclude that the combination of multi-level modulation, digital signal processing and photonic integration, can enable robust and cost-effective optical transmission systems with the capacity to transport the data required for tomorrow’s Internet applications.

<sup>2</sup>Partial DPSK is the state-of-the-art binary modulation format for 40-Gb/s transmission, and is therefore used here as the reference.

<sup>3</sup>The nonlinear tolerance depends strongly on the bit rate and dispersion map, the denoted comparison is an estimation at a 40-Gb/s bit rate.

<sup>4</sup>The transponder complexity denoted in the table does not include either optical dispersion or PMD compensation, as this is different for each transmission link and not strictly determined by the choice in modulation format.

# A

---

## List of symbols & abbreviations

### A.1 List of symbols

$\langle \cdot \rangle$	Ensemble average
$var(\cdot)$	Ensemble variance
$\nabla$	Vector differential operator
$\alpha$	Fiber attenuation
$\beta_n$	Group velocity of the $n^{th}$ order
$\gamma$	Fiber nonlinearly
$\hat{\gamma}$	Path-averaged fiber nonlinearly
$\Delta\tau$	mean DGD
$\epsilon_0$	Permittivity of vacuum
$\theta$	Optical polarization angle
$\lambda$	Optical wavelength
$\lambda_0$	Zero-dispersion wavelength
$\mu$	Statistical mean
$\mu_0$	Permeability of vacuum
$\langle \rho \rangle$	Nonlinear phase noise
$\sigma$	Statistical variance
$\vec{\tau}$	PMD vector
$\phi$	Optical phase
$\phi_{SPM}$	SPM-induced phase shift
$\chi^{(n)}$	Susceptibility of the $n^{th}$ order
$\psi$	Optical polarization phase

## Appendix A. List of symbols & abbreviations

---

$\omega$	Angular frequency
$\omega_0$	Optical carrier frequency
$A_{eff}$	Effective area of a fibers core
$B_0$	Signal bandwidth ( $B_0 = 1/T_0$ )
$c$	Speed of light ( $c = 2.99792 \cdot 10^8$ m/s)
$D$	Dispersion parameter
$D_{local}$	Local dispersion
$E(z,t)$	Optical field as a function of time and distance
$f$	Optical frequency
$f_0$	Optical carrier frequency
$F$	Noise figure (optical amplifier)
$g_R$	Raman gain coefficient
$G$	Gain (optical amplifier)
$h$	Planck's constant ( $h = 6.626068 \cdot 10^{-34}$ m <sup>2</sup> kg/s)
$I$	In-phase tributary
$n$	Refractive index
$n_0$	Linear refractive index
$n_2$	Nonlinear refractive index
$n_{sp}$	Spontaneous emission factor
$N_0$	Noise power spectral density
$N_{span}$	Number of spans in the transmission link
$P$	Optical power
$P_0$	Optical input power
$PD\lambda$	Polarization dependent wavelength shift
$L$	Fiber length
$L_D$	Normalized dispersion length
$L_{eff}$	Effective fiber length
$L_{span}$	Fiber span length
$L_W$	Walk-off length
$Q$	Quadrature tributary
$S$	Dispersion slope parameter
$t, T$	Time
$T_0$	Symbol time
$v_p$	Phase velocity
$V_\pi$	Characteristic voltage of a modulator
$V_{pp}$	Peak-to-peak voltage
$z$	Transmission distance

## A.2 List of abbreviations

ADC	Analog-to-digital converter
AGC	Automatic gain control
Al <sub>2</sub> O <sub>3</sub>	Aluminium Oxide
AM	Amplitude modulation
APol	Alternating polarization modulation
ASE	Amplitude spontaneous emission
ASIC	Application specific integrated circuit
AWG	Arrayed waveguide grating
BER	Bit-error-rate
BERT	Bit-error-rate tester
BPF	Band pass filter
BSF	Band selection filter
BPSK	Binary phase shift keying
CDR	Clock and data recovery
CMA	Constant modulus algorithm
CPE	Carrier phase estimation
CR	Clock recovery
CRZ	Chirped return-to-zero
CSF	Channel selection filter
CSRZ	Carrier-suppressed return-to-zero
CW	Continuous wave
DD	Decision-directed
DCF	Dispersion compensated fiber
DCM	Dispersion compensation unit
DFB	Distributed feedback
DFF	Data flip-flop
DFG	Difference frequency generation
DGD	Differential Group Delay
DGE	Dynamic gain equalizer
DML	Directly modulated laser
DPSK	Differential phase shift keying
DOP	Degree of polarization
DQPSK	Differential quadrature phase shift keying
DSF	Dispersion shifted fiber
DSL	Digital subscriber line
DSO	Digital Storage Oscilloscope
EAM	Electro-absorption modulator
ECL	External cavity laser
EDFA	Erbium doped fiber amplifier
EO	Eye opening
EOP	Eye opening penalty

## Appendix A. List of symbols & abbreviations

---

Er <sup>3+</sup>	Erbium
FBG	Fiber Bragg grating
FEC	Forward error correction
FIR	Finite impulse response
FFT	Fast Fourier transform
FWM	Four wave mixing
GaAs	Gallium Arsenide
GDR	Group delay ripple
GeO <sub>2</sub>	Germanium Oxide
GVD	Group velocity dispersion
IFWM	Intra-channel four wave mixing
InP	Indium Phosphite
INT	Interleaver
ISI	Inter symbol interference
ITU	International telecommunication union
IXPM	Intra-channel cross polarization modulation
JD	Joint decision
LiNbO <sub>3</sub>	Lithium Niobate
LMS	Least mean square
LSPS	Loop-synchronous polarization scrambler
MEMS	Micro electro-mechanical system
MLSE	Maximum likelihood sequence estimation
MSPE	Multi-symbol phase estimation
MZM	Mach-zehnder modulator
MZDI	Mach-Zehnder delay interferometer
NRZ	Non-return-to-zero
NZDSF	Non-zero dispersion shifted fiber
OADM	Optical add-drop multiplexer
OH <sup>-</sup>	Hydroxyl
OPC	Optical phase conjugation
OOK	On-off keying
OSNR	Optical signal-to-noise ratio
OTN	Optical transport network
PBF	Pump block filter
PBS	Polarization beam splitter
PC	Polarization controller
PCD	Polarization chromatic dispersion
PDF	Probability density function
PDL	Polarization dependent loss
PDM	Polarization division multiplexing
PM	Phase modulator
PMD	Polarization mode dispersion
POLMUX	Polarization multiplexing
POLSK	Polarization shift keying

PPLN	Periodically-poled lithium Niobate
PRBS	Pseudo random bit sequence
PRQS	Pseudo random quaternary sequence
PSBT	Phase shaped binary transmission
PSD	Power spectral density
PSK	Phase shift keying
PSP	Principle state of polarization
PXC	Photonic cross connect
QPM	Quasi phase matching
QPSK	Quadrature phase shift keying
RIN	Relative intensity noise
RX	Receiver
RZ	Return-to-zero
SBS	Stimulated Brillouin scattering
SHG	Second harmonic generation
SiO <sub>2</sub>	Silicon Oxide
SOP	State of polarization
SOPMD	Second order polarization mode dispersion
SPM	Self phase modulation
SRS	Stimulated Raman scattering
SSMF	Standard single mode fiber
TDC	Tunable dispersion compensator
TX	Transmitter
VOA	Variable optical attenuator
WDM	Wavelength division multiplexing
WSS	Wavelength selective switch
XPIC	Cross polarization interference canceler
XPM	Cross phase modulation
XPolM	Cross Polarization modulation





# B

---

## Definition of the Q-factor and eye opening penalty

The experimental results discussed in this thesis use the bit-error-ratio (BER) to quantify transmission impairments and pulse degradations. The BER quantifies the fraction of errors that occurred in a given time interval  $\Delta T$ , according to,

$$BER = \frac{k(\Delta T)}{K(\Delta T)}, \quad (\text{B.1})$$

where  $k(\Delta T)$  are the bit errors counted during the time interval  $\Delta T$  and  $K(\Delta T)$  is the total number of received bits during this interval. The BER is normally measured as a function of the OSNR, in order to define the *required OSNR* for a certain BER. The impact of isolated transmission impairments, such as chromatic dispersion or DGD, can then be quantified as a function of the required OSNR for a chosen BER.

The impact of isolated transmission impairments in a long-haul WDM transmission system is more difficult to quantify. The OSNR is normally determined by dividing signal and ASE power, where the ASE power is measured at a wavelength close to the signal. The more accurate measurement is to take the average of the noise power at a slightly higher and lower wavelengths, as this corrects for a (linear) tilt in the spectrum. However, with co-propagating WDM channels it is difficult to quantify the noise level. As a result, the OSNR cannot easily be measured with high accuracy using this method. We therefore use the BER/Q-factor to quantify the performance in the long-haul WDM transmission experiments.

## B.1 Q-factor

The Q-factor is related to the signal-to-noise ratio at the decision circuit expressed in terms of the photocurrent [445]. It is defined as the distance from the decision threshold to the mean photocurrent divided through the standard deviation, e.g.

$$Q_0 = \frac{\mu_0 - I}{\sigma_0} \tag{B.2}$$

$$Q_1 = \frac{\mu_1 - I}{\sigma_1}$$

where  $\mu_0$  and  $\mu_1$  are the mean photocurrents of the marks ('1's) and spaces ('0's) level, respectively, and  $\sigma_0 / \sigma_1$  is the standard deviation. This is valid independently of the specific distribution of the noise probability density functions.

When a hard-decision threshold receiver takes a binary decision on a signal degraded by ASE, the *optimum* decision threshold  $I_D$  is defined as,

$$I_D = \frac{\sigma_0 \mu_1 + \sigma_1 \mu_0}{\sigma_0 + \sigma_1}, \tag{B.3}$$

which is visualized in Figure B.1a. The Q-factor can then be defined as,

$$Q = \frac{\mu_1 - I_D}{\sigma_1} = \frac{I_D - \mu_0}{\sigma_0}. \tag{B.4}$$

This can be written independently of the optimum threshold  $I_D$  by combining Equations B.3 and B.4,

$$Q = \frac{\mu_1 - \mu_0}{\sigma_0 + \sigma_1}. \tag{B.5}$$

The photocurrent of an ideal photodiode has a Chi-square distribution when the amplitude of the ASE noise is Gaussian distributed. This is a result of the quadratic relation between photocurrent and incident optical power. However, for a direct detected OOK modulated signal the Chi-square distribution can be approximated with a Gaussian distribution. This approximation is valid under certain conditions, such as a high enough OSNR ( $>10$  dB) and low ISI. The Q-factor can then be used to approximate the BER, as shown by *Bergano et. al.* in [445].

$$BER \equiv \frac{1}{2} \operatorname{erfc}\left(\frac{Q}{\sqrt{2}}\right) \approx \frac{1}{\sqrt{2\pi}Q} \exp\left(-\frac{Q^2}{2}\right), \tag{B.6}$$

where  $\operatorname{erfc}(\cdot)$  is the complementary error function and the approximation is valid for a BER lower than  $10^{-2}$ .

For direct detected phase modulated formats, *Bosco and Poggiolini* showed in [446] that a Gaussian approximation of the Chi-square distributed photocurrent is not accurate. This results from

the phase demodulation with an MZDI and subsequent balanced detection, which affects the probability density distribution of the noise. We note that the Q-factor can still be defined for phase modulated formats, but it is not accurate to compute the BER using Equation B.6. Alternatively, BER estimation for phase modulated formats is possible through the Eigenfunction Expansion Method [288] or using the Karhunen–Loève approximation [299]. Both BER estimation approaches have been used in the analytical simulations of this thesis.

The Q-factor is often defined in logarithmic units,

$$Q(\text{dB}) = 20 \cdot \log_{10}(Q). \quad (\text{B.7})$$

Using Q(dB) as an indication of transmission performance has the advantage that it is proportional to the OSNR. Hence, a 1 dB increase in OSNR will result in a  $\sim 1$  dB increase in Q(dB). This property is used to express the *system margin* in long-haul transmission systems. When a transmission operates at a 3 dB margin with respect to the FEC limit, this implies that either the Q(dB) or OSNR can be lowered by 3 dB before the FEC limit is reached. Figure B.1b visualizes the relation between  $\log(\text{BER})$  and Q(dB). We note that Equation B.6 is still valid for phase modulated formats, and can be used to compute the Q-factor based on a known BER. This is used in this thesis to compute Q(dB) for D(Q)PSK modulation, which gives an indication of the system margin.

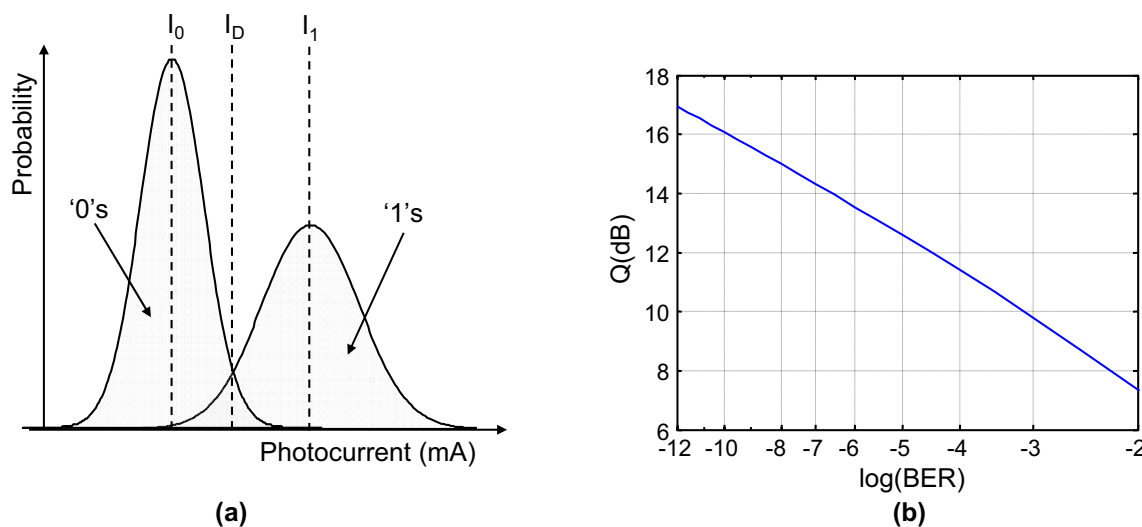


Figure B.1: (a) Definition of the optimum decision threshold and (b) relation between Q and BER.

## B.2 Eye opening penalty

In the analytical simulations, the eye opening penalty (EOP) is used as a measure besides the BER to qualify signal impairments. The EOP is not dependent on the OSNR but it is computed only from the shape of the eye diagram. It has therefore the advantage that it can be computed

## Appendix B. Definition of the Q-factor and eye opening penalty

---

with relatively low computational effort. Several definitions of the EOP exist in literature, but in this thesis we defined it as,

$$EOP = \frac{2 \cdot \text{mean}}{EO}, \quad (\text{B.8})$$

where *mean* defines the average value of all lines in the eye diagram and EO is the eye opening. The definition of the eye opening is the largest square box with a width equal to 20% of the symbol period that fits into the eye diagram. The 20% eye opening width is used here to account for signal jitter. Figure B.1 graphically depicts the definition of the EOP, where  $T_0$  is the bit interval. The EOP is not always a good approximation of the OSNR penalty. In particular in the presence of ISI, such as chromatic dispersion or PMD, it can be a factor of 2-3 smaller than the OSNR penalty [330].

The EOP is usually defined in logarithmic units as,

$$EOP(\text{dB}) = 10 \cdot \log_{10}(EOP). \quad (\text{B.9})$$

The EOP(dB) is zero for an ideal NRZ-OOK eye diagram, but it can be lower than zero for other modulation formats. In particular RZ pulse carving lowers the EOP below zero. In the comparison between modulation formats, such as for example in Chapter 8, the EOP is therefore normalized with respect to the EOP in the absence of transmission impairments

We note that the EOP can be computed either from the optical eye diagram (before the photodiode) or the electrical eye diagram. The EOP based on the electrical eye diagram is a more realistic definition as it includes the impact of narrowband electrical filtering. For phase modulated formats, the necessity to include balanced detection limits the EOP computation to the electrical eye diagram.

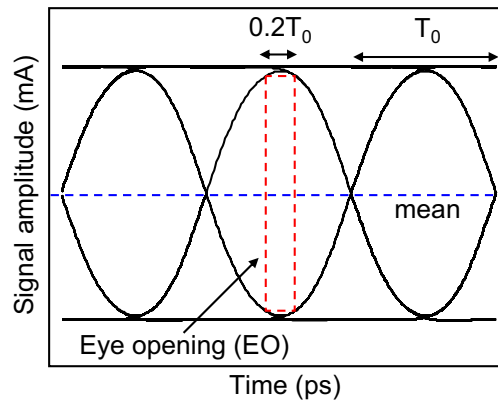


Figure B.2: Definition of the EOP and its relation to the shape of the (electrical) eye diagram.

## Asymmetric 3 x 3 coupler for coherent detection

As discussed in Chapter 10, a coherent receiver requires a  $90^\circ$  hybrid for detection of the in-phase and quadrature components. In this thesis this has been realized using an asymmetric  $3 \times 3$  fiber coupler. In this appendix we will give the proof that an asymmetric  $3 \times 3$  fiber coupler can be used as a  $90^\circ$  Hybrid. The configuration of a coherent receiver using an asymmetric fiber coupler is depicted, for a single polarization, in C.1. The two input signals of the fiber coupler consist of the received optical signal and the LO laser.

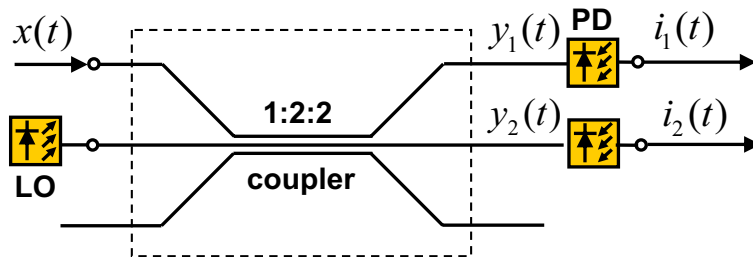


Figure C.1: Coherent receiver using an asymmetric  $3 \times 3$  coupler with 2:2:1 output ratio

The input vector  $\vec{x}$  can thus be defined as,

$$\vec{x}(t) = \begin{pmatrix} \sqrt{P_s} \exp(j[\omega_0 t + \varphi(t)]) \\ \sqrt{P_{LO}} \exp(j[\omega_0 t + \varphi_{LO}]) \end{pmatrix}, \quad (\text{C.1})$$

where we assume that the information is carried in the optical phase  $\varphi(t)$  and both the received signal and local oscillator have the same carrier frequency  $\omega_0$ . The output vector  $\vec{y}$  of the asym-

### Appendix C. Asymmetric 3 x 3 coupler for coherent detection

---

metric 3x3 coupler is now defined by multiplication of the input vector with a 3x3 scattering matrix  $S$ . The elements of  $S$  can be written as,

$$S_{ik} = s_{ik}e^{j\phi_{ik}}, \quad (\text{C.2})$$

where  $i$  and  $k$  are the matrix indexes. The scattering matrix derivation for a generalized 3x3 coupler has been analyzed by *Pietzsch* in [447]. We now follow this derivation to compute the scattering matrix of an asymmetric coupler with a 1 : 2 : 2 output ratio. For simplicity, we assume the coupler to be lossless. In this case the dissipated power is zero and the scattering matrix has to be unitary, i.e.,

$$\sum_{k=1}^3 s_{ik}^2 = \sum_{i=1}^3 s_{ik}^2 = 1. \quad (\text{C.3})$$

The amplitude coefficients of  $S$  are therefore directly defined by the output ratio. For a 1 : 2 : 2 output ratio we then find,

$$s^2 = \begin{pmatrix} 0.2 & 0.4 & 0.4 \\ 0.4 & 0.2 & 0.4 \\ 0.4 & 0.4 & 0.2 \end{pmatrix}. \quad (\text{C.4})$$

By variation of the optical path lengths in and out of the fiber coupler it can be shown that five of the nine angle coefficients can be chosen arbitrarily (see for example also [448]). Using the normalization of the scattering matrix given in [447], this results in,

$$\phi_{12} = \phi_{21}, \quad \phi_{23} = \phi_{32}, \quad \phi_{11} = \phi_{22} = \phi_{33} = 0. \quad (\text{C.5})$$

The remaining amplitude coefficients of  $S$  can be computed directly out of the amplitude coefficients,

$$\cos(\phi_{ik} - \phi_{il} - \phi_{jk} + \phi_{jl}) = \frac{s_{ml}^2 s_{mk}^2 - s_{jl}^2 s_{jk}^2 - s_{il}^2 s_{ik}^2}{2s_{il} s_{ik} s_{jl} s_{jk}}, \quad (\text{C.6})$$

where  $i \neq j \neq m$  and  $l \neq k$ .

Solving this set of equations for a 1 : 2 : 2 output ratio results in the following scattering matrix  $S$ ,

$$S = \frac{1}{\sqrt{5}} \begin{pmatrix} 1 & \sqrt{2}\exp(j\frac{\pi}{4}) & \sqrt{2}\exp(j\frac{\pi}{2}) \\ \sqrt{2}\exp(j\frac{\pi}{4}) & 1 & \sqrt{2} \\ -\sqrt{2} & \sqrt{2} & 1 \end{pmatrix}. \quad (\text{C.7})$$

The output vector  $\vec{y}(t)$  follows now out of  $\vec{y}(t) = S\vec{x}(t)$ ,

$$\vec{y}(t) = \frac{1}{\sqrt{5}} \begin{pmatrix} \sqrt{P_s}\exp(j[\omega_0(t) + \varphi(t)]) & + & \sqrt{2P_{LO}}\exp(j[\omega_0(t) + \varphi_{LO} + \frac{\pi}{4}]) \\ \sqrt{2P_s}\exp(j[\omega_0(t) + \varphi(t) + \frac{\pi}{4}]) & + & \sqrt{P_{LO}}\exp(j([\omega_0(t) + \varphi_{LO}]) \\ \sqrt{2P_s}\exp(j[\omega_0(t) + \varphi(t) + \pi]) & + & \sqrt{2P_{LO}}\exp(j[(\omega_0(t) + \varphi_{LO}]) \end{pmatrix}. \quad (\text{C.8})$$

---

The third fiber output of the coupler can be detected with a third photodiode and used to cancel out the DC term  $\sqrt{P_s}$ . But in the work described in this thesis the third output is not used and the DC term  $\sqrt{P_s}$  is canceled out using a high LO to signal ratio  $P_{LO}/P_s$ . The current after an ideal photodiode is then given by  $i(t) = |\vec{y}(t)\vec{y}^*(t)|$ ,

$$\vec{i}(t) = \frac{1}{5} \begin{pmatrix} P_s + 2P_{LO} + \sqrt{2P_{LO}P_s}[\exp(j[\varphi(t) - \varphi_{LO} - \frac{\pi}{4}]) + \exp(-j[\varphi(t) - \varphi_{LO} - \frac{\pi}{4}])] \\ 2P_s + P_{LO} + \sqrt{2P_{LO}P_s}[\exp(j[\varphi(t) - \varphi_{LO} + \frac{\pi}{4}]) + \exp(-j[\varphi(t) - \varphi_{LO} + \frac{\pi}{4}])] \end{pmatrix},$$

where we neglect all high-frequency terms at the carrier frequency. This we can rewrite as,

$$\vec{i}(t) = \frac{P_s}{5} \begin{pmatrix} 1 \\ 2 \end{pmatrix} + \frac{P_{LO}}{5} \begin{pmatrix} 2 \\ 1 \end{pmatrix} + \frac{2\sqrt{2P_{LO}P_s}}{5} \begin{pmatrix} \cos(\varphi(t) - \varphi_{LO} - \frac{\pi}{4}) \\ \cos(\varphi(t) - \varphi_{LO} + \frac{\pi}{4}) \end{pmatrix}. \quad (C.9)$$

And with  $\varphi_0 = \frac{\pi}{4}$

$$\vec{i}(t) = \frac{P_s}{5} \begin{pmatrix} 1 \\ 2 \end{pmatrix} + \frac{P_{LO}}{5} \begin{pmatrix} 2 \\ 1 \end{pmatrix} + \frac{2\sqrt{2P_{LO}P_s}}{5} \begin{pmatrix} \sin(\varphi(t)) \\ \cos(\varphi(t)) \end{pmatrix}. \quad (C.10)$$

Equation C.10 is equal to the photocurrents described in [449]





---

# Bibliography

- [1] [Online]. Available: <http://www.skype.com>
- [2] [Online]. Available: <http://www.youtube.com>
- [3] [Online]. Available: <http://earth.google.com>
- [4] [Online]. Available: <http://www.telegeography.com>
- [5] N. J. Frigo, P. P. Iannone, and K. C. Reichmann, "A View of Fiber to the Home Economics," *IEEE Commun. Mag.*, vol. 42, no. 8, pp. S16–S23, Aug. 2004.
- [6] T. Koonen, "Fiber to the Home/Fiber to the Premises: What, Where and When?" *Proc. IEEE*, vol. 94, no. 5, pp. 911–934, May 2006.
- [7] P. J. Winzer and R.-J. Essiambre, "Advanced Optical Modulation Formats," *Proc. IEEE*, vol. 94, no. 5, pp. 952–985, May 2006.
- [8] G. Raybon, S. Chandrasekhar, A. Agarwal *et al.*, "Limitations of Optical Add/Drop Filtering on 42.7-Gb/s Transmission with 50-GHz Channel Spacing," in *Proc. Eur. Conf. Optical Commun. (ECOC)*, Stockholm, Sweden, September 2004, paper Mo4.5.1.
- [9] J. A. Lázaro, W. Idler, R. Dischler, and A. Kleinkamp, "Filtering and Linear Crosstalk Penalties of ASK and DPSK 43Gb/s DWDM Systems with 50GHz Channel Spacing," in *Proc. Eur. Conf. Optical Commun. (ECOC)*, Stockholm, Sweden, September 2004, paper We3.4.1.
- [10] J. M. Kahn and K.-P. Ho, "Spectral Efficiency Limits and Modulation/Detection Techniques for DWDM Systems," *IEEE J. Sel. Topics Quantum Electron.*, vol. 10, no. 2, pp. 259–272, Mar/Apr. 2004.
- [11] J. H. Sinkov, A. Adamiecki, L. Buhl *et al.*, "107-Gbit/s Opto-Electronic Receiver with Hybrid Integrated Photodetector and Demultiplexer," in *Proc. Optical Fiber Commun. Conf. (OFC)*, Anaheim, CA, U.S.A., Mar. 2007, post-deadline paper PDP30.
- [12] P. J. Winzer, G. Raybon, C. R. Doerr *et al.*, "107-Gb/s Optical Signal Generation Using Electronic Time-Division Multiplexing," *J. Lightwave Technol.*, vol. 24, no. 8, p. 3107–3113, Aug. 2006.
- [13] M. Daikoku, I. Morita, H. Taga *et al.*, "100-Gb/s DQPSK Transmission Experiment without OTDM for 100G Ethernet Transport," *J. Lightwave Technol.*, vol. 25, no. 1, pp. 139–145, Jan. 2007.
- [14] P. J. Winzer, G. Raybon, C. R. Doerr *et al.*, "2000-km WDM Transmission of 10x107-Gb/s RZ-DQPSK," in *Proc. Eur. Conf. Optical Commun. (ECOC)*, Cannes, France, Sep. 2006, post-deadline paper Th4.1.3.
- [15] P. J. Winzer, G. Raybon, S. Chandrasekhar *et al.*, "10 x 107-Gb/s NRZ-DQPSK Transmission at 1.0 b/s/Hz over 12 x 100 km Including 6 Optical Routing Nodes," in *Proc. Optical Fiber Commun. Conf. (OFC)*, Anaheim, CA, U.S.A., Mar. 2007, post-deadline paper PDP24.
- [16] G. E. Moore, "No Exponential is Forever: But "Forever" Can Be Delayed!" in *Proc. IEEE Int. Solid-State Circ. Conf. (ISSCC)*, San Francisco, CA, U.S.A., Feb. 2003, paper 1.1.

## Bibliography

---

- [17] P. Schvan, D. Pollex, S.-C. Wang *et al.*, “A 22GS/s 5b ADC in 0.13 $\mu$ m SiGe BiCMOS,” in *Proc. IEEE Int. Solid-State Circ. Conf. (ISSCC)*, San Francisco, CA, U.S.A., Feb. 2006, paper 31.4.
- [18] P. Schvan, J. Bach, C. Falt *et al.*, “A 24GS/s 6b ADC in 90nm CMOS,” in *Proc. IEEE Int. Solid-State Circ. Conf. (ISSCC)*, San Francisco, CA, U.S.A., Feb. 2008, paper 30.3.
- [19] A. Färbert, S. Langenbach, N. Stojanovic *et al.*, “Performance of a 10.7 Gb/s Receiver with Digital Equaliser using Maximum Likelihood Sequence Estimation,” in *Proc. Eur. Conf. Optical Commun. (ECOC)*, vol. 6, Stockholm, Sweden, September 2004, post-deadline paper Th4.1.5.
- [20] T. Kupfer, J. Whiteaway, and S. Langenbach, “PMD Compensation using Electronic Equalization particular Maximum Likelihood Sequence Estimation,” in *Proc. Optical Fiber Commun. Conf. (OFC)*, Anaheim, CA, U.S.A., March 2007, paper OMH1.
- [21] S. L. Jansen, “Optical Phase Conjugation in Fiber-Optic Transmission Systems,” Ph.D. dissertation, Eindhoven University of Technology, Jun. 2006.
- [22] K. C. Kao and G. A. Hockham, “Dielectric-Fiber Surface Waveguides for Optical Frequencies,” *Proc. Inst. Elect. Eng.*, vol. 113, no. 7, pp. 1151–1158, Jul. 1966.
- [23] S. R. Nagel, J. B. MacChesney, and K. L. Walker, “An Overview of the Modified Chemical Vapor Deposition (MCVD) Process and Performance,” *IEEE J. Quantum Electron.*, vol. 18, no. 4, pp. 459–476, Apr. 1982.
- [24] T. Kato, Y. Koyano, and M. Nishimura, “Temperature Dependence of Chromatic Dispersion in Various Types of Optical Fibers,” in *Proc. Optical Fiber Commun. Conf. (OFC)*, Baltimore, MD, U.S.A, Mar. 2000, paper TuG7.
- [25] *ITU-T G.652, Characteristics of a Single-Mode Optical Fibre and Cable*, Jun. 2005.
- [26] Y. Chigusa, Y. Yamamoto, T. Yokokawa *et al.*, “Low-loss Pure-Silica-Core Fibers and Their Possible Impact on Transmission Systems,” *J. Lightwave Technol.*, vol. 23, no. 11, pp. 3541–3550, Nov. 2005.
- [27] K. Nagayama, M. Kakui, M. Matsui *et al.*, “Ultra-Low-Loss (0.1484 dB/km) Pure Silica Core Fibre and Extension of Transmission Distance,” *Electron. Lett.*, vol. 38, no. 20, pp. 1168–1169, Sep. 2002.
- [28] H. Maeda, G. Funatsu, and A. Naka, “Ultra-Long-Span 500 km 16 x 10 Gbit/s WDM Unrepeateded Transmission using RZ-DPSK Format,” *Electron. Lett.*, vol. 41, no. 1, pp. 34–35, Jan. 2005.
- [29] G. P. Agrawal, *Fiber-Optic Communication Systems*, 3rd ed. John Wiley & Sons, 2002.
- [30] C. F. Bohren and D. Huffman, *Absorption and Scattering of Light by Small Particles*. New York, NY, U.S.A: John Wiley, 1983.
- [31] K. Mochizuki and Y. Namihira, “Transmission Loss Increase in Optical Fibres due to Hydrogen Permeation,” *Electron. Lett.*, vol. 19, no. 18, pp. 743–745, Sep. 1983.
- [32] K. H. Chang, D. Kalish, and M. Pearsall, “New Hydrogen Aging Loss Mechanism in the 1400 nm Window,” in *Proc. Optical Fiber Commun. Conf. (OFC)*, San Diego, CA, U.S.A., Feb. 1999, post-deadline paper PD22.
- [33] *ITU-T G.Sup39, Optical System Design and Engineering Considerations*, Feb. 2006.
- [34] A. H. Gnauck, G. Charlet, P. Tran *et al.*, “25.6-Tb/s C+L-Band Transmission of Polarization-Multiplexed RZ-DQPSK Signals,” in *Proc. Optical Fiber Commun. Conf. (OFC)*, Anaheim, CA, U.S.A, Mar. 2007, post-deadline paper PDP19.
- [35] M. Duelk, “Next-Generation 100G Ethernet,” in *Proc. Eur. Conf. Optical Commun. (ECOC)*, Glasgow, United Kingdom, Sep. 2005, paper Tu.3.1.2.
- [36] I. Sogawa, N. Kaida, K. Iwai *et al.*, “Study on Full-Spectrum Directly Modulated CWDM Transmission of 10 Gb/s per Channel over Water-Peak-Suppressed Nonzero Dispersion Shifted Fiber,” in *Proc. Eur. Conf. Optical Commun. (ECOC)*, Copenhagen, Denmark, Sep. 2002, paper 8.2.1.
- [37] H. J. Thiele, P. J. Winzer, J. H. Sinsky *et al.*, “160-Gb/s CWDM Capacity Upgrade using 2.5-Gb/s Rated Uncooled Directly Modulated Lasers,” *IEEE Photon. Technol. Lett.*, vol. 16, no. 10, pp. 2389–2391, Oct. 2004.

- 
- [38] E.-G. Neumann, *Single Mode Fibers I: Fundamentals*. Springer Verlag, 1988.
- [39] J. Lee, G. H. Song, U.-C. Paek, and Y. G. Seo, "Design and Fabrication of a Nonzero-Dispersion Fiber with a Maximally Flat Dispersion Spectrum," *IEEE Photon. Technol. Lett.*, vol. 13, no. 4, pp. 317–319, Apr. 2001.
- [40] *ITU-T G.653, Characteristics of a Dispersion-Shifted Single-Mode Optical Fibre and Cable*, Dec. 2006.
- [41] *ITU-T G.655, Characteristics of a Non-Zero Dispersion-Shifted Single-Mode Optical Fibre and Cable*, Mar. 2003.
- [42] G. P. Agrawal, *Nonlinear Fiber Optics*, 3rd ed. Academic Press, 2001.
- [43] S. Huard, *Polarization of Light*, 1st ed. John Wiley & Sons, 1997.
- [44] R. B. Dyott, *Elliptical Fiber waveguides*, 1st ed. Artec House, 1995.
- [45] S. C. Rashleigh and R. Ulrich, "Polarization-Mode Dispersion in Single-Mode Fibers," *Opt. Lett.*, vol. 3, no. 2, pp. 60–62, Aug. 1978.
- [46] P. Rosenau, "Random Walker and the Telegrapher's Equation: A Paradigm of a Generalized Hydrodynamics," *Phys. Rev. E*, vol. 48, no. 2, pp. 655–657, Aug. 1993.
- [47] L. E. Nelson and R. Jopson, "Introduction to Polarization Mode Dispersion in Optical Systems," in *Proc. Venice Summer School on PMD*, Venice, Italy, Jun. 2002, paper Mon-1.
- [48] A. Papoulis, *Probability, Random Variables, and Stochastic Processes*. New York, NY, U.S.A: McGraw-Hill, 1991.
- [49] G. J. Foschini and C. D. Poole, "Statistical Theory of Polarization Dispersion in Single Mode Fibers," *J. Lightwave Technol.*, vol. 9, no. 11, pp. 1439–1456, Nov. 1991.
- [50] M. Karlsson, "Probability Density Functions of the Differential Group Delay in Optical Fiber Communication Systems," *J. Lightwave Technol.*, vol. 19, no. 3, pp. 324–331, Mar. 2001.
- [51] *ITU-T G.650.2, Definitions and Test Methods for Statistical and Non-Linear Related Attributes of Single-Mode Fibre and Cable*, Jan. 2005.
- [52] C. Antonelli and A. Mecozzi, "Theoretical Characterization and System Impact of the Hinge Model of PMD," *J. Lightwave Technol.*, vol. 24, no. 11, pp. 4064–4074, Nov. 2006.
- [53] H. Kogelnik and P. J. Winzer, "PMD Outage Probabilities Revisited," in *Proc. Optical Fiber Commun. Conf. (OFC)*, Anaheim, CA, U.S.A, Mar. 2007, paper OTuN3.
- [54] G. V. de Faria, M. R. Jimenez, and J. P. von der Weid, "PMD Variations From Factory to Field in OPGW Cabled Fibers," *J. Lightwave Technol.*, vol. 18, no. 1, pp. 250–252, Jan. 2006.
- [55] A. Galtarossa, L. Palmieri, and A. Pizzinat, "Low-PMD Spun Fibers," in *Proc. Venice Summer School on PMD*, Venice, Italy, Jun. 2002, paper Tue-8.
- [56] D. Derickson, *Fiber Optic Test and Measurement*, 1st ed. Prentice-Hall, 1998.
- [57] A. Mecozzi and M. Shtaif, "Signal-to-Noise-Ratio Degradation Caused by Polarization-Dependent Loss and the Effect of Dynamic Gain Equalization," *J. Lightwave Technol.*, vol. 22, no. 8, pp. 1856–1871, Aug. 2004.
- [58] C. Xie and L. F. Mollenauer, "Performance Degradation Induced by Polarization-Dependent Loss in Optical Fiber Transmission Systems with and without Polarization-Mode Dispersion," *J. Lightwave Technol.*, vol. 21, no. 9, pp. 1953–1957, Sep. 2003.
- [59] M. Shtaif and O. Rosenberg, "Polarization-Dependent Loss as a Waveform-Distorting Mechanism and its Effect on Fiber-Optic Systems," *J. Lightwave Technol.*, vol. 23, no. 2, pp. 923–930, Feb. 2005.
- [60] T. Okuno, M. Onishi, T. Kashiwada *et al.*, "Silica-based Functional Fibers with Enhanced Nonlinearity and Their Applications," *IEEE J. Sel. Topics Quantum Electron.*, vol. 5, no. 5, pp. 1385–1391, Sep-Oct. 1999.
- [61] D. J. Richardson, K. Furusawa, H. Ebendorff-Heidepriem *et al.*, "Practical Applications of Holey Optical Fibers," in *Proc. Optical Fiber Commun. Conf. (OFC)*, Los Angeles, CA, U.S.A., Mar. 2004, paper ThA1.
-

## Bibliography

---

- [62] J.-P. Elbers, A. Farbert, and C. Scheerer, "Reduced Model to Describe SPM-Limited Fiber Transmission in Dispersion-Managed Light Wave Systems," *IEEE J. Sel. Topics Quantum Electron.*, vol. 6, no. 2, pp. 276–281, March–April 2000.
- [63] L. F. Mollenauer, R. H. Stolen, and J. P. Gordon, "Experimental Observation of Picosecond Pulse Narrowing and Solitons in Optical Fibers," *Phys. Rev. Lett.*, vol. 44, no. 13, p. 1095–1098, Sep. 1980.
- [64] L. F. Mollenauer, J. P. Gordon, and M. N. Islam, "Soliton Propagation in Long Fibers with Periodically Compensated Loss," *IEEE J. Quantum Electron.*, vol. 22, no. 1, p. 157–173, Jan. 1986.
- [65] P. V. M. L. F. Mollenauer and M. J. Neubelt, "Demonstration of Soliton WDM Transmission at 6 and 7 x 10 gbit/s, Error Free over Transoceanic Distances," *Electron. Lett.*, vol. 32, no. 5, p. 471–473, Feb. 1996.
- [66] P. V. Mamyshev and L. F. Mollenauer, "Pseudo-Phase-Matched Four-Wave Mixing in Soliton Wavelength-Division Multiplexing Transmission," *Opt. Lett.*, vol. 21, no. 6, p. 396–398, Mar. 1996.
- [67] I. Morita, K. Tanaka, N. Edagawa, and M. Suzuki, "40 Gb/s Single-Channel Soliton Transmission over Transoceanic Distances by Reducing Gordon-Haus Timing Jitter and Soliton-Soliton Interaction," *J. Lightwave Technol.*, vol. 17, no. 12, pp. 2506 – 2511, Dec. 1999.
- [68] L. Rapp, "Experimental Investigation of Signal Distortions Induced by Cross-Phase Modulation Combined with Dispersion," *IEEE Photon. Technol. Lett.*, vol. 9, no. 12, p. 1592–1594, Dec. 1997.
- [69] H. J. Thiele, R. I. Killey, and P. Bayvel, "Influence of Fibre Dispersion on XPM Pulse Distortion in WDM Systems," in *Proc. Eur. Conf. Optical Commun. (ECOC)*, vol. 1, Barcelona, Spain, Sep. 1998, p. 593–594.
- [70] Y. Yamada, S.-I. Nakagawa, K. Takashina *et al.*, "25-GHz Spacing Ultra-Dense WDM Transmission Experiment of 1-Tbit/s (100 WDMx10Gbit/s) over 7300 km using Non Pre-Chirped RZ Format," *Electron. Lett.*, vol. 35, no. 25, pp. 2212–2213, Dec. 1999.
- [71] Y. Zhu, W. Lee, P. Lobb *et al.*, "Polarization-Channel-Interleaved Carrier-Suppressed CS-RZ Transmission at 40Gbit/s with 0.8 bit/s/Hz Spectral Efficiency," *Electron. Lett.*, vol. 38, no. 8, pp. 381–382, Apr. 2002.
- [72] D. F. Grosz, A. Agrawal, S. Basnerjee *et al.*, "5.12 Tbit/s (128 x 42.7 Gb/s) Transmission with 0.8 bit/s/Hz Spectral Efficiency over 1280 km of Standard Single-Mode Fiber using All-Raman Amplification and Strong Signal Filtering," in *Proc. Eur. Conf. Optical Commun. (ECOC)*, Copenhagen, Denmark, Sep. 2002, post-deadline paper PD4.3.
- [73] G. Bellotti and S. Bigo, "Cross-Phase Modulation Suppressor for Multi-Span Dispersion-Managed WDM Transmission," in *Proc. Eur. Conf. Optical Commun. (ECOC)*, vol. 1, Nice, France, Sep. 1999, p. 204–205.
- [74] S. Chandrasekhar and A. H. Gnauck, "Performance of MLSE Receiver in a Dispersion-Managed Multispan Experiment at 10.7 Gb/s Under Nonlinear Transmission," *J. Lightwave Technol.*, vol. 18, no. 23, pp. 2448–2450, Dec. 2006.
- [75] P. Poggiolini, G. Bosco, M. Visintin *et al.*, "MLSE-EDC versus Optical Dispersion Compensation in a Single-Channel SPM-limited 800 km Link at 10 Gbit/s," in *Proc. Eur. Conf. Optical Commun. (ECOC)*, Berlin, Germany, Sep. 2007, paper Th9.1.3.
- [76] M. Karlsson and H. Sunnerud, "Effects of Nonlinearities on PMD-induced System Impairments," *J. Lightwave Technol.*, vol. 24, no. 11, p. 4127–4137, Nov. 2006.
- [77] L. F. Mollenauer, J. P. Gordon, and F. Heismann, "Polarization Scattering by Soliton-Soliton Collisions," *Opt. Lett.*, vol. 20, no. 20, pp. 2060–2062, Oct. 1995.
- [78] B. C. Collings and L. Boivin, "Nonlinear Polarization Evolution Induced by Cross-Phase Modulation and its Impact on Transmission Systems," *IEEE Photon. Technol. Lett.*, vol. 12, no. 11, pp. 1582–1584, Nov. 2000.
- [79] R. Stolen and J. Bjorkholm, "Parametric amplification and frequency conversion in optical fibers," *IEEE J. Quantum Electron.*, vol. 18, no. 7, pp. 1062–1072, Jul. 1982.
- [80] H. Onaka, K. Otsuka, H. Miyata, and T. Chikama, "Measuring the Longitudinal Distribution of Four-Wave Mixing Efficiency in Dispersion-Shifted Fibers," *IEEE Photon. Technol. Lett.*, vol. 6, no. 12, pp. 1454–1456, Dec. 1994.

- 
- [81] M. Eiselt, "Limits on WDM systems due to Four-Wave Mixing: A Statistical Approach," *J. Lightwave Technol.*, vol. 17, no. 11, p. 2261–2267, Nov. 1999.
- [82] F. Forghieri, A. H. Gnauck, R. W. Thach *et al.*, "Repeaterless Transmission of eight Channels at 10 Gb/s over 137 km (11 Tb/s-km) of Dispersion-Shifted Fiber using Unequal Channel Spacing," *IEEE Photon. Technol. Lett.*, vol. 6, no. 11, pp. 1374–1376, Nov. 1994.
- [83] F. Forghieri, R. W. Thach, and A. R. Chraplyvy, "WDM Systems with Unequally Spaced Channels," *IEEE Photon. Technol. Lett.*, vol. 13, no. 5, pp. 889–897, May 1995.
- [84] H. Masuda, H. Kawakami, S. Kuwahara *et al.*, "1.28 Tbit/s (32x43 Gbit/s) Field Trial over 528km (6x88 km) DSF using L-band Remotely-Pumped EDF-Distributed Raman Hybrid Inline Amplifiers," *Electron. Lett.*, vol. 39, no. 23, pp. 1668–1670, Nov. 2003.
- [85] I. Shake, K. Takara, S. Kawanishi, and Y. Yamabayashi, "Influence of Inter-Bit Four-Wave Mixing in Optical TDM Transmission," *Electron. Lett.*, vol. 34, no. 16, pp. 1600–1601, Aug. 1998.
- [86] R.-J. Essiambre, B. Mikkelsen, and G. Raybon, "Intra-Channel Cross-Phase Modulation and Four-Wave Mixing in Highspeed TDM Systems," *Electron. Lett.*, vol. 35, no. 18, p. 1576–1578, Sep. 1999.
- [87] P. V. Mamyshev and N. A. Mamysheva, "Pulse-overlapped Dispersion-Managed Data Transmission and Intrachannel Four-Wave Mixing," *Opt. Lett.*, vol. 24, no. 21, p. 1454–1456, Nov. 1999.
- [88] A. Mecozzi, C. B. Clausen, M. Shtaif *et al.*, "Cancellation of Timing and Amplitude Jitter in Symmetric Links using Highly Dispersed Pulses," *IEEE Photon. Technol. Lett.*, vol. 13, no. 5, p. 445–447, May 2001.
- [89] J. P. Gordon and L. F. Mollenauer, "Phase Noise in Photonic Communications Systems Using Linear Amplifiers," *Opt. Lett.*, vol. 15, no. 23, pp. 1351–1353, Dec. 1990.
- [90] H. Kim and A. H. Gnauck, "Experimental Investigation of the Performance Limitation of DPSK Systems Due to Nonlinear Phase Noise," *IEEE Photon. Technol. Lett.*, vol. 15, no. 2, pp. 320–322, Feb. 2003.
- [91] S. L. Jansen, D. van den Borne, C. C. Monsalve *et al.*, "Reduction of Gordon-Mollenauer Phase Noise by Mid-Link Spectral Inversion," *IEEE Photon. Technol. Lett.*, vol. 17, no. 4, pp. 923–925, Jan. 2005.
- [92] S. L. Jansen, S. Calabró, B. Spinnler *et al.*, "Nonlinear Phase Noise Reduction in DPSK Transmission by Optical Phase Conjugation," in *Proc. Optoelectronics Commun. Conf. (OECC)*, Seoul, Korea, Jul. 2005, paper 6B1-3.
- [93] V. S. Grigoryan, M. Shin, P. Devgan *et al.*, "SOA-based Regenerative Amplification of Phase-Noise-Degraded DPSK signals: Dynamic Analysis and Demonstration," *J. Lightwave Technol.*, vol. 24, no. 1, pp. 135–142, Jan. 2006.
- [94] J. Hansryd, J. van Howe, and C. Xu, "Experimental Demonstration of Nonlinear Phase Jitter Compensation in DPSK Modulated Fiber Links," *IEEE Photon. Technol. Lett.*, vol. 17, no. 1, pp. 232–234, Jan. 2005.
- [95] K.-P. Ho and J. M. Kahn, "Electronic Compensation Technique to Mitigate Nonlinear Phase Noise," *J. Lightwave Technol.*, vol. 22, no. 3, pp. 779–783, Mar. 2004.
- [96] C. Xu and X. Liu, "Postnonlinearity Compensation with Data-driven Phase Modulators in Phase-Shift Keying Transmission," *Opt. Lett.*, vol. 27, no. 18, pp. 1619–1621, Sep. 2002.
- [97] P. M. Krummrich, R. E. Neuhauser, and G. Fischer, "Experimental Comparison of Raman Thresholds of Different Transmission Fibre Types," in *Proc. Eur. Conf. Optical Commun. (ECOC)*, vol. 4, Munich, Germany, Sep. 2000, paper, pp. 133–134.
- [98] M. N. Islam, *Raman amplifiers for telecommunications 1*. Springer Verlag, 2004.
- [99] K.-P. Ho, "Statistical Properties of Stimulated Raman Crosstalk in WDM Systems," *J. Lightwave Technol.*, vol. 18, no. 7, pp. 915–921, Jul. 2000.
- [100] A. R. Chraplyvy, "Limitations on Lightwave Communications Imposed by Optical-Fiber Nonlinearities," *J. Lightwave Technol.*, vol. 8, no. 10, pp. 1548–1557, October 1990.
-

## Bibliography

---

- [101] M. N. Islam, *Raman amplifiers for telecommunications 2*. Springer Verlag, 2004.
- [102] B. Huiszoon, R. J. W. Jonker, P. K. van Bennekom *et al.*, “Cost-Effective Up to 40 Gb/s Transmission Performance of 1310 nm Directly Modulated Lasers for Short- to Medium-Range Distances,” *J. Lightwave Technol.*, vol. 23, no. 3, pp. 1116–1125, Mar. 2005.
- [103] U. Troppenz, J. Kreissl, W. Rehbein *et al.*, “40 Gb/s Directly Modulated InGaAsP Passive Feedback Laser,” in *Proc. Eur. Conf. Optical Commun. (ECOC)*, Cannes, France, Sep. 2006, post-deadline paper Th4.5.5.
- [104] Y. Matsui, D. Mahgerefteh, X. Zheng *et al.*, “Chirp-Managed Directly Modulated Laser (CML),” *IEEE Photon. Technol. Lett.*, vol. 18, no. 2, pp. 385–387, Jan. 2006.
- [105] Y. Yu, R. Lewen, S. Irmscher *et al.*, “80-Gb/s ETDM Transmitter with a Traveling-Wave Electroabsorption Modulator,” in *Proc. Eur. Conf. Optical Commun. (ECOC)*, Glasgow, United Kingdom, Sep. 2005, paper OWE1.
- [106] L. Mach, “Über einen Interferenzrefraktor,” *Zeitschr. für Instrumentenkunde*, vol. 12, pp. 89–93, 1892.
- [107] L. Zehnder, “Ein neuer Interferenzrefraktor,” *Zeitschr. für Instrumentenkunde*, vol. 11, pp. 275–285, 1891.
- [108] M. Doi, M. Sugiyama, K. Tanaka, and M. Kawai, “Advanced  $LiNbO_3$  Optical Modulators for Broadband Optical Communications,” *IEEE J. Sel. Topics Quantum Electron.*, vol. 12, no. 4, pp. 745–750, Jul.-Aug. 2006.
- [109] R. A. Griffin, R. G. Walker, and R. I. Johnstone, “Integrated Devices for Advanced Modulation Formats,” in *Proc. IEEE/LEOS Workshop Advanced Modulation Formats*, San Francisco, CA, U.S.A, Jul. 2004, paper FC1.
- [110] S. Akiyama, H. Itoh, T. Takeuchi *et al.*, “Mach–Zehnder Modulator Driven by 1.2 v Single Electrical Signal,” *Electron. Lett.*, vol. 41, no. 1, p. 40–41, Jan. 2005.
- [111] A. H. Gnauck, X. Liu, X. Wei *et al.*, “Comparison of Modulation Formats for 42.7-Gb/s Single-Channel Transmission Through 1980 km of SSMF,” *IEEE Photon. Technol. Lett.*, vol. 16, no. 3, p. 909–911, Mar. 2004.
- [112] W. Idler, A. Klekamp, R. Dischler *et al.*, “System Performance and Tolerances of 43-Gb/s ASK and DPSK Modulation Formats,” in *Proc. Eur. Conf. Optical Commun. (ECOC)*, Rimini, Italy, Sep. 2003, paper Th2.6.3.
- [113] H. Sunnerud, M. Karlsson, and P. A. Andrekson, “A Comparison Between NRZ and RZ Data Formats with Respect to PMD-Induced System Degradation,” *IEEE Photon. Technol. Lett.*, vol. 13, no. 5, pp. 448–450, May 2001.
- [114] A. H. Gnauck, G. Raybon, P. G. Bernasconi *et al.*, “1-Tb/s (6 x 170.6 Gb/s) Transmission over 2000-km NZDF Using OTDM and RZ-DPSK Format,” *IEEE Photon. Technol. Lett.*, vol. 15, no. 11, p. 1618–1620, Nov. 2003.
- [115] K.-P. Ho and C. Lin, “Performance Analysis of Optical Transmission System with Polarization-Mode Dispersion and Forward Error Correction,” *J. Lightwave Technol.*, vol. 9, no. 9, pp. 1288–1290, Sep. 1997.
- [116] W. D. Grover, “Forward Error Correction in Dispersion-Limited Lightwave Systems,” *J. Lightwave Technol.*, vol. 6, no. 5, pp. 643–654, May 1988.
- [117] P. M. Gabla, J. L. Pamart, R. Uhel *et al.*, “401km, 622Mb/s and 357km, 2.488Gb/s IM/DD Repeaterless Transmission Experiments using Erbium-Doped Fiber Amplifiers and Error Correcting Code,” *J. Lightwave Technol.*, vol. 4, no. 10, pp. 1148–1152, Oct. 1992.
- [118] *ITU-T G.975, Forward Error Correction for Submarine Systems*, Oct. 2000.
- [119] *ITU-T G.975.1, Forward Error Correction for High Bit Rate DWDM Submarine Systems*, Feb. 2004.
- [120] T. Mizuoichi, “Recent Progress in Forward Error Correction and its Interplay with Transmission Impairments,” *IEEE J. Sel. Topics Quantum Electron.*, vol. 12, no. 4, pp. 544–554, Jul-Aug. 2006.

- [121] C. Rasmussen, T. Fjelde, J. Bennike *et al.*, “DWDM 40G Transmission over Trans-Pacific Distance (10 000 km) using CSRZ-DPSK, Enhanced FEC, and All-Raman-Amplified 100-km UltraWave Fiber Spans,” *J. Lightwave Technol.*, vol. 22, no. 1, pp. 203–207, Jan. 2004.
- [122] G. Charlet, P. Tran, H. Mardoyan *et al.*, “151x43Gb/s Transmission over 4,080km based on Return-to-Zero Differential Quadrature Phase-shift Keying,” in *Proc. Eur. Conf. Optical Commun. (ECOC)*, Glasgow, United Kingdom, Sep. 2005, post-deadline paper Th4.1.3.
- [123] G. Charlet, E. Corbel, J. Lazaro *et al.*, “Comparison of System Performance at 50, 62.5 and 100 GHz Channel Spacing over Transoceanic Distances at 40 Gbit/s Channel Rate using RZ-DPSK,” *Electron. Lett.*, vol. 41, no. 3, pp. 145–146, Feb. 2005.
- [124] R. J. Mears, L. Reekie, M. Jauncey, and D. N. Payne, “Low-Noise Erbium-Doped Fiber Amplifier Operating at 1.54  $\mu\text{m}$ ,” *Electron. Lett.*, vol. 23, no. 19, pp. 1026–1028, Sep. 1987.
- [125] E. Desurvire, J. R. Simpson, , and P. C. Becker, “High-Gain Erbium-Doped Traveling-Wave Fiber Amplifier,” *Opt. Lett.*, vol. 12, no. 11, pp. 888–890, Nov. 1987.
- [126] E. Desurvire, *Erbium-Doped Fiber Amplifiers*. Wiley Interscience, 1994.
- [127] R. B. Sargent, “Recent Advances in Thin Film Filters,” in *Proc. Optical Fiber Commun. Conf. (OFC)*, Anaheim, CA, U.S.A., Mar. 2004, paper TuD2.
- [128] A. M. Vengsarkar, J. R. Pedrazzani, J. B. Judkins *et al.*, “Long-Period Fiber-Grating-based Gain Equalizers,” *Opt. Lett.*, vol. 21, no. 5, p. 336–338, Mar. 1996.
- [129] L. Tancevski, A. Bononi, and L. A. Rusch, “Output Power and SNR Swings in Cascades of EDFAs for Circuit- and Packet-Switched Optical Networks,” *J. Lightwave Technol.*, vol. 17, no. 5, pp. 733–742, May 1999.
- [130] A. Einstein, “Zur Quantentheorie der Strahlung,” *Physikalische Zeitschrift*, vol. 18, pp. 121–128, 1917.
- [131] M. J. F. Digonnet, *Rare Earth Doped Fiber Lasers and Amplifiers*. New York, NY, U.S.A: Marcel Dekker, 1993.
- [132] M. Karasek, “Optimum Design of Er<sup>3+</sup>-Yb<sup>3+</sup> Codoped Fibers for Large-Signal High-Pump-Power Applications,” *IEEE J. Quantum Electron.*, vol. 33, no. 10, pp. 1699–1705, Oct. 1997.
- [133] M. Laroche, S. Girard, J. K. Sahu *et al.*, “Accurate Efficiency Evaluation of Energy-Transfer Processes in Phosphosilicate Er<sup>3+</sup>-Yb<sup>3+</sup>-Codoped Fibers,” *J. Opt. Soc. Am. B*, vol. 23, no. 2, pp. 195–202, Feb. 2006.
- [134] R. H. Stolen, E. P. Ippen, and A. R. Tynes, “Raman Oscillation in Glass Optical Waveguide,” *Appl. Phys. Lett.*, vol. 20, no. 2, pp. 62–64, Jan. 1972.
- [135] J. Hegarty, N. A. Olsson, and L. Goldner, “CW Pumped Raman Pre-amplifier in a 45 km-Long Fibre Transmission System Operating at 1.15 $\mu\text{m}$  and 1Gbit/s,” *Electron. Lett.*, vol. 21, no. 7, pp. 290–292, Mar. 1985.
- [136] T. N. Nielsen, A. J. Stentz, K. Rottwitt *et al.*, “3.28-Tb/s Transmission over 3 x 100 km of Nonzero-Dispersion Fiber using Dual C- and L-band Distributed Raman Amplification,” *IEEE Photon. Technol. Lett.*, vol. 12, no. 8, pp. 1079–1081, Aug. 2000.
- [137] B. Bristiel, S. Jiang, P. Gallion, and E. Pincemin, “New Model of Noise Figure and RIN Transfer in Fiber Raman Amplifiers,” *IEEE Photon. Technol. Lett.*, vol. 18, no. 8, pp. 980–982, Apr. 2006.
- [138] S. Namiki, K. Seo, N. Tsukiji, and S. Shikii, “Challenges of Raman Amplification,” *Proc. IEEE*, vol. 94, no. 5, p. 1024–1035, May 2006.
- [139] S. Namiki and Y. Emori, “Ultrabroad-Band Raman Amplifiers Pumped and Gain-Equalized by Wavelength-Division-Multiplexed High-Power Laser Diodes,” *IEEE J. Sel. Topics Quantum Electron.*, vol. 7, no. 1, pp. 3–16, Jan-Feb. 2001.
- [140] P. M. Krummrich, R. E. Neuhauser, and C. Glingener, “Bandwidth Limitations of Broadband Distributed Raman Fiber Amplifiers for WDM Systems,” in *Proc. Optical Fiber Commun. Conf. (OFC)*, Anaheim, CA, U.S.A., Mar. 2001, paper MI3.

## Bibliography

---

- [141] *IEC Tech. rep. 61292-4, Maximum Permissible Optical Power for the Damage-Free and Safe Use of Optical Amplifiers Including Raman Amplifiers*, Aug. 2004.
- [142] *ITU-T G.664, Optical Safety Procedures and Requirements for Optical Transport Systems*, Mar. 2006.
- [143] L. Gruner-Nielsen, M. Wandel, P. Kristensen *et al.*, “Dispersion-Compensating Fibers,” *J. Lightwave Technol.*, vol. 23, no. 11, pp. 3566–3579, Nov. 2005.
- [144] G. P. Agrawal, *Lightwave Technology*, 1st ed. John Wiley & Sons, 2005.
- [145] B. Bakhshi, M. Manna, G. Mohs *et al.*, “First Dispersion-Flattened Transpacific Undersea System: from Design to Terabit/s Field Trial,” *J. Lightwave Technol.*, vol. 22, no. 1, pp. 233–241, Jan. 2004.
- [146] R. I. Killey, V. Mikhailov, S. Appathurai, and P. Bayvel, “Investigation of Nonlinear Distortion in 40-Gb/s Transmission with Higher Order Mode Fiber Dispersion Compensators,” *J. Lightwave Technol.*, vol. 20, no. 12, pp. 2282–2289, Dec. 2002.
- [147] C. Lin, H. Kogelnik, and L. G. Cohen, “Optical-Pulse Equalization of Low-Dispersion Transmission in Single-Mode Fibers in the 1.3-1.7- $\mu$ m Spectral Region,” *Opt. Lett.*, vol. 5, no. 11, pp. 476–478, Nov. 1980.
- [148] J. M. Dugan, A. J. Price, M. Ramadan *et al.*, “All-Optical, Fiber-based 1550 nm Dispersion Compensation in a 10 Gb/s, 150 km Transmission Experiment over 1310 nm Optimized Fiber,” in *Proc. Optical Fiber Commun. Conf. (OFC)*, San Jose, CA, U.S.A, Feb. 1992, post-deadline paper PD14.
- [149] J. Chesnoy, P. Nouchi, J. Y. Boniort *et al.*, “Optimum Dispersion Compensating Fiber: Birefringence and PMD Simulation and Fiber Process Improvement,” in *Proc. Int. Wire and Cable Symp. (IWCS)*, Philadelphia, PA, U.S.A, Nov. 1995, paper PD14.
- [150] M. J. Hamp, J. Wright, M. Hubbard, and B. Brimacombe, “Investigation into the Temperature Dependence of Chromatic Dispersion in Optical Fiber,” *IEEE Photon. Technol. Lett.*, vol. 14, no. 11, pp. 1524–1526, Nov. 2002.
- [151] R. Lachance, M. Morin, and Y. Painchaud, “Group Delay Ripple in Fibre Bragg Grating Tunable Dispersion Compensators,” *Electron. Lett.*, vol. 38, no. 24, pp. 1505–1507, Nov. 2002.
- [152] H. Bissessur, C. Bastide, and A. Hugbart, “Performance Characterization of Components with Phase Ripple for Different 40Gb/s Formats,” in *Proc. Optical Fiber Commun. Conf. (OFC)*, Anaheim, CA, U.S.A, Feb. 2006, paper OFN4.
- [153] D. J. Moss, S. McLaughlin, G. Randall *et al.*, “Multichannel Tunable Dispersion Compensation using All-Pass Multicavity Etalons,” in *Proc. Optical Fiber Commun. Conf. (OFC)*, Anaheim, CA, U.S.A., Feb. 2002, paper TuT2.
- [154] T. Georges, “Extended Path-Averaged Soliton Regime in Highly Dispersive Fibers,” *Opt. Lett.*, vol. 22, no. 10, p. 679–681, May 1997.
- [155] R. I. Killey, H. J. Thiele, V. Mikhailov, and P. Bayvel, “Reduction of Intrachannel Nonlinear Distortion in 40-Gb/s-based WDM Transmission over Standard Fiber,” *IEEE Photon. Technol. Lett.*, vol. 12, no. 12, pp. 1624–1626, Dec. 2000.
- [156] A. G. Striegler and B. Schmauss, “Compensation of intrachannel effects in symmetric dispersion-managed transmission systems,” *J. Lightwave Technol.*, vol. 22, no. 8, pp. 1877–1882, Aug. 2004.
- [157] N. Kikuchi, K. Sekine, , and S. Sasaki, “Analysis of Cross-Phase Modulation (XPM) Effect on WDM Transmission Performance,” *Electron. Lett.*, vol. 33, no. 8, p. 653–654, Apr. 1997.
- [158] M. Shtaif, “Analytical Description of Cross-Phase Modulation in Dispersive Optical Fibers,” *Opt. Lett.*, vol. 23, no. 15, p. 1191–1193, Aug. 1998.
- [159] A. V. T. Cartaxo, “Cross-Phase Modulation in Intensity Modulation-Direct Detection WDM Systems with Multiple Optical Amplifiers and Dispersion Compensators,” *J. Lightwave Technol.*, vol. 17, no. 2, p. 178–190, Feb. 1999.



- [160] A. Sano, Y. Miyamoto, S. Kuwahara, and H. Toba, "A 40-Gb/s/ch WDM Transmission with SPM/XPM Suppression Through Prechirping and Dispersion Management," *J. Lightwave Technol.*, vol. 18, no. 11, pp. 1519–1527, Nov. 2000.
- [161] T.-K. Chiang, N. Kagi, T. K. Fong *et al.*, "Cross-Phase Modulation in Dispersive Fibers: Theoretical and Experimental Investigation of the Impact of Modulation Frequency," *IEEE Photon. Technol. Lett.*, vol. 6, no. 6, p. 733–736, Jun. 1994.
- [162] S. Banerjee, A. Agarwal, D. F. Grosz *et al.*, "Doubly Periodic Dispersion Maps for 10 and 40 Gbit/s Ultra-Long-Haul Transmission," *Electron. Lett.*, vol. 40, no. 20, pp. 1287–1288, Sep. 2004.
- [163] S. Chandrasekhar, C. R. Doerr, and L. L. Buhl, "Demonstration of 100 percent precompensated DWDM transmission over 1280 km of SSMF with no inline dispersion compensation using interconnected recirculating loops," *IEEE Photon. Technol. Lett.*, vol. 18, no. 1, pp. 256–258, Jan. 2006.
- [164] M. Vaa, E. Golovchenko, L. Rahman *et al.*, "Dense WDM RZ-DPSK Transmission over Transoceanic Distances without Use of Periodic Dispersion Management," in *Proc. Eur. Conf. Optical Commun. (ECOC)*, Stockholm, Sweden, Sep. 2004, post-deadline paper Th4.4.4.
- [165] P. B. Hansen, L. Eskildsen, A. J. Stentz *et al.*, "Rayleigh scattering limitations in distributed Raman pre-amplifiers," *IEEE Photon. Technol. Lett.*, vol. 10, no. 1, p. 159–161, Jan. 1998.
- [166] P. Parolari, L. Marazzi, L. Bernardini, and M. Martinelli, "Double Rayleigh scattering noise in lumped and distributed Raman amplifiers," *J. Lightwave Technol.*, vol. 21, no. 10, pp. 2224–2228, Oct. 2003.
- [167] K. O. Hill and G. Meltz, "Fiber Bragg Grating Technology Fundamentals and Overview," *J. Lightwave Technol.*, vol. 15, no. 8, pp. 1263–1276, Aug. 1997.
- [168] H. S. Fewes, M. F. Stephens, A. Straw *et al.*, "Experimental Comparison of Fibre and Grating-based Dispersion Compensation Schemes for 40 channel 10Gb/s DWDM Systems," in *Proc. Eur. Conf. Optical Commun. (ECOC)*, Cannes, France, Sep. 2006, paper Th3.2.5.
- [169] K. O. Hill, Y. Fujii, D. C. Johnson, and B. S. Kawasaki, "Photosensitivity in Optical Fiber Waveguides: Application to Reflection Filter Fabrication," *Appl. Phys. Lett.*, vol. 32, no. 10, pp. 647–649, May 1978.
- [170] Y. Painchaud, A. Mailoux, H. Chotard *et al.*, "Multichannel Fiber Bragg Gratings for Dispersion and Slope Compensation," in *Proc. Optical Fiber Commun. Conf. (OFC)*, Anaheim, CA, U.S.A., Feb. 2002, paper THAA5.
- [171] H. Li, M. Li, Y. Sheng, and J. E. Rothenberg, "Advances in the Design and Fabrication of High-Channel-Count Fiber Bragg Gratings," *IEEE Photon. Technol. Lett.*, vol. 25, no. 9, pp. 2739–2750, Sep. 2007.
- [172] C. Scheerer, C. Glingener, G. Fischer *et al.*, "Influence of Filter Group Delay Ripples on System Performance," in *Proc. Eur. Conf. Optical Commun. (ECOC)*, Nice, France, Sep. 1999, paper I-410.
- [173] X. Fan, D. Labrake, and J. Brennan, "Chirped Fiber Gratings Characterization with Phase Ripples," in *Proc. Optical Fiber Commun. Conf. (OFC)*, Atlanta, GA, U.S.A., Mar. 2003, paper FC2.
- [174] Y. Painchaud, M. Lapointe, and M. Guy, "Slope-matched tunable dispersion compensation over the full C-band based on fiber Bragg gratings," in *Proc. Eur. Conf. Optical Commun. (ECOC)*, Stockholm, Sweden, Sep. 2004, paper we3.3.4.
- [175] Y. Painchaud, C. Paquet, M. Poulin *et al.*, "Low-Penalty Cascade of Low-Ripple FBG-based Dispersion Compensators," in *Proc. Eur. Conf. Optical Commun. (ECOC)*, Cannes, France, Sep. 2006, post-deadline paper Th4.2.7.
- [176] V. Veljanovski, D. van den Borne, W. Schairer, and N. Hanik, "Equalisation of Fibre Bragg Gratings' Group Delay Ripple by means of Maximum Likelihood Sequence Estimation," in *Proc. IEEE/LEOS Annual Meeting*, Montreal, Quebec, Canada, Nov. 2006, paper ThH4.
- [177] X. Liu, C. R. Giles, X. Wei *et al.*, "Demonstration of Broad-Band PMD Mitigation in the Presence of PDL Through Distributed Fast Polarization Scrambling and Forward-Error Correction," *IEEE Photon. Technol. Lett.*, vol. 17, no. 5, pp. 1109–1111, May 2005.

## Bibliography

---

- [178] A. Klekamp, B. Junginger, and H. Bülow, "Experimental PMD Mitigation for 43-Gb/s DPSK by Distributed Polarisation Scrambling over 4 spans SMF Fibre," in *Proc. Eur. Conf. Optical Commun. (ECOC)*, Cannes, France, Sep. 2006, post-deadline paper Th4.3.6.
- [179] T. Ono, S. Yamazaki, H. Shimizu, and H. Emura, "Polarization Control Method for Suppressing Polarization Mode Dispersion in Optical Transmission Systems," *J. Lightwave Technol.*, vol. 12, no. 5, pp. 891–898, May 1994.
- [180] F. Heismann, D. Fishman, and D. Wilson, "Automatic Compensation of First Order Polarization Mode Dispersion in a 10Gb/s Transmission System," in *Proc. Eur. Conf. Optical Commun. (ECOC)*, vol. 1, Madrid, Spain, Sep. 1998, pp. 529 – 530.
- [181] J. Patscher and R. Eckhardt, "Component for Second-Order Compensation of Polarization-Mode Dispersion," *Electron. Lett.*, vol. 33, no. 13, p. 1157–1159, Jun. 1997.
- [182] M. Bohn, W. Rosenkranz, and P. M. Krummrich, "Adaptive distortion compensation with integrated optical finite impulse response filters in high bitrate optical communication systems," *IEEE J. Sel. Topics Quantum Electron.*, vol. 10, no. 2, pp. 273–280, Mar.-Apr. 2004.
- [183] H. Sunnerud, M. Karlsson, C. Xie, and P. A. Andrekson, "Polarization-Mode Dispersion in High-Speed Fiber-Optic Transmission Systems," *J. Lightwave Technol.*, vol. 20, no. 12, pp. 2204–2219, Dec. 2002.
- [184] H. Bülow, "PMD Mitigation Techniques and Their Effectiveness in Installed Fiber," in *Proc. Optical Fiber Commun. Conf. (OFC)*, Baltimore, MD, U.S.A., Mar. 2000, paper ThH1.
- [185] D. Waddy, P. Lu, L. Chen, and X. Bao, "Fast State of Polarization Changes in Aerial Fiber under Different Climatic Conditions," *IEEE Photon. Technol. Lett.*, vol. 13, no. 9, pp. 1035–1037, Sep. 2001.
- [186] J. Wuttke, P. M. Krummrich, and J. Rösch, "Polarization Oscillations in Aerial Fiber Caused by Wind and Power-Line Current," *IEEE Photon. Technol. Lett.*, vol. 15, no. 6, pp. 882–884, Jun. 2003.
- [187] P. M. Krummrich, E.-D. Schmidt, W. Weiershausen, and A. Mattheus, "Field Trail Results on Statistics of Fast Polarization Changes in Long Haul WDM Transmission Systems," in *Proc. Optical Fiber Commun. Conf. (OFC)*, Anaheim, CA, U.S.A., Feb. 2005, paper OThT6.
- [188] E. B. Basch, R. Egorov, S. Gringeri, and S. Elby, "Architectural Tradeoffs for Reconfigurable Dense Wavelength-Division Multiplexing Systems," *IEEE J. Sel. Topics Quantum Electron.*, vol. 12, no. 4, pp. 615–626, Jul.-Aug. 2006.
- [189] A. R. Ranalli, B. A. Scott, and J. P. Kondis, "Liquid Crystal-based Wavelength Selectable Cross-Connect," in *Proc. Eur. Conf. Optical Commun. (ECOC)*, vol. 1, Nice, France, Sep. 1999, pp. 68–69.
- [190] L. Y. Lin, E. L. Goldstein, and R. W. Tkach, "Free-space Micromachined Optical Switches for Optical Networking," *IEEE J. Sel. Topics Quantum Electron.*, vol. 5, no. 1, pp. 4–9, Jan.-Feb. 1999.
- [191] A. Yariv, D. Fekete, and D. M. Pepper, "Compensation for Channel Dispersion by Nonlinear Optical Phase Conjugation," *Opt. Lett.*, vol. 4, no. 2, pp. 52–54, Feb. 1979.
- [192] S. Watanabe, G. Ishikawa, T. Naito, and T. Chikama, "Generation of Optical Phase-Conjugate Waves and Compensation for Pulse Shapes Distorsion in a Single Mode Fiber," *J. Lightwave Technol.*, vol. 12, no. 12, pp. 2139–2146, Dec. 1994.
- [193] C. Lorattanasane and K. Kikuchi, "Design Theory of Long-Distance Optical Transmission Systems using Midway Optical Phase Conjugation," *J. Lightwave Technol.*, vol. 15, no. 6, pp. 948–955, Jun. 1997.
- [194] A. Chowdhury, G. Raybon, R.-J. Essiambre, and C. R. Doerr, "Optical Phase Conjugation in a WDM CSRZ Pseudo-Linear 40 Gb/s System for 4,800 km Transmission," in *Proc. Eur. Conf. Optical Commun. (ECOC)*, Stockholm, Sweden, Sep. 2004, post-deadline paper Th4.5.6.
- [195] A. Chowdhury, G. Raybon, R.-J. Essiambre *et al.*, "Compensation of Intrachannel Nonlinearities in 40-Gb/s Pseudolinear Systems using Optical-Phase Conjugation," *J. Lightwave Technol.*, vol. 23, no. 1, pp. 172–177, Jan. 2005.

- [196] S. Watanabe, S. Kaneko, G. Ishikawa *et al.*, “20-Gb/s Fiber Transmission Experiment over 3000-km Waveform Precompensation using Fiber Compensator and Optical Phase Conjugator,” in *Proc. Integr. Optics and Optical Fiber Commun. Conf. (IOCC)*, Hong Kong, Jul. 1995, post-deadline paper PD2-6.
- [197] U. Feiste, R. Ludwig, E. Dietrich *et al.*, “40 Gbit/s Transmission over 434 km Standard-Fiber using Polarisation Independent Mid-Span Spectral Inversion,” *Electron. Lett.*, vol. 34, no. 21, pp. 2044–2045, Oct. 1998.
- [198] S. Ayotte, S. Xu, H. Rong *et al.*, “Dispersion Compensation by Optical Phase Conjugation in Silicon Waveguide,” *Electron. Lett.*, vol. 43, no. 19, pp. 1037–1039, Sep. 2007.
- [199] S. J. B. Yoo, C. Caneau, R. Bhat, and M. A. Koza, “Wavelength Conversion by Quasi-Phase Matched Difference Frequency Generation in AlGaAs Waveguides,” in *Proc. Optical Fiber Commun. Conf. (OFC)*, San Diego, CA, U.S.A., Feb. 1995, post-deadline paper PD-13.
- [200] C. Q. Xu, H. Okayama, and M. Kawahara, “1.5  $\mu\text{m}$  Band Efficient Broadband Wavelength Conversion by Difference Frequency Generation in a Periodically Domain-Inverted LiNbO<sub>3</sub> Channel Waveguide,” *Appl. Phys. Lett.*, vol. 63, no. 26, pp. 3559–3561, Dec. 1993.
- [201] M. H. Chou, J. Hauden, M. A. Arbore, and M. M. Fejer, “1.5- $\mu\text{m}$ -Band Wavelength Conversion based on Difference-Frequency Generation in LiNbO<sub>3</sub> Waveguides with Integrated Coupling Structures,” *Opt. Lett.*, vol. 23, no. 13, pp. 1004–1006, Jul. 1998.
- [202] C. Q. Xu, H. Okayama, and M. Kawahara, “Wavelength Conversions Between the Two Silica Fibre Loss Windows at 1.31 and 1.55 $\mu\text{m}$  using Difference Frequency Generation,” *Electron. Lett.*, vol. 30, no. 25, pp. 2168–2169, Dec. 2004.
- [203] S. L. Jansen, G. D. Khoe, H. de Waardt *et al.*, “Mixed Data Rate and Format Transmission (40Gbit/s NRZ, 40Gbit/s Duobinary, 10Gbit/s NRZ) using Mid-Link Spectral Inversion,” *Opt. Lett.*, vol. 29, no. 20, pp. 2348–2350, Oct. 2004.
- [204] G. Schreiber, H. Suche, Y. L. Lee *et al.*, “Efficient Cascaded Difference Frequency Conversion in Periodically Poled Ti:LiNbO<sub>3</sub> Waveguides using Pulsed and CW Pumping,” *Appl. Phys. B*, vol. 73, no. 5-6, pp. 501–504, Oct. 2001.
- [205] J. Yamawaku, H. Takara, T. Ohara *et al.*, “Simultaneous 25GHz-spaced DWDM Wavelength Conversion of 1.03 Tbit/s (103x10Gbit/s) Signals in PPLN Waveguide,” *Electron. Lett.*, vol. 39, no. 21, pp. 1144–1145, Oct. 2003.
- [206] C. Q. Xu, H. Okayama, and Y. Ogawa, “Photorefractive Damage of LiNbO<sub>3</sub> Quasiphase Matched Wavelength Converters,” *J. Appl. Phys.*, vol. 87, no. 7, pp. 3203–3208, Apr. 2000.
- [207] Y. Furukawa, K. Kitamura, S. Takekawa *et al.*, “Stoichiometric MgLiNbO<sub>3</sub> as an Effective Material for Nonlinear Optics,” *Opt. Lett.*, vol. 23, no. 24, pp. 1892–1894, Dec. 1998.
- [208] I. Brener, M. H. Chou, E. Chaban *et al.*, “Polarization-Insensitive Parametric Wavelength Converter based on Cascaded Nonlinearities in LiNbO<sub>3</sub> Waveguides,” in *Proc. Optical Fiber Commun. Conf. (OFC)*, Baltimore, MA, U.S.A., Mar. 2000, paper TuF1-1.
- [209] D. Caccioli, A. Paoletti, A. Schiffrini *et al.*, “Field Demonstration of In-Line All-Optical Wavelength Conversion in a WDM Dispersion Managed 40-Gbit/s Link,” *IEEE J. Sel. Topics Quantum Electron.*, vol. 10, no. 2, pp. 356–362, Mar-Apr. 2004.
- [210] S. L. Jansen, D. van den Borne, P. M. Krummrich *et al.*, “Transmission of 42.8-Gbit/s RZ-DQPSK over 42x94.5-km SSMF Spans using Optical Phase Conjugation and EDFA only Amplification,” in *Proc. Eur. Conf. Optical Commun. (ECOC)*, Cannes, France, Sep. 2006, paper Mo3.2.3.
- [211] S. Watanabe, S. Takeda, G. Ishikawa *et al.*, “Simultaneous Wavelength Conversion and Optical Phase Conjugation of 200 Gb/s (5x40 Gb/s) WDM Signal using a Highly Nonlinear Fiber Four-wave Mixer,” in *Proc. Eur. Conf. Optical Commun. (ECOC)*, London, United Kingdom, Sep. 1997, post-deadline paper TH3A.

## Bibliography

---

- [212] X. Shu, K. Chisholm, and K. Sugden, "Design and Realization of Dispersion Slope Compensators using Distributed Gires-Tournois Etalons," *IEEE Photon. Technol. Lett.*, vol. 16, no. 4, pp. 1092–1094, Apr. 2004.
- [213] K. Kikuchi, C. Lorattanasane, F. Futami, and S. Kaneko, "Observation of Quasi-Phase Matched Four-Wave Mixing Assisted by Periodic Power Variation in a Long-Distance Optical Amplifier Chain," *IEEE Photon. Technol. Lett.*, vol. 7, no. 11, p. 1378–1380, Nov. 1995.
- [214] X. Tang and Z. Wu, "Nonlinear Noise Amplification in Optical Transmission Systems with Optical Phase Conjugation," *J. Lightwave Technol.*, vol. 23, no. 5, pp. 1866–1873, May 2005.
- [215] —, "Suppressing Modulation Instability in Midway Optical Phase Conjugation Systems by using Dispersion Compensation," *IEEE Photon. Technol. Lett.*, vol. 17, no. 4, pp. 926–928, Apr. 2005.
- [216] S. L. Jansen, S. Spälter, G.-D. Khoe *et al.*, "16x40Gbit/s over 800km of SSMF using Mid-Link Spectral Inversion," *IEEE Photon. Technol. Lett.*, vol. 16, no. 7, pp. 1763–1765, Jul. 2004.
- [217] C. J. McKinstrie, S. Radic, and C. Xie, "Reduction of Soliton Phase Jitter by In-Line Phase Conjugation," *Opt. Lett.*, vol. 28, no. 17, pp. 1519–1521, Sep. 2003.
- [218] A. Hirano, Y. Miyamoto, K. Yonenaga *et al.*, "40 Gbit/s L-band Transmission Experiment Using SPM-tolerant Carrier-Suppressed RZ format," *Electron. Lett.*, vol. 35, no. 25, p. 2213–2215, Dec. 1999.
- [219] E. A. Golovchenko, N. S. Bergano, C. R. Davidson, and A. N. Pilipetskii, "Modeling vs. Experiments of 16 x 10 Gbit/s WDM Chirped RZ Pulse Transmission over 7500 km," in *Proc. Optical Fiber Commun. Conf. (OFC)*, San Diego, CA, U.S.A., Feb. 1999, paper ThQ3.
- [220] B. Bakhshi, M. Vaa, E. A. Golovchenko *et al.*, "Comparison of CRZ, RZ and NRZ Modulation Formats in a 64 x 12.3 Gb/s WDM Transmission Experiment over 9000 km," in *Proc. Optical Fiber Commun. Conf. (OFC)*, Anaheim, CA, U.S.A., Mar. 2001, paper WF4.
- [221] R. A. Griffin, R. G. Walker, R. I. Johnstone *et al.*, "Integrated 10 Gb/s Chirped Return-To-Zero Transmitter Using GaAs-AlGaAs Modulators," in *Proc. Optical Fiber Commun. Conf. (OFC)*, Anaheim, CA, U.S.A., Mar. 2001, post-deadline paper PD15.
- [222] D. Penninckx, M. Chbat, L. Pierre, and J.-P. Thiery, "The Phase-Shaped Binary Transmission (PSBT): A New Technique to Transmit Far Beyond the Chromatic Dispersion Limit," *IEEE Photon. Technol. Lett.*, vol. 9, no. 2, pp. 259–261, Feb. 1997.
- [223] A. Lender, "The Duobinary Technique for High Speed Data Transmission," *IEEE Trans. on Communications and Electronics*, vol. 82, pp. 214–218, May 1963.
- [224] —, "Correlative Digital Communication Techniques," *IEEE Trans. on Communication Technology*, vol. 12, no. 4, pp. 128–135, Dec. 1964.
- [225] M. J. O'Mahony, "Duobinary Transmission with p-i-n F.E.T. Optical Receivers," *Electron. Lett.*, vol. 16, no. 19, pp. 752–753, Sep. 1980.
- [226] S. Walklin and J. Conradi, "On the Relationship Between Chromatic Dispersion and Transmitter Filter Response in Duobinary Optical Communication Systems," *Electron. Lett.*, vol. 9, no. 7, pp. 1005–1007, Jul. 1997.
- [227] A. J. Price and N. L. Mercier, "Reduced Bandwidth Optical Digital Intensity Modulation with Improved Chromatic Dispersion Tolerance," *Electron. Lett.*, vol. 31, no. 1, pp. 58–59, Jan. 1995.
- [228] K. Yonenaga, S. Kuwano, S. Norimatsu, and N. Shibata, "Optical Duobinary Transmission System with no Receiver Sensitivity Degradation," *Electron. Lett.*, vol. 31, no. 4, pp. 302–304, Feb. 1995.
- [229] W. Kaiser, A. Ehrhardt, W. Rosenkranz, and N. Hanik, "Field Trail of Optical Duobinary Transmission over 1720 km at 10Gb/s," in *Proc. Eur. Conf. Optical Commun. (ECOC)*, Copenhagen, Denmark, Sep. 2002, paper P3.3.
- [230] H. Kim, G. Lee, H. Lee *et al.*, "On the Use of 2.5-Gb/s Mach-Zehnder Modulators to Generate 10-Gb/s Optical Duobinary Signals," *IEEE Photon. Technol. Lett.*, vol. 16, no. 11, p. 2577–2579, Nov. 2004.

- 
- [231] D. M. Gill, A. H. Gnauck, X. Liu *et al.*, “42.7-Gb/s Cost-Effective Duobinary Optical Transmitter Using a Commercial 10-Gb/s Mach–Zehnder Modulator With Optical Filtering,” *IEEE Photon. Technol. Lett.*, vol. 17, no. 4, pp. 917–919, Apr. 2005.
- [232] H. Kim and C. X. Yu, “Optical Duobinary Transmission System Featuring Improved Receiver Sensitivity and Reduced Optical Bandwidth,” *IEEE Photon. Technol. Lett.*, vol. 14, no. 8, p. 1205–1207, Aug. 2002.
- [233] I. Lyubomirsky and B. Pitchumani, “Impact of Optical Filtering on Duobinary Transmission,” *IEEE Photon. Technol. Lett.*, vol. 16, no. 8, pp. 1969–1971, Aug. 2004.
- [234] I. Lyubomirsky and C. Chien, “Experimental Demonstration of a Theoretically Optimum Optical Duobinary Transmission System,” in *Proc. Optical Fiber Commun. Conf. (OFC)*, Anaheim, CA, U.S.A., Feb. 2005, paper OME53.
- [235] —, “Optical Duobinary Spectral Efficiency versus Transmission Performance: Is There a Tradeoff?” in *Proc. Conf. Lasers and Electro-Optics (CLEO 2005)*, Baltimore, MD, U.S.A., May 2005, paper JThE72.
- [236] G. Bosco, A. Carena, V. Curri *et al.*, “Quantum Limit of Direct-Detection Receivers Using Duobinary Transmission,” *IEEE Photon. Technol. Lett.*, vol. 15, no. 1, pp. 102–104, Jan. 2003.
- [237] C. Xie, L. Möller, and R. Ryf, “Improvement of Optical NRZ- and RZ-Duobinary Transmission Systems With Narrow Bandwidth Optical Filters,” *IEEE Photon. Technol. Lett.*, vol. 16, no. 9, p. 2162–2164, Sep. 2004.
- [238] P. M. Krummrich and M. Bohn, “A novel, Easy to Use Emulator for Deterministic Generation of Pure First and Second Order PMD,” in *Proc. Optical Fiber Commun. Conf. (OFC)*, Anaheim, CA, U.S.A., Mar. 2007, paper OMH3.
- [239] W. Kaiser, T. Wuth, M. Wichers, and W. Rosenkranz, “Reduced Complexity Optical Duobinary 10-Gb/s Transmitter Setup Resulting in an Increased Transmission Distance,” *IEEE Photon. Technol. Lett.*, vol. 13, no. 8, pp. 884–886, Aug. 2001.
- [240] G. Charlet, J.-C. Antona, S. Lanne *et al.*, “From 2,100 km to 2,700 km Distance Using Phase-Shaped Binary Transmission at 6.3 Tbit/s Capacity,” in *Proc. Optical Fiber Commun. Conf. (OFC)*, Atlanta, GA, U.S.A., Mar. 2003, paper WE3.
- [241] G. Charlet, S. Lanne, L. Pierre *et al.*, “Cost-optimized 6.3-Tbit/s Capacity Terrestrial Link over 17×100 km Using Phase-Shaped Binary Transmission in a Conventional All-EDFA SMF-based System,” in *Proc. Optical Fiber Commun. Conf. (OFC)*, Atlanta, GA, U.S.A., Mar. 2003, post-deadline paper PD25.
- [242] M. Birk, C. Skolnick, B. Curto *et al.*, “Field Trial of a 40 Gbit/s PSBT Channel Upgrade to an Installed 1700 km 10 Gbit/s System,” in *Proc. Optical Fiber Commun. Conf. (OFC)*, Anaheim, CA, U.S.A., Feb. 2005, paper OTuH3.
- [243] T. Ono, Y. Yano, K. Fukuchi *et al.*, “Characteristics of Optical Duobinary Signals in Terabit/s Capacity, High-Spectral Efficiency WDM Systems,” *J. Lightwave Technol.*, vol. 16, no. 5, pp. 788–797, May 1998.
- [244] E. Forestieri and G. Prati, “Novel Optical Line Codes Tolerant to Fiber Chromatic Dispersion,” *J. Lightwave Technol.*, vol. 19, no. 11, pp. 1675–1684, Nov. 2001.
- [245] S. Walklin and J. Conradi, “Multilevel Signaling for Increasing the Reach of 10 Gb/s Lightwave Systems,” *J. Lightwave Technol.*, vol. 17, no. 11, pp. 2235–2248, Nov. 1999.
- [246] R. S. Vodhanel, “5 Gbit/s direct optical DPSK modulation of a 1530-nm DFB laser,” *IEEE Photon. Technol. Lett.*, vol. 1, no. 8, pp. 218–220, Aug. 1989.
- [247] D. Penninckx, H. Bissessur, P. Brindle *et al.*, “Optical Differential Phase Shift Keying (DPSK) Direct Detection Considered as a Duobinary Signal,” in *Proc. Eur. Conf. Optical Commun. (ECOC)*, Amsterdam, The Netherlands, Sep. 2001, paper We.P.40.
- [248] X. Wei, X. Lui, S. Chandrasekhar *et al.*, “40 Gb/s Duobinary and Modified Duobinary Transmitter Based on an Optical Delay Interferometer,” in *Proc. Eur. Conf. Optical Commun. (ECOC)*, Copenhagen, Denmark, Sep. 2002, paper 9.6.3.
-

## Bibliography

---

- [249] F. Seguin and F. Gonthier, "Tuneable All-Fiber Delay-Line Interferometer for DPSK Demodulation," in *Proc. Optical Fiber Commun. Conf. (OFC)*, Anaheim, CA, U.S.A., Mar. 2005, paper OFL5.
- [250] L. Christen, Y. K. Lizé, S. Nuccio *et al.*, "Fiber Bragg Grating Balanced DPSK Demodulation," in *Proc. IEEE/LEOS Annual Meeting*, Montreal, QC, Canada, Nov. 2006, paper WP2.
- [251] J. Hsieh, C. Ai, V. Chien *et al.*, "Athermal Demodulator for 42.7-Gb/s DPSK Signals," in *Proc. Eur. Conf. Optical Commun. (ECOC)*, Glasgow, United Kingdom, Sep. 2005, paper Th1.5.6.
- [252] A. H. Gnauck, X. Liu, S. Chandrasekhar, and X. Wei, "Optical Duobinary Format From Demodulation of DPSK Using Athermal Delay Interferometer," *IEEE Photon. Technol. Lett.*, vol. 18, no. 4, pp. 637–639, Feb. 2006.
- [253] O. K. Tonguz and R. E. Wagner, "Equivalence between Preamplified Direct Detection and Hetrodyme Receivers," *IEEE Photon. Technol. Lett.*, vol. 3, no. 9, pp. 835–837, Sep. 1991.
- [254] W. A. Atia and R. S. Bondurant, "Demonstration of Return-to-Zero Signaling in both OOK and DPSK formats to Improve Receiver Sensitivity in an Optical Preamplified Receiver," in *Proc. IEEE/LEOS Annual Meeting*, San Francisco, CA, U.S.A., Nov. 1999, paper TuM3.
- [255] J. H. Sinsky, A. Ademiecki, A. H. Gnauck *et al.*, "A 42.7-Gb/s Integrated Balanced Optical Front End with Record Sensitivity," in *Proc. Optical Fiber Commun. Conf. (OFC)*, Atlanta, GA, U.S.A., Feb. 2003, post-deadline paper PD39.
- [256] M. Salsi, J. Renaudier, G. Charlet *et al.*, "Investigation of Single-Channel Nonlinear Impairments on 40Gb/s Coherent Polarization Division Multiplexed QPSK in Dispersion-Managed or Digitally Post Compensated Systems," in *Proc. Eur. Conf. Optical Commun. (ECOC)*, Berlin, Germany, Sep. 2007, paper Th10.4.2.
- [257] P. J. Winzer and H. Kim, "Degradations in Balanced DPSK Receivers," *IEEE Photon. Technol. Lett.*, vol. 15, no. 9, p. 1282–1284, Sep. 2003.
- [258] G. Bosco and P. Poggiolini, "The Impact of Receiver Imperfections on the Performance of Optical Direct-Detection DPSK," *J. Lightwave Technol.*, vol. 23, no. 2, pp. 842–848, Feb. 2005.
- [259] H. Kim and P. J. Winzer, "Robustness to Laser Frequency Offset in Direct-Detection DPSK and DQPSK Systems," *J. Lightwave Technol.*, vol. 21, no. 9, pp. 1887–1891, Sep. 2003.
- [260] H. C. Ji, P. K. Park, H. Kim *et al.*, "A Novel Frequency-Offset Monitoring Technique for Direct-Detection DPSK systems," *IEEE Photon. Technol. Lett.*, vol. 18, no. 8, pp. 950–952, Apr. 2006.
- [261] N. Yoshikane, I. Morita, and N. Edagawa, "Benefit of Half-Bit Delay Demodulation For Severely Bandlimited RZ-DPSK Signal," in *Proc. Eur. Conf. Optical Commun. (ECOC)*, Rimini, Italy, Sep. 2003, paper We3.5.2.
- [262] Y. K. Lize, L. Christen, P. Saghari *et al.*, "Implication of Chromatic Dispersion on Frequency Offset and Bit Delay Mismatch Penalty in DPSK Demodulation," in *Proc. Eur. Conf. Optical Commun. (ECOC)*, Cannes, France, Sep. 2006, paper Mo3.2.5.
- [263] A. D'Errico, R. Proietti, L. Giorgi *et al.*, "WDM-DPSK detection by means of frequency-periodic Gaussian filtering," *Electron. Lett.*, vol. 42, no. 2, pp. 112–113, Jan. 2006.
- [264] B. Mikkelsen, C. Rasmussen, P. Mamyshev, and F. Liu, "Partial DPSK With Excellent Filter Tolerance and OSNR sensitivity," *Electron. Lett.*, vol. 42, no. 23, pp. 1363 – 1364, Nov. 2006.
- [265] C. Malouin, J. Bennike, and T. Schmidt, "DPSK Receiver Design – Optical Filtering Considerations," in *Proc. Optical Fiber Commun. Conf. (OFC)*, Anaheim, CA, U.S.A, Mar. 2007, paper We3.5.2.
- [266] Y. K. Lizé, L. Christen, X. Wu *et al.*, "Free Spectral Range Optimization of Return-to-Zero Differential Phase Shift Keyed Demodulation in the Presence of Chromatic Dispersion," *Opt. Express*, vol. 15, no. 11, pp. 6817–6822, May 2007.
- [267] S. Benedetto, R. Gaudino, and P. Poggiolini, "Direct detection of optical digital transmission based on polarization shift keying modulation," *IEEE J. Sel. Areas Commun.*, vol. 13, no. 3, pp. 531–542, Apr. 1995.

- [268] Y. Han and G. Li, "Theoretical Sensitivity of Direct-Detection Multilevel Modulation Formats for High Spectral Efficiency Optical Communications," *IEEE J. Sel. Topics Quantum Electron.*, vol. 12, no. 4, pp. 571–580, Jul.-Aug. 2006.
- [269] C. Xu, X. Liu, and X. Wei, "Differential Phase-shift Keying for High Spectral Efficiency Optical Transmissions," *IEEE J. Sel. Topics Quantum Electron.*, vol. 10, no. 2, pp. 281–293, Mar/Apr. 2004.
- [270] M. Seimetz, M. Noelle, and E. Patzak, "Optical Systems With High-Order DPSK and Star QAM Modulation Based on Interferometric Direct Detection," *J. Lightwave Technol.*, vol. 25, no. 6, pp. 1515–1530, Jun. 2007.
- [271] R. A. Griffin, R. I. Johnstone, R. G. Walker *et al.*, "10Gb/s Optical Differential Quadrature Phase Shift Key (DQPSK) Transmission using GaAs/AlGaAs Integration," in *Proc. Optical Fiber Commun. Conf. (OFC)*, Anaheim, CA, U.S.A., Feb. 2002, paper FD6.
- [272] C. Wree, J. Leibrich, and W. Rosenkranz, "RZ-DQPSK format with High Spectral Efficiency and High Robustness towards Fiber Nonlinearities," in *Proc. Eur. Conf. Optical Commun. (ECOC)*, Copenhagen, Denmark, Sep. 2002, paper 9.6.6.
- [273] M. Ohm and T. Freckmann, "Comparison of Different DQPSK Transmitters with NRZ and RZ Impulse Shaping," in *Proc. IEEE/LEOS Workshop Advanced Modulation Formats*, San Francisco, CA, U.S.A., Jul. 2004, paper ThB2.
- [274] M. Serbay, C. Wree, and W. Rosenkranz, "Comparison of six Different RZ-DQPSK Transmitter Set-ups Regarding their Tolerance towards Fibre Impairments in 8x40Gb/s WDM-Systems," in *Proc. IEEE/LEOS Workshop Advanced Modulation Formats*, San Francisco, CA, U.S.A., Jul. 2004, paper ThB3.
- [275] C. R. Doerr, L. Zhang, P. J. Winzer *et al.*, "Compact High-Speed InP DQPSK Modulator," *IEEE Photon. Technol. Lett.*, vol. 19, no. 15, pp. 1184–1186, Aug. 2007.
- [276] H. G. Weber, S. Ferber, M. Kroh *et al.*, "Single Channel 1.28 Tbit/s and 2.56 Tbit/s DQPSK Transmission," *Electron. Lett.*, vol. 42, no. 3, pp. 178–179, Feb. 2006.
- [277] C. R. Doerr, D. M. Gill, A. H. Gnauck *et al.*, "Monolithic Demodulator for 40-Gb/s DQPSK using a Star Coupler," *J. Lightwave Technol.*, vol. 24, no. 1, pp. 171–174, Jan. 2006.
- [278] C. R. Doerr, L. Zhang, S. Chandrasekhar, and L. L. Buhl, "Monolithic DQPSK Receiver in InP with Low Polarization Sensitivity," *IEEE Photon. Technol. Lett.*, vol. 19, no. 21, pp. 1765–1767, Nov. 2007.
- [279] M. Oguma, Y. Nasu, H. Takahashi *et al.*, "Single MZI-based 1x4 DQPSK demodulator," in *Proc. Eur. Conf. Optical Commun. (ECOC)*, Berlin, Germany, Sep. 2007, paper Th10.3.4.
- [280] Z. Tao, A. Isomura, T. Hoshida, and J. C. Rasmussen, "Dither-free, Accurate, and Robust Phase Offset Monitor and Control Method for Optical DQPSK Demodulator," in *Proc. Eur. Conf. Optical Commun. (ECOC)*, Berlin, Germany, Sep. 2007, paper Tu3.5.2.
- [281] M. Serbay, C. Wree, and W. Rosenkranz, "Implementation of Differential Precoder for High-Speed Optical DQPSK Transmission," *Electron. Lett.*, vol. 40, no. 20, pp. 1288–1289, Sep. 2004.
- [282] M. Serbay, C. Wree, A. Schöpflin *et al.*, "Coding Gain of FEC encoded 21.42Gb/s RZ-D(Q)PSK using an Electrical Differential Quaternary Precoder," in *Proc. Eur. Conf. Optical Commun. (ECOC)*, Glasgow, United Kingdom, Sep. 2005, paper We4.P.10.
- [283] Y. Konishi, K. Ishida, K. Kubo, and T. Mizuochi, "True PRBS Transmission of DQPSK by Differential Precoder Employing Parallel Prefix Network," in *Proc. Optical Fiber Commun. Conf. (OFC)*, Anaheim, CA, U.S.A., Feb. 2006, paper OThR3.
- [284] K. Sekine, C. Hasegawa, N. Kikuchi, and S. Sasaki, "A Novel Bias Control Technique for MZ Modulator with Monitoring Power of Backward Light for Advanced Modulation Formats," in *Proc. Optical Fiber Commun. Conf. (OFC)*, Anaheim, CA, U.S.A., Mar. 2007, paper OTuH5.
- [285] K.-P. Ho, "The Effect of Interferometer Phase Error on Direct-Detection DPSK and DQPSK Signals," *IEEE Photon. Technol. Lett.*, vol. 16, no. 1, pp. 308–310, Jan. 2004.

## Bibliography

---

- [286] X. Zhou, J. Yu, T. Wang, and G. Zhang, "Impact of Strong Optical Filtering on DQPSK Modulation Formats," in *Proc. Eur. Conf. Optical Commun. (ECOC)*, Berlin, Germany, Sep. 2007, paper P094.
- [287] M. Haris, J. Yu, and G.-K. Chang, "Impact of Free Spectral Range Optimization on RZ/NRZ DQPSK Modulation Format with Strong Optical Filtering for Ultra-High Data Rate Systems," in *Proc. IEEE/LEOS Annual Meeting*, Orlando, FL, U.S.A., Oct. 2007, paper MP2.
- [288] J.-S. Lee and C.-S. Shim, "Bit-error-rate Analysis of Optically Preamplified Receivers using an Eigenfunction Expansion Method in Optical Frequency Domain," *J. Lightwave Technol.*, vol. 12, no. 7, pp. 1224–1229, Jul. 1994.
- [289] C. Wree, M. Serbay, and W. Rosenkranz, "Toward 1.6 b/s/Hz Spectral Efficiency by Strong Optical Filtering of RZ-DQPSK," in *Proc. Eur. Conf. Optical Commun. (ECOC)*, Rimini, Italy, Sep. 2003, paper We4.P.126.
- [290] N. Yoshikane and I. Morita, "160 percent Spectrally-Efficient 5.12 Tb/s (64 x 85.4 Gb/s RZ-DQPSK) Transmission without Polarisation Demultiplexing," in *Proc. Eur. Conf. Optical Commun. (ECOC)*, Stockholm, Sweden, Sep. 2004, post-deadline paper Th4.4.3.
- [291] A. H. Gnauck, P. J. Winzer, S. Chandrasekhar, and C. Dorrer, "Spectrally Efficient (0.8 b/s/Hz) 1-Tb/s (25 x 42.7Gb/s) RZ-DQPSK Transmission over 28 100-km SSMF Spans with 7 Optical Add/Drops," in *Proc. Eur. Conf. Optical Commun. (ECOC)*, Stockholm, Sweden, Sep. 2004, post-deadline paper Th4.4.1.
- [292] M. Serbay, J. Leibrich, W. Rosenkranz *et al.*, "Experimental Investigation of Asymmetrical Filtered 43 Gb/s RZ-DQPSK," in *Proc. IEEE/LEOS Annual Meeting*, Montreal, QC, Canada, Nov. 2006, paper WH5.
- [293] B. Spinnler, N. Hecker-Denschlag, S. Calabrò *et al.*, "Nonlinear Tolerance of Differential Phase Shift Keying Modulated Signals Reduced by XPM," in *Proc. Optical Fiber Commun. Conf. (OFC)*, Los Angeles, CA, U.S.A., Mar. 2004, paper TuF3.
- [294] C. Fürst, J.P-Elbers, M. Camera *et al.*, "43 Gb/s RZ-DQPSK DWDM Field Trail over 1047 km with Mixed 43 Gb/s and 10.7 Gb/s Channels at 50 and 100 GHz Channel Spacing," in *Proc. Eur. Conf. Optical Commun. (ECOC)*, Cannes, France, Sep. 2006, post-deadline paper Th4.1.4.
- [295] M. Daikoku, I. Morita, and H. Tanaka, "Study of 40 Gbit/s Modulation Format to Upgrade 10 Gbit/s Long-haul Transmission Systems with 50 GHz Channel Spacings," in *Proc. Eur. Conf. Optical Commun. (ECOC)*, Cannes, France, Sep. 2006, paper Tu4.2.3.
- [296] G. Charlet, H. Mardoyan, P. Tran *et al.*, "Nonlinear Interactions Between 10 Gb/s NRZ Channels and 40 Gb/s Channels with RZ-DQPSK or PSBT Format, over Low-dispersion Fiber," in *Proc. Eur. Conf. Optical Commun. (ECOC)*, Cannes, France, Sep. 2006, paper Mo3.2.6.
- [297] A. H. Gnauck, P. J. Winzer, and S. Chandrasekhar, "Hybrid 10/40-G Transmission on a 50-GHz Grid Through 2800 km of SSMF and Seven Optical Add-drops," *Proc. IEEE*, vol. 17, no. 10, p. 2203–2205, Oct. 2005.
- [298] L. K. Wickham, R.-J. Essiambre, A. H. Gnauck *et al.*, "Bit Pattern Length Dependence of Intrachannel Nonlinearities in Pseudolinear Transmission," *IEEE Photon. Technol. Lett.*, vol. 16, no. 6, pp. 1591–1593, June 2004.
- [299] E. Forestieri, "Evaluating the Error Probability in Lightwave Systems with Chromatic Dispersion, Arbitrary Pulse Shape and Pre- and Postdetection Filtering," *J. Lightwave Technol.*, vol. 18, no. 11, pp. 1493–1503, Nov. 2000.
- [300] B. Spinnler and C. Xie, "Performance Assessment of DQPSK using Pseudo-Random Quaternary Sequences," in *Proc. Eur. Conf. Optical Commun. (ECOC)*, Berlin, Germany, Sep. 2007, paper Mo2.3.6.
- [301] H. Griesser and J.-P. Elbers, "Influence of Cross-Phase Modulation Induced Nonlinear Phase Noise on DQPSK Signals from Neighbouring OOK Channels," in *Proc. Eur. Conf. Optical Commun. (ECOC)*, Cannes, France, Sep. 2005, paper Tu1.2.2.
- [302] K. Ishida, T. Kobayashi, J. Abe *et al.*, "A Comparative Study of 10 Gb/s RZ-DPSK and RZ-ASK WDM Transmission over Transoceanic Distances," in *Proc. Optical Fiber Commun. Conf. (OFC)*, Baltimore, MD, U.S.A., Mar. 2003, paper ThE2.



- 
- [303] X. Liu, L. F. Mollenauer, and X. Wei, "Impact of Group-Delay ripple in Transmission Systems Including Phase-Modulated Formats," *IEEE Photon. Technol. Lett.*, vol. 16, no. 1, pp. 305–307, Jan. 2004.
- [304] N. Cheng and J. C. Carterledge, "Effect of Residual Dispersion and Phase Response Ripple at 40Gb/s using a Tunable Chirped Fiber Bragg Grating," in *Proc. Optical Fiber Commun. Conf. (OFC)*, Anaheim, CA, U.S.A., Feb. 2006, paper OWI46.
- [305] M. H. Eiselt, C. B. Clausen, and R. W. Tkach, "Performance Characterization of Components with Group Delay Fluctuations," *IEEE Photon. Technol. Lett.*, vol. 15, no. 8, pp. 1076–1078, Aug. 2003.
- [306] G. Charlet, E. Corbel, J. Lazaro *et al.*, "WDM Transmission at 6-Tbit/s Capacity over Transatlantic Distance, Using 42.7-Gb/s Differential Phase-Shift Keying Without Pulse Carver," *J. Lightwave Technol.*, vol. 23, no. 1, pp. 104–107, Jan. 2005.
- [307] J.-X. Cai, M. Nissov, C. R. Davidson *et al.*, "Improved Margin in Long-Haul 40 Gb/s Systems using Bit-Synchronously Modulated RZ-DQPSK," in *Proc. Optical Fiber Commun. Conf. (OFC)*, Anaheim, CA, U.S.A., Feb. 2006, post-deadline paper PDP33.
- [308] S. L. Jansen, D. van den Borne, A. Schöpflin *et al.*, "26x42.8-Gbit/s DQPSK Transmission with 0.8-bit/s/Hz Spectral Efficiency over 4,500 km SSMF using Optical Phase Conjugation," in *Proc. Eur. Conf. Optical Commun. (ECOC)*, Glasgow, United Kingdom, Sep. 2005, post-deadline paper Th4.1.5.
- [309] T. Hoshida, T. Takahara, Y. Akiyama *et al.*, "Design Optimization of 40 Gb/s RZ-DQPSK Transceiver for High OSNR and PMD Tolerance under Fast Polarization Changes," in *Proc. Eur. Conf. Optical Commun. (ECOC)*, Berlin, Germany, Sep. 2007, paper P064.
- [310] T. Xia, G. Wellbrock, W. Lee *et al.*, "Transmission of 107-Gb/s DQPSK over Verizon 504-km Commercial LambdaXtreme® Transport System," in *Proc. Optical Fiber Commun. Conf. (OFC)*, San Diego, CA, U.S.A., Mar. 2007, paper NMC2.
- [311] P. N. Ji, A. Dogariu, L. Xu *et al.*, "Optical tunable asymmetric interleaver," in *Proc. Optical Fiber Commun. Conf. (OFC)*, Anaheim, CA, U.S.A., Feb. 2006, paper OTuM7.
- [312] D. van den Borne, S. L. Jansen, E. Gottwald *et al.*, "Line Optimization in Long-Haul Transmission Systems with 42.8-Gbit/s RZ-DQPSK modulation," in *Proc. Optical Fiber Commun. Conf. (OFC)*, Anaheim, CA, U.S.A., Feb. 2006, paper OFD2.
- [313] J. S. G. Evangelides, L. F. Mollenauer, J. P. Gordon, and N. S. Bergano, "Polarization multiplexing with solitons," *J. Lightwave Technol.*, vol. 10, no. 1, pp. 28–35, Jan. 1992.
- [314] K. Iwatsuki, K. Suzuki, S. Nishi, and M. Saruwatari, "80 Gb/s Optical Soliton Transmission over 80 km with Time/Polarization Division Multiplexing," *IEEE Photon. Technol. Lett.*, vol. 5, no. 2, pp. 245–248, Feb. 1993.
- [315] M. Nakazawa, K. Suzuki, E. Yoshida *et al.*, "160 Gbit/s Soliton Data Transmission over 200km," *Electron. Lett.*, vol. 31, no. 7, pp. 565–566, Mar. 1995.
- [316] A. R. Chraplyvy, A. H. Gnauck, R. W. Tkach *et al.*, "1-Tb/s Transmission Experiment," *IEEE Photon. Technol. Lett.*, vol. 8, no. 9, pp. 1264–1266, Sep. 1996.
- [317] T. Ito, K. Fukuchi, K. Sekiya *et al.*, "6.4 Tb/s (160 x 40 Gb/s) WDM Transmission Experiment with 0.8 bit/s/Hz Spectral Efficiency," in *Proc. Eur. Conf. Optical Commun. (ECOC)*, Munich, Germany, Sep. 2000, post-deadline paper PD1.1.
- [318] Y. Frignac, G. Charlet, W. Idler *et al.*, "Transmission of 256 Wavelength-Division and Polarization-Division-Multiplexed Channels at 42.7Gb/s (10.2 Tb/s Capacity) over 3x100km of Teralight Fiber," in *Proc. Optical Fiber Commun. Conf. (OFC)*, Anaheim, CA, U.S.A., Mar. 2002, post-deadline paper FC5.
- [319] K. Kukuchi, T. Kasamatsu, M. Morie *et al.*, "10.92-Tb/s (273 x 40-Gb/s) Triple-Band/Ultra-Dense WDM Optical-Repeated Transmission Experiment," in *Proc. Optical Fiber Commun. Conf. (OFC)*, Anaheim, CA, U.S.A., Feb. 2001, post-deadline paper PD24.
-

## Bibliography

---

- [320] S. Bigo, Y. Frignac, G. Charlet *et al.*, “10.2 Tbit/s (256 x 42.7 Gbit/s PDM/WDM) Transmission over 100km Terahertz Fiber with 1.28 bits/s/Hz Spectral Efficiency,” in *Proc. Optical Fiber Commun. Conf. (OFC)*, Anaheim, CA, U.S.A., Mar. 2001, post-deadline paper PD25.
- [321] H. Masuda, A. Sano, T. Kobayashi *et al.*, “20.4-Tb/s (204 x 111 Gb/s) Transmission over 240 km using Bandwidth-Maximized Hybrid Raman/EDFAs,” in *Proc. Optical Fiber Commun. Conf. (OFC)*, Anaheim, CA, U.S.A., Mar. 2007, post-deadline paper PDP20.
- [322] N. E. Hecker, E. Gottwald, K. Kotten *et al.*, “Automated Polarization Control Demonstrated in a 1.28 Tbit/s (16x2x40Gbit/s) Polarization Multiplexed DWDM Field Trail,” in *Proc. Eur. Conf. Optical Commun. (ECOC)*, Amsterdam, The Netherlands, Sep. 2001, paper Mo.L.3.1.
- [323] C. Herard and A. Lacourt, “Three Channel Multiplexing using Polarization of Light,” *Opt. Comm.*, vol. 60, no. 1-2, pp. 27–31, Oct. 1986.
- [324] —, “New Multiplexing Technique using Polarization of Light,” *Appl. Opt.*, vol. 30, no. 2, pp. 222–231, Jan. 1991.
- [325] C. Chen, *Elements of Optoelectronics and Fiber Optics*, 1st ed. Irwin Professional Publishing, 1996.
- [326] L. E. Nelson and H. Kogelnik, “Coherent Crosstalk Impairments in Polarization Multiplexed Transmission due to Polarization Mode Dispersion,” *Opt. Express*, vol. 7, no. 10, pp. 350–361, Nov. 2000.
- [327] R. Noé, S. Hinz, D. Sandel, and F. Wust, “Crosstalk Detection Schemes for Polarization Division Multiplexed Transmission Experiments,” *J. Lightwave Technol.*, vol. 19, no. 10, pp. 1469–1475, Oct. 2001.
- [328] F. Heismann, P. Hansen, S. Korotky *et al.*, “Automatic Polarization Demultiplexer for Polarization-Multiplexed Transmission Systems,” *Electron. Lett.*, vol. 29, no. 22, pp. 1965–1966, Oct. 1993.
- [329] A. O. Dal-Forno, A. Paradisi, R. Passy, and J. P. von der Weid, “Experimental and Theoretical Modeling of Polarization Mode Dispersion in Single-Mode Fibers,” *IEEE Photon. Technol. Lett.*, vol. 12, no. 3, pp. 296–298, Mar. 2000.
- [330] H. Kogelnik, L. E. Nelson, and P. J. Winzer, “Second-Order PMD outage of First-Order Compensated Fiber Systems,” *IEEE Photon. Technol. Lett.*, vol. 16, no. 4, pp. 1053–1055, Apr. 2004.
- [331] S. Hinz, D. Sandel, F. Wüst, and R. Noé, “PMD Tolerance of Polarization Division Multiplex Transmission using Return-to-Zero Coding,” *Opt. Express*, vol. 9, no. 3, pp. 136–140, Jul. 2001.
- [332] S. Song, C. Allen, K. Demarest, and R. Hui, “A Novel Method for Measuring Polarization-Mode Dispersion using Four-Wave Mixing,” *J. Lightwave Technol.*, vol. 17, no. 12, pp. 2530–2533, Dec. 1999.
- [333] S. Hinz, D. Sandel, F. Wust, and R. noé, “Polarization Multiplexed 2x20Gbit/s RZ transmission using Interference detection,” in *Proc. Optical Fiber Commun. Conf. (OFC)*, Anaheim, CA, U.S.A., Mar. 2001, paper WM4.
- [334] L. E. Nelson, T. N. Nielsen, and H. Kogelnik, “Observation of PMD-Induced Coherent Crosstalk in Polarization- Multiplexed Transmission,” *IEEE Photon. Technol. Lett.*, vol. 13, no. 7, pp. 738–740, Jul. 2001.
- [335] B. S. Marks and C. R. Menyuk, “Polarization-mode Dispersion Enhancements of Nonlinear Propagation,” in *Proc. Eur. Conf. Optical Commun. (ECOC)*, Rimini, Italy, Sep. 2003, paper Mo3.7.1.
- [336] D. Sandel, F. Wüst, V. Mirvoda, and R. Noé, “Standard (NRZ 1x40Gbit/s, 210km) and Polarization Multiplex (CS-RZ, 2x40Gb/s, 212 km) Transmissions with PMD compensation,” *IEEE Photon. Technol. Lett.*, vol. 14, no. 8, pp. 1181–1183, Aug. 2002.
- [337] C. Furst, J.-P. Elbers, C. Scheerer, and C. Glingener, “Limitations of Dispersion-Managed DWDM Systems due to Cross-Phase Modulation,” in *Proc. IEEE/LEOS Annual Meeting*, November 2000, paper MB3.
- [338] D. Wang and C. R. Menyuk, “Reduced model of the Evolution of the Polarization States in Wavelength-Division-Multiplexed Channels,” *Opt. Lett.*, vol. 23, no. 21, pp. 1677–1679, Nov. 1998.

- [339] T. Tolke, P. A. Andersson, Y. Geng *et al.*, "Generation, Transmission and Wavelength Conversion of a 80Gbit/s RZ-DBPSK-ASK Signal," in *Proc. Conf. Lasers and Electro-Optics (CLEO 2005)*, Baltimore, MD, U.S.A., May 2005, paper CMQ4.
- [340] N. Kikuchi, K. Mandai, K. Sekine, and S. Sasaki, "First Experimental Demonstration of Single-Polarization 50-Gbit/s 32-level (QASK and 8-DPSK) Incoherent Optical Multilevel Transmission," in *Proc. Optical Fiber Commun. Conf. (OFC)*, Anaheim, CA, U.S.A., Mar. 2007, post-deadline paper PDP21.
- [341] T. Tolke, M. Serbay, Y. Geng *et al.*, "Penalty-free Transmission of Multilevel 240 Gbit/s RZ-DQPSK-ASK using only 40 Gbit/s Equipment," in *Proc. Eur. Conf. Optical Commun. (ECOC)*, Glasgow, United Kingdom, Sep. 2005, post-deadline paper Th4.1.6.
- [342] R. A. Griffin, "Advanced Optical Modulators on InP," in *Proc. IEEE/LEOS Annual Meeting*, Orlando, FL, U.S.A., Oct. 2007, paper ThX1.
- [343] D. F. Welch, F. A. Kish, S. Melle *et al.*, "Large-Scale InP Photonic Integrated Circuits: Enabling Efficient Scaling of Optical Transport Networks," *IEEE J. Sel. Topics Quantum Electron.*, vol. 13, no. 1, pp. 22–31, Jan.-Feb. 2007.
- [344] G. Charlet, S. Lanne, L. Pierre *et al.*, "Cost-Optimized 6.3Tbit/s-Capacity Terrestrial Link over 17x100km using Phase-Shaped Binary Transmission in a Conventional All-EDFA SMF-based System," in *Proc. Optical Fiber Commun. Conf. (OFC)*, Atlanta, GA, U.S.A., Mar. 2003, post-deadline paper PDP25.
- [345] B. Zhu, L. E. Nelson, S. Stulz *et al.*, "6.4-Tb/s (160x 42.7 Gb/s) Transmission With 0.8 bits/s/Hz Spectral Efficiency over 32 x 100 km of Fiber Using CSRZ-DPSK Format," in *Proc. Optical Fiber Commun. Conf. (OFC)*, Atlanta, GA, U.S.A., Mar. 2003, post-deadline paper PDP19.
- [346] I. Morita and N. Edgawa, "50GHz-spaced 64 x 42.7Gbit/s Transmission over 8200km Using Pre-filtered CS-RZ DPSK Signal and EDFA Repeaters," in *Proc. Eur. Conf. Optical Commun. (ECOC)*, Rimini, Italy, Sep. 2003, paper Mo4.3.1.
- [347] H. Sotobayashi, W. Chujo, and K. Kitayama, "1.6 bits/s/Hz, 6.4 Tbit/s OCDM/WDM (4 OCDM x 40 WDM x 40Gbit/s) Transmission Experiment," *IEEE J. Sel. Topics Quantum Electron.*, vol. 10, no. 2, pp. 250–258, Mar.-Apr. 2004.
- [348] C. Wree, N. E. Hecker-Denschlag, E. Gottwald *et al.*, "High Spectral Efficiency 1.6-b/s/Hz Transmission (8 x 40 Gb/s with a 25-GHz Grid) over 200-km SSMF using RZ-DQPSK and Polarization-Multiplexing," *IEEE Photon. Technol. Lett.*, vol. 15, no. 9, pp. 1303–1305, Sep. 2003.
- [349] B. Milivojevic, A. F. Abas, A. Hidayat *et al.*, "1.6-b/s/Hz 160-Gb/s 230-km RZ-DQPSK Polarization Multiplex Transmission," *IEEE Photon. Technol. Lett.*, vol. 17, no. 2, pp. 495–498, Feb. 2005.
- [350] D. van den Borne, S. L. Jansen, E. Gottwald *et al.*, "1.6-b/s/Hz Spectrally Efficient Transmission Over 1,700 km of SSMF Using 40 x 85.6-Gbit/s POLMUX-RZ-DQPSK," *J. Lightwave Technol.*, vol. 25, no. 1, pp. 222–232, Jan. 2007.
- [351] G. Charlet, J. Renaudier, H. Mardoyan *et al.*, "12.8Tbit/s Transmission of 160 PDM-QPSK (160x2x40Gbit/s) Channels with Coherent Detection over 2,550km," in *Proc. Eur. Conf. Optical Commun. (ECOC)*, Berlin, Germany, Sep. 2007, post-deadline paper PDP17.
- [352] P. S. Cho, G. Harston, C. J. Kerr *et al.*, "Investigation of 2-b/s/Hz 40-Gbit/s DWDM Transmission over 4 x 100 km SMF-28 Fiber using RZ-DQPSK and Polarization-Multiplexing," *IEEE Photon. Technol. Lett.*, vol. 16, no. 2, pp. 656–658, Feb. 2004.
- [353] C. R. S. Fludger, T. Duthel, D. van den Borne *et al.*, "10 x 111 Gbit/s, 50 GHz Spaced, POLMUX-RZ-DQPSK Transmission over 2375 km Employing Coherent Equalisation," in *Proc. Optical Fiber Commun. Conf. (OFC)*, Anaheim, CA, U.S.A., Mar. 2007, post-deadline paper PDP22.
- [354] S. Tsukamoto, D.-S. Ly-Gagnon, K. Katoh, and K. Kikuchi, "Coherent Demodulation of 40-Gbit/s Polarization-Multiplexed QPSK Signals with 16-GHz Spacing after 200-km Transmission," in *Proc. Optical Fiber Commun. Conf. (OFC)*, Anaheim, CA, U.S.A., Feb. 2005, post-deadline paper PDP29.

## Bibliography

---

- [355] D.-S. Ly-Gagnon, S. Tsukamoto, K. Katoh, and K. Kikuchi, "Coherent Detection of Optical Quadrature Phase-Shift Keying Signals with Carrier Phase Estimation," *J. Lightwave Technol.*, vol. 24, no. 1, pp. 12–21, Jan. 2006.
- [356] S. L. Jansen, I. Morita, and H. Tanaka, "16x52.5-Gb/s, 50-GHz spaced, POLMUX-CO-OFDM transmission over 4,160 km of SSMF enabled by MIMO processing," in *Proc. Eur. Conf. Optical Commun. (ECOC)*, Berlin, Germany, Sep. 2007, post-deadline paper PD1.3.
- [357] B. Schmidt, A. J. Lowery, and J. Armstrong, "Experimental Demonstrations of 20 Gbit/s Direct-Detection Optical OFDM and 12 Gbit/s with a colorless transmitter," in *Proc. Optical Fiber Commun. Conf. (OFC)*, Anaheim, CA, U.S.A., Mar. 2007, post-deadline paper PDP18.
- [358] D. McGhan, C. Laperle, A. Savchenko *et al.*, "5120-km RZ-DPSK Transmission over G.652 Fiber at 10 Gb/s without Optical Dispersion Compensation," *IEEE Photon. Technol. Lett.*, vol. 18, no. 2, pp. 400–402, Jan. 2006.
- [359] R. I. Killey, P. M. Watts, V. Mikhailov *et al.*, "Electronic Dispersion Compensation by Signal Predistortion using Digital Processing and a Dual-Drive Mach-Zehnder Modulator," *IEEE Photon. Technol. Lett.*, vol. 17, no. 3, pp. 714–716, Mar. 2005.
- [360] G. Goeger, "Modulation Format with Enhanced SPM-Robustness for Electronically Pre-Distorted Transmission," in *Proc. Eur. Conf. Optical Commun. (ECOC)*, Cannes, France, Sep. 2006, paper Tu4.2.6.
- [361] C. Weber, J. K. Fischer, C.-A. Bunge, and K. Petermann, "Electronic Precompensation of Intra-Channel Nonlinearities at 40 Gbit/s," in *Proc. Eur. Conf. Optical Commun. (ECOC)*, Cannes, France, Sep. 2006, paper We1.5.4.
- [362] R. I. Killey, P. M. Watts, M. Glick, and P. Bayvel, "Electronic precompensation Techniques to Combat Dispersion and Nonlinearities in Optical Transmission," in *Proc. Eur. Conf. Optical Commun. (ECOC)*, Glasgow, United Kingdom, Sep. 2005, paper Tu4.2.1.
- [363] R.-J. Essiambre and P. J. Winzer, "Fibre Nonlinearities in Electronically Pre-Distorted Transmission," in *Proc. Eur. Conf. Optical Commun. (ECOC)*, Glasgow, United Kingdom, Sep. 2005, paper Tu3.2.2.
- [364] T. Nielsen and S. Chandrasekhar, "OFC2004 workshop on optical and electronic mitigation of impairments," *J. Lightwave Technol.*, vol. 23, no. 1, p. 131–141, Jan. 2005.
- [365] J. Winters and R. D. Gitlin, "Electrical signal processing techniques in long-haul fiber-optic systems," *IEEE Trans. Commun.*, vol. 38, no. 9, p. 1439–1453, Sep. 1990.
- [366] H. Bülow, R. Ballentin, W. Baumert *et al.*, "Adaptive PMD mitigation at 10 Gbit/s using an electronic SiGe equaliser IC," in *Proc. Eur. Conf. Optical Commun. (ECOC)*, Nice, France, Sep. 1999, p. 138–139.
- [367] P. M. Watts, V. Mikhailov, S. Savory *et al.*, "Performance of Single-Mode Fiber Links using Electronic Feed Forward and Decision Feedback Equalizers," *IEEE Photon. Technol. Lett.*, vol. 17, no. 10, pp. 2206–2208, Oct. 2005.
- [368] C. Xia and W. Rosenkranz, "Nonlinear Electrical Equalization for Different Modulation Formats with Optical Filtering," *IEEE Photon. Technol. Lett.*, vol. 25, no. 4, pp. 996–1001, Apr. 2007.
- [369] N. Kikuchi, K. Mandai, S. Sasaki, and K. Sekine, "Proposal and First Experimental Demonstrations of Digital Incoherent Optical Field Detector for Chromatic Dispersion Compensation," in *Proc. Eur. Conf. Optical Commun. (ECOC)*, Cannes, France, Sep. 2006, post-deadline paper Th4.4.4.
- [370] J. M. Gene, P. J. Winzer, S. Chandrasekhar, and H. Kogelnik, "Joint PMD and Chromatic Dispersion Compensation Using an MLSE," in *Proc. Eur. Conf. Optical Commun. (ECOC)*, Cannes, France, Sep. 2006, paper We2.5.2.
- [371] J. P. Elbers, H. Wernz, H. Griesser *et al.*, "Measurement of the Dispersion Tolerance of Optical Duobinary with an MLSE-Receiver at 10.7 Gb/s," in *Proc. Optical Fiber Commun. Conf. (OFC)*, Anaheim, CA, U.S.A., Feb. 2005, paper OThJ4.

- 
- [372] F. Adachi and M. Sawahashi, "Decision Feedback Differential Phase Detection of M-ary DPSK Signals," *IEEE Trans. Veh. Technol.*, vol. 44, no. 2, pp. 203–210, May 1995.
- [373] D. Divsalar and M. K. Simon, "Multiple-symbol Differential Detection of MPSK," *IEEE Trans. Commun.*, vol. 38, no. 3, pp. 300–308, Mar. 1990.
- [374] H. Leib, "Data-aided Noncoherent Demodulation of DPSK," *IEEE Trans. Commun.*, vol. 43, no. 234, pp. 722–725, Feb-Mar-Apr. 1995.
- [375] Y. Yadin, A. Bilenca, and M. Nazarathy, "Soft Detection of Multichip DPSK over the Nonlinear Fiber-Optic Channel," *IEEE Photon. Technol. Lett.*, vol. 17, no. 9, pp. 2001–2003, Sep. 2005.
- [376] Y. Yadin, M. Nazarathy, A. Bilenca, and M. Orenstein, "Multichip Differential Phase-Shift-Keyed Transmission over (Non)Linear Optical Channels," *J. Lightwave Technol.*, vol. 25, no. 6, pp. 1431–1440, Jun. 2007.
- [377] X. Lui, "Receiver Sensitivity Improvement in Optical DQPSK and DQPSK/ASK Through Data-Aided Multisymbol Phase Estimation," in *Proc. Eur. Conf. Optical Commun. (ECOC)*, Cannes, France, Sep. 2006, paper We2.5.6.
- [378] X. Liu, S. Chandrasekhar, A. H. Gnauck *et al.*, "DSP-enabled Compensation of Demodulator Phase Error and Sensitivity Improvement in Direct-Detection 40-Gb/s DQPSK," in *Proc. Eur. Conf. Optical Commun. (ECOC)*, Cannes, France, Sep. 2006, post-deadline paper Th4.4.5.
- [379] C. P. Kaiser, P. J. Smith, , and M. Shafi, "An Improved Optical Heterodyne DPSK Receiver to Combat Laser Phase Noise," *J. Lightwave Technol.*, vol. 13, no. 3, pp. 525–533, Mar. 1995.
- [380] S. Savory and A. Hadjifotiou, "Laser Linewidth Requirements for Optical DQPSK Systems," *IEEE Photon. Technol. Lett.*, vol. 16, no. 3, pp. 930–932, Mar. 2004.
- [381] T. M. M. Funabashi, H. Nasu, T. Kimoto, T. Shinagawa *et al.*, "Recent Advantages in DFB Lasers for Ultradense WDM Applications," *IEEE J. Sel. Topics Quantum Electron.*, vol. 10, no. 2, pp. 312–320, Mar-Apr. 2004.
- [382] E. Ip and J. M. Kahn, "Feedforward Carrier Recovery for Coherent Optical Communications," *J. Lightwave Technol.*, vol. 25, no. 9, pp. 2675–2692, Sep. 2007.
- [383] M. G. Taylor, "Accurate Digital Phase Estimation Process for Coherent Detection using a Parallel Digital Processor," in *Proc. Eur. Conf. Optical Commun. (ECOC)*, Glasgow, United Kingdom, Sep. 2005, paper Tu4.2.6.
- [384] S. Norimatsu and K. Iwashita, "Linewidth Requirements for Optical Synchronous Detection Systems with Nonnegligible Loop Delay Time," *J. Lightwave Technol.*, vol. 10, no. 3, pp. 341–349, Mar. 1992.
- [385] J. R. Barry and J. M. Kahn, "Carrier Synchronization for Homodyne and Heterodyne Detection of Optical Quadrature-Phase-Shift Keying," *J. Lightwave Technol.*, vol. 10, no. 12, pp. 1939–1951, Dec. 1992.
- [386] J. D. Berger, Y. Zhang, J. D. Grade, and H. Lee, "Widely Tunable External Cavity Diode Laser using a MEMS Electrostatic Rotary Actuator," in *Proc. Eur. Conf. Optical Commun. (ECOC)*, Amsterdam, The Netherlands, Sep. 2001, paper Tu.F.3.3.
- [387] J. Prat and J. M. Fàbrega, "New Homodyne Receiver with Electronic I & Q Differential Demodulation," in *Proc. Eur. Conf. Optical Commun. (ECOC)*, Glasgow, United Kingdom, Sep. 2005, paper We4.P.104.
- [388] J. G. Proakis and D. K. Manolakis, *Digital Signal Processing*, 4th ed. Prentice Hall, 2006.
- [389] G. F. Jr., "Maximum-likelihood sequence estimation of digital sequences in the presence of intersymbol interference," *IEEE Trans. Inf. Theory*, vol. 18, no. 3, pp. 363–378, May 1972.
- [390] O. E. Agazzi, M. R. Hueda, H. S. Carrer, and D. E. Crivelli, "Maximum-Likelihood Sequence Estimation in Dispersive Optical Channels," *J. Lightwave Technol.*, vol. 23, no. 2, pp. 749–763, Feb. 2005.
- [391] S. Savory, A. Napoli, B. Thomsen *et al.*, "Robust Optical Systems Using Maximum Likelihood Sequence Estimators," in *Proc. IEE Seminar on Optical Fiber Commun. and Elec. Sig. Proc.*, London, United Kingdom, Dec. 2005, paper 11.
-

## Bibliography

---

- [392] A. Napoli, S. Savory, B. C. Thomsen *et al.*, “Limits of Maximum-Likelihood Sequence Estimation in Chromatic Dispersion Limited Systems,” in *Proc. Optical Fiber Commun. Conf. (OFC)*, Anaheim, CA, U.S.A., Feb. 2006, paper JThB36.
- [393] P. Poggiolini, G. Bosco, S. Savory *et al.*, “1,040 km Uncompensated IMDD Transmission over G.652 Fiber at 10 Gbit/s using a Reduced-state SQRT-Metric MLSE receiver,” in *Proc. Eur. Conf. Optical Commun. (ECOC)*, Cannes, France, Sep. 2006, post-deadline paper Th4.4.6.
- [394] N. Alic, G. C. Papen, R. E. Saperstein *et al.*, “Experimental demonstration of 10 Gb/s NRZ extended dispersion-limited reach over 600 km-SMF link without optical dispersion compensation,” in *Proc. Optical Fiber Commun. Conf. (OFC)*, Anaheim, CA, U.S.A., Feb. 2006, paper OWB7.
- [395] S. J. Savory, Y. Benlachtar, R. I. Killey *et al.*, “IMDD Transmission over 1,040 km of Standard Single-Mode Fiber at 10Gbit/s using a One-Sample-per-Bit Reduced-Complexity MLSE Receiver,” in *Proc. Optical Fiber Commun. Conf. (OFC)*, Anaheim, CA, U.S.A., Mar. 2007, paper OThK2.
- [396] C. Xia and W. Rosenkranz, “Electrical Dispersion Compensation for Different Modulation Formats with Optical Filtering,” in *Proc. Optical Fiber Commun. Conf. (OFC)*, Anaheim, CA, U.S.A., Feb. 2006, paper OWR2.
- [397] M. Cavallari, C. R. S. Fludger, and P. J. Anslow, “Electronic Signal Processing for Differential Phase Modulation Formats,” in *Proc. Optical Fiber Commun. Conf. (OFC)*, Los Angeles, CA, U.S.A., Mar. 2004, paper TuG2.
- [398] M. C. Jeruchim, “Techniques for Estimating the Bit Error Rate in the Simulation of Digital communication systems,” *IEEE J. Sel. Areas Commun.*, vol. 2, no. 1, pp. 153 – 170, Jan. 1984.
- [399] E. Forestierie, *Optical Communication Theory and Techniques*. Springer Verlag, 2004.
- [400] F. N. Hauske, B. Lankl, C. Xie, and E.-D. Schmidt, “Iterative Electronic Equalization Utilizing Low Complexity MLSEs for 40 Gbit/s DQPSK Modulation,” in *Proc. Optical Fiber Commun. Conf. (OFC)*, Anaheim, CA, U.S.A., Mar. 2007, paper OMG2.
- [401] J. Zhao, L.-K. Chen, and C.-K. Chan, “Maximum Likelihood Sequence Estimation for Chromatic Dispersion and Polarization Mode Dispersion Compensation in 3-Chip DPSK Modulation Format,” in *Proc. Optical Fiber Commun. Conf. (OFC)*, Anaheim, CA, U.S.A., Mar. 2007, paper OMG3.
- [402] —, “Maximum Likelihood Sequence Estimation for Impairment Compensation in Advanced Modulation Formats,” in *Proc. Optoelectronics Commun. Conf. (OECC)*, Yokohama, Japan, Jul. 2007, paper 13B2-1.
- [403] D. J. Maylon, T. G. Hodgkinson, D. W. Smith *et al.*, “PSK Homodyne Receiver Sensitivity Measurements at 1.5 $\mu$ m,” *Electron. Lett.*, vol. 19, no. 4, pp. 144–146, Feb. 1983.
- [404] A. W. Davis, M. J. Pettitt, J. P. King, and S. Wright, “Phase Diversity Techniques for Coherent Optical Receivers,” *J. Lightwave Technol.*, vol. 5, no. 4, pp. 561–571, Apr. 1987.
- [405] C. Wree, D. Becker, D. Mohr, and A. Joshi, “Optical Coherent Receivers for 2.5 and 5Gb/s,” in *Proc. IEEE/LEOS Annual Meeting*, Montreal, QC, Canada, Nov. 2006, paper WM1.
- [406] D. J. Maylon, “Digital Fibre Transmission using Optical Homodyne Detection,” *Electron. Lett.*, vol. 20, no. 7, pp. 281–283, Mar. 1984.
- [407] E. Basch and T. Brown, “Introduction to coherent optical fiber transmission,” *IEEE Commun. Mag.*, vol. 23, no. 5, pp. 23–30, May 1985.
- [408] G. Nicholson, “Probability of the Error for Optical Hetrodyne DPSK System with Quantum Phase Noise,” *Electron. Lett.*, vol. 20, no. 24, pp. 1005–1007, Nov. 1984.
- [409] R. A. Linke, B. L. Kasper, N. A. Olsson, and R. C. Alferness, “Coherent Lighthwave Transmission over 150 km Fibre Lengths at 400 Mbit/s and 1 Gbit/s Data Rates using Phase Modulation,” *Electron. Lett.*, vol. 22, no. 1, pp. 30–31, Jan. 1986.

- [410] C. Wree, D. Becker, D. Mohr, and A. Joshi, "Coherent Receivers for Phase-Shift Keyed Transmission," in *Proc. Optical Fiber Commun. Conf. (OFC)*, Anaheim, CA, USA, Mar. 2007, paper OMP6.
- [411] A. W. Davis, M. J. Pettitt, J. P. King, and S. Wright, "Coherent Optical Receiver for 680 Mbit/s using Phase Diversity," *Electron. Lett.*, vol. 22, no. 1, pp. 9–11, Jan. 1986.
- [412] F. Derr, "Coherent Optical QPSK Intradyne System: Concept and Digital Receiver Realization," *J. Lightwave Technol.*, vol. 10, no. 9, pp. 1290–1296, Sep. 1992.
- [413] S. Norimatsu, K. Iwashita, and K. Noguchi, "An 8 Gb/s QPSK Optical Homodyne Detection Experiment using External-Cavity Laser Diodes," *IEEE Photon. Technol. Lett.*, vol. 4, no. 7, pp. 765–767, Jul. 1992.
- [414] F. Derr, "Optical QPSK Transmission System with Novel Digital Receiver concept," *Electron. Lett.*, vol. 27, no. 23, pp. 2177–2179, Nov. 1991.
- [415] R. Noé, H. J. Rodler, A. Ebberg *et al.*, "Comparison of Polarization Handling Methods in Coherent Optical Systems," *J. Lightwave Technol.*, vol. 9, no. 10, pp. 1353–1366, Oct. 1991.
- [416] T. Okoshi, S. Ryu, and K. Kikuchi, "Polarization-Diversity Receiver for Heterodyne/Coherent Optical Fiber Communications," in *Proc. Integr. Optics and Optical Fiber Commun. Conf. (IOCC)*, Tokyo, Japan, Jun. 1983, paper 3OC3-2.
- [417] B. Glance, "Polarization Independent Coherent Optical Receiver," *J. Lightwave Technol.*, vol. 5, no. 2, pp. 274–276, Feb. 1987.
- [418] T. Okoshi, O. Ishida, and K. Kikuchi, "Optical QPSK Homodyne Transmission of 280 Mbit/s," *Electron. Lett.*, vol. 24, no. 2, pp. 120–122, Jan. 1988.
- [419] T. Okoshi and Y. H. Cheng, "Four-port Homodyne Receiver for Optical Fibre Communications Compromising Phase and Polarization Diversities," *Electron. Lett.*, vol. 23, no. 8, pp. 377–388, Apr. 1987.
- [420] S. Savory, A. Stewart, S. Wood *et al.*, "Digital Equalisation of 40Gbit/s per Wavelength Transmission over 2480km of Standard Fibre without Optical Dispersion Compensation," in *Proc. Eur. Conf. Optical Commun. (ECOC)*, Cannes, France, Sep. 2006, paper Th2.5.5.
- [421] G. Charlet, J. Renaudier, M. Salsi *et al.*, "Efficient Mitigation of Fiber Impairments in an Ultra-Long Haul Transmission of 40Gbit/s Polarization-Multiplexed Data, by Digital Processing in a Coherent Receiver," in *Proc. Optical Fiber Commun. Conf. (OFC)*, Anaheim, CA, U.S.A, Mar. 2007, post-deadline paper PDP17.
- [422] C. Laperle, B. Villeneuve, Z. Zhang *et al.*, "Wavelength Division Multiplexing (WDM) and Polarization Mode Dispersion (PMD) Performance of a Coherent 40Gbit/s Dual-Polarization Quadrature Phase Shift Keying (DP-QPSK) Transceiver," in *Proc. Optical Fiber Commun. Conf. (OFC)*, Anaheim, CA, U.S.A, Mar. 2007, post-deadline paper PDP16.
- [423] Z. Tao, H. Zhang, A. Isomura *et al.*, "Simple, Robust, and Wide-Range Frequency Offset Monitor for Automatic Frequency Control in Digital Coherent Receivers," in *Proc. Eur. Conf. Optical Commun. (ECOC)*, Berlin, Germany, Sep. 2007, paper Tu3.5.4.
- [424] K. Poulton, R. Neff, B. Setterberg *et al.*, "A 20GS/s 8b ADC with a 1MB Memory in 0.18 $\mu$ m CMOS," in *Proc. IEEE Int. Solid-State Circ. Conf. (ISSCC)*, San Francisco, CA, U.S.A., Feb. 2003, paper 18.1.
- [425] R. Noé, T. Pfau, O. Adamczyk *et al.*, "Real-time Digital Carrier & Data Recovery for a Synchronous Optical Quadrature Phase Shift Keying Transmission System," in *Proc. IEEE/MTT-S Int. Micr. Symp.*, Honolulu, HI, U.S.A., Jun. 2007, paper, pp. 1503–1506.
- [426] DPO/DSA 70000 series application notes. [Online]. Available: <http://www.tek.com>
- [427] J. Sitch, "Implementation Aspects of High-Speed DSP for Transmitter and Receiver Signal Processing," in *Proc. LEOS Summer Topicals*, Portland, OR, U.S.A., Jul. 2007, paper MA4.3.
- [428] H. Sun, K.-T. Wu, and K. Roberts, "Continuous real-time measurements are shown from a coherent 40 Gb/s transmission system that uses Dual-Polarization Quadrature Phase Shift Keying (DP-QPSK) modulation," *Opt. Express*, vol. 16, no. 2, pp. 873–879, Feb. 2008.

## Bibliography

---

- [429] M. C. Jeruchim, P. Balaban, and K. S. Shanmugan, *Simulation of Communication Systems*. New York, NY, U.S.A.: Plenum, 1992.
- [430] M. Oerder and H. Meyr, "Digital Filter and Square Timing Recovery," *IEEE Trans. Commun.*, vol. 36, no. 5, pp. 605–612, May 1988.
- [431] M. T. Core, "Cross Polarization Interference Cancellation for Fiber Optics Systems," *J. Lightwave Technol.*, vol. 24, no. 1, pp. 305–312, Jan. 2006.
- [432] S. Calabro, T. Dullweber, E. Gottwald *et al.*, "An Electrical Polarization-state Controller and Demultiplexer for Polarization Multiplexed Optical Signals," in *Proc. Eur. Conf. Optical Commun. (ECOC)*, Rimini, Italy, Sep. 2003, paper Th2.2.2.
- [433] G. Ungerboeck, "Fractional Tap-Spacing Equalizer and Consequences for Clock Recovery in Data Modems," *IEEE Trans. Commun.*, vol. 24, no. 8, pp. 856–864, Aug. 1976.
- [434] D. N. Godard, "Self-Recovering Equalization and Carrier Tracking in Two-Dimensional Data Communication Systems," *IEEE Trans. Commun.*, vol. 28, no. 11, pp. 1867–1875, Nov. 1980.
- [435] S. J. Savory, G. Gavioli, R. I. Killey, and P. Bayvel, "Electronic Compensation of Chromatic Dispersion using a Digital Coherent Receiver," *OSA Optics Express*, vol. 15, no. 5, pp. 2120–2126, Mar. 2007.
- [436] N. Benvenuto and G. Cherubini, *Algorithms for Communications Systems and their Applications*, 1st ed. Wiley, 2002.
- [437] Y. Han and G. Li, "Coherent Optical Communication using Polarization Multiple-Input-Multiple-Output," *OSA Optics Express*, vol. 13, no. 19, pp. 7527–7534, Sep. 2005.
- [438] K. Roberts, "Electronic Dispersion Compensation Beyond 10 Gb/s," in *Proc. LEOS Summer Topicals*, Portland, OR, U.S.A., Jul. 2007, paper MA2.3.
- [439] F. N. Hauske, J. C. Geyer, M. Kuschnerov *et al.*, "Optical Performance Monitoring from FIR Filter Coefficients in Coherent Receivers," in *Proc. Optical Fiber Commun. Conf. (OFC)*, San Diego, CA, U.S.A., Feb. 2008, paper OThW2.
- [440] J. C. Geyer, F. N. Hauske, C. R. S. Fludger *et al.*, "Channel Parameter Estimation for Polarization Diverse Coherent Receivers," *Submitted to IEEE Photon. Technol. Lett.*, 2008.
- [441] A. J. Viterbi and A. M. Viterbi, "Nonlinear Estimation of PSK-Modulated Carrier Phase with Applications to Burst Digital Transmission," *IEEE Trans. Inf. Theory*, vol. 29, no. 4, pp. 543–551, Jul. 1983.
- [442] O. B. Pardo, J. Renaudier, H. Mardoyan *et al.*, "Investigation of Design Options for Overlaying 40Gb/s Coherent PDM-QPSK Channels over a 10Gb/s System Infrastructure," in *Proc. Optical Fiber Commun. Conf. (OFC)*, San Diego, CA, U.S.A., Feb. 2008, paper OTuM5.
- [443] C. R. S. Fludger, T. Duthel, T. Wuth, and C. Schulien, "Uncompensated Transmission of 86Gbit/s Polarization Multiplexed RZ-QPSK over 100km of NDSF Employing Coherent Equalisation," in *Proc. Eur. Conf. Optical Commun. (ECOC)*, Cannes, France, Sep. 2006, post-deadline paper Th4.3.3.
- [444] E. Ip and J. M. Kahn, "Digital Equalization of Chromatic Dispersion and Polarization Mode Dispersion," *J. Lightwave Technol.*, vol. 25, no. 8, pp. 2033–2043, Aug. 2007.
- [445] N. S. Bergano, F. W. Kerfoot, and C. R. Davidsion, "Margin measurements in optical amplifier system," *IEEE Photon. Technol. Lett.*, vol. 5, no. 3, pp. 304 – 306, Mar. 1993.
- [446] G. Bosco and P. Poggiolini, "On the Q factor inaccuracy in the performance analysis of optical direct-detection DPSK systems," *IEEE Photon. Technol. Lett.*, vol. 16, no. 2, pp. 665 – 667, Feb. 2004.
- [447] J. Pietzsch, "Scattering Matrix Analysis of 3x3 Fiber Couplers," *J. Lightwave Technol.*, vol. 7, no. 2, pp. 303–307, Feb. 1989.
- [448] R. G. Priest, "Analysis of Fiber Interferometer Utilizing 3 x 3 Fiber Coupler," *IEEE Trans. Microw. Theory Tech.*, vol. 30, no. 10, pp. 1589–1591, Oct. 1982.
- [449] P. J. Anslow, C. R. S. Fludger, S. Savory *et al.*, "Frequency Selective Coherent Receiver for Agile Networks," in *Proc. Eur. Conf. Optical Commun. (ECOC)*, Cannes, France, Sep. 2006, paper Mo4.2.4.



---

# List of publications

## Invited contributions

- c1. D. van den Borne, S. L. Jansen, E. Gottwald, E. D. Schmidt, G. D. Khoe, and H. de Waardt, "DQPSK Modulation for Robust Optical Transmission", in *Proc. Optical Fiber Commun. Conf. (OFC)*, San Diego, USA, Feb. 2008, paper OMQ1.
- c2. S. L. Jansen, I. Morita, T. C. W. Schenk, D. van den Borne, and H. Tanaka, "Optical OFDM - A Candidate for Future Long-Haul Optical Transmission Systems", in *Proc. Optical Fiber Commun. Conf. (OFC)*, San Diego, USA, Feb. 2008, paper OMU3.
- c3. M. S. Alfiad, D. van den Borne, A. Napoli, F. N. Hauske, A. M. J. Koonen, and H. de Waardt, "A 10.7-Gb/s DPSK Receiver with 4000-ps/nm Dispersion Tolerance Using a Shortened MZDI and 4-State MLSE", in *Proc. Optical Fiber Commun. Conf. (OFC)*, San Diego, USA, Feb. 2008, paper OWT3.
- c4. C. R. S. Fludger, T. Duthel, D. van den Borne, C. Schulien, E. D. Schmidt, T. Wuth, J. Geyer, E. de Man, G. D. Khoe, and H. de Waardt, "Coherent Equalisation and POLMUX-RZDQPSK for Robust 100GE Transmission", Accepted for invited publication in *J. Lightwave Technol.*, Jan. 2008.
- c5. S. L. Jansen, D. van den Borne, P. M. Krummrich, S. H. Spaelter, H. Suche, W. Sohler, G. D. Khoe, H. de Waardt, I. Morita, and H. Tanaka, "Overview of important results concerning the application of optical phase conjugation to increase system robustness", in *Proc. Asia-Pacific Optical Commun. Conf. (APOC)*, Wuhan, China, Nov. 2007, paper 6783-37.
- c6. D. van den Borne, T. Duthel, C. R. S. Fludger, E-D. Schmidt, T. Wuth, C. Schulien, E. Gottwald, G. D. Khoe, and H. de Waardt, "Electrical PMD Compensation in 43-Gb/s POLMUX-NRZ-DQPSK enabled by Coherent Detection and Equalization", in *Proc. Eur. Conf. Optical Commun. (ECOC)*, Berlin, Germany, Sep. 2007, paper We8.3.1.
- c7. D. van den Borne, S. L. Jansen, E. Gottwald, P.M. Krummrich, G. D. Khoe, and H. de Waardt, "1.6-b/s/Hz Spectrally Efficient Transmission Over 1,700 km of SSMF Using 40 x 85.6-Gbit/s POLMUX-RZ-DQPSK", *J. Lightwave Technol.*, Vol. 25, No 1, pp. 222-232, Jan. 2007.
- c8. S. L. Jansen, D. van den Borne, P. M. Krummrich, S. Spälter, H. Suche, W. Sohler, G. D. Khoe, and H. de Waardt, "Phase Conjugation for Increased System Robustness", in *Proc. Optical Fiber Commun. Conf. (OFC)*, Anaheim, USA, Feb. 2006, paper OtuK3.
- c9. S. L. Jansen, D. van den Borne, B. Spinnler, S. Calabrò, H. Suche, P. M. Krummrich, W. Sohler, G. D. Khoe, and H. de Waardt, "Optical Phase Conjugation for Ultra Long-haul Phase Shift Keyed Transmission", *J. Lightwave Technol.*, Vol. 24, No 1, pp. 54-64, Jan. 2006.
- c10. S. L. Jansen, D. van den Borne, P. M. Krummrich, S. Spälter, G. D. Khoe, and H. de Waardt, "Long-Haul DWDM Transmission Systems Employing Optical Phase Conjugation", *IEEE J. Sel. Topics Quantum Electron.*, Vol. 12, No. 4, pp. 505-520, Jul.-Aug. 2006.

### Journal Papers

- c11. D. van den Borne, V. Veljanovski, U. Gaubatz, C. Paquet, Y. Painchaud, E. Gottwald, G. D. Khoe, and H. de Waardt, "Bit Pattern Dependence in Optical DQPSK Modulation", *Electron. Lett.*, Vol. 43, No. 22, pp. 1223-1225, Oct. 2007.
- c12. D. van den Borne, V. Veljanovski, U. Gaubatz, C. Paquet, Y. Painchaud, E. Gottwald, G. D. Khoe, and H. de Waardt, "42.8-Gb/s RZ-DQPSK Transmission with FBG-based in-line Dispersion Compensation", *IEEE Photon. Technol. Lett.*, Vol. 19, No. 14, pp. 1069-1071, Jul. 2007.
- c13. D. van den Borne, N. E. Hecker-Denschlag, G. D. Khoe, and H. de Waardt, "PMD induced transmission penalties in polarization multiplexed transmission", *J. Lightwave Technol.*, Vol. 23, No. 12, pp. 4004-4015, Dec. 2005.
- c14. S. L. Jansen, H. Chayet, E. Granot, S. Ben Ezra, D. van den Borne, P. M. Krummrich, D. Chen, G. D. Khoe, and H. de Waardt, "Wavelength conversion of a 40Gbit/s NRZ signal across the entire C band by an asymmetric Sagnac loop", *IEEE Photon. Technol. Lett.*, Vol. 17, No. 10, pp. 2137-2139, Oct. 2005.
- c15. S. L. Jansen, D. van den Borne, C. Climent, S. Spälter, P. M. Krummrich, G. D. Khoe, and H. de Waardt, "Reduction of Gordon-Mollenauer phase noise by mid-link spectral inversion", *IEEE Photon. Technol. Lett.*, Vol. 17, No. 4, pp. 923-925, Apr. 2005.
- c16. D. van den Borne, S. L. Jansen, N. E. Hecker-Denschlag, G. D. Khoe, and H. de Waardt, "Reduction of Nonlinear Penalties Through Polarization Interleaving in 2x10 Gb/s Polarization-Multiplexed Transmission", *IEEE Photon. Technol. Lett.*, Vol. 17, No. 6, pp. 1337-1339, Jun. 2005.
- c17. D. van den Borne, S. L. Jansen, G. D. Khoe, H. de Waardt, S. Calabrò, P. M. Krummrich, W. Schairer, and C.-J. Weiske, "Inter-channel nonlinear transmission penalties in polarization-multiplexed 2x10Gbit/s DPSK transmission", *Opt. Lett.*, Vol. 30, No. 12, pp. 1443-1445, Jun. 2005.
- c18. D. van den Borne, N. E. Hecker-Denschlag, G. D. Khoe, and H. de Waardt, "PMD and nonlinearity induced penalties on polarization multiplexed transmission", *IEEE Photon. Technol. Lett.*, Vol. 16, No. 9, pp. 2174-2176, Sep. 2004.

### International Peer-reviewed Conferences

- c19. M. S. Alfiad, D. van den Borne, F. Hauske, A. Napoli, B. Lankl, T. Koonen, and H. de Waardt, "Dispersion Tolerant 21.4-Gb/s DQPSK Using Simplified Gaussian Joint-Symbol MLSE", in *Proc. Optical Fiber Commun. Conf. (OFC)*, San Diego, USA, Feb. 2008, paper OThO3.
- c20. F. N. Hauske, J. C. Geyer, M. Kuschnerov, K. Piyawanno, T. Duthel, C. R. S. Fludger, D. van den Borne, E.-D. Schmidt, B. Spinnler, H. de Waardt, and B. Lankl, "Optical Performance Monitoring from FIR Filter Coefficients in Coherent Receivers", in *Proc. Optical Fiber Commun. Conf. (OFC)*, San Diego, USA, Feb. 2008, paper OThW2.
- c21. D. van den Borne, C. R. S. Fludger, T. Duthel, T. Wuth, E.-D. Schmidt, C. Schulien, E. Gottwald, G. D. Khoe, and H. de Waardt, "Carrier phase estimation for coherent equalization of 43-Gb/s POLMUX-NRZ-DQPSK transmission with 10.7 Gb/s NRZ neighbors", in *Proc. Eur. Conf. Optical Commun. (ECOC)*, Berlin, Germany, Sep. 2007, paper We8.3.1.
- c22. T. Duthel, C. R. S. Fludger, D. van den Borne, C. Schulien, E.-D. Schmidt, T. Wuth, E. Gottwald, G. D. Khoe, and H. de Waardt, "Impairment tolerance of 111Gbit/s POLMUX-RZ-DQPSK using a reduced complexity coherent receiver with a T-spaced equaliser", in *Proc. Eur. Conf. Optical Commun. (ECOC)*, Berlin, Germany, Sep. 2007, paper Mo1.3.2.

- 
- c23. M. S. Alfiad, D. van den Borne, F. N. Hauske, A. Napoli, A. M. J. Koonen, and H. de Waardt, "Robust Detection of 10.7-Gb/s DPSK Using Joint Decision Maximum Likelihood Sequence Estimation", in *Proc. Eur. Conf. Optical Commun. (ECOC)*, Berlin, Germany, Sep. 2007, paper Th9.1.2.
- c24. D. van den Borne, E. Gottwald, G. D. Khoe, and H. de Waardt, "Pseudo-Random Sequences for Modeling of Quaternary Modulation Formats", in *Proc. Optoelectronics Commun. Conf. (OECC)*, Jul. 2007, paper 13P-10.
- c25. D. van den Borne, T. Duthel, C. R. S. Fludger, E-D. Schmidt, T. Wuth, C. Schulien, E. Gottwald, G. D. Khoe, and H. de Waardt, "Coherent Equalization versus Direct Detection for 111 Gb/s Ethernet Transport", in *Proc. LEOS Summer Topicals*, Jul. 2007, paper MA2.4.
- c26. C. R. S. Fludger, T. Duthel, D. van den Borne, C. Schulien, E-D. Schmidt, T. Wuth, E. de Man, G. D. Khoe, and H. de Waardt, "10 x 111 Gbit/s, 50 GHz spaced, POLMUX-RZ-DQPSK transmission over 2375 km employing coherent equalization", in *Proc. Optical Fiber Commun. Conf. (OFC)*, Anaheim, USA, Mar. 2007, Post-Deadline paper PDP22.
- c27. D. van den Borne, V. Veljanovski, E. de Man, U. Gaubatz, C. Zuccaro, C. Paquet, Y. Painchaud, S. L. Jansen, E. Gottwald, G. D. Khoe, and H. de Waardt, "Cost-effective 10.7 Gbit/s Long-Haul Transmission using Fiber Bragg Gratings for In-line Dispersion Compensation", in *Proc. Optical Fiber Commun. Conf. (OFC)*, Anaheim, USA, Mar. 2007, paper OThS5.
- c28. S. L. Jansen, R. H. Derksen, C. Schubert, X. Zhou, M. Birk, C. J. Weiske, M. Bohn, D. van den Borne, P. M. Krummrich, M. Möller, F. Horst, B. J. Offrein, H. de Waardt, G. D. Khoe, and A. Kirstädter, "107-Gb/s full-ETDM transmission over field installed fiber using vestigial sideband modulation", in *Proc. Optical Fiber Commun. Conf. (OFC)*, Anaheim, USA, Mar. 2007, paper OWE3.
- c29. S. L. Jansen, I. Morita, D. van den Borne, G. D. Khoe, H. de Waardt, and P. M. Krummrich, "Experimental study of XPM in 10-Gbit/s NRZ pre-compensated transmission systems", in *Proc. Optical Fiber Commun. Conf. (OFC)*, Anaheim, USA, Mar. 2007, paper OThS6.
- c30. S. C. J. Lee, F. Breyer, S. Randel, B. Spinnler, I. L. Lobato Polo, D. van den Borne, J. Zeng, E. de Man, H. P. A. van den Boom, and A. M. J. Koonen, "10.7 Gbit/s Transmission over 220 m Polymer Optical Fiber using Maximum Likelihood Sequence Estimation", in *Proc. Optical Fiber Commun. Conf. (OFC)*, Anaheim, USA, Mar. 2007, paper OMR2.
- c31. V. Veljanovski, D. van den Borne, W. Schairer, and N. Hanik, "Equalisation of Fibre Bragg Gratings' Group Delay Ripple by means of Maximum Likelihood Sequence Estimation", in *Proc. IEEE/LEOS Annual Meeting*, Montreal, Quebec, Canada, Nov. 2006, paper ThH4.
- c32. D. van den Borne, S. L. Jansen, E. Gottwald, G. D. Khoe, and H. de Waardt, "Lumped Dispersion Management in Long-Haul 42.8-Gbit/s RZ-DQPSK Transmission", in *Proc. Eur. Conf. Optical Commun. (ECOC)*, Cannes, France, Sep. 2006, paper Mo3.2.2.
- c33. S. L. Jansen, D. van den Borne, P. M. Krummrich, H. Suche, W. Sohler, G. D. Khoe, and H. de Waardt, "Transmission of 42.8-Gbit/s RZ-DQPSK over 42x94.5-km SSMF Spans using Optical Phase Conjugation and EDFA only Amplification", in *Proc. Eur. Conf. Optical Commun. (ECOC)*, Cannes, France, Sep. 2006, paper Mo3.2.3.
- c34. I. L. Lobato Polo, D. van den Borne, E. Gottwald, H. de Waardt, and E. Brinkmeyer, "Comparison of Maximum Likelihood Sequence Estimation equalizer performance with OOK and DPSK at 10.7 Gb/s", in *Proc. Eur. Conf. Optical Commun. (ECOC)*, Cannes, France, Sep. 2006, paper We2.5.3.
- c35. D. van den Borne, S. L. Jansen, E. Gottwald, G. D. Khoe, and H. de Waardt, "Optical Filtering tolerances of 42.8-Gbit/s RZ-DQPSK Modulation", in *Proc. Optoelectronics Commun. Conf. (OECC)*, Kaohsiung, Taiwan, Jul. 2006, paper 5F3-5.
- c36. D. van den Borne, S. L. Jansen, E. Gottwald, P. M. Krummrich, G. D. Khoe, and H. de Waardt, "1.6-b/s/Hz Spectrally Efficient 40 x 85.6-Gb/s Transmission Over 1,700 km of SSMF Using POLMUX-RZ-DQPSK", in *Proc. Optical Fiber Commun. Conf. (OFC)*, Anaheim, USA, Feb. 2006, Post-Deadline paper PDP34.
-

## Appendix C. List of publications

---

- c37. D. van den Borne, S. L. Jansen, E. Gottwald, G. D. Khoe, and H. de Waardt, "A Comparison between Multi-level Modulation Formats: 21-4Gbit/s RZ-DQPSK and POLMUX-RZ-DPSK", in *Proc. Optical Fiber Commun. Conf. (OFC)*, Anaheim, USA, Feb. 2006, paper OThR2.
- c38. D. van den Borne, S. L. Jansen, E. Gottwald, G. D. Khoe, and H. de Waardt, "Line Optimization in Long-Haul Transmission Systems with 42.8-Gbit/s RZ-DQPSK modulation", in *Proc. Optical Fiber Commun. Conf. (OFC)*, Anaheim, USA, Feb. 2006, paper OFD2.
- c39. D. van den Borne, S. Calabrò, S. L. Jansen, E. Gottwald, G. D. Khoe, and H. de Waardt, "Differential Quadrature Phase Shift Keying with close to Homodyne Performance based on Multi-Symbol Phase Estimation", in *Proc. IEE seminar on electrical signal processing in optical communications*, London, United Kingdom, Dec. 2006, paper 12.
- c40. S. L. Jansen, D. van den Borne, A. Schöpflin, E. Gottwald, P. M. Krummrich, G. D. Khoe, and H. de Waardt, "26x42.8-Gbit/s DQPSK Transmission with 0.8-bit/s/Hz Spectral Efficiency over 4,500-km SSMF using Optical Phase Conjugation", in *Proc. Eur. Conf. Optical Commun. (ECOC)*, Glasgow, United Kingdom, Sep. 2005, Post-Deadline paper Th4.1.5.
- c41. S. L. Jansen, D. van den Borne, P. M. Krummrich, G. D. Khoe, and H. de Waardt, "Experimental Comparison of Optical Phase Conjugation and DCF Aided DWDM 2x10.7Gbit/s DQPSK Transmission", in *Proc. Eur. Conf. Optical Commun. (ECOC)*, Glasgow, United Kingdom, Sep. 2005, paper Th2.2.3.
- c42. M. Serbay, C. Wree, A. Schöpflin, C.-J. Weiske, D. van den Borne, S. L. Jansen, G. D. Khoe, P. M. Krummrich, P. Leisching, and W. Rosenkranz, "Coding Gain of FEC encoded 21.42Gb/s RZ-D(Q)PSK Using an Electrical Differential Quaternary Precoder", in *Proc. Eur. Conf. Optical Commun. (ECOC)*, Glasgow, United Kingdom, Sep. 2005, paper We4.P.10.
- c43. S. Calabrò, D. van den Borne, S. L. Jansen, G. D. Khoe, and H. de Waardt, "Improved detection of differential phase shift keyed transmission through multi-symbol phase estimation", in *Proc. Eur. Conf. Optical Commun. (ECOC)*, Glasgow, United Kingdom, Sep. 2005, paper We4.P.118.
- c44. S. L. Jansen, D. van den Borne, P. M. Krummrich, G. D. Khoe, and H. de Waardt, "Nonlinear phase noise degradation in ultra-long haul 2x10Gbit/s DQPSK transmission", in *Proc. Optoelectronics Commun. Conf. (OECC)*, Seoul, South Korea, Jul. 2005, Post-Deadline paper PDP04.
- c45. S. L. Jansen, S. Calabrò, B. Spinnler, D. van den Borne, P. M. Krummrich, G. D. Khoe, and H. de Waardt, "Nonlinear Phase Noise Reduction in DPSK Transmission by Optical Phase Conjugation", in *Proc. Optoelectronics Commun. Conf. (OECC)*, Seoul, South Korea, Jul. 2005, paper 6B1-3.
- c46. S. L. Jansen, D. van den Borne, C. Climent, M. Serbay, C.-J. Weiske, H. Suche, P. M. Krummrich, S. Spälter, S. Calabró, N. E. Hecker-Denschlag, P. Leisching, W. Rosenkranz, W. Sohler, G. D. Khoe, T. Koonen, and H. de Waardt, "10,200km 22x2x10Gbit/s RZ-DQPSK Dense WDM Transmission without Inline Dispersion Compensation through Optical Phase Conjugation", in *Proc. Optical Fiber Commun. Conf. (OFC)*, Anaheim, USA, Feb. 2005, Post-Deadline paper PDP28.
- c47. S. L. Jansen, D. van den Borne, C. Climent, S. Spälter, P. M. Krummrich, G. D. Khoe, and H. de Waardt, "Reduction of nonlinear phase noise by mid-link spectral inversion in a DPSK based transmission system", in *Proc. Optical Fiber Commun. Conf. (OFC)*, Anaheim, USA, Feb. 2005, paper OThO5.
- c48. D. van den Borne, S. L. Jansen, G. D. Khoe, H. de Waardt, S. Calabró, and N. E. Hecker-Denschlag, "Polarization interleaving to reduce inter-channel nonlinear penalties in polarization multiplexed transmission", in *Proc. Optical Fiber Commun. Conf. (OFC)*, Anaheim, USA, Feb. 2005, paper JWA41.
- c49. D. van den Borne, N. E. Hecker-Denschlag, G. D. Khoe, and H. de Waardt, "Cross phase modulation induced depolarization penalties in 2x10Gbit/s polarization-multiplexed transmission", in *Proc. Eur. Conf. Optical Commun. (ECOC)*, Stockholm, Sweden, Sep. 2004, paper Mo4.5.5.
- c50. B. Spinnler, N. Hecker-Denschlag, S. Calabro, M. Herz, C.J. Weiske, E. D. Schmidt, D. van den Borne, G. D. Khoe, and H. de Waardt, R. Griffen, S. Wadsworth, "Nonlinear Tolerance of differential phase shift keying modulated signals reduced by XPM", in *Proc. Optical Fiber Commun. Conf. (OFC)*, Anaheim, USA, Feb. 2004, paper TuF3.

---

## Local Conferences

- c51. D. van den Borne, V. Veljanovski, E. Gottwald, G. D. Khoe, and H. de Waardt, "Fiber Bragg Gratings for In line Dispersion Compensation in Cost effective 10.7 Gbit/s Long-Haul Transmission", in *Proc. IEEE/LEOS BENELUX Annual Symposium*, Eindhoven, pp. 17-20, Dec. 2006.
- c52. S. C. J. Lee, F. Breyer, S. Randel, B. Spinnler, I. L. Lobato Polo, D. van den Borne, J. Zeng, E. de Man, H. P. A. van den Boom, and A. M. J. Koonen, "Performance of Maximum Likelihood Sequence Estimation in 10 Gb/s Transmission Systems with Polymer Optical Fiber", In *Proc. IEEE/LEOS BENELUX Annual Symposium*, Eindhoven, pp. 177-180, Dec. 2006.
- c53. D. van den Borne, S. L. Jansen, E. Gottwald, P. M. Krummrich, P. Leisching, G. D. Khoe, and H. de Waardt, "A robust modulation format for 42.8-Gbit/s long-haul transmission: RZ-DPSK or RZ-DQPSK?", in *ITG Fachbericht 193, 7th ITG-fachtagung on Photonic Networks*, pp. 113-120, Leipzig, Germany, Apr. 2006.
- c54. S. L. Jansen, D. van den Borne, P. M. Krummrich, G. D. Khoe, and H. de Waardt, "Compensation of nonlinear phase noise impairments through optical phase conjugation in long-haul transmission systems", In *Proc. IEEE/LEOS BENELUX Annual Symposium*, pp. 129-132, Mons, Belgium, Dec. 2005.
- c55. D. van den Borne, S. L. Jansen, E. Gottwald, G. D. Khoe, and H. de Waardt, "Inter-channel Depolarization Impairments in 21.4-Gbit/s POLMUX OOK and DPSK Transmission", In *Proc. IEEE/LEOS BENELUX Annual Symposium*, pp. 133-136, Mons, Belgium, Dec. 2005.



---

## Samenvatting

Sinds de introductie van de eerste glasvezelcommunicatiesystemen is de transmissiecapaciteit voortdurend toegenomen en zijn de kosten per verzonden bit continue verlaagd. De kern van het wereldwijde telecommunicatienetwerk bestaat tegenwoordig uit golflengte gestapelde (wavelength division multiplexed, WDM) optische langeafstandstransmissiesystemen. WDM is een aantrekkelijke technologie omdat het een hoge spectrale efficiëntie mogelijk maakt, i.e. de efficiëntie waarmee de beschikbare bandbreedte van een fiber wordt benut. Commerciële WDM transmissiesystemen gebruiken tegenwoordig maximaal 80 kanalen met een 50-GHz kanaalafstand en 10-Gb/s of soms 40-Gb/s per golflengte kanaal. Dit vertaalt zich in een spectrale efficiëntie van 0.2 tot 0.8-b/s/Hz. Echter, op basis van de voorspelde toename van het dataverkeer zal het binnen niet al te lange tijd nodig zijn om een volgende generatie van transmissiesystemen te ontwikkelen. Deze systemen zullen naar verwachting 40 Gb/s of 100 Gb/s per kanaal transporteren met een spectrale efficiëntie tussen 0.8 tot 2.0-b/s/Hz. Daarnaast is het een vereiste dat de tolerantie ten opzichte van signaalverstoringen vergelijkbaar is met de huidige generatie van transmissiesystemen.

Van oudsher maken optische transmissiesystemen gebruik van intensiteit gemoduleerde signalen. Voor de volgende generatie van transmissiesystemen is intensiteitsmodulatie echter ongeschikt. Het vereist doorgaans een te grote kanaalafstand, heeft een hoge signaal-ruis verhouding (optical signal-to-noise ratio, OSNR) nodig en genereert sterke niet-lineaire verstoringen op de transmissielijn. De transmissiesystemen die momenteel worden ontwikkeld, maken daarom meestal gebruik van differentiële fasemodulatie (differential phase-shift keying, DPSK). Vergeleken met intensiteitsmodulatie, genereert DPSK minder niet-lineaire verstoringen en voldoet een lagere OSNR in de ontvanger. Maar door de hoge symboolsnelheid (e.g. 40 Gbaud) is de robuustheid ten opzichte van de belangrijkste lineaire verstoringen, namelijk chromatische dispersie en polarisatiemodus dispersie (polarization mode dispersion, PMD), nog steeds beperkt.

Het eerste gedeelte van deze dissertatie behandelt modulatieformaten die het mogelijk maken om de capaciteit en transmissieafstand van optische transmissiesystemen verder te verbeteren. Zo kunnen niet-binaire modulatieformaten met meer dan twee signaalniveaus worden gebruikt. Deze formaten zijn dispersie bestendig en gaan daarnaast zuinig om met optische bandbreedte (en maken daardoor een hogere spectrale efficiëntie mogelijk). In het bijzonder 40-Gb/s differentiële kwadratuur fasemodulatie (differential quadrature phase shift keying, DQPSK) wordt uitgebreid besproken in deze dissertatie. 40-Gb/s DQPSK moduleert 2 bits per symbool en ben-

odigd daardoor slechts een symboolsnelheid van 20-Gbaud. Niet-binaire modulatie heeft echter zowel voor- als nadelen. Het verbetert de tolerantie ten opzichte van chromatische dispersie en PMD, maar resulteert ook in een meer complexe zender en ontvanger structuur, een verhoging van de benodigde OSNR en een lagere tolerantie ten opzichte van niet-lineaire verstoringen. We bespreken de mogelijkheid om langeafstandstransmissie te realiseren met 40-Gb/s DQPSK modulatie en laten zien dat een maximale afstand van 2,800-km kan worden overbrugd met 0.8-b/s/Hz spectrale efficiëntie. Gecombineerd met optische fase omkering (optical phase conjugation) kan dit verder worden verbeterd en is het mogelijk om een transmissieafstand van 4,500-km te overbruggen. We beschrijven daarnaast de combinatie van 40-Gb/s DQPSK modulatie met verschillende dispersie compensatie technieken, zoals de concentratie van dispersie compensatie op slechte enkele punten langs de transmissielijn en dispersie compenserende fiber-Bragg gratings.

In het tweede deel van deze dissertatie komen polarisatie gestapelde (POLMUX) signalen aan de orde. Deze techniek moduleert de beide orthogonale polarisaties in een fiber onafhankelijk van elkaar. Hierdoor kan de spectrale efficiëntie worden verdubbeld en de symboolsnelheid worden gehalveerd in vergelijking tot niet-polarisatie gestapelde signalen. Om de spectrale efficiëntie verder te verhogen, kan POLMUX signalering worden gecombineerd met DQPSK, waardoor modulatie met 4 bits per symbool wordt gerealiseerd. We bespreken een transmissie experiment met 80-Gb/s POLMUX-RZ-DQPSK over een transmissie afstand van 1,700 km en een spectrale efficiëntie van 1.6-b/s/Hz. Echter, de wisselwerking tussen PMD en andere signaalverstoringen maakt het problematisch om deze techniek toe te passen zonder de compensatie van PMD.

In het derde deel van deze dissertatie behandelen we elektrische compensatie methoden. Deze kunnen worden ingezet om de nadelige eigenschappen van DQPSK modulatie en POLMUX signalen te verminderen. Voor incoherente ontvangers kan multi-symbol phase estimation (MSPE) worden gebruikt om zowel de OSNR als de niet-lineaire tolerantie van D(Q)PSK modulatie te verbeteren. Daarnaast kan Maximum likelihood sequence estimation (MLSE) worden gebruikt om de chromatische dispersie en PMD tolerantie te verhogen. Elektrische compensatie is echter bijzonder effectief wanneer het wordt gecombineerd met een coherente ontvanger. In een coherente ontvanger wordt niet alleen de amplitude, maar het volledige optische basisband veld (amplitude, fase en polarisatie) overgezet naar het elektrische domein. Daardoor kunnen bijna onbeperkt hoge chromatische dispersie en PMD waardes worden gecompenseerd en tegelijkertijd kan een polarisatie gestapeld signaal worden opgesplitst in de beide polarisatiecomponenten. We bespreken de benodigde systeemarchitectuur voor een digitale coherente ontvanger en behandelen daarnaast een 100-Gb/s POLMUX-DQPSK transmissie experiment over 2,375 km met 2.0-b/s/Hz spectrale efficiëntie.

Op basis van de resultaten in dit proefschrift kunnen we concluderen dat met behulp van niet-binaire modulatieformaten het mogelijk is om langeafstandstransmissie te realiseren met zowel 40-Gb/s als 100-Gb/s per golflengte kanaal en een 50-GHz kanaalafstand. Elektronische compensatie versimpelt daarnaast het systeemontwerp en maakt deze modulatieformaten robuust tegen signaalverstoringen.



---

# Acknowledgement

*"A dwarf standing on the shoulders of a giant may see farther than the giant himself." (Didacus Stella)*

The end of a Ph.D. project is a very suitable moment in time to look back and reflect on the years past. Doing so, I can wholeheartedly conclude that the past three and a half years have been an exciting time, both professionally as well as in private life. This would not have been possible without the support of many, to whom I would like to express my sincere gratitude here.

I am very grateful to Prof. Djan Khoe for his support during these years. He offered me a chance to pursue research in fiber-optic transmission by arranging for me to go to Munich for my graduation project. His continuing support throughout my Ph.D. project as well as his flexibility in the cooperation with Nokia Siemens Networks (previously Siemens Communications) have been of great value to me. I also would like to thank Dr. Nancy Hecker-Denschlag, for supervising my graduation project within Siemens and, later on, for offering me the possibility to pursue my Ph.D. there. In a time when engineering positions were hard to come by this provided me with the best possible choice I could have made. I am also greatly indebted to Dr. Huug de Waardt for being my supervisor during all these years. Despite the challenge posed by the distance between Eindhoven and Munich, he was always only a phone call away when I need advice or a trusted opinion. It is an interesting observation, that together we discussed all aspects of a Ph.D. on fiber-optic transmission systems while using exactly such systems. As well, I would like to thank Dr. Stefano Calabrò and Dr. Erich Gottwald, for supervising my Ph.D. project within Nokia Siemens Networks and for all the stimulating technical discussions we had over the years.

I would further like to express my thanks to Prof. Palle Jeppesen, Prof. Peter Krummrich, Prof. Ton Koonen, Dr. Robert Killey and Dr. Jos van der Tol for the time they invested in reading this thesis and providing me with feedback. I am as well indebted to Dr. Antonio Napoli, Vladimir Veljanovski and Mohammad Alfiad for reading parts of this thesis and helping me to improve this work through their comments.

The most intensive and rewarding cooperation during my Ph.D. has without doubt been with Dr. Sander Jansen. The research project we pursued together have redefined my definition of teamwork. His "let's get this working" mentality was instrumental in building up the highly complicated transmission experiments of which some are described in this thesis. As well, I will fondly remember the many parties, in all corners of the world, that we celebrated together during these years.

I also received support from many other co-workers and students within Nokia Siemens Networks throughout the Ph.D. project. In particular, I would like to thank Claus-Jörg Weiske,

## Appendix C. Acknowledgement

---

Andreas Schöpflin and Erik de Man. Without their help on all things electrical, it would not have been possible to build up many of the optical transmission experiments covered in this thesis. I also very much enjoyed working together with Ernst-Dieter Schmidt, and I'm grateful for the effort he put into organizing the various cooperations. As well, although he never convinced me of his theory on group velocity dispersion, I'm grateful to Dr. Ulrich Gaubatz for the helpful advice he has given over the years. I further would like to thank Vladimir Veljanovski for his everlasting good mood and our after-work parties in 'Dilingers'. Dr. Sebastian Randel is gratefully acknowledged for his work on the DPSK receiver software and our many technical discussions. Furthermore, I want to express my thanks to, without the intention to forget someone, Dr. Gottfried Lehmann, Dr. Lutz Rapp, Dr. Bernhard Spinnler, Dr. Patrick Leisching, Dr. Uwe Feiste, Dr. Torsten Wuth, Dr. Hans-Joerg Thiele, Dr. Arne Striegler, Dr. Cornelius Cremer, Dr. Achim Autenrieth, David Stahl, Wolfgang Schairer, Dr. Alessandro Bianciotto, Dr. Dario Setti, Dr. Juraj Slovak, Christian Sanabria von Walter, Christian Palm and Carlos Climent. Finally, I would like to thank Dr. Stefan Spälter for the effort he put into keeping me at Nokia Siemens Networks after finishing my Ph.D.

From Eindhoven University of Technology I would further like to thank, without the intention to forget someone, Jeffrey Lee, Bas Huiszoon, Johan van Zantvoort, Maria García Larrodé, Prof. Harm Dorren, Dr. Eduard Tangdiongga and Dr. Nicola Calabretta. As well, I am indebted to the secretaries of the department, Susan de Leeuw, Els Gerittsen and José Hakkens for their great help with the administrative work. A word of encouragement and thanks here also to Mohammad Alfiad, for his excellent master thesis work, which covers most of the results in Section 9.2. I hope that your Ph.D. project at Nokia Siemens Networks will be as successful as your master thesis.

During my Ph.D. project, I have been in the privileged position to cooperate with many people from other universities and companies. I particularly would like to thank Murat Serbay from the University of Kiel for his work during our first long-haul RZ-DQPSK transmission experiment, Fabian Hauske of the Federal Armed Forces University Munich for his work on MLSE receivers, Maxim Kuschnerov of the Federal Armed Forces University Munich for our fruitful discussions on signal processing algorithms, Dr. Chris Fludger, Dr. Thomas Duthel and Dr. Christoph Schulien of CoreOptics for our cooperation on the transmission experiments with a digital coherent receiver, Carl Paquet and Yves Painchaud of Teraxion for supplying me with FBG samples to measure the impact of phase ripple on DQPSK modulation, Dr. Bernt Satorius and Carsten Bornholdt from the Heinrich-Hertz Institute for our cooperation on DPSK regeneration and the Enterprise Services group from T-Systems for their support during our DQPSK field-trail.

I am very grateful to my parents Walter and Antoinette, my sister Marieke, her husband Dolf and my brother Gijs for supporting me throughout these years. As well, the many trips to Düsseldorf airport when I was coming from or going to Munich are very much appreciated. I also would like to thank my mother for correcting the Dutch summary in this thesis.

And finally, I would like to thank Iveth for her support, encouragement, patience, as well as for reading and correcting large parts of this thesis. But most of all I would like to thank her, to finish with the words of Moliere, because to live without loving is not really to live.

---

## Curriculum Vitae

Dirk van den Borne was born in Bladel, The Netherlands, on October 7, 1979. After completing the VWO (secondary school) at the PIUS-X college in Bladel in 1998, he started studying electrical engineering at the Eindhoven University of Technology. In 2002-2003 he spend 4 months, as part of the M.Sc. programm, at the Fujitsu laboratories Ltd. in Kawasaki, Japan, working on super-continuum generation and pulse compression. Later on, he performed his Master's thesis work at Siemens AG in Munich, Germany, working on polarization-mode dispersion related impairments in polarization-multiplexed transmission. He received his M.Sc. degree, cum laude, in 2004.

In June 2004, he started working towards the Ph.D. degree in electrical engineering at the Eindhoven University of Technology. The research was carried out in the long-haul optical transmission R&D department of Nokia Siemens Networks (previously Siemens AG) in Munich, Germany. His Ph.D. work focused on improvements in long-haul optical transmission systems using robust modulation formats, alternative dispersion compensation schemes and electronic impairment mitigation.

During his Ph.D. studies, he has authored and co-authored more than 50 peer-reviewed journal papers and conference contributions, of which 10 were invited contributions. In addition, he wrote 5 patents related to fiber-optic communications. In 2007 he received the telecommunication award from the Royal Institution of Engineers in the Netherlands (KIVI-NIRIA) and the IEEE Laser & Electro-Optics Society (LEOS) graduate student fellowship.

Since March 2008, Dirk is with Nokia Siemens Networks in Munich, Germany.



---

# Index

- AGC, 39
- AMI, 77
- amplification
  - EDFA, 41
  - hybrid EDFA/Raman, 44
  - Raman, 44
- analog-to-digital converters, 7, 209, 234
- ASE, 43
- C-band, 14
- coherent receivers, 203
  - analog, 204
  - digital, 207
  - heterodyne, 205
  - homodyne, 205
  - intra-dyne, 206
  - polarization diversity, 207
- CRZ, 69
- CSRZ, 38, 69
- CWDM, 14
- cycle slips, 218
- DCF, 49
  - attenuation, 49
  - index profile, 49
  - system penalty, 49
- differential group delay, 19
- digital coherent receiver, 207
  - baud-rate equalizers, 234
  - chromatic dispersion, 223, 227
  - DGD, 220, 227
  - long-haul transmission, 228
  - OSNR requirement, 219, 225
  - polarization dependent loss, 221
- digital signal processing, 7, 210
  - baud-rate, 234
  - carrier recovery, 216
  - clock recovery, 211
  - CMA, 212
  - coherent, 207
  - differential decoding, 218
  - direct detection, 173
  - equalization, 212
  - FFT, 215
  - LMS, 214
  - MLSE, 184
  - MSPE, 175
  - performance monitoring, 215
  - polarization de-multiplexing, 212
- dispersion compensation, 48
  - DCF, 49
  - FBG, 55, 113
  - in-line, 48
  - OPC, 62, 121
  - tunable, 51
- dispersion maps, 25, 51
  - accumulated dispersion, 50
  - inline under-compensation, 52
  - lumped, 54, 111
  - optimization of, 106, 109
  - post-compensation, 52
  - pre-compensation, 52
- dispersion slope, 15
- DPSK, 74
  - balanced detection, 77
  - chromatic dispersion, 82
  - demodulation, 76
  - DGD, 82
  - OSNR requirement, 79
  - partial, 83
  - single-ended detection, 77

- DQPSK, 87
  - chromatic dispersion, 97
  - demodulation, 89
  - DGD, 97
  - long-haul transmission, 106
  - narrowband filtering, 94
  - nonlinear tolerance, 99
  - OSNR requirement, 92
  - precoder, 89
  - PRQS, 101
- DSF, 16
- duobinary, 69, 76
  - chromatic dispersion, 73
  - DGD, 73
  - electrical, 71
  - optical, 72
  - OSNR requirement, 71
  - polybinary, 73
  - PSBT, 69
- EDFA, 41
  - amplifier structure, 43
  - ASE, 47
  - noise figure, 47
  - stimulated emission, 42
- FBG, 55
  - cascading of, 117
  - DQPSK, 113
  - GDR, 56
  - phase ripple, 57
  - tunable, 57
  - wavelength de-tuning, 116
- FEC, 40
- group velocity, 15
- group velocity dispersion, 15
- Kerr effect, 23
- L-band, 14, 30
- laser linewidth, 180
- long-haul transmission, 1
- Mach-Zehnder modulator, 36
- meshed networks, 5, 58
- MLSE, 184
  - DPSK, 189
  - Gaussian model method, 187
  - histogram method, 186
  - joint-symbol, 191, 197
  - OOK, 188
  - partial DPSK, 194
  - trellis decoding, 186
- modulation, 36
  - direct, 36
  - DPSK, 75
  - DQPSK, 88
  - duobinary, 70
  - electro-absorption, 36
  - Mach-Zehnder, 36
  - OOK, 67
  - POLMUX, 134
  - POLMUX-DQPSK, 158
- MSPE, 175
  - laser linewidth, 180
  - nonlinear phase noise, 182
  - OSNR requirement, 178
  - principle of, 176
- multi-level modulation, 87
- MZDI, 76
  - amplitude imbalance, 81
  - colorless, 77
  - constructive port, 76
  - destructive port, 76
  - differential delay, 83, 93
  - phase offset, 82, 93
  - polarization dependence, 77, 138
- NLSE, 23
- nonlinear impairments, 22
  - FWM, 29
  - IFWM, 30
  - IXPM, 30
  - nonlinear phase noise, 31
  - SPM, 25, 145
  - SRS, 33
  - XPM, 27, 150
  - XPolM, 28, 150, 230
- nonlinear phase noise, 31
  - compensation, 63, 182

- 
- nonlinear Schrödinger equation, 23
  - NRZ-OOK, 67
  - NZDSF, 16
  
  - OADM, 5, 58
  - OOK, 67
  - optical fiber, 11
    - birefringence, 18
    - chromatic dispersion, 14
    - effective length, 25
    - insertion loss, 12
    - manufacturing, 12
    - nonlinear coefficient, 23
    - nonlinearity, 22
    - polarization, 16
  - optical phase conjugation, 59
    - conversion efficiency, 121
    - dispersion compensation, 62
    - DQPSK, 121
    - nonlinear phase noise, 63
    - polarization dependence, 61
    - PPLN, 60
  
  - partial DPSK, 83, 194
  - photodiode, 38
  - polarization
    - degree of, 18
    - dependent loss, 22, 143, 221
    - interleaving, 28
    - Jones vector, 17
    - Poincaré sphere, 18
    - principle states of, 19
    - state of, 16
    - Stokes parameters, 17
  - polarization diversity, 207
  - polarization interleaving, 164
  - polarization mode dispersion, 20
    - depolarization, 21
    - distribution, 20
    - optical compensation, 57
    - outage, 20
    - POLMUX, 138
    - second order, 21
  - polarization multiplexing, 131
  - POLMUX, 131
    - depolarization, 150
    - dispersion tolerance, 142
    - nonlinear tolerance, 145
    - OSNR requirement, 137
    - PMD tolerance, 138
    - polarization dependent loss, 143
    - polarization interleaving, 152
    - principle, 132
    - XPolM, 150
  - POLMUX-DQPSK, 157
    - coherent detection, 207
    - direct detection, 159
    - long-haul transmission, 162, 228
    - narrowband filtering, 162, 226
    - nonlinear tolerance, 166
    - OSNR requirement, 160
    - PMD, 165
  - power map, 25
  - PRQS, 101
  - pulse carving, 37
  
  - Raman amplification, 44
    - all-Raman, 45
    - amplifier structure, 46
    - backward pumping, 44
    - effective noise figure, 45
    - forward pumping, 45
    - safety, 46
  - re-circulating loop, 106
  - robustness, 4
  
  - spectral efficiency, 4, 169
  - SSMF, 12
  
  - transponder, 4
  
  - WDM, 3
  - WSS, 58
-

